Stationary in-situ measurements of aerosols, gaseous pollutants and meteorology: Chemical and physical characterization of natural and anthropogenic sources

DISSERTATION

ZUR ERLANGUNG DES GRADES

"DOKTOR DER NATURWISSENSCHAFTEN"

IM PROMOTIONSFACH CHEMIE

AM FACHBEREICH CHEMIE, PHARMAZIE UND GEOWISSENSCHAFTEN

DER JOHANNES GUTENBERG-UNIVERSITÄT MAINZ

vorgelegt von

Jovana-Maria Diesch

geboren in Riedlingen

Mainz, July 2012

Dekan:

1. Berichterstatter:

2. Berichterstatter:

Tag der mündlichen Prüfung: 24.08.2012

Dedicated To

Abstract

Natural and anthropogenic emissions of gaseous and particulate matter affect the chemical composition of the atmosphere, impact visibility, air quality, clouds and climate. Concerning climate, a comprehensive characterization of the emergence, composition and transformation of aerosol particles is relevant as their influence on the radiation budget is still rarely understood. Regarding air quality and therefore human health, the formation of atmospheric aerosol particles is of particular importance as freshly formed, small particles penetrate into the human alveolar region and can deposit. Additionally, due to the long residence times of aerosol particles in the atmosphere it is crucial to examine their chemical and physical characteristics.

This cumulative dissertation deals with stationary measurements of particles, trace gases and meteorological parameters during the DOMINO (*Diel Oxidant Mechanism In relation to Nitrogen Oxide*) campaign at the southwest coast of Spain in November/December 2008 and the ship emission campaign on the banks of the Elbe in Freiburg/Elbe in April 2011. Measurements were performed using the Mobile research Laboratory "MoLa" which is equipped with state-of-the-art aerosol particle and trace gas instruments as well as a meteorological station.

A variety of emitted pollutants which were affected by meteorological conditions contribute to the air quality on the south coast of Spain. The change of the measured parameters could be attributed to continental, urban and marine air masses which were in detail analyzed regarding their physical and chemical properties. While marine air masses are characterized by lowest average submicron particle number (1000 cm^{-3}) and mass (2 $\mu g\ m^{-3}$) concentrations, submicron particles mainly consisted of sulfuric acid. In contrast, aerosol of continental and urban origin was primarily composed of organic matter. This could be assigned to four different types of organic aerosol that are associated with various aerosol sources and components: low-volatile and semi-volatile oxygenated organic aerosol as well as hydrocarbon-like and wood-burning organic aerosol. In addition to the air mass origin, the meteorological situation affects trace gases as well as the occurrence and temporal evolution of new particle formation events which were also examined in the context of this thesis. While new particle formation was not observed in marine air masses, measured parameters show substantial differences between nucleation events observed under clean conditions and with superimposed pollution. The so-called regional events occurred over large spatial scales on the continent and are characterized by a sharp transition to a predominant mode at 10 nm particle diameter and a subsequent and persistent growth over several hours. When pollution was superimposed on regionally formed nucleation events increased formation rates and bimodal size distributions were obtained which reflect the additional influence of freshly produced small particles of industrial origin. The results show that sulfuric acid is an important new particle

formation precursor. In contrast, during particle growth mainly oxidized organic matter was identified in the mass spectral fingerprints.

The detailed analysis of the DOMINO data leads to the result that the variability of the air composition associated with the different source regions and the distance from sources affects particle loading, composition, size distribution and acidity as well as trace gas parameters. Although meteorological parameters impact particle formation and growth, the variability of the air composition was found as more important factor. Even though by means of factor analysis a separation of the organic matter was accomplished, the complete attribution to individual sources remains in the focus of future research. Details of the new particle formation mechanism are also currently in the focus of numerous scientists, as the present technology does not allow the chemical analysis of particles around 1 nm.

A further goal of this work was to characterize well identifiable anthropogenic emissions of ships which contribute to the air pollution and therefore impact local and regional air quality. Emission factors of particle number and submicron mass positively correlate with the fuel sulfur content and depend on the engine type and performance. Submicron particles were composed of organic matter (72%), sulfate (22%) and black carbon (6%). While both, the trace gases SO_2, resulting from the fuel sulfur, and NO_x, which depends on the combustion temperature, increased, O_3 significantly decreased when a ship passed the site. Particulate emissions of ships typically exhibit a bimodal size distribution with a dominant nucleation mode around 10 nm and a combustion aerosol mode at approximately 35 nm particle diameter. Since additionally to the measured parameters various ship information for each vessel were registered, the vessels could be classified according to their gross tonnage levels. While the emission factors of particle number, black carbon and PAHs decrease with increasing gross tonnage levels, emission factors of SO_2, NO_x, particulate organic and sulfate matter and the submicron particle mass increase. A further part of this thesis is the investigation of the ship emission impact on local air quality. While the influence of the vessel immissions related to total immissions strongly depends on the respective air quality parameter, container, tanker and cargo ships together covered approximately 85% of the ship-related immissions. By detailed analysis of the mass spectra typical signatures of unburned fuel and lubricating oil could be identified. While the organic aerosol fraction mainly consists of hydrocarbon-like organic aerosol, sulfuric acid, which was found to be the most abundant sulfate species, leads to a highly acidic aerosol.

The results obtained during this work reveal that emission factors of the measured parameters depend on a variety of factors e.g. the fuel sulfur content, engine type, performance and the exhaust system. The impact of ship emissions on local air quality is especially important when considering the nearby located populated regions. For this reason, the work is valuable for assessing further limitations of individual parameters and emission-control strategies to limit total emissions.

Zusammenfassung

Natürliche und anthropogene Emissionen von Gasen und Partikeln beeinflussen die chemische Zusammensetzung der Atmosphäre und wirken sich auf die Sichtverhältnisse, die Luftqualität und das Klima aus. Bezüglich des Klimas ist eine umfassende Charakterisierung der Entstehung, Zusammensetzung und Umwandlung von Aerosolpartikeln relevant da deren Einfluss auf den Strahlungsantrieb mit sehr großen Unsicherheiten verbunden ist. Besondere Bedeutung im Hinblick auf die Gesundheit spielt die Bildung von atmosphärischen Aerosolpartikeln da vor allem frisch gebildete, kleine Partikel in die Alveolen gelangen und sich absetzen können. Auch aufgrund ihrer langen Aufenthaltsdauer in der Atmosphäre ist es wichtig chemische und physikalische Aerosolpartikeleigenschaften zu untersuchen.

Diese kumulative Dissertation konzentriert sich auf die stationären Untersuchungen von Partikeln, Spurengasen und meteorologischen Parametern während der DOMINO (*Diel Oxidant Mechanism In relation to Nitrogen Oxide*) Kampagne an der südwest-atlantischen Küste von Spanien im November/Dezember 2008 sowie der Schiffsemissionsmesskampagne am Elbeufer in Freiburg im April 2011. Die Messungen wurden mit einem Mobilen Aerosolforschungs-Labor „MoLa“, das mit modernsten Aerosolpartikel- und Spurengas-Instrumenten und einer meteorologischen Station ausgestattet ist, durchgeführt.

Eine Vielzahl an emittierten Schadstoffen, welche durch meteorologische Bedingungen beeinflusst werden, wirken sich auf die Luftqualität an der Südküste Spaniens aus. Die Veränderung der gemessenen Parameter war auf die jeweiligen kontinentalen, urbanen und marinen Luftmassen zurückzuführen, welche detailliert hinsichtlich ihrer physikalischen und chemischen Eigenschaften untersucht wurden. Marine Luftmassen wiesen die kleinsten Partikelanzahl- (1000 cm^{-3}) und Massenkonzentrationen (2 $\mu g\ m^{-3}$) auf, wobei die Partikel kleiner 1 µm Durchmesser größtenteils aus Schwefelsäure bestanden. Aerosol kontinentalen und urbanen Ursprungs war stattdessen hauptsächlich aus organischer Materie zusammengesetzt. Diese konnte vier verschiedenen organischen Aerosoltypen zugeordnet werden: geringflüchtigem, semiflüchtigem, kohlenwasserstoffähnlichem organischem Aerosol und organischem Aerosol aus Holzverbrennungsprozessen. Zusätzlich zur Luftmassenherkunft wirkte sich die meteorologische Situation auf die Variabilität der Spurengase sowie das Auftreten und die zeitliche Entwicklung von Partikelneubildungsereignissen aus, welche im Rahmen dieser Dissertation untersucht wurden. Während in marinen Luftmassen keine Partikelneubildungsereignisse beobachtet wurden, zeigten gemessene Partikelneubildungsereignisse welche unter kontinentalen Bedingungen und zusätzlich von urbaner Luft überlagert wurden erhebliche Unterschiede. Die sogenannten “regionalen” Ereignisse traten großflächig über mehrere hundert Kilometer hinweg auf dem Kontinent auf und sind gekennzeichnet durch einen Größenverteilungsmode bei 10 nm. Dieser Partikeldurchmesser

wächst kontinuierlich über mehrere Stunden an. Die von urbaner Luft beeinflussten regionalen Ereignisse weisen erhöhte Partikelbildungsraten und bimodale Partikelgrößenverteilungen während der Wachstumsphase auf, welche den zusätzlichen Einfluss der frisch gebildeten Partikel städtischen Ursprungs reflektieren. Die Resultate zeigen, dass Schwefelsäure ein wichtiger Ausgangsstoff zur Partikelneubildung darstellt. Im Unterschied hierzu wurden während des Partikelwachstums mittels massenspektrometrischer Analyse hauptsächlich oxidierte organische Komponenten identifiziert.

Die detaillierte Analyse der DOMINO Daten führte zum Ergebnis, dass die Luftzusammensetzung welche mit den unterschiedlichen Quellregionen assoziiert ist und die Distanz zu den Quellen die Partikelbeladung, Zusammensetzung, Größenverteilung und Acidität sowie Spurengasparameter beeinflusst. Obwohl sich meteorologische Parameter auf die Partikelneubildung und deren Wachstum auswirken, so beeinflusste die Luftzusammensetzung die Ereignisse stärker. Auch wenn mittels Faktorenanalyse eine Separierung der organischen Materie gelang, so bleibt die vollständige Zuordnung zu einzelnen Quellen in der Umgebungsluft weiter ein aktuelles Forschungsgebiet. Auch Details der Partikelneubildungsmechanismen blieben bislang verborgen da die gegenwärtige Technologie es nicht erlaubt, Partikel von ungefähr 1 nm chemisch zu analysieren.

Ein weiteres Ziel dieser Arbeit war es, Emissionen von Schiffen welche zu hoher Luftverschmutzung beitragen und somit die lokale und regionale Luftqualität beeinflussen, zu untersuchen. Die Emissionsfaktoren der Partikelanzahl und Masse nahmen mit dem Schwefelgehalt im Treibstoff zu und hingen vom Motortyp und dessen Leistung ab. Partikel kleiner 1 μm Durchmesser bestanden aus 72% organischer Materie, 22% Sulfat und 6% Ruß. Während sowohl das Spurengas SO_2, das vom Schwefelgehalt im Treibstoff resultiert, als auch NO_x, das von der Verbrennungstemperatur abhängt, anstieg, so zeigte O_3 eine signifikante Abnahme sofern ein Schiff den Messort passierte. Die Partikelemissionen von Schiffen weisen typischerweise eine bimodale Größenverteilung mit einem Nukleationsmode bei 10 nm und einem Verbrennungsaerosolmode bei 35 nm Durchmesser auf. Da zusätzlich zu den gemessenen Parametern diverse Schiffsdaten zu jedem Schiff registriert wurden, konnten die Schiffe anhand ihrer Bruttoraumzahl klassifiziert werden. Im Gegensatz zu den Emissionsfaktoren der Anzahlkonzentration, des Rußes und der PAHs welche mit zunehmender Schiffsgröße sanken, wurde eine Zunahme der Emissionsfaktoren von SO_2, NO_x, Organik, Sulfat und der Massenkonzentration der Partikel bis zu einem 1 μm beobachtet. Ein weiterer Bestandteil der Dissertation ist die Untersuchung des Einflusses der Schiffsemissionen auf die lokale Luftqualität. Während der Einfluss der Schiffsimmissionen bezogen auf die Gesamtimmissionen stark vom jeweiligen Luftqualitätsparameter abhängt, so tragen Container, Tanker und Frachtschiffe ungefähr zu 85% zu den Gesamtschiffsimmissionen bei. Durch detaillierte Analyse der Massenspektren konnten typische Signaturen von unverbranntem Öl und Treibstoff in den Massenspektren identifiziert werden. Während der organische Anteil hauptsächlich aus kohlenwasserstoffähnlichen Fragmenten bestand, so bestand das Sulfataerosol hauptsächlich aus Schwefelsäure, was zu einer hohen Acidität des Aerosols führte.

Abschließend lässt sich sagen, dass die Emissionsfaktoren der gemessenen Parameter von einer Vielzahl von Faktoren abhängen, unter anderem dem Schwefelgehalt des Treibstoffs, dem Motortyp, der Motorleistung und dem Verbrennungssystem. Die Untersuchung der Einflüsse auf die lokale Luftqualität sind insbesondere im Hinblick auf nahegelegene bevölkerungsreiche Regionen wichtig um niedrigere Grenzwerte bezüglich einzelner Luftqualitätsparameter festzusetzen und Emissionskontrollstrategien zu entwickeln um die Gesamtimmissionen zu limitieren.

Contents

1

Introduction

Although "climate change" is frequently used in conjunction with human-specific impacts on the Earth´s atmosphere, to which degree human activities contribute is still poorly understood. While radiative forcing by long-lived greenhouse gases such as CO_2, CH_4, N_2O and O_3 is positive and leads to a global warming, anthropogenic inputs to the atmospheric aerosol (e.g. organics, sulfate, black carbon, nitrate) might even produce a cooling effect but are yet largely uncertain (Forster et al., 2007). Although climate change which refers to global changes (e.g. of temperature, precipitation, sea levels) and poor air quality where issues like ground-level ozone, particulate matter and release of other air contaminants occur in the lowest part of the atmosphere, implying in the air we breathe are different phenomena, both are affected by air pollutants from diverse sources and activities (Seinfeld and Pandis et al., 2006).

Furthermore, depending on their size and the composition particulate air pollutants are potentially hazardous to human health. Especially particles in the nanometer size range which were inhaled can enter the respiratory tract, the lung or even reach the blood cycle (Oberdorster et al., 2002; Geller et al., 2006). Since small particles are characterized by a relatively large surface area, they are of special importance as diverse gases can adsorb onto, particles coagulate and chemical reactions take part. However, due to its complexity detailed knowledge of the gas-to-particle conversion and the atmospheric reactions taking place on a molecular level are scarce as current technology does not allow studying the chemical composition of particles of sizes around 1 nm. Due to the adverse health effects in recent years several emission control strategies to limit anthropogenic pollution were introduced. These regulations were especially adopted next to populated regions to directly affect local air quality and therefore the important property, human health.

Playing important roles in terms of the mentioned effects, several aspects of air pollutants have to be taken into account. For getting an improved understanding of the emissions and their impacts on air quality and atmospheric chemistry, a detailed characterization of aerosol particles and investigation of precursor gases, the processing of particles and the change of the chemical and physical properties was investigated within the scope of this thesis. To study these topics, field campaigns were performed at the southwest coast of Spain in November/December 2008 and on the banks of the Elbe near Freiburg, Germany in April 2011. To evaluate the variety of aspects and links, on the one hand sophisticated aerosol measurement instrumentation measuring with high time resolution and low detection limits, on the other hand information of trace gases and meteorological parameters are essential. For an extended analysis, further tools like trajectory models for reproducing air mass transport processes on larger spatial scales and vessel information gathered via Automated Identification System broadcasts were used. Furthermore, measuring valuable data in atmospheric environments and sampling single anthropogenic emission sources as

well as evaluating the large amount of data is complex. Additionally, knowledge of the gas and particulate characteristics of the probed types of emission sources is important for their interpretation.

For this reason, the structure of this cumulative thesis is as following: Chapter 2 gives an overview of the methodology and a scientific background of the atmospheric aerosol. A description of the conducted field campaigns, the description of the Mobile research Laboratory "MoLa", its instrumentation and the data analysis is followed by a short scientific background of the sources, evolution and properties of the atmospheric aerosol. Chapter 3 contains all publications written throughout this work. The thesis closes with a discussion of the results, a conclusion and an outlook over possible future research activities (Chapter 4). Finally, all publications together with the information in which way being involved as a co-author are presented in the Appendix.

References

Forster, P., Ramaswamy, V., Artaxo, P., Berntsen, T., Betts, R., Fahey, D. W., Haywood, J., Lean, J., Lowe, D. C., Myhre, G., Nganga, J., Prinn, R., Raga, G., Schulz, M., and Van Dorland, R.: Changes in Atmospheric Constituents and in Radiative Forcing. In: Climate Change 2007: The Physical Science Basis. Contribution of Working Group I to the fourth Assessment Report of the Intergovernmental Panel on Climate Change. [Solomon, S., D. Qin, M. Manning, Z. Chen, M. Marquis, K.B. Averyt, M.Tignor and H.L. Miller (eds.)]. Cambridge University Press, Cambridge, United Kingdom and New York, NY, USA, 2007.

Geller, M. D., Ntziachristos, L., Mamakos, A., Samaras, Z., Schmitz, D. A., Froines, J. R., and Sioutas, C.: Physicochemical and redox characteristics of particulate matter (pm) emitted from gasoline and diesel passenger cars, Atmospheric Environment, 40(36):6988-7004, 2006.

Oberdorster, G., Sharp, Z., Atudorei, V., Elder, A., Gelein, R., Lunts, A., Kreyling, W., and Cox, C.: Extrapulmonary translocation of ultrafine carbon particles following whole-body inhalation exposure of rats, J Toxicol Env Heal A, 65, 1531-1543, 2002.

Seinfeld, J. H. and Pandis, S. N.: Atmospheric Chemistry and Physics: From air pollution to climate change, John Wiley & Sons, 2nd ed, 2006.

2

Methodology and Scientific Background

2.1 Sources, evolution and properties of the atmospheric aerosol

Before I focus on the specific sources sampled during the DOMINO and the ship emission campaign, typical chemical and physical properties of aerosols, as well as their formation and transformation processes taking part in the atmosphere are introduced.

Aerosol particles were either directly emitted into the atmosphere by natural or anthropogenic sources such as primary organic carbon, soot, sea salt or mineral dust (primary aerosol particles) or formed by gas-to-particle conversion (nucleation or condensation) of low-volatile vapors of inorganic trace gases such as NO_x, NH_3, SO_2 or organic substances (e.g. VOCs, DMS) (Seinfeld and Pandis, 2006). Freshly formed atmospheric particles were measured in the nanometer size range (Fig. 2.1). Additionally, primary aerosol particles from combustion processes were emitted in the ultrafine particle size range (d_p = 10-100 nm). Nucleation mode particles can either grow by condensation of low volatile vapors or by coagulation with pre-existing particles to accumulation mode particles (Fig. 2.1). By these processes internally mixed aerosol particles were formed as different kinds of chemical components originating from different aerosol sources condense onto each other. Externally mixed aerosol represents different source origins and emissions and includes individual particles of the same components. Primary particles generated by mechanical processes show size distributions in the coarse mode. The lifetime of particles depends on their particle size (Fig. 2.1). Shortest lifetimes exist for nucleation mode particles (10^{-3} days) as they quickly coagulate or evaporate as well as for coarse mode particles (10^{-3}-10 days) which fast sediment due to their relatively large mass. The lifetime of accumulation mode particles which were mainly eliminated by rainout lies between 1-10 days in the troposphere.

Both, during the formation of aerosol particles and their conversion in the atmosphere chemical reactions play an important role. Chemical reactions occur in the gas phase, on the aerosol surface and within the particles and influence both, gas phase chemistry and properties of particles (Hoffmann et al., 2007). In the following, primary and secondary tropospheric aerosol sources that affected the sampling sites during both campaigns and their formation and transformation processes are introduced.

Fig. 2.2 displays the emission sources and the corresponding primary aerosol particles and precursor gases which were emitted, transformed and afterwards probed during the DOMINO and the ship emission measurement campaign using the Mobile research Laboratory "MoLa" (centered). While on the right side large scale natural emissions that influenced the measurement site are shown (continental and marine source region), anthropogenic urban and ship emissions are

illustrated on the left. On the one hand, continental and marine air masses were registered without anthropogenic influences, on the other hand they are affected by industrial and vessel emissions. However, anthropogenic point sources during the field campaigns cannot be probed without the influence of continental or marine air masses. Arrows indicate the pathways of the trajectories and the transported emissions observed during the campaigns.

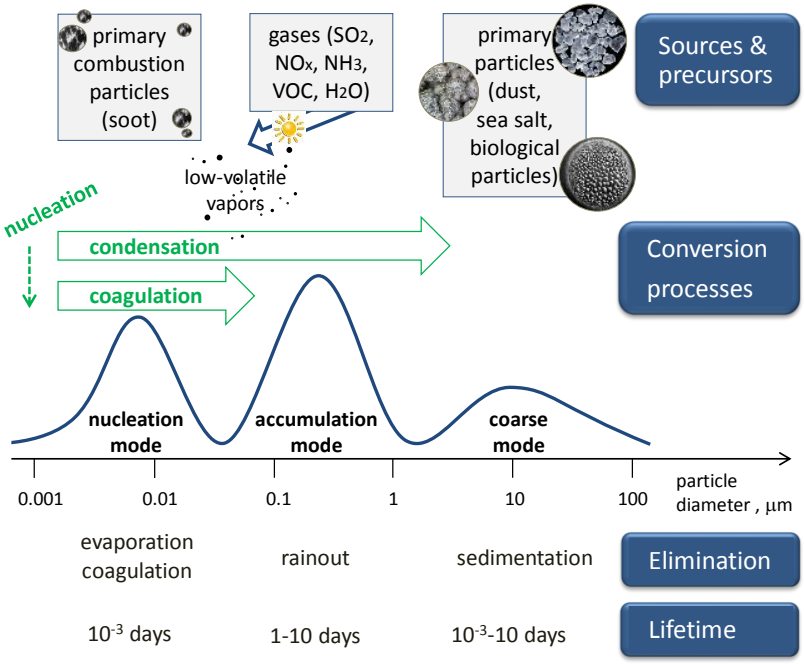

Figure 2.1: Schematics of the size distributions and atmospheric conversion processes, removal processes and particulate lifetimes. The figure is modified according to those presented by Seinfeld and Pandis (2006) and Jaenicke (1988).

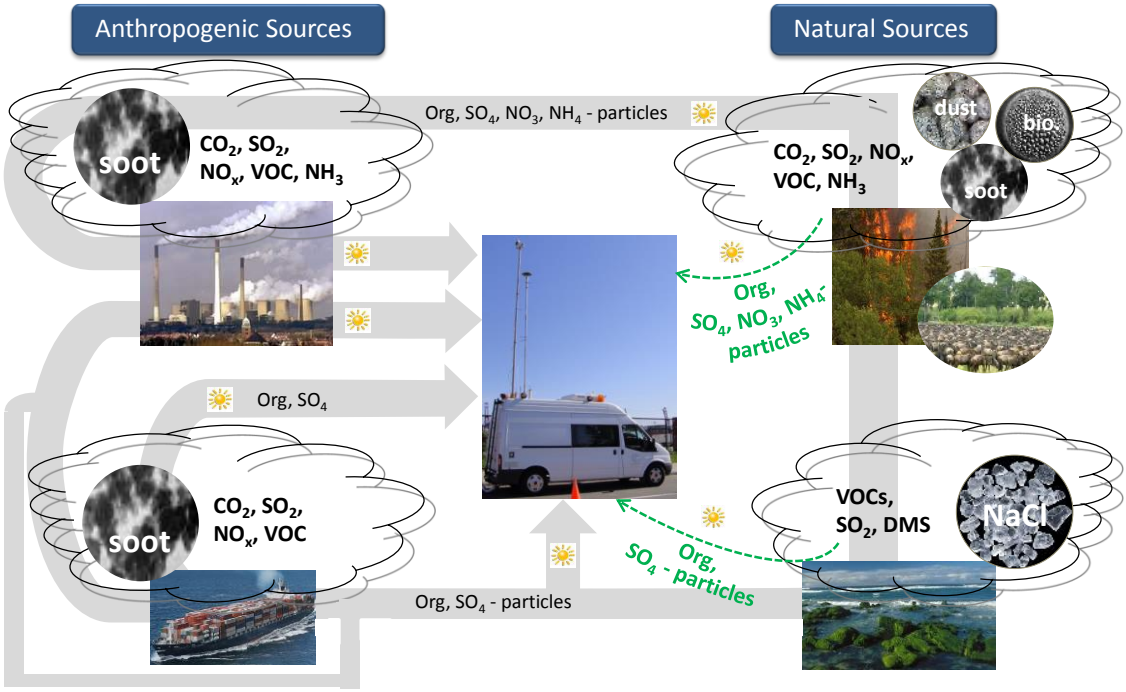

Figure 2.2: The main emission sources probed during this work. Some of the transformation processes of the aerosol are indicated along the transport pathways.

Probed primary aerosol sources

In the *marine source region* large amounts of sea salt particles are emitted into the atmosphere. The major generation processes of sea spray which depend on wind speed are called bubble bursting and spume spray generation (Schulz et al., 2004) and occur when air bubbles at the ocean´s surface burst. Thereby, drops were formed which mainly include sodium chloride. After the evaporation of water, particles consist of organic and inorganic species of marine biota, but mainly sea salt. These include organic and sulfur compounds originating from phytoplankton and anaerobic bacteria (Ramanathan et al., 2001; Schulz et al., 2004). Also gas phase species like DMS are emitted into the marine boundary layer. DMS for example is oxidized by hydroxyl radicals (OH^*) mainly to sulfur dioxide (SO_2) and gaseous sulfuric acid (H_2SO_4) but also methanesulfonic acid (CH_3SO_3H, MSA) can be observed (von Glasow and Crutzen, 2004).
A dominant part of the atmospheric aerosol from *continental source regions* can consist of mineral dust particles which are transported from arid regions after wind erosion over large spatial scales. For this reason, these particles are mainly composed of earth crust components (Zender and Tegen, 2004). Additionally, primary biological organic aerosol species such as microorganisms, spores or pollen can be directly emitted into the atmosphere (Penner et al., 2001; Jaenicke, 2005).

So far, the mentioned primary aerosol particles of natural origin have an influence on larger spatial scales and they are characterized by larger diameters (>1 µm, coarse mode particles). In contrast, primary aerosol particles from *anthropogenic emission sources* generally affect the atmosphere on smaller spatial scales. However, fine mode particles (10-100 nm) originating from combustion processes include soot particles which are of special importance in terms of the atmospheric chemistry (Kanakidou et al., 2005).

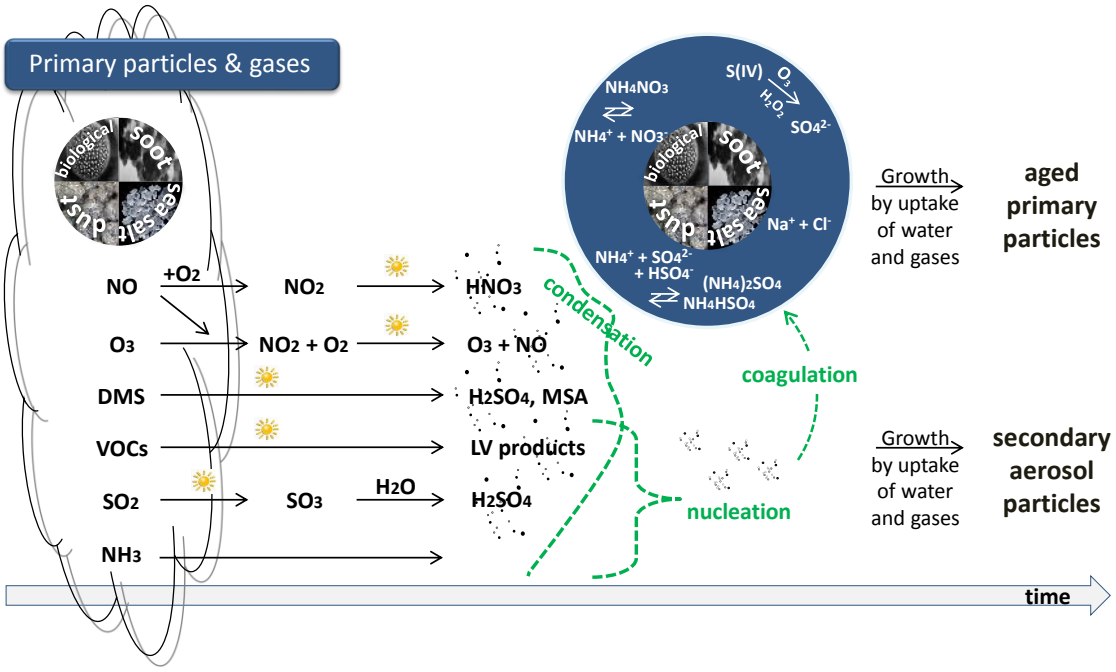

Figure 2.3: Schematics of formation and transformation processes of aerosol particles to aged primary and secondary particles. They are formed by condensation or nucleation of low-volatile vapors. Some reactions occurring in the atmosphere and within the particles surface are exemplarily demonstrated.

Probed secondary aerosol sources

Secondary atmospheric aerosol particles are formed by conversion of low-volatile vapors to particles (gas-to-particle conversion) while low-volatile condensable species are formed by oxidation of precursor gases (see Fig. 2.3). For example, the precursor gas sulfur dioxide (SO_2) is oxidized by hydroxyl radicals (OH^*) and reacts with water to sulfuric acid (H_2SO_4). Condensable organic and inorganic products can condense onto pre-existing particles if sufficient particle surface is available. Then, the aerosol particle can be chemically modified as shown in Fig. 2.3. By subsequent uptake of gas molecules and water the aerosol particles grow. Accumulation mode particles can serve as cloud condensation nuclei (CCN), if they are water soluble, where further water vapor condenses onto the surface. On the one hand, further water condensation can result in the formation of droplets which are mainly eliminated through precipitation, on the other hand droplets can evaporate as well.

When not enough particle surface for condensation exists, along with distinct low-volatile vapors, under certain conditions (e.g. meteorological) it is possible that new particle formation via nucleation of low-volatile vapors occurs. Firstly, thermodynamically stable clusters of about 1 nm diameter were formed. However, their lifetime is typically very short being removed primarily by coagulation. These clusters grow by the uptake of further gas molecules and water. Similarly as explained for primary particles grown via condensation, particles formed by nucleation can act as CCN by further uptake of gas molecules and water. After the gas-to-particle conversion, a complex mixture of different components exists in the particle phase and further chemical reactions take part, which depend on the pH value (Fig. 2.3). Sulfur species like $SO_2 \cdot H_2O$, H_2SO_3 and SO_3^{2-} often exist in the liquid phase and can be oxidized by hydrogen peroxide (H_2O_2) or ozone (O_3) to sulfate (SO_4^{2-}). Additionally, reactions like the neutralization of the anions sulfate, nitrate (NO_3^-) and chloride (Cl^-) by ammonium (NH_4^+) can occur.

In addition to a detailed investigation of the acidification meaning the neutralization of anions by the cation ammonium, much effort within the scope of this thesis has been put into the separation of the organic aerosol. By using Positive Matrix Factorization (PMF) four different organic aerosol classes were identified that can be associated with various factors which are linked to aerosol sources and components. Close to anthropogenic emission sources, a hydrocarbon-like organic aerosol (HOA) resulting from unburnt fuel was found. This corresponds to the primary organic aerosol (POA). If the distance to the source increases, however, HOA is transformed which leads in addition to a semi-volatile oxidized organic aerosol (SV-OOA or OOA II, Zhang et al., 2005). In addition, SV-OOA represents altered particles formed by nucleation. Further atmospheric processing of the organic aerosol (OA) leads to a low-volatile, highly-oxidized OA which is characterized by largest ratios of CO_2^+ (m/z 44) in the mass spectra to total OA (Jimenez et al., 2009). Additionally, continentally influenced air masses showed organic particles from wood burning (WBOA) characterized by fragments of levoglucosan (m/z 60 and m/z 73, Schneider et al., 2006; Alfarra et al., 2007), a marker for decomposed cellulose debris (Simoneit et al., 1999). A detailed description of the OA components is given in section 3.1 and 3.2.

However, the large amount of organic substances in the atmosphere which were firstly oxidized to low-volatile substances and condense in the particle phase is even more complex than suggested (Hoffmann et al., 2007) and remain in the field of research. In addition, regarding heterogeneous reactions, for example the interaction between trace gases (such as NO_x, O_3 and oxidized compounds) with particles as well as the trace gas chemistry itself is complex (indicated in Fig. 2.3). For this reason, a number of outstanding questions have to be addressed.

2.2 Field campaigns and their foci

Results of this work base on data which were obtained during the DOMINO campaign, 2008 and the ship emission measurement campaign, 2011 using the Mobile research Laboratory "MoLa". Firstly, I will introduce the objectives of the campaigns and give a short overview about the sampled source regions and aerosol types.

2.2.1 DOMINO campaign

The 2008 DOMINO (*Diel Oxidant Mechanisms In relation to Nitrogen Oxides*) research campaign took place from November 20 until December 9 at the atmospheric research station "El Arenosillo" (37° 5´ 47.76" N, 6° 44´ 6.94" W) in the southwest of Spain (Fig. 2.4) operated by the INTA (National Institute for Aerospace Technology). The main objective of the campaign was to study the atmospheric oxidation chemistry, to compare the radical and nighttime chemistry and to characterize the self-cleaning efficiency of the atmosphere in different air mass types. Our contribution to this project was to study the variability of aerosol, gaseous pollutants and meteorological characteristics associated with changes in air mass origin. The aerosol particle composition and chemistry during formation and transformation processes was also investigated.

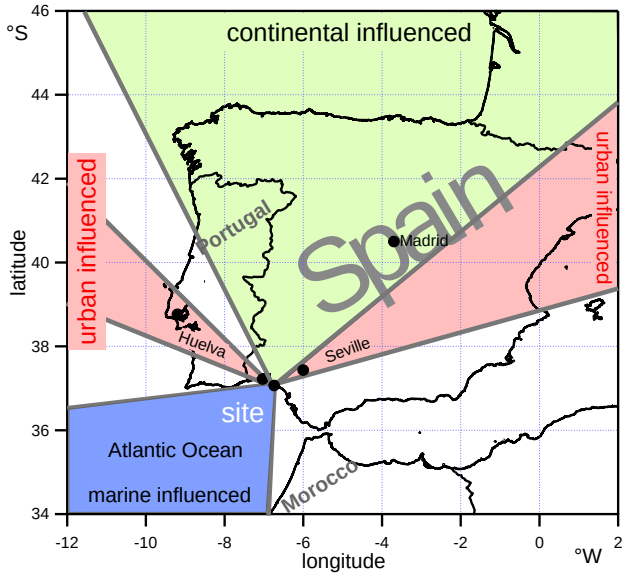

Figure 2.4: Map of Spain showing the location of the DOMINO field measurement campaign and the source regions continental, urban and marine that were sampled and analyzed in detail.

The "El Arenosillo" research station lies within a Protected Natural Area with a large variety of ecosystems in between very different source regions and types. The Atlantic Ocean, the towns of Huelva (20 km distance) and Seville (70 km distance) and the continent (see Fig. 2.4) surrounded the measurement site. Huelva is a highly industrialized town with three large chemical estates where fertilizer production industries, petrochemical industries, ammonia and urea industries as well as paper production industries are situated (Carretero et al., 2005; Alastuey et al., 2006; Querol et al., 2002; Querol et al., 2004; Fernandez-Camacho et al., 2010a). At 70 km distance from the site lies the city of Seville which is less industrialized than Huelva. The predominant wind directions at the station during the time the study took place are WSW, NW and NNE transporting air from Seville, Huelva, the Continent and the Atlantic Ocean to the measurement site.

2.2.2 Ship emission measurement campaign

The ship emission measurement campaign was conducted near the Elbe river mouth in Northern Germany between April 25 and 29, 2011 using the mobile research laboratory "MoLa" (Fig. 2.5a). 178 commercial marine vessels were encountered during the 5 days of sampling. The measurement sites were located near Freiburg/Elbe between Cuxhaven and Hamburg on the banks of the Elbe (53°50' N, 9°20' E) chosen to be located directly downwind of the ship tracks (Fig. 2.5b). The Elbe is daily passed by numerous ocean-going vessels entering and leaving the port of Hamburg, the second largest freight port of Europe. The measurements were conducted in an emission control area (ECA) where the ship fuel sulfur content is legally fixed not to exceed 1% by weight since July 01, 2010. The objective of this campaign was to study chemical and physical as well as trace gas properties of ship emissions and their impact on local air quality.

The predominant wind directions during the study period were N-NW transporting relatively clean air from the Baltic and North Sea to the measurement sites. At the measurement sites, the Elbe is about 2 km wide. For this reason most vessels were probed and identified at a distance of about 0.8 and 1.2 km dependant on the location of main shipping lanes downstream and upstream the Elbe.

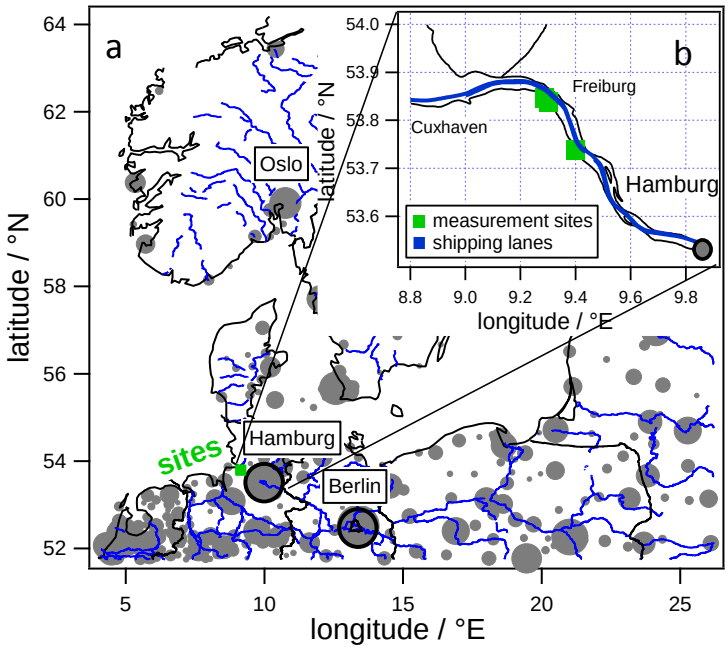

Figure 2.5: Map showing the measurement sites located between Cuxhaven and Hamburg, Northern Germany on a large scale (a) and in a close-up showing the positions where MoLa was operated (b).

2.3 Description of MoLa, the on-board instrumentation and data analysis

To obtain a better understanding of various information about atmospheric aerosols, the compact Mobile aerosol research Laboratory "MoLa" which was developed at the Max Planck Institute for Chemistry (MPIC) was used for stationary measurements of aerosol, trace gas and meteorological characteristics during both field campaigns. In this section the mobile laboratory MoLa, the general set up of the instruments, data acquisition and the analysis of the dataset using several tools (Squirrel, PMF, PIKA) is described. Additionally, the Hybrid Single-Particle Lagrangian Integrated Trajectory (HYSPLIT) model to assign different air masses to individual source regions and the Automated Identification System (AIS) tool which provides various information of the vessels is introduced in this section.

2.3.1 Mobile aerosol research Laboratory "MoLa"

The mobile laboratory MoLa is based on a Ford Transit vehicle which is modified and equipped with numerous state-of-the art instruments for research purposes. The aerosol was sampled through an extendable inlet tube system at a height of 10 m during the DOMINO and about 7 m during the ship emission campaign (Fig. 2.6). Next to the inlet line, the meteorological station was fixed on a separate mast. While during the DOMINO campaign electrical power for the instruments operation was obtained from the grid, during the ship emission campaign on-board electrical power was used. For this reason, MoLa´s engine emissions were transported downwind using an exhaust removal system to avoid self-contamination of our measurements. A detailed technical description of MoLa can be found in Drewnick et al. (2012). In table 2.1 the measured quantities, particle size ranges and distinct details for the instruments implemented in MoLa during both campaigns are summarized.

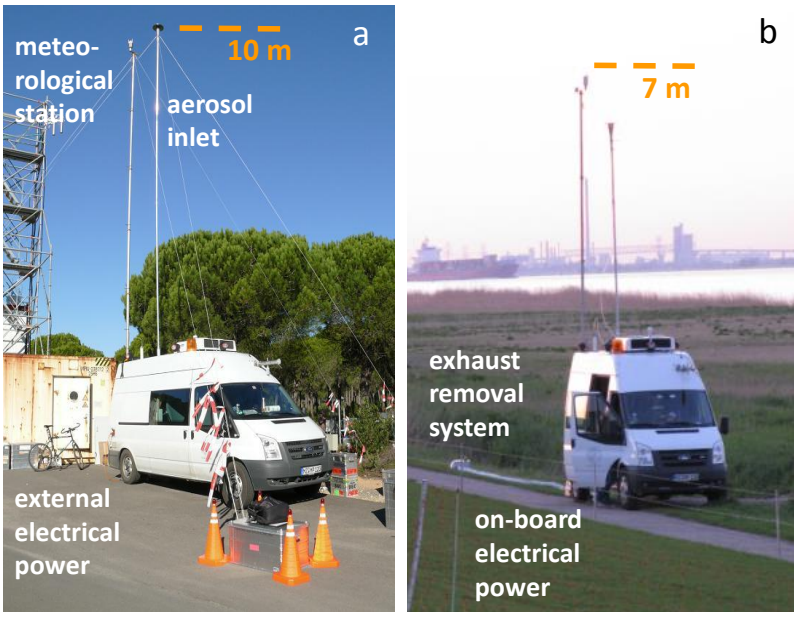

Figure 2.6: The mobile laboratory during stationary measurements on the south coast of Spain during DOMINO (a) and the ship emission measurement campaign (b). While external electrical power was used during DOMINO, on-board electrical power was used during the ship emission measurement campaign. For this reason, the engine´s emissions were removed during the ship emission measurement campaign by the exhaust removal system which releases pollutants about 25 m downwind of the vehicle to avoid self-contamination.

Measurements of physical aerosol particle properties

Ultrafine water-based Condensation Particle Counter (UW-CPC, TSI Model 3786): The particle number concentration is one of the most important aerosol physical properties. Particles larger than 2.5 nm are detected with a time resolution of 1 s by entering the inlet system before they get into the saturation chamber and enter a cooled condensation line. Due to the decrease of temperature air is supersaturated and particles act as condensation nuclei. By condensation of water particles grow and can therefore be optically detected.

Filter Dynamics Measurement System-Tapered Element Oscillating Microbalance (FDMS-TEOM, Rupprecht & Patashnick Co., Inc.): Particulate matter below 1 μm aerodynamic diameter (PM_1) was probed with the TEOM mass sensor (15 min time resolution) as a PM_1 cyclone was fixed at the inlet system. The measurement is based on a frequency change of an oscillating tapered element which changes its eigenfrequency dependant on the accumulated mass on the element. The mass concentration is calculated from the increased mass, the time and flow rate.

Environmental Dust Monitor (EDM, Grimm Model 180): The particles pass a laser beam and scatter light which is collected using a mirror and transferred to a detector attached on the opposite site. The particle size can be calculated from the intensity of the scattered light. The particle number for each size bin is obtained by the counting rate and volumetric flow rate. When the particle diameter and density is known, particulate mass of particles smaller 1, 2.5 and 10 μm with a 6 s time resolution can be determined from the particle size distribution.

Fast Mobility Particle Sizer (FMPS, TSI Model 3091): Particles were size classified according to their electrical mobility after cations were generated by an electrical diffusion charger. The measurement column consists of an inner positively charged high voltage electrode and an outer cylinder divided into several sensing electrodes. Between both a high voltage is applied. In the resulting electrical field positively charged particles migrate towards the outer sensing cylinder perpendicular to the aerosol flow through the cylinder. If particles exhibit a large electrical mobility (small particles) they reach an electrode near the top of the measurement column otherwise they are traveling further downstream (large particles). Due to their charge, particles can be detected by electrometers with a time resolution of 1 s in 32 size channels (7-523 nm).

Aerodynamic Particle Sizer (APS, TSI Model 3321): The APS measures particle size distributions in the 0.37-20 μm diameter size range. Particles are separated into 52 channels according to their flight time by passing two laser beams. Particles are accelerated by an air expansion in a nozzle, reach a velocity which depends on their aerodynamic diameter and scatter light when they pass the laser beams. Scattered light is collected and focused by an elliptical mirror and detected with a solid-state photodetector (1 s time resolution).

Optical Particle Counter (OPC, Grimm Model 1.109): The optical particle sizer measures the particle size distribution between 250 nm and 32 μm in 31 channels and and with a time resolution of 6 s. When particles pass a laser beam scattered light is collected using a mirror and transferred to a detector attached on the opposite site. The particle size can be calculated from the intensity of the scattered light using a calibration with PSL particles.

Measurements of chemical aerosol particle properties

High-resolution Time-of-Flight Aerosol Mass Spectrometer (HR-ToF-AMS, Aerodyne Res., Inc.): The C-ToF-AMS and the vacuum system is described in Jayne et al. (2003), the HR-ToF-AMS and the data acquisition is explained in Drewnick et al. (2005). DeCarlo et al. (2006) described the HR-ToF-AMS as well while the PhD thesis of Hings (2006) focuses on a detailed characterization of the C-ToF-AMS. Therefore only a short summary of the instrument and its operation will follow.

The HR-ToF-AMS is integrated in a rack which is fixed in MoLa and contains the vacuum system, the mass spectrometer and the electronics. The vacuum system consists of:
- aerosol sampling chamber
- particle sizing chamber
- particle evaporation and ionization chamber
- chemical analysis and detection chamber.

Firstly, the aerosol is introduced into the instrument through the critical orifice and the aerodynamic lens assembly. Then it passes a skimmer where most of the surrounding gas is separated. Particles in the ~40-600 nm size range are focused by the aerodynamic lens into the vacuum chamber with an efficiency of almost 100%. Then particles enter the particle sizing chamber and pass through a chopper which provides the starting point of the particle flight time for the determination of the aerodynamic particle size. Afterwards, particles impact onto a porous tungsten vaporizer heated up to temperatures of about 600°C where the non-refractory components flash-vaporize. After being ionized by electron impact (70 eV), positively charged ions were extracted, orthogonally accelerated by a pulsed electrical field into the time-of-flight mass spectrometer and detected by multi-channel plates.

The AMS is able to quantitatively measure size-resolved mass concentrations. For this reason, the instrument operates in the mass spectrum (MS) and particle time-of-flight (PTOF) mode, alternately. In the MS mode, mass concentrations of individual non-refractory aerosol components in ambient air (chopper open) and the instrument background (chopper closed) were measured providing average aerosol mass spectra by subtraction. Species-resolved size distribution data were obtained based on the particle velocity between chopper and vaporizer implying their specific flight times.

Multi Angle Absorption Photometer (MAAP, Carusso Model 5012): Black carbon concentrations are measured with a time resolution of 1 min by optical absorption and scattering of light at particles collected on a filter tape. Multiple detectors simultaneously register the transmitted and scattered light to account for the influence of non-absorbing particles.

Polycyclic aromatic hydrocarbon sensor (EcoChem Model, PAS 2000): Polycyclic aromatic hydrocarbons (PAH) on particles can be measured by a photoelectrical aerosol sensor of which the basic principle is based on the photoelectric ionization of particles. When particles are irradiated with electromagnetic radiation and the photon energy is larger than the photoelectric threshold function, an electron is emitted and the particle gets positively charged. As PAHs exhibit ionization energies below the UV photon energy they can be measured in contrast to other species. After the charged particles were absorbed on a filter, situated in a faraday cup, the electrical current can be measured, providing a measure of the total PAH content on and near the surface of the aerosol particles (12 s time resolution).

Measurements of trace gases

Airpointer gas measurement system (Recordum GmbH): In an air-conditioned enclosure, several modules are integrated. Each of them provides different measurement techniques for registering the individual trace gases sulfur dioxide (SO_2), nitrogen oxide, nitrogen dioxide (NO, NO_2), ozone (O_3) and CO.

SO_2 is determined by absorption of ultraviolet light (214 nm wavelength). Excited SO_2 molecules emit fluorescence light (330 nm) which is detected by a fluorescence detector.

NO_x and NO are measured based on chemiluminescence via gas phase titration with the following reactions underlying the process:

$$NO + O_3 \rightarrow NO_2^* + O_2 \quad (R2.1)$$
$$NO_2^* \rightarrow NO_2 + hv \quad (R2.2)$$

NO mixing ratios can be determined by reaction with ozone. The thereby established excited NO_2^* molecules emit photons which are detected by a photomultiplier.
To measure NO_2 it is firstly converted into NO (Mo = molybdenum):

$$3\ NO_2 + Mo \rightarrow 3\ NO + MoO_2 \quad (R2.3)$$

Afterwards the same reactions occur (R2.1 and R2.2) to achieve NO_2 mixing ratios which actually correspond to NO_x mixing ratios. By subtraction of the NO mixing ratios from those of NO_x, NO_2 mixing ratios are obtained.

The O_3 analyzer contains a measurement cell with ultraviolet light of 254 nm. Decreased light intensity due to absorption of O_3 can be measured. By using a chemical O_3 scrubber which eliminates O_3, the reference signal can be registered and subtracted from the signal.

The CO module uses a heated element to generate an infrared beam with a wavelength of 4.7 μm. The beam is conducted through the CO probe cell consisting of two mirrors on both ends to reflect the beam between them. The decreased beam intensity due to absorption of CO can be registered by a photodetector.

Licor gas analyzer (LI-COR Inc., Model 840): The infrared CO_2 and H_2O gas analyzer uses an optical path where H_2O and CO_2 are measured due to the absorption of infrared light (1 s time resolution). H_2O absorbs IR light at a wavelength of 2.595 μm, CO_2 absorbs IR light at a wavelength of 4.26 μm. CO_2 and H_2O mixing ratios are calculated from the difference in the IR absorption between reference and sample.

Measurements of meteorological parameters

Weather station (Vaisala, Model WXT520): Wind direction and wind speed are measured using an ultrasonic anemometer. An acoustic sensor registers rain drops and is used to measure precipitation via piezoelectric detection. Different parameters such as temperature, ambient pressure and relative humidity can be measured with capacitive sensors (1 s time resolution).

Table 2.1: Summary of measured quantities, size ranges and the corresponding particle losses, sampling time delays and detection limits for the instruments implemented in the mobile laboratory (MoLa). Particle losses within the given size range boundaries are lower than those provided here; therefore the given losses are upper limits.

Measurement Instrument	Measured Quantity (time resolution)	Size Range/ (Particle losses)	Sampling Delay	Detection Limits/Accuracy
AMS Aerosol Mass Spectrometer	size-resolved Aerosol Chemical Composition (1 min)	40 nm (6%) – 600 nm (2%) (vacuum aerodynamic diameter)	43 s	sulfate: 0.04 µg m^{-3} nitrate: 0.02 µg m^{-3} ammonium: 0.05 µg m^{-3} chloride: 0.02 µg m^{-3} organics: 0.09 µg m^{-3}
MAAP Multi Angle Absorption Photometer	Black Carbon Particle Mass Concentration (1 min)	10 nm (4%) – 1 µm (0.2%)	7 s	0.1 µg m^{-3}
PAH-Sensor Polycyclic Aromatic Hydrocarbons Sensor	total PAH Mass Concentration (12 s)	10 nm (11%) – 1 µm (0.3%)	8 s	1 ng m^{-3}
CPC Condensation Particle Counter	Particle Number Concentration (1 s)	2.5 nm (45%) – 3 µm (0.8)	7 s	Max. Konz. 10^5 # cm^{-3}
TEOM Tapered Element Oscillating Microbalance	Particle Mass Concentration (PM_1) (15 min)	< 1 µm (0.5-9%)	9 s	2.5 µg m^{-3}
FMPS Fast Mobility Particle Sizer	Particle Size Distribution based on Electrical Mobility (1 s)	7 nm (9%) – 523 nm (0.1%) (D_{mob})	7 s	N/A
APS Aerodynamic Particle Sizer	Particle Size Distribution based on Aerodynamic Sizing (1 s)	0.37 µm (0.1%) - 20 µm (45%) (D_{aero})	7 s	N/A
OPC Optical Particle Counter	Particle Size Distribution based on Light Scattering (6s)	0.25 µm (0.05%) – 32 µm (0.002%) (D_{opt})	8 s	N/A
Airpointer	O_3, SO_2, CO and NO, NO_2 Mixing Ratio (1 min)	N/A	6 s	O_3/SO_2: < 1.0 nmol mol^{-1} CO: < 0.08 µmol mol^{-1} NO_x: < 2.0 nmol mol^{-1}
LICOR LI840	CO_2 and H_2O Mixing Ratio (1 s)	N/A	8 s	CO_2: 1 µmol mol^{-1} (accuracy) H_2O: 0.01 pmol mol^{-1}
Met. Station	Wind speed & Direction Temperature, RH, Rain intensity, Pressure (1 s)	N/A	0 s	Accuracy: WSp: 0.3 m s^{-1}, WDir: 3°, Temp.: 0.3 C°, RH: 3% Precipitation: 5% Pressure: 0.5 hPa

2.3.2 Data preparation for analysis

Before analyzing the large amount of data gained by the instruments in MoLa within short time periods, data preparation is a challenge. As DOMINO was the first campaign after MoLa was built, new approaches of data processing have to be developed to extract data step by step with the consideration which information are necessary for the subsequent analysis. For this reason, different data preparation procedures for both campaigns were applied for a better handling of the datasets.

After the data were converted from diverse instrument formats/software into a common standard format/software (IGOR PRO), outliers due to the instrument failures and local pollution contaminations, for example by vehicles passing MoLa were hand-selected and removed. Both are typically characterized by relatively short, large peaks and are therefore clearly visible in the measured data (see Fig. 2.7). Similarly invalid data points where individual instruments did not work due to calibrations, software problems, interrupted power supply etc. were removed.

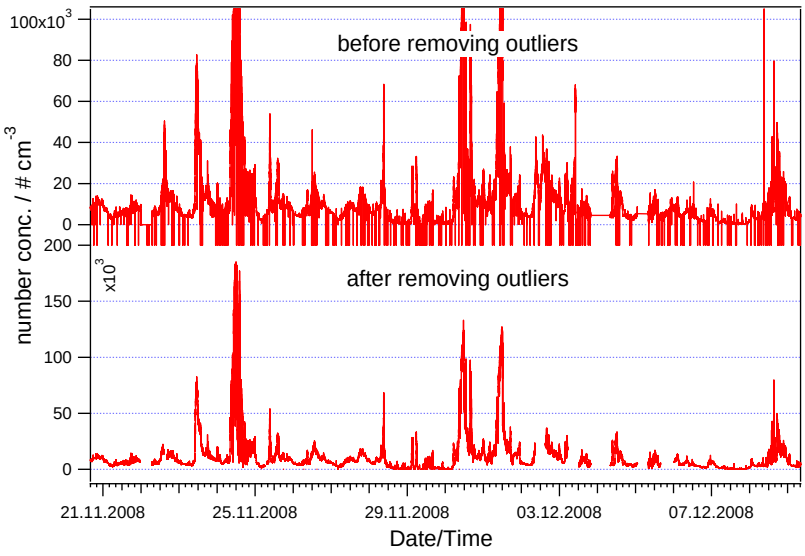

Figure 2.7: Particulate number concentration time series (CPC instrument) before and after removing of invalid data points and outliers (measured during the DOMINO campaign).

Before all DOMINO data are converted into a consistent data set including a common 1 min time axis, the measurement times due to the residence times of the aerosol in the tube system has to be corrected for. The delays due to the aerosol transport from the roof inlet to the instruments were subtracted from the time stamps to get the correct sampling time. The sampling delays for the individual instruments are listed in section 3.1. They are calculated by the individual instrument flow rates and the geometry of the tube system (delay = $\pi r^2 h$/flow rate).

Additionally, particle losses during the aerosol transport have been calculated using the Particle Loss Calculator (von der Weiden et al., 2009). The software accounts for the most important sampling and transport effects (e.g. diffusion, sedimentation, deposition) that affect the measurements though a sampling probe. While particle losses have a maximum of 45% for 20 µm particles for the APS, for the most instruments and particle sizes used during the campaigns maximum particle losses are below 25% (see Fig. 2.8). The respective losses are relatively small in the size range where the majority of relevant particle mass concentrations for this work are collected: In the size range from 30 nm to 2 µm calculated particle losses are below 3% (without

regarding the AMS: <8%). Therefore, the occurring particle losses can be neglected, since they do not influence the measurement results significantly and the ambient aerosol was measured mostly unbiased in this range.

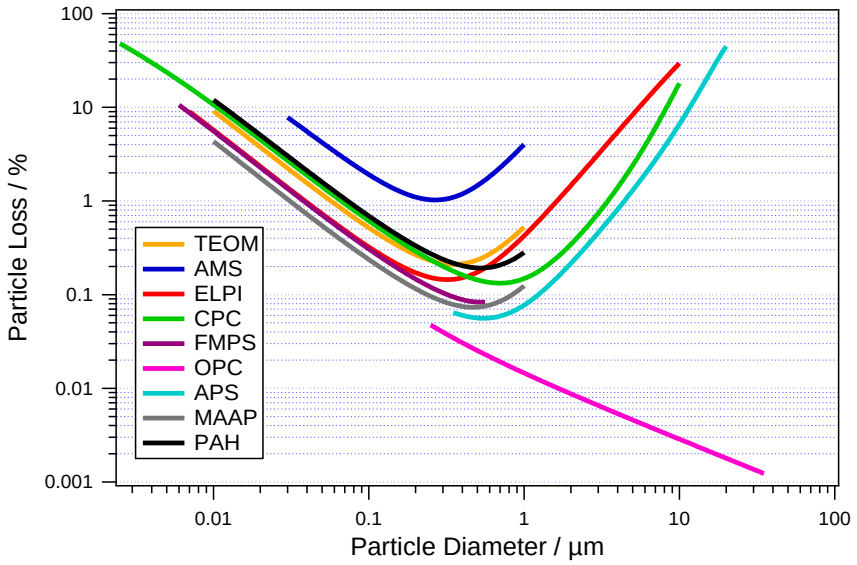

Figure 2.8: Calculated particle losses for the roof inlet as a function of the particle diameter for all instruments implemented in MoLa during the DOMINO campaign.

For the analysis of ship plume events, a comprehensive data analysis tool was programmed by Thomas Klimach for an objective and more efficient handling. On the one hand, the analysis tool supports characterizing ship emissions by the calculation of the average concentrations and integrated concentrations "area" for each ship and parameter. On the other hand background levels without the impact of ship emissions can be obtained using a template. As a detailed description can be found in the publications in section 3.3 and 3.4, only a short overview is given here.

Transport times through the sampling line and individual internal measurement time constants of the instruments result in constant delays and broadenings of the individual parameters. The particle number concentration was the first parameter that quickly increased apparently without instrument-related delays and it was always enhanced when a ship passed the site. Therefore, the average number concentration of each ship plume was determined from the start until the end point of the associated peak, both defined manually. These start and end points of the particle number concentration of each plume were used as a reference to which the offset and broadening of all other parameters were referred to. The background concentrations of the measured aerosol and gas phase species were subtracted from the total concentrations using a linear fit between manually defined background intervals (pre- and post-plume). Then, the average concentrations, the area of the peaks and the background can be obtained.

2.3.3 AMS data acquisition, calibrations, detection limits and analysis tools

In the following the examination of the AMS data is described. Several calibrations have to be performed and correction factors must be determined and implemented in the data analysis software for providing meaningful quantitative results of the non-refractory aerosol species. Together with several complex analysis tools large information about aerosol properties can be obtained (Canagaratna et al., 2007; Sun et al., 2010; Zhang et al., 2011). On the one hand, the

organic aerosol fraction can be separated in different sources and components using Positive Matrix Factorization (PMF). On the other hand, the chemical information of single peaks in the high-resolution mass spectra using Peak Integration by Key Analysis (PIKA) can be obtained.

AMS operations

During the DOMINO campaign the AMS collected averaged high resolution mass spectra and species-resolved size distributions by alternating through the related operation modes (general alternation mode), spending 50% of the sampling time in each mode. Since during the expected short plume intercepts during the ship emission campaign no reasonable size distribution measurement with the AMS is possible and for not losing measurement time, the AMS was operated in MS mode only, measuring aerosol mass spectra without size information. For both campaigns, final AMS data have a time resolution of 1 minute.

AMS calibrations

For data quality assurance a variety of calibrations of the AMS were performed before and during the campaigns. A particle Time-of-Flight calibration was accomplished prior to the campaigns, used to convert particle flight times into the corresponding particle diameters. To relate an ion flight time to the respective m/z, dominant peaks like N^+ (m/z 14.003), N_2^+ (m/z 28.006), O_2^+ (m/z 31.990), Ar^+ (m/z 39.962) or W^+ (m/z 183.951) are used. The so-called single ion (SI) calibration is used to determine the signal of background ions and aims to convert the signals into ions s^{-1}. A calibration of the Ionization efficiency (IE) of the ion source was conducted once a week. Hereby, the ionization efficiency for nitrate (ca. 10^{-7} ions/molecule) is determined and related to the other species. A collection efficiency (CE) factor (Huffman et al., 2005) has to be determined to account for the fraction of particles that are not detected as they bounce off the vaporizer before evaporation and to correct for incomplete transmission of particles through the inlet of the instrument. By comparing AMS together with black carbon measurements with results from the TEOM (DOMINO) and EDM (ship emission campaign) PM_1 instruments, a CE factor of 0.5 for the AMS mass concentrations (organics, sulfate, nitrate, ammonium and chloride) for both campaigns was found. Very high relative humidity implies less particle bounce resulting in a CE factor closer to 1 (no bounce). However, when using the CE factor of 0.5, the time series of the ToF-AMS mass concentrations summed with the MAAP black carbon mass concentrations show a good agreement with PM_1 mass concentrations (see Fig. 2.9 for the DOMINO campaign).

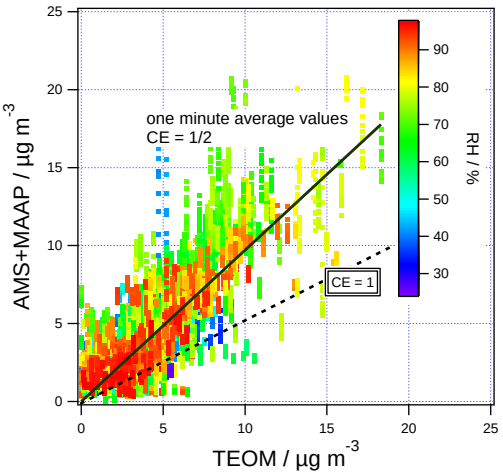

Figure 2.9: Correlation between AMS+MAAP and TEOM PM_1 mass concentrations during DOMINO using a CE factor of 0.5. Data points are color-coded according to the relative humidity. (The dotted line represents the correlation of the PM_1 mass concentrations if a CE of 1 would be used.)

AMS detection limits

Additionally, detection limits (LOD) for each species were evaluated on the basis of the method described by Drewnick et al. (2009). They are defined as:

$$LOD = 3 \cdot \sqrt{2} \cdot \sigma(I) \tag{2.1}$$

with $\sigma(I)$ the standard deviation of the background signals (1 min) of the respective species. Generally, a value of a measurement is considered to be significant if it is at least three times the standard deviation of the background. The average mass spectrum (difference spectrum) is determined by subtraction of the background spectrum (closed spectrum, chopper closed) from the complete mass spectrum (open spectrum, chopper open). As both measurements exhibit the same standard deviations, the standard deviation has to be multiplied with the square root of two to obtain the LOD for the mass concentrations. AMS species generally are characterized by large changes in the background signals originating from contaminations. For this reason, a sliding window over the whole campaign data set was used for the calculation of the standard deviation.

AMS analysis software

As the AMS generated large data sets during both campaigns and for an easier examination the standard analysis software SQUIRREL (SeQUential Igor data REtRivaL, versions 1.47-1.51) was used. By means of the analysis software, parameters gained by the calibrations can be included. Finally, objectively determined chemically resolved time series and particle size distributions are obtained. The software tools explained in the following are based on the scientific graphing, data analysis, image processing and programming software IGOR Pro (Wavemetrics, 2012).

Positive Matrix Factorization (PMF, Ulbrich et al., 2009) was used to extract typical organic mass spectral signatures to different kinds of emission sources and components during the DOMINO campaign. Beside the marine air mass origins where sulfate is most abundant, in all continentally influenced source regions organic species dominated the total submicron aerosol mass. For this reason, being probably involved in particle formation and certainly playing an important role as condensable species during growth, transformation processes of the organic aerosol in the atmosphere were analyzed using PMF as well. The PMF model extracts factors corresponding to those sources and components explaining the majority of the variance of the organic data matrix. For this reason, PMF allows distinguishing between different aged organic aerosol species implying an investigation of the oxidation state. However, the selection of the number of factors being measured is a critical step. Usually, the most reasonable result is taken, explaining the high subjectivity of this method. This means that PMF data were compared with time series of other instruments during DOMINO and mass spectra from known sources. After this comparisons, the four factor solution was selected for this data set including a highly oxidized, low-volatile organic aerosol (OOA I), a semi-volatile oxidized OA (OOA II), a hydrocarbon-like OA (HOA) and a wood-burning OA (WBOA). Details about the four factor solution, the identification of the sources and parameters using correlations with time series of other measured parameters and reference mass spectra, the uncertainties obtained by choosing different user inputs and a detailed interpretation of the PMF results can be found within the DOMINO publications in section 3.1 and 3.2. For the ship emission measurement campaign no separation of the organic mass fraction using PMF was performed as the registered ship plume events vary between 1-5 minutes which probably cannot be resolved by PMF because for statistical reasons, PMF needs a certain number of data points. Otherwise, the software probably has difficulties in the processing. However, typical marker peaks in the mass spectra exist for the different PMF species. Hereby, differences in the mass spectra are characterized by m/z 44 (mainly CO_2^+) and m/z 43 (mainly $C_3H_7^+$). While the

OOA II exhibits a higher ratio of m/z 44 versus total organics and a lower ratio of m/z 43 versus total organics than OOA II, HOA can be clearly distinguished from both OOA mass spectra and generally exhibit a marker fragment at m/z 43. For this reason, both marker fragments were used to assign differences in the mass spectra. Finally, a separation of the m/z 44 and m/z 43 to the total organic mass fraction shows that the background was mainly composed of oxidized organic aerosol while freshly formed HOA dominated in ship emission plumes (section 3.4).

For the speciation of sulfur compounds occurring in marine influenced air masses, PIKA (Peak Integration by Key Analysis) was used which is a further AMS analysis tool based on SQUIRREL. PIKA allows the separation of different species with the same nominal mass based on exact m/z ratios. For this reason, PIKA was used to deconvolve the m/z 79 signal into three peaks from three different contributions: bromine (Br^+), a methanesulfonic acid (MSA) fragment ($CH_3SO_2^+$) and an organic fragment ($C_6H_7^+$, see Fig. 2.10). In contrast to Zorn et al. (2008) who used the software tool TADA which allows to fit the main contributors by Gaussian functions, PIKA additionally considers the peak shape in the calculation of the mass concentrations. This is particularly important in the DOMINO data analysis as MSA concentrations are registered near the detection limit (LOD = 6 ng m^{-3}). Zorn et al. (2008) directly measured on the Atlantic Ocean and found MSA levels being approximately a factor of 10 larger within a lower aerosol background. A detailed description of marine sources (MSA etc.), further information and interpretation about MSA concentrations can be found in section 3.1.

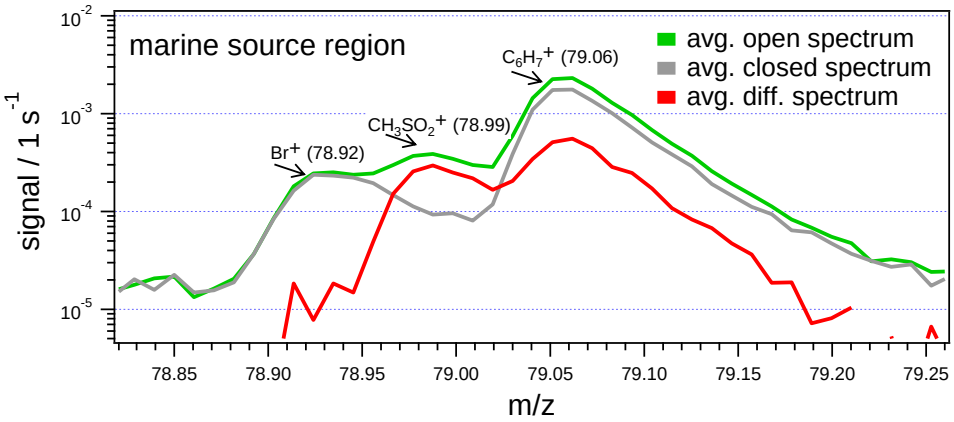

Figure 2.10: Separation of the high-resolution m/z 79 signal into a bromine (Br^+), methanesulfonic acid (MSA, $CH_3SO_2^+$) and an organic ($C_6H_7^+$) fraction using PIKA. While the average open spectrum recorded during beam open measurements is shown in green, the average closed one which represents background measurements when the beam is blocked is shown in grey. The average difference spectrum is gained by subtraction of the background from the open spectrum (red). This indicates that MSA is present in marine air masses during the DOMINO campaign.

2.3.4 Hybrid Single-Particle Lagrangian Integrated Trajectory (HYSPLIT)

The Hybrid Single-Particle Lagrangian Integrated Trajectory (HYSPLIT) model offered by the National Oceanic and Atmospheric Administration (NOAA) Air Resource Laboratory provides an online calculation of air parcel back trajectories (http://www.arl.noaa.gov/ready.html). Back trajectories show the history of the air masses on their way to the measurement site. For this reason, back trajectories allow drawing a conclusion about source regions and their influences and 48 h back trajectories for every 2 hour interval during both campaigns were calculated. However, it has to be considered that HYSPLIT is intended for transport processes on regional scales due to its

relatively low grid resolution. Especially for lower trajectory altitudes the model suffers from severe limitations as small scale processes are not considered (e.g. land-sea breeze, small scale topography (hills, river valleys)). For this reason and as for the DOMINO campaign trajectories are used to assign different air masses to source regions, local meteorology was used as second approach for the identification of the air mass origin. A detailed description of both methods together with a graph for comparison reasons is shown in section 3.1. However, I want to mention that both methods of associating measurement data to the source regions provide similar results except those trajectories spreading directly along the coastline. By detailed analysis it was found that this effect results from the land-sea-circulation (see Fig. 2.11). The land-sea breeze twist locally measured wind directions when air is flowing along the coastline in contrast to the back trajectories that were not influenced by this small scale process. Dependant on the time of day the temperature between land and sea varies as both heat up differently. While during day the temperature raise is larger on land implying wind directions are located further north, at night the situation changed and wind directions were measured further south compared to the back trajectories. For this reason, back trajectories which pass along the coastline differ slightly but systematically from locally measured wind directions.

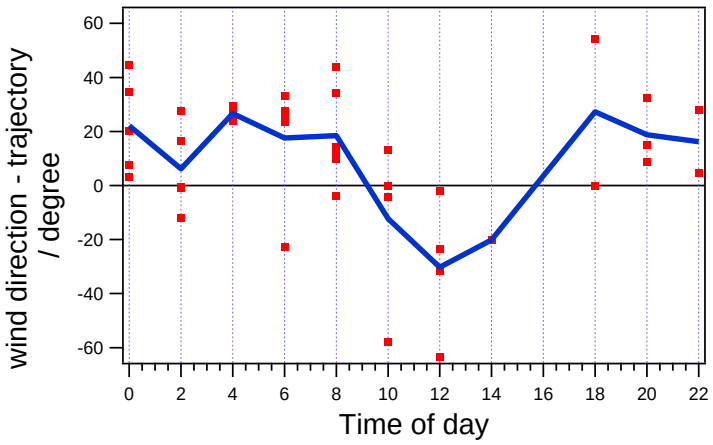

Figure 2.11: The graph shows differences between wind directions and back trajectories, both determined by hand in degree during the same time period. While the red dots represent values of individual days, the blue colored cycle represents average values of the red dots of each day.

2.3.5 Automated Identification System (AIS)

Ship information including ship name, commercial type, length, breath, deepness, speed, position, gross tonnage and maximum engine power was collected from Automated Identification System (AIS) broadcasts (www.vesseltracker.com). AIS is a globally implemented identification system mandatory in all vessels larger than 20 m length or 300 gross tonnages. Specific data of each vessel are broadcast continuously and serve for the prevention of collisions between vessels. The system was used to identify the individual ships passing the measurement site and thus assigning the specific ship characteristics to each of the registered plumes and to classify the measured vessels into different types.

References

Alfarra, M. R., Prevot, A. S. H., Szidat, S., Sandradewi, J., Weimer, S., Lanz, V. A., Schreiber, D., Mohr, M., and Baltensperger, U.: Identification of the Mass Spectral Signature of Organic Aerosols from Wood Burning Emissions, Environ. Sci. Technol., 41, 5770-5777, 2007.

Canagaratna, M. R., Janye, J. T., Jimenez, J. L., Allan, J. D., Alfarra, M. R., Zhang, Q., Onasch, T. B., Drewnick, F., Coe, H., Middelbrook, A., Delia, A., Williams, L. R., Trimborn, A. M., Northway, M. J., DeCarlo, P. F., Kolb, C. E., Davidovits, R. and Worsnop, D. R.: Chemical and microphysical characterization of ambient aerosols with the Aerodyne aerosol mass spectrometer, Mass Spectrom. Rev., 26, 185-222, 2007.

Carretero, M. I., Bernabe, J. M., and Galan, E.: Mineralogy and origin of atmospheric particles in the industrial area of Huelva (SW Spain), Atmos. Environ., 39, 6777-6789, 2005.

Alastuey, A., Querol, X., Plana, F., Viana, M., Ruiz, C. R., de la Campa, A. S., de la Rosa, J., Mantilla, E., and dos Santos, S. G.: Identification and chemical characterization of industrial particulate matter sources in southwest Spain, Journal of the Air & Waste Management Association, 56, 993-1006, 2006.

Drewnick, F., Hings, S. S., Alfarra, M. R., Prevot, A. S. H., and Borrmann, S.: Aerosol quantification with the Aerodyne Aerosol Mass Spectrometer: detection limits and ionizer background effects, Atmospheric Measurement Techniques, 2, 33-46, 2009.

Drewnick, F., Böttger, T., von der Weiden-Reinmüller, S.-L., Zorn, S. R., Klimach, T., Schneider, J., and Borrmann, S.: Design of a mobile aerosol research laboratory and data processing tools for effective stationary and mobile field measurements, Atmos. Meas. Tech. Discuss., 5, 2273-2313, doi: 10.5194/amtd-5-2273-2012, 2012.

Fernandez-Camacho, R., de la Rosa, J., de la Campa, A. M. S., Gonzalez-Castanedo, Y., Alastuey, A., Querol, X., and Rodriguez, S.: Geochemical characterization of Cu-smelter emission plumes with impact in an urban area of SW Spain, Atmos Res, 96, 590-601, 2010a.

Hings, S. S.: Characterization and Field Deployment of a Novel Quantitative Time-of-Flight Aerosol Mass Spectrometer (ToF-AMS), PhD, Fachbereich Physik, Mathematik und Informatik, Johannes Gutenberg-Universität Mainz, 2006.

Hoffmann, T., Zetzsch, C., Rossi, M. J.: Chemie von Aerosolen, Chem. Unserer Zeit, 41, 232-246, 2007.

Huffman, J. A., Jayne, J. T., Drewnick, F., Aiken, A. C., Onasch, T., Worsnop, D. R., and Jimenez, J. L.: Design, modeling, optimization, and experimental tests of a particle beam width probe for the aerodyne aerosol mass spectrometer, Aerosol Sci. Technol., 39, 1143-1163, 2005.

Jaenicke, R.: Aerosol physics and chemistry, in: Landholt-Börnstein, Zahlenwerte und Funktionen aus Naturwissenschaft und Technik, edited by: Fischerr, G., Springer-Verlag, Berlin, 391-457, 1988.

Jaenicke, R.: Abundance of cellular material and proteins in the atmosphere, Science, 308, 73-73, DOI 10.1126/science.1106335, 2005.

Jimenez, J. L., Canagaratna, M. R., Donahue, N. M., Prevot, A. S. H., Zhang, Q., Kroll, J. H., DeCarlo, P. F., Allan, J. D., Coe, H., Ng, N. L., Aiken, A. C., Docherty, K. S.,

Ulbrich, I. M., Grieshop, A. P., Robinson, A. L., Duplissy, J., Smith, J. D., Wilson, K. R., Lanz, V. A., Hueglin, C., Sun, Y. L., Tian, J., Laaksonen, A., Raatikainen, T., Rautiainen, J., Vaattovaara, P., Ehn, M., Kulmala, M., Tomlinson, J. M., Collins, D. R., Cubison, M. J., Dunlea, E. J., Huffman, J. A., Onasch, T. B., Alfarra, M. R., Williams, P. I., Bower, K., Kondo, Y., Schneider, J., Drewnick, F., Borrmann, S., Weimer, S., Demerjian, K., Salcedo, D., Cottrell, L., Griffin, R., Takami, A., Miyoshi, T., Hatakeyama, S., Shimono, A., Sun, J. Y., Zhang, Y. M., Dzepina, K., Kimmel, J. R., Sueper, D., Jayne, J. T., Herndon, S. C., Trimborn, A. M., Williams, L. R., Wood, E. C., Middlebrook, A. M., Kolb, C. E., Baltensperger, U., and Worsnop, D. R.: Evolution of Organic Aerosols in the Atmosphere, Science, 326, 1525-1529, 10.1126/science.1180353, 2009.

Kanakidou, M., Seinfeld, J. H., Pandis, S. N., Barnes, I., Dentener, F. J., Facchini, M. C., Van Dingenen, R., Ervens, B., Nenes, A., Nielsen, C. J., Swietlicki, E., Putaud, J. P., Balkanski, Y., Fuzzi, S., Horth, J., Moortgat, G. K., Winterhalter, R., Myhre, C. E. L., Tsigaridis, K., Vignati, E., Stephanou, E. G., and Wilson, J.: Organic aerosol and global climate modelling: A review, Atmos. Chem. Phys., 5, 1053-1123, 2005.

Penner, J. E., Hegg, D., and Leaitch, R.: Unraveling the role of aerosols in climate change, Environ. Sci. Technol., 35, 332a-340a, 2001.

Querol, X., Alastuey, A., de la Rosa, J., Sanchez-de-la-Campa, A., Plana, F., and Ruiz, C. R.: Source apportionment analysis of atmospheric particulates in an industrialised urban site in southwestern Spain, Atmos. Environ., 36, 3113-3125, 2002.

Querol, X., Alastuey, A., Rodriguez, S., Viana, M. M., Artinano, B., Salvador, P., Mantilla, E., do Santos, S. G., Patier, R. F., de La Rosa, J., de la Campa, A. S., Menendez, M., and Gil, J. J.: Levels of particulate matter in rural, urban and industrial sites in Spain, Sci. Total Environ., 334, 359-376, 2004.

Ramanathan, V., Crutzen, P. J., Kiehl, J. T., and Rosenfeld, D.: Aerosols, Climate, and the Hydrological Cycle, Science 294, 2119-2124, and Supplemental Data, 2001.

Schneider, J., Weimer, S., Drewnick, F., Borrmann, S., Helas, G., Gwaze, P., Schmid, O., Andreae, M. O., and Kirchner, U.: Mass spectrometric analysis and aerodynamic properties of various types of combustion-related aerosol particles, Int. J. Mass Spectrom., 258, 37-49, 10.1016/j.ijms.2006.07.008, 2006.

Schulz, M., de Leeuw, G., and Balkanski, Y.: Sea-salt aerosol source functions and emissions, in: Emissions of atmospheric trace compounds, edited by: Granier, C., Artaxo, P., and Reeves, C. E., Advances in global change research, Kluwer Academic Publishers, Dortrecht, The Netherlands, 333-360, 2004.

Seinfeld, J. H., and Pandis, S. N.: Atmospheric Chemistry and Physics: From Air Pollution to Climate Change, 2nd ed., Wiley-Interscience, 2006.

Simoneit, B. R. T., Schauer, J. J., Nolte, C. G., Oros, D. R., Elias, V. O., Fraser, M. P., Rogge, W. F., and Cass, G. R.: Levoglucosan, a tracer for cellulose in biomass burning and atmospheric particles, Atmos. Environ., 33, 173-182, 1999.

Sun, J., Zhang, Q., Canagaratna, M. R., Zhang, Y., Ng, N. L., Sun, Y., Jayne, J. T., Zhang, X., Zhang, X. and Worsnop, D. R.: Highly time- and size-resolved characterization of submicron aerosol particles in Beijing using an Aerodyne Aerosol Mass Spectrometer, Atmos. Environ., 44, 131-140, 2010.

Ulbrich, I. M., Canagaratna, M. R., Zhang, Q., Worsnop, D. R., and Jimenez, J. L.: Interpretation of organic components from Positive Matrix Factorization of aerosol mass spectrometric data, Atmos. Chem. Phys., 9, 2891-2918, 2009.

von der Weiden, S. L., Drewnick, F., and Borrmann, S.: Particle Loss Calculator - a new software tool for the assessment of the performance of aerosol inlet systems, Atmospheric Measurement Techniques, 2, 479-494, 2009.

Zender, C.S., Miller, R.L., and Tegen, I.: Quantifying mineral dust mass budgets: Terminology, constraints, and current estimates, Eos Trans. Amer. Geophys. Union, 85(48), 509, 512, 2004.

Zhang, Q., Alfarra, M. R., Worsnop, D. R., Allan, J. D., Coe, H., Canagaratna, M. R., and Jimenez, J. L.: Deconvolution and quantification of hydrocarbon-like and oxygenated organic aerosols based on aerosol mass spectrometry, Environ. Sci. Technol., 39, 4938-4952, 10.1021/es048568I, 2005.

Zhang, Q., Jimenez, J. L., Canagaratna, M. R., Ulbrich, I. M., Ng, N. L., Worsnop, D. R., Sun, Y.: Understanding atmospheric organic aerosols via factor analysis of aerosol mass spectrometry: a review, Anal. Bioanal. Chem., 401 (10), 3045-3067, 2011.

Zorn, S. R., Drewnick, F., Schott, M., Hoffmann, T., and Borrmann, S.: Characterization of the South Atlantic marine boundary layer aerosol using an aerodyne aerosol mass spectrometer, Atmos. Chem. Phys., 8, 4711-4728, 2008.

3

Results

3.1 Variability of aerosol, gaseous pollutants and meteorological characteristics associated with changes in air mass origin at the SW Atlantic coast of Iberia[1]

J.-M. Diesch[1], F. Drewnick[1], S. R. Zorn[1,*], S.-L. von der Weiden-Reinmüller[1], M. Martinez[2] and S. Borrmann[1, 3]

[1] Particle Chemistry Department, Max Planck Institute for Chemistry, Mainz, Germany

[2] Atmospheric Chemistry Department, Max Planck Institute for Chemistry, Mainz, Germany

[3] Institute for Atmospheric Physics, Johannes Gutenberg University Mainz, Mainz, Germany

[*] now at: AeroMegt GmbH, Hilden, Germany

Published in Atmospheric Chemistry and Physics, Volume 12, 1-22, doi: 10.51947/acp-12-1-2012

Abstract

Measurements of the ambient aerosol were performed at the Southern coast of Spain, within the framework of the DOMINO (*Diel Oxidant Mechanisms In relation to Nitrogen Oxides*) project. The field campaign took place from November 20 until December 9, 2008 at the atmospheric research station "El Arenosillo" (37° 5´ 47.76" N, 6° 44´ 6.94" W). As the monitoring station is located at the interface between a natural park, industrial cities (Huelva, Seville) and the Atlantic Ocean a variety of physical and chemical parameters of aerosols and gas phase could be characterized in dependency on the origin of air masses. Backwards trajectories were examined and compared with local meteorology to classify characteristic air mass types for several source regions. Aerosol number and mass as well as polycyclic aromatic hydrocarbons and black carbon concentrations were measured in PM_1 and size distributions were registered covering a size range from 7 nm up to 32 μm. The chemical composition of the non-refractory submicron aerosol (NR-PM_1) was measured by means of an Aerosol Mass Spectrometer (Aerodyne HR-ToF-AMS). Gas phase analyzers monitored various trace gases (O_3, SO_2, NO, NO_2, CO_2) and a weather station provided meteorological parameters.

Lowest average submicron particle mass and number concentrations were found in air masses arriving from the Atlantic Ocean with values around 2 μg m^{-3} and 1000 cm^{-3}. These mass concentrations were about two to four times lower than the values recorded in air masses of

[1] Original text and figures published in Atmospheric Chemistry and Physics.

continental and urban origins. For some species PM_1-fractions in marine air were significantly larger than in air masses originating from Huelva, a closely located city with extensive industrial activities. The largest fraction of sulfate (54%) was detected in marine air masses and was to a high degree not neutralized. In addition small concentrations of methanesulfonic acid (MSA), a product of biogenic dimethyl sulfate (DMS) emissions could be identified in the particle phase.

In all air masses passing the continent the organic aerosol fraction dominated the total NR-PM_1. For this reason, using Positive Matrix Factorization (PMF) four organic aerosol (OA) classes that can be associated with various aerosol sources and components were identified: a highly-oxygenated OA is the major component (43% OA) while semi-volatile OA accounts for 23%. A hydrocarbon-like OA mainly resulting from industries, traffic and shipping emissions as well as particles from wood burning emissions also contribute to total OA and depend on the air mass origin. A significant variability of ozone was observed that depends on the impact of different air mass types and solar radiation.

3.1.1 Introduction

Studying tropospheric aerosols is becoming increasingly important as they influence the Earth´s climate (IPCC, 2007), continental, urban and marine ecosystems and visibility (Querol et al., 2009). In addition they can have a significant influence on human health (Pope and Dockery, 2006). To study the influence of natural and anthropogenic pollutants emitted by local and regional sources measurement campaigns at remote sites are required where the complex mixture of components in the atmosphere can be observed. This mixture depends on the various source regions influencing the measurement site as well as their distance, since chemical and physical processing takes place in an air mass during transport. In addition, particularly in Southern Europe, the season plays an important role. In the summer months African dust outbreaks, re-circulation of air masses, strong photochemistry and long-range transport from NW Europe or Western Iberia (Sanchez de la Campa et al., 2007; Pey et al., 2008) affect the atmospheric composition and levels. The SW of Spain lies next to the Atlantic Ocean and the Strait of Gibraltar, a major ship route. There are several large towns and cities, the largest of them Seville, important ports like the one of Huelva, as well as large agricultural plantations and forests.

The air quality close to the heavily industrialized area around the city of Huelva is significantly degraded at times. Epidemiological studies (CSIC, 2002) as well as the distribution of cancer incidents in Spain (Benach et al., 2003) suggest that certain kinds of cancers (e.g. lung cancer) occur in this region at an elevated rate. Therefore, a number of studies were performed, mainly in and around Huelva to evaluate the impact of industrial emissions and their characterization in terms of the chemical composition and potential origin (Fernandez-Camacho et al., 2010b; de la Rosa et al., 2010; Perez-Lopez et al., 2010; de la Campa et al., 2011; Toledano et al., 2009). In addition, the interaction of high solar radiation levels as they occur in Andalusia together with elevated anthropogenic and natural ozone precursor emissions lead to enhanced photochemical ozone production that can be measured downwind of industrialized regions where the ozone precursor substances are emitted (Adame et al., 2010a,b; Adame et al., 2008).

So far no comprehensive studies investigating the chemical composition of aerosol particles in conjunction with measurements of a variety of trace gases were conducted in Southern Spain. The aim of this study is to present a detailed investigation of the variability of aerosol, trace gas characteristics and meteorological conditions depending on continental, urban and marine sources surrounding the measurement site in "El Arenosillo". Backwards trajectories were calculated and

compared to local meteorology to classify different air mass categories. The non-refractory submicron aerosol composition was determined depending on the air mass categories. The sulfate fraction was further investigated regarding aerosol acidity for the individual air mass types. A focus is also on organic components of the aerosol, their sources and variations. Furthermore, the dependence of the diurnal ozone variation associated with meteorological conditions and different air masses was analyzed.

3.1.2 Overview of the 2008 DOMINO campaign

The 2008 DOMINO (*Diel Oxidant Mechanisms In relation to Nitrogen Oxides*) research campaign took place from the 20th of November until the 9th of December at the atmospheric research station "El Arenosillo" (37° 5´ 47.76" N, 6° 44´ 6.94" W) in the southwest of Spain (Fig. 3.1a), operated by the INTA (National Institute for Aerospace Technology). The main objective of the campaign was to characterize the oxidative capacity of the troposphere. For this reason, the focus was to study the atmospheric oxidation chemistry, to compare the radical and nighttime chemistry and to characterize the self-cleaning efficiency of the atmosphere in different air mass types. Our contribution to this project was the investigation of the aerosol particle chemistry, composition, formation and transformation processes. Therefore, we measured a large number of atmospheric parameters simultaneously.

The "El Arenosillo" research station lies within a Protected Natural Area in between 3 very different source regions: the Atlantic Ocean, the town of Huelva (20 km distance) and the nearby National Park of Doñana. The Atlantic Ocean itself has relatively low levels of pollutants, however there are shipping emissions from heavy ship traffic in the Strait of Gibraltar (Pey et al., 2008). Huelva is a highly industrialized town with three large chemical estates where fertilizer production industries, petrochemical industries, ammonia and urea industries as well as paper production industries are situated (Carretero et al., 2005; Alastuey et al., 2006; Querol et al., 2002; Querol et al., 2004; Fernandez-Camacho et al., 2010a). The nearby National Park of Doñana on the other hand is a Nature Preserve Park with a large variety of ecosystems and a unique biodiversity (de la Campa et al., 2009). Situated in the west of the Guadalquivir River, it is a UNESCO Biosphere Reserve and Heritage of Mankind consisting of marshlands, pine forests, preserves and moving sand dunes. Beyond it at 70 km distance from the site lies the city of Seville, the capital of Andalusia (population: 704,000). However it is less industrialized than Huelva (population: 149,000) which is located at the southwestern end of the Andalusian region and is surrounded by the rivers Odiel and Tinto and the Atlantic Ocean (Fig. 3.1c). The predominant wind directions at the station during the time the study took place are WSW, NW and NNE transporting air from Seville, Huelva, the Continent and the Atlantic Ocean to the measurement site (Fig. 3.1b).

In order to study the variability of the particle loading, composition, size distributions as well as trace gas and meteorological parameters in different types of air masses whose origin is well defined, the campaign was conducted in winter. This offers the advantage to achieve a better understanding of the characteristics, sources and processes as typical summer features in this part of Southern Europe are reduced: enhanced photochemistry or recirculation periods that typically occur in spring and summer seasons in this part of Southern Europe (Pey et al., 2008) would contribute to a more complex study scenario.

In the beginning of the campaign from 20th of November until the 3rd of December fair weather conditions with sunny days and clear sky prevailed. Therefore, a stable nocturnal boundary layer existed and low altitude emissions for example from Huelva were accumulated and measured at

elevated concentrations. Only on two nights (November, 28-29 and November, 29-30) short precipitation periods occurred which did not change the atmospheric composition significantly as the wind originated from the marine source region and concentrations remained as low as before. During the last 6 days of the campaign (December, 3-9), it was cloudy with nearly constant temperature, relative humidity and air pressure near ground.

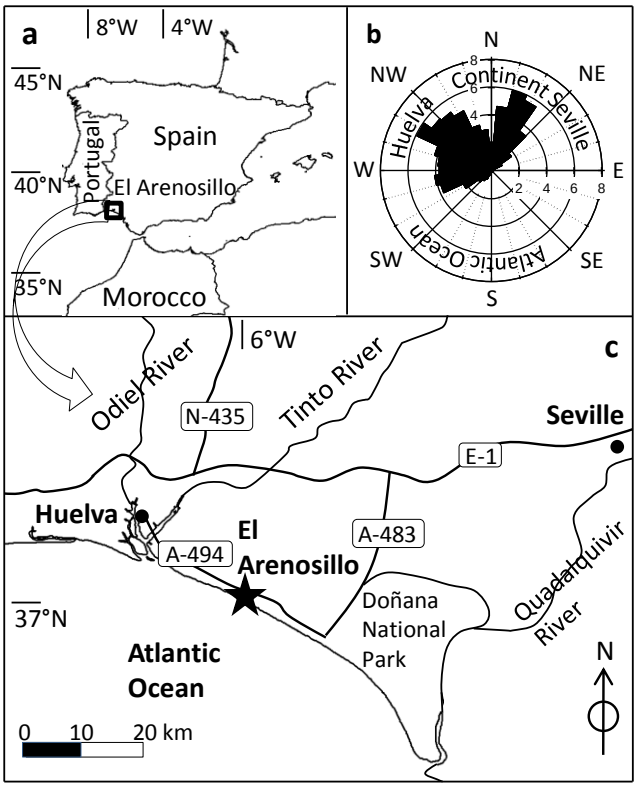

Figure 3.1: Map of Spain (a) showing the location of the field measurements (c) and an angular histogram of the wind directions recorded during the campaign (b).

3.1.2.1 Setup for ground based measurements of aerosol, gas phase species and meteorology

Key instrumentation

Measurements of the ambient aerosol and several trace gas mixing ratios were performed using MoLa, a mobile platform for aerosol research (Drewnick et al., 2012). During this campaign physical aerosol particle properties in PM_1 were detected by the ultrafine water-based Condensation Particle Counter in the 5 nm to 3 μm size range (CPC 3786, TSI, Inc.) as well as the Filter Dynamics Measurement System Tapered Element Oscillating Microbalance (FDMS-TEOM, Rupprecht & Patashnick Co., Inc.) (see Table 3.1). For particle size information, a Fast Mobility Particle Sizer (FMPS 3091, TSI, Inc.), an Aerodynamic Particle Sizer (APS 3321, TSI, Inc.) as well as an Optical Particle Counter (OPC 1.109, Grimm) were used to cover a particle size range from 7 nm until 32 μm. The chemical composition of the non-refractory (NR) aerosol in the submicron range was measured by means of a High-Resolution Time-of-Flight Aerosol Mass Spectrometer using the "V-mode" (HR-ToF-AMS, Aerodyne Res., Inc.). The black carbon concentration in PM_1 was determined by a Multi Angle Absorption Photometer (MAAP, Thermo E.C.) and polycyclic aromatic hydrocarbons on particles were appointed by the PAH-Monitor (PAS 2000, EcoChem. Analytics). MoLa is also equipped with two instruments to detect various trace gases. An Airpointer (Recordum GmbH) measures the gas phase species SO_2, CO, NO, NO_2 and O_3. CO_2 and H_2O

were monitored using a LICOR 840 gas analyzer (LI-COR, Inc.). A weather station (WXT 510, Vaisala) provided the most important weather parameters such as ambient temperature, relative humidity, air pressure, wind speed, wind direction and rain intensity.

Sampling setup

During the field campaign the roof inlet of MoLa, which is normally available for stationary measurements was used. Next to the roof inlet an extendable mast with the meteorological station was fixed, both for measurements in 10 meters height. Short branches were used to connect several instruments with the main inlet system. The sampling line is optimized for a flow rate of about 90 l min^{-1} and therefore a pump with flow control was used for regulating this flow independant of the set of instruments operating. The inlet was optimized and characterized for transport losses and sampling artifacts (von der Weiden et al., 2009). One of the main characteristics is the occurring aerosol particle loss. Table 3.1 contains particle loss information for all instruments calculated using the *Particle Loss Calculator* (von der Weiden et al., 2009). While particle losses have a maximum of 45% for 20 µm particles for the APS, for all other instruments used during the campaign maximum particle losses are below 25%. The respective losses are relatively small in the size range where the majority of relevant data for this work is collected: In the size range from 30 nm to 2 µm calculated particle losses are below 3% (without regarding the AMS: <8%). Therefore the occurring particle loss can be neglected since they do not influence the measurement results significantly and the ambient aerosol was measured mostly unbiased in this range.

Transport times through the sampling line differ slightly for the individual instruments, so the sampling and measurement times are not identical. Therefore the time stamp for each instrument has to be corrected dependent on the residence time of the aerosol in the tube system. The calculated delays for all instruments were subtracted from the time stamps to get the correct sampling time. The sampling delays for the individual instruments are also presented in Table 3.1. The time resolution used for this analysis was 1 min for all instruments beside the TEOM which generated 15 min data.

Quality assurance for aerosol chemical composition measurements

For data quality assurance a variety of calibrations of the AMS were performed before and during the campaign. A particle Time-of-Flight calibration was accomplished prior to the campaign, used to convert particle flight times into the corresponding particle diameters. For determination of the instrument background and several distinct instrument parameters, measurements using a high-efficiency particulate air (HEPA) filter as well as a calibration of the Ionization efficiency (IE) of the ion source were conducted once a week. The sensitivity of the detector was monitored permanently and calibrated frequently as well.

A collection efficiency (CE) factor (Huffman et al., 2005) has to be determined to account for the fraction of particles that are not detected as they bounce off the vaporizer before evaporation and to correct for incomplete transmission of particles through the inlet of the instrument. Usually this factor is determined by comparing AMS measurements with results from other instruments or filter measurements. This factor usually ranges between 0.5 (for 50% particle loss) and 1 (no bounce) and depends mainly on the measurement conditions, for example relative humidity or particle composition. For the DOMINO campaign, a CE factor of 0.5 for the AMS mass concentrations (organics, sulfate, nitrate, ammonium and chloride) was used. When using this typical CE factor, the time series of the ToF-AMS mass concentrations summed with the MAAP black carbon mass concentrations show a good agreement with TEOM PM_1 mass concentrations (ratio $PM_{AMS+MAAP}/PM_{TEOM} = 0.97$, $R^2=0.6$).

Table 3.1: Summary of measured quantities, size ranges and the corresponding particle losses, sampling time delays and detection limits for the instruments implemented in the mobile laboratory (MoLa). Particle losses within the given size range boundaries are lower than those provided here; therefore the given losses are upper limits.

Measurement Instrument	Measured Quantity	Size Range/ (Particle losses)	Sampling Delay	Detection Limits/Accuracy
AMS Aerosol Mass Spectrometer	size-resolved Aerosol Chemical Composition	40 nm (6%) – 600 nm (2%) (vacuum aerodynamic diameter)	43 s	sulfate: 0.04 µg m^{-3} nitrate: 0.02 µg m^{-3} ammonium: 0.05 µg m^{-3} chloride: 0.02 µg m^{-3} organics: 0.09 µg m^{-3}
MAAP Multi Angle Absorption Photometer	Black Carbon Particle Mass Concentration	10 nm (4%) – 1 µm (0.2%)	7 s	0.1 µg m^{-3}
PAH-Sensor Polycyclic Aromatic Hydrocarbons Sensor	total PAH Mass Concentration	10 nm (11%) – 1 µm (0.3%)	8 s	1 ng m^{-3}
CPC Condensation Particle Counter	Particle Number Concentration	5 nm (25%) – 3 µm (0.8)	7 s	N/A
TEOM Tapered Element Oscillating Microbalance	Particle Mass Concentration (PM_1)	< 1 µm (0.5-9%)	9 s	2.5 µg m^{-3}
FMPS Fast Mobility Particle Sizer	Particle Size Distribution based on Electrical Mobility	7 nm (9%) – 523 nm (0.1%) (D_{mob})	7 s	N/A
APS Aerodynamic Particle Sizer	Particle Size Distribution based on Aerodynamic Sizing	0.37 µm (0.1%) – 20 µm (45%) (D_{aero})	7 s	N/A
OPC Optical Particle Counter	Particle Size Distribution based on Light Scattering Cross Section	0.25 µm (0.05%) – 32 µm (0.002%) (D_{opt})	8 s	N/A
Airpointer	O_3, SO_2, CO and NO, NO_2 Mixing Ratio	N/A	6 s	O_3: < 1.0 nmol mol^{-1} SO_2: < 1.0 nmol mol^{-1} CO: < 0.08 µmol mol^{-1} NO_x: < 2.0 nmol mol^{-1}
LICOR LI840	CO_2 and H_2O Mixing Ratio	N/A	8 s	CO_2: 1 µmol mol^{-1} (accuracy) H_2O: 0.01 pmol mol^{-1}
Met. Station	Wind speed & Direction Temperature, RH, Rain intensity, Pressure	N/A	0 s	N/A

During normal operation, the AMS collected averaged high resolution mass spectra and species-resolved size distributions by alternating through the related operation modes, spending 50% of the sampling time in each mode. The detection limits (LOD, Table 3.1) for each species were evaluated on the basis of the method described by Drewnick et al. (2009). They are defined as:

$$\mathrm{LOD} = 3 \cdot \sqrt{2} \cdot \sigma(\mathrm{I}) \tag{3.1}$$

with $\sigma(I)$ the standard deviation of the background signals of the respective species.

3.1.2.2 Back trajectories and air mass classification

To classify different source regions that are reflected in the aerosol and trace gas composition of the air arriving at the measurement site, 48 h back trajectories at 10 m arrival height above ground level were calculated for every 2 h during the whole campaign using the HYSPLIT (*Hybrid Single Particle Lagrangian Integrated Trajectory*) model (Draxler and Rolph, 2003). To analyze the measured data of chemical and physical aerosol particle properties as well as gas phase parameters that are associated with different source regions the whole dataset was divided according to back trajectories that correspond to similar air mass histories. For this assignment we assume that the respective data one hour before the arrival time and one hour thereafter "belong" to each trajectory and associate these data in the further analysis with the source region defined by the trajectory. Fig. 3.2 shows a map including back trajectories classified into 6 air mass categories based on air mass origins and pathways. The resulting air mass categories with the corresponding angles of the limiting trajectory arrival directions as well as the measurement time in percent of the entire measurement period are:

- "Seville" (65°-82°, 6%)
- "Continental" (340°-65°, 15%)
- "Portugal+Huelva" (310°-328°, 3%)
- "Marine+Huelva" (285°-310°, 18%)
- "Portugal+Marine" (265°-285°, 15%)
- "Marine" (140°-265°, 6%).

To be classified as "Seville" calculated back trajectories had to cross Seville (latitude and longitude for "Seville" category borders: 37°16´11´´N, 5°54´33´´W and 37°24´55´´N, 6°5´1´´W) before approaching the measurement site. Air masses labeled as "Continental" contain air transported from Spanish inland areas over pine and eucalyptus forests to the station. While "Portugal+Huelva" trajectories mainly travel over Portugal before passing Huelva and then the site, trajectories corresponding to "Marine+Huelva" firstly travelled over the Atlantic Ocean (Huelva category borders: 37°19´1´´N, 6°50´36´´W and the coastline). In contrast to "Portugal+Huelva" air masses with trajectories spreading preferentially over the northern part of Huelva city, "Marine+Huelva" trajectories extend over the whole area of the city. Finally, the fifth ("Portugal+Marine") and sixth ("Marine") category include marine influenced air masses with the difference that "Portugal+Marine" trajectories also passed Portugal. For each air mass type aerosol as well as gas phase and meteorological parameters were analyzed separately. In total, 63% of the measured data were considered in our examinations. The remaining data are associated with trajectories that passed along the boundaries of the categories and cannot reliably be associated with any of the six categories.

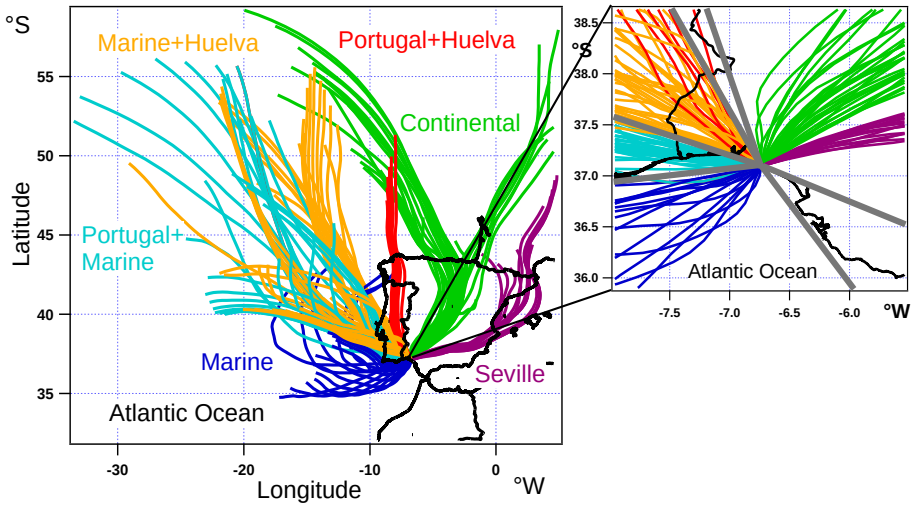

Figure 3.2: On the left side a map of the Iberian Peninsula is shown including 48 h backwards trajectories calculated for every 2 hours using HYSPLIT. The zoom-in at the right shows the transport direction of the classified air mass types at the measurement site. 6 air mass categories corresponding to different source regions were separated: "Seville" (purple), "Continental" (green), "Portugal+Huelva" (red), "Marine+Huelva" (orange), "Portugal+Marine" (light blue), "Marine" (blue).

HYSPLIT is intended for transport processes on larger spatial scales due to its relatively low grid resolution. Especially for lower trajectory altitudes the model suffers from severe limitations. Therefore, under the influence of mesoscale processes, HYSPLIT is not able to reproduce local meteorology adequately. However, during the DOMINO campaign synoptic conditions dominated also regional transport which can therefore be reproduced sufficiently accurate down to the lower boundary layer by HYSPLIT calculations as was shown by thorough sensitivity analyses and comparison to measurement data (personal communication, J. A. Adame Carnero, 2012).

As second approach for the identification of the air mass origin local meteorology was used measured at the sampling site. Here the whole measured data set was divided into different sectors according to the wind direction registered by the meteorological station in 10 m height. In order to avoid associating stagnant air masses with potential contamination from local sources with individual source sectors all data measured during times with wind speeds below 1 m s^{-1} were not used for further processing. Hereafter, 3 different source regions associated with individual wind directions were identified, called "Continental", "Urban" and "Marine".

In Fig. 3.3 locally measured wind direction data were compared for both classification methods. The three different wind direction ranges of the "Continental" (340°-110°), "Urban" (285°-330°) and "Marine" (140°-265°) sectors are shown as grey shaded areas. Red colored box plots reflect the local wind directions measured during the arrival times of the back trajectories associated with various air mass categories. For the "Seville", "Continental", "Marine+Huelva" and "Marine" air mass categories the measured wind directions agree quite well with the wind sectors associated with the same source regions. Contrary, measured wind directions of the "Portugal+Marine" air masses are not located within any of the wind direction ranges because this air mass type could not be separated using the wind direction method since a gap had to be selected between land (Huelva) and marine influenced air masses. For the "Portugal+Huelva" and "Marine+Huelva" air mass categories the directions of the trajectories differ slightly but systematically from locally measured wind directions because registered wind directions are influenced by the land-sea-circulation. This effect results in wind directions measured at the site, which was located directly at the shore,

oriented further south – compared to the direction of the trajectories – during daytime while during the night they are rotated more towards the north.

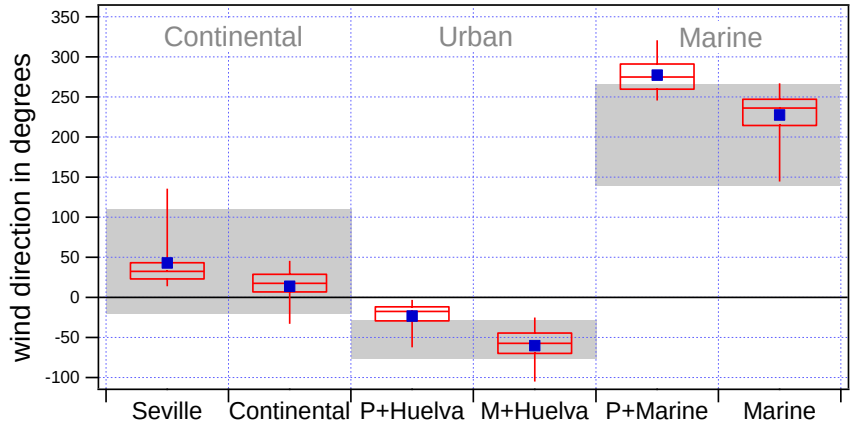

Figure 3.3: Comparison of wind directions associated with the classified air mass categories (HYSPLIT) with wind direction ranges used for the identification of the three sectors. The wind directions associated with the HYSPLIT air mass categories are presented as box plots (blue marker: mean, box: 25-75% percentiles with median, whiskers: 5% and 95% percentiles) while the wind direction ranges are shown as grey shaded area.

In summary, the classification of air mass types made on the basis of back trajectories is more robust than that based on wind directions. HYSPLIT enables a more exact apportionment of air masses as it considers not only local conditions but also regional and long-range transport influences. However, both methods of associating measurement data to source regions provide similar results when regarding both "Huelva"-related air mass categories as "Urban" and the "Seville" and "Continental" air mass categories as "Continental". Although very similar results are obtained with both methods the use of HYSPLIT to identify air masses gives the possibility to separate the data into additional air mass types that cannot be identified on the basis of wind directions alone (e.g. "Seville").

In Fig. 3.4 time series for several of the measured parameters that are discussed below are shown for the whole campaign. The time intervals associated with the classified air mass categories are indicated as shaded areas in different colors. As shown in this figure, for the "Continental", "Marine+Huelva" and "Portugal+Marine" air mass categories the air mass origin persisted over relatively long periods on several days. Therefore the influx from other source regions into these air masses is very unlikely. On the other hand, the "Portugal+Huelva" category was registered only for short time intervals and only on a single day. Therefore for this air mass category, influx from other source regions by re-circulation of air masses in varying wind fields cannot be excluded, even though the back trajectories do not show any evidence for this effect. The "Seville" category was measured during two approximately half-day long periods on two different days. Significant differences in the measured parameters have been found for the two time intervals because different phases of new particle formation events have been probed during these times. However, even though mixing with "Continental" air masses is likely, the increased concentrations measured during these two periods, compared to typical "Continental" concentrations, suggest that actually air masses that at least partially passed Seville have been probed here. Generally both "Marine" periods show very similar evolution of the measured time series, characterized by low concentrations over extended time intervals. During the early phase of the first period increased concentrations of some aerosol parameters could be an indication of re-circulation of continentally influenced air masses. However, also ship emissions could be the cause of these elevated

concentrations. Land-sea breeze has been identified to slightly twist locally measured wind directions when air is flowing along the coastline. However, its effect seems to be sufficiently small to prevent significant mixing of marine and continentally influenced air masses in the identified source categories. As also shown in Fig. 3.4, the highest concentrations observed on Nov 28, 2011 were not considered in the study due to an air mass change occurring during this time. Trajectories for this time period show a complex path and a trend, moving further to the West from hour to hour. Therefore, they were not classified into one of the categories. A more in-depth analysis of the influence of topography and transport height on trajectory calculations was performed by scientists of INTA (National Institute for Aerospace Technology) and will be published elsewhere.

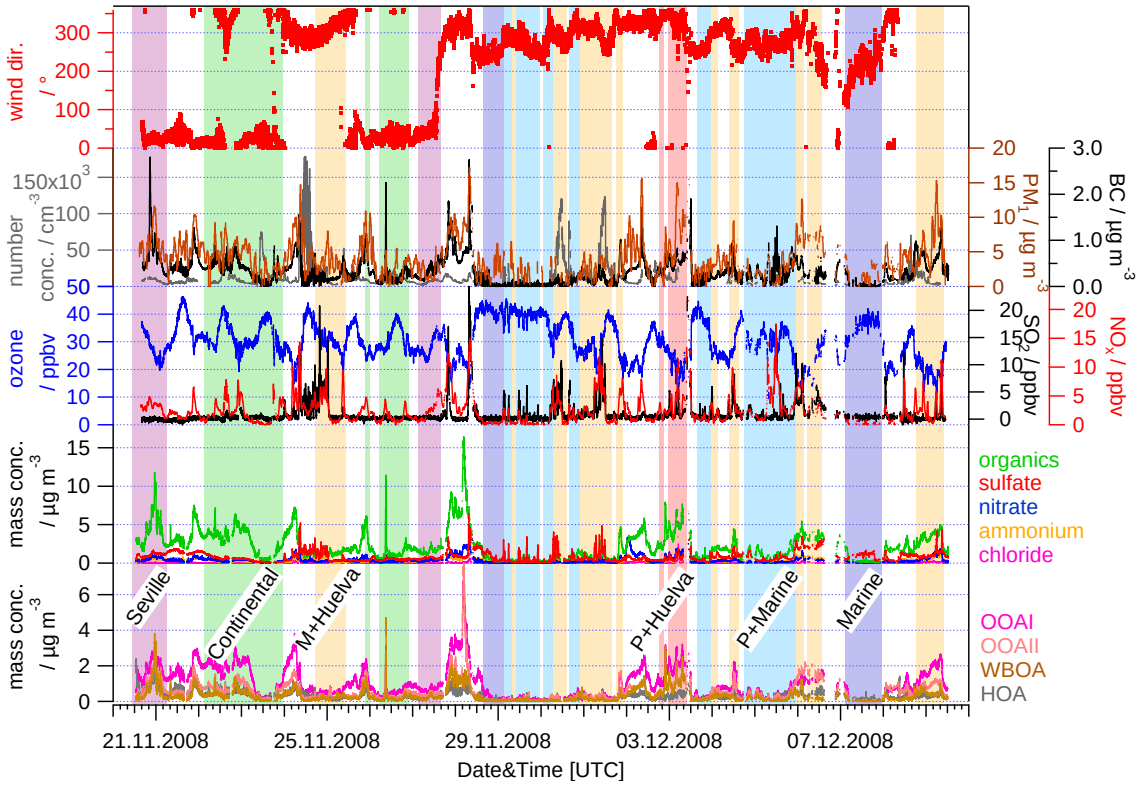

Figure 3.4: Time series of several parameters (wind direction (red), number (grey) and PM_1 mass (brown) concentrations, black carbon (black), ozone (blue), sulfur dioxide (SO_2, black), nitrogen oxide (NO_x, red), AMS species (organics (green), sulfate (red), nitrate (blue), ammonium (orange), chloride (purple), OOAI (purple), OOAII (salmon), WBOA (brown), HOA (grey)) measured during the DOMINO campaign and discussed in the paper. The classified air mass categories are indicated as shaded areas behind the traces ("Seville" (purple), "Continental" (green), "Portugal+Huelva" (red), "Marine+Huelva" (orange), "Portugal+Marine" (light blue), "Marine" (blue)).

3.1.3 Results

3.1.3.1 Aerosol composition of selected air mass categories

PM_1 concentrations: The chemical composition of the submicron aerosol, divided into the most common AMS species (organics, sulfate, nitrate, ammonium, chloride) and black carbon (BC) is presented for each of the air masses in Table 3.2 and in the pie charts of Fig. 3.5. Here the total PM_1 mass concentrations are defined as the sum of all AMS and BC mass concentrations. The lowest average PM_1 mass concentration was found in air masses transported over the Atlantic Ocean (1.7±1.1 μg m^{-3}) (see Table 3.2). This value was about two to four times lower than the values recorded in air masses of "Continental" (3.9±2.6 μg m^{-3}) and urban ("Huelva"/"Seville", 4.0±3.1 and 6.9±3.4 μg m^{-3}) origins. Even though the difference in PM_1 concentrations is not significant within the one standard deviation boundaries, the trend is clearly evident. Despite the large variability within each category the values for the air from the Atlantic Ocean largely differ from those of the other two categories. Regarding the whole campaign, total PM_1 average mass concentrations were 4.0±2.5 μg m^{-3} while black carbon contributes 7.9% (0.32 μg m^{-3}) to this value.

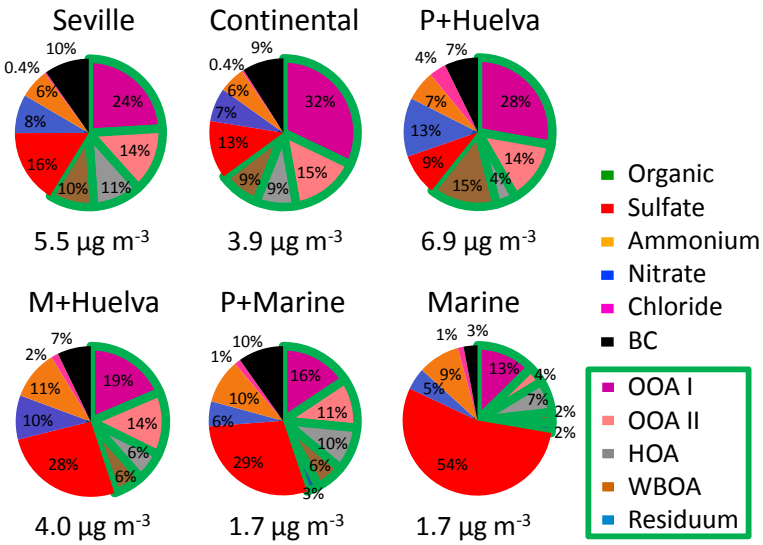

Figure 3.5: Pie charts of the submicron aerosol composition of the PM_1 for each air mass type consisting of organics (green), sulfate (red), ammonium (orange), nitrate (blue), chloride (purple) and black carbon (black). Organic material was further separated into OOA I (dark purple), OOA II (salmon), HOA (grey) and WBOA (brown) using PMF. The residuum (light blue) cannot be associated with any of these sources or components.

Particulate organics: Firstly, we note that the organics, sulfate and nitrate NR-PM_1 (non-refractory particulate matter with $d_p \leq 1$ μm) aerosol concentrations show the most significant levels and also the most contrasting variations dependent on air mass origin. Therefore they largely determine the chemical character of the aerosol. The highest organic matter fraction (64%) was measured in the "Continental" air mass category. Biogenic precursor emissions in addition to emissions from frequent biomass burning activities originating from the surrounding pine and eucalyptus forests and the agricultural fields were transported downwind towards the coastal measurement site and generate secondary organic aerosol mass. In addition, anthropogenic sources also result in the generation of organic particulate matter. While the consistently high organics content is the dominant fraction in all air masses that passed the continent, in the "Marine" category sulfate plays the major role. To distinguish between different types of organics and to gain

further insights into sources and processes affecting the organic composition results of a factor analysis study are presented in section 3.4.

Non-sea-salt particulate sulfate: Generally, sulfate is a more regionally influenced component. While in "Continental" influenced air masses 13% (0.49±0.27 μg m^{-3}) of PM_1 consists of "sulfate", in the "Marine+Huelva" air mass category a fraction of 28% (1.1±0.81 μg m^{-3}) was registered. In the marine boundary layer (MBL) sulfur compounds are quite common (Charlson et al., 1987; Zorn et al., 2008) as the ocean is a large source for atmospheric sulfur (Barnes et al., 2006). In addition, shipping emissions of marine transport in the Strait of Gibraltar play an important role as reported by Pey et al. (2008). Therefore, "sulfate" is the most abundant species of the "Marine" submicron non-refractory aerosol with a fraction of 54% (0.91±0.43 μg m^{-3}). The "sulfate" aerosol is further characterized (see section 3.3) by analyzing the acidity since it affects aerosol hygroscopic growth, toxicity and heterogeneous reactions (Sun et al., 2010).

Particulate nitrate: As a result of a wide variety of industrial and traffic emission sources located in Huelva, nitrate formed by photochemical oxidation of nitrous oxides is the major inorganic fraction of the aerosol composition in the "Portugal+Huelva" (13%, 0.88±0.50 μg m^{-3}) air mass category. While in "Marine+Huelva" (9.5%, 0.38±0.36 μg m^{-3}) and "Seville" (8.4%, 0.46±0.22 μg m^{-3}) air masses nitrate occurs as second most abundant inorganic fraction. It is well known that nitrate is a major content in fine particles from cities, urban and industrial regions (Takami et al., 2005). In addition, source apportionment studies conducted in the Andalusian region showed higher average nitrate values in stations with a high traffic influence (de la Rosa et al., 2010). However, ammonium nitrate is volatile and reacts quickly during transport (Takami et al., 2005). The large variability of concentrations within the air mass categories is caused by the different kinds of emissions from short distances and changing wind directions.

Particulate ammonium: As a major fraction of total inorganic species, nitrate is followed by ammonium in all air mass types except both "Marine" categories where even less nitrate than ammonium was observed. Nevertheless, ammonium precursor sources in the marine boundary layer (Jickells et al., 2003) are not sufficiently abundant to neutralize the present sulfate. For the continentally influenced air masses instead, sources of ammonium include agricultural activities, manures, biomass burning or soils (Bouwman et al., 1997; Hock et al., 2008). The fertilizer production industries in Huelva (Perez-Lopez et al., 2010) provide an increased delivery of ammonia (Carretero et al., 2005) resulting in highest ammonium concentrations in "Portugal+Huelva" (0.45±0.38 μg m^{-3}) and "Marine+Huelva" (0.43±0.33 μg m^{-3}) air masses.

Particulate chloride: The measured chloride content is in the order of 0.4% to 3.6% within all air masses. However, average chloride values are not dominant in the "Marine" air mass categories as the ToF-AMS cannot measure sea salt (sodium chloride) with significant efficiency (Zorn et al., 2008). In contrast, both "Portugal+Huelva" (3.6%; 0.25±0.55 μg m^{-3}) and "Marine+Huelva" (1.6%, 0.062±0.060 μg m^{-3}) air masses are influenced by industrial emissions (e.g. organic chloride species) likely responsible for up to nine times enhanced PM_1 chloride concentrations compared to "Continental" (0.41%; 0.016 ±0.047 μg m^{-3}) air mass types. Lowest chloride values were registered in the "Seville" category (0.36%, 0.020±0.020 μg m^{-3}). Since the measured chloride concentrations are either below the detection limit (0.02 μg m^{-3}) or the resulting mass concentrations show large variability we cannot identify clear differences within the individual source categories for this species.

Table 3.2: Averaged submicron mass concentrations and fractions of total PM_1 for the common HR-ToF-AMS species and black carbon within the categorized air masses. For each category the total time of measurements is listed that are used for the evaluation. For each species, standard deviations are listed as an estimate for the inner-category variability.

in µg m^{-3}	Seville 26 h	Continental 60 h	P+Huelva 11 h	M+Huelva 75 h	P+Marine 59 h	Marine 26 h
AMS-Org	3.2±2.2	2.5±1.7	4.2±1.5	1.8±1.3	0.78±0.63	0.46±0.42
%	58	64	61	45	46	27
AMS-SO_4	0.88±0.29	0.49±0.27	0.62±0.33	1.1±0.81	0.50±0.44	0.91±0.43
%	16	13	9.0	28	29	54
AMS-NH_4	0.35±0.12	0.22±0.11	0.45±0.38	0.43±0.33	0.17±0.15	0.15±0.089
%	6.4	5.6	6.5	11	10	8.8
AMS-NO_3	0.46±0.22	0.29±0.18	0.88±0.50	0.38±0.36	0.094±0.078	0.080±0.054
%	8.4	7.4	13	9.5	5.5	4.7
AMS-Chl	0.020±0.020	0.016±0.047	0.25±0.55	0.062±0.060	0.023±0.027	0.022±0.024
%	0.36	0.41	3.6	1.6	1.4	1.3
BC	0.54±0.43	0.35±0.24	0.5±0.14	0.29±0.23	0.17±0.17	0.050±0.082
%	9.8	9.0	7.2	7.3	10	2.9
Total Conc. µg m^{-3}	**5.5**±3.3	**3.9**±2.6	**6.9**±3.4	**4.0**±3.1	**1.7**±1.5	**1.7**±1.1
TEOM Conc. µg m^{-3}	**4.4**±2.8	**3.3**±2.5	**6.4**±3.6	**4.2**±2.8	**2.1**±1.4	**2.2**±1.4

Black carbon: The influence of air mass histories is also evident in average black carbon (BC) mass concentrations. Enhanced average BC fractions were measured in polluted Huelva (7%) and "Continental" (9%) air masses (see Table 3.2) while lowest BC mass fractions occur in the "Marine" (3%) influenced air mass category, being typically below the detection limit (0.1 µg m^{-3}). Therefore, an air mass history change leads to a change in measured BC mass concentrations at the site as well.

Aerosol mass concentrations: Fig. 3.6 illustrates the dependence of average mass concentrations measured with the TEOM (filled brown) and AMS+MAAP (hatched brown) in PM_1 as well as averaged aerosol number concentrations (CPC, grey) on air mass types. Although both mass concentrations are characterized by large variability (in terms of standard deviations), it is obvious that for all marine influenced source regions TEOM slightly exceed AMS+MAAP mass concentrations. This is likely due to sea spray which is the major source of particulate matter within the marine boundary layer, consisting of sodium chloride aerosol particles (Warneck, 1988), which cannot be measured efficiently with the AMS. For the "Seville", "Continental" and "Portugal+Huelva" air mass categories AMS+MAAP concentrations are larger than TEOM mass concentrations. This could be due to volatile substances that are potentially not completely registered using the TEOM.

Particle number concentrations: The number concentration levels within the "Continental", "Marine+Huelva", "Portugal+Marine" and "Marine" air mass categories show significant variability, reflected in large standard deviations. For the first two of these source sectors the large variability is caused by the frequent occurrence of particle nucleation events. For the "Portugal+Marine" category particle nucleation is also possible however, we can neither clearly

identify nor exclude such events unambiguously. Another potential cause is the inhomogeneous mixture of polluted continental air with clean marine air, and for the "Marine" category the generally low values are associated with significant variability, potentially caused by individual ship emission plumes. Despite the strong variations in number concentrations, a general trend is clearly visible and major differences occur between the group of "Continental", "Marine+Huelva" and "Portugal+Marine" air masses compared to the group of "Seville", "Portugal+Huelva" and "Marine" air masses: The ratios of particle number to particle mass concentration bar heights in Fig. 3.6 differ significantly between these two groups of air masses. While the brown colored bars corresponding to PM_1 mass concentrations referred to the grey ones representing number concentrations are approximately four times as high for the "Marine" category and 2 times as high for "Seville", almost the same bar heights were obtained for the "Continental" and "Portugal+Marine" air mass categories. The presence of freshly produced aerosol originating from nearby particle sources in "Marine+Huelva" air mass types affect both physical aerosol concentrations in a way that large particle number concentrations associated with lower aerosol mass concentrations were measured, compared to the other air mass types. On the other hand the aging of the aerosol during regional transport of urban emissions like it is the case for "Seville" or aged "Marine" aerosol is expressed in lower number but enhanced particle mass concentrations. Due to the fact that "Marine+Huelva" air mass trajectories extend over the whole area of Huelva city compared to "Portugal+Huelva" crossing mainly the north of the city, related concentrations behave differently. Typically, the relation of the particle mass and number concentration shows low correlation (Buonanno et al., 2010). Similar information is provided by the following particle size distributions with additional details.

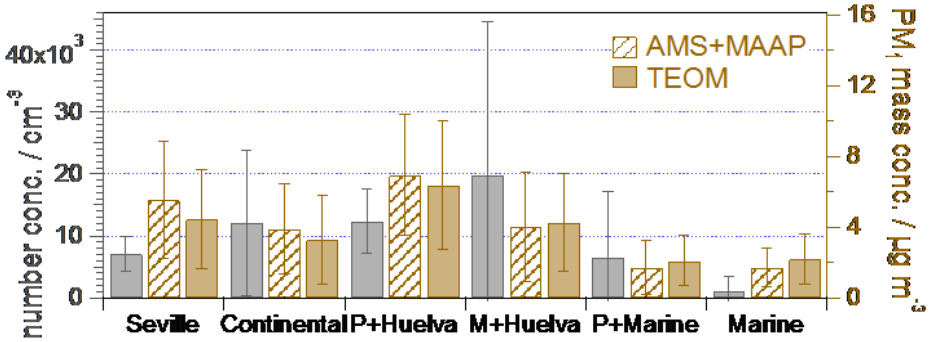

Figure 3.6: Averaged particle number (grey) and mass (brown) concentrations for the individual air mass categories. While hatched brown bars represent averaged submicron PM_1 mass concentrations determined by adding HR-ToF-AMS species and black carbon concentrations, brown filled bars show PM_1 mass concentrations measured using the TEOM. Standard deviations show the variability for the mentioned parameters within each air mass category.

3.1.3.2 Variability of particle size distributions

Fig. 3.7 shows the size distributions of averaged number, surface and volume concentrations measured for the different air mass categories using the FMPS (a) and the OPC (b). The FMPS covers the particle size range 7-523 nm (a), whereas the OPC particle size range is from 320 nm until 32 µm (b). The FMPS registers the mobility diameter of the aerosol particles while the OPC measures the optical particle diameter. Since the optical properties of the measured particles are not known well enough, no attempt was made to convert these different particle diameters into a common type of particle diameter. Therefore, both size distributions are shown in separate panels and each mode is discussed separately.

Aging of aerosol particles is often associated with coagulation of small particles with each other or onto larger pre-existing particles and with condensational growth of vapors onto available particle surfaces, resulting in an increase of particle size with time, in a decrease of number concentrations and in a change of the particle composition as well. Under the condition that particles are larger than 40 nm several hours after particle formation started, e.g. during the growth phase of a nucleation event, changes in particle composition can be investigated using the AMS. However, this topic is the focus of a future publication.

Within the measured FMPS mobility diameter size range, modes in the averaged number distributions were found in the nuclei mode nearly without exception within all continental and Huelva influenced air mass categories. FMPS number size distributions are clearly influenced by frequently occurring particle formation events within these air mass categories. This impact is shown in Fig. 3.7a using solid and dotted lines of the same color for data where all measurements are considered or where nucleation periods are excluded for the "Continental" and "Marine+Huelva" air mass categories. For the "Portugal+Marine" category we also measured a mode around 10 nm but we can neither identify nor exclude unambiguously new particle formation events for this source category. The significant urban pollution in Huelva causes the highest particle number concentrations for "Portugal+Huelva" including particles in a wide size range with a mode diameter around 30 nm. In Huelva-related air masses, new particles are also formed by nucleation. In addition industrial exhaust gases condense onto pre-existing particles. Nevertheless, as new particle formation is dealed within a future paper, we will not further go into details here. For the "Marine" air mass category, the monomodal number size distribution with low total number concentrations indicates processed aerosol.

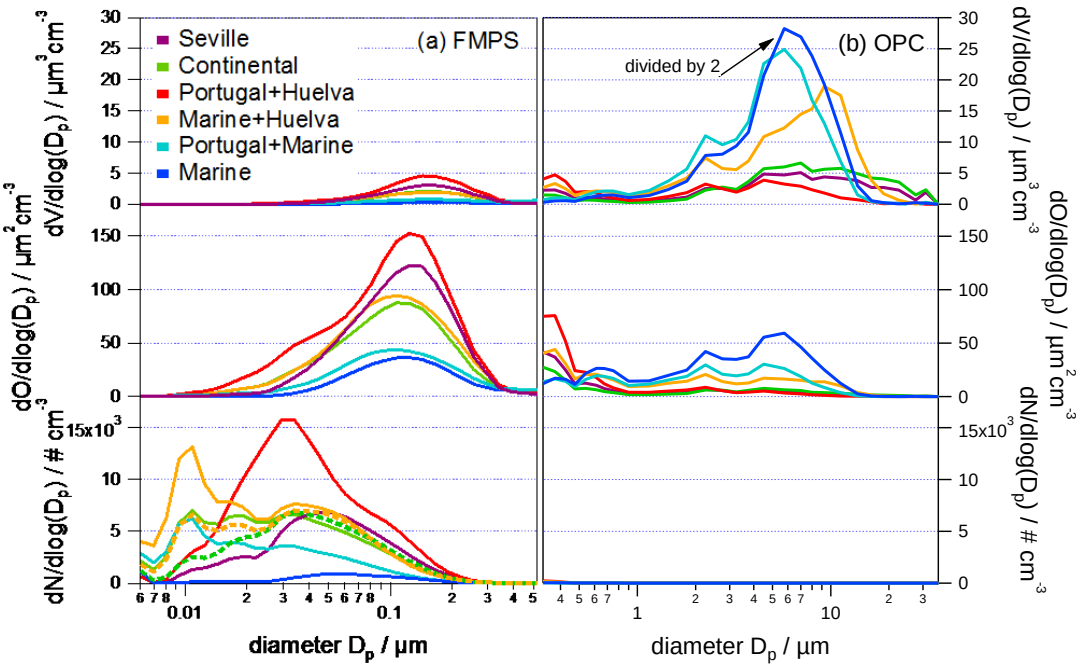

Figure 3.7: Averaged particle size distributions in the size range of 7 nm until 32 µm for all air mass types using the FMPS (a) and OPC (b) data. The FMPS registers particle diameters in a size range of 7-523 nm (D_{mob}) while the OPC covers the particle size range 320 nm until 32 µm (D_{opt}). Dotted lines in the number distribution show averaged concentrations without considering new particle formation events for the "Marine+Huelva" and the "Continental" categories. The observed discrepancies could be due to the fact that both instruments base on different measurement methods and both reach their limits regarding the smallest and largest channels.

The surface area size distributions (Fig. 3.7) with accumulation mode diameters around 150 nm have a similar monomodal shape for each category beside for the "Portugal+Huelva" air masses which are five times as high as those from "Marine" air mass types. The extreme urban pollution in Huelva with maximum number concentrations in the 30 nm size range result in maximum surface area concentrations and in a fronting of the particle surface area distribution as well.

The volume size distributions measured primarily using the OPC (Fig. 3.7b) show interesting features in the coarse mode up to 2 μm optical particle diameter. Volume concentrations of all marine influenced air masses are higher than those originating from "Continental" or urban source regions. While the averaged volume size distributions for "Marine" and "Portugal+Marine" air masses both have their maxima at 5.7 μm and also a similar shape, the "Marine+Huelva" size distribution is clearly shifted towards larger diameters and therefore has its dominant mode around 10 μm. The major particle source in marine enviroments is sea spray therefore sodium chloride particles contribute significantly to the volume size distributions in "Marine" and "Portugal+Marine" air masses. The "Marine+Huelva" size distribution is affected by both, sea salt particles and particles originating from Huelva's industries. "Continental" and "Seville" categories have nearly the same volume concentrations and shape, but compared to all marine influenced air masses they are shifted towards larger optical particle sizes.

3.1.3.3 Variation of the acidity of the submicron aerosol

The aerosol variability between different air mass types was further characterized by analyzing the contributors that influence the aerosols' acidity since it has an important impact on both, aerosol hygroscopic growth, toxicity as well as heterogeneous reactions (Sun et al., 2010). In this context we examined the relative abundance of the inorganic ToF-AMS species sulfate, ammonium and nitrate in the submicron PM_1 aerosol, particularly with regard to the differences in the ion balance in dependence of the air mass types.

A scatter plot of the sum of molar sulfate, nitrate and chloride versus molar ammonium is shown in Fig. 3.8a to illustrate the degree of neutralization for the individual air mass classes. Sulfate was multiplied by a factor of 2 to reflect the molar ratio of sulfate versus ammonium in ammonium sulfate. The black line (1:1) indicates fully neutralized aerosol. Data points below this line are associated with alkaline aerosol as ammonium concentrations are higher than needed to neutralize the anions while points lying above this line are associated with acidic aerosol. For most of the points primarily in "Seville", "Continental", "Marine+Huelva" and "Portugal+Marine" air masses the correlation of measured ammonium versus inorganic anions indicates that a major fraction of PM_1 submicron aerosol was slightly acidic for most of the time while also neutralized aerosols occur. In "Portugal+Huelva" air masses the sum of all inorganic AMS anionic compounds (sulfate, nitrate, chloride) exceeds ammonium which implies an acidic aerosol. As mentioned before, acidic sulfate originating from "Marine" air masses measured at this coastal site is due to negligible contribution of ammonium in this region. Like shown in the studies of Jickells et al. (2003) ammonium sources are not very abundant in the MBL therefore particulate ammonium concentrations are much smaller than the concentration necessary for the neutralization of sulfate and nitrate (Coe et al., 2006; Allan et al., 2004; Allan et al., 2008). Although sodium chloride is the most abundant species in the marine boundary layer, the AMS only measures the NR-PM_1 aerosol fraction and therefore does not measure sodium chloride with significant efficiency (Zorn et al., 2008). For this reason we assume measured chloride is mostly present as ammonium chloride if it is neutralized, hence it is included in the calculations of the ion balance. Regarding all air mass

categories the averaged equivalent ratio is larger than one (see Fig. 3.8a), indicating that the aerosol at the measurement site was generally rather acidic.

Another focus was put on speciation of sulfur compounds expected to be found in the aerosol from the different source regions. While previous studies in Pittsburgh identified a sulfur mixture of ammonium sulfate ($(NH_4)_2SO_4$), ammonium bisulfate (NH_4HSO_4) and also small amounts of sulfuric acid (H_2SO_4) (Zhang et al., 2007), Zorn et al. (2008) included the identification and quantification of methanesulfonic acid (MSA) in the analysis, which can be found ubiquitously in marine environments. Fig. 3.8b shows a scatter plot of acid-related hydrogen (H^+) present in the particle phase versus the molar sulfate concentration in the submicron particles. The H^+ molar concentration was estimated by subtracting the ammonium (NH_4^+) molar concentration from the molar concentrations of the anions sulfate (SO_4^{2-}), nitrate (NO_3^-) and chloride (Cl^-) (Zhang et al., 2007):

$$[H^+] = 2 * [SO_4^{2-}] + [NO_3^-] + [Cl^-] - [NH_4^+] \quad (3.2)$$

The black lines in Fig. 3.8b indicate the molar ratios that would correspond to $(NH_4)_2SO_4$, NH_4HSO_4 and H_2SO_4; the dashed line agrees with 50% $(NH_4)_2SO_4$ and 50% NH_4HSO_4. To quantify the various "sulfate" aerosol components for the different air mass types in Table 3.3 the percentage of ammonium sulfate ($(NH_4)_2SO_4$), ammonium bisulfate (NH_4HSO_4), sulfuric acid (H_2SO_4) and methanesulfonic acid (MSA) were calculated as follows:

NH_4^+ excess (mol)	= NH_4^+ (mol) – NO_3^- (mol) – Cl^- (mol)	(3.3)
SO_4^{2-} excess (mol)	= SO_4^{2-} (mol) – NH_4^+excess (mol) / 2	(3.4)
% H_2SO_4	= SO_4^{2-} excess (mol) / SO_4^{2-}total (mol) * 100	(3.5)
% MSA	= MSA (mol) / SO_4^{2-}total (mol) * 100	(3.6)
% $(NH_4)_2SO_4$	= 100 – % H_2SO_4 – % MSA	(3.7)

The fraction of NH_4HSO_4 for each category can be calculated stoichiometrically based on the molar ratios of $(NH_4)_2SO_4$ and H_2SO_4.

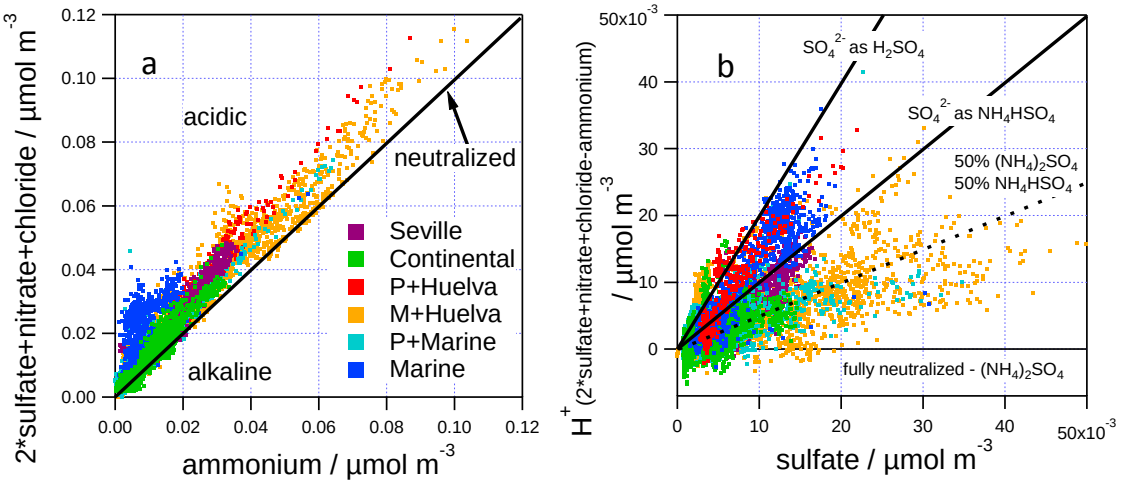

Figure 3.8: Correlations illustrating the difference of the ion balance (a) dependent on the air mass origin. The scatter plot (b) serves for the identification of the sulfur species ammonium sulfate ($(NH_4)_2SO_4$), ammonium bisulfate (NH_4HSO_4) and sulfuric acid (H_2SO_4) within the different aerosols. Points represent 2 min average values.

The "sulfate" classes $(NH_4)_2SO_4$, NH_4HSO_4 and H_2SO_4 were distinguished on the basis of the presence of the potential counter ions as we cannot separate the different sulfate species directly in our measurements. Therefore, we assume that ammonium first reacts with nitrate and chloride in the particles and chemical equilibrium exists. Likewise, excess ammonium reacts with sulfate to form ammonium sulfate in an equilibrium reaction. Finally, sulfate that could not be neutralized by ammonium has to be present as ammonium bisulfate or sulfuric acid. In Table 3.3 the relative contributions of the species $(NH_4)_2SO_4$, NH_4HSO_4 and H_2SO_4 to total "sulfate" are presented. For calculating MSA concentrations the *Peak Integration by Key Analysis* software (PIKA, http://cires.colorado.edu/jimenez-group/ToFAMSResources, De Carlo et al. (2006)) was used to deconvolve the m/z 79 signal into three peaks: Bromine, a MSA fraction, and an organic fragment ($C_6H_7^+$) as described in Zorn et al. (2008). As shown in Table 3.3, the analysis indicates that MSA accounts for only a minor degree (1%) of the total "sulfate" component class when "Marine" air masses arrive at the measurement site while MSA concentrations in the other categories are below the detection limit (6 ng m^{-3}).

Table 3.3: Percentage contribution of ammonium sulfate ($(NH_4)_2SO_4$), ammonium bisulfate (NH_4HSO_4), sulfuric acid (H_2SO_4) and methanesulfonic acid (MSA) to the species class "sulfate" for the selected air mass categories.

%	ammonium sulfate ($(NH_4)_2SO_4$)	ammonium bisulfate (NH_4HSO_4)	sulfuric acid (H_2SO_4)	methanesulfonic acid (MSA)
Seville	28	72	0	below LOD
Continental	50	50	0	below LOD
Portugal+Huelva	0	72	28	below LOD
Marine+Huelva	32	68	0	below LOD
Portugal+Marine	26	74	0	below LOD
Marine	0	74	26	1

Unlike in the studies of Zorn et al. (2008) a major fraction of the "sulfate" class in the "Marine" air mass category is contributed by ammonium bisulfate (74%) while sulfuric acid (26%) is the second major contributor (Fig. 3.8b). While sulfuric acid is produced from dimethyl sulfide (DMS) originating from phytoplankton or anaerobe bacteria (Charlson et al., 1987) and from sulfur dioxide (SO_2) from shipping emissions (Zorn et al., 2008), ammonium bisulfate is the result of the neutralization reaction between sulfuric acid and ammonia. In comparison, "Portugal+Huelva" air masses are influenced by nitrate precursor emission sources in Southern Huelva, causing the binding of a significant fraction of the available ammonium. This results in an ammonium bisulfate (72%) to sulfuric acid (28%) ratio that is even more acidic than those within the "Marine" air mass category (Table 3.3). On the contrary, ammonia is mostly present in the terrestrial boundary layer hence sulfurous aerosols are mostly composed of ammonium bisulfate and ammonium sulfate in the "Seville", "Marine+Huelva" and "Portugal+Marine" air mass types. For the "Continental" air mass category the ammonium sulfate to ammonium bisulfate ratio is balanced. This can also be seen in Fig. 3.8b based on the corresponding data points reflecting the 50% $(NH_4)_2SO_4$/50% NH_4HSO_4 line. Similar results were found during the OOMPH (Organics over the Ocean Modifying Particles in both Hemispheres) campaign: Zorn et al. (2008) found only a minor fraction (20-50%) of neutralized aerosol during pristine marine dominated periods while continentally influenced air masses are often neutralized.

3.1.3.4 Factor analysis of the organic aerosol using Positive Matrix Factorization (PMF)

Another major objective of this study is to identify the main components and sources of the submicron organic aerosol. For this purpose positive matrix factorization (PMF) (Paatero, 1997; Paatero and Tapper, 1994) was used to analyze the AMS organics information using the evaluation tool developed by Ulbrich et al. (2009). Results of this analysis for the whole campaign period show four "factors", representing different aerosol types that explain an average of 97% of the total organic mass and can be associated with aerosol sources and components. Oxygenated organic aerosol (OOA I) was the major component that contributes on average 43% of the particulate organic mass during the whole measurement period. While OOA I, a highly-oxygenated OA mostly represents secondary organic aerosol (SOA), OOA II accounting for additional 23% of the organic mass, represents a less-oxygenated/processed, semi-volatile OA (Ulbrich et al., 2009). A hydrocarbon-like organic aerosol type (HOA, 16%) as well as aerosol from wood burning emissions (WBOA, 15%) were identified in this study by comparing the mass spectra of the PMF factors to measured ambient reference spectra (http://cires.colorado.edu/jimenez-group/AMSsd/).

Comparison of mass spectra with reference spectra

In Fig. 3.9a calculated average mass spectra of all four PMF factors (OOA I, OOA II, HOA, WBOA) are shown. Significant mass fragments for highly-aged OOA I (Fig. 3.9a/1) are m/z 18, 27, 41, 43, 44, 55, 69 while marker peaks at m/z 27, 29, 41, 43, 55, 67, 79 are characteristic for OOA II (Fig. 3.9a/2). Both factors correlate well with reference spectra shown in Lanz et al. (2007) (R^2=0.96 for OOA I; R^2=0.90 for OOA II). Unlike in the studies of Lanz et al. (2007), Zhang et al. (2005) and Ulbrich et al. (2009) the HOA mass spectrum found in this work (Fig. 3.9a/3) is dominated by m/z 44 and therefore m/z 18 and 17 mass fragments are enhanced as well because their calculation was bound to m/z 44 in the analysis. Apart from this, the typical characteristic peaks for hydrocarbons (m/z 41, 43, 55, 57, 69, 81, 95) exist. Therefore, we assume this factor represents a "slightly oxidized HOA". For this reason, the HOA reference spectrum (Zhang et al., 2005) does not correlate very well (R^2=0.58) with our HOA spectrum. Moreover, regarding the high resolution mass spectra at m/z 44, the $C_3H_8^+$ peak (m/z 44.06) overlaps the CO_2^+ peak (m/z 43.99) and could not be separated with the AMS as the mass resolution was too low. Therefore, this could also be a reason for the enhanced m/z 44 signal which is not associated with oxidized organic aerosol. In addition a spectral pattern was determined in the fourth factor in this study which is similar to the wood burning reference spectrum in Lanz et al. (2007) (R^2=0.83), containing prominent peaks at m/z 15, 29, 41, 55, 60, 69, 73, 91 (WBOA, Fig. 3.9a/4).

Quality assurance for the mathematically calculated PMF results

To validate the PMF results a variety of tests has been performed with the data set. One of these validation exercises concerned the weighting of particular m/z. For these tests PMF has been performed using different sets of input parameters (weighting of particular m/z in the input mass spectra) and the related results have been compared to each other. According to these calculations the individual m/z in the average mass spectra of the four factors (OOA I, OOA II, HOA, WBOA) have an uncertainty in the order of 5%; also the calculated mass concentrations associated with the four factors have an uncertainty of approximately 5% if lowest aerosol mass concentrations were not considered. PMF computations consider so-called "fpeak" values that allow examining "rotations" and "seeds" to explore additional solutions by starting the algorithm from several pseudorandoms (Ulbrich et al., 2009). Both variables have to be set by the user in the data analysis process. Since no clear rules exist which values have to be used for "fpeak" and "seeds" this results in an additional uncertainty of the peak intensities of the mass spectra of 17-34% dependent on the

factor if "fpeaks" were varied, while the uncertainty varies between 2-19% with a change of the "seeds". The uncertainty of averaged mass concentrations of the time series varies between 13-36% for the different factors when "fpeak" is varied. For a variation of the "seeds" this uncertainty is in the order of 1-10%. Generally the HOA and WBOA factors have a larger uncertainty than OOA I and OOA II. After several tests were conducted with PMF, we decided to take the four factor solution using "fpeak" and "seed" values of zero. However, it has to be noted that these factors are subjectively selected and result in the uncertainties in both the mass spectra and average mass concentrations described above. Additionally, the instrument uncertainty of the AMS (25-30%) has also to be taken into account.

By adding an additional fifth factor in the PMF analysis a meaningless factor appears as a consequence of "splitting" of one of the previous factors like also described in the studies of Sun et al. (2010). Therefore, this factor did not improve the PMF results. To assure the best possible PMF solution the factors were further tested, not only on the basis of the mass spectral (MS) signature but also correlations of the OOA I, OOA II, HOA and WBOA mass concentration time series (see Fig. 3.9b) with those of other measured aerosol species, trace gases and meteorological parameters were accomplished.

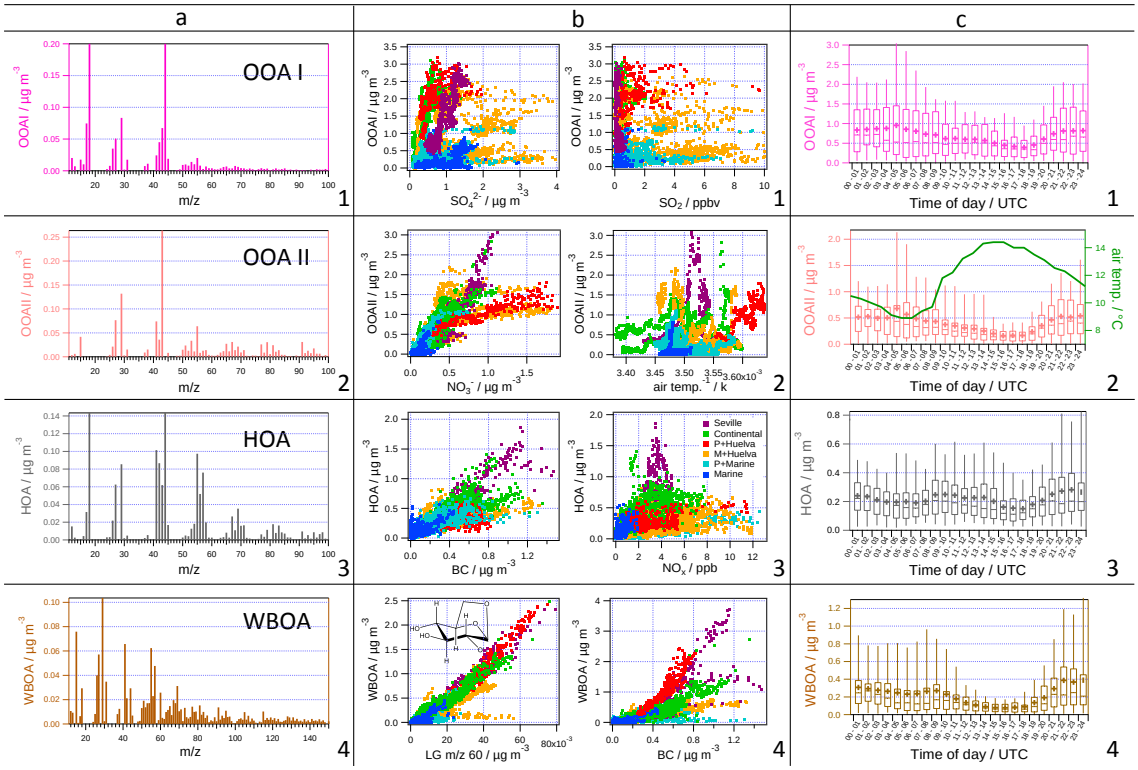

Figure 3.9: Mass spectra (a), correlations (b) and diurnal variation box plots (c) of OOA I (dark purple, 1), OOA II (salmon, 2), HOA (grey, 3) and WBOA (brown, 4) organic aerosol types. Mass spectral markers were compared to reference spectra (not shown). The four factors were correlated with aerosol species (sulfate, nitrate, m/z 60 as levoglucosan tracer, black carbon), trace gases (nitrogen oxide, sulfur dioxide) and meteorological parameters (air temperature) (b). Box plots of the diurnal variation for the whole campaign (c) show the median, mean and the 25%/75% percentiles. The whiskers indicate the 5%/95% interquartile span. Points in the correlations (b) represent 2 min average values.

Diurnal cycles and correlations of particulate organics with aerosol and gas phase species

In Fig. 3.9b/1 the sulfate mass concentrations are correlated with those of the PMF OOA I factor. Unlike in the studies of Lanz et al. (2007), Zhang et al. (2005) and Ulbrich et al. (2009) OOA I is

only weakly correlated with particulate sulfate. This might be due to the variety of types of emission sources around the measurement site. On the one hand the strongly industrialized Huelva estuary or the marine category, where sulfate plays an important role (54% of total aerosol, Table 3.2) and on the other hand source categories with lower sulfate abundance cause extreme changes of sulfate concentrations as discussed in section 3.1.3.3 with changing meteorological conditions (wind directions). For this reason, also the sulfur dioxide mixing ratios vary between 0.3 ppb in the "Marine" and 2 ppb in the "Marine+Huelva" air mass category and correlate reasonably with sulfate concentrations (R^2=0.4) but not with OOA I. These variations in sulfur dioxide and sulfate concentrations do not necessarily have to be associated with changes in OOA I concentrations since OOA I has its sources in a different set of air mass categories compared to sulfate.

According to the diurnal cycle (Fig. 3.9c/1) OOA I does only show a weak photochemical dependence as expected, since it reflects aged highly-oxidized OA. Contrary, the temporal behavior of OOA II, a less aged semi-volatile organic aerosol component shows typical maximum concentrations at night. This could be explained by the strong anti-correlation of the diurnal OOA II cycle with the temperature cycle (Fig. 3.9c/2) which could be the reason for an accumulation of oxidized organic products in the vapor phase during the day that condense onto the particles surfaces preferentially during the night (Lanz et al., 2007). AMS-nitrate is also a temperature-sensitive species correlating reasonably well with OOA II (R^2=0.5, Fig. 3.9b/2).

As observed in many previous studies (Lanz et al., 2007; Zhang et al., 2005) prominent features of the HOA diurnal patterns around 08:00-13:00 UTC and 20:00 UTC (Fig. 3.9c/3) result from morning and evening rush-hours and other human activities. The HOA time series is correlated with the primary emission tracer black carbon (R^2=0.6) but not with NO_x (R^2=0.2). NO_x is formed by oxidation of nitrogen in combustion engines at high temperatures and is also emitted by industrial sources and biomass burning. Hence, like mentioned by Lanz et al. (2007) NO_x is not only a marker for traffic emissions and HOA should not be regarded as pure vehicle exhaust marker, likely resulting in the relatively poor correlation observed between these species.

The WBOA temporal evolution was correlated with AMS m/z 60, which is typically associated with Levoglucosan known as major molecular marker for fine particulate wood and biomass burning emissions (Alfarra et al., 2007; Schneider et al., 2006). Fig. 3.9b/4 shows the temporal behavior of both mass concentrations which are correlated well (R^2=0.9), supporting the identification of this factor. The WBOA diurnal pattern shows increased concentrations during the night until the late morning which decrease afterwards, likely due to a combination of domestic heating and boundary layer height cycles. However, WBOA concentrations are more dominant in the evening (Fig. 3.9c/4) similar to studies carried out in Zurich (Lanz et al., 2008). Maximum average values of the WBOA diurnal pattern at night probably result from domestic heating. Comparing the results for the different source regions the characteristic daily cycles of the four factors resemble each other because independant of the source strengths in the individual air mass categories effects like boundary layer height or temperature cycle affect all air mass categories in the same way.

Particulate organics in the different air mass types

As discussed in section 3.1.3.1 Fig. 3.5 depicts the average composition of NR-PM_1 that belongs to the individual air mass categories. Here the total organic signal frames the average mass fractions of each of the OA components (OOA I, OOA II, HOA, WBOA) as well as the residuum in the green pie. The fractional contribution of the four components differs dependent on the air mass category. Nevertheless, low-volatile OOA I can be found in each air mass type as the major submicron aerosol fraction besides all marine influenced air masses where sulfate plays the most important role

(section 3.3). Referred to the OA fraction OOA I is approximately in the same order (35% in "Portugal+Marine" up to 49% in "Continental") in all air mass categories. The less aged OOA II component appears as second most abundant fraction of the OA in all air mass types with a contribution of approximately 25% beside the "Marine" category that has a lower OOA II fraction of 13%. Over marine environments particle aging is a characteristic feature (Topping et al., 2004), resulting in a more oxygenated and a less volatile aerosol. In contrast, in continentally influenced air masses typically freshly produced biogenic and anthropogenic organic material exists, resulting in OOA II aerosol after photochemical processing. HOA concentrations are expected to be most prominent downwind of the urban city Huelva, however HOA aerosol undergoes rapid losses due to oxidation while it is transported (Zhang et al., 2007). Like in the studies of Zhang et al. (2007), we also found OOA concentrations similar or even enriched when the air was transported downwind of urban areas, likely due to condensation of vapors onto the pre-existing particles and oxidation of HOA, respectively. In contrast to all other air mass types, the "Marine" category contained HOA as the second most abundant organic aerosol component (25% of total OA) potentially originating from shipping emissions. In "Portugal+Huelva" air masses WBOA levels are more prominent and exceed HOA which is likewise the case for the city Zurich (Lanz et al., 2008). Due to the beginning of the winter season in the south of Spain with cooler temperatures and rain, domestic heating is an important contributor to this aerosol type as people heat using wood. This becomes apparent in increased WBOA concentrations especially in the evenings. In addition, as the measurement site is surrounded by pines and eucalyptus forests with agricultural activity WBOA average values around 7% in all continentally influenced air mass categories were measured.

3.1.3.5 Meteorological conditions and ozone variability

In order to evaluate ozone behavior it is necessary to understand the conditions and processes like the regional transport of ozone and its precursors as well as meteorological variables that have a significant influence on ozone production. To study the impact of meteorological conditions on ozone variability at the measurement site, wind speed and direction, temperature and relative humidity data were analyzed. The measured temperatures exhibit a characteristic diurnal cycle as expected (Fig. 3.10a) for the El Arenosillo location. The ozone mixing ratio is strongly associated with wind speed and direction as these meteorological parameters affect the transport and dispersion of ozone and its precursors (Adame et al., 2010). As indicated in Fig. 3.1 the wind blew mainly from the first, third and fourth quadrant and therefore air masses from Continental Europe and from the Atlantic Ocean arrive at the measurement station.

Using only the data from the "Continental" source region, we found a general characteristic daily ozone cycle in "El Arenosillo" that mainly follows this scheme (Fig. 3.10a):
- In the early morning hours minimum ozone levels exist around 07:00 UTC until ozone mixing ratios increase as photochemical reactions begin.
- Then, the ozone levels follow the intensity of the solar radiation with a delay of approximately 3 h. Maximum ozone mixing ratios occur at approximately 15:00 UTC.
- When the solar radiation intensity decreases ozone levels also decrease and reach the lowest values at night (around 23:00 UTC) when the night inversion layer is present. Low nocturnal ozone mixing ratios are caused by the absence of ozone generation associated with in-situ destruction of ozone, titration by NO and dry deposition (Adame et al., 2010a).
This general pattern agrees with previous findings at coastal sites in the Southwest of the Iberian Peninsula in El Arenosillo (Adame et al., 2010a,b).

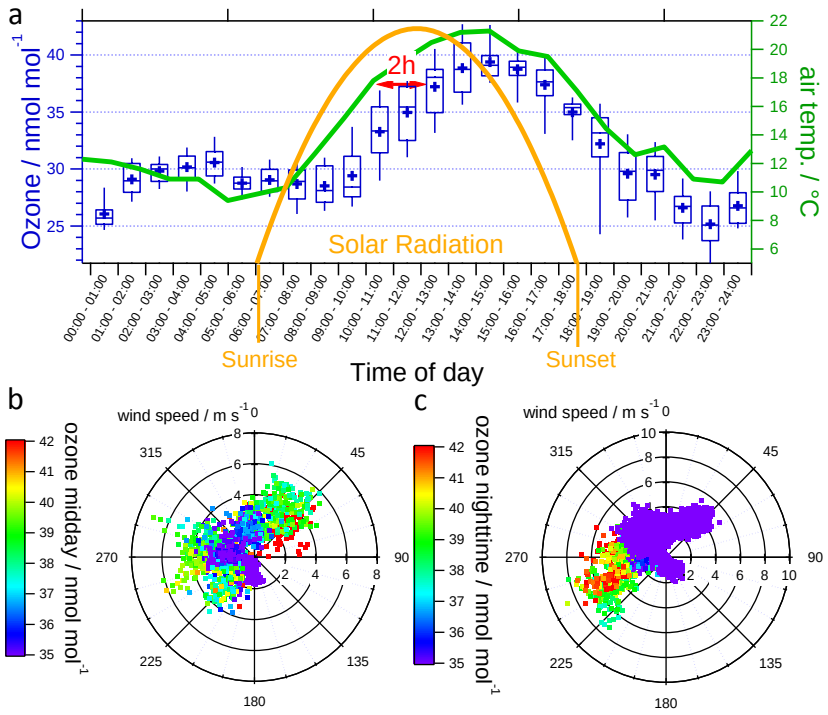

Figure 3.10: Summary of the ozone variability at the measurement site. A general characteristic evolution of the daily ozone cycle for "El Arenosillo" using the "Continental" air mass category data is presented in (a). The temperature was measured using a meteorological station while solar radiation values are just for illustration. While ozone levels follow the solar radiation with a delay of approximately 3 h, a delay of 2 h was registered relatively to the temperature trends. Wind roses (speed and direction) colored by the ozone mixing ratio at early afternoon (12:00-16:00 UTC) (b) and at night (21:00-06:00 UTC) (c) show that the ozone levels depend not only on the diurnal solar radiation cycle, but also on air mass origin associated with different precursor concentrations and composition.

To study both, the diurnal variability of ozone and its association with various air masses, we display wind roses of ozone mixing ratios (showing the wind direction and speed dependence) around its concentration maximum (12:00-16:00 UTC) and at night (21:00-06:00 UTC) in Fig. 3.10b and 10c. The variability of ozone at this coastal measurement site depends both, on meteorological conditions (diurnal cycle of solar radiation and temperature) as well as on the transport of air masses with ozone precursors originating from different source regions. Maximum ozone mixing ratios (47 nmol mol^{-1}) were reached in the afternoon around 15:00 UTC with largest levels in air masses coming from NE where ozone precursor substances (like NO_x, CO and VOC) from Seville have sufficient time to form ozone before arriving at the measurement site. During the nocturnal period lowest ozone mixing ratios with values of about 23 nmol mol^{-1} were measured for this wind direction. A similar behavior but with smaller amplitude of the diurnal cycle is observed in "Continental" air masses. Due to the low number of data points from the "Seville" air mass category, the associated diurnal cycle is not well represented. Therefore, we show the diurnal cycle of the "Continental" air mass category in Fig. 3.10a. This source region is not as strongly affected by the transport of industrial and traffic emissions therefore midday ozone mixing ratios are lower (39 nmol mol^{-1}) compared to "Seville" air masses. As a consequence of the absence of solar activity at night the ozone mixing ratios decrease to 25 nmol mol^{-1}. Ozone mixing ratios in the NW wind direction are influenced by the strong urban pollution including different types of emissions originating from Huelva. The wide spectrum of emissions leads to decreased ozone levels caused by titration by nitrogen oxides that are produced by industries and traffic. In contrast to the "Seville" category, the transport distance (20 km) for "Huelva" air masses to the station is not sufficient to

allow the ozone precursor substances to generate ozone completely. Therefore ozone mixing ratios for this air mass type are low and vary between 36 nmol mol^{-1} at noon and 16 nmol mol^{-1} at night. Compared to all the other diurnal cycles discussed before, the ozone pattern is quite different in the "Marine" category (SW) where about 40 nmol mol^{-1} occur late at night (13:00 UTC). Interestingly, almost the same concentrations were measured during afternoon. We assume that no ozone destroying substances are available over marine environments.

3.1.3.6 Inner- and inter-category variability

The variability of particulate and trace gas concentrations and composition within the individual air mass categories has also been determined. This allows comparing the observed differences between air mass categories (inter-category variability) with the variability of the same parameters within the individual air masses (inner-category variability). The inner-category variability was determined as the relative standard deviation of the concentration values associated with the air mass in question. Contrary the inter-category variability was calculated as the relative standard deviation of the average concentrations of all air mass categories.

Generally, for most of the species the inner-category variability is larger than the inter-category variability. While for several parameters like organic aerosol concentrations (Table 3.2) or ozone both types of variability are very similar, only for nitrate larger differences are observed between the different air masses than within the individual air masses (Table 3.2). For the ozone mixing ratios the lowest variability was observed. While for total particle mass concentration and the concentrations of most of the secondary aerosol components (ammonium, sulfate, nitrate, OOA I) medium inner-category variability levels were observed, the largest variation in aerosol parameters was observed for the particle number concentrations as well as for the concentrations of black carbon, semi-volatile OOA (OOA II) and biomass-burning related organic aerosol (WBOA). As an example, Fig. 3.11 shows the time series of the particle number concentration data for three different air masses ("Continental", "Marine+Huelva", "Marine). Standard deviations of the number concentrations represent the inner-category variability and show the large variations within the individual air mass categories, which exceed the differences between the various average values.

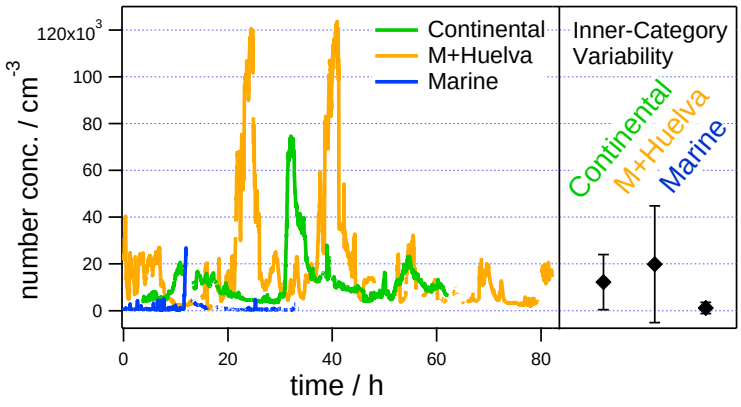

Figure 3.11: Time series of the number concentration (CPC) for three different air masses ("Continental", "Marine+Huelva" and "Marine") and corresponding inner-category variability determined based on the relative standard deviations of the measured data.

Significant differences from the above-mentioned general trends have been observed for several air quality parameters in some of the air mass categories. Extraordinary large inner-category variability for several parameters like black carbon, total and PMF-classified organics and particle number and

mass concentrations have been observed for the marine influenced air mass categories. This is due to very low background concentrations that are interspersed with much larger concentrations in emission plumes, e.g. from individual ships. Contrary to this high variability, for ozone the lowest inner-category variability is observed in the "Marine" category likely due to the wide absence of sources and sinks. Particularly low variability was observed for inorganic secondary species concentrations as well as particle number concentrations in the "Seville" and partially "Continental" air mass categories, likely associated with reasonably well-aged and mixed aerosol and low abundance of sources in the close vicinity of the measurement site.

3.1.4 Discussion & Summary

The aim of our study is to evaluate typical values and the variability of aerosol, trace gas and meteorological parameters using measurements with the mobile laboratory (MoLa) at the interface of marine, urban and continentally influenced air masses in Southern Spain. This provides both, valuable information about the air composition in this part of Spain and how these parameters vary with air mass origin. To evaluate separate air masses with differentiated continental, urban and marine origin, the campaign was accomplished in winter. The advantage compared to summer measurements in this region is a well-defined origin of air masses with lower disturbance by intensive photochemistry and recirculation periods which affect the aerosol and trace gas phenomenology additionally and therefore contribute to a more complex study scenario.

To provide the best possibility of studying the variability of air quality parameters with varying source regions not only air mass trajectories but also local meteorology measured at the sampling site was used to classify different types of air masses. Although similar results were obtained from both methods, the classification made on basis of backwards trajectories is more conclusive compared to that using wind directions measured with the meteorological station. Consequently, using backwards trajectories six air mass types ("Seville", "Continental", "Portugal+Huelva", "Marine+Huelva", "Portugal+Marine", "Marine") were distinguished and associated aerosol and trace gas parameters were further characterized.

Organics, sulfate and nitrate NR-PM_1 aerosol mass concentrations show the most significant variations and therefore they largely determine the chemical character of the aerosol from different source regions. While 64% of the PM_1 in "Continental" air masses consisted of organics, sulfate is the most abundant species in the "Marine" air mass category (54%).

Like in the studies of Phinney et al. (2006) who identified sulfuric acid to be a dominant sulfate species in the marine environment, further analysis regarding the acidity show that in the "Marine" air mass type the species class "sulfate" is mainly composed of ammonium bisulfate (74%) and sulfuric acid (26%) as ammonium concentrations are significantly too low for sulfate neutralization. Similar as in the studies of Zorn et al. (2008) we also identified MSA in marine air masses, resulting from oxidized DMS that is released from phytoplankton. Nevertheless, it only contributes to a minor degree to the total sulfate fraction (1%). On the contrary, ammonia is more abundant in the terrestrial than in the marine boundary layer. Hence, sulfurous aerosols are mostly composed of ammonium bisulfate and ammonium sulfate in "Continental", "Marine+Huelva" and "Portugal+Marine" air masses.

As a result of a large number of industrial emission sources and road traffic in Huelva, nitrate is the major inorganic fraction of the aerosol composition in the "Portugal+Huelva" influenced air mass category. However, compared to a number of studies performed next to urban locations (DeCarlo

et al., 2008; Stolzenburg and Hering, 2000; Salcedo et al., 2006) registered nitrate concentrations in this work are substantially lower. As reported in source apportionment studies in the Andalusian region, higher nitrate values were observed with increased influence of traffic (de la Rosa et al., 2010). As the number of registered cars in Huelva is low (Viana et al., 2007), this is a possible reason why in the corresponding air masses lower nitrate concentrations were measured.

The influence of air mass histories is reflected in average black carbon concentrations as well as in number and volume size distributions. Air masses originating from polluted Huelva and "Seville" source regions are associated with larger particle number concentrations and smaller particle sizes while lowest number concentration values with larger particle sizes are associated with "Marine" air mass types.

By using Positive Matrix Factorization (PMF) we showed that almost the entire organic aerosol can be categorized into one of the four classes OOA I, OOA II, HOA and WBOA. Our measurements show that OOA I is the most abundant submicron aerosol fraction in those air masses ("Seville", "Continental", "Portugal+Huelva") that have not been in contact with marine air masses where sulfate plays a more important role. As mentioned by Topping et al. (2004) over marine environments particle aging is a characteristic feature, thus the highly-oxygenated OOA I occurs also as major organic aerosol fraction in the "Marine" category. HOA was found as second most abundant organic aerosol fraction in this air mass type, possibly originating from ship emissions. In the "Seville", "Continental", "Marine+Huelva" and "Portugal+Marine" air mass categories, the less aged OOA II is the second dominant organic fraction**.** Although we have expected large HOA fractions in "Huelva" air mass categories, because urban areas are typically rich of HOA sources, only relatively low HOA levels have been observed, likely due to rapid losses of HOA that can result in decreased levels already at locations close to the emissions (Zhang et al., 2007). In addition, as traffic emissions are low due to the low number of registered cars in Huelva (Viana et al., 2007) HOA concentrations are probably reduced as well. Beside OOA I, WBOA occurs as a further dominant species in "Portugal+Huelva" air masses likely resulting from domestic heating. As people are using wood for heating purposes the wood burning source strength is becoming more apparent in the evening and night, in agreement with our findings of the WBOA cycle. Previous studies (Lanz et al., 2007; Zhang et al., 2005) observed prominent features of the HOA diurnal patterns around 08:00-13:00 UTC and 20:00 UTC from various anthropogenic activities. The diurnal variability of organic particle types can also be influenced by the solar radiation and temperature cycle. As OOA I reflects highly-aged processed OA, it only shows a weak photochemical dependence. In contrast, the temporal behavior of OOA II shows typical maximum concentrations at night as a consequence of accumulation of oxidized organic products in the vapor phase during day that condense onto particle surfaces at night like mentioned by Lanz et al. (2007).

Another main interest of our study was the investigation of ozone mixing ratios that depend on the solar radiation modified by precursor concentrations, chemical and physical processes and meteorological parameters. In agreement with previous findings at coastal sites (Adame et al., 2010a,b) a general characteristic daily ozone cycle was observed in the continental and urban air mass types. Contrary, in marine air masses almost the same concentrations during day and night were registered, potentially due to the general absence of sources or sinks. Largest ozone mixing ratios were measured in the "Seville" category where ozone precursor substances had sufficient time to form ozone by photochemical reactions (Liu and Chan, 2002; Cremades et al., 2006) during the transport from Seville (70 km distance) to the site. Huelva air masses instead are characterized by lower ozone mixing ratios likely caused by titration of ozone by nitrogen oxides and transport times that were too short to allow the formation of ozone from precursors. Consequently, the

registered maximum and minimum concentrations depend more on the source regions and source distances, the diurnal variability of ozone levels depends more on meteorological conditions (solar radiation/temperature).

The variability within and between the categories were calculated in order to compare the observed differences between the air mass categories with the variations within the individual air masses. Generally, for most of the species the inner-category variability is larger than the inter-category variability. Large inner-category variability for several parameters such as black carbon, PMF-classified organics and particle number and mass concentrations have been observed for marine influenced air masses, likely due to the generally very low background concentrations that are interspersed with much larger concentrations in emission plumes, e.g. from individual ships. Nitrate concentrations instead show the highest inner-category variability due to different kinds of source regions and their characteristic emission types. Generally, for most of the species the inner-category variability is larger than the inter-category variability, therefore the measured concentrations vary to a larger degree within the individual air masses than the average concentrations of the different air masses differ. Although the inner-category variability is often larger than the inter-category variability, which is calculated over the whole set of source categories, there are significant differences between individual categories for individual parameters.

In summary, the variability of the air composition associated with different source regions and distance from sources affects the particle loading, composition, size distributions and acidity as well as trace gas and meteorological parameters at a certain site. Additionally, the season has an important effect on the air composition and levels. Therefore, to provide a full characterization of the variability long-time measurements are required to study the characteristics, sources and processes in this part of Southern Europe where several different influences lead to a complex study scenario. However, in the context of this study an overview of typical air mass characteristics dependent on various source regions for this season can be obtained.

Acknowledgements. This research was supported by the DOMINO (Diel Oxidant Mechanisms In relation to Nitrogen Oxides) project, funded internally by the Max Planck Society. The authors wish to acknowledge T. Böttger for technical support. Furthermore, we thank the INTA (National Institute for Aerospace Technology) for providing facilities at the measurement site. We gratefully acknowledge the NOAA Air Resources Laboratory (ARL) for the provision of the HYSPLIT transport and dispersion model (http://www.arl.noaa.gov/ready.html) used in this paper. J.-M. Diesch and S. R. Zorn also thank the German Research Foundation (DFG) for financing their work through the Research Training School GRK 826.

References

Adame, J. A., Lozano, A., Bolivar, J. P., De la Morena, B. A., Contreras, J., and Godoy, F.: Behavior, distribution and variability of surface ozone at an arid region in the south of Iberian Peninsula (Seville, Spain), Chemosphere, 70, 841-849, 2008.

Adame, J. A. A., Bolivar, J. P., and de la Morena, B. A.: Surface ozone measurements in the southwest of the Iberian Peninsula (Huelva, Spain), Environ Sci Pollut R, 17, 355-368, 2010a.

Adame, J. A., Serrano, E., Bolivar, J. P., and de la Morena, B. A.: On the Tropospheric Ozone Variations in a Coastal Area of Southwestern Europe under a Mesoscale Circulation, Journal of Applied Meteorology and Climatology, 49, 748-759, 2010b.

Alastuey, A., Querol, X., Plana, F., Viana, M., Ruiz, C. R., de la Campa, A. S., de la Rosa, J., Mantilla, E., and dos Santos, S. G.: Identification and chemical characterization of industrial particulate matter sources in southwest Spain, Journal of the Air & Waste Management Association, 56, 993-1006, 2006.

Alfarra, M. R., Prevot, A. S. H., Szidat, S., Sandradewi, J., Weimer, S., Lanz, V. A., Schreiber, D., Mohr, M., and Baltensperger, U.: Identification of the mass spectral signature of organic aerosols from wood burning emissions, Environ. Sci. Technol., 41, 5770-5777, 2007.

Allan, J. D., Bower, K. N., Coe, H., Boudries, H., Jayne, J. T., Canagaratna, M. R., Millet, D. B., Goldstein, A. H., Quinn, P. K., Weber, R. J., and Worsnop, D. R.: Submicron aerosol composition at Trinidad Head, California, during ITCT 2K2: Its relationship with gas phase volatile organic carbon and assessment of instrument performance, J. Geophys. Res.-Atmos., 109, 16, 2004.

Allan, J. D., Baumgardner, D., Raga, G. B., Mayol-Bracero, O. L., Morales-Garcia, F., Garcia-Garcia, F., Montero-Martinez, G., Borrmann, S., Schneider, J., Mertes, S., Walter, S., Gysel, M., Dusek, U., Frank, G. P., and Kramer, M.: Clouds and aerosols in Puerto Rico - a new evaluation, Atmos. Chem. Phys., 8, 1293-1309, 2008.

Barnes, I., Hjorth, J., and Mihalopoulos, N.: Dimethyl sulfide and dimethyl sulfoxide and their oxidation in the atmosphere, Chemical Reviews, 106, 940-975, 2006.

Benach, J., Yasui, Y., Borrell, C., Rosa, E., Pasarin, M. I., Benach, N., Espanol, E., Martinez, J. M., and Daponte, A.: Examining geographic patterns of mortality - The Atlas of mortality in small areas in Spain (1987-1995), European Journal of Public Health, 13, 115-123, 2003.

Bouwman, A. F., Lee, D. S., Asman, W. A. H., Dentener, F. J., VanderHoek, K. W., and Olivier, J. G. J.: A global high-resolution emission inventory for ammonia, Global Biogeochemical Cycles, 11, 561-587, 1997.

Buonanno, G., Stabile, L., Avino, P., and Vanoli, R.: Dimensional and chemical characterization of particles at a downwind receptor site of a waste-to-energy plant, Waste Manag, 30, 1325-1333, 2010.

Carretero, M. I., Bernabe, J. M., and Galan, E.: Mineralogy and origin of atmospheric particles in the industrial area of Huelva (SW Spain), Atmos. Environ., 39, 6777-6789, 2005.

Charlson, R. J., Lovelock, J. E., Andreae, M. O., and Warren, S. G.: Oceanic phytoplankton, atmospheric sulfur, cloud albedo and climate, Nature, 326, 655-661, 1987.

Coe, H., Allan, J. D., Alfarra, M. R., Bower, K. N., Flynn, M. J., McFiggans, G. B., Topping, D. O., Williams, P. I., O'Dowd, C. D., Dall'Osto, M., Beddows, D. C. S., and Harrison, R. M.: Chemical and physical characteristics of aerosol particles at a remote coastal location, Mace Head, Ireland, during NAMBLEX, Atmos. Chem. Phys., 6, 3289-3301, 2006.

Cremades, L. V., Toro, M. V., and Calbo, J.: Relationship between VOC and NOx emissions and chemical production of tropospheric ozone in the Aburra Valley (Colombia), Chemosphere, 65, 881-888, 2006.

CSIS: Segundo informe sobre Evaluacion Ambiental de la Ria de Huelva, available at: http://csis.es,2002.

de la Campa, A. M. S., Pio, C., de la Rosa, J. D., Querol, X., Alastuey, A., and Gonzalez-Castanedo, Y.: Characterization and origin of EC and OC particulate matter near the Donana National Park (SW Spain), Environmental Research, 109, 671-681, 2009.

de la Campa, A. M. S., de la Rosa, J., Gonzalez-Castanedo, Y., Fernandez-Camacho, R., Alastuey, A., Querol, X., Stein, A. F., Ramos, J. L., Rodriguez, S., Orellana, I. G., and Nava, S.: Levels and chemical composition of PM in a city near a large Cu-smelter in Spain, J Environ Monitor, 13, 1276-1287, 2011.

de la Rosa, J. D., de la Campa, A. M. S., Alastuey, A., Querol, X., Gonzalez-Castanedo, Y., Fernandez-Camacho, R., and Stein, A. F.: Using PM(10) geochemical maps for defining the origin of atmospheric pollution in Andalusia (Southern Spain), Atmos. Environ., 44, 4595-4605, 2010.

DeCarlo, P. F., Kimmel, J. R., Trimborn, A., Northway, M. J., Jayne, J. T., Aiken, A. C., Gonin, M., Fuhrer, K., Horvath, T., Docherty, K. S., Worsnop, D. R., and Jimenez, J. L.: Field-deployable, high-resolution, time-of-flight aerosol mass spectrometer, Analytical Chemistry, 78, 8281-8289, 2006.

DeCarlo, P. F., Dunlea, E. J., Kimmel, J. R., Aiken, A. C., Sueper, D., Crounse, J., Wennberg, P. O., Emmons, L., Shinozuka, Y., Clarke, A., Zhou, J., Tomlinson, J., Collins, D. R., Knapp, D., Weinheimer, A. J., Montzka, D. D., Campos, T., and Jimenez, J. L.: Fast airborne aerosol size and chemistry measurements above Mexico City and Central Mexico during the MILAGRO campaign, Atmos. Chem. Phys., 8, 4027-4048, 2008.

Draxler, R. R. and Rolph, G. D.:HYSPLIT (Hybrid Single-Particle Lagrangian Integrated Trajectory). NOAA Air Resources Laboratory, Silver Spring, MD. Model access via NOAA ARL READY Website (http://www.arl.noaa.gov/ready/hysplit4.html), 2003.

Drewnick, F., Hings, S. S., Alfarra, M. R., Prevot, A. S. H., and Borrmann, S.: Aerosol quantification with the Aerodyne Aerosol Mass Spectrometer: detection limits and ionizer background effects, Atmospheric Measurement Techniques, 2, 33-46, 2009.

Drewnick, F., Böttger, T., von der Weiden-Reinmüller, S.-L., Zorn, S. R., Klimach, T., Schneider, S., and Borrmann, S.: Design of a mobile aerosol research laboratory and data processing tools for effective stationary and mobile measurements, Atmos. Meas. Tech. Discuss., 5, 2273-2313, doi: 10.5194/amtd-5-2273-2012, 2012.

Fernandez-Camacho, R., de la Rosa, J., de la Campa, A. M. S., Gonzalez-Castanedo, Y., Alastuey, A., Querol, X., and Rodriguez, S.: Geochemical characterization of Cu-smelter emission plumes with impact in an urban area of SW Spain, Atmos Res, 96, 590-601, 2010a.

Fernandez-Camacho, R., Rodriguez, S., de la Rosa, J., de la Campa, A. M. S., Viana, M., Alastuey, A., and Querol, X.: Ultrafine particle formation in the inland sea breeze airflow in Southwest Europe, Atmos. Chem. Phys., 10, 9615-9630, 2010b.

Hock, N., Schneider, J., Borrmann, S., Rompp, A., Moortgat, G., Franze, T., Schauer, C., Poschl, U., Plass-Dulmer, C., and Berresheim, H.: Rural continental aerosol properties and processes observed during the Hohenpeissenberg Aerosol Characterization Experiment (HAZE2002), Atmos. Chem. Phys., 8, 603-623, 2008.

Huffman, J. A., Jayne, J. T., Drewnick, F., Aiken, A. C., Onasch, T., Worsnop, D. R., and Jimenez, J. L.: Design, modeling, optimization, and experimental tests of a particle beam width probe for the aerodyne aerosol mass spectrometer, Aerosol Sci. Technol., 39, 1143-1163, 2005.

IPCC: Climate Change 2007: The Physical Science Basis. Contribution of Working Group I to the Fourth Assessment Report of the Intergovernmental Panel on Climate Change, edited by: Solomon, S., Qin, D., Manning, M., Chen, Z., Marquis, M., Averyt, K. B., Tignor, M., and Miller, H. L., Cambridge University Press, Cambridge, UK and New York, NY, USA, 996 pp., 2007.

Jickells, T. D., Kelly, S. D., Baker, A. R., Biswas, K., Dennis, P. F., Spokes, L. J., Witt, M., and Yeatman, S. G.: Isotopic evidence for a marine ammonia source, Geophys Res Lett, 30, 2003.

Lanz, V. A., Alfarra, M. R., Baltensperger, U., Buchmann, B., Hueglin, C., and Prevot, A. S. H.: Source apportionment of submicron organic aerosols at an urban site by factor analytical modelling of aerosol mass spectra, Atmos. Chem. Phys., 7, 1503-1522, 2007.

Lanz, V. A., Alfarra, M. R., Baltensperger, U., Buchmann, B., Hueglin, C., Szidat, S., Wehrli, M. N., Wacker, L., Weimer, S., Caseiro, A., Puxbaum, H., and Prevot, A. S. H.: Source attribution of submicron organic aerosols during wintertime inversions by advanced factor analysis of aerosol mass spectra, Environ. Sci. Technol., 42, 214-220, 2008.

Liu, H. P., and Chan, J. C. L.: An investigation of air-pollutant patterns under sea-land breezes during a severe air-pollution episode in Hong Kong, Atmos. Environ., 36, 591-601, 2002.

Paatero, P., and Tapper, U.: POSITIVE MATRIX FACTORIZATION - A NONNEGATIVE FACTOR MODEL WITH OPTIMAL UTILIZATION OF ERROR-ESTIMATES OF DATA VALUES, Environmetrics, 5, 111-126, 1994.

Paatero, P.: Least squares formulation of robust non-negative factor analysis, Chemometrics and Intelligent Laboratory Systems, 37, 23-35, 1997.

Perez-Lopez, R., Nieto, J. M., Lopez-Coto, I., Aguado, J. L., Bolivar, J. P., and Santisteban, M.: Dynamics of contaminants in phosphogypsum of the fertilizer industry of Huelva (SW Spain): From phosphate rock ore to the environment, Appl Geochem, 25, 705-715, 2010.

Pey, J., Querol, X., de la Rosa, J., Gonzalez-Castanedo, Y., Alastuey, A., Gangoiti, G., de la Campa, A. S., Alados-Arboledas, L., Sorribas, M., Pio, C., Cachorro, V., Pineiro, M., Lopez-Mahia, P., and Garcia-Gacio, D.: Characterization of a long range transport pollution episode affecting PM in SW Spain, J Environ Monitor, 10, 1158-1171, 2008.

Phinney, L., Leaitch, W. R., Lohmann, U., Boudries, H., Worsnop, D. R., Jayne, J. T., Toom-Sauntry, D., Wadleigh, M., Sharma, S., and Shantz, N.: Characterization of the aerosol over the sub-arctic north east Pacific Ocean, Deep-Sea Research Part Ii-Topical Studies in Oceanography, 53, 2410-2433, 2006.

Pope, C. A., and Dockery, D. W.: Health effects of fine particulate air pollution: Lines that connect, Journal of the Air & Waste Management Association, 56, 709-742, 2006.

Querol, X., Alastuey, A., de la Rosa, J., Sanchez-de-la-Campa, A., Plana, F., and Ruiz, C. R.: Source apportionment analysis of atmospheric particulates in an industrialised urban site in southwestern Spain, Atmos. Environ., 36, 3113-3125, 2002.

Querol, X., Alastuey, A., Rodriguez, S., Viana, M. M., Artinano, B., Salvador, P., Mantilla, E., do Santos, S. G., Patier, R. F., de La Rosa, J., de la Campa, A. S., Menendez, M., and Gil, J. J.: Levels of particulate matter in rural, urban and industrial sites in Spain, Sci. Total Environ., 334, 359-376, 2004.

Querol, X., Alastuey, A., Pey, J., Cusack, M., Perez, N., Mihalopoulos, N., Theodosi, C., Gerasopoulos, E., Kubilay, N., and Kocak, M.: Variability in regional background aerosols within the Mediterranean, Atmos. Chem. Phys., 9, 4575-4591, 2009.

Salcedo, D., Onasch, T. B., Dzepina, K., Canagaratna, M. R., Zhang, Q., Huffman, J. A., DeCarlo, P. F., Jayne, J. T., Mortimer, P., Worsnop, D. R., Kolb, C. E., Johnson, K. S., Zuberi, B., Marr, L. C., Volkamer, R., Molina, L. T., Molina, M. J., Cardenas, B., Bernabe, R. M., Marquez, C., Gaffney, J. S., Marley, N. A., Laskin, A., Shutthanandan, V., Xie, Y., Brune, W., Lesher, R., Shirley, T., and Jimenez, J. L.: Characterization of ambient aerosols in Mexico City during the MCMA-2003 campaign with Aerosol Mass Spectrometry: results from the CENICA Supersite, Atmos. Chem. Phys., 6, 925-946, 2006.

Sanchez de la Campa, A. M., de la Rosa, J., Querol, X., Alastuey, A., and Mantilla, E.: Geochemistry and origin of PM10 in the Huelva region, Southwestern Spain, Environmental Research, 103, 305-316, 2007.

Schneider, J., Weimer, S., Drewnick, F., Borrmann, S., Helas, G., Gwaze, P., Schmid, O., Andreae, M. O., and Kirchner, U.: Mass spectrometric analysis and aerodynamic properties of various types of combustion-related aerosol particles, Int J Mass Spectrom, 258, 37-49, 2006.

Stolzenburg, M. R., and Hering, S. V.: Method for the automated measurement of fine particle nitrate in the atmosphere, Environ. Sci. Technol., 34, 907-914, 2000.

Sun, J. Y., Zhang, Q., Canagaratna, M. R., Zhang, Y. M., Ng, N. L., Sun, Y. L., Jayne, J. T., Zhang, X. C., Zhang, X. Y., and Worsnop, D. R.: Highly time- and size-resolved characterization of submicron aerosol particles in Beijing using an Aerodyne Aerosol Mass Spectrometer, Atmos. Environ., 44, 131-140, 2010.

Takami, A., Miyoshi, T., Shimono, A., and Hatakeyama, S.: Chemical composition of fine aerosol measured by AMS at Fukue Island, Japan during APEX period, Atmos. Environ., 39, 4913-4924, 2005.

Toledano, C., Cachorro, V. E., de Frutos, A. M., Torres, B., Berjón, A., Sorribas, M., and Stone, R. S.: Airmass Classification and Analysis of Aerosol Types at El Arenosillo (Spain), Journal of Applied Meteorology and Climatology, 48, 962-981, 2009.

Topping, D., Coe, H., McFiggans, G., Burgess, R., Allan, J., Alfarra, M. R., Bower, K., Choularton, T. W., Decesari, S., and Facchini, M. C.: Aerosol chemical characteristics from sampling conducted on the Island of Jeju, Korea during ACE Asia, Atmos. Environ., 38, 2111-2123, 2004.

Ulbrich, I. M., Canagaratna, M. R., Zhang, Q., Worsnop, D. R., and Jimenez, J. L.: Interpretation of organic components from Positive Matrix Factorization of aerosol mass spectrometric data, Atmos. Chem. Phys., 9, 2891-2918, 2009.

Viana, M., Querol, X., Gotschi, T., Alastuey, A., Sunyer, J., Forsberg, B., Heinrich, J., Norback, D., Payo, F., Maldonado, J. A., and Kunzli, N.: Source apportionment of ambient PM2.5 at five Spanish centres of the European Community Respiratory Health Survey (ECRHS II), Atmos. Environ., 41, 1395-1406, 2007.

von der Weiden, S. L., Drewnick, F., and Borrmann, S.: Particle Loss Calculator - a new software tool for the assessment of the performance of aerosol inlet systems, Atmospheric Measurement Techniques, 2, 479-494, 2009.

Warneck, P.: Chemistry of the natural atmosphere, in: International geophysics series, Academic Press Inc., 1988.

Zhang, Q., Alfarra, M. R., Worsnop, D. R., Allan, J. D., Coe, H., Canagaratna, M. R., and Jimenez, J. L.: Deconvolution and quantification of hydrocarbon-like and oxygenated organic aerosols based on aerosol mass spectrometry, Environ. Sci. Technol., 39, 4938-4952, 2005.

Zhang, Q., Jimenez, J. L., Worsnop, D. R., and Canagaratna, M.: A case study of urban particle acidity and its influence on secondary organic aerosol, Environ. Sci. Technol., 41, 3213-3219, 2007.

Zorn, S. R., Drewnick, F., Schott, M., Hoffmann, T., and Borrmann, S.: Characterization of the South Atlantic marine boundary layer aerosol using an aerodyne aerosol mass spectrometer, Atmos. Chem. Phys., 8, 4711-4728, 2008.

3.2 New particle formation and growth events observed under clean conditions and with superimposed pollution on the coast of SW Spain[2]

J.-M. Diesch[1], F. Drewnick[1], V. Sinha[2,6], J. A. Adame[3], M. Sorribas[3,*], J. Williams[2], M. Martinez[4] and S. Borrmann[1,5]

[1] Particle Chemistry Department, Max Planck Institute for Chemistry, Mainz, Germany

[2] Air Chemistry Department, Max Planck Institute for Chemistry, Mainz, Germany

[3] Atmospheric Research and Instrumentation, National Institute for Aerospace Technology (INTA), Huelva, Spain

[4] Atmospheric Chemistry Department, Max Planck Institute for Chemistry, Mainz, Germany

[5] Institute for Atmospheric Physics, Gutenberg University Mainz, Mainz, Germany

[6] Indian Institute of Science Education and Research, Mohali Sector 81, S. A. S. Nagar, Manauli PO, Punjab, India 140306

[*]now at: Andalusian Center for Environmental Research (CEAMA), University of Granada, Spain

Submitted to Atmospheric Environment, in review, 2012

Abstract

The variability of the air composition associated with advection from different source regions affects the emergence and temporal evolution of particle nucleation events. Physical and chemical parameters of the ambient aerosol (particle number and mass concentration, size distributions from 7-523 nm), various trace gases (NO_x, SO_2, O_3, H_2O), the OH reactivity and meteorological parameters (solar UV radiation, ambient temperature, relative humidity, air pressure, wind speed, wind direction and precipitation) were simultaneously measured in "El Arenosillo" on the SW coast of Spain. The DOMINO (*Diel Oxidant Mechanisms In relation to Nitrogen Oxides*) campaign took place from November 20 until December 9, 2008. As the monitoring site was located at an airshed interface between an industrial city (Huelva), the Spanish continental interior and the Atlantic Ocean, new particle formation and growth events were classified according to associated back trajectories and local meteorology. Additionally, new particle formation events were separated according to the strength of particle formation and the growth profile. "Regional" nucleation occurred over large spatial scales of several hundred kilometers over the continent, characterized by a sharp transition of the fine particle aerosol fraction to a predominant mode around 10 nm, with subsequent and persistent growth. "Plume" events were measured when pollution from the industrialized Huelva estuary was superimposed on regionally formed nucleation events. These were characterized by stronger particle bursts and clear bimodal size distributions during the growth period indicating the addition of freshly formed particles of urban origin. Thus, different influences of anthropogenic and biogenic emissions onto particle formation and growth in urban and continental source regions can be identified. Here, we focus on precursor gases which favor the occurrence of new particle formation and characterize the chemical submicron particle composition before new particle formation and during growth using the Aerosol Mass Spectrometer (Aerodyne HR-ToF-AMS). Sulfuric acid, which was dependent on the availability of anthropogenic SO_2 is suggested to be the main precursor contributing to particle formation. Sulfate concentrations were substantially higher during the initial formation stages of "plume" events compared to "regional" events that were characterized by lower PM_1 concentrations principally composed of organics. All new particle formation events exhibited organic matter as predominant constituent during the

[2] Original text and figures not yet published (June 2012) but submitted and reviewed by Atmospheric Environment. A shortened version has been accepted.

growth period. A detailed analysis of the organic mass spectral fingerprint shows oxidized organic compounds being the main contributors to growth. As one aspect of this study was to identify favorable nucleation conditions we also focus on non-event days observed when air masses originate from the Atlantic Ocean.

3.2.1 Introduction

Atmospheric particle formation and subsequent growth have been observed in different locations including forested (Kulmala et al., 1998; Dal Maso et al., 2005), coastal (O'Dowd et al., 2002a; Liu et al., 2008), rural (Weber et al., 1997; Wiedensohler et al., 2002; Paasonen et al., 2009) and urban areas (Alam et al., 2003; Stanier et al., 2004; Wehner et al., 2004; Fernandez-Camacho et al., 2010). Although the latter locations were expected to be less favored for such processes due to the higher condensational sink causing loss of condensable species onto pre-existing particles, numerous studies have now established that nucleation events also occur in urban or polluted environments. However, very limited data exist concerning new particle formation events that are superimposed by pollution plumes. While Wu et al. (2007) mentioned to observe a so-called "plume" event, Sakurai and coworkers investigated "plume" events regarding hygroscopicity and volatility (Sakurai et al., 2005). However, the influence of pollution plumes (e.g. industrial or ship emissions) overlapping new particle formation events has not been investigated in detail although it is known that they emit additional precursors and could therefore strongly affect the particle formation and growth processes from regular nucleation events.

Regardless of the environment, nucleation events are characterized by bursts of ultrafine particles which are potentially hazardous to human health (Oberdorster et al., 2002). Once grown to ca. 40-100 nm, these particles have a radiative effect on climate since they may act as cloud condensation nuclei (Spracklen et al., 2008; Merikanto et al., 2009). Literature on the identification of natural and anthropogenic precursor species contributing to particle nucleation and growth is relatively rare or limited to few species. While laboratory measurements of Sipilä et al. (2010) proposed that one or two sulfuric acid molecules and water in the atmosphere are sufficient for new particle formation, Metzger et al. (2010) and Zhang et al. (2009) suggested organic precursors (organic acids) additionally play a role in the formation of a critical nucleus. Kerminen et al. (2010) found ammonia in laboratory measurements being involved in nucleation, however based on quantum chemical calculations they suggested amines to be more important than ammonia in assisting nucleation. Measurement studies of the nanoparticle chemical composition performed by Wang et al. (2010) showed organics are involved in heterogeneous reactions forming non-volatile compounds which contribute to particle growth.

In recently published measurements at the CERN Proton Synchrotron, it was found that nucleating sulfuric acid clusters include nitrogen-containing bases or amides (Kirkby et al., 2011). As ternary (NH_3-H_2SO_4-H_2O) nucleation theory is unable to quantitatively explain atmospheric boundary-layer nucleation, Kirkby et al. (2011) suggested organic compounds to be involved in atmospheric nucleation. However, as current technology does not allow studying the composition of particles of sizes around 1 nm directly, the details of the nucleation mechanism cannot be finally described yet (Zhang, 2010). Additionally, dependent on location and meteorological conditions, the precursors can vary substantially (Kulmala et al., 2005; Boy et al., 2008). In urban areas, for example, more sulfuric acid is available contributing to particle nucleation and growth compared to less human affected environments (Kulmala et al., 2005; Zhang et al., 2009).

Uncertainties also exist about the meteorological influence on particle nucleation events. Some studies (Birmili and Wiedensohler, 2000; Boy and Kulmala, 2002; Stanier et al., 2004) found solar UV radiation to be an important meteorological factor that triggers photochemical reactions. Other environmental factors such as low temperature and relative humidity are suggested to have significant influence on new particle formation (Hamed et al., 2007). However, not all particle nucleation studies agree on these influences making it difficult to predict events or derive parameterizations.

The aim of this study is to present a detailed investigation of the characteristics and differences of new particle formation and growth events that occurred over large spatial scales and are partially affected by different kinds of pollution sources depending on the air mass origin. Back trajectories were calculated to investigate the variability of the air composition associated with advection from different source regions. Additionally, we focus on precursor gases which favor the occurrence of new particle formation and we characterize the chemical particle composition during new particle formation and growth. Finally, meteorological and gas phase conditions under which new particle formation events occurred or are inhibited are juxtaposed.

3.2.2 Methodology

3.2.2.1 Sampling time and location

The measurements during the DOMINO (*Diel Oxidant Mechanisms In relation to Nitrogen Oxides*) campaign were conducted at the "El Arenosillo"-Atmospheric Sounding Station (37° 05' 47.76" N, 6° 44' 6.49" W), a platform of the Atmospheric Research and Instrumentation Branch of the Spanish National Institute for Aerospace Technology (INTA) dedicated to atmospheric measurements in the southwest of Spain (Fig. 3.12) from November 20 until December 9, 2008. The site was located near the Doñana National Park, a large nature reserve of pine forests and marshlands with sandy soil, near the Atlantic coast (300 m) to the south of the site. In relation to the measurement station, the city Huelva (pop. ca. 0.5 million) is located 20 km to the northwest while the distance to Seville (pop. ca. 2 million) is about 70 km to the northeast.

3.2.2.2 Predominant wind directions and transport of pollutants

As the monitoring site is located at an airshed interface (Fig. 3.12) local air composition and quality was affected by advection from various continental, urban and marine sources determined by the transport patterns of air arriving at the measurement site. Predominant wind directions during this study period ranged from WSW through NW to NNE being untypical during winter time in this sampling area (Adame et al., 2010). They transported polluted air from Seville (and continental Spain) and more locally, from the strongly industrialized area of Huelva characterized by different kinds of industrial point sources (Querol et al., 2004; Alastuey et al., 2006; Sanchez de la Campa et al., 2007). These include the production and processing of metals and mineral and chemical industries (fertilizer production industries, petrochemical industries, ammonia and urea industries) in the southeast of Huelva city (Punta del Sebo and Nuevo Puerto areas). Towards the north, paper and wood processing industry and the food and beverage sector is situated (Tartessos area). Waste and waste water management as well as the energy sector is geographically scattered around Huelva. Air masses from the continent and the Atlantic Ocean affected the site as well. Moreover, desert dust is also a prevalent aerosol type in this region occurring mostly during February-March and in the summer months (Toledano et al., 2007), however not during the study period. In addition, the land-sea breeze system may affect atmospheric processes but this mainly occurs in spring and

summer time with lowest occurrence in the cold months and up to 30% of the days between May to September with a maximum of 70% in August (Adame et al., 2010). A detailed investigation of the different kinds of air masses, their characteristics, processes, typical sources of aerosols and trace gases during the DOMINO campaign can be found in Diesch et al. (2012). Previous publications on surface measurements in this area show levels and temporal variations of surface ozone (Adame et al., 2010), particulate mass levels (gravimetric) and chemical composition (de la Campa et al., 2009), submicron particle size distributions (Sorribas et al., 2011).

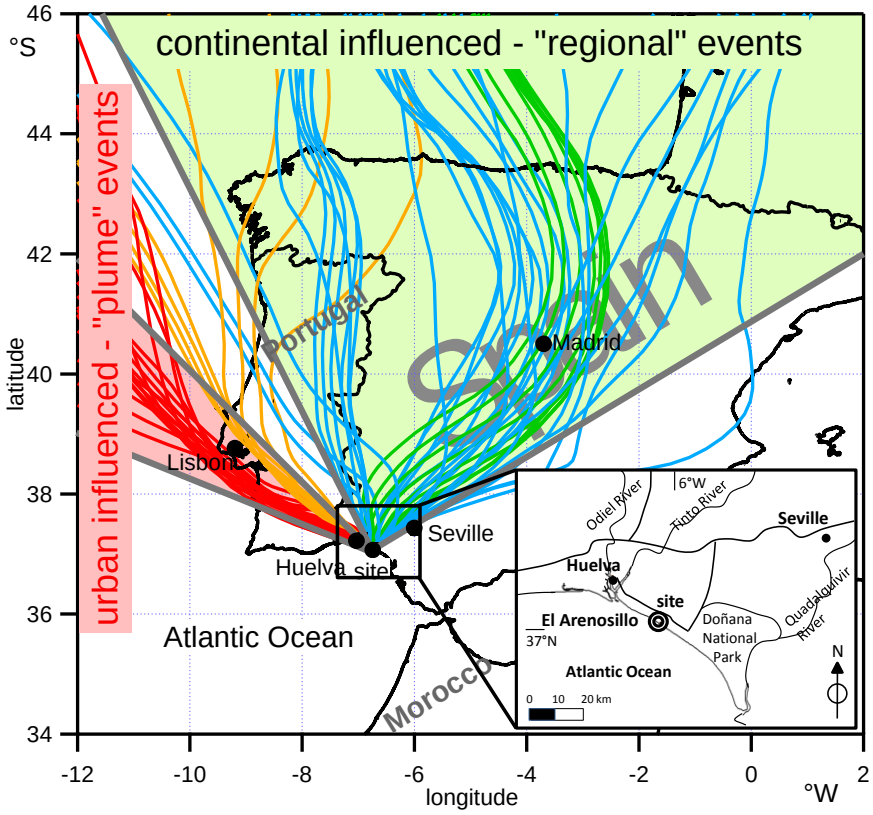

Figure 3.12: Map of Spain including 48 h backwards trajectories calculated for every 2 hours using HYSPLIT. Dependent on the trajectory pathways and air mass origins (continental/urban) new particle formation events were classified into "regional" (green and blue) and "plume" (red and orange) events. The zoom-in at the lower right shows the location of the monitoring station.

3.2.2.3 Instrumentation and data quality

Measurements of ambient aerosol were performed using the mobile laboratory "MoLa", a mobile platform for aerosol research (Drewnick et al., 2012). The complete set of instrumentation implemented in MoLa and used for the analysis of nucleation events during this study is listed in Table 3.4. PM_1-number and mass concentrations were measured and a size distribution instrument was used to cover the particle size range from 7 to 523 nm. The chemical composition of the non-refractory (NR) aerosol was measured by means of an Aerosol Mass Spectrometer (AMS) as well as the black carbon concentration (MAAP) was determined in PM_1. Gas phase species measurement instruments monitored various trace gases (NO, NO_2, SO_2, O_3, H_2O) in the air and a weather station provided meteorological parameters (ambient temperature, relative humidity, air pressure, wind speed, wind direction and precipitation). The integrated ultraviolet solar irradiance was registered from 286 to 363 nm. The mixing layer height calculations are based on meteorological balloon soundings by R. Sander twice a day during the campaign (unpublished data). The OH

comparative reactivity instrument, that determines species in the gas phase (Sinha et al., 2008; Sinha et al., 2009; Sinha et al., 2010) was located in a measurement container adjacent to MoLa. For stationary measurements the roof inlet of MoLa with a sampling height of 10 m above ground level was used next to a second extendable mast (10m) housing the meteorological station.

Table 3.4: Instruments implemented in the mobile laboratory (MoLa) and in its vicinity, used to investigate new particle formation events in this study.

Measured parameter	Instrument	Model
number concentration	ultrafine water-based Condensation Particle Counter	CPC 3786, TSI, Inc.
mass concentration	Filter Dynamics Measurement System Tapered Element Oscillating Microbalance	FDMS-TEOM, Rupprecht&Patashnick Co., Inc.
particle size distribution	Fast Mobility Particle Sizer (7-523 nm)	FMPS 3091, TSI, Inc.
chemical composition	High-Resolution Time-of-Flight Aerosol Mass Spectrometer	HR-ToF-AMS, Aerodyne Res., Inc.
black carbon	Multi Angle Absorption Photometer	MAAP, Thermo E.C.
SO_2, NO, NO_2 and O_3	Airpointer	Recordum GmbH
H_2O	LICOR 840 gas analyzer	LI-COR, Inc.
ambient temperature, relative humidity, air pressure, wind speed, wind direction, rain intensity	weather station	WXT 510, Vaisala
ultraviolet solar irradiance (from 286 to 363 nm)	Brewer MK-III double monochromator spectrometer	Scintec-Kipp & Zonen
OH Reactivity	Comparative Reactivity (Glass reactor and Quadrupole Proton Transfer Reaction-Mass Spectrometer)	Custom built and integrated at MPI, Mainz

For data quality assurance:

- particle losses for all instruments were estimated using the *Particle Loss Calculator* Software (von der Weiden et al., 2009). It was found that particle losses can be neglected as in the size range where the majority of relevant data were measured, particle losses do not influence the measurement results significantly.
- transport delays through the sampling inlet were determined and subtracted from the time stamps for each instrument to calculate the sampling times from the measurement times.
- calibrations of the AMS (particle sizing calibration (once per campaign), detector gain calibration (every second day), ionization efficiency calibration (once per week)) were performed regularly during the campaign and a collection efficiency (CE) factor of 0.5 for the AMS mass concentrations was determined by comparing AMS (PM_1 non-refractory species) plus MAAP (PM_1 black carbon) with TEOM PM_1 mass concentrations to correct for incomplete transmission and collection of the particles in the AMS.
- detection limits were calculated for each parameter, measured by the AMS, as described in Drewnick et al. (2009).

A summary of the measured quantities, size ranges, particle losses, sampling time delays and detection limits for all instruments implemented in MoLa during this study as well as detailed information on the operation and the data analysis is presented in Diesch et al. (2012). Further information of the mobile aerosol research platform is given in Drewnick et al. (2012). For this analysis, a uniform 1-min time resolution for all instruments was used except for the TEOM where the smallest time resolution amounts to 15 min. The detection limit for the OH reactivity measurements during this study was 3.5 s^{-1} and the overall uncertainty of the measured OH reactivity was ~20% (Sinha et al., 2012).

Two different types of diameters were used in this study: the FMPS size distribution instrument registers the electrical mobility diameter (D_{mob}), the AMS measures the aerodynamic particle diameter in the free-molecular flow regime (D_{va}). Both diameters depend on the dynamic shape factor (χ) and D_{va} in addition, on the particle density. While the aerodynamic lens of the AMS is able to focus particles with 100% efficiency in the 40-600 nm vacuum-aerodynamic particle size range (Liu et al., 2007), particles in the 20-1200 nm size range can be detected as well, but with decreased efficiency. Nevertheless, the AMS is not able to measure freshly formed particles in the early nucleation stages and therefore it is not possible to investigate chemical species that form the nucleus, but those that contribute to growth. To distinguish between particles that were involved in growth and the background aerosol, the AMS size distribution was divided into the "ultrafine" (<100 nm) and the "accumulation" mode (>100 nm).

3.2.2.4 Back trajectory analysis and classification of new particle formation events

In order to determine bulk air mass motion affecting the site, 48-h back trajectories at 10 m arrival height above ground level were calculated for every 2 h during the entire measurement period using the HYSPLIT (Hybrid Single Particle Lagrangian Integrated Trajectory) model (Draxler et al., 2009). The GDAS (Global Data Analysis System) generated and maintained by the ARL (Air Resources Laboratory) have been used as meteorological data input. To analyze different categories of new particle formation and growth events, the measured physical and chemical aerosol particle as well as gas phase parameters were segregated on the basis of the back trajectories showing similar air mass histories. For this purpose we assume that the measured data one hour before the arrival time and one hour thereafter "belong" to each trajectory. Fig. 3.12 shows a map including the back trajectories that correspond to each of the identified types of new particle formation events.

Dependent on the trajectory pathways and air mass origins new particle formation events were classified into 2 classes:
- "regional" events occurring in continentally influenced air masses (green traces) and
- "plume" events measured when trajectories pass the urban source region Huelva (red traces).

Continentally influenced air masses contain air transported from Spanish and Portuguese inland areas over pine forests to the station in contrast to Huelva-influenced air masses that firstly travelled over the Atlantic Ocean (beside the 3 orange trajectories), then passed Portugal and Huelva before they reached the site.

The HYSPLIT trajectory analysis addresses the regional and long-range transport properties of air masses, but as a second criterion for the evaluation of new particle formation events, local meteorology at the sampling site was taken into account. The following wind direction ranges limited by the different air mass histories for each of the measured events were used for the analysis:

-340-65° for "regional" events
-285-310° for "plume" events.
Further information about the different classification methods can be found in Diesch et al. (2012). Furthermore, in order to avoid stagnant air masses with potential contamination from local sources to influence the results, all data measured during times with wind speed below 1 m s^{-1} were not used for further processing.

3.2.2.5 Formation rate, growth rate, and condensational sink

The following three parameters were used for the description of new particle formation events:
- Particle formation rates (FR, particles cm^{-3} s^{-1}) were estimated on the basis of the particle number concentration in the 7 up to 20 nm size range from the event starting time until the time of maximum number concentration assuming a linear increase without accounting for coagulation losses. The start time of an event is characterized by an abrupt rise in the particle number concentration.
- Particle growth rates (GR, nm h^{-1}) were determined by fitting the increase of the arithmetic mean diameter (AMD) for the size distribution range below 100 nm linearly between the event start (smallest AMD) and the maximum diameter when the growth has ended as described in Jeong et al. (2010).
- The condensational sink[3] (CS, cm^{-2}) was determined by integration of the size distribution over the 7 nm to 523 nm (i.e. the FMPS upper size limit) size range based on the formulation by Stanier et al. (2004):

$$CS = \sum_i \beta_i D_{mob,i} N_i \tag{3.8}$$

where β_i is the transitional regime correction factor which is in the range of 0.04 to 0.83, $D_{mob,i}$ the particle mobility diameter and N_i the particle number concentration of the size bin i.
The transitional regime correction factor was calculated according to Fuchs and Sutugin (1970):

$$\beta = \frac{Kn+1}{1.33\,Kn^2+1.71\,Kn+1} \tag{3.9}$$

by using the Knudsen number:

$$Kn = \frac{2\lambda}{D_{mob}} \tag{3.10}$$

where λ represents the mean free path of gas molecules (under standard conditions λ =67 nm). As the condensational sink was integrated over the size range of the FMPS only, the actual condensational sink would be slightly underestimated when larger particles exist, particularly when aged air masses are present. However, in order to avoid the even larger uncertainty when merging data from the FMPS and OPC instruments, particles larger than 523 nm were neglected which account for <10% of the total particle surface (see Diesch et al., 2012).

[3] The condensational sink provides a measure of the available surface area for condensation of gases. The larger the condensational sink the less favourable the new particle formation.

3.2.3 Results

3.2.3.1 Characteristics of the nucleation events

New particle formation and growth events were identified on the basis of the evolution of the particle size distributions and the particle number concentrations. From November 20 until December 9, 2008 eight new particle formation and growth events were observed. The events started in the morning between 9.30 a.m. and 1.30 p.m. (UTC) and grew between 12-20 hours until the particles reached sizes of about 100 nm.

For in-depth discussion of the new particle formation events, the events have been divided into two classes and two sub-classes with similar conditions as follows:
- The so-called "regional" nucleation events (Fig. 3.12, associated with the green and blue colored trajectories) occurred in air masses that have a large geographical homogeneity and are characterized by starting times in the morning or early afternoon. They have a sustained growth profile over several hours (Kulmala et al., 2004; Stanier et al., 2004).
- Pollution-influenced nucleation events (red and orange in Fig. 3.12); hereafter called "plume" events were measured when pollution from a point source, in our case the strongly industrialized Huelva estuary, was superimposed over a "regionally" formed nucleation event as also found by Sakurai et al. (2005) and Wu et al. (2007).
- "Regional" nucleation events were further classified by the methods described in Mäkelä et al. (2000) and Dal Maso et al. (2005) according to the intensity of the particle formation (formation rate) and the distinctness of the particle growth profile. A "Class 1" new particle formation event (green colored in Fig. 3.12) exhibits intensive particle formation as well as continuous growth with only small size distribution fluctuations. Also for "Class 2" events (blue colored) clear particle formation and a following growth period are observed. However, Class 2 events did not exhibit such an intensive particle formation and also showed larger fluctuations in the size distributions.
- As one aspect of this study was to identify conditions that favor new particle formation, in addition, days without nucleation (non-event days) as well as days that can either be classified as non-event or event-day are also considered.

Although nucleation events were detected under sea-breeze and non-sea-breeze conditions in a long-term study from 15 July 2004 to 31 July 2006 performed at the "El Arenosillo" station, Sorribas et al. (2011) found no differences in the observed "regional" nucleation events within both types of conditions. In contrast, differences were found during the growth period of the "plume" events. However, since in winter the sea breeze is less pronounced, we did not further evaluate this influence on the measured new particle formation events. Although we only observed 8 new particle formation events during the DOMINO campaign, comparing the major features of these individual case studies with those observed over a two year period by Sorribas et al. (2011), they appear to be representative for the "El Arenosillo" area.

In Fig. 3.13, diel variations of the particle number concentration in the 7 up to 20 nm size range for all days of the classified new particle formation events are shown. The start of the individual events is characterized by a significant increase of nucleation mode particles reaching maximum number concentrations from $N_{7\text{-}20}$ = 4600 up to 80,000 cm^{-3} while the maximum particle number concentrations range between N_{tot} = 20,000 and 180,000 cm^{-3}, respectively (Table 3.5). To show the differences in the particle number concentrations between nucleation and non-nucleation event days, as an example, one of these days was added in Fig. 3.13.

Depending on the air mass origin, new particle formation events differ in the starting times and intensity. While "plume" events (starting times between 9:30 and 10:40 a.m.) are characterized by the largest formation rates (4-13 cm^{-3} s^{-1}), a lower rate was determined for the "regional" Class 1 event (3.9 cm^{-3} s^{-1}) and the lowest formation rates were found for Class 2 events (0.6-2.2 cm^{-3} s^{-1}) (Table 3.5). Compared to "regional" events, in "plume" events relatively strong industrial emissions are superimposed onto the advected particle concentrations, leading to increased particle number concentrations and resulting in higher formation rates. However, the formation rates of "plume" events are difficult to determine. Due to the different kinds of point sources situated in Huelva City (see Section 2.3) that do not have a constant level, particle number concentrations show significant variations dependent on the path of the air masses through this area and the time. Both, "regional" Class 1 and Class 2 nucleation events are continentally influenced and have similar air mass histories. For this reason they exhibit similar characteristics. However, different intensities and starting times of the events depend on the particular characteristics of the measurement day. Class 2 events started between 00:30 and 01:30 p.m. (UTC) on workdays (incl. Saturday) characterized by high particle number (blue traces in Fig. 3.13), nitrogen oxide and particulate organics concentrations between 8 and 10 a.m. (Fig. 3.14) probably originating from vehicular traffic emissions. Likewise, before the start of the Class 2 events higher mass concentrations were observed in contrast to the Class 1 event that was registered on a Sunday starting at 10:30 a.m. (Table 3.5). Additionally, during the "regional" Class 1 event, the height of the boundary layer was 1300 m in the afternoon (4 p.m.) and a relatively high UV solar irradiance was observed. The relatively high boundary layer led to lower concentrations in the early morning hours while due to the high UV solar irradiance a high particle formation rate was observed. Instead, "regional" Class 2 events are characterized either by high UV solar irradiance or by a high boundary layer height (see Table 3.5) which results in lower particle formation rates due to the loss of precursors onto pre-existing particles.

Comparing the diel patterns of particle number and mass concentrations of nucleation and non-nucleation event days, particle formation caused substantially higher number, as opposed to mass concentrations as also found by Alam et al. (2003). Number concentrations vary significantly between continental, urban and marine source regions. However, new particle formation events even cause larger variations in the number concentrations.

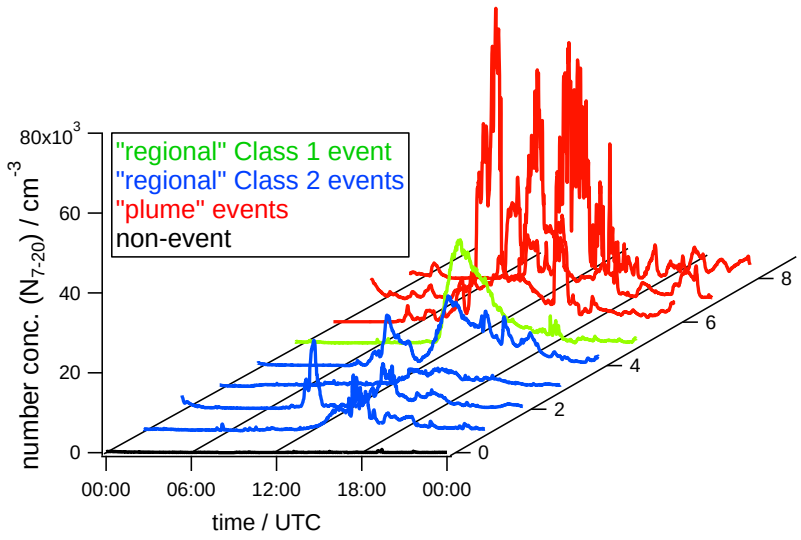

Figure 3.13: Diurnal variations in particle number concentrations ($N_{7\text{-}20}$) for all new particle formation event classes are shown. Additionally one of the days without nucleation (black) is added for comparison.

Table 3.5: Summary of times, types, conditions and corresponding parameters determined for the different new particle formation events (*indicates average values calculated during the nucleation period). The boundary layer heights were determined by the change of the potential temperature gradient at approximately 4 p.m.. The UV solar radiation levels reflect daily average values.

Date	Starting time	Event	Formation rate /cm^{-3} s^{-1}	Growth rate /nm h^{-1}	cond. sink* /cm^{-2}
22.11.2008	01:00 p.m.	Class 2	0.6±0.05	4.5±0.04	0.009
23.11.2008	10:30 a.m.	Class 1	3.9±0.2	2.8±0.04	0.003
24.11.2008	10:40 a.m.	"plume"	12.9±2.2	-	0.008
25.11.2008	01:30 p.m.	Class 2	1.6±0.2	2.8±0.2	0.006
26.11.2008	01:00 p.m.	Class 2	0.7±0.07	4.2±0.1	0.004
30.11.2008	09:30 a.m.	"plume"	10.3±0.8	2.3±0.05	0.009
01.12.2008	09:30 a.m.	"plume"	4.0±0.4	2.0±0.1	0.01
02.12.2008	00:30 p.m.	Class 2	2.2±0.1	2.1±0.03	0.006

Date	Starting time	Event	max. $N_{7\text{-}20}$ /cm^{-3}	max. N_{tot} /cm^{-3}	SO_2* / ppbv
22.11.2008	01:00 p.m.	Class 2	5925	20202	0
23.11.2008	10:30 a.m.	Class 1	26038	73941	0.5
24.11.2008	10:40 a.m.	"plume"	59087	177730	2.9
25.11.2008	01:30 p.m.	Class 2	11388	30682	0.3
26.11.2008	01:00 p.m.	Class 2	4647	23078	0.04
30.11.2008	09:30 a.m.	"plume"	78555	120570	4.4
01.12.2008	09:30 a.m.	"plume"	30823	100830	9.8
02.12.2008	00:30 p.m.	Class 2	17185	38917	0.4

Date	Starting time	Event	NO_x* / ppbv	max. O_3 /ppbv	H_2O* / pptv
22.11.2008	01:00 p.m.	Class 2	1.9	43	9.5
23.11.2008	10:30 a.m.	Class 1	0.3	41	8.2
24.11.2008	10:40 a.m.	"plume"	3.4	44	10.5
25.11.2008	01:30 p.m.	Class 2	0.6	40	7.3
26.11.2008	01:00 p.m.	Class 2	0.9	40	3.6
30.11.2008	09:30 a.m.	"plume"	4.6	40	8.5
01.12.2008	09:30 a.m.	"plume"	8.3	40	8.0
02.12.2008	00:30 p.m.	Class 2	0.9	37	6.0

Date	Starting time	Event	min. RH /%	max. T /°C	avg. UV /Wm^{-2}	Boundary layer height /m
22.11.2008	01:00 p.m.	Class 2	35	23	18	80
23.11.2008	10:30 a.m.	Class 1	29	22	16	1300
24.11.2008	10:40 a.m.	"plume"	47	18	11	1300
25.11.2008	01:30 p.m.	Class 2	41	15	8	1250
26.11.2008	01:00 p.m.	Class 2	24	13	12	150
30.11.2008	09:30 a.m.	"plume"	49	14	17	450
01.12.2008	09:30 a.m.	"plume"	52	12	15	1450
02.12.2008	00:30 p.m.	Class 2	37	14	17	-

3.2.3.2 Particle size distributions of classified new particle formation events

Before analyzing the size distributions of the classes of new particle formation events, we briefly discuss the limitations of the analysis of such events when measurements are observed at a single fixed site. Measurements at a fixed location imply different air parcels arriving at different times and therefore not the same air mass can be observed over extended time intervals. This means that the air masses have to be relatively homogeneous over larger spatial scales (Kulmala et al., 2001; Stanier et al., 2004; Lunden et al., 2006) in order to be able to observe particle formation events over several hours as in our studies. Otherwise the typical size distribution pattern would be interrupted.

The top panels of Fig. 3.14 a-c display image plots of the temporal evolution of the particle size distribution for the "regional" Class 2 (Fig. 3.14a), a Class 1 (Fig. 3.14b), and a "plume" event (Fig. 3.14c) measured by the FMPS. All three events started on average 4.2±1.7 hours after sunrise and show a sustained growth profile over an extended time period reaching maximum arithmetic mean particle diameters between 35 and 60 nm. These data indicate that new particle formation occurred after the break-up of the nocturnal inversion layer, initiated and driven by the photochemistry.

The evolution of the size distribution of a "plume" event (Fig. 3.14c) clearly differs from those of non-pollution-influenced "regional" events (Fig. 3.14a,b) by showing an additional mode at about 10 nm that indicates the occurrence of freshly formed particles of industrial origin relatively close to the measurement site. In addition, large fluctuations in the size distribution pattern were observed for this type of event due to the fact that small changes in wind directions cause diverse industrial point sources and emissions to influence the measurement site. Additionally, these emissions are not constant over time. Therefore, "plume" impacted nucleation events are typically characterized by a broader "banana"-shaped size distribution trend. For the same reason, the evolution of the arithmetic mean diameter (AMD) of particles determined by fitting the FMPS size distribution differs for "regional" and "plume" events. Both event types are characterized by an abrupt decrease in the AMD at the start of the event due to the formation of newly formed particles and a subsequent gradual increase during the growth period. Due to the additional influence of freshly produced particles formed in Huelva "plume" events frequently show a second mode around 10 nm.

By fitting the increase of the AMD over the growth period linearly, the average growth rate of nucleated particles during this study was determined to be 3.0±1.0 nm h^{-1} and varied from 2.0 to 4.5 nm h^{-1} during the individual events (Table 3.5). Regarding average growth rates for the different nucleation event classes, the lowest mean rate was determined for "plume"-impacted nucleation events (2.2 nm h^{-1}) while larger growth rates were observed for the "regional" Class 1 (2.8 nm h^{-1}) and Class 2 (3.4 nm h^{-1}) events. Therefore, an inverse trend in the particle growth rates compared to the formation rates is recognizable, which also exists within the group of Class 2 events.

Together with the existing background aerosol newly formed particles compete for the available condensable material. In addition to condensational growth they can be scavenged by the background aerosol particles. Thus, under conditions of high condensational sink new particle formation only occurs when the condensable vapor concentrations are sufficiently large, resulting in fast growth of nuclei mode particles before they are scavenged by larger ones. Therefore, larger growth rates were typically observed in more polluted areas (Birmili et al., 2003; Kulmala et al., 2005) while smaller ones are a feature for relatively clean environments (Weber et al., 1997; Dal Maso et al., 2005). In case of the "plume" events identified in our measurements, particles were formed and initially grow over the continent like during "regional" nucleation events. Therefore,

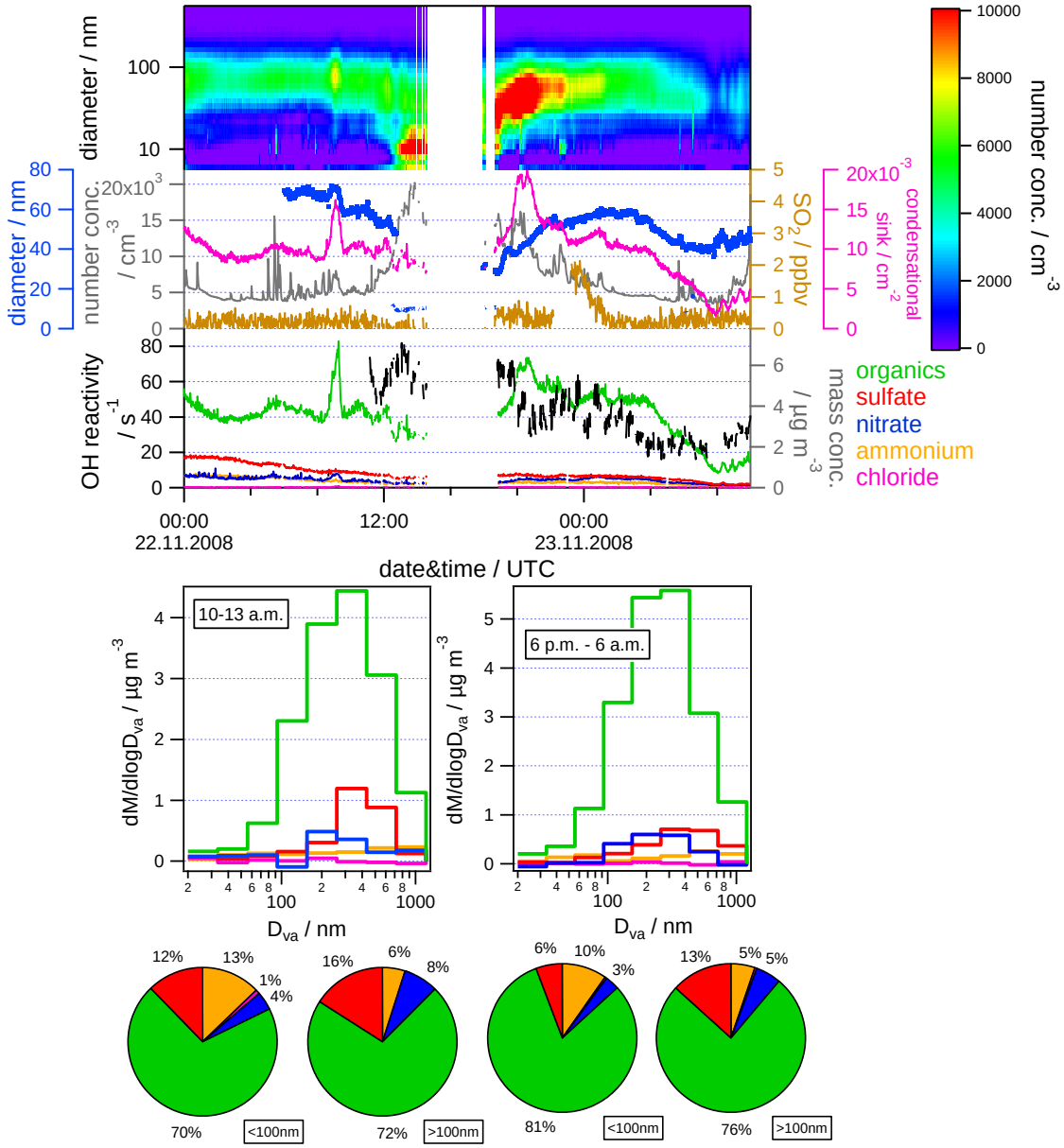

Figure 3.14a: Changes of the particle size distribution and the corresponding arithmetic mean diameter, variations in the particle number concentration, condensational sink, SO_2 mixing ratios as well as mass concentrations of the typical AMS species (organics, sulfate, nitrate, ammonium, chloride) for a "regional" Class 2 event are depicted. Mass distributions for periods before the nucleation event started and during the growth period together with corresponding pie charts of particle composition are shown integrated over the ultrafine (<100 nm) and accumulation mode (>100 nm) size range, respectively. The gaps in the graph result from periods where either wind speeds are smaller than 1 m s^{-1} or wind directions did not fall into the limited range.

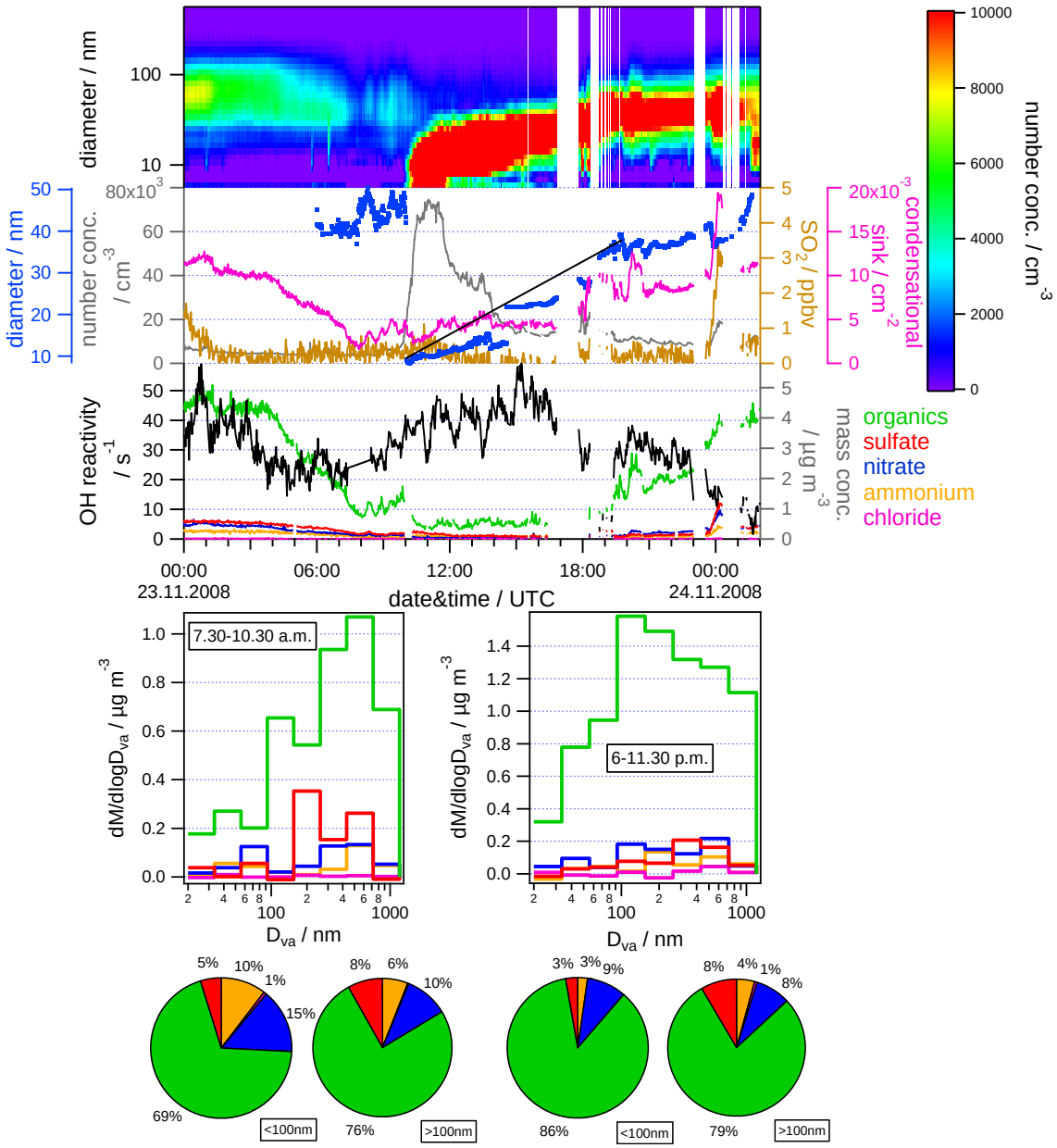

Figure 3.14b: Symbols and variables as in Figure 3.14a for a "regional" Class 1 event are depicted.

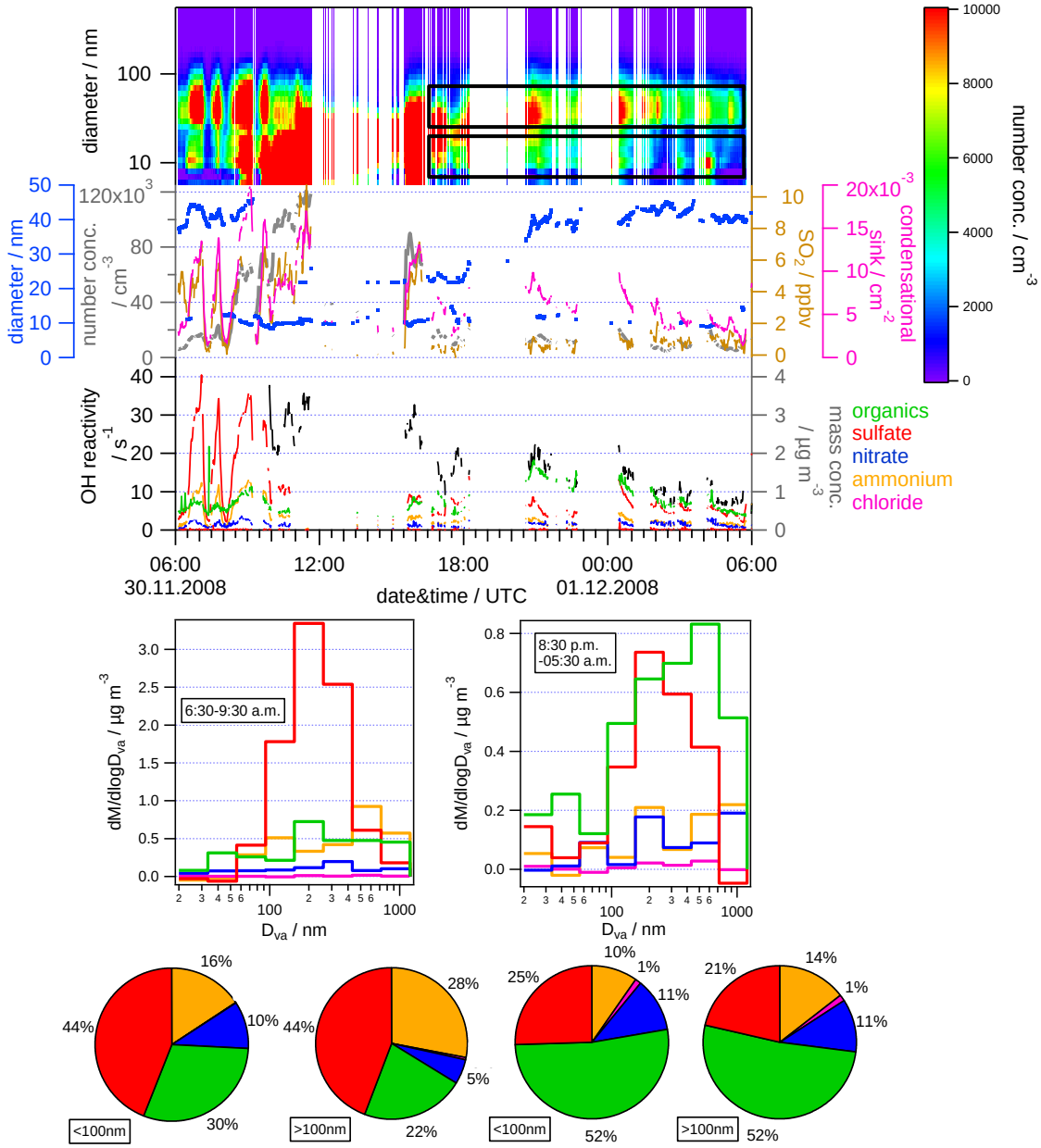

Figure 3.14c: Symbols and variables as in Figure 3.14a for a "plume" event are depicted.

comparable growth rates were observed for both types of events. However, when "plume" event air masses pass the city of Huelva they are impacted by diverse pollution sources that both, affect the nucleation period and also contribute material during the growth phase, resulting in an additional mode around 10 nm. As growth rates depend upon the available condensable vapor concentrations but also on the available particle surface, this additional particle surface area leads to slightly decreased average growth rates for "plume" events. The negative correlation that exists between the formation and growth rates within Class 2 events indicates that the fewer particles that are formed, the stronger they can grow, assuming that similar condensable vapor concentrations and meteorological conditions exist. Furthermore, it suggests that different kinds of species are involved in nucleation and in growth processes. Therefore the potential contribution of species to nucleation and growth is discussed in detail in the following sections.

The "plume" event corresponding to the orange colored trajectories (Fig. 3.12) differs from the two others, both in red. The air masses that were observed during its particle formation phase included a more aged and processed aerosol since the associated trajectories have passed over the continent for a long time before reaching Huelva and the site. In contrast, during the growth period a relatively fresh aerosol was observed because the associated air mass trajectories spent a shorter time over the continent. Due to this difference in air mass conditions for the two phases, the particle formation period cannot be compared with the growth period. Therefore, no growth rate was determined for this event.

3.2.3.3 Atmospheric conditions and composition during the nucleation periods

In the following, the prevailing atmospheric conditions observed during the nucleation periods (first hour after the onset of the new particle formation events) is investigated and compared using a range of measured parameters.

An important parameter, the condensational sink (CS), which is calculated from the FMPS size distribution provides a measure of the available surface area for condensation. Based on our calculations, the average CS during the nucleation period for the "regional" Class 1 event (CS = 0.003 cm^{-2}) is lower than that observed during the start of the Class 2 events (CS = 0.006 ± 0.002 cm^{-2}; average ± standard deviation) (Table 3.5). The CS of the Class 1 event decreased in the early morning hours due to the development of the boundary layer and consequently a lower average CS was observed for this event. Instead, during Class 2 events conditions are less favorable for nucleation due to a higher CS. Even though these CS values decreased after 10:00 h (UTC) at the beginning of the events the values were still higher than those of the Class 1 event. "Plume" events exhibit larger CS values (CS = 0.01 ± 0.003 cm^{-2}) during the nucleation period due to the influence of the pollutants in the urban atmosphere (Table 3.5). High levels of condensational sink can suppress new particle formation by scavenging freshly formed particles and absorbing condensable vapors (Kerminen et al., 2001; Monkkonen et al., 2004) resulting generally in higher formation rates of "clean" compared to "pollution" events. However, in case of the "plume" events observed in this study a strong nucleation (formation rate) characterized by high particle number concentrations was observed. In addition during these events high sulfur dioxide (SO_2) concentrations were present (Fig. 3.14). Generally, a wide range of concentrations was observed for SO_2 (Table 3.5). For "regional" events lowest average SO_2 mixing ratios (0-0.5 ppbv) were measured during the nucleation period. While higher average SO_2 mixing ratios (2.9-9.8 ppbv) characterized by large fluctuations were measured during "plume" events that were influenced by a variety of industrial emission sources. As SO_2 is the main precursor for gaseous sulfuric acid (H_2SO_4) which is thought to be one of the key species in particle formation (Kulmala et al., 2005; Boy et al., 2008; Berndt et

al., 2010) the product of ultraviolet (UV) light intensity (integrated over the 286-363 nm wavelength range) and SO_2 mixing ratios during the nucleation period can be used as a proxy for the H_2SO_4 production (Stanier et al., 2004). In Fig. 3.15, a scatter plot of the CS versus this H_2SO_4–proxy ($UV*SO_2$) is shown for the nucleation periods of all events. Depending on whether favorable conditions for nucleation exist or not, the graph was divided into two regions: in the upper part with large condensational sinks and low sulfuric acid-proxy, nucleation is observed fairly rare, while in the lower region new particle formation is more common as favorable conditions are present (Stanier et al., 2004). All data points corresponding to the "plume" and "regional" Class 1 events are below this CS : $UV*SO_2$ line. The relative locations of the data points for these two types of events imply that the nucleation periods of the pollution-influenced nucleation events are characterized by higher SO_2 levels and condensational sinks compared to the Class 1 "regional" nucleation event. "Regional" Class 2 events differ from both other classes as some of the data points fall into the upper left region where nucleation is not as favored because the sulfuric acid production is low and additionally the existing surface area for condensation is slightly enhanced compared to the "regional" Class 1 event. In agreement with the findings by Stanier et al. (2004) and Hamed et al. (2007), while this plot generally represents important parameters for particle nucleation also microphysics and meteorology may play important roles.

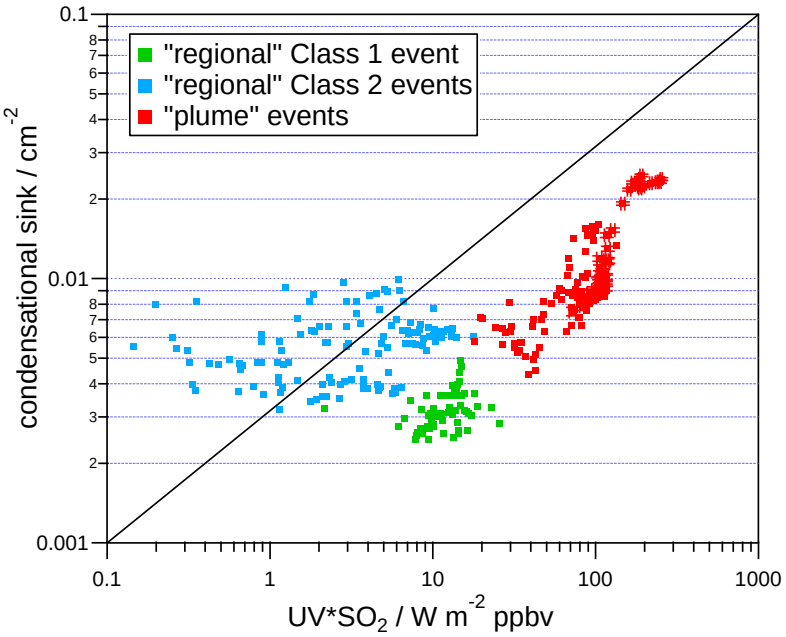

Figure 3.15: The condensational sink correlates with the product of ultraviolet light (UV) and SO_2, a proxy for the H_2SO_4 production for "regional" Class 1 (green-shaded), Class 2 (blue-shaded) and "plume" (red-shaded) events. The black line separates regions where nucleation is generally observed (lower right) and regions were nucleation is not very common (upper left). Data are one minute averages during the nucleation period (1 hour after the start of the individual events). The repeatability of the data points is exemplarily represented at some points.

In order to examine the differences in condensational sinks of "regional" Class 1 and Class 2 events compared to the "plume" events during the nucleation period, the chemical particle composition measured using the AMS was further analyzed. During the nucleation period, the non-refractory submicron aerosol composition was dominated either by organics or sulfate depending on the classification of the new particle formation events. In Fig. 3.16 the correlation of organics versus sulfate is shown for all nucleation periods, color-coded with the CS. While organics dominated the submicron aerosol during the nucleation period of the "regional" Class 2 events, sulfur species were

the major components which influenced the condensational sink during "plume" events. For the "regional" Class 1 event lowest CS values associated with lowest organic and sulfate concentrations were observed. Both, organics and sulfate are largely determined by the aerosol sources. On the one hand due to biogenic precursor emissions originating from the surrounding pine forests, on the other hand due to the influence of anthropogenic emission sources. For this reason, the particle composition during the nucleation and growth period is further investigated in the next section.

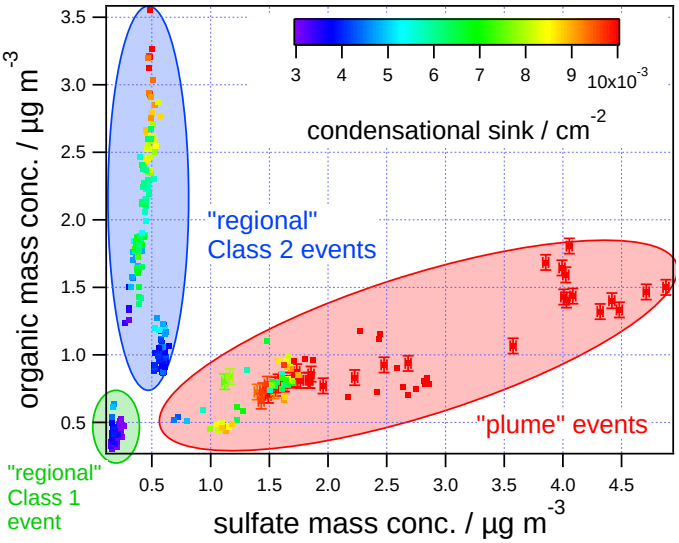

Figure 3.16: Scatter plot of the non-refractory submicron organic versus sulfate aerosol mass concentrations color-coded with the condensational sink for the nucleation period of "regional" and "plume" nucleation events. The repeatability of the data points is exemplarily represented at several points.

3.2.3.4 Particle composition during new particle formation events

Classical binary (H_2SO_4, H_2O) and ternary (H_2SO_4, H_2O, NH_3) nucleation theories failed to explain the frequency and intensity of new particle formation events. Thus, further species such as organic components were suggested to contribute to nucleation and growth as well (Kulmala et al., 2002; Kirkby et al., 2011). Here, we provide results from measurements of the chemical composition of the submicron aerosol during the new particle formation events and identify the species that participate in "regional" and "plume" nucleation events.

Temporal variation of submicron aerosol species

The evolution of the particle composition during "regional" Class 1, Class 2 and "plume" nucleation events is pictured in Fig. 3.14 (third panel from top). The aerosol particle characteristics before particle formation, during the nucleation and during the growth periods significantly differ between the classified types of events. Already before the nucleation starts, different influences of anthropogenic and biogenic emissions onto the aerosol composition in air masses from urban and continental source regions can be identified. Days of "regional" nucleation events are characterized by high organic mass concentrations of 4-5 µg m^{-3} very early in the morning. Due to the development of the mixing layer height the organics concentrations decreased and reached minimum levels (0.5-2.5 µg m^{-3}) during the new particle formation periods. Due to the morning rush hour days of Class 2 events exhibit an increased aerosol mass loading dominated by organics and nitrate, starting at about 9 h. A clear difference to this behavior is observed before the start and during the initial stages of "plume" events where the submicron aerosol is substantially affected by

sulfate, neutralized to a certain degree by ammonium. This is caused by the additional occurrence of freshly formed particles of industrial origin.

The growth period of "regional"-influenced new particle formation events is characterized by an increase of the organics, sulfate, nitrate and ammonium concentrations, starting 5-8 hours after the nucleation bursts occurred. However, the organics were the first species that contribute to growth and provide the largest fraction to it. The time delay between the rise of the number concentration ($N_{7\text{-}20}$), associated with the nucleation start, and the increase of the AMS mass concentrations is needed for freshly formed particles to reach the size range that can be registered by the AMS (i.e. diameter larger than 20-40 nm). Particle mass concentrations during "plume"-influenced nucleation events varied strongly depending on the additional influence of anthropogenic emissions. In contrast, during the growth period comparatively low mass concentrations were measured dominated by organics and sulfate. Sulfate and ammonium both show the same evolution during "regional" and "plume" nucleation events. As also mentioned by Zhang et al. (2004) and Allan et al. (2006) aerosol particles were mostly acidic during nucleation events as there was not enough ammonia present to fully neutralize the existing sulfate, nitrate and chloride. Sometimes condensable nitrate species were available in the gas phase and significantly contributed to the particle composition during the growth period of "regional" and "plume" events as well. Besides the four species (organics, sulfate, ammonium and nitrate) chloride played only a minor role in particle growth.

Dynamics of the size-resolved AMS composition

As the AMS simultaneously measures the particle composition and size distribution, it enables a detailed investigation of the species that contribute to growth, represented by the ultrafine mode (d_{va}<100 nm), as well as of the background aerosol, represented by particles larger than d_{va}=100 nm (accumulation mode). Since some of the size distribution data are significantly affected by electronic noise, before averaging and integration over the 20-100 and 100-1200 nm size range, those data with more than three times the regular noise were removed.

The chemical particle composition and corresponding total mass concentrations of the ultrafine and accumulation modes depend strongly on the sampled air masses. "Regional" events that occurred in less-polluted air masses from continental source regions are characterized by an accumulation mode mainly composed of organics (AMS size distributions in Fig. 3.14a,b). As shown in the pie charts in Fig. 3.14a,b that correspond to the time periods before nucleation started and to the growth periods of "regional" Class 1 and Class 2 events, respectively, the organic content in the >100 nm size range amounts to more than 70% while sulfate, ammonium and nitrate only contributed to a minor degree to the composition of the background aerosol. In contrast, sulfate dominated the background aerosol (44%) during the start of "plume" events (Fig. 3.14c) while organic matter is the main contributor (52%) during the growth period of these events. This suggests that for "plume" events both, organic species as well as sulfate play important roles in aerosol growth. As the ammonium fraction is smaller than needed to neutralize the sulfate mass fraction, particles were slightly acidic.

Although only very small mass concentrations were observed in the ultrafine mode, the aerosol composition for this size range can be characterized using the AMS. Since in all measured cases new particle formation started on the continent, the ultrafine mode aerosol is dominated by organic matter during the growth period of "regional" (>80%) as well as "plume" (52%) events. This indicates that the growth is mainly driven by condensable organic species. However, ammonium, sulfate and nitrate were also found to be present in ultrafine particles during the growth period.

Nevertheless, the fraction of these three inorganic compounds is appreciably smaller during "regional" compared to "plume" events where a large fraction of sulfate (25%), ammonium (10%) and nitrate (11%) was involved in particle growth (Fig. 3.14c).

Investigation of the organic mass spectral fingerprint

To further investigate those species that mainly contribute to the growth of the particles, the average mass spectrum of the background aerosol (that was assumed to be the same as before the growth period) was subtracted from the average mass spectrum during the growth period in order to obtain organic mass spectral fingerprints of the freshly condensed material. Mass spectra of the "regional" and "plume" events obtained by this method are shown in Fig. 3.17. They indicate that the different characteristic m/z fractions occurred, independant of whether nucleation events were continentally or urban influenced.

Mass spectra of the growth periods of "regional" Class 1 and Class 2 and of "plume" events (Fig. 3.17) show an increased contribution of m/z 44 compared to m/z 29, representing a rather oxidized organic aerosol. The ratio of these signals is larger during "regional" compared to "plume" events, implying a more processed and therefore more aged aerosol. Instead, the signal at m/z 43 ($C_3H_7^+$, $C_2H_3O^+$) results from primary as well as secondary organic matter. Although the allocation is not distinct it serves as a marker when comparing the m/z 44 with the m/z 43 signal to total organics as it is shown in Fig. 3.30 and explained in section 3.4.3.2. Elevated ion signals at m/z 27 and m/z 29 indicate biogenic, less aged secondary OA (SOA) potentially produced by the oxidation of VOCs from plants (Kiendler-Scharr et al., 2009) while those at m/z 41, 43, 55, 57, 69, 81, 95 ($C_nH_{2n+1}^+$, $C_nH_{2n-1}^+$) mainly correspond to heavily saturated and non-oxidized hydrocarbon-like organic aerosol species.

Using the Positive Matrix Factorization (PMF) tool (Ulbrich et al., 2009) to separate the submicron organic aerosol, four classes associated with various aerosol sources and components were identified: a highly-oxygenated and low volatile OA (OOA I), a semi-volatile OA (OOA II), a hydrocarbon-like OA (HOA) and a wood burning-related OA (WBOA). While a detailed analysis of these factors during the DOMINO campaign is presented in Diesch et al. (2012), in this study we focus on the variability of these organic aerosol classes during new particle formation and growth.

The increase of the total organic mass concentration during particle growth is mainly linked to an increase of OOA I. OOA I reflects a highly-oxidized OA while the m/z 27, 29, 41, 43, 55, 67, 79 mass fragments primarily correspond to OOA II. This behavior reflects the photochemical processes associated with the generation of secondary organic aerosol, which showed larger OOA concentrations during growth due to the accumulation of oxidized organic compounds in the vapor phase during the day that condensed onto the particle surfaces. HOA is enhanced during morning and evening rush hours and other human activities while WBOA, characterized by m/z 60, is a marker for fine particulate wood and biomass burning emissions. The m/z signals associated with HOA and WBOA are enhanced during both, "regional" and "plume" events (Fig. 3.17) indicating that species originating from anthropogenic emissions condensed onto the submicron aerosol. However, due to the strong industrial emissions originating from the Huelva estuary, "plume" events are characterized by larger m/z signals corresponding to these classes, compared to "regional" events (Fig. 3.17).

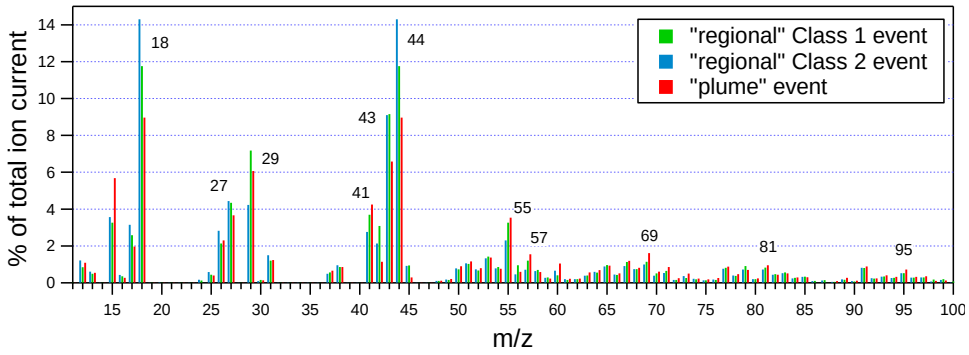

Figure 3.17: Comparison between organic mass spectral signatures observed during growth periods of "regional" and "plume" nucleation events. For comparability the mass spectra were normalized to the total ion current.

3.2.3.5 OH Reactivity

Characteristic features are also found in the total atmospheric OH reactivity values, measured as reciprocal OH lifetimes. The OH reactivity provides a measure of the concentration of species that can be oxidized by OH radicals. This includes a subset of potential aerosol precursors. Considering all days where nucleation took place, a diel variation of this parameter was observed in the profiles with average maximum OH reactivity levels of 42 s^{-1} between 1-2 p.m. (UTC) and lowest values (average: 20 s^{-1}) in the early morning hours (Fig. 3.18). Thus, the OH reactivity shows a delay of 1-2 h relative to the solar UV radiation cycle and correlates well with the temperature cycle. The median of 20-40 s^{-1} (Fig. 3.18) is significantly higher than the range observed for the entire campaign period (8 to 22 s^{-1}, Sinha et al. (2012)). Thus it appears that higher OH reactivity levels create favorable conditions for nucleation.

Regarding the temporal evolution of the OH reactivity in Fig. 3.14, maximum values were typically observed prior to the increase in the organic mass concentrations, indicating a large load of chemically reactive species in the atmosphere. The highest OH reactivity was observed for the "regional" Class 2 event with an average value of 70 s^{-1} during the new particle formation period (Fig. 3.14). However, due to a wind direction change values from 2 until 7 p.m. were not considered as they did not fall into the defined wind direction range. The "regional" Class 1 event reached lower average maximum values of about 50 s^{-1} while lowest maximum OH reactivity values of about 30 s^{-1} exist during the "plume" event in Fig. 3.14. Generally, for continentally influenced air masses, these values are markedly higher compared to those observed during studies in the tropical rainforest of Suriname where highest observed reactivity values of about 60 s^{-1} were measured (Sinha et al., 2008). For comparison, in boreal forests values in the order of 9 s^{-1} were found (Sinha et al., 2010). The values measured during DOMINO are broadly comparable to those measured in suburban Japan (average values of 30 s^{-1} in Tokyo, Sadanaga et al., 2005).

During the growth periods of all new particle formation event classes, the OH reactivity markedly decreases and reaches lowest values in the early morning hours at the end of the particle growth as a consequence of consumption of the potential precursor species during the night. In comparison, during non-event days the OH reactivity stays quite constant during this period with average values of 12 s^{-1} (Sinha et al., 2012).

Generally, it was found that higher OH reactivity levels during the nucleation period subsequently lead to a higher particle growth rate and higher organic mass concentrations as more precursors for

condensable vapors are available that condense onto the particle surface later on (Fig. 3.18). For one of the "regional" Class 2 events we observed an opposite OH reactivity behavior in relation to this general finding. However we do not have any explanations for this.

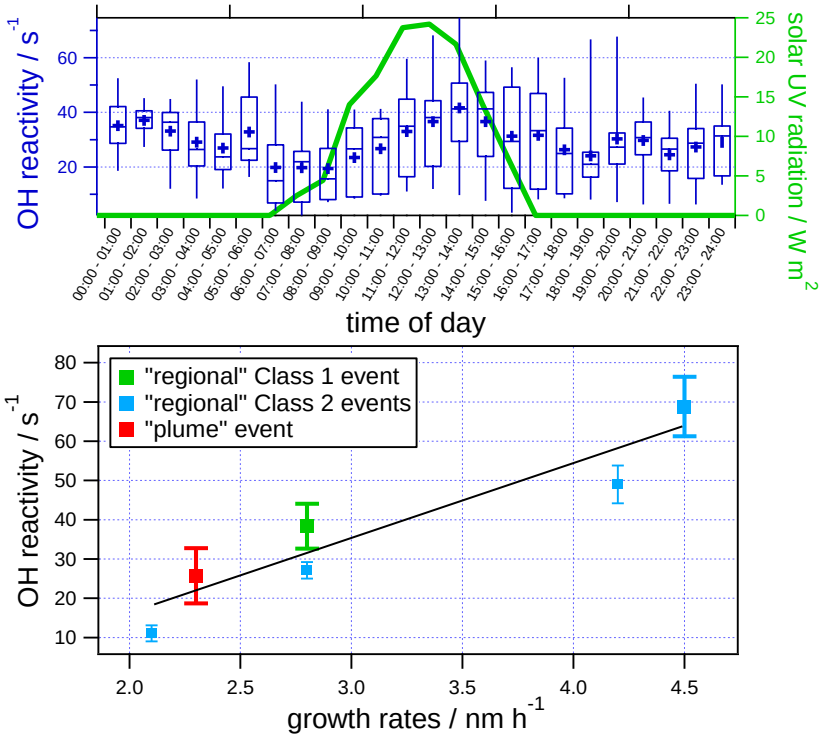

Figure 3.18: Diurnal variability of the OH reactivity shown as box plots (blue marker: mean, box: 25-75% percentiles with median, whiskers: 5% and 95% percentiles) and solar UV radiation cycle on nucleation-event days show good correlation. In the lower plot, the correlation between the OH reactivity during the nucleation period (1 hour after the start of the individual events) and corresponding growth rates are shown for all events where OH reactivity data were measured (coefficient values: a = -22±11; b = 19±3.4). The three new particle formation events of which the temporal evolutions are presented in Fig. 3.14 are bold highlighted.

3.2.3.6 Meteorological and gas phase parameters during new particle formation events

A further focus of this study is to analyze the effects and differences of meteorological and gas phase parameters on the occurrence and type of nucleation events. Relationships between meteorological and gas phase conditions during new particle formation events are also discussed as part of this section.

The wind direction has the most important influence on new particle formation events observed at a certain site, because it defines the advection of air masses from different source regions to the site. The calculated air mass back trajectories that agree well with the locally measured wind directions (Diesch et al., 2012) indicate that nucleation events took place only when the site was influenced by continental air masses while under marine conditions they do not occur. The reason for this behavior is likely the low abundance of precursor gases e.g. organics and ammonia and adverse meteorological conditions (high relative humidity levels, low wind speeds) in the marine environment that prevent the formation and growth of particles, although enhanced SO_2 levels together with a low condensational sink were found. In the 60-90° wind direction range (air masses passing over Southern Spain only) new particle formation occurred as well. However, as this wind

direction range was registered rarely during the campaign only snatches of growth were observed that cannot be further evaluated.

Significant differences were found in the relative humidity (RH) values associated with the different nucleation event types. The more the air masses were affected by the Atlantic Ocean, the higher the RH. Therefore, "regional" events are characterized by low RH levels frequently below 45% around noon, associated with the highest daily RH variation. Slightly higher RH values (~50% during noon) with similar diel cycles were measured for "plume" events. In contrast, during non-event days with marine influenced air masses no strong daily RH variation was observed and minimum RH levels around 75% occurred. Additionally, RH levels above 90% were registered during two nights of the campaign. Since precipitation occurred on these days, the growth period of a "plume" nucleation event was inhibited and the event was therefore not further evaluated.

Variations of the discernible humidity during cloudy days, when the solar UV radiation was reduced, did not have a effect on the occurrence of particle formation and growth events. Although generally a higher relative humidity leads to a higher condensational sink due to the growth of pre-existing aerosol particles (also dependent on other atmospheric parameters), nucleation can also take place under such conditions as shown in the case of the "plume" events. Although clouds occurred at times during the nucleation events, particle nucleation event days are typically characterized by diurnal solar UV radiation cycles with maximum values around 25 W m^{-2}.

As for the solar UV radiation, typical strong daily temperature cycles during "regional" and "plume" event days were gathered contrary to days where no nucleation was observed, which are characterized by smaller temperature variations. Daily average temperatures were found to be lower (20%) on event than on non-event days.

Although low average wind speeds were obtained during the whole campaign, average wind speeds were slightly higher on event days than on non-event days (about 10% before the start of the new particle formation events). A negative correlation of the wind speed and the condensational sink was observed because stronger winds are likely associated with a better mixing of the boundary layer leading to lower aerosol concentrations and thus condensational sink values.

Ozone plays an important role in the production of condensable organic species directly through reactions with VOCs and indirectly by contribution to the formation of OH by daytime photolysis. These condensable organics then speed up the growth of initially formed molecular clusters which indirectly prevents coagulation scavenging as there is less time available for coagulation (Hamed et al., 2007). Water vapor reduces new particle formation as it was suggested to react with the stabilized Criegee intermediates that were formed during the ozonolysis reaction with organics (Bonn et al., 2002). The reaction products decompose into volatile, non-condensable products (Boy et al., 2008). The absolute water vapor concentrations are enhanced during non-event days and anti-correlate with ozone mixing ratios whose diurnal cycle and concentrations are lower during non-event days. Considering only nucleation event days, we find larger growth rates on days with enhanced ozone mixing ratios. This is an indication that the above mentioned processes also occurred during this study.

The fact that the production term of the H_2SO_4 proxy ($UV*SO_2$) increased in line with the particle formation rates of the different nucleation event classes indicates that sulfuric acid plays an important role during new particle formation as also mentioned in several other studies (Stanier et al., 2004; Hamed et al., 2010; Yue et al., 2010). Especially before and during the initial formation

stages of "plume" events high SO_2 mixing ratios originating from the urban Huelva estuary were measured that were converted into H_2SO_4 as soon as the photochemistry began. Therefore, highest formation rates were observed during sulfur-rich "plume" events compared to sulfur-poor "regional" events that were associated with lower formation rates as in the studies of Yue et al. (2010).

The differences in particle formation rates between the two subtypes of the "regional" events are likely associated with the weekday morning rush hour identified by elevated NO_x, organics and number concentrations prior to the Class 2 events while the Class 1 event was observed on a Sunday and did not show such features. Additionally, the Class 1 event is characterized by both, a high solar UV radiation and a high boundary layer height in contrast to the Class 2 events. For this reason, higher condensational sinks existed during the start of the Class 2 events, which depleted condensable vapors and therefore reduced the formation of particles.

3.2.4 Discussion

Numerous studies have dealt with particle formation in urban atmospheres (Dunn et al., 2004; Wehner et al., 2004; Wu et al., 2007) where generally a high condensational sink is responsible for a lower formation rate (Alam et al., 2003; Gao et al., 2009; Jeong et al., 2010). The "plume"-impacted events observed in this study differ in their characteristics from the so-called pollution events formed in urban environments by the fact that during the growth period a second mode around d_p=10 nm was observed. As Sakurai et al. (2005) who measured "plume" events superimposed upon regional events in Atlanta which were characterized by extremely high sub-10 nm particle concentrations, we also think that the second mode was photochemically formed during the transport of the plume to the measurement site. Thus this mode reflects freshly formed particles that have roughly constant age over extended measurement time intervals due to the constant transport times from the confined source of Huelva to our measurement site. In addition, high anthropogenic SO_2 emissions coincided with 10 nm particle number concentrations as also found by Sakurai et al. (2005). This additional particle surface and the associated loss of condensable material results in smaller average growth rates during "plume" compared to "regional" nucleation events. While particle formation rates are positively correlated with SO_2 mixing ratios and the H_2SO_4 proxy, average growth rates show an inverse dependence, indicating different species were involved in particle formation and growth as mentioned by Kulmala (2003). This anti-correlation between the formation and growth rates also exists within the group of Class 2 events that are subjected to similar conditions. If one assumes that similar condensable vapor concentrations and meteorological conditions existed during the particle growth of these events, the less freshly formed particles are produced, the stronger particles can grow with the same amount of available condensable matter. A further possible explanation for this phenomenon has been shown by Kiendler-Scharr et al. (2009) who conducted simulation experiments in a plant chamber and found that isoprene suppressed the formation but increased the growth of freshly formed particles (Yue et al., 2010). Isoprene reacts with OH which is necessary to produce nucleating vapors. The isoprene OH oxidation products did not contribute to the nucleation process but instead to growth. However, biogenic emissions (isoprene, acetone, benzene, toluene) from the surrounding forest were not strong during this period (Song et al., 2012).

Under atmospheric conditions, it was generally thought that organic vapors do not participate in the initial particle formation (Kulmala et al., 2004), but there is some evidence that biogenic emissions might play a role in this process (Becker et al., 1999; O'Dowd et al., 2002b). Likewise, our study is in agreement with these observations as no events were observed when clean marine air

masses passed the site although favorable conditions for new particle formation existed characterized by low condensational sinks and elevated SO_2 levels. Therefore, in agreement with the findings by Stanier et al. (2004) and Hamed et al. (2010) non-event days cannot be distinguished reliably from event days in the condensational sink – H_2SO_4 proxy scatter plot (Fig. 3.15) and thus this diagram shows favorable, though not necessary, conditions for new particle formation. This indicates that either the low presence of (a) certain essential precursor gas(es) such as organics/ammonia or meteorological conditions were not sufficiently available in the marine environment for particle formation and growth. Other possible contributors responsible for new particle formation at a coastal site in Ireland (Mace Head) are iodine-containing species released from macro-algae (O'Dowd and Hoffmann, 2005, Hoffmann et al., 2001), that did not play a significant role in the present study.

Due to the limited measurement capabilities of the AMS we cannot directly investigate which species were involved in the initial new particle formation process. Nevertheless, measurement results of the chemistry and dynamics of ultrafine and accumulation mode particles during "regional" and "plume" nucleation events show that primarily oxidized organic compounds condensed onto the freshly formed particles. Therefore, these species played the most import role during the growth periods as also pointed out in several previous studies (Allan et al., 2006; Ziemba et al., 2010; Cottrell et al., 2008). In agreement with a study in Pittsburgh presented by Zhang et al. (2004) who found sulfuric acid in the earliest formation stages, we also found sulfate to dominate the submicron aerosol prior and during "plume" particle formation coinciding with large SO_2 mixing ratios before and during nucleation. While nitrate from NO_x emission sources only temporarily contributed to the non-refractory submicron aerosol, Hock et al. (2008) found significant amounts of aerosol nitrate being involved in growth events, observed in rural southern Germany.

The source region variability did not only influence aerosol and gas phase parameters during particle formation and growth but also affected the meteorological parameters as well. Favorable conditions for the nucleation events observed in this study are relatively low H_2O concentrations associated with low RH levels, otherwise high condensational sinks can prevent new particle formation as found in several other studies (Jeong et al., 2010; Boy and Kulmala, 2002; Komppula et al., 2003). Linked to this, when we observed higher wind speeds we found lower condensational sinks likely due to a better mixing of the boundary layer, resulting in more favorable conditions for new particle formation. In this study, during the presence of low pressure systems, which are often associated with precipitation, we did not observe new particle formation. However, only on two nights (November, 28-29 and November, 29-30) short precipitation periods occurred and the wind originated from the marine source region where generally no new particle formation events occur. Instead a strong solar UV radiation and temperature cycle was found to be crucial for producing precursor gases essential for nucleation like also mentioned by Hamed et al. (2007). Additionally, the OH reactivity was found to correlate with the temperature cycle on nucleation-event days. In our study the OH reactivity levels have been on average 70 s^{-1} for the "regional" Class 2 and 50 s^{-1} for the "regional" Class 1 event before particle growth started. Compared to studies performed in the tropical rainforest of Suriname where highest observed reactivity values were measured in the order of 60 s^{-1} during the peak of diel emissions (Sinha et al., 2008), measured average levels in our study are markedly higher which indicates the high load of chemical reactants.

3.2.5 Summary

Variations in particle loading and composition, measured size distributions and gas phase parameters have been associated with variations in the wind direction linked to different types of source regions surrounding a measurement site at the southwestern coast of Spain. Only very limited data exists concerning new particle formation events which are superimposed by pollution plumes as most studies have focused on new particle formation in "clean" or in "polluted" ambient air. For this reason, a detailed analysis of "regional" and "plume"-affected new particle formation and growth events, observed when continental and urban influenced air masses reached the measurement site, was accomplished within the framework of the DOMINO project. Although the characteristics and differences of only eight events were addressed in this study, implying only a few case studies were presented, they seem to be representative for the "El Arenosillo" area. Nucleation events occurred under sunny conditions with elevated SO_2 mixing ratios and low condensational sinks indicating a significant contribution of H_2SO_4 to this process. Comparing "plume" with "regional" events, an increase in anthropogenic SO_2 in the "plume"-related events is associated with increased particle number concentrations and corresponding formation rates. A different finding, the delineation between particle formation and growth rates can be understood in terms of different sources contributing to the individual nucleation stages: SO_2 is mainly emitted by anthropogenic, organic matter instead by both, biogenic and anthropogenic sources. However, there is some evidence that other species (e.g. organics, ammonia, iodine) are, in addition to H_2SO_4, involved in the initial new particle formation process as non-event days were associated with marine air masses despite existing favorable conditions like minimum condensational sink and ubiquitous existence of sulfurous species. A study of the ultrafine and accumulation mode aerosol particles during the growth period of "regional" and "plume" nucleation events showed that they were principally organic in composition. Inorganic particulate mass (sulfate, nitrate, ammonium) was also detected in the particles, more in the case of "plume" events and less during "regional" events. By detailed analysis of the mass spectral signatures during growth preferentially oxidized organic species were found to condense onto the particle surfaces. We also examined meteorological and gas phase parameters that were present during particle nucleation and found a typical diurnal solar UV radiation, temperature, wind speed and ozone cycle to be favorable for such events while high relative humidity, water vapor concentration and precipitation associated with low atmospheric pressure inhibited new particle formation events. However, the largest influence on "regional" and "plume" new particle formation events was found to be the air composition associated with different air mass origins. This is also the first study that investigates the link between OH reactivity and new particle formation in the atmosphere. Combining OH reactivity measurements in future aerosol studies could provide a valuable proxy for gas phase reactivity levels favoring aerosol formation.

Acknowledgements. This research was supported by the German Research Foundation (DFG) through the Research Training School GRK 826. The DOMINO (*Diel Oxidant Mechanisms In relation to Nitrogen Oxides*) project was internally funded by the Max Planck Society. The authors wish to acknowledge S. R. Zorn, S.-L. von der Weiden-Reinmüller, T. Klimach and T. Böttger for support during the field measurements. We also thank R. Sander for the balloon soundings that were launched with Graw radiosondes. Furthermore, we thank the INTA (National Institute for Aerospace Technology) for providing facilities at the measurement site. We gratefully acknowledge the NOAA Air Resources Laboratory (ARL) for the provision of the HYSPLIT transport and dispersion model (http://www.arl.noaa.gov/ready.html) used in this paper.

References

Adame, J. A., Serrano, E., Bolivar, J. P., and de la Morena, B. A.: On the Tropospheric Ozone Variations in a Coastal Area of Southwestern Europe under a Mesoscale Circulation, Journal of Applied Meteorology and Climatology, 49, 748-759, 2010.

Alam, A., Shi, J. P., and Harrison, R. M.: Observations of new particle formation in urban air, J. Geophys. Res.-Atmos., 108, -, 2003.

Alastuey, A., Querol, X., Plana, F., Viana, M., Ruiz, C. R., de la Campa, A. S., de la Rosa, J., Mantilla, E., and dos Santos, S. G.: Identification and chemical characterization of industrial particulate matter sources in southwest Spain, J Air Waste Manage, 56, 993-1006, 2006.

Allan, J. D., Alfarra, M. R., Bower, K. N., Coe, H., Jayne, J. T., Worsnop, D. R., Aalto, P. P., Kulmala, M., Hyotylainen, T., Cavalli, F., and Laaksonen, A.: Size and composition measurements of background aerosol and new particle growth in a Finnish forest during QUEST 2 using an Aerodyne Aerosol Mass Spectrometer, Atmos. Chem. Phys., 6, 315-327, 2006.

Becker, E. J., O'Dowd, C. D., Hoell, C., Aalto, P., Makela, K. M., and Kulmala, M.: Organic contribution to sub-micron aerosol evolution over a boreal forest - a case study, PCCP Phys. Chem. Chem. Phys., 1, 5511-5516, 1999.

Berndt, T., Stratmann, F., Sipila, M., Vanhanen, J., Petaja, T., Mikkila, J., Gruner, A., Spindler, G., Mauldin, R. L., Curtius, J., Kulmala, M., and Heintzenberg, J.: Laboratory study on new particle formation from the reaction OH + SO(2): influence of experimental conditions, H(2)O vapour, NH(3) and the amine tert-butylamine on the overall process, Atmos. Chem. Phys., 10, 7101-7116, 2010.

Birmili, W., and Wiedensohler, A.: New particle formation in the continental boundary layer: Meteorological and gas phase parameter influence, Geophys Res Lett, 27, 3325-3328, 2000.

Birmili, W., Berresheim, H., Plass-Dulmer, C., Elste, T., Gilge, S., Wiedensohler, A., and Uhrner, U.: The Hohenpeissenberg aerosol formation experiment (HAFEX): a long-term study including size-resolved aerosol, H2SO4, OH, and monoterpenes measurements, Atmos. Chem. Phys., 3, 361-376, 2003.

Bonn, B., Schuster, G., and Moortgat, G. K.: Influence of water vapor on the process of new particle formation during monoterpene ozonolysis, J Phys Chem A, 106, 2869-2881, 2002.

Boy, M., and Kulmala, M.: Nucleation events in the continental boundary layer: Influence of physical and meteorological parameters, Atmos. Chem. Phys., 2, 1-16, 2002.

Boy, M., Karl, T., Turnipseed, A., Mauldin, R. L., Kosciuch, E., Greenberg, J., Rathbone, J., Smith, J., Held, A., Barsanti, K., Wehner, B., Bauer, S., Wiedensohler, A., Bonn, B., Kulmala, M., and Guenther, A.: New particle formation in the front range of the colorado rocky mountains, Atmos. Chem. Phys., 8, 1577-1590, 2008.

Cottrell, L. D., Griffin, R. J., Jimenez, J. L., Zhang, Q., Ulbrich, I., Ziemba, L. D., Beckman, P. J., Sive, B. C., and Talbot, R. W.: Submicron particles at Thompson Farm during ICARTT measured using aerosol mass spectrometry, J. Geophys. Res.-Atmos., 113, -, 2008.

Dal Maso, M., Kulmala, M., Riipinen, I., Wagner, R., Hussein, T., Aalto, P. P., and Lehtinen, K. E. J.: Formation and growth of fresh atmospheric aerosols: eight years of aerosol size distribution data from SMEAR II, Hyytiala, Finland, Boreal Environ. Res., 10, 323-336, 2005.

de la Campa, A. M. S., Pio, C., de la Rosa, J. D., Querol, X., Alastuey, A., and Gonzalez-Castanedo, Y.: Characterization and origin of EC and OC particulate matter near the Donana National Park (SW Spain), Environmental Research, 109, 671-681, 2009.

Diesch, J.-M., Drewnick, F., Zorn, S. R., von der Weiden-Reinmüller, S.-L., Martinez, M., and Borrmann, S.: Variability of aerosol, gaseous pollutants and meteorological characteristics associated with continental, urban and marine air masses at the SW Atlantic coast of Iberia, Atmos. Chem. Phys., 12, 1-22, 2012.

Draxler, R., Stunder, B., Rolph, G., Stein, A., Taylor, A., 2009. Hysplit4 User's Guide. National Oceanic and Atmospheric Administration. http://www.arl.noaa.gov/documents/ reports/hysplit_user_guide. pdf (accessed 20.04.09).

Drewnick, F., Hings, S. S., Alfarra, M. R., Prevot, A. S. H., and Borrmann, S.: Aerosol quantification with the Aerodyne Aerosol Mass Spectrometer: detection limits and ionizer background effects, Atmospheric Measurement Techniques, 2, 33-46, 2009.

Drewnick, F., Böttger, T., von der Weiden-Reinmüller, S.-L., Zorn, S. R., Klimach, T., Schneider, S., and Borrmann, S.: Design of a mobile aerosol research laboratory and data processing tools for effective stationary and mobile measurements, Atmos. Meas. Tech. Discuss., 5, 2273-2313, doi: 10.5194/amtd-5-2273-2012, 2012.

Dunn, M. J., Jimenez, J. L., Baumgardner, D., Castro, T., McMurry, P. H., and Smith, J. N.: Measurements of Mexico City nanoparticle size distributions: Observations of new particle formation and growth, Geophysical Research Letters, 31, -, 2004.

Fernandez-Camacho, R., Rodriguez, S., de la Rosa, J., de la Campa, A. M. S., Viana, M., Alastuey, A., and Querol, X.: Ultrafine particle formation in the inland sea breeze airflow in Southwest Europe, Atmos. Chem. Phys., 10, 9615-9630, 2010.

Gao, J., Wang, T., Zhou, X. H., Wu, W. S., and Wang, W. X.: Measurement of aerosol number size distributions in the Yangtze River delta in China: Formation and growth of particles under polluted conditions, Atmos. Environ., 43, 829-836, 2009.

Hamed, A., Joutsensaari, J., Mikkonen, S., Sogacheva, L., Dal Maso, M., Kulmala, M., Cavalli, F., Fuzzi, S., Facchini, M. C., Decesari, S., Mircea, M., Lehtinen, K. E. J., and Laaksonen, A.: Nucleation and growth of new particles in Po Valley, Italy, Atmos. Chem. Phys., 7, 355-376, 2007.

Hamed, A., Birmili, W., Joutsensaari, J., Mikkonen, S., Asmi, A., Wehner, B., Spindler, G., Jaatinen, A., Wiedensohler, A., Korhonen, H., Lehtinen, K. E. J., and Laaksonen, A.: Changes in the production rate of secondary aerosol particles in Central Europe in view of decreasing SO2 emissions between 1996 and 2006, Atmos. Chem. Phys., 10, 1071-1091, 2010.

Hock, N., Schneider, J., Borrmann, S., Rompp, A., Moortgat, G., Franze, T., Schauer, C., Poschl, U., Plass-Dulmer, C., and Berresheim, H.: Rural continental aerosol properties and processes observed during the Hohenpeissenberg Aerosol Characterization Experiment (HAZE2002), Atmos. Chem. Phys., 8, 603-623, 2008.

Hoffmann, T., O´Dowd, C. D., and Seinfeld, J. H.: Iodine oxide homogeneous nucleation: An explanation for coastal new particle production, Geophys. Res. Lett., 28, 1949-1952, 2001.

Jeong, C. H., Evans, G. J., McGuire, M. L., Chang, R. Y. W., Abbatt, J. P. D., Zeromskiene, K., Mozurkewich, M., Li, S. M., and Leaitch, A. R.: Particle formation and growth at five rural and urban sites, Atmos. Chem. Phys., 10, 7979-7995, 2010.

Kerminen, V. M., Pirjola, L., and Kulmala, M.: How significantly does coagulational scavenging limit atmospheric particle production?, J. Geophys. Res.-Atmos., 106, 24119-24125, 2001.

Kerminen, V. M., Petaja, T., Manninen, H. E., Paasonen, P., Nieminen, T., Sipila, M., Junninen, H., Ehn, M., Gagne, S., Laakso, L., Riipinen, I., Vehkamaki, H., Kurten, T., Ortega, I. K., Dal Maso, M., Brus, D., Hyvarinen, A., Lihavainen, H., Leppa, J., Lehtinen, K. E. J., Mirme, A., Mirme, S., Horrak, U., Berndt, T., Stratmann, F., Birmili, W., Wiedensohler, A., Metzger, A., Dommen, J., Baltensperger, U., Kiendler-Scharr, A., Mentel, T. F., Wildt, J., Winkler, P. M., Wagner, P. E., Petzold, A., Minikin, A., Plass-Dulmer, C., Poschl, U., Laaksonen, A., and Kulmala, M.: Atmospheric nucleation: highlights of the EUCAARI project and future directions, Atmos. Chem. Phys., 10, 10829-10848, 2010.

Kiendler-Scharr, A., Wildt, J., Dal Maso, M., Hohaus, T., Kleist, E., Mentel, T. F., Tillmann, R., Uerlings, R., Schurr, U., and Wahner, A.: New particle formation in forests inhibited by isoprene emissions, Nature, 461, 381-384, 2009.

Kirkby, J., Curtius, J., Almeida, J., Dunne, E., Duplissy, J., Ehrhart, S., Franchin, A., Gagne, S., Ickes, L., Kuerten, A., Kupc, A., Metzger, A., Riccobono, F., Rondo, L., Schobesberger, S., Tsagkogeorgas, G., Wimmer, D., Amorim, A., Bianchi, F., Breitenlechner, M., David, A., Dommen, J., Downard, A., Ehn, M., Flagan, R. C., Haider, S., Hansel, A., Hauser, D., Jud, W., Junninen, H., Kreissl, F., Kvashin, A., Laaksonen, A., Lehtipalo, K., Lima, J., Lovejoy, E. R., Makhmutov, V., Mathot, S., Mikkila, J., Minginette, P., Mogo, S., Nieminen, T., Onnela, A., Pereira, P., Petaja, T., Schnitzhofer, R., Seinfeld, J. H., Sipila, M., Stozhkov, Y., Stratmann, F., Tome, A., Vanhanen, J., Viisanen, Y., Vrtala, A., Wagner, P. E., Walther, H., Weingartner, E., Wex, H., Winkler, P. M., Carslaw, K. S., Worsnop, D. R., Baltensperger, U., and Kulmala, M.: Role of sulphuric acid, ammonia and galactic cosmic rays in atmospheric aerosol nucleation, Nature, 476, 429-U477, 2011.

Komppula, M., Dal Maso, M., Lihavainen, H., Aalto, P. P., Kulmala, M., and Viisanen, Y.: Comparison of new particle formation events at two locations in northern Finland, Boreal Environ. Res., 8, 395-404, 2003.

Kulmala, M., Toivonen, A., Makela, J. M., and Laaksonen, A.: Analysis of the growth of nucleation mode particles observed in Boreal forest, Tellus Ser. B-Chem. Phys. Meteorol., 50, 449-462, 1998.

Kulmala, M., Dal Maso, M., Makela, J. M., Pirjola, L., Vakeva, M., Aalto, P., Miikkulainen, P., Hameri, K., and O'Dowd, C. D.: On the formation, growth and composition of nucleation mode particles, Tellus Ser. B-Chem. Phys. Meteorol., 53, 479-490, 2001.

Kulmala, M., Korhonen, P., Napari, I., Karlsson, A., Berresheim, H., and O'Dowd, C. D.: Aerosol formation during PARFORCE: Ternary nucleation of H2SO4, NH3, and H2O, J. Geophys. Res.-Atmos., 107, 11, 2002.

Kulmala, M.: How particles nucleate and grow, Science, 302, 1000-1001, 2003.

Kulmala, M., Vehkamaki, H., Petaja, T., Dal Maso, M., Lauri, A., Kerminen, V. M., Birmili, W., and McMurry, P. H.: Formation and growth rates of ultrafine atmospheric particles: a review of observations, J Aerosol Sci, 35, 143-176, 2004.

Kulmala, M., Petaja, T., Monkkonen, P., Koponen, I. K., Dal Maso, M., Aalto, P. P., Lehtinen, K. E. J., and Kerminen, V. M.: On the growth of nucleation mode particles: source rates of condensable vapor in polluted and clean environments, Atmos. Chem. Phys., 5, 409-416, 2005.

Liu, P. S. K., Deng, R., Smith, K. A., Williams, L. R., Jayne, J. T., Canagaratna, M. R., Moore, K., Onasch, T. B., Worsnop, D. R., and Deshler, T.: Transmission efficiency of an aerodynamic focusing lens system: Comparison of model calculations and laboratory measurements for the Aerodyne Aerosol Mass Spectrometer, Aerosol Sci. Technol., 41, 721-733, 2007.

Liu, S., Hu, M., Wu, Z. J., Wehner, B., Wiedensohler, A., and Cheng, Y. F.: Aerosol number size distribution and new particle formation at a rural/coastal site in Pearl River Delta (PRD) of China, Atmos. Environ., 42, 6275-6283, 2008.

Lunden, M. M., Black, D. R., Mckay, M., Revzan, K. L., Goldstein, A. H., and Brown, N. J.: Characteristics of fine particle growth events observed above a forested ecosystem in the Sierra Nevada Mountains of California, Aerosol Sci. Technol., 40, 373-388, 2006.

Makela, J. M., Dal Maso, M., Pirjola, L., Keronen, P., Laakso, L., Kulmala, M., and Laaksonen, A.: Characteristics of the atmospheric particle formation events observed at a borel forest site in southern Finland, Boreal Environ. Res., 5, 299-313, 2000.

Merikanto, J., Spracklen, D. V., Mann, G. W., Pickering, S. J., and Carslaw, K. S.: Impact of nucleation on global CCN, Atmos. Chem. Phys., 9, 8601-8616, 2009.

Metzger, A., Verheggen, B., Dommen, J., Duplissy, J., Prevot, A. S. H., Weingartner, E., Riipinen, I., Kulmala, M., Spracklen, D. V., Carslaw, K. S., and Baltensperger, U.: Evidence for the role of organics in aerosol particle formation under atmospheric conditions, P Natl Acad Sci USA, 107, 6646-6651, 2010.

Monkkonen, P., Koponen, I. K., Lehtinen, K. E. J., Uma, R., Srinivasan, D., Hameri, K., and Kulmala, M.: Death of nucleation and Aitken mode particles: observations at extreme atmospheric conditions and their theoretical explanation, J Aerosol Sci, 35, 781-787, 2004.

O'Dowd, C. D., Hameri, K., Makela, J., Vakeva, M., Aalto, P., de Leeuw, G., Kunz, G. J., Becker, E., Hansson, H. C., Allen, A. G., Harrison, R. M., Berresheim, H., Geever, M., Jennings, S. G., and Kulmala, M.: Coastal new particle formation: Environmental conditions and aerosol physicochemical characteristics during nucleation bursts, J. Geophys. Res.-Atmos., 107, -, 2002a.

O'Dowd, C. D., Hameri, K., Makela, J. M., Pirjola, L., Kulmala, M., Jennings, S. G., Berresheim, H., Hansson, H. C., de Leeuw, G., Kunz, G. J., Allen, A. G., Hewitt, C. N., Jackson, A., Viisanen, Y., and Hoffmann, T.: A dedicated study of New Particle Formation and Fate in the Coastal Environment (PARFORCE): Overview of objectives and achievements, J. Geophys. Res.-Atmos., 107, 16, 2002b.

O'Dowd, C. D., and Hoffmann, T.: Coastal new particle formation: A review of the current state-of-the-art, Environmental Chemistry, 2, 245-255, 2005.

Oberdorster, G., Sharp, Z., Atudorei, V., Elder, A., Gelein, R., Lunts, A., Kreyling, W., and Cox, C.: Extrapulmonary translocation of ultrafine carbon particles following whole-body inhalation exposure of rats, J Toxicol Env Heal A, 65, 1531-1543, 2002.

Paasonen, P., Sihto, S. L., Nieminen, T., Vuollekoski, H., Riipinen, I., Plass-Dulmer, C., Berresheim, H., Birmili, W., and Kulmala, M.: Connection between new particle formation and sulphuric acid at Hohenpeissenberg (Germany) including the influence of organic compounds, Boreal Environ. Res., 14, 616-629, 2009.

Querol, X., Alastuey, A., Rodriguez, S., Viana, M. M., Artinano, B., Salvador, P., Mantilla, E., do Santos, S. G., Patier, R. F., de La Rosa, J., de la Campa, A. S., Menendez, M., and Gil, J. J.: Levels of particulate matter in rural, urban and industrial sites in Spain, Sci. Total Environ., 334, 359-376, 2004.

Sadanaga, Y., Yoshino, A., Kato, S., and Kajii, Y.: Measurements of OH reactivity and photochemical ozone production in the urban atmosphere, Environ. Sci. Technol., 39, 8847-8852, 2005.

Sakurai, H., Fink, M. A., McMurry, P. H., Mauldin, L., Moore, K. F., Smith, J. N., and Eisele, F. L.: Hygroscopicity and volatility of 4-10 nm particles during summertime atmospheric nucleation events in urban Atlanta, J. Geophys. Res.-Atmos., 110, -, 2005.

Sanchez de la Campa, A. M., de la Rosa, J., Querol, X., Alastuey, A., and Mantilla, E.: Geochemistry and origin of PM10 in the Huelva region, Southwestern Spain, Environmental Research, 103, 305-316, 2007.

Shirley, T. R., Brune, W. H., Ren, X., Mao, J., Lesher, R., Cardenas, B., Volkamer, R., Molina, L. T., Molina, M. J., Lamb, B., Velasco, E., Jobson, T., and Alexander, M.: Atmospheric oxidation in the Mexico City Metropolitan Area (MCMA) during April 2003, Atmos. Chem. Phys., 6, 2753-2765, 2006.

Sinha, V., Williams, J., Crowley, J. N., and Lelieveld, J.: The comparative reactivity method - a new tool to measure total OH reactivity in ambient air, Atmos. Chem. Phys., 8, 2213-2227, 2008.

Sinha, V., Custer, T. G., Kluepfel, T., and Williams, J.: The effect of relative humidity on the detection of pyrrole by PTR-MS for OH reactivity measurements, Int J Mass Spectrom, 282, 108-111, 2009.

Sinha, V., Williams, J., Lelieveld, J., Ruuskanen, T. M., Kajos, M. K., Patokoski, J., Hellen, H., Hakola, H., Mogensen, D., Boy, M., Rinne, J., and Kulmala, M.: OH Reactivity Measurements within a Boreal Forest: Evidence for Unknown Reactive Emissions, Environ. Sci. Technol., 44, 6614-6620, 2010.

Sinha, V., Williams, J., Diesch, J.-M., Drewnick, F., Martinez, M., Harder, H., Regelin, E., Kubistin, D., Bozem, H., Hosaynali-Beygi, Z., Fischer, H., Andrés-Hernández, M. D., Kartal, D., Adame, J. A., and Lelieveld, J.: OH reactivity measurements in a coastal location in Southwestern Spain during DOMINO, Atmos. Chem. Phys. Discuss., 12, 4979-5014, 2012.

Sipila, M., Berndt, T., Petaja, T., Brus, D., Vanhanen, J., Stratmann, F., Patokoski, J., Mauldin, R. L., Hyvarinen, A. P., Lihavainen, H., and Kulmala, M.: The Role of Sulfuric Acid in Atmospheric Nucleation, Science, 327, 1243-1246, 2010.

Spracklen, D. V., Carslaw, K. S., Kulmala, M., Kerminen, V. M., Sihto, S. L., Riipinen, I., Merikanto, J., Mann, G. W., Chipperfield, M. P., Wiedensohler, A., Birmili, W., and Lihavainen, H.: Contribution of particle formation to global cloud condensation nuclei concentrations, Geophys Res Lett, 35, 2008.

Stanier, C. O., Khlystov, A. Y., and Pandis, S. N.: Nucleation events during the Pittsburgh air quality study: Description and relation to key meteorological, gas phase, and aerosol parameters, Aerosol Sci. Technol., 38, 253-264, 2004.

Toledano, C., Cachorro, V. E., de Frutos, A. M., Sorribas, M., Prats, N., and de la Morena, B. A.: Inventory of African desert dust events over the southwestern Iberian Peninsula in 2000-2005 with an AERONET Cimel Sun photometer, J. Geophys. Res.-Atmos., 112, 2007.

Ulbrich, I. M., Canagaratna, M. R., Zhang, Q., Worsnop, D. R., and Jimenez, J. L.: Interpretation of organic components from Positive Matrix Factorization of aerosol mass spectrometric data, Atmos. Chem. Phys., 9, 2891-2918, 2009.

von der Weiden, S. L., Drewnick, F., and Borrmann, S.: Particle Loss Calculator - a new software tool for the assessment of the performance of aerosol inlet systems, Atmospheric Measurement Techniques, 2, 479-494, 2009.

Wang, L., Khalizov, A. F., Zheng, J., Xu, W., Ma, Y., Lal, V., and Zhang, R. Y.: Atmospheric nanoparticles formed from heterogeneous reactions of organics, Nat Geosci, 3, 238-242, 2010.

Weber, R. J., Marti, J. J., McMurry, P. H., Eisele, F. L., Tanner, D. J., and Jefferson, A.: Measurements of new particle formation and ultrafine particle growth rates at a clean continental site, J. Geophys. Res.-Atmos., 102, 4375-4385, 1997.

Wehner, B., Wiedensohler, A., Tuch, T. M., Wu, Z. J., Hu, M., Slanina, J., and Kiang, C. S.: Variability of the aerosol number size distribution in Beijing, China: New particle formation, dust storms, and high continental background, Geophys Res Lett, 31, -, 2004.

Wiedensohler, A., Wehner, B., and Birmili, W.: Aerosol number concentrations and size distributions at mountain-rural, urban-influenced rural, and urban-background sites in Germany, J. Aerosol Med.-Depos. Clear. Eff. Lung, 15, 237-243, 2002.

Wu, Z. J., Hu, M., Liu, S., Wehner, B., Bauer, S., Ssling, A. M., Wiedensohler, A., Petaja, T., Dal Maso, M., and Kulmala, M.: New particle formation in Beijing, China: Statistical analysis of a 1-year data set, J. Geophys. Res.-Atmos., 112, -, 2007.

Yue, D. L., Hu, M., Zhang, R. Y., Wang, Z. B., Zheng, J., Wu, Z. J., Wiedensohler, A., He, L. Y., Huang, X. F., and Zhu, T.: The roles of sulfuric acid in new particle formation and growth in the mega-city of Beijing, Atmos. Chem. Phys., 10, 4953-4960, 2010.

Zhang, Q., Stanier, C. O., Canagaratna, M. R., Jayne, J. T., Worsnop, D. R., Pandis, S. N., and Jimenez, J. L.: Insights into the chemistry of new particle formation and growth events in Pittsburgh based on aerosol mass spectrometry, Environ. Sci. Technol., 38, 4797-4809, 2004.

Zhang, R. Y., Wang, L., Khalizov, A. F., Zhao, J., Zheng, J., McGraw, R. L., and Molina, L. T.: Formation of nanoparticles of blue haze enhanced by anthropogenic pollution, P Natl Acad Sci USA, 106, 17650-17654, 2009.

Zhang, R. Y.: Getting to the Critical Nucleus of Aerosol Formation, Science, 328, 1366-1367, 2010.

Ziemba, L. D., Griffin, R. J., Cottrell, L. D., Beckman, P. J., Zhang, Q., Varner, R. K., Sive, B. C., Mao, H., and Talbot, R. W.: Characterization of aerosol associated with enhanced small particle of number concentrations in a suburban forested environment, J. Geophys. Res.-Atmos., 115, -, 2010.

3.3 Investigation of gaseous and particulate emissions from various marine vessel types measured on the banks of the Elbe in Northern Germany[4]

J.-M. Diesch[1], F. Drewnick[1], T.Klimach[1] and S. Borrmann[1,2]
[1] Particle Chemistry Department, Max Planck Institute for Chemistry, Mainz, Germany
[2] Institute of Atmospheric Physics, Johannes Gutenberg University Mainz, Mainz, Germany

Submitted in Atmospheric Chemistry and Physics, 2012

Abstract
Measurements of the ambient aerosol, various trace gases and meteorological parameters using a mobile laboratory (MoLa) were performed on the banks of the Lower Elbe in an emission control area (ECA) which is passed by numerous private and commercial marine vessels reaching and leaving the port of Hamburg, Germany. From April 25-30, 2011 a total of 178 vessels were probed at a distance of about 0.8-2 km with high temporal resolution. 139 ship emission plumes were of sufficient quality to be analyzed further and to determine emission factors (EFs).

Concentrations of aerosol number and mass as well as polycyclic aromatic hydrocarbons (PAH) and black carbon were measured in PM_1 and size distribution instruments covered the size diameter range from 7 nm up to 32 μm. The chemical composition of the non-refractory submicron aerosol was measured by means of an Aerosol Mass Spectrometer (Aerodyne HR-ToF-AMS). Gas phase species analyzers monitored various trace gases (O_3, SO_2, NO, NO_2, CO_2) in the air and a weather station provided wind, precipitation, UV solar radiation and other parameters. Together with ship information for each vessel obtained from Automatic Identification System (AIS) broadcasts, a detailed characterization of the individual ship types and of features affecting gas and particulate emissions is provided.

Particle number EFs (average 2.6e+16 # kg^{-1}) and PM_1 mass EFs (average 2.4 g kg^{-1}) positively correlate with the fuel sulfur content and depend on the engine type and performance. Observed PM_1 composition of the vessel emissions was dominated by organic matter (72%), sulfate (22%) and black carbon (6%) while PAHs only account for 0.2% of the submicron aerosol mass. Measurements of gaseous components showed an increase of SO_2 (average EF: 7.7 g kg^{-1}) and NO_x (average EF: 53 g kg^{-1}) while O_3 decreased when a ship plume reached the sampling site. The particle number size distributions of the vessels are generally characterized by a bimodal size distribution, with the nucleation mode in the 10-20 nm diameter range and a combustion aerosol mode centered at about 35 nm while particles > 1 μm were not found. "High particle number emitters" are characterized by a dominant nucleation mode. By contrast, a third weaker mode at 150 nm primarily occurred for "high black carbon emitters". Classifying the vessels according to their gross tonnage shows a decrease of the number, black carbon and PAH EFs while EFs of SO_2, NO, NO_2, NO_x, AMS species (particulate organics, sulfate) and PM_1 mass concentration increase with increasing gross tonnages.

3.3.1 Introduction

Gaseous and particulate emissions from marine vessels gain increasing attention due to their significant contribution to the anthropogenic burden of the atmosphere, the change of the

[4] Text and Figures submitted in Atmospheric Chemistry and Physics.

atmospheric composition and the impact on local and regional air quality and climate (Corbett and Fischbeck, 1997; Endresen et al., 2003; Eyring et al., 2005a; Eyring et al., 2010). Increased NO_x levels caused by ship emissions can be seen along the shipping routes via satellite measurements (Beirle et al., 2004). In addition, these emissions have a significant impact on the ozone chemistry and increase hydroxyl radical concentrations thereby having an influence on the oxidation power of the atmosphere (Lawrence and Crutzen, 1999). Ship emission-related black carbon, a major light-absorbing species and sulfuric acid, an efficient light-scattering species, both formed during combustion processes are suggested to have an important impact on the earth's radiation budget (Endresen et al., 2003; Petzold et al., 2008; Eyring et al., 2010). Cloud condensation nuclei (CCN) in ship exhaust indirectly affect global radiative forcing, visible in satellite images as so-called "ship tracks", regions downwind of ships characterized by increased solar reflectivity due to marine stratiform clouds (Hobbs et al., 2000; Durkee et al., 2000; Dusek et al., 2006).

Due to the large variety of impacts a broad interest exists in emissions from marine vessels. However, only sparse literature is available on the large range of ship emissions that depend on engine type and technology, operation conditions and the different kinds of fuel types. The available experimental studies can be separated in:
-Laboratory engine studies (Lyyranen et al., 1999; Kasper et al., 2007; Sarvi et al., 2008)
-On-board studies performed on a ship in operation (Cooper, 2001; Agrawal et al., 2008; Fridell et al., 2008; Moldanova et al., 2009)
-Studies tracking individual ship emission plumes by using aircrafts or ships (Hobbs et al., 2000; Osborne et al., 2001; Sinha et al., 2003; Chen et al., 2005; Petzold et al., 2008; Lack et al., 2009; Murphy et al., 2009; Williams et al., 2009; Moldanova et al., 2009)
-Stationary measurements affected by ship plumes (e.g. harbors) (Lu et al., 2006; Agrawal et al., 2009; Healy et al., 2009; Ault et al., 2010; Jonsson et al., 2011).

Since a significant fraction of the emissions even from ocean-going vessels occurs close to land, such emissions may have a strong impact on air quality in coastal and port regions (Corbett et al., 1999). For this reason, global regulations exist to restrict commercial marine vessel emissions (IMO, 2009). Additionally, so-called emission control areas (ECA) have been defined to reduce local and regional ship-related pollution. Having a potentially important role as air pollutant and on climate an improved understanding of the emissions, a detailed characterization of the chemical composition and processing of particles and their dependence on characteristic vessel parameters is desirable. However, literature is only sparse as recently summarized in Jonsson et al. (2011).

In this study, highly time-resolved stationary measurements of air pollutants were performed on the banks of the Lower Elbe which is passed by a large number of ocean-going vessels of different types entering and leaving the port of Hamburg. Using a mobile laboratory, chemical and physical aerosol properties as well as trace gas properties of ship emissions were characterized in this ECA next to populated areas. Emission factors (EFs) were determined for individual vessels for particle number and black carbon, polycyclic aromatic hydrocarbons and chemical PM_1 species as well as the trace gases sulfur dioxide and nitrogen oxide. In addition particle size distributions were measured for each ship separately. By using ship information data gathered via Automated Identification System (AIS) broadcasts, we are able to extract vessel characteristics that affect gas and particulate emissions. The number of vessels sampled allows the categorization of ships into different types and the identification of relationships between EFs and ship properties.

3.3.2 Experimental Methods

3.3.2.1 Measurement campaign

The ship emission measurement campaign was conducted near the Elbe river mouth in Northern Germany (Fig. 3.19a) between April 25 and 29, 2011. 178 commercial and private vessels were probed during the 5 days of sampling, with 139 of the measured ship plumes being of sufficient quality to be considered in the analysis. The remaining ships could not be evaluated because plumes overlapped, e.g. when vessels from both directions pass the Elbe and their plumes reach the measurement site at the same time. The measurement sites (53°50' N, 9°20' E; Fig. 3.19b) were located near Freiburg/Elbe between Cuxhaven and Hamburg on the banks of the Elbe, chosen to be located directly downwind of the ship tracks. The Elbe is daily passed by numerous ocean-going vessels entering and leaving the port of Hamburg, the second largest freight port of Europe. The measurements were conducted in an emission control area (ECA) where the ship fuel sulfur content is legally fixed not to exceed 1% by weight since July 01, 2010. The predominant wind directions during the study period were N-NO (see trajectories in Fig. 3.19a) transporting relatively clean air from the Baltic and North Sea to the measurement sites. At the measurement sites, the Elbe is about 2 km wide. For this reason most vessels were probed and identified at a distance of about 0.8 and 1.2 km, reflecting the main shipping lanes (downstream/upstream the Elbe). During the 5 days of sampling similar meteorological conditions existed (no rain, similar temperatures, RH) which allows to directly compare individual vessel plumes.

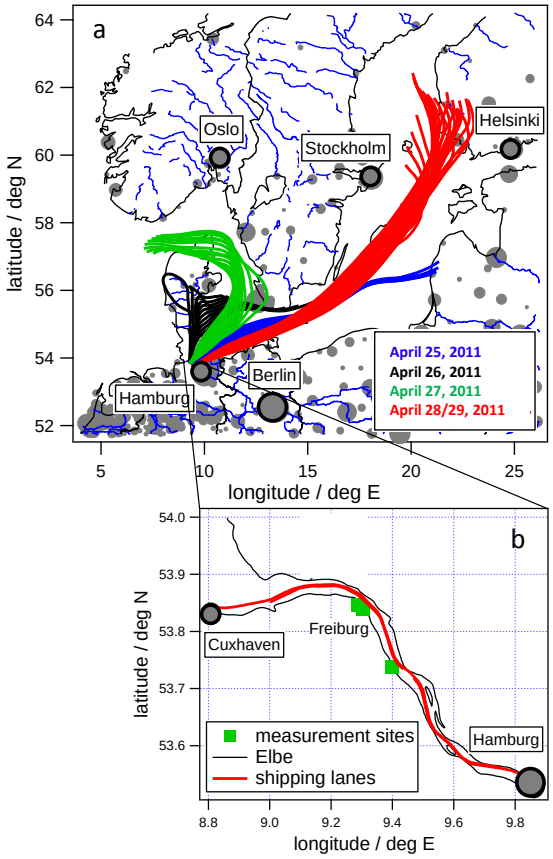

Figure 3.19: Map showing the location of the measurement sites including 48 h backwards trajectories calculated for every hour using HYSPLIT for each measurement day (a). As the wind direction range was N-NO, the measurement sites were located downwind the Elbe. The zoom-in at the lower right shows the positions of the measurement sites (green points) and the shipping lanes on the Elbe (b).

3.3.2.2 Instrumentation

During the campaign, a comprehensive set of aerosol and trace gas instruments was used, implemented in the mobile laboratory MoLa, a mobile platform for aerosol research (Drewnick et al., 2012). This included an ultrafine water-based Condensation Particle Counter (CPC 3786, TSI, Inc., 2.5 nm-3 μm) for particle number concentration measurement and an Environmental Dust Monitor (EDM 180, Grimm) measuring PM_1, $PM_{2.5}$ and PM_{10}. Size distributions in the size range from 7 nm until 32 μm were measured using a Fast Mobility Particle Sizer (FMPS 3091, TSI, Inc., d_{mob} = 7-523 nm), an Aerodynamic Particle Sizer (APS 3321, TSI, Inc., d_{aero} = 0.37-20 μm) as well as an Optical Particle Counter (OPC 1.109, Grimm, d_{opt} = 0.25-32 μm). Concentrations of non-refractory (NR) submicron aerosol species were detected by means of a High-Resolution Time-of-Flight Aerosol Mass Spectrometer (HR-ToF-AMS, Aerodyne Res., Inc.) using the medium mass resolution mode ("V-mode"). A Multi Angle Absorption Photometer (MAAP, Thermo E.C.) registered black carbon concentrations in PM_1 and polycyclic aromatic hydrocarbons on particles were measured by the PAH-Monitor (PAS 2000, EcoChem. Analytics, size range: 10 nm-1 μm). Additionally, for measuring various trace gases MoLa is equipped with the Airpointer (Recordum GmbH) which monitors SO_2, CO, NO, NO_2 and O_3 mixing ratios and the LICOR 840 gas analyzer (LI-COR, Inc.) that measures CO_2. The WXT 510 weather station (Vaisala) provided meteorological parameters (ambient temperature, relative humidity, air pressure, wind speed, wind direction and rain intensity) – for further information see Drewnick et al. (2012).

During the ship plume measurements the roof inlet of MoLa was used which is designed for stationary measurements. Alongside the inlet line, an extendable mast with the meteorological station was fixed, both reaching a height of 7 m above ground level. In order to capture as many data points of the ship plumes as possible, high time resolution of the measurements is essential. Most instruments have a time resolution of 12 s or less, besides the AMS and MAAP instruments that measured in 1 min time intervals. Since during the expected short plume intercepts no reasonable size distribution measurement with the AMS is possible and not to lose measurement time, the AMS was operated in MS mode only, measuring aerosol mass spectra without size information.

3.3.2.3 Data quality assurance

Although the sampling inlet of MoLa was optimized for minimal transport losses and sampling artifacts, characteristic particle losses for all instruments were estimated using the Particle Loss Calculator (von der Weiden et al., 2009). In the size range where the majority of data were measured the respective losses are relatively small (particle losses for all instruments were below 3% and AMS <8% in the 30 nm to 2 μm size range). For this reason, the occurring particle losses were neglected as the measurement results were not significantly influenced and the ambient aerosol was measured widely unbiased.

Several AMS calibrations were conducted during the study. A calibration of the Ionization Efficiency (IE) of the ion source was performed before the beginning of the campaign and after its end. Several distinct instrument parameters and the instrument background were determined using measurements through a High-Efficiency Particulate Air (HEPA) filter. Every second day, the detector gain was calibrated. To account for particles that cannot be detected as they bounce off the vaporizer before evaporation or due to incomplete transmission through the AMS inlet system a Collection Efficiency (CE) factor has to be determined (Huffman et al., 2005). This CE factor was estimated by comparing the sum of the AMS species (organics, sulfate, nitrate, ammonium and

chloride) concentrations and the MAAP black carbon mass concentrations with the EDM PM_1 mass concentrations. When using the typical CE factor of 0.5 for the AMS measurements a satisfying mass closure was generally found. However, occasionally the AMS plus MAAP speciated aerosol concentrations are lower than the EDM PM_1 mass concentrations. This difference is likely due to sea salt, which cannot be measured with the AMS with high efficiency.

3.3.2.4 Analysis of plume events to determine emission factors

For an objective and more efficient handling of the comprehensive data set of chemical, physical and gas phase characteristics from 139 individual ship exhaust plumes, a data analysis tool (Fig. 3.20a) was custom-programmed. The analysis tool supports the characterization of the ship emissions as it calculates emission factors for each ship and parameter using the CO_2 balance method which assumes that all of the carbon in the fuel is emitted as CO_2 (Hobbs et al., 2000). Therefore, this approach of calculating emission factors of the pollutants accounts for dilution of the exhaust plume.

The emission factor of the species x (EF_x) is provided in grams or number of x emitted per kilogram of fuel burned (g kg^{-1} or # kg^{-1}). It is defined as the ratio between the average excess concentration of species x (Δx) in µg m^{-3} (3.11) or # cm^{-3} (3.12) in the measured emission plume above the ambient background level and the average excess CO_2 concentration (ΔCO_2) in mg m^{-3}. In addition, the molar ratios of CO_2 (44 g mol^{-1}) and carbon (12 g mol^{-1}) convert CO_2 to carbon concentrations. The mass fraction of carbon in marine diesel fuel is w_c=0.865 (Lloyd´s Register, 1995). Thus, the emission factor in grams of a certain species per kg fuel burned is:

$$EF_x\ (g\ kg^{-1}) = \frac{\Delta x\ (\mu g\ m^{-3})}{\Delta CO_2\ (\mathrm{mg}\ m^{-3}) \cdot \frac{C\ (g\ mol^{-1})}{CO_2\ (g\ mol^{-1})}} \cdot w_c \qquad (3.11)$$

The uncertainties of the emission factors were calculated by means of Gaussian error propagation as follows: $\sqrt{(\Delta x)^2 + (\Delta CO_2)^2}$. Size-separated particle number emission factors ($dEF_N/dlogD_p$) were determined by using equation (3.12) for each of the particle size bins individually:

$$EF_x\ (\#\ kg^{-1}) = \frac{\Delta x\ (\#\ cm^{-3})}{\Delta CO_2\ (\mathrm{mg}\ m^{-3}) \cdot \frac{C\ (g\ mol^{-1})}{CO_2\ (g\ mol^{-1})}} \cdot w_c \cdot 10^{12} \qquad (3.12)$$

Determination of emission factors using the plume analysis tool

- Firstly, the average concentrations of all measured parameters of each ship plume were calculated. Dependent on the instrument, ship emissions were registered with different but constant delays and broadenings as shown in the time series in Fig. 3.21. These effects result from the transport times through the sampling line that slightly differ for the individual instruments and the internal measurement time constants of the instruments. Therefore, the sampling and the measurement times are not identical and this delay must be corrected for. As shown in Fig. 3.21, the number concentration was the first parameter that quickly increased apparently without instrument-related delays and it was always enhanced when a ship passed the site. Therefore, the average number concentration of each ship plume was determined from the start until the end point of the associated peak, both defined manually (Fig. 3.20b, blue lines). These start and end points of each plume in the number concentration data were used as a reference to which the offset and broadening of all other parameters were referred to. The offsets and broadenings for each parameter were identified using several very distinct plume events and are shown in the third

column of the table in Fig. 3.20a. Some measured parameters which did not exhibit an offset and broadening are explained in section 3.
- Secondly, the CO_2 balance method implies the removal of the background from each ship plume and parameter individually to calculate the excess concentrations. The background concentrations of the measured aerosol and gas phase species were subtracted using a linear fit between the manually defined background intervals 1 and 2 (pre- and post-plume, green lines in Fig. 3.20a and b).

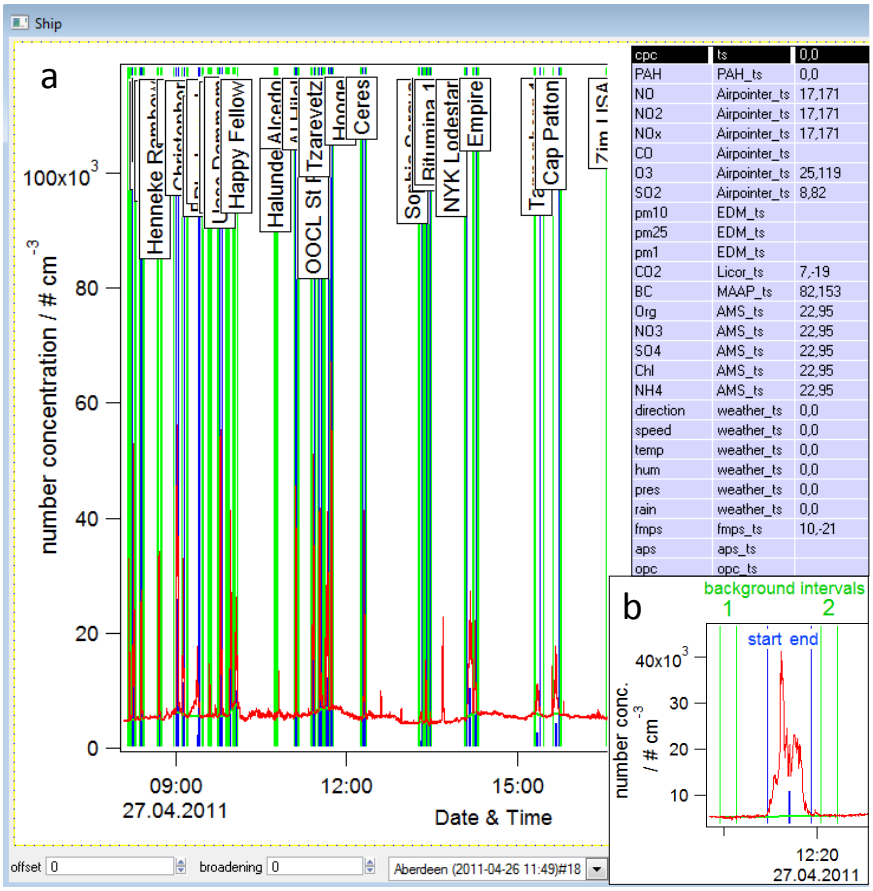

Figure 3.20: Cutout of the ship analysis tool which calculates emission factors for each ship and parameter showing particle number concentration (CPC) time series (a). Emission factors were calculated using manually selected start and end points in the number concentration time series for each ship plume (b). For the other parameters a constant delay and broadening (a, third column of the table on the right) with respect to the number concentration measurement was applied for calculating the average concentrations. The background was subtracted by using a linear fit between the background intervals 1 before and 2 after the ship plume, both hand-selected for each plume and parameter (b).

By referring the excess of the emitted species Δx to ΔCO_2 and therefore to the quantity of fuel used, plume dilution can be corrected under the assumption that the ratio of the emitted species x to CO_2 is conserved during plume expansion. For this reason, we assume that the same dilution of x compared to the chemically inert tracer gas CO_2 exists. This method is limited by all field measurements as transformation processes cannot be completely excluded. For non-conservable emissions, where quick particle coagulation, deposition and chemical processing occur downwind of the ship exhaust emissions Petzold et al. (2008) utilized the term "emission indices". However, according to Hinds (1999) coagulation processes of emissions after leaving the stack did not occur to any significant degree. For this reason and as we cannot identify which species are not conserved the term "emission factor" will be retained in this study. It should be noted that relatively fresh

emission plumes were probed during this study. Dependent on the meteorological situation and the distance between ship and sampling site the ages of the registered plumes vary between 1-5 minutes.

A further limitation of the method is that in addition to CO_2, carbon is emitted as carbon monoxide (CO), methane (CH_4), non-methane organic compounds (NMOC) and particulate carbon (PC). A CO enhancement was not registered during any of the ship plume encounters. The occurrence of CH_4, NMOC and PC is assumed to be relatively small. Therefore the assumption that most of the carbon is emitted as CO_2 is a good approximation providing an upper limit for the EFs.

3.3.2.5 Different types of ships studied

Ship information including ship name, commercial type, length, breadth, deepness, speed, position, gross tonnage and engine power was collected from Automated Identification System (AIS) broadcasts. AIS is a globally implemented identification system mandatory in all vessels larger than 20 m length or 300 gross tonnages. Specific data of each vessel are broadcasted continuously and serve for the prevention of collisions between vessels. The system allows identification of the individual ships passing the measurement site and thus assigning the specific ship characteristics to each of the registered plumes and to classify the measured vessels into different types.
The resulting 7 vessel types and the corresponding number counts as well as the length range of each type measured are:
- Container ships (89, 99-366 m)
- Tankers (35, 35-265 m)
- Ferries & RoRos (9, 51-180 m)
- Cargo ships (15, 82-193 m)
- Reefer & bulkcarriers (5, 145-229 m)
- Riverboats (17, <30 m-134 m)
- Others: tugboat, coast guard and dredging ship (8, 27-56 m).

Although only a limited number of ships for some of the vessel types were measured, the aim of this study to cover a spectrum of ship types and volumes for evaluating the associated dependencies in the emission factors was reached. Within individual ship types a large range of ship volumes/lengths exists. For this reason, the gross tonnage is a key parameter for characterizing the variety of vessels. The gross tonnage is a measure for the ships volume and depends on the ships length by a power function (Hulskotte and van der Gon, 2010). Additionally, the ships gross tonnage is typically directly proportional to the engine power.

3.3.3 Results

3.3.3.1 Identification of plume-related species

The ship plumes registered by MoLa can be identified as more or less pronounced peaks in the time series of several parameters (Fig. 3.21). Those parameters for which a significant enhancement over the background level was observed when a ship passed the site were considered in the further analysis. For this reason, as for every parameter the Limit of Detection (LOD) is different the number of ships for which EFs could be determined varies. The cutout of the time series (Fig. 3.21) shows 9 ship plumes. An individual plume lasted for about 5 minutes, dependent on the characteristic broadening of each parameter that was caused by the different instrumental time constants. For the third event in the depicted time series two plumes were registered

simultaneously. Therefore they cannot be separated and further evaluated. Additionally, the signals are not perfectly synchronous in time as the aerosol transport times through the sampling line slightly differ for the individual instruments.

Figure 3.21 shows several typical characteristics of the measured plumes. In the top panel the size-resolved particle number concentrations are displayed showing dominant modes in the 10-120 nm size range when ship exhaust was sampled. A sharp increase was also observed in the total number, black carbon, PAH, SO_2, NO_x, CO_2 and the particulate organic and sulfate mass concentrations which are directly affected by ship engine exhaust. In addition, apparently some of the emitted species indirectly affect particulate ammonium and chloride which were observed to increase in several of the plumes. Finally, O_3 was indirectly affected which often rapidly decreases from background concentrations at the plume onset due to reaction of ozone with NO forming NO_2 (Lawrence and Crutzen, 1999).

No significant increase compared to the background levels was found in the particle size distributions of the APS and OPC. Apparently the impact of the ship plumes on the aerosol in the size range larger than 250 nm is either very small or simply not reflected in the data due to the poor counting statistics in this particle size range. This is also the reason that no enhancement in the $PM_{2.5,10}$ was observed due to ship emissions. EDM PM_1 instead did not increase when a ship passed the site as particles smaller 250 nm cannot be measured by this instrument but were determined by approximation based on size distributions in the 250 nm-32 µm size range. Finally, for CO no significant variations due to the plume were observed, reflecting very small CO concentrations within the emissions.

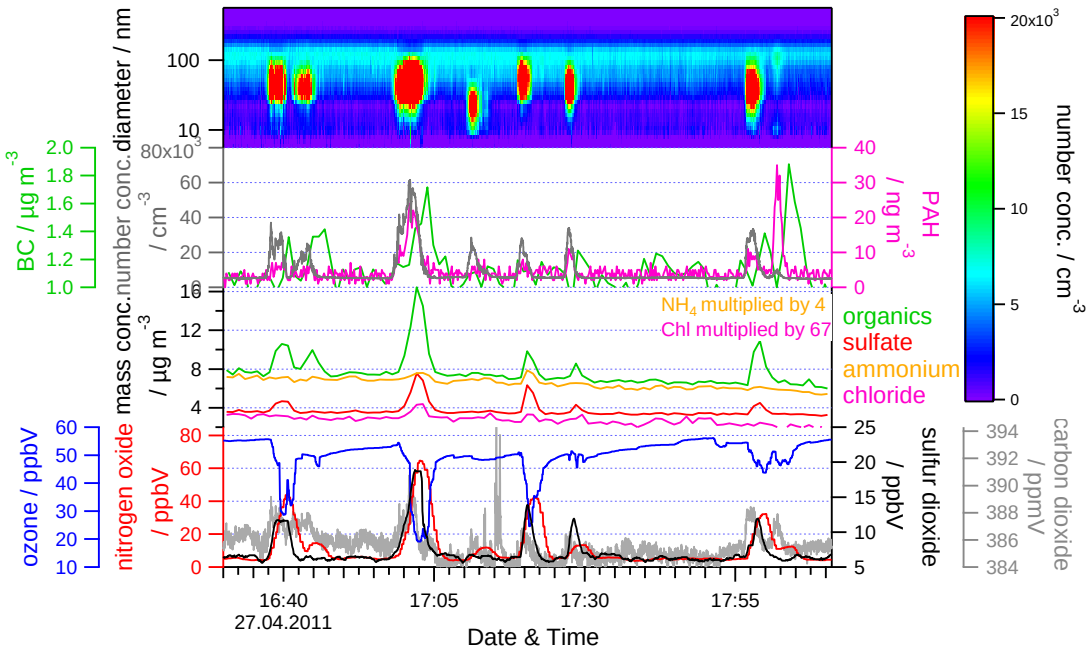

Figure 3.21: Cutout of the time series for relevant parameters showing 9 ship plumes. Here the third plume event consists of two different ship emission plumes which are overlapped and were therefore not further evaluated. Shown are aerosol measurements like the size-resolved and total number concentration (FMPS, CPC), black carbon (MAAP), PAH (PAS) and non-refractory species (organics, sulfate, ammonium, chloride, AMS) concentrations as well as gas phase measurements of SO_2, NO_x, CO_2 and O_3 (Airpointer, Licor).

3.3.3.2 Characterization of emissions

In this section the typical emission factors (EFs) for the measured parameters and particle size distributions for all measured vessels are presented while a detailed characterization for separated types of vessels is discussed in the next section. The EFs (in terms of quantities emitted per kg of fuel burned) of all parameters averaged for all vessel plumes measured during the campaign are summarized in Table 3.6. An overview of the correlations between EFs and vessel characteristics together with the Pearson correlation coefficients (R^2) are listed in Table 3.7. Although the obtained correlation coefficients are generally low, trends observed within this study for the parameters are visible and depend on a variety of factors which are discussed.

Particle number EFs: All vessel plumes were found to contain particles in the 10-250 nm size range (Fig. 7). However, large differences of the particle number EFs between the individual vessels were observed (EF_{min}=5.7e+14 # kg^{-1}, EF_{max}=1.4e+17 # kg^{-1}; see Fig. 3.22). The emitted particle number concentrations mainly depend on the kind of fuel the vessels used. As sulfuric acid is known to be an efficient particle nucleation precursor (Schneider et al., 2005), the sulfur content in fuel is a key parameter influencing the particle number emissions. The average particle number EF for all vessels encountered is 2.6e+16 ± 1.9e+16 # kg^{-1} (Table 3.6).

Black carbon EFs: A completely different relationship to the vessel characteristics was observed for black carbon (BC) EFs. While also a large range of BC emissions (EF_{min}<LOD (0.1 µg m^{-3}), EF_{max}=0.84 g kg^{-1}; see Fig. 3.22) were measured for various ships, generally BC values increased with decreasing vessel speed. A lower vessel speed implies a lower engine load and less complete combustion process for which reason BC is formed. Therefore, we assume BC EFs depend mainly on the operating conditions of the engine. The average BC EF determined for all vessels in this study is 0.15±0.17 g kg^{-1} (Table 3.6).

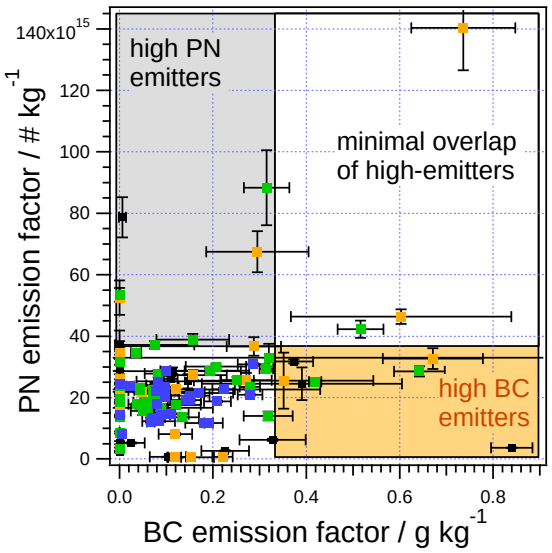

Figure 3.22: Scatter plot of particle number versus black carbon emission factors for the individual vessel types ("Type 1": orange, "Type 2": green, "Type 3": blue). While the grey box highlights the highest 10% of PN emitters, the brown one reflects the 10% highest BC emitters. Only a small overlap (3 vessels) exists with high-emitters of both pollutants which were therefore not considered in the analysis. High PN or BC emitters are among the smaller vessels. Dots which represent gross tonnage values larger than 30000 (blue) show a proportionality of PN and BC EFs. Some vessels are black-coded as no gross tonnage values exist for vessels smaller than 20 m length or 300 gross tonnages. Error bars were determined by means of Gaussian error propagation.

Fig. 3.22 shows a scatter plot of particle number and BC EFs for all ships probed during this study. The grey box highlights the 10% highest particle number emitters (10 vessels as EFs of 99 ship emission plumes could be calculated for both, PN and BC emitters), the brown box highlights the 10% highest BC emitters (10 vessels). While the highest 10% of PN emitters account for 23% of the total average particle number EF, the highest 10% of BC emitters cover 37% of the total black carbon EF. Only a minimal overlap among the two types of high-emitters exists – three vessels are characterized by both, high particle number as well as high BC EFs. The lack of overlap can be explained by the different processes leading to high particle number or high BC emissions: New particle formation is less favored when high black carbon concentrations exist as the larger surface area causes loss of condensable species onto pre-existing particles. Therefore, high black carbon emissions suppress new particle formation by scavenging freshly formed particles and absorbing condensable vapors (Kerminen et al., 2001) resulting in lower particle number concentrations – and vice versa. However, considering all vessel plumes a weak positive correlation of the particle number and BC EFs was obtained (EF_{CPC} (BC[g kg^{-1}]) [# kg^{-1}] = 1.9e+16 + 3.4e+16 · BC[g kg^{-1}], R^2=0.1) as generally a more incomplete combustion process leads to higher particulate as well as BC emissions.

Sulfur dioxide EFs: SO_2 emissions depend on the sulfur content of fuel burned and therefore on the type of fuel used. A higher fuel quality requires lower fuel sulfur content resulting in reduced SO_2 emissions. From the average SO_2 EF of 7.7±6.7 g kg^{-1} (Table 3.6) and the particulate SO_4 EF (0.54±0.46 g kg^{-1}), the sulfur content in fuel can be calculated as follows:

$$\%\, S\ by\ weight = \left[\frac{EF\ [SO_2\ (kg\ kg^{-1})]}{SO_2\ (\mathrm{g}\ mol^{-1})} \cdot S\ (g\ mol^{-1}) + \frac{EF\ [SO_4\ (kg\ kg^{-1})]}{SO_4\ (\mathrm{g}\ mol^{-1})} \cdot S\ (g\ mol^{-1}) \right] \cdot 100 \quad (3.13)$$

Typically in the measured plumes the first term which accounts for the SO_2-related sulfur in the fuel contributes 95% of the total fuel sulfur content, as expected. In agreement with the marine fuel regulations in the North and Baltic Seas (ECA, MARPOL Annex VI, 2010) which requires vessels to burn low-sulfur fuel not to exceed 1% sulfur by weight, the average sulfur content in this study amounts to 0.4% averaged for all vessels (see Table 3.6). Two vessels did not stand on the rules and exhibit larger levels (see Fig. 3.23a). However, when considering the measurement uncertainties only one vessel exhibited slightly enhanced fuel sulfur contents.
As shown in Fig. 3.23a the particle number EFs increase with increasing SO_2 EFs (EF_{CPC} (EF_{SO2}[g kg^{-1}]) [# kg^{-1}] = 1.7e+16 + 1.0e+15 · EF_{SO2}[g kg^{-1}], R^2=0.2), and thus with higher fuel sulfur contents (EF_{CPC}(sulfur[%]) [# kg^{-1}] = 1.7e+16 + 2.0e+16 · sulfur[%], R^2=0.2). This results from the oxidation of sulfur species in fuel to SO_2 and SO_3 which reacts to sulfuric acid (H_2SO_4), the main precursor for new particle formation.

Nitrogen oxide EFs: In contrast to SO_2, emission factors of NO_x (average value: 53±27 g kg^{-1}, see Table 3.6) apparently depend exclusively on the power of the ship engine. More powerful engines operating at higher temperatures emit more NO_x (Sinha et al., 2003). In addition to an increase of NO, NO_2 and NO_x, a tendency of higher NO/NO_2 ratio was found with increased engine power ($EF_{NO/NO2}$(enginepower[kW]) = 0.5 + 3.7e-06 · enginepower[kW], R^2=0.01) and vessel speed ($EF_{NO/NO2}$(speed[kts]) = 0.3 + 0.02 · speed[kts], R^2=0.02) levels. As nitrogen oxide reacts with ozone (O_3) to NO_2, the higher the NO concentrations emitted by the vessels, the lower the measured O_3 concentrations. However, further downwind ozone precursors like hydrocarbons and NO_x will form additional O_3 photochemically.

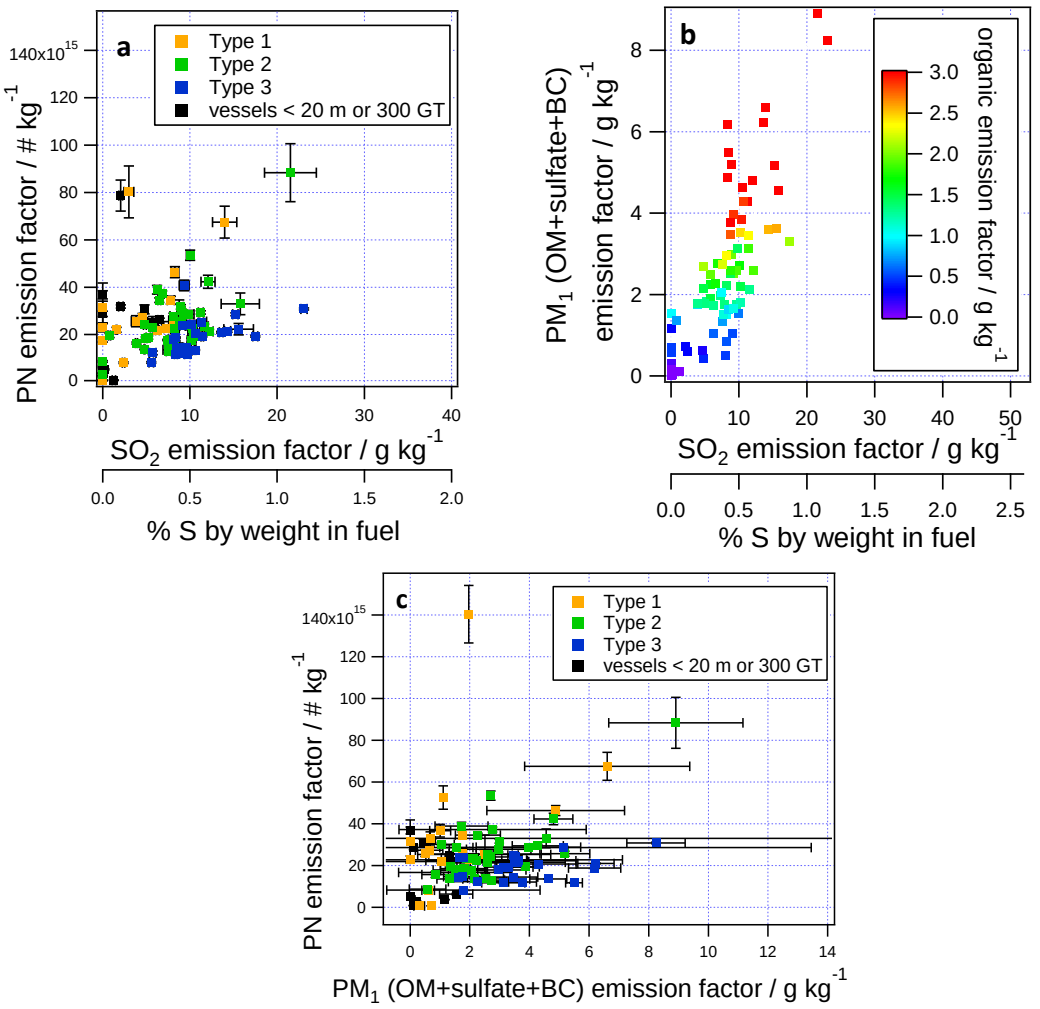

Figure 3.23: Correlation of the particle number (a) and the submicron aerosol mass (PM_1) emission factors (b) with sulfur dioxide emission factors which are associated with the weight percentage of fuel sulfur. Additionally, the particle number versus PM_1 emission factors are shown (c). While graphs (a) and (c) are colored dependent on the vessel type ("Type 1": orange, "Type 2": green, "Type 3": blue, those not registered by the AIS system: black), the graph (c) is color-coded with the organic mass concentration emission factors. The graphs indicate that with increasing fuel sulfur content, the particle number as well as PM_1 mass emission factors increase. Error bars were determined by means of Gaussian error propagation.

Chemical particle composition: Ship engine exhaust aerosol is composed of combustion particles consisting mainly of organic matter (OM), sulfate and black carbon (BC). Ash, a further exhaust component which was not registered during the campaign, accounts generally for a few percent to PM_1 (Petzold et al., 2008). Additionally, in some plumes particulate ammonium and chloride were measured (see Fig. 3.21) possibly formed by reactions of exhaust species with pre-existing sea salt and ammonia in the air. However, most of the sulfate species in the plumes are existent as sulfuric acid making the submicron aerosol acidic.

Analysis of the submicron aerosol (average PM_1 EF for all vessels: 2.4±1.8 g kg^{-1}, see Table 3.6) shows that sulfate EFs (EF_{SO4}(sulfur[%]) [g kg^{-1}] = 0.06 + 0.3 · sulfur[%], R^2=0.5) as well as OM EFs (EF_{Org}(sulfur[%]) [g kg^{-1}] = 0.06 + 4.4 · sulfur[%], R^2=0.7) are strongly linearly correlated with the fuel sulfur content (see Fig. 3.23b). While the relation between fuel sulfur content, SO_2 and SO_4 is obvious, the increase of the organics EF with increasing fuel sulfur content can be explained as follows: In the cylinders of the engine a fraction of the lubricating oil for neutralizing acidic products to prevent corrosion is consumed. The higher the fuel sulfur content the more lubricating

oil is needed (Lack et al., 2009) and consequently emitted. Additionally, the quantity of lubricating oil use depends on the engine type and performance. Therefore, OM EFs (average value for all vessels: 1.8±1.7 g kg^{-1}, see Table 3.6) for individual ships depend on the engine type and the amount of unburned fuel, i.e. the efficiency of combustion. In contrast to studies which were not performed in an ECA (Lack et al., 2009; Moldanova et al., 2009) we found OM but not sulfate (average EF: 0.54±0.46 g kg^{-1}) to be the most abundant submicron aerosol species (see Fig. 3.24). While OM accounts for 72% averaged over all vessels sulfate amounts to 22% of the PM_1 mass. The fraction of black carbon EFs to total PM_1 amounts to 6% considering all vessels. In summary, PM_1 emissions depend on fuel sulfur content with EF_{PM1}(sulfur[%]) [g kg^{-1}] = 0.19 + 6.1 · sulfur[%], R^2=0.6 (see Fig. 3.23b)), the engine type and engine operating conditions. Further insights into the AMS mass spectral signatures indicate typical fragments of diesel exhaust organic and sulfate matter which result from unburned fuel and lubricating oil.

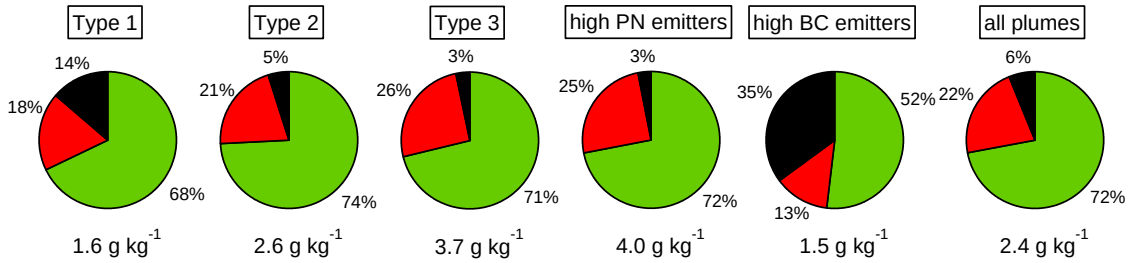

Figure 3.24: Averaged chemical PM_1 composition for the classified "Type 1", "Type 2" and "Type 3" vessels, high PN/BC emitters and for all plumes calculated using total and chemically speciated PM_1 EFs. The PM_1 composition of all vessel plumes include organics (green), sulfate (red) and black carbon (black) while organic matter is the most abundant PM_1 fraction. Sulfate species represent the second most abundant aerosol fraction beside for the high BC emitters.

Polycyclic aromatic hydrocarbons: PAHs are aromatic compounds formed frequently during incomplete combustion processes. As some PAHs are classified as human carcinogens, PAHs are important to be considered. We found PAH EFs weakly depend on the engine power (EF_{PAH}(engine power[kW]) [g kg^{-1}] = 0.005 – 3.5e-08 · engine power[kW], R^2=0.03) - smaller vessels which include lower power engines emit more PAHs due to a more incomplete combustion. For this reason, PAH EFs positively correlate with BC EFs (EF_{PAH}(EF_{BC}[g kg^{-1}]) [g kg^{-1}] = 0.003 + 0.02 · EF_{BC}[g kg^{-1}], R^2=0.3). Due to different volatilities of these compounds their presence in the particle phase depends also on the exhaust temperature (Moldanova et al., 2009). However, with an average EF of 5.3±4.7 mg kg^{-1} for all vessels, PAHs account on average for 0.2% of the total emitted submicron aerosol mass.

Particle size distributions: The particle number size distribution EFs of the measured ship emission plumes covered the size range from 7 to 250 nm (see Fig. 3.25). The relatively fresh ship exhaust particle number size distributions are characterized by either uni-, bi- or tri-modal structures. One mode is centered at around 10 nm, the second one at 35 nm and a third, weaker one is located around 150 nm (brown, Fig. 3.25) particle mobility diameter. However, as shown in Fig. 3.25 for all vessel plumes (red), the majority of plumes exhibit a bimodal size distribution with average mode diameters at 10 and 35 nm. Larger than 250 nm, no significant increase of the particle number concentration compared to the background aerosol was found.
The intensity of the first mode, the nucleation mode varies strongly dependent on the kind of vessel. The strong variations in particle number EFs of the nucleation mode can be explained by the different kind of fuels the vessels used and the different engine types (efficiency of operation and combustion). The formation of H_2SO_4, the most important new particle formation precursor,

depends on the sulfur content in the fuel and the engine operation conditions. The efficiency of coagulation and condensation of freshly formed particles before emission from the stack differ for the individual vessels for which reason nucleation mode particles vary in size from 10-20 nm.

The second mode, the so-called combustion aerosol mode (Petzold et al., 2008) centered around 35 nm is present in most size distributions of the measured vessel plumes and exhibits the largest particle number EFs values (Fig. 3.25). Generally, the combustion aerosol mode contains combustion particles as OM and ash (Petzold et al., 2008). For this reason, lower variations in the level of particle number EFs were observed as OM is the largest fraction of the PM_1.

The particle number EFs of the third mode for particles larger than 100 nm are typically 3 orders of magnitude lower in relation to those of the combustion aerosol mode (Fig. 3.25). The intensity of this "exhaust particle mode" increases with decreasing speed of the vessels implying a more incomplete combustion process and a simultaneous increase of black carbon. As only a small number of high black carbon emitters was measured, the average particle number EFs for all plumes in Fig. 3.25 (red) did not show this mode.

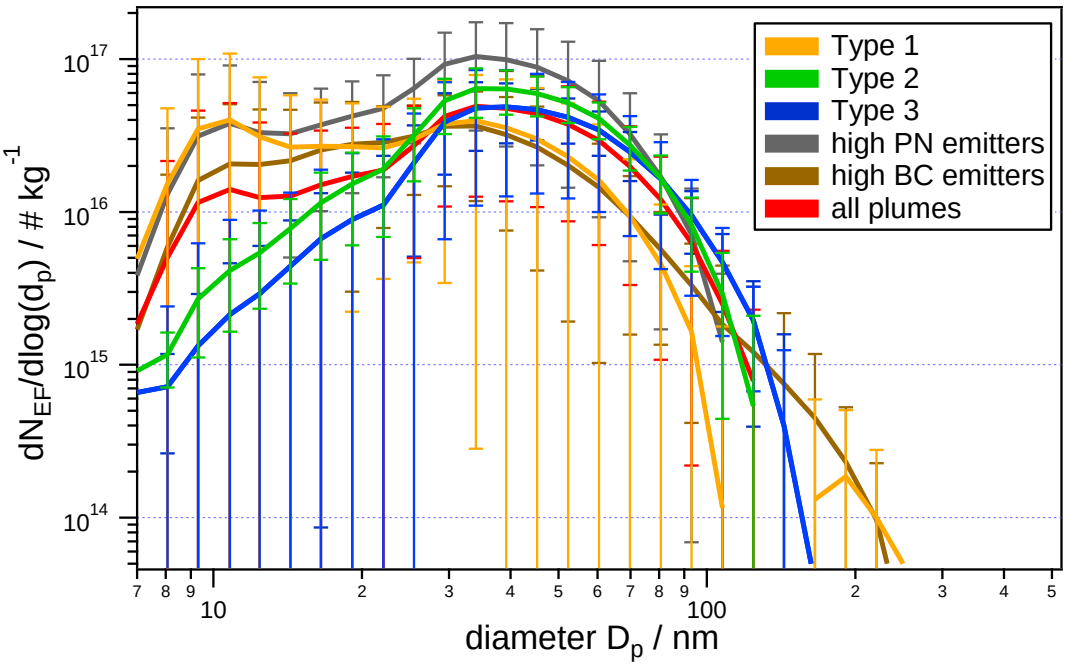

Figure 3.25: Averaged size-resolved particle number emission factors in the 7 up to 523 nm size range for the three types of ship plumes, high PN/BC emitters and for all plumes measured during the campaign. Error bars represent the variability (standard deviation) within the ship plumes for each size bin.

3.3.3.3 Classification into different vessel types

Using AIS, the vessels were separated into 7 types (container ships, tankers, ferries & RoRos, cargo ships, reefer & bulkcarriers, riverboats and others). However, the characteristics of the individual vessels (size, speed, gross tonnage and engine power) within each of the classified ship types differ strongly resulting in large variations of the emissions. By detailed analysis, we found the gross tonnage to be a key factor in grouping different kinds of vessels.

For this reason, vessels were classified in
- "Type 1" vessels which exhibit gross tonnages less than 5000,
- "Type 2" vessels are characterized by gross tonnages from 5000 up to 30,000 and
- "Type 3" vessels exhibit a gross tonnage level larger than 30,000.

Additionally, two vessel types were identified according to their particle number and black carbon EFs as follows (see Fig. 3.22):
- "high PN emitters" represent those vessels which correspond to the 10% highest particle number emitters (grey box) while
- "high BC emitters" are characterized being one of the 10% highest black carbon polluters (brown box).

Table 3.6 summarizes averaged AIS data and chemical, physical as well as gas phase EFs which are explained in the following for all vessel classes. As three vessels are characterized by both, high particle number as well as black carbon EFs they were neither considered as "high PN emitters" nor "high BC emitters".

Comparison of number and black carbon EFs (see Fig. 3.22): "High PN emitters" are characterized by high number and typically moderate black carbon EFs. "High BC emitters" show a completely different behavior – they exhibit high black carbon and moderate particle number EFs. High black carbon concentrations imply a larger surface area where potential new particle formation precursors condense onto instead of nucleating. Additionally, high black carbon emissions inhibit the growth of freshly formed particles as they are scavenged during coagulation. For this reason, "high BC emitters" exhibit moderate particle number EFs only and vice versa. While "Type 1" vessels exhibit largest BC and PN EFs, with increasing gross tonnages of the "Type 2" and "Type 3" vessels, PN and BC EFs decreased, on average. For "Type 3" vessels, particle number and black carbon EFs are proportional within the measurement uncertainty and relatively low in contrast to "Type 1" and "Type 2" vessels. Lower particle number and black carbon EFs can be explained by a more complete combustion which implies higher combustion temperatures. High BC EFs instead are found for those vessels with typically lower vessel speeds, engine loads and therefore likely a more incomplete combustion. In contrast to "high PN emitters" and "high BC emitters" that both are characterized by small average gross tonnages, lengths and engine powers, "Type 3" vessels with an average length of 286 m reflect the largest ocean-going vessels passing the Elbe. For this reason, the engine systems of these ships likely differ from those of the smaller "Type 1" and "Type 2" vessels. Additionally, the exhaust system of the "Type 3" vessels is larger therefore we suggest that due to an increased residence time of the aerosol in the ship exhaust system transformation (coagulation and condensation) processes occur increased. These processes likely result in smaller particle number EFs compared to "Type 1" and "Type 2" vessels.

Table 3.6: Overview of ship characteristics and Emission Factors (EFs) for the different types of vessels investigated in this study. Averaged ship data from the AIS system (speed, gross tonnage, volume, length, engine power), observed mode maximum, sulfur (S) by weight in fuel and EFs (in # per kg fuel or g per kg fuel) are tabulated. *Sulfur by weight in fuel was calculated as described in section 3.3.3.2.

	Type 1 (39 vessels)	**Type 2** (59 vessels)	**Type 3** (41 vessels)
speed / knots	13 ± 6	14 ± 3	13 ± 2
gross tonnage / 3.57 m^3	2051 ± 1205	13983 ± 6189	70190 ± 29816
volume / m^3	4580 ± 3163	32178 ± 13935	124000 ± 45000
length / m	80 ± 22	158 ± 26	286 ± 49
engine power / kW	2738 ± 2251	11055 ± 5238	39064 ± 23033
mode maximum / nm	28 ± 16	42 ± 6.2	44 ± 6.6
sulfur (S) by weight in fuel* / %	0.22 ± 0.21	0.46 ± 0.40	0.55 ± 0.20
particle number EF/ # kg^{-1}	3.38e+16±3.10e+16	2.64e+16±1.48e+15	1.96e+16±6.96e+15
black carbon EF/ g kg^{-1}	0.21 ± 0.23	0.14 ± 0.16	0.12 ± 0.08
nitrogen oxide (NO_x) EF/ g kg^{-1}	43 ± 29	57 ± 28	65 ± 23
nitrogen monoxide (NO) EF/ g kg^{-1}	8.6 ± 6.0	18 ± 12	25 ± 11
nitrogen dioxide (NO_2) EF/ g kg^{-1}	35 ± 25	38 ± 21	40 ± 17
NO/NO_2	0.31 ± 0.29	0.66 ± 0.82	0.67 ± 0.32
sulfur dioxide (SO_2) EF/ g kg^{-1}	4.5 ± 4.1	9.3 ± 7.9	11 ± 4.0
sulfate (SO_4) EF/ g kg^{-1}	0.28 ± 0.38	0.58 ± 0.39	0.92 ± 0.39
organics (Org) EF/ g kg^{-1}	1.0 ± 1.3	2.1 ± 1.9	2.6 ± 1.4
PAHs EF/ g kg^{-1}	0.0080 ± 0.0065	0.0044 ± 0.0030	0.0034 ± 0.0017
$PM_{1(Org+SO4+BC)}$ EF / g kg^{-1}	1.6 ± 1.7	2.6 ± 1.5	3.7 ± 1.7

	high PN (7 vessels)	**high BC** (7 vessels)	**all plumes** (139)
speed / knots	14 ± 3	9.1 ± 3	13 ± 4
gross tonnage / 3.57 m^3	6925 ± 4884	9618 ± 8037	27214 ± 32813
volume / m^3	13984 ± 11024	15266 ± 16470	42632 ± 53341
length / m	121 ± 30	101 ± 52	153 ± 88
engine power / kW	6608 ± 4047	6273 ± 5167	15545 ± 18206
mode maximum / nm	29 ± 9	26 ± 12	35 ± 15
sulfur (S) by weight in fuel* / %	0.51 ± 0.34	0.30 ± 0.23	0.38 ± 0.34
particle number EF/ # kg^{-1}	5.95e+16±1.94e+16	2.46e+16±9.77e+15	2.55e+16±1.91e+16
black carbon EF/ g kg^{-1}	0.12 ± 0.14	0.53 ± 0.19	0.15 ± 0.17
nitrogen oxide (NO_x) EF/ g kg^{-1}	57 ± 23	43 ± 11	53 ± 27
nitrogen monoxide (NO) EF/ g kg^{-1}	12 ± 3.5	9 ± 6	16 ± 12
nitrogen dioxide (NO_2) EF/ g kg^{-1}	45 ± 24	34 ± 7	37 ± 20
NO/NO_2	0.36 ± 0.22	0.27 ± 0.18	0.55 ± 0.59
sulfur dioxide (SO_2) EF/ g kg^{-1}	10 ± 6.9	5.9 ± 4.5	7.7 ± 6.7
sulfate (SO_4) EF/ g kg^{-1}	0.99 ± 0.82	0.20 ± 0.28	0.54 ± 0.46
organics (Org) EF/ g kg^{-1}	2.8 ± 2.2	0.8 ± 0.6	1.8 ± 1.7
PAHs EF/ g kg^{-1}	0.0096 ± 0.0036	0.0074 ± 0.0090	0.0053 ± 0.0047
$PM_{1(Org+SO4+BC)}$ EF / g kg^{-1}	4.0 ± 3.2	1.5 ± 1.1	2.4 ± 1.8

Table 3.7: Overview of the parameterizations of EF dependencies on vessel characteristics or dependencies between each other together with the Pearson correlation coefficients (R^2) observed during this study (ep = engine power).

correlations **y = a + bx**	**a**	**b**	**R^2**
EF_{CPC} (BC[g kg^{-1}]) [# kg^{-1}]	1.9e+16	3.4e+16	0.1
EF_{CPC} (EF_{SO2}[g kg^{-1}]) [# kg^{-1}]	1.7e+16	1.0e+15	0.2
EF_{CPC}(sulfur[%]) [# kg^{-1}]	1.7e+16	2.0e+16	0.2
$EF_{NO/NO2}$(engine power[kW])	0.5	3.7e-06	0.01
$EF_{NO/NO2}$(speed[kts])	0.3	0.02	0.02
EF_{PM1}(sulfur[%]) [g kg^{-1}]	0.19	6.1	0.6
EF_{PAH}(engine power[kW]) [g kg^{-1}]	0.005	-3.5e-08	0.03
EF_{PAH}(EF_{BC}[g kg-1]) [g kg^{-1}]	0.003	0.02	0.3
EF_{CPC}(EF_{PM1}[g kg-1]) [# kg^{-1}]	1.7e+16	3.0e+15	0.1
EF_{Org}(sulfur[%]) [g kg^{-1}]	0.06	4.4	0.7
EF_{SO4}(sulfur[%]) [g kg^{-1}]	0.06	0.3	0.5

Comparison of SO_2 and NO_x EFs: The average EFs of both, SO_2 and NO_x gas phase species are higher for "high PN emitters" and "Type 3" vessels compared to "high BC emitters". Additionally, with increasing gross tonnage levels ("Type 1", "Type 2", "Type 3") SO_2 and NO_x (NO, NO_2 and NO/NO_2) EFs increase (Table 3.6). SO_2 emissions depend on the sulfur content in the fuel which also has an impact on the particle number concentrations by production of sulfuric acid (Fig. 3.23a). Additionally, as shown in Fig. 3.23a, PN EFs did not only depend on the fuel sulfur content but also on the classified vessel types and therefore on the engine type, performance and the combustion or exhaust system. In contrast, NO_x (NO, NO_2) is generated by oxidation processes with nitrogen in air. For this reason, NO_x EFs are combustion temperature-dependent. The higher the gross tonnage levels the higher the NO_x EFs and the NO/NO_2 ratio of the vessels likely due to higher combustion temperatures.

Comparison of PM_1 EFs: The particle number EFs increase with increasing PM_1 EFs (Fig. 3.23c; EF_{CPC}(EF_{PM1}[g kg^{-1}]) [# kg^{-1}] = 1.7e+16 + 3.0e+15 · EF_{PM1}[g kg^{-1}], R^2=0.1) as the ship emissions are characterized by similar size distribution shapes or rather similar ratio of smaller/larger particles. PM_1 EFs increase from "Type 1", "Type 2" to "Type 3" vessels (Fig. 3.23c and Table 3.6). Regarding the averaged chemical composition (see Fig. 3.24), OM was found as the most abundant submicron aerosol fraction for all types of vessels, while sulfate is the second most abundant fraction in PM_1 with ~22%. In contrast, due to the incomplete combustion conditions of "high BC emitters", the black carbon fraction (35%) is more abundant than the sulfate fraction (13%) for this type of vessels. Likewise to the BC EFs, PAH EFs anti-correlate with the vessel size (smallest PAH EFs for "Type 3" vessels) due to the strong dependence of this value on the combustion process efficiency.

Comparison of size distributions: Comparing the size distributions and EFs for particle components of the different vessel types we found the size of the ship engine exhaust aerosol to

strongly depend on the size of vessel that was probed. Although several factors like fuel quality, engine type, efficiency of combustion, cooling and dilution of the exhaust or the design of the exhaust system likely affect size distributions, general differences between the different vessel types can be identified in Fig. 3.25. Smaller "Type 1" vessels, "high PN emitters" and "high BC emitters" emit particulate matter composed of freshly formed particles likely from sulfuric acid nucleating in the expanding plume (mode around 10 nm) and combustion aerosol particles (mode around 35 nm). Larger fuel sulfur contents imply higher sulfate and organic EFs for which reason both modes are more pronounced for "high PN emitters". In contrast, "high BC emitters" exhibit an additional mode larger than 100 nm. The mode could possibly originate from large soot particles which were deposited on walls of the exhaust tube system and are then re-entrained into the exhaust gas stream. "Type 2" and "Type 3" vessels show a totally different behavior with a less pronounced nucleation mode and no mode larger than 100 nm, reflecting both, the lower number and BC EFs. The average plumes for all vessel types, exhibited the combustion aerosol mode (~35 nm) likely including OM or ash. With increasing gross tonnage levels implying "Type 1", "Type 2" and "Type 3" vessels, larger mode diameters were found (Table 3.6).

3.3.4 Discussion with respect to previous studies

The fact that the formation of new particles increases in line with SO_2 emissions via the formation of SO_3 and H_2SO_4 indicates that the fuel quality, i.e. the sulfur content in the fuel, has an important impact on particle number EFs as also mentioned in several other studies of passenger car and ship emissions (Schneider et al., 2005; Chen et al., 2005; Lu et al., 2006; Petzold et al., 2008). For this reason, limiting the fuel sulfur content can result in a direct reduction of the particle number emissions. However, as already pointed out by Lack et al. (2009), we also found that beside the fuel type, the engine type and operation conditions (efficiency of combustion) and probably the engine and exhaust system play important roles. The average particle number EF of 2.55e+16 # kg^{-1} for all vessels during this study is within the range presented in the literature varying from 0.4e+16 to 6.2e+16 # kg^{-1} (Hobbs et al., 2000; Chen et al., 2005; Lack et al., 2009; Murphy et al., 2009). A very similar average particle number EF as our average value was reported by Jonsson et al. (2011) who measured and evaluated particle number and mass EFs also in an ECA. However, our average SO_2 emission factor of 7.7 g kg^{-1} which corresponds to an average fuel sulfur content of 0.4% is lower compared to those in non-ECA studies which probed ships burning marine fuel oil with an average fuel sulfur content of 2.7% (Corbett and Koehler, 2003; Endresen et al., 2003).

We found a positive correlation between the particle number EFs, fuel sulfur and PM_1 EFs. OM is the most abundant PM_1 fraction (average of 72%): On the one hand, OM increases with increasing SO_4 (average contribution to PM_1: 22%) as more cylinder lubricating oil is needed to neutralize corrosive sulfur species. On the other hand, OM emissions depend on the type of engine and the operation conditions as unburned fuel increases the organic emissions as well as those of black carbon. The average contribution of black carbon to PM_1 emissions was 6%, similar to the 4% measured by Sinha et al. (2003). Our studies show that black carbon depends on the vessel speed and therefore likely engine load and operation conditions, which might influence the degree of incomplete combustion. For this reason, not only the fuel sulfur content has a significant impact on total PM_1, also the engine type and operation additionally play important roles. The observed PM composition clearly differs from those by Lack et al. (2009) who reported 46% particulate SO_4, 39% OM and 15% BC for 211 encountered commercial and private marine vessels in the Gulf of Mexico. Due to the reduction of the fuel sulfur to 1% by weight, in the ECA in this study higher OM than sulfate EFs were measured. As a consequence of the reduced fuel sulfur contents, the reduction of sulfate EFs leads to a less acidic aerosol which positively affects the environment and

the aerosol chemistry and therefore climate when considering the formation of CCNs. However, total PM_1 ($EF_{PM1=AMS+BC}$) emission factors of 3.3 g kg^{-1} found by Lack et al. (2009) are comparable with the 2.4 g kg^{-1} determined during this study. In comparison, Jonsson et al. (2011) who also conducted measurements in an ECA in Scandinavia reported an average $EF_{PM(5.6\text{-}560\ nm)}$ of 2.0 g kg^{-1} determined for 734 individual ships. For this reason, both, particulate mass and number EFs are well comparable with those received under similar conditions (Jonsson et al., 2011) and, as expected, they are lower than the global average values of 5.9-7.6 g kg^{-1} (Endresen et al., 2003; Eyring et al., 2005b).

When comparing black carbon and particle number emissions of the ships a totally different behavior of both features was observed. Similar as shown by Ban-Weiss et al. (2009) for individual heavy-duty trucks we found minimal overlap between both high black carbon emitters and high particle number emitters due to the fact that increased black carbon emissions suppress new particle formation (Kerminen et al., 2001; Monkkonen et al., 2004). This relationship between the emission levels for both parameters is also reflected in the associated size distributions. An increased availability of sulfuric acid tends to result in an increase of nucleation mode particles as also mentioned by Petzold et al. (2008). In contrast, high black carbon emitters exhibit a mode larger than 100 nm as also mentioned in studies performed by Petzold et al. (2010). Sinha et al. (2003) as well as Petzold et al. (2008) who analyzed black carbon mass EFs from cruising ships reported an EF_{BC} of about 0.18 g kg^{-1} which is slightly larger than the average EF_{BC} of 0.15 g kg^{-1} determined for all measured plumes during this study. We found that for enhanced black carbon EFs, NO_x EFs drop by up to 50%. Lower combustion temperatures lead to a decrease in NO, NO_2 and NO_x EFs (Sinha et al., 2003) and the NO/NO_2 ratio because under these conditions the oxidation of nitrogen is less favored. For this reason, NO_x EFs (average $EF_{NOx}=53 \pm 27$ g kg^{-1}) largely depend on the engine power and a large range of EFs from 20 to over 100 g kg^{-1} were reported in the literature (Hobbs et al., 2000; Sinha et al., 2003; Chen et al., 2005; Williams et al., 2009).

Vessels with a gross tonnage of less than 5000 ("Type 1") exhibit the largest black carbon and particle number EFs. Due to the different setup of the ship engine system, its performance and exhaust tubes, emissions of larger vessels ("Type 3") commonly differ strongly from those of smaller vessels. For this reason, the gross tonnage is an important parameter for distinguishing different kinds of vessels in terms of emission characteristics as also mentioned by Hulskotte et al. (2010). Comparing "high PN emitters" with the largest ocean-going vessels characterized by gross tonnages of more than 30000 ("Type 3"), similar EFs for all particulate physical and chemical as well as trace gas parameters were found. The only exception is the average particle number EF of the large vessels which amounts to only a third compared to those of the smaller ships. This difference is reflected in the average size distributions with less distinct nucleation modes for the larger vessels, on average. We suggest that the aerosol in the larger exhaust tube systems of the large ships has more time to coagulate and thus to reduce the number concentrations of very small particles. PM_1 mass EFs instead are similar for "high PN emitters" and "Type 3" vessels and investigated size distributions did not show enhanced EFs of particles above 100 nm. This feature was also found by Hobbs et al. (2000), Murphy et al. (2009), Petzold et al. (2008) and Kasper et al. (2007) who investigated size distributions of marine diesel engine emissions and measured major modes in the 10-100 nm size range but hardly any particles larger than 250 nm. Also, the PAH EFs depend on the gross tonnage of the vessels: While smaller vessels exhibit larger PAH EFs, the decrease of PAH EFs with increasing vessel size can be explained by a more incomplete combustion process in the smaller "Type 1" vessels. In contrast to all other EFs of the registered parameters (NO, NO_2, SO_2, SO_4, Org, PM_1) which increase with increasing gross tonnages (i.e.

from "Type 1" over "Type 2" to "Type 3" vessels) the number, black carbon and PAH EFs decrease when larger vessels were probed.

3.3.5 Summary & Conclusions

Chemical, physical and gas phase species were measured in a large number of commercial marine vessel plumes on the banks of the Lower Elbe in April 2011. During the 5 days of sampling 178 ship emission plumes were of sufficient quality to be analyzed providing emission factors. The information of Automated Identification System broadcasts for the vessels allows providing a detailed characterization of parameters affecting gas and particulate emissions.

Total particle number EFs were found to increase with increasing fuel sulfur content. Additionally, the engine and performance as well as the exhaust system appear to affect the particle number EFs. Smaller particle number EFs were observed for larger vessels, possibly due to enhanced coagulation in the exhaust system of the larger engines and the more efficient combustion process due to higher combustion temperatures. For these reasons, the particle number EFs depend on a variety of parameters like fuel composition as well as engine type, operation and exhaust system.

Similar dependences (on fuel sulfur content, engine type and load) were found for the emission factors of particulate matter and particle chemical components which are dominated by OM, sulfate and black carbon. The EFs of the most abundant PM_1 fraction, the organic matter are positively correlated with EFs of sulfate, which in turn depend on the fuel sulfur content. In addition, OM is also dependent on engine type and load because it is associated with unburned fuel and lubricating oil. Black carbon emissions appear to be mainly a function of the engine type. While contributing only to a minor degree to PM_1 on average, black carbon concentrations in the emissions have a strong impact on particle number EFs. PAHs instead account for 0.2% of the emitted submicron aerosol mass and are larger the smaller the vessels.

The measurements performed during this study also show an increase of SO_2 and NO_x mixing ratios while O_3 significantly decreased due to reactions with NO when ships passed the site. While SO_2 is directly related to fuel sulfur content, NO, NO_2 and NO_x EFs increase with vessel speed and engine power, associated with increased engine load and combustion temperatures.

The size distributions of the ship plume aerosol also show a dependence on fuel sulfur content. The intensity of the nucleation mode from freshly formed particles in the 10-20 nm diameter range depends on the sulfur content in the fuel, the engine and the size of the exhaust system which likely reduces small particles by coagulation and condensation processes. The combustion aerosol mode in the 35 nm size range was measured for all types of vessels. Vessels characterized by large black carbon EFs additionally show an additional mode above 100 nm particle diameter. Generally the exhaust particle size distributions are influenced by numerous factors including the engine size and load, cooling and dilution of the exhaust gases as well as the sulfur content in the fuel.

In summary, emission factors of particle number concentrations and size distributions, the submicron particle chemical components and total submicron particulate matter as well as the trace gas mixing ratios depend on a multitude of factors including fuel sulfur content, the engine type, load and performance, and probably the size of the ship exhaust system. Especially fuel sulfur regulations, as adopted within the emission control areas next to populated regions, directly affect local climate, air quality and health.

Acknowledgements. This research was partially funded by the German Research Foundation (DFG, GRK 826) and internal sources from the Max-Planck Society. The authors wish to acknowledge T. Böttger for technical support and J. Schneider for helpful discussions. We gratefully acknowledge the NOAA Air Resources Laboratory (ARL) for the provision of the HYSPLIT transport and dispersion model.

References

Agrawal, H., Welch, W. A., Miller, J. W., and Cocker, D. R.: Emission measurements from a crude oil tanker at sea, Environ. Sci. Technol., 42, 7098-7103, 2008.

Agrawal, H., Eden, R., Zhang, X., Fine, P. M., Katzenstein, A., Miller, J. W., Ospital, J., Teffera, S., and Cocker, D. R.: Primary Particulate Matter from Ocean-Going Engines in the Southern California Air Basin, Environ. Sci. Technol., 43, 5398-5402, 2009.

Ault, A. P., Gaston, C. J., Wang, Y., Dominguez, G., Thiemens, M. H., and Prather, K. A.: Characterization of the Single Particle Mixing State of Individual Ship Plume Events Measured at the Port of Los Angeles, Environ. Sci. Technol., 44, 1954-1961, 2010.

Ban-Weiss, G. A., Lunden, M. M., Kirchstetter, T. W., and Harley, R. A.: Measurement of Black Carbon and Particle Number Emission Factors from Individual Heavy-Duty Trucks, Environ. Sci. Technol., 43, 1419-1424, 2009.

Beirle, S., Platt, U., von Glasow, R., Wenig, M., and Wagner, T.: Estimate of nitrogen oxide emissions from shipping by satellite remote sensing, Geophys. Res. Lett., 31, 2004.

Chen, G., Huey, L. G., Trainer, M., Nicks, D., Corbett, J., Ryerson, T., Parrish, D., Neuman, J. A., Nowak, J., Tanner, D., Holloway, J., Brock, C., Crawford, J., Olson, J. R., Sullivan, A., Weber, R., Schauffler, S., Donnelly, S., Atlas, E., Roberts, J., Flocke, F., Hubler, G., and Fehsenfeld, F.: An investigation of the chemistry of ship emission plumes during ITCT 2002, J. Geophys. Res. Atmos., 110, 2005.

Cooper, D. A.: Exhaust emissions from high speed passenger ferries, Atmos. Environ., 35, 4189-4200, 2001.

Corbett, J. J., and Fischbeck, P.: Emissions from ships, Science, 278, 823-824, 1997.

Corbett, J. J., Fischbeck, P. S., and Pandis, S. N.: Global nitrogen and sulfur inventories for oceangoing ships, J. Geophys. Res. Atmos., 104, 3457-3470, 1999.

Corbett, J. J., and Koehler, H. W.: Updated emissions from ocean shipping, J. Geophys. Res. Atmos., 108, 2003.

Diesch, J.-M., Drewnick, F., Zorn, S. R., von der Weiden-Reinmüller, S.-L., Martinez, M., and Borrmann, S.: Variability of aerosol, gaseous pollutants and meteorological characteristics associated with continental, urban and marine air masses atthe SW Atlantic coast of Iberia, Atmos. Chem. Phys., 12, 1-22, 2012.

Draxler, R., Stunder, B., Rolph, G., Stein, A., Taylor, A., 2009. Hysplit4 User's Guide. National Oceanic and Atmospheric Administration. http://www.arl.noaa.gov/documents/ reports/hysplit_user_guide. pdf (accessed 20.04.09).

Drewnick, F., Böttger, T., von der Weiden-Reinmüller, S.-L., Zorn, S. R., Klimach, T., Schneider, S., and Borrmann, S.: Design of a mobile aerosol research laboratory and data processing tools for effective stationary and mobile measurements, Atmos. Meas. Tech. Discuss., 5, 2273-2313, doi: 10.5194/amtd-5-2273-2012, 2012.

Durkee, P. A., Chartier, R. E., Brown, A., Trehubenko, E. J., Rogerson, S. D., Skupniewicz, C., Nielsen, K. E., Platnick, S., and King, M. D.: Composite ship track characteristics, J. Atmos. Sci., 57, 2542-2553, 2000.

Dusek, U., Frank, G. P., Hildebrandt, L., Curtius, J., Schneider, J., Walter, S., Chand, D., Drewnick, F., Hings, S., Jung, D., Borrmann, S., and Andreae, M. O.: Size matters more than chemistry for cloud-nucleating ability of aerosol particles, Science, 312, 1375-1378, 2006.

Endresen, O., Sorgard, E., Sundet, J. K., Dalsoren, S. B., Isaksen, I. S. A., Berglen, T. F., and Gravir, G.: Emission from international sea transportation and environmental impact, J. Geophys. Res. Atmos., 108, 2003.

Eyring, V., Kohler, H. W., Lauer, A., and Lemper, B.: Emissions from international shipping: 2. Impact of future technologies on scenarios until 2050, J. Geophys. Res. Atmos., 110, 2005a.

Eyring, V., Kohler, H. W., van Aardenne, J., and Lauer, A.: Emissions from international shipping: 1. The last 50 years, J. Geophys. Res. Atmos., 110, 2005b.

Eyring, V., Isaksen, I. S. A., Berntsen, T., Collins, W. J., Corbett, J. J., Endresen, O., Grainger, R. G., Moldanova, J., Schlager, H., and Stevenson, D. S.: Transport impacts on atmosphere and climate: Shipping, Atmos. Environ., 44, 4735-4771, 2010.

Fridell, E., Steen, E., and Peterson, K.: Primary particles in ship emissions, Atmos. Environ., 42, 1160-1168, 2008.

Healy, R. M., O'Connor, I. P., Hellebust, S., Allanic, A., Sodeau, J. R., and Wenger, J. C.: Characterisation of single particles from in-port ship emissions, Atmos. Environ., 43, 6408-6414, 2009.

Heywood, J. B. (1988), Internal Combustion Engine Fundamentals, 930 pp., McGraw-Hill, New York.

Hinds, C.: Aerosol technology: properties, behavior, and measurement of airborne particles, John Wiley & Sons, New York, 1999.

Hobbs, P. V., Garrett, T. J., Ferek, R. J., Strader, S. R., Hegg, D. A., Frick, G. M., Hoppel, W. A., Gasparovic, R. F., Russell, L. M., Johnson, D. W., O'Dowd, C., Durkee, P. A., Nielsen, K. E., and Innis, G.: Emissions from ships with respect to their effects on clouds, J. Atmos. Sci., 57, 2570-2590, 2000.

Huffman, J. A., Jayne, J. T., Drewnick, F., Aiken, A. C., Onasch, T., Worsnop, D. R., and Jimenez, J. L.: Design, modeling, optimization, and experimental tests of a particle beam width probe for the aerodyne aerosol mass spectrometer, Aerosol Sci. Technol., 39, 1143-1163, 2005.

Hulskotte, J. H. J., and van der Gon, H. A. C. D.: Fuel consumption and associated emissions from seagoing ships at berth derived from an on-board survey, Atmos. Environ., 44, 1229-1236, 2010.

International Maritime Organization (IMO) (2009), Revised MARPOL Annex VI & NOx Technical Code 2008, 224 pp., Int. Marit. Org., London.

Jonsson, A. M., Westerlund, J., and Hallquist, M.: Size-resolved particle emission factors for individual ships, Geophys Res Lett, 38, 2011.

Kasper, A., Aufdenblatten, S., Forss, A., Mohr, M., and Burtscher, H.: Particulate emissions from a low-speed marine diesel engine, Aerosol Sci. Technol., 41, 24-32, 2007.

Kerminen, V. M., Pirjola, L., and Kulmala, M.: How significantly does coagulational scavenging limit atmospheric particle production?, J. Geophys. Res. Atmos., 106, 24119-24125, 2001.

Lack, D. A., Corbett, J. J., Onasch, T., Lerner, B., Massoli, P., Quinn, P. K., Bates, T. S., Covert, D. S., Coffman, D., Sierau, B., Herndon, S., Allan, J., Baynard, T., Lovejoy, E., Ravishankara, A. R., and Williams, E.: Particulate emissions from commercial shipping: Chemical, physical, and optical properties, J. Geophys. Res. Atmos., 114, 2009.

Lawrence, M. G., and Crutzen, P. J.: Influence of NOx emissions from ships on tropospheric photochemistry and climate, Nature, 402, 167-170, 1999.

Lloyd´s Register (1995), Marine Exhaust Emissions Research Program, London.

Lu, G., Brook, J. R., Alfarra, M. R., Anlauf, K., Leaitch, W. R., Sharma, S., Wang, D., Worsnop, D. R., and Phinney, L.: Identification and characterization of inland ship plumes over Vancouver, BC, Atmos. Environ., 40, 2767-2782, 2006.

Lyyranen, J., Jokiniemi, J., Kauppinen, E. I., and Joutsensaari, J.: Aerosol characterisation in medium-speed diesel engines operating with heavy fuel oils, J. Aerosol. Sci., 30, 771-784, 1999.

Moldanova, J., Fridell, E., Popovicheva, O., Demirdjian, B., Tishkova, V., Faccinetto, A., and Focsa, C.: Characterisation of particulate matter and gaseous emissions from a large ship diesel engine, Atmos. Environ., 43, 2632-2641, 2009.

Monkkonen, P., Koponen, I. K., Lehtinen, K. E. J., Uma, R., Srinivasan, D., Hameri, K., and Kulmala, M.: Death of nucleation and Aitken mode particles: observations at extreme atmospheric conditions and their theoretical explanation, J Aerosol Sci, 35, 781-787, 2004.

Murphy, S. M., Agrawal, H., Sorooshian, A., Padro, L. T., Gates, H., Hersey, S., Welch, W. A., Jung, H., Miller, J. W., Cocker, D. R., Nenes, A., Jonsson, H. H., Flagan, R. C., and Seinfeld, J. H.: Comprehensive simultaneous shipboard and airborne characterization of exhaust from a modern container ship at sea, Environ. Sci. Technol., 43, 4626-4640, 2009.

Osborne, S. R., Johnson, D. W., Bower, K. N., and Wood, R.: Modification of the aerosol size distribution within exhaust plumes produced by diesel-powered ships, J. Geophys. Res. Atmos., 106, 9827-9842, 2001.

Petzold, A., Hasselbach, J., Lauer, P., Baumann, R., Franke, K., Gurk, C., Schlager, H., and Weingartner, E.: Experimental studies on particle emissions from cruising ship, their characteristic properties, transformation and atmospheric lifetime in the marine boundary layer, Atmos. Chem. Phys., 8, 2387-2403, 2008.

Petzold, A., Weingartner, E., Hasselbach, I., Lauer, P., Kurok, C., and Fleischer, F.: Physical Properties, Chemical Composition, and Cloud Forming Potential of Particulate Emissions from a Marine Diesel Engine at Various Load Conditions, Environ. Sci. Technol., 44, 3800-3805, 2010.

Sarvi, A., Fogelholm, C. J., and Zevenhoven, R.: Emissions from large-scale medium-speed diesel engines: 2. Influence of fuel type and operating mode, Fuel Process Technol, 89, 520-527, 2008.

Schneider, J., Hock, N., Weimer, S., and Borrmann, S.: Nucleation particles in diesel exhaust: Composition inferred from in situ mass spectrometric analysis, Environ. Sci. Technol., 39, 6153-6161, 2005.

Sinha, P., Hobbs, P. V., Yokelson, R. J., Christian, T. J., Kirchstetter, T. W., and Bruintjes, R.: Emissions of trace gases and particles from two ships in the southern Atlantic Ocean, Atmos. Environ., 37, 2139-2148, 2003.

von der Weiden, S. L., Drewnick, F., and Borrmann, S.: Particle Loss Calculator - a new software tool for the assessment of the performance of aerosol inlet systems, Atmos. Meas. Tech., 2, 479-494, 2009.

Williams, E. J., Lerner, B. M., Murphy, P. C., Herndon, S. C., and Zahniser, M. S.: Emissions of NO(x), SO(2), CO, and HCHO from commercial marine shipping during Texas Air Quality Study (TexAQS) 2006, J. Geophys. Res. Atmos., 114, 2009.

3.4 Ship emission impact on local air quality and atmospheric chemistry: Measurements at the Elbe river[5]

J.-M. Diesch[1], F. Drewnick[1] and S. Borrmann[1,2]
[1] Particle Chemistry Department, Max Planck Institute for Chemistry, Mainz, Germany
[2] Institute of Atmospheric Physics, Johannes Gutenberg University Mainz, Mainz, Germany

Abstract
The impact of marine vessel emissions on air quality, climate and the atmospheric chemistry is increasingly of concern. Due to the fact that ship emissions are a significant source of air pollution and contribute to poor air quality in coastal areas fuel regulations exist to limit the emission impact. To investigate the ship emission impact on local air quality and atmospheric chemistry, in April 25-29, 2011 a variety of particulate and gaseous measurements were performed on the banks of the Elbe which is passed by numerous vessels reaching the port of Hamburg, the second largest freight port of Europe. Emission plumes of 178 ships were individually sampled in the emission control area (ECA) at a distance of about 0.8-2 km with high time resolution. The vessel plumes were identified by a more or less pronounced increase of SO_2, NO_x, CO_2 mixing ratios, particle counts, black carbon and PAH concentrations. The chemical submicron aerosol species organics, sulfate, ammonium and chloride were measured by means of an Aerosol Mass Spectrometer (Aerodyne HR-ToF-AMS). Ship information for each vessel gathered via Automatic Identification System (AIS) broadcasts were used to classify vessels into different types.

Container, tanker and cargo vessels together covered ~85% of the ship-related immissions on the banks of the Elbe as they passed the measurement site most frequently. By detailed analysis of the submicron aerosol, ship emissions were found to have a contribution of 4% to total PM_1 which was composed of organics (71%), sulfate (21%) and black carbon (6%). Additionally, ammonium (2%) and chloride (0.002%) contributed to PM_1 as both are formed after emissions left the exhaust stack. The AMS mass spectral signature exhibited typical fragments of diesel exhaust organic and sulfate matter. Ship emissions were dominated by a freshly formed hydrocarbon-like organic aerosol while the background aerosol was composed of an oxygenated organic aerosol. Being the most abundant sulfate species formed in the expanding plumes, sulfuric acid makes the submicron aerosol highly acidic. Emitted nitrogen oxide is found to decrease ground-level ozone by 0.4%, on average at the measurement site.

3.4.1 Introduction

More than 80% of the world's volume of sales is transported by ships with increasing trends for the future (Bughaug et al., 2009). This fuel efficient means of transport emits harmful pollutants such as NO_x, SO_2 and particles (Corbett and Fischbeck, 1997; Eyring et al., 2010) and the International Maritime Organization (IMO) introduced fuel regulations in 2008 to reduce NO_x and SO_2 emissions. While today the average global fuel sulfur content amounts to ~2.7% for vessels, it will be below 0.5% starting from 2020. Special emission control areas (ECA), for example in the North and Baltic Sea exist which will reduce today´s limit for the sulfur content from 1% to 0.1% in 2015.

[5] First draft of a publication which is intended to be submitted to Environmental Science & Technology.

Particulate and gaseous emissions from vessels contribute to the anthropogenic pollution and thereby affect local and regional air quality and climate (Fuglestvedt et al., 2009; Eyring et al., 2010). While black carbon, CO_2 and O_3 cause positive radiative forcing the contribution of sulfate is negative. Particles can indirectly affect radiative forcing and therefore climate due to their ability to act as cloud condensation nuclei (CCN) (Hobbs et al., 2000) which is sometimes visible from the so-called "ship tracks" (Schreier et al., 2006). Therefore, present-day net radiative forcing from vessels is estimated to be negative (Endresen et al., 2003; Lauer et al., 2007; Eyring et al., 2010). NO_x emissions from vessels increase the O_3 and OH levels and therefore also the oxidation power of the troposphere (Lawrence and Crutzen, 1999). This leads to decreased lifetimes of reactive greenhouse gases and in turn to a production of aerosol particles. The emitted species also significantly affect the atmospheric chemical composition (Petzold et al., 2008; Sarvi et al., 2011) and may contribute to the environmental acidification (Dalsoren et al., 2009; Lonati et al., 2010).

Considerable influences of ship emissions on local air quality exist in coastal areas and in the vicinity of major harbors where they directly affect a large population (Corbett et al., 2007). In this connection, Corbett et al. (2007) estimated up to 60,000 premature deaths result annually. To investigate the significance of the pollution sources, generally emission inventories on a global basis were compiled (Corbett and Fischbeck, 1997; Corbett and Koehler, 2003; Endresen et al., 2003; Eyring et al., 2007). They found that shipping contributes to 15-30% of global anthropogenic production of NO_x while SO_2 amounts to 5-8% of global anthropogenic SO_2 emissions. A few authors have analyzed the impact of ship emissions next to harbor areas by conducting stationary measurements (Agrawal et al., 2009; Healy et al., 2009; Hellebust et al., 2010), others used dispersion modeling for this purpose (Isakson et al., 2001; Saxe and Larsen, 2004; Viana et al., 2009). Alastuey et al. (2007) addressed the estimation of harbor activities which impact ambient particulate matter concentrations. Lu et al. (2006) investigated the composition of emitted particles in Vancouver. Summarized, the mentioned studies found a considerable impact of shipping on local air quality in the vicinity of major harbours, particularly caused from NO_x, SO_2, PM_1 and VOC (volatile organic carbon) species.

In this study we focus on chemical, physical and trace gas properties of emissions from ships of different types and their immission impact. The measurements were performed on the banks of the Elbe, Northern Germany in an emission control area, in close proximity to populated regions. A detailed investigation of the submicron aerosol fraction and the chemistry of the ship plumes compared to the atmospheric background is also provided.

3.4.2 Experimental Approach

3.4.2.1 Measurements

The reported measurements were conducted on April 25-29, 2011 near the Elbe river mouth in Northern Germany which is located in an emission control area with fuel sulfur contents restricted to 1% by weight. The measurement sites (53°50' N, 9°20' E; see Fig. 3.26, orange) were located between Hamburg and Cuxhaven on the banks of the Elbe. The Elbe was passed by commercial marine vessels, most of them entering and leaving the port of Hamburg. The 178 vessels were sampled in 0.8-2 km distance from the shipping lanes (Fig. 3.26) using the Mobile research Laboratory "MoLa". Predominant wind directions are N-NO transporting air from Denmark, Sweden, the Baltic and North Sea to the measurement sites (Fig. 3.26). During the 5 days of sampling similar meteorological conditions existed (no rain, similar temperatures, RH) which allows to directly compare individual vessel plumes.

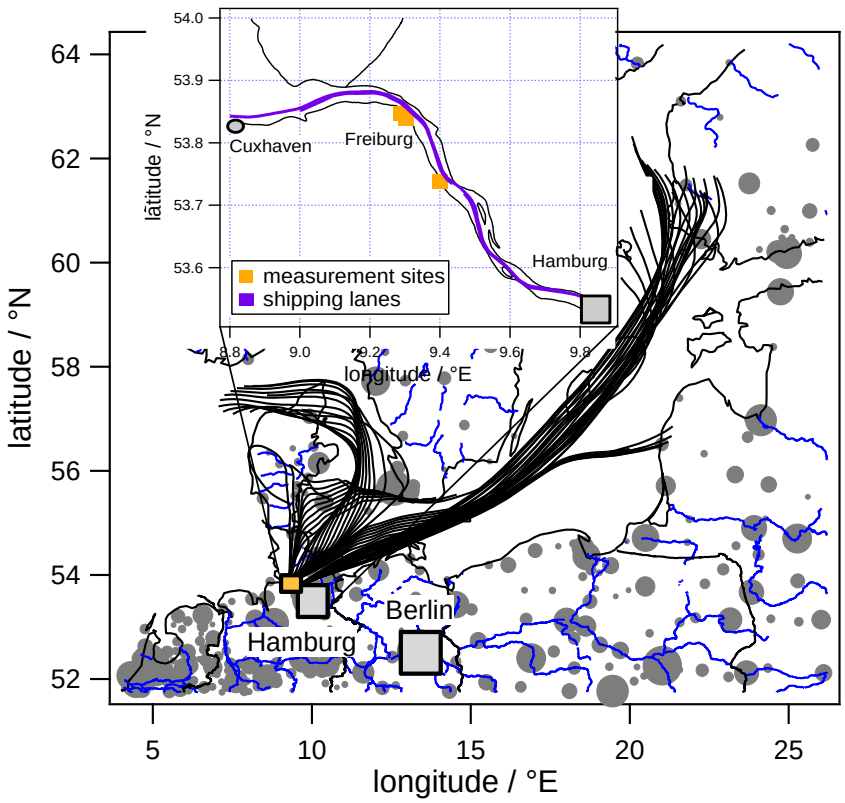

Figure 3.26: Map showing the location around the measurement site including 48 h HYSPLIT backwards trajectories calculated for every hour during the campaign. The zoom-in shows the location of the measurement sites (orange points) and the shipping lanes on the Elbe (purple) commonly used.

3.4.2.2 Instrumentation

On the platform of the mobile laboratory MoLa, a comprehensive set of state-of-the-art instruments were operated to measure physical and chemical aerosol and trace gas parameters (Drewnick et al., 2012). While the complete list of instruments implemented in MoLa during the study is given in Diesch et al. (2012), here only the instruments and techniques required for the measurements presented in this manuscript are described.

Particle number concentrations from 2.5 nm-3 µm were detected by the ultrafine water-based Condensation Particle Counter (CPC 3786, TSI, Inc.). The chemical composition of the non-refractory submicron aerosol was measured using a High-Resolution Time-of-Flight Aerosol Mass Spectrometer (HR-ToF-AMS, Aerodyne Res., Inc.). The black carbon concentration in PM_1 was determined by a Multi Angle Absorption Photometer (MAAP, Thermo E.C.) and polycyclic aromatic hydrocarbons (PAH) on particles were appointed by the PAH-Monitor (PAS 2000, EcoChem. Analytics). MoLa is also equipped with two instruments to detect various trace gases. The Airpointer (Recordum GmbH) measures the trace gases SO_2, NO_x and O_3 while CO_2 was monitored using the LICOR 840 gas analyzer (LI-COR, Inc.). The WXT 510 weather station (Vaisala) provided the most common weather parameters. In Table 3.8 all instruments and corresponding parameters are listed. Details on the instrumental parameters, LODs, errors etc. are provided in Drewnick et al. (2012) and Diesch et al. (2012).
During the ship measurement campaign the roof inlet mast of MoLa was used which was fixed next to an extendable mast with the meteorological station, both at the sampling height of 7 m above ground level. The sampling inlet was optimized and characterized for transport losses and sampling

artifacts (von der Weiden et al., 2009). For measuring the short plume events all instruments were operated at their highest possible sampling frequency. For the CPC and LICOR the time resolutions are: 1s, for the PAS: 13s and for the Airpointer: 4s. The AMS and MAAP instruments measured in 1 min time intervals. Although the AMS is able to measure the particle composition and size distribution by alternating through the high resolution mass spectra (MS) mode and the particle time of flight (PTOF) mode, in this study the AMS only operated in the MS-mode. AMS calibrations (ionization efficiency calibration, detector gain calibration) were conducted during the study and a collection efficiency factor of 0.5 for the AMS mass concentrations was determined. Further information on the data quality assurance for the campaign can be obtained from Diesch et al. (2012).

3.4.2.3 Identification and analysis of ship plumes

Typical ship emissions were registered based on abruptly changing levels of numerous parameters which persist for 1-5 minutes. The signals are more or less enhanced dependent on the kind of vessel, the engine type and performance as well as the fuel sulfur content (Diesch et al., 2012). Typically a ship plume event consisted of a significant enhancement of the total number, black carbon, PAH, SO_2, NO_x, CO_2 and AMS organics, sulfate, ammonium, chloride concentration and a reduction of O_3. A time series of the measured parameters including several ship plumes is shown in Diesch et al. (2012). The age of the respective plumes vary between 1-5 minutes dependent on the meteorological situation.

By means of the Automated Identification System (AIS) characteristic ship data (e.g. ship name, position, speed, type, sizes, gross tonnage) are registered which allow the measured plumes to be attributed to individual vessels. The system is required in all ships larger than 20 m or 300 gross tonnages and broadcasts the vessel-specific parameters continuously for collision prevention reasons.
For investigating the impact of certain vessel types to total immissions on the Elbe, the measured vessels were classified into 7 types (including the number of encountered vessels and the vessel lengths):
- Container ships (89, 99-366 m)
- Tankers (35, 35-265 m)
- Ferries and RoRos (9, 51-180 m)
- Cargo ships (15, 82-193 m)
- Reefer and bulkcarriers (5, 145-229 m)
- Riverboats (17, <30 m-134 m)
- Others: tugboat, coast guard and dredging ship (8, 27-56 m).

For a more objective handling of the comprehensive data set of the 178 ship exhaust plumes, a data analysis tool was custom-programmed based on IGOR Pro.
- For evaluating the emission characteristics, the analysis tool calculates the average values of each parameter and ship plume from the start until the end of the peak. The peak start and end position of the particle number concentrations was defined by the operator as this was the first, fastest and most reliable parameter that increased when a ship passed the site. Dependent on the kind of instrument, ship emissions were registered with different but constant delays and broadenings. The delay results from the aerosol transport times through the sampling line while the broadening occurred from the internal data recording and individual time constants that differ for the individual instruments. For this reason, the start and end of the particle number concentration was used as a reference to which the offset and broadening of the other parameters were referred.

During background conditions no ships passed the site influencing the measurements and the resulting concentration levels. For this reason, those levels were subtracted using a linear fit between the background intervals 1 and 2. These were manually defined before and after each ship and parameter.
- The ship emission impact was determined using the integral over the concentrations as a function of time implying the area of each peak and parameter corresponding to a vessel without considering background concentrations. For comparison with the background impact, the sum of the areas of the individual peaks was related to the measurement time from the beginning until the end of the campaign.
- The background impact was determined with the help of a mask which includes the ship periods and subsequently removes increased levels caused by ship emissions. The integral from the beginning until the end of the campaign hereby represents the background level.
A cutout of the analysis tool and an illustration of the evaluation proceeding based on a single ship plume as well as the delays and offsets of each parameter are shown in Diesch et al. (2012).

3.4.3 Results and Discussion

3.4.3.1 Impact of ship plumes to total immissions

In this section the immission impact of the ships is discussed together with the influence of the different ship types to total immissions. The average levels of the background with ("BG+plumes") and without ("BG") ship emission plumes as well as the percentage fractions of the background and those impacting the site due to ship emission plumes are provided in Table 3.8. Fig. 3.27 shows the contribution of the different ship types to total immissions.

The impact of gaseous emissions which can cause health damages or influence climate differ strongly dependent on the kind of parameter. While SO_2 emissions which depend on the fuel sulfur content contributed to 7% to total SO_2 immissions, emissions of NO_x even contributed to 39% to total NO_x pollutant immissions observed at the measurement site. The fuel sulfur content amounted on average to 0.4% since fuel regulations only allow vessels to burn low-sulfur fuel with maximum sulfur contents of 1% in this area. NO_x emissions depend on the engine type and the vessel speed implying more nitrogen is oxidized the more powerful the engine and the higher the combustion temperature of the vessel (Sinha et al., 2003). NO_x emissions presently range from 9.8-17 g/kWh dependent on the vessel speed (MARPOL Annex IV, 2010) but they have to reach less than 3.4 g/kWh starting 2016. When the emission impact of SO_2 and NO_x is compared, the stricter fuel sulfur regulations possibly result in the lower average ship emission influences. Due to reactions with NO to NO_2 and O_2, local O_3 concentrations decreased when a ship passed the site thereby having an impact of -0.4% related to the total immissions. However, photochemical reactions of precursor species (e.g. NO_x, hydrocarbons) will contribute to a substantial increase of O_3 further downwind (Lelieveld et al., 2004). For this reason, the contribution from shipping emissions to the air quality of regions downwind from the emission source depends on the intensity of local precursor emissions (Song et al., 2010). As carbon dioxide is a major greenhouse gas and a natural constituent of air it contributed at least to total immissions regarding all gas phase parameters.

Emissions of particulate matter from vessels also affect the measurement site. With an average contribution of 20% to total immissions, the particle number concentration was found to depend strongly on the kind of fuel used and the engine operation conditions (Diesch et al., 2012). As ship plumes were found to contain primarily particles in the 10-250 nm size range the relatively small

particles can penetrate and diffuse into the lung, circulatory system or accumulate in organs (Kennedy, 2007). However, the required low fuel sulfur content also reduces the formation of sulfuric acid which acts as particle formation precursor and results finally in decreased particle number concentrations. Black carbon emissions instead were produced increasingly with decreasing speed due to incomplete combustion and accounted for 3% of the total immission impact. Ship engine exhaust is also composed of particulate organic matter (OM) and sulfate (SO_4) matter while both, ammonium (NH_4) and chloride (Chl) were indirectly formed. The highest contribution of 6% was observed for OM. OM depends on the fuel sulfur content, the amount of unburned fuel and oil and the engine type (Diesch et al., 2012). Particulate SO_4 instead depends on the fuel sulfur content and affected the sampling site by 4%. Due to their indirect formation, NH_4 (0.7%) and Chl (0.02%) instead contributed only less to the total immission impact compared to the other measured PM_1 compounds. PAHs which account for 0.2% to the submicron aerosol mass have an important role as some of them are being classified as human carcinogens. With a contribution of 12% they had a relatively strong impact to the total immissions. Comparing the particulate number and PM_1 mass concentrations a fivefold influence of the number concentration (20%) compared to the mass concentration (4%) was found as most particles are freshly formed and therefore emitted in a size range less than 100 nm.

In Fig. 3.27, the fraction of the ship-related immissions dependent on the different vessel types is shown. The immissions are dominated by container ships (~70%), tankers (~15%) and cargo ships (~10%) which together cover 80-95% (BC, PAH: ~80%; PN, NO_x, CO_2: ~90%; SO_2, organics, sulfate: ~95%) of the ship-related air quality impact. This can be explained by the fact that these ship types were registered most frequently during the campaign. Comparing these results with the emissions of 89 seagoing ships at berth in the harbor of Rotterdam, oil tankers (30%), container ships (25%) and ferries & RoRos (20%) were found to cover ~75% of total ship emissions (Hulskotte and van der Gon, 2010).

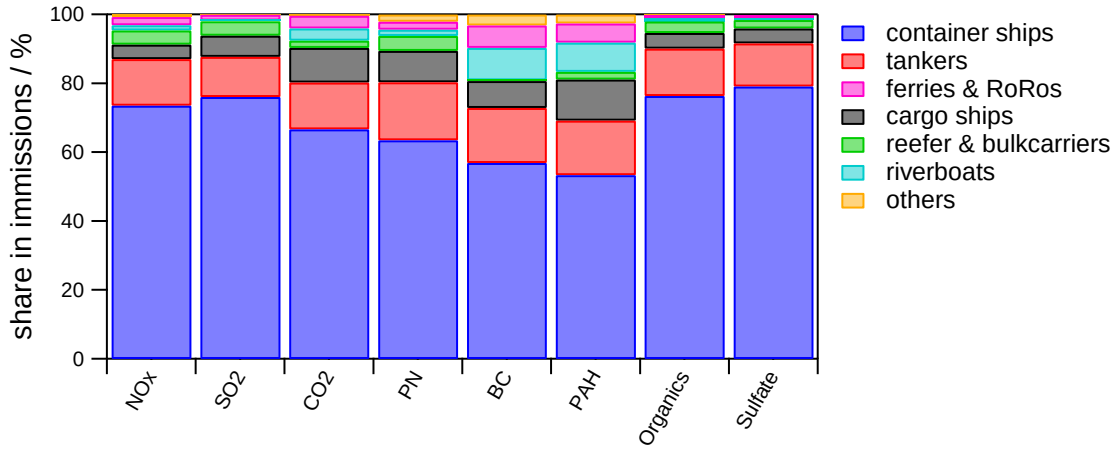

Figure 3.27: Share in immissions of the different ship types to total ship-related immissions on the banks of the Elbe during the campaign.

Table 3.8: Instrumentation and measured variables of (1) background (BG, i.e. ship plume measurements removed from dataset), and (2) data including background and ship exhaust plumes (BG+plumes). The values are averages (with standard deviations) over the entire campaign period from April 25-29, 2011.

MoLa instrumentation	measured quantity	average concentrations		impact in %	
		BG	BG+plumes	BG	plumes
Trace Gases					
Airpointer	NO_x (ppbv)	4.6 ± 1.8	7.5 ± 8.7	61	39
	SO_2 (ppbv)	5.4 ± 0.6	5.9 ± 1.7	93	7
	O_3 (ppbv)	50.4 ± 10.7	50.2 ± 11.4	100.4	-0.4
LICOR gas analyzer	CO_2 (ppbv)	387.8 ± 5.9	388.0 ± 6.0	99.9	0.1
Particle Properties					
ultrafine water-based Condensation Particle Counter	counts (cm^{-3}) (2.5nm-3µm)	6500 ± 2500	8200 ± 7000	80	20
Multi Angle Absorp. Photom.	black carbon (µg m^{-3}; <PM_1)	0.72 ± 0.26	0.74 ± 0.27	97	3
PAH-Monitor	PAHs (ng m^{-3}) (10nm-1µm)	3.1 ± 1.5	3.5 ± 2.3	88	12
High-Resolution Time-of-Flight	Org (µg m^{-3})	4.6 ± 1.5	4.9 ± 1.9	94	6
Aerosol Mass Spectrometer	SO_4 (µg m^{-3})	2.0 ± 0.7	2.1 ± 0.8	96	4
HR-ToF-AMS	NO_3 (µg m^{-3})	1.5 ± 1.1	1.5 ± 1.1	100	0
	NH_4 (µg m^{-3})	0.966 ± 0.4	0.973 ± 0.4	99.3	0.7
	Chl (µg m^{-3}) (<PM_1)	~0.04 ± 0.03	~0.04 ± 0.03	99.98	0.02
sum of Org, SO_4, NO_3, NH_4, Chl and BC	mass (µg m^{-3}) (<PM_1)	9.9 ± 4.0	10.3 ± 4.5	96	4

3.4.3.2 Impact of ship plumes on aerosol chemistry

For a detailed analysis of the ship plume chemistry, emitted particulate chemical species were further analyzed regarding their atmospheric composition, the acidification and the change of the oxidation degree. In each subsection the differences between background and plume immissions were compared to evaluate the ship plume impact.

Atmospheric composition

The submicron aerosol chemical composition of the background and ship plume-related immissions averaged for the campaign period are shown in Fig. 3.28. The PM_1 composition of the background aerosol which contained 47% organic matter (OM), 21% sulfate, 15% nitrate, 10% ammonium and 7% BC and 0.5% chloride clearly differed from that of the ship emissions. Particulate emissions from ship engines consisted exclusively of combustion aerosol particles OM (71%), BC (6%) and of sulfate (21%) particles formed from sulfuric acid in the expanding plume. Ammonium (2%) and chloride (0.002%) were found to contribute to PM_1 as well. However, both were formed indirectly through reactions with ammonia and chloride originating from sodium chloride (NaCl) in sea salt particles. According to Petzold et al. (2008) ash also accounts to a few percent of the total mass, however, it was not measured during this study. In inventory studies of Eyring et al. (2005) sulfate was estimated (14% OM and 5% BC) to contribute with 81% to global PM mass. For this reason, along with other studies (Lloyd´s Register, 1995; Sax and Alexis, 2007) they suggested PM emissions mainly result from the fuel sulfur. With a composition of 46% SO_4, 39% OM and 15% BC, Lack et al. (2009) found a weaker relationship between fuel sulfur and PM. Although using different methods to best represent the composition of emissions, large differences occur. However, comparing the study performed by Lack et al. (2009) who sampled >200 vessels in the Gulf of Mexico, the smaller than expected fraction of sulfate in PM_1 found in this study can be explained by sampling in an emission control area. Although the adopted fuel sulfur regulations lead to significant changes in PM properties, it has to be considered that the engine type and performance affected OM and BC and therefore PM mass and composition as well (Diesch et al., 2012).

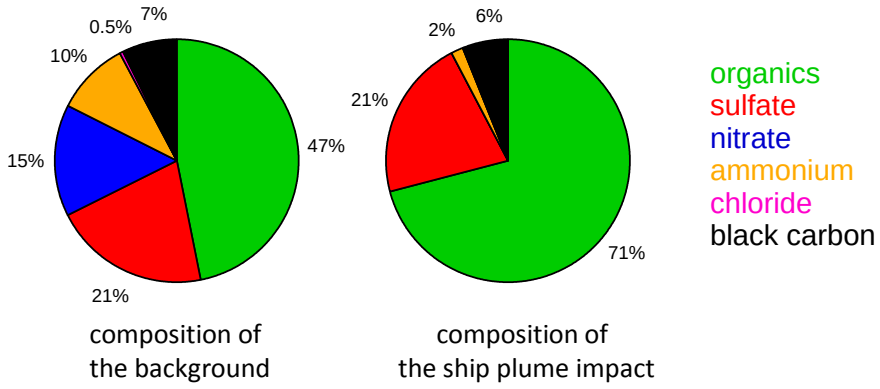

Figure 3.28: Chemical submicron aerosol composition when no ship plume influenced the measurement site (background) and the impact of ship plumes without the background. Variations (relative standard deviations) of the impact of the background and ship plume PM_1 composition are shown in table 3.8.

Acidification

Since the aerosol acidity may have an influence on hygroscopic growth, toxicity and heterogeneous reactions (Sun et al., 2010) the relative abundance of inorganic submicron aerosol species (SO_4^{2-}, NO_3^- and Chl^-) versus those of the cation NH_4^+ was investigated. To illustrate the neutralization degree of both, background and ship plume immissions, the scatter plot (Fig. 3.29) shows the acid-related hydrogen (H^+) versus particulate sulfate. Molar H^+ concentrations were estimated by subtracting molar NH_4^+ concentrations from the molar concentrations of the anions SO_4^{2-}, NO_3^- and Cl^-. In this calculation molar SO_4^{2-} concentrations were multiplied by 2 due to the molar ratio of NH_4^+ in $(NH_4)_2SO_4$. The black lines in Fig. 3.29 reflect molar ratios corresponding to a fully neutralized aerosol (ammonium sulfate, $(NH_4)_2SO_4$), a slightly acidic (ammonium bisulfate, NH_4HSO_4) and strongly acidic aerosol (sulfuric acid, H_2SO_4). We assume NH_4^+ firstly reacts with NO_3^- and Chl^- while remaining NH_4^+ reacts with SO_4^{2-}. By investigating the aerosol acidity differences in the ion balance are clearly visible. The background aerosol was slightly acidic as ammonium sources in the marine boundary layer are not as abundant as would be necessary for neutralizing the anions SO_4^{2-} and NO_3^- (Coe et al., 2006; Allan et al., 2008). Ship immissions instead affect the environment due to their high acidity as particulate SO_4^{2-} consists of sulfuric acid formed by oxidation of fuel sulfur. Although NH_4^+ was found to be enhanced during the ship plumes, the contribution to PM_1 and therefore to the acidification is negligible. In addition to sulfur compounds, nitrogen species are important because they affect the acidification and eutrophication of ecosystems as well as the biodiversity (Eyring et al., 2007). For this reason, further limitations of SO_2 implying fuel sulfur as well as NO_x from 2016 will have favorable consequences.

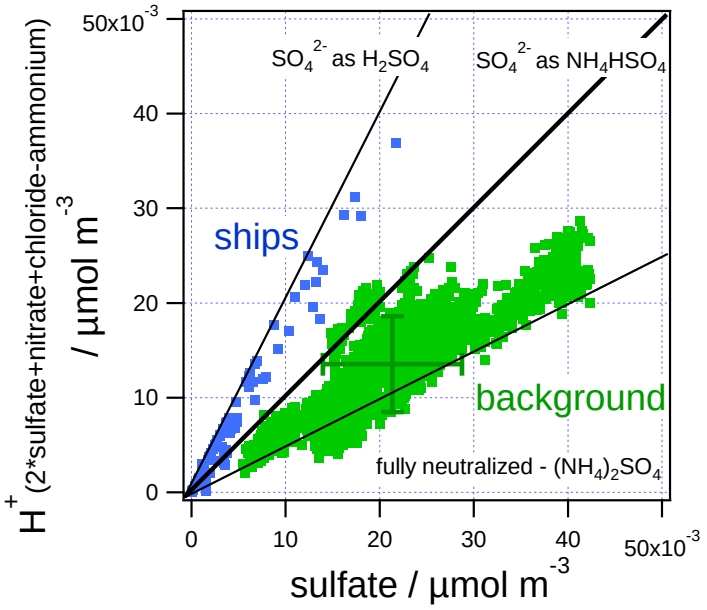

Figure 3.29: Correlation illustrating the difference of the ion balance between background (green points) and ship plumes (blue points). The scatter plot serves for the identification of the sulfur species ammonium sulfate ($(NH_4)_2SO_4$), ammonium bisulfate (NH_4HSO_4) and sulfuric acid (H_2SO_4). While background aerosol is slightly acidic, ship emissions mainly consist of sulfuric acid which leads to a highly acidic aerosol.

Oxidation degree

In this section we focus on the characteristics and properties of the background and plume-related emissions of the organic aerosol (OA), the largest fraction of PM_1. Total OM can be separated into a low-volatile oxygenated OA (LV-OOA), a semi-volatile oxygenated OA (SV-OOA) and a

hydrocarbon-like OA (HOA) dependant on differences in the respective mass spectra. While LV-OOA, a high-oxygenated OA mostly represents secondary OA with significant mass fragments at *m/z* of 18, 27, 41, 43, 44, 55, 69, SV-OOA represents a less-oxygenated/processed aerosol with marker peaks at *m/z* of 27, 29, 41, 43, 55, 67, 79. The typical characteristic peaks for hydrocarbons (*m/z* 41, 43, 55, 57, 69, 81, 95) exist in HOA. To clearly distinguish between the different OA species PMF have been used for the evalution. However, as being typical marker peaks an allocation to different OA components is also possible based on different fractions of m/z 44 (CO_2^+) and m/z 43 ($C_2H_3O^+$, $C_3H_7^+$) to total organics. While LV-OOA exhibit higher f_{44} (ratio of m/z 44 versus total organics) and lower f_{43} (ratio of m/z 43 versus total organics) levels than SV-OOA, HOA can be clearly distinguished from both OOA mass spectra and generally exhibit low CO_2^+ (m/z 44). As presented in Fig. 3.30, we added the f_{44} associated with SV-OOA and LV-OOA reported in Ng et al. (2010) who analyzed 43 AMS datasets and found f_{44} of the LV-OOA ranged between 0.13 and 0.21 while SV-OOA amounted from 0.03 up to 0.11. Comparing the ambient OA of this study without considering ship emission plumes (background) oxidized organic aerosol mainly contributed to total OA. The degree of oxidation can also be expressed as the ratio between the oxygen and carbon content of the aerosol.

By detailed analysis of several ambient and chamber studies, Aiken et al. (2008) found the following relationship between f_{44} and the O:C ratio which was used to calculate the O:C ratio stated in Fig. 3.30:

$$O{:}C = (0.0382 \pm 0.0005) * f_{44} + (0.0794 \pm 0.0070) \quad (3.14)$$

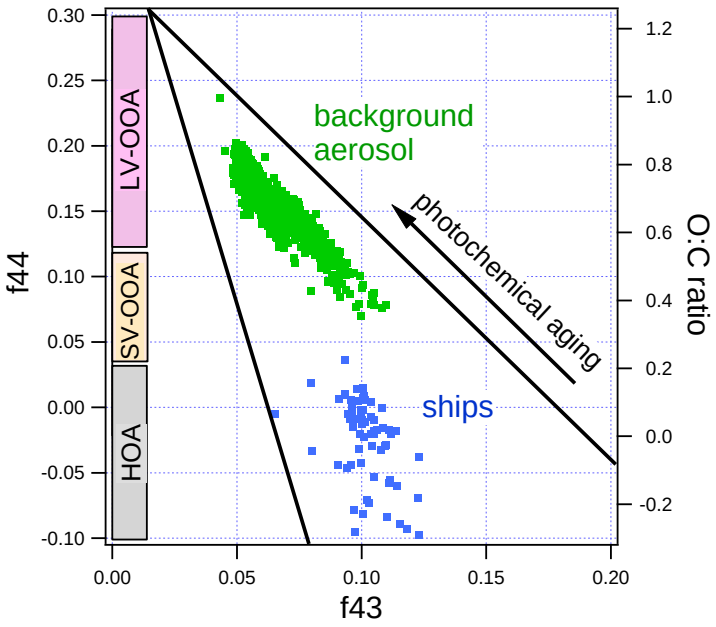

Figure 3.30: Scatter plot showing the ratio of m/z 44 to total organics (f44) and m/z 43 to total organics (f43) to represent the degree of oxidation. F44 is associated with the O:C ratio. The correlation shows freshly formed hydrogenated organic aerosol (HOA) reach the sampling site from ship emission plumes while the background is mainly composed of an oxidized organic aerosol.

For the correlation in Fig. 3.30 it has to be considered that the AMS measures CO_2 in the particle and gas phase. Normally, gas phase CO_2 is subtracted by measuring its contribution during a filter period. As ship emissions increase gas phase CO_2, the measured particulate CO_2 signal of each vessel was corrected for this effect. An increase from 0 to 388 ppm leads to an increase in the m/z

44 signal of 0.035101 µg m^{-3} which has to be subtracted dependant on the increase of the CO_2 level as follows:

corrected signal = uncorrected signal – 0.035101 / 388 ppm * (388+x) ppm 3.14

Fig. 3.30 shows a scatter plot of f_{44} and f_{43} to compare the differences of the organic aerosol between background and the ship emissions that affected the sampling site. In contrast to the background aerosol, the organic aerosol consisted of a non-oxidized organic aerosol when ship emissions reach the sampling site. This likely consisted of primary combustion aerosol species. Fig. 3.31 shows an averaged mass spectrum of the sampled vessel plumes. The relatively fresh exhaust aerosol was dominated by organic (green) and sulfate (red) fragments likely originating from diesel fuel and lubricating oil. The organic fragments show dominant features of freshly formed HOA species: n-alkane, branched alkanes, cycloalkanes and aromatics (mono- and polycyclic aromatic hydrocarbons). The same result is given in Fig. 3.30 based on the O:C ratio which was below 0.2 for the plume OA compared to 0.7, on average for the background aerosol. For this reason dominant ion series including $C_nH_{2n+1}^+$ (m/z 29, 43, 57, 71, 85) which are typical of saturated and branched alkanes while $C_nH_{2n-1}^+$ (m/z 27, 41, 55, 69, 83) fragments are representative of alkenes. Fragments belonging to the $C_nH_{2n-3}^+$ (m/z 67, 79, 81, 95, 107, 109, 123) series are common markers of cycloalkane and $C_6H_5C_nH_{2n}^+$ (m/z 77, 91, 105, 119) are indicators for aromatics (McLafferty and Turecek, 1993). Sulfate components (red) of the exhaust are inferred from the ions S^+, SO^+, SO_2^+, SO_3^+, HSO_3^+, $H_2SO_4^+$ (m/z = 32, 48, 64, 80, 81, 98). Fragments above 200 known to be associated to PAHs additionally exist in the mass spectra. Comparing the ship exhaust mass spectra with those from other studies (Lu et al., 2006; Phinney et al., 2006; Murphy et al., 2009) the major peaks are the same. However, as ship particulate emissions depend on the engine type, the operation conditions and fuel sulfur content, variations in the relative peak intensities were found dependent on the kind of vessel. Additionally, as the exhaust plumes mix with the background aerosol during dilution after leaving the stack, the relative intensity of the peaks observed during different diesel exhaust studies also vary.

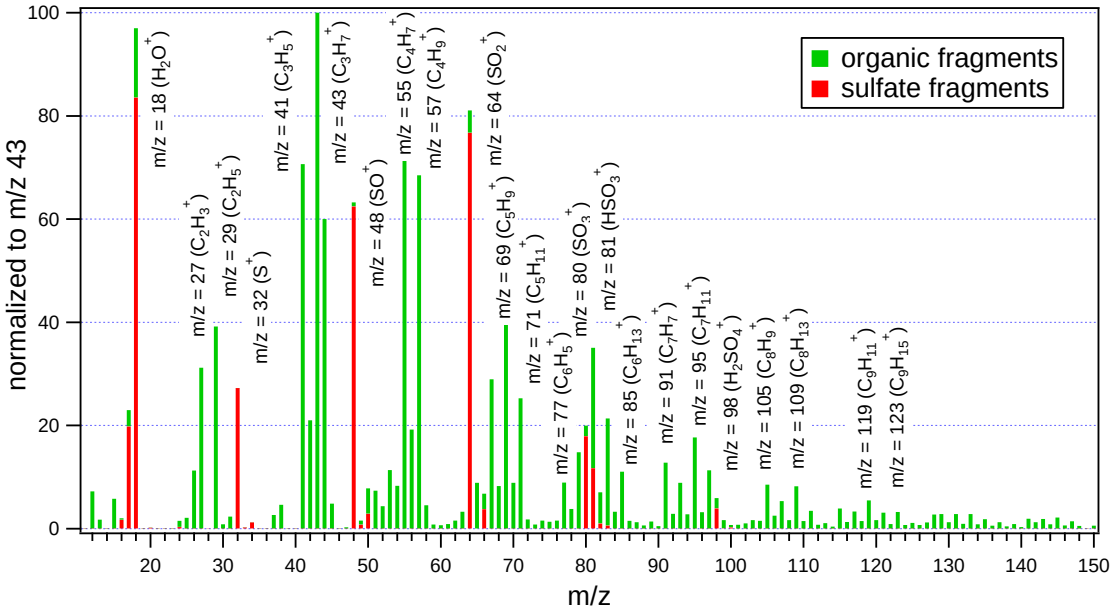

Figure 3.31: Averaged HR-ToF-AMS mass spectrum obtained for all (178) ship plumes measured during the campaign without considering the background. The organic (green) and sulfate (red) mass fractions were normalized to m/z 43 which always was the highest peak.

3.4.4 Summary and Conclusions

The measurements reported here were performed in Northern Germany between Hamburg and Cuxhaven in April 2011. Emissions of 178 vessels were sampled on the banks of the Elbe which is located in an emission control area. A wide range of chemical and physical parameters and trace gases were measured with high time resolution to investigate the impact of the vessel immissions on local air quality and the atmospheric chemistry.

With the information of AIS broadcasts vessels were classified into different types to evaluate their contribution to the total immission impact.
- By detailed investigation of the influence of gaseous species emitted by the vessels, CO_2 was found to contribute by 0.1% to total immissions while O_3 levels decreased on average by 0.4%. Although the sulfur content in fuel is limited, SO_2 even contributed with 7% to total immissions. NO_x was found to contribute 39% to total pollutant immissions. However, stricter NO_x regulations from 2016 associated with changes in the engine technology and emission control systems will lead to a significant decrease of the immission impact.
- Although a reduction of fuel sulfur leads to a decrease of the particulate number immissions, with an average contribution of 20%, the registered contribution is crucial. Predominantly when considering that mainly small particles (<100 nm) influence the sampling site that strongly affect human health. This also explains the fivefold contribution of the number concentration compared to the mass concentration (4%). The relative influence of ship emitted PAHs with an immission contribution of 12% need to be mentioned as well, because some of them are classified as human carcinogens.
- In contrast to several other studies which found sulfate to be the most abundant PM_1 aerosol species our study showed OM (71%; 6% immission impact) was the main contributor to PM_1 while sulfate (21%; 4% immission impact) and black carbon (6%; 3% immission impact) contributed less. In addition, ammonium (2%; 0.7% immission impact) and chloride (0.002%; 0.02% immission impact) affect PM_1 composition. This results in a number of factors contributing to the PM_1 composition and mass and subsequent air quality issues. Hereby, the engine type and performance in addition to the fuel sulfur content were found to play important roles. For this reason, this study is useful to compare the influence of the adopted fuel sulfur regulations which will be stricter in the next years.
- The evaluation of the ship plume chemistry indicates the environmental influence due to the high acidity of particulate sulfate which is composed of sulfuric acid. In addition to particulate sulfate, mass spectra are typically dominated by hydrocarbon-like organic aerosol of unburned fuel and lubricating oil spectral signatures (n-alkanes, branches alkanes, cycloalkanes and aromatics).
- The relative impact of the ship-related immissions during the campaing was dominated by container ships (~60%), tankers (~15%) and cargo ships (~10%) which cover 80-95% (BC, PAH: ~80%; PN, NO_x, CO_2: ~90%; SO_2, organics, sulfate: ~95%) of the air quality impact.

Measuring ship emission plumes has been highlighted to evaluate their impact on local air quality and atmospheric chemistry, particularly next to populated regions. However, data on ship emissions are still sparse implying this work contributes to the assessment of potential effects of several emission-control strategies which will be tightened in the coming years worldwide.

Acknowledgements. This research was funded internally by the Max-Planck Society. The authors wish to acknowledge T. Klimach for programming the analysis tool, T. Böttger for technical support and J. Schneider for helpful discussions. We gratefully acknowledge the NOAA Air Resources Laboratory (ARL) for the provision of the HYSPLIT transport and dispersion model (http://www.arl.noaa.gov/ready.html). J.-M. Diesch also thanks the German Research Foundation (DFG) for financing her position through the Research Training School GRK 826.

References

Agrawal, H., Eden, R., Zhang, X., Fine, P. M., Katzenstein, A., Miller, J. W., Ospital, J., Teffera, S., and Cocker, D. R.: Primary Particulate Matter from Ocean-Going Engines in the Southern California Air Basin, Environ. Sci. Technol., 43, 5398-5402, 2009.

Aiken, A. C., Decarlo, P. F., Kroll, J. H., Worsnop, D. R., Huffman, J. A., Docherty, K. S., Ulbrich, I. M., Mohr, C., Kimmel, J. R., Sueper, D., Sun, Y., Zhang, Q., Trimborn, A., Northway, M., Ziemann, P. J., Canagaratna, M. R., Onasch, T. B., Alfarra, M. R., Prevot, A. S. H., Dommen, J., Duplissy, J., Metzger, A., Baltensperger, U., and Jimenez, J. L.: O/C and OM/OC ratios of primary, secondary, and ambient organic aerosols with high-resolution time-of-flight aerosol mass spectrometry, Environ. Sci. Technol., 42, 4478-4485, 2008.

Alastuey, A., Moreno, N., Querol, X., Viana, M., Artinano, B., Luaces, J. A., Basora, J., and Guerra, A.: Contribution of harbour activities to levels of particulate matter in a harbour area: Hada Project-Tarragona Spain, Atmos. Environ., 41, 6366-6378, 2007.

Allan, J. D., Baumgardner, D., Raga, G. B., Mayol-Bracero, O. L., Morales-Garcia, F., Garcia-Garcia, F., Montero-Martinez, G., Borrmann, S., Schneider, J., Mertes, S., Walter, S., Gysel, M., Dusek, U., Frank, G. P., and Kramer, M.: Clouds and aerosols in Puerto Rico - a new evaluation, Atmos. Chem. Phys., 8, 1293-1309, 2008.

Buhaug, Ø. et al.: Second IMO GHG Study 2009, Int. Marit. Organ., London, 2009.

Coe, H., Allan, J. D., Alfarra, M. R., Bower, K. N., Flynn, M. J., McFiggans, G. B., Topping, D. O., Williams, P. I., O'Dowd, C. D., Dall'Osto, M., Beddows, D. C. S., and Harrison, R. M.: Chemical and physical characteristics of aerosol particles at a remote coastal location, Mace Head, Ireland, during NAMBLEX, Atmos. Chem. Phys., 6, 3289-3301, 2006.

Corbett, J. J., and Fischbeck, P.: Emissions from ships, Science, 278, 823-824, 1997.

Corbett, J. J., and Koehler, H. W.: Updated emissions from ocean shipping, J. Geophys. Res.-Atmos., 108, 2003.

Corbett, J. J., Winebrake, J. J., Green, E. H., Kasibhatla, P., Eyring, V., and Lauer, A.: Mortality from ship emissions: A global assessment, Environ. Sci. Technol., 41, 8512-8518, 2007.

Dalsoren, S. B., Eide, M. S., Endresen, O., Mjelde, A., Gravir, G., and Isaksen, I. S. A.: Update on emissions and environmental impacts from the international fleet of ships: the contribution from major ship types and ports, Atmos. Chem. Phys., 9, 2171-2194, 2009.

Diesch, J.-M., Drewnick, F., Zorn, S. R., von der Weiden-Reinmüller, S.-L., Martinez, M., and Borrmann, S.: Variability of aerosol, gaseous pollutants and meteorological characteristics associated with continental, urban and marine air masses atthe SW Atlantic coast of Iberia, Atmos. Chem. Phys., 12, 1-22, 2012.

Draxler, R., Stunder, B., Rolph, G., Stein, A., Taylor, A., 2009. Hysplit4 User's Guide. National Oceanic and Atmospheric Administration. http://www.arl.noaa.gov/documents/ reports/hysplit_user_guide. pdf (accessed 20.04.09).

Drewnick, F., Böttger, T., von der Weiden-Reinmüller, S.-L., Zorn, S. R., Klimach, T., Schneider, S., and Borrmann, S.: Design of a mobile aerosol research laboratory and data processing tools for effective stationary and mobile measurements, Atmos. Meas. Tech. Discuss., 5, 2273-2313, doi: 10.5194/amtd-5-2273-2012, 2012.

Endresen, O., Sorgard, E., Sundet, J. K., Dalsoren, S. B., Isaksen, I. S. A., Berglen, T. F., and Gravir, G.: Emission from international sea transportation and environmental impact, J. Geophys. Res.-Atmos., 108, 2003.

Eyring, V., Kohler, H. W., Lauer, A., and Lemper, B.: Emissions from international shipping: 2. Impact of future technologies on scenarios until 2050, J. Geophys. Res.-Atmos., 110, 2005.

Eyring, V., Stevenson, D. S., Lauer, A., Dentener, F. J., Butler, T., Collins, W. J., Ellingsen, K., Gauss, M., Hauglustaine, D. A., Isaksen, I. S. A., Lawrence, M. G., Richter, A., Rodriguez, J. M., Sanderson, M., Strahan, S. E., Sudo, K., Szopa, S., van Noije, T. P. C., and Wild, O.: Multi-model simulations of the impact of international shipping on Atmospheric Chemistry and Climate in 2000 and 2030, Atmos. Chem. Phys., 7, 757-780, 2007.

Eyring, V., Isaksen, I. S. A., Berntsen, T., Collins, W. J., Corbett, J. J., Endresen, O., Grainger, R. G., Moldanova, J., Schlager, H., and Stevenson, D. S.: Transport impacts on atmosphere and climate: Shipping, Atmos. Environ., 44, 4735-4771, 2010.

Fuglestvedt, J., Berntsen, T., Eyring, V., Isaksen, I., Lee, D. S., and Sausen, R.: Shipping Emissions: From Cooling to Warming of Climate-and Reducing Impacts on Health, Environ. Sci. Technol., 43, 9057-9062, 2009.

Healy, R. M., O'Connor, I. P., Hellebust, S., Allanic, A., Sodeau, J. R., and Wenger, J. C.: Characterisation of single particles from in-port ship emissions, Atmos. Environ., 43, 6408-6414, 2009.

Hellebust, S., Allanic, A., O'Connor, I. P., Jourdan, C., Healy, D., and Sodeau, J. R.: Sources of ambient concentrations and chemical composition of PM(2.5-0.1) in Cork Harbour, Ireland, Atmos Res, 95, 136-149, 2010.

Hobbs, P. V., Garrett, T. J., Ferek, R. J., Strader, S. R., Hegg, D. A., Frick, G. M., Hoppel, W. A., Gasparovic, R. F., Russell, L. M., Johnson, D. W., O'Dowd, C., Durkee, P. A., Nielsen, K. E., and Innis, G.: Emissions from ships with respect to their effects on clouds, J Atmos Sci, 57, 2570-2590, 2000.

Hulskotte, J. H. J., and van der Gon, H. A. C. D.: Fuel consumption and associated emissions from seagoing ships at berth derived from an on-board survey, Atmos. Environ., 44, 1229-1236, 2010.

International Maritime Organization (IMO), Regulations for the prevention of air pollution from ships, MARPOL Annex IV, 2010

Isakson, J., Persson, T. A., and Lindgren, E. S.: Identification and assessment of ship emissions and their effects in the harbour of G(o)over-circleteborg, Sweden, Atmos. Environ., 35, 3659-3666, 2001.

Kennedy, I. M.: The health effects of combustion-generated aerosols, P Combust Inst, 31, 2757-2770, 2007.

Lack, D. A., Corbett, J. J., Onasch, T., Lerner, B., Massoli, P., Quinn, P. K., Bates, T. S., Covert, D. S., Coffman, D., Sierau, B., Herndon, S., Allan, J., Baynard, T., Lovejoy, E., Ravishankara, A. R., and Williams, E.: Particulate emissions from commercial shipping: Chemical, physical, and optical properties, J. Geophys. Res.-Atmos., 114, 2009.

Lauer, A., Simon, M. A., Banning, J. L., Andre, E., Duncan, K., and Harris, R. N.: Common cutaneous bacteria from the eastern red-backed salamander can inhibit pathogenic fungi, Copeia, 630-640, 2007.

Lawrence, M. G., and Crutzen, P. J.: Influence of NOx emissions from ships on tropospheric photochemistry and climate, Nature, 402, 167-170, 1999.

Lelieveld, J., van Aardenne, J., Fischer, H., de Reus, M., Williams, J., and Winkler, P.: Increasing ozone over the Atlantic Ocean, Science, 304, 1483-1487, 2004.

Lloyd´s Register Engineering Services (1995), *Marine Exhaust Emissions Research Program*, London.

Lonati, G., Cernuschi, S., and Sidi, S.: Air quality impact assessment of at-berth ship emissions. Case-study for the project of a new freight port, Sci. Total Environ., 409, 192-200, 2010.

Lu, G., Brook, J. R., Alfarra, M. R., Anlauf, K., Leaitch, W. R., Sharma, S., Wang, D., Worsnop, D. R., and Phinney, L.: Identification and characterization of inland ship plumes over Vancouver, BC, Atmos. Environ., 40, 2767-2782, 2006.

McLafferty, F. W., Turecek, F., 1993. Interpretation of mass spectra. University Science Books, Mill Valley, CA.

Murphy, S. M., Agrawal, H., Sorooshian, A., Padro, L. T., Gates, H., Hersey, S., Welch, W. A., Jung, H., Miller, J. W., Cocker, D. R., Nenes, A., Jonsson, H. H., Flagan, R. C., and Seinfeld, J. H.: Comprehensive Simultaneous Shipboard and Airborne Characterization of Exhaust from a Modern Container Ship at Sea, Environ. Sci. Technol., 43, 4626-4640, 2009.

Ng, N. L., Canagaratna, M. R., Zhang, Q., Jimenez, J. L., Tian, J., Ulbrich, I. M., Kroll, J. H., Docherty, K. S., Chhabra, P. S., Bahreini, R., Murphy, S. M., Seinfeld, J. H., Hildebrandt, L., Donahue, N. M., DeCarlo, P. F., Lanz, V. A., Prevot, A. S. H., Dinar, E., Rudich, Y., and Worsnop, D. R.: Organic aerosol components observed in Northern Hemispheric datasets from Aerosol Mass Spectrometry, Atmos. Chem. Phys., 10, 4625-4641, 2010.

Petzold, A., Hasselbach, J., Lauer, P., Baumann, R., Franke, K., Gurk, C., Schlager, H., and Weingartner, E.: Experimental studies on particle emissions from cruising ship, their characteristic properties, transformation and atmospheric lifetime in the marine boundary layer, Atmos. Chem. Phys., 8, 2387-2403, 2008.

Phinney, L., Leaitch, W. R., Lohmann, U., Boudries, H., Worsnop, D. R., Jayne, J. T., Toom-Sauntry, D., Wadleigh, M., Sharma, S., and Shantz, N.: Characterization of the aerosol over the sub-arctic north east Pacific Ocean, Deep-Sea Research Part Ii-Topical Studies in Oceanography, 53, 2410-2433, 2006.

Sarvi, A., Lyyranen, J., Jokiniemi, J., and Zevenhoven, R.: Particulate emissions from large-scale medium-speed diesel engines: 2. Chemical composition, Fuel Process Technol, 92, 2116-2122, 2011.

Sax, T., and Alexis , A. (2007), A critical review of ocean-going vessel particulate matter emission factors, Calif. Air Resour. Board, Sacramento, Calif.

Saxe, H., and Larsen, T.: Air pollution from ships in three Danish ports, Atmos. Environ., 38, 4057-4067, 2004.

Schreier, M., Kokhanovsky, A. A., Eyring, V., Bugliaro, L., Mannstein, H., Mayer, B., Bovensmann, H., and Burrows, J. P.: Impact of ship emissions on the microphysical, optical and radiative properties of marine stratus: a case study, Atmos. Chem. Phys., 6, 4925-4942, 2006.

Sinha, P., Hobbs, P. V., Yokelson, R. J., Christian, T. J., Kirchstetter, T. W., and Bruintjes, R.: Emissions of trace gases and particles from two ships in the southern Atlantic Ocean, Atmos. Environ., 37, 2139-2148, 2003.

Song, S. K., Shon, Z. H., Kim, Y. K., Kang, Y. H., Oh, I. B., and Jung, C. H.: Influence of ship emissions on ozone mixing ratios around coastal areas during summer season, Atmos. Environ., 44, 713-723, 2010.

Sun, J. Y., Zhang, Q., Canagaratna, M. R., Zhang, Y. M., Ng, N. L., Sun, Y. L., Jayne, J. T., Zhang, X. C., Zhang, X. Y., and Worsnop, D. R.: Highly time- and size-resolved characterization of submicron aerosol particles in Beijing using an Aerodyne Aerosol Mass Spectrometer, Atmos. Environ., 44, 131-140, 2010.

Viana, M., Amato, F., Alastuey, A., Querol, X., Moreno, T., Dos Santos, S. G., Herce, M. D., and Fernandez-Patier, R.: Chemical Tracers of Particulate Emissions from Commercial Shipping, Environ. Sci. Technol., 43, 7472-7477, 2009.

von der Weiden, S. L., Drewnick, F., and Borrmann, S.: Particle Loss Calculator - a new software tool for the assessment of the performance of aerosol inlet systems, Atmospheric Measurement Techniques, 2, 479-494, 2009.

Wang, C., Corbett, J. J., and Firestone, J.: Improving spatial representation of global ship emissions inventories, Environ. Sci. Technol., 42, 193-199, 2008.

Winnes, H., and Fridell, E.: Particle Emissions from Ships: Dependence on Fuel Type, J Air Waste Manage, 59, 1391-1398, 2009.

4

Conclusions and Outlook

At the beginning of this work, the Max Planck Institute for Chemistry (MPIC) developed a compact Mobile aerosol research Laboratory MoLa for the determination of a multitude of chemical and physical aerosol parameters, trace gas and meteorological characteristics. It is designed for stationary as well as mobile measurements e.g. pollutant mapping, chasing of mobile sources or quasi-Lagrangian-type investigations.

Within this work, the application during two stationary field campaigns, the DOMINO and ship emission measurement campaign has demonstrated that the instruments implemented in the mobile laboratory MoLa are capable of providing valuable quantitative data with high time resolution. Chemical and physical particulate information, meteorology and trace gas mixing ratios allow the characterization of natural and anthropogenic emissions. In addition with complementary tools such as the HYSPLIT trajectory model and the Automated Identification System (AIS) broadcasts, a comprehensive analysis of a large variety of aspects and links between emission sources, formation and transformation processes of emissions and related aerosol properties was possible.

Experimental Aspects I: Limitations of stationary MoLa measurements

For measuring high-quality data and for an extensive analysis including a variety of aspects (measurement location, meteorological conditions (season), distance from sources) it is necessary to critically discuss and consider specific issues and limitations of stationary measurements using the mobile laboratory MoLa.

Stationary measurements using a mobile laboratory have the advantage that measurement locations which are not influenced by local pollution sources can be selected and locations can be changed within short times if conditions suddenly change (wind direction, local pollution, precipitation). Although the measurement sites were situated at a single fixed site during DOMINO and on the same side of the Elbe during the ship emission campaign, a wind change would have allowed driving the mobile laboratory MoLa on the other side of the Elbe, to be located directly downwind of the ship tracks.

A disadvantage of stationary measurements compared to mobile measurements is the loss of spatial flexibility. However, depending on the measurement location and the meteorological conditions (wind shifts) different source regions and emission plumes can be sampled. During the DOMINO campaign, the monitoring station was located at an interface between the continent, two industrial cities in different distances and the Atlantic Ocean. For this reason, the variability of aerosol, gaseous pollutants and meteorological characteristics associated with changes in air mass origin was investigated within the scope of this thesis.

Additionally, a limitation of stationary measurements is that only snapshots of a certain air parcel can be measured implying not the same air parcel can be observed over extended time intervals. For this reason, the detailed investigation of particle formation and transformation processes during transport of emissions from anthropogenic sources cannot be examined at a single fixed site with the exception that source regions are relatively homogeneous over large spatial scales as observed during the DOMINO campaign. During our studies new particle formation and growth events occurred over several hours and were in detail analyzed with the focus of the characterization of events that are observed under clean conditions and with superimposed pollution.

Furthermore, the sampling line of the mobile laboratory MoLa during stationary measurements could be extended to 10 m (10 m during DOMINO, ~7m during the ship emission campaign). For such low altitudes the HYSPLIT trajectory model, used for data separation according to different source regions, suffers from severe limitations. As HYSPLIT is intended for the calculation of transport processes on larger spatial scales due to its relatively low grid resolution, as second approach for the identification of the air mass origin during DOMINO, local meteorology was used measured at the sampling site. As no hindrance e.g. hill, building blocked the wind flow similar results were obtained for both methods. Additionally, influx from other source regions in winter can be neglected as synoptic conditions dominated and re-circulation of air masses (land-sea breeze) is relatively low. Nevertheless, HYSPLIT enables a more exact apportionment of air masses to source regions as it considers the regional/long-range transport processes.

Experimental aspects II: Data processing/Quality assurance

Since the mobile laboratory MoLa was used in the field for the first time during the DOMINO campaign, no experience existed in the handling of such a large amount of coherent data and the data processing. Therefore, time and effort was spent in the preparation of the raw data sets to obtain useful results.

This includes the
-transfer of different formats into a common standard format
-adjustment of data with the MoLa laboratory notebook to remove individual features e.g. power supply interruptions
-removal of outliers (instrument failures, contaminations) and calibration periods
-application of correction factors
-data quality assurance measures (calibrations, particle losses and transport delays through the sampling line)
-averaging onto a consistent common time axis (UTC)
to get a consistent and corrected dataset that enables to efficiently investigate all measured parameters and to extract reliable results for further analysis.

In the meanwhile a common data acquisition software in the mobile laboratory MoLa exists which displays all measured parameters in real-time and allows the operator to subsequently fix a problem "close-to-real-time" if an instrument does not work. Additionally, the acquisition software allows collecting the large amount of data produced by all instruments in a single IGOR experiment file. This feature saves a lot of time of adding and converting different kinds of individual instrument files into a single IGOR file with a common time axis.

Experimental aspects III: AMS data acquisition, calibrations and analysis tools

Much work has been done to assign ambient particulate concentrations to individual sources. On the one hand a recently developed tool, Positive Matrix Factorization (PMF) was used to identify and separate different sources of the organic aerosol. On the other hand, the Peak Integration by Key Analysis (PIKA) tool was used for speciation and quantification of MSA in the high-resolution mass spectra. However, although both advanced analysis methods developed to HR-ToF-AMS standard analysis techniques in the meantime, the uncertainties and limitations of the methods to carefully extract and interpret the processed data have to be considered. Additionally, those of the AMS instrument are also relevant which will be discussed in the following.

Firstly, regarding the HR-ToF-AMS instrumental limitations, it has to be considered that
-the AMS intake system is only able to measure with 100% transmission efficiency in the 40-600 nm particle size range. Larger particles increasingly impact on the critical orifice and do generally not enter the aerodynamic lens system, smaller particles are not focused in the aerodynamic lens system.
-the vaporizer temperature of ~600°C only allows the determination of non-refractory particles and
-remarkable fragmentation due to electron impact ionization was obtained making the analysis difficult.

Secondly, it is necessary that the instrument is tuned and calibrated correctly to
-get a maximal mass resolving power including Gaussian-like peak shapes
-obtain a good signal to noise ratio implying lower mass concentration detection limits (SI calibration)
-convert measured ion signals into aerosol mass concentrations (IE calibration)
-convert particle flight times into corresponding particle diameters (PTOF calibration)
-account for particles that bounce off the vaporizer (CE factor).

In addition to the estimated 25-30% uncertainty introduced by the AMS measurement, further uncertainties result from the individual user inputs in PMF and PIKA analysis. For this reason and as the mobile laboratory MoLa provides the facilities of measuring various parameters, time series of different aerosol types obtained by using PMF were compared with those of other instruments and with ambient reference mass spectra to validate PMF solutions. For this study PIKA has been applied to deconvolve and quantify a marker fragment at m/z 79 corresponding to methanesulfonic acid (MSA). As the MSA calculation was also involved in older software, the ToF-AMS Data Analysis (TADA) tool was used for comparison purposes. However, TADA does not allow fitting the peak shape. As MSA concentrations were registered near the detection limit, PIKA was found to be the better alternative.

Ongoing work on the improvement of the data acquisition tools which help to simplify HR-ToF-AMS data is done by the Jimenez group of the University of Colorado at Boulder. To improve the identification of organic emission sources based on environmental data with PMF, further insights are expected by the recently undertaken custom-programmed tool for high-resolution ToF-AMS data (HR-PMF). Using HR-PMF, the deconvolution of species with the same nominal mass allows a more exact identification and quantification of organic aerosol sources. However, further insights into the organic aerosol fraction are often associated with additional errors (e.g. uncertainties due to inaccurate fitting/m/z calibration/assignment to individual peaks...). For this reason an exact calibration, evaluation and quality assurance is essential for a highly qualitative data interpretation.

A further challenge regarding the PIKA data analysis was to include APES (Analytic Procedure for Elemental Separation) into the PIKA software. This provides the opportunity to firstly fit each peak in the high-resolution mass spectrum using PIKA and afterwards calculate immediately for example the O/C ratio with APES.

Scientific results: Main outcomes of data interpretation, outlook and comparison of datasets

After data were processed as described, a detailed investigation and interpretation have been performed which contribute to the limited knowledge in terms of several aspects which are summarized in the following.

DOMINO campaign

The DOMINO campaign provides both, valuable information about the air composition in this part of Spain and how these parameters vary with air mass origin. To evaluate separate air masses with differentiated continental, urban and marine origin, the campaign was accomplished in winter. The advantage compared to summer measurements in this region is a well-defined origin of air masses with lower disturbance by intensive photochemistry and recirculation periods which affect the aerosol and trace gas phenomenology additionally and therefore contribute to a more complex study scenario. As a result, the variability of the air composition associated with different source regions and the distance from sources affects the particle loading, composition, size distributions and acidity as well as trace gas and meteorological parameters at a certain site. While local pollution sources are characterized by large enhancements of distinct parameters, the components are quickly diluted and transformed with increasing distance to the sources. Regional pollution instead is characterized by a more aged, oxidized aerosol with larger O/C ratios as during the transport of the aerosol transformation processes occur. For this reason, in comparison with urban source regions, more well-mixed air masses originating from continental and marine source regions were sampled. These are characterized by time series with lower inner-category variations implying variations within the air masses. However, comparing the inner-category variability with the inter-category variability (variations between different source regions), variations within the air mass categories are generally larger as very low background concentrations (e.g. marine) are interspersed with individual emissions from point sources (e.g. ships). Additionally, a focus was put on speciation of sulfur compounds. While sulfate was found to be the most abundant PM_1 species in the marine air mass category mainly composed of ammonium bisulfate and sulfuric acid, in addition small amounts of MSA were identified. Due to the high scientific interest, part of this study was to identify the main components and sources of the organic aerosol. This was found to be dominant in all continental source regions and could be categorized into four PMF classes: OOA I, OOA II, HOA and WBOA. Although results reveal the identification of some emission sources in ambient air, improving source apportionment tools will continue to be a challenge as several parameters (time, location, season, meteorology, different kinds of combustion processes (wood burning, fossil fuel combustion) influence altering of source profiles.

Among the results obtained by detailed evaluation of different air masses and their variability, the analysis of individual case studies – of eight "regional" and "plume"-affected new particle formation and growth events – was accomplished within the framework of the DOMINO campaign as well. Only very limited data exist that deal with "plume" events, although it is of particular interest considering most of the continentally formed atmospheric new particle formation events are superimposed by pollution while being transported, changing the chemical composition,

concentration of distinct compounds and aerosol properties by intrusion of anthropogenic pollution. Nucleation events occurred under sunny conditions with elevated sulfur dioxide mixing ratios and low condensational sinks indicating a significant contribution of sulfuric acid to particle formation. For this reason, comparing "plume" with "regional" events, an increase in anthropogenic sulfur dioxide in the "plume"-related events is associated with increased particle formation rates. A different finding, the delineation between particle formation and growth rates can be understood in terms of different sources contributing to the individual nucleation stages (particle formation and growth): sulfur dioxide is mainly emitted by anthropogenic, organic matter instead by both, biogenic and anthropogenic sources. For this reason, by detailed analysis of the mass spectral signatures during particle growth preferentially oxidized organic species were found to condense onto the particle surfaces. The new finding in this context is the positive correlation between the OH reactivity and particle growth in the atmosphere. This shows that the combination of OH reactivity measurements in future field and chamber studies could provide a valuable proxy for gas phase reactivity levels potentially favoring aerosol formation.

For this reason, it will be a future challenge to develop an instrument capable of measuring the chemical composition of particles in this size range. This will allow studying new particle formation processes in detail. Together with the investigation of the variability of air masses, these research fields are particularly important considering the fast industrial development of Asian regions connected with an increase of anthropogenic emissions. In this context it is important to understand characteristics of urban source regions and the formation and transformation processes affected by pollution precursors in contrast to those observed under clean conditions. Additionally, it is necessary to improve the knowledge of the properties and impact of the atmospheric aerosol from different sources considering air quality and the important property human health. Also the radiative impact of the atmospheric aerosol is highly uncertain. For this reason, the investigation of the background aerosol and its properties plays an important role. To further investigate these aspects measurement campaigns using MoLa in megacities and further downwind of the emission sources until real background concentrations are measured is of great importance.

Ship emission measurement campaign

The increase of industrial activities in many countries associated with the increased volume of international trade implies also an increase of ship traffic. Ship traffic significantly contributes to the anthropogenic burden of the atmosphere, changes the atmospheric composition and impacts on local and regional air quality and climate. Since a significant fraction of the emissions even from ocean-going vessels occurs close to land, such emissions may have a strong impact on air quality in coastal and port regions. For this reason, global regulations exist to restrict commercial marine vessel emissions. However, it is worthwhile to mention that only sparse literature of ship emission measurements exists which are valuable for assessing the potential effects of several emission-control strategies. Especially fuel sulfur regulations, as adopted within the emission control areas next to populated regions, directly affect local air quality and atmospheric chemistry. As a result it was found that the impact of ships to total immissions depends largely on the kind of the measured parameter. However, container ships, tankers and cargo vessels together covered most of the ship-related immissions. In addition to the immission impact, submicron sulfate aerosol was found to be highly acidic which negatively affects the environment by acidification. The main outcome within the scope of a detailed analysis of vessel plume characteristics is that emission factors of particle number concentrations and size distributions, the submicron aerosol composition and total submicron particulate matter as well as the trace gas mixing ratios depend on a multitude of factors.

These include the fuel sulfur content, the engine type, load and performance, and probably the size of the ship exhaust system.

Further restrictions are on the way dealing with a reduction of nitrogen oxide which can be affected by changes in the engine technology. Stricter regulations of sulfur dioxide from 2016 will further limit the immissions impact, respectively. For this reason, a further measurement campaign in an emission control area in 2016 and on the open ocean using MoLa is important. This will provide the opportunity to compare trends in emissions changes not only on a local scale but even on a global scale as emission control areas will be created globally in future – based on the results obtained in the existing ones. For this reason, it is essential that emission inventories implement up-to-date information in global modeling studies to estimate future changes and the actual impact of ship emissions.

Comparison of datasets at very different locations

DOMINO campaign

For a better classification of the DOMINO results with those obtained from measurements at very different environments, key parameters from this work are compared with those from measurement campaigns in the following regions:

- the Mediterranean region (Crete) in summer, during the MINOS 2001 campaign
- a rural continental region (Hohenpeissenberg), during HAZE 2002
- the South Atlantic remote marine boundary layer, during the OOMPH 2007 cruise
- a rural continental region (Feldberg), during PARADE 2011 and
- an urban megacity (Paris), during the summer MEGAPOLI 2009 campaign.

During DOMINO, particle number concentrations did not only vary strongly due to the influence of different kinds of air masses but also nucleation events caused abrupt changes in the number concentrations, resulting in large inner-category variability (see Table 4.1). For the same reason, number concentrations exceeding 10^4 cm^{-3} occurred during HAZE compared to nighttime background levels of $1\text{-}2 \cdot 10^3$ cm^{-3} (Hock et al., 2008). Additionally, during the PARADE and the MEGAPOLI campaign new particle formation events in continentally influenced air masses were observed resulting in large variations of the particle number concentration. However, average number concentrations during the summer MEGAPOLI campaign (13013 ± 6742 cm^{-3}) are considerably higher than during DOMINO due to the influence of the Paris emission plume (Freutel et al., 2012). During MINOS, number concentration levels range between $2\text{-}6 \cdot 10^3$ cm^{-3} (Schneider et al., 2004). These relatively high levels for a remote region can be explained by backwards trajectories travelling over Eastern Europe.

During DOMINO the lowest average PM_1 concentrations were measured in "Marine" air masses (1.7 ± 1.1 $\mu g\ m^{-3}$) with "sulfate" being the dominant species. Values for PM_1 which are two to four times higher were recorded in "Continental" and urban air masses where "organics" contributed a major fraction to the total aerosol mass (mean: 4.0 ± 2.5 $\mu g\ m^{-3}$). For comparison, at typical rural sites in central Europe (Hohenpeissenberg: 6.6 ± 5.4 $\mu g\ m^{-3}$; Feldberg: 5.6 ± 4.4 $\mu g\ m^{-3}$) and during MINOS (Crete, 6.6 ± 0.93 $\mu g\ m^{-3}$) higher average PM_1 concentrations were registered. In addition, the aerosol was composed of a balanced organic to inorganic ratio during HAZE, while "sulfate" as the major species was measured in Crete. The highest PM_1 levels and variations were registered during MEGAPOLI. This can be explained by the influence of different source regions

(continentally influenced air masses and the Paris megacity emission plume) surrounding the suburban measurement site. As typical for marine environments, "sulfate" was also the dominating species during OOMPH (Zorn et al., 2008). However, in comparison with all other mentioned campaigns, as being mostly within the remote marine boundary layer, lowest average PM_1 concentrations (0.6 ± 0.6 μg m^{-3}) were obtained during the OOMPH project.

An in-depth investigation of the "sulfate" fraction of the aerosol showed a strong acidification of the aerosol during DOMINO and MINOS. However, the largest acidity of the aerosol occurred during OOMPH where sulfuric acid was the most abundant "sulfate" species. Completely different conditions were observed during HAZE, PARADE and MEGAPOLI, where particles mainly consisted of ammonium sulfate, ammonium nitrate and organics. The organic aerosol was mainly composed of a highly-oxygenated OA during DOMINO and HAZE (see Table 4.1) and together with the semi-volatile OA, both were approximately four times as abundant as hydrocarbon-like OA. A totally different OOA/HOA ratio was obtained during the MEGAPOLI campaign probably due to the increased influence of industrial and traffic emissions from the Paris megacity.

The Mediterranean region is influenced by high solar radiation intensities in the summer months that lead to high ozone levels reaching 60 ppbv during MINOS in Crete (Berresheim et al., 2003). With the additional influence of polluted air for example from Eastern Europe during MINOS or from the Po Valley region (Italy) during HAZE (49 ppbv), high ozone concentrations are the consequence. The influence of season on ozone levels could be recognized when comparing MINOS/HAZE and PARADE with DOMINO, which took place in November/December where lower ozone concentrations were recorded. Although measurements were performed in summer during the MEGAPOLI campaign, lower ozone levels were observed as being titrated by NO. Since the cleanest air was found over the Atlantic Ocean even less ozone (17 ppbv) was found during OOMPH (Williams et al., 2010).

Table 4.1. Overview of the number concentrations, PM_1 mass concentrations, aerosol neutralization, OOA/HOA ratios and ozone levels and corresponding standard deviations within this study and during HAZE 2002, MINOS 2001, OOMPH 2007, PARADE 2011 and MEGAPOLI 2009.

	number conc. / # cm^{-3}	PM_1 conc. / μg m^{-3}	aerosol neutralization	OOA/HOA	O_3 / ppbv
DOMINO 2008	300-178000	4.0±2.5	acidic	4	30±7
HAZE 2002	1000-11000	6.6±5.4	neutralized	4	49±14
MINOS 2001	2000-6000	6.6±0.93	acidic	-	60
OOMPH 2007	-	0.6±0.6	acidic	-	17±2
PARADE 2011	500-23000	5.6±4.4	neutralized	-	38±13
MEGAPOLI 2009	1700-231000	7.9±5.9	neutralized	1.4	29±15

Ship emission measurement campaign

Diesel motor emissions gain increasing attention due to their significant contribution to the anthropogenic atmospheric burden, chemical composition and the impact on local and regional air quality and climate. As diesel engines are also used in cars and trucks, the results obtained from the ship emission measurement campaign were compared with measurements:

- of 226 individual heavy-duty trucks (Ban-Weiss et al., 2009) and
- emissions registered near a German autobahn and test rig studies (Schneider et al., 2005).

When comparing black carbon and particle number emissions of the ships totally different properties were observed. Similar as shown by Ban-Weiss et al. (2009) for individual heavy-duty trucks we found minimal overlap between high black carbon emitters and high particle number emitters due to the fact that increased black carbon emissions suppress new particle formation (Kerminen et al., 2001; Monkkonen et al., 2004). This relationship between the emission levels for both parameters is also reflected in the associated size distributions. An increased availability of sulfuric acid tends to result in an increase of nucleation mode particles as also found by Schneider et al. (2005). The fact that the formation of new particles increases in line with SO_2 emissions via the formation of SO_3 and H_2SO_4 indicates that the fuel quality, i.e. the sulfur content in the fuel, has an important impact on particle number EFs as mentioned by Schneider et al. (2005). For this reason, limiting the fuel sulfur content can result in a direct reduction of the particle number emissions. In contrast, high black carbon emitters exhibit an additional mode larger than 100 nm as also reported by Petzold et al. (2008) who analyzed black carbon mass EFs from cruising ships. As a further result, for enhanced black carbon EFs, NO_x EFs drop by up to 50%. Lower combustion temperatures lead to a decrease in NO_x and the NO/NO_2 ratio because under these conditions the oxidation of nitrogen is less favored (Schneider et al., 2005). While the overall ratio of organics to sulfate is strongly dependent on the engine load during test rig studies performed by Schneider et al. (2005), particulate emissions from ship engines consisted mainly of organic aerosol (organics: 70%, sulfate: 20%). Generally, it has to be considered that ships in contrast to most cars and trucks did not have particle traps known to efficiently remove soot particles but are not designed to remove nucleation particles.

References

Ban-Weiss, G. A., Lunden, M. M., Kirchstetter, T. W., and Harley, R. A.: Measurement of Black Carbon and Particle Number Emission Factors from Individual Heavy-Duty Trucks, Environ. Sci. Technol., 43, 1419-1424, 2009.

Berresheim, H., Plass-Dulmer, C., Elste, T., Mihalopoulos, N., and Rohrer, F.: OH in the coastal boundary layer of Crete during MINOS: Measurements and relationship with ozone photolysis, Atmos. Chem. Phys., 3, 639-649, 2003.

Freutel, F., Schneider, J., Drewnick, F., von der Weiden-Reinmüller, S.-L., Crippa, M., Prévôt, A. S. H., Baltensperger, U., Poulain, L., Wiedensohler, A., Sciare, J., Sarda-Estève, R., Burkhart, J. F., Eckhardt, S., Stohl, A., Gros, V., Colomb, A., Michoud, V., Doussin, J. F., Borbon, A., Haeffelin, M., Morille, Y., Beekmann, M., and Borrmann, S.: Aerosol particle measurements at three stationary sites in the megacity of Paris during summer 2009: Meteorology and air mass origin dominate aerosol particle composition and size distribution, Atmos. Chem. Phys., To be Submitted, 2012.

Hock, N., Schneider, J., Borrmann, S., Rompp, A., Moortgat, G., Franze, T., Schauer, C., Poschl, U., Plass-Dulmer, C., and Berresheim, H.: Rural continental aerosol properties and processes observed during the Hohenpeissenberg Aerosol Characterization Experiment (HAZE2002), Atmos. Chem. Phys., 8, 603-623, 2008.

Kerminen, V. M., Pirjola, L., and Kulmala, M.: How significantly does coagulational scavenging limit atmospheric particle production?, J. Geophys. Res.-Atmos., 106, 24119-24125, 2001.

Monkkonen, P., Koponen, I. K., Lehtinen, K. E. J., Uma, R., Srinivasan, D., Hameri, K., and Kulmala, M.: Death of nucleation and Aitken mode particles: observations at extreme atmospheric conditions and their theoretical explanation, J Aerosol Sci, 35, 781-787, 2004.

Petzold, A., Hasselbach, J., Lauer, P., Baumann, R., Franke, K., Gurk, C., Schlager, H., and Weingartner, E.: Experimental studies on particle emissions from cruising ship, their characteristic properties, transformation and atmospheric lifetime in the marine boundary layer, Atmos. Chem. Phys., 8, 2387-2403, 2008.

Schneider, J., Borrmann, S., Wollny, A. G., Blasner, M., Mihalopoulos, N., Oikonomou, K., Sciare, J., Teller, A., Levin, Z., and Worsnop, D. R.: Online mass spectrometric aerosol measurements during the MINOS campaign (Crete, August 2001), Atmos. Chem. Phys., 4, 65-80, 2004.

Schneider, J., Hock, N., Weimer, S., and Borrmann, S.: Nucleation particles in diesel exhaust: Composition inferred from in situ mass spectrometric analysis, Environ. Sci. Technol., 39, 6153-6161, 2005.

Williams, J., Custer, T., Riede, H., Sander, R., Jockel, P., Hoor, P., Pozzer, A., Wong-Zehnpfennig, S., Beygi, Z. H., Fischer, H., Gros, V., Colomb, A., Bonsang, B., Yassaa, N., Peeken, I., Atlas, E. L., Waluda, C. M., van Aardenne, J. A., and Lelieveld, J.: Assessing the effect of marine isoprene and ship emissions on ozone, using modelling and measurements from the South Atlantic Ocean, Environmental Chemistry, 7, 171-182, 2010.

Zorn, S. R., Drewnick, F., Schott, M., Hoffmann, T., and Borrmann, S.: Characterization of the South Atlantic marine boundary layer aerosol using an aerodyne aerosol mass spectrometer, Atmos. Chem. Phys., 8, 4711-4728, 2008.

Appendix A

List of Figures

List of Tables

List of Abbreviations & Symbols

Abbreviations

AIS	Automated Identification System
AMD	Arithmetic Mean Diameter
APS	Aerodynamic Particle Sizer
BC	Black Carbon
CCN	Cloud Condensation Nuclei
CE	Collection Efficiency
CERN	Conseil Européen pour la Recherche Nucléaire
CS	Condensational Sink
DOMINO	Diel Oxidant Mechanism In relation to Nitrogen Oxide
DMS	DiMethyl Sulfide
ECA	Emission Control Area
EDM	Environmental Dust Monitor
EF	Emission Factor
EP	Engine Power
FDMS-TEOM	Filter Dynamics Measurement System-Tapered Element Oscillating Microbalance
FMPS	Fast Mobility Particle Sizer
FR	Formation Rate
GR	Growth Rate
HEPA	High-Efficiency Particulate Air
HOA	Hydrocarbon-like Organic Aerosol
HR-ToF-AMS	High-resolution Time-of-Flight Aerosol Mass Spectrometer
HYSPLIT	Hybrid Single-Particle Lagrangian Integrated Trajectory
IE	Ionization Efficiency
INTA	Instituto Nacional de Técnica Aeroespacial
LOD	Limit of Detection
LV-OOA (OOAI)	Low-Volatile Oxidized Organic Aerosol
MAAP	Multi Angle Absorption Photometer
MBL	Marine Boundary Layer
MoLa	Mobile research Laboratory
MS	Mass Spectrum
MSA	MethaneSulfonic Acid
NOAA	National Oceanic and Atmospheric Administration
NR	Non-Refractory
OA	Organic Aerosol

OC	Organic Carbon
OM	Organic Matter
OOMPH	Organics over the Ocean Modifying Particles in both Hemispheres
OPC	Optical Particle Counter
PAH	Polycyclic Aromatic Hydrocarbon
PIKA	Peak Integration by Key Analysis
PM	Particulate Matter
PMF	Positive Matrix Factorization
PN	Particle Number
PLC	Particle Loss Calculator
PTOF	Particle Time-Of-Flight
RH	Relative Humidity
RoRo	Roll-on Roll-off
SOA	Secondary Organic Aerosol
SQUIRREL	SeQUential Igor data REtRivaL
SV-OOA (OOAII)	Semi-Volatile Oxidized Organic Aerosol
TADA	Tof-AMS Data Analyzer
UV	UltraViolet
UW-CPC	Ultrafine water-based Condensation Particle Counter
VOC	Volatile Organic Carbon
WBOA	Wood-burning Organic Aerosol

Symbols

β_i	transitional regime correction factor of size bin i
CE	collection efficiency
ΔCO_2	average excess CO_2 concentration
CS	condensational sink
D_{aero}	particle aerodynamic diameter
D_{mob}	particle electrical mobility diameter
D_{opt}	particle optical diameter
D_p	particle diameter
D_{va}	particle vacuum aerodynamic diameter
EF_x	emission factor of species x
IE	ionization efficiency
Kn	Knudsen number
λ	mean free path of gas molecules
LOD	limit of detection
m/z	mass-to-charge ratio
N_i	particle number concentration of the size bin i
N_{tot}	total particle number concentration
R^2	Pearson's correlation coefficient
$\sigma(I)$	standard deviation of the background signal
w_c	fraction of carbon in fuel
Δx	average excess concentration of species x
f_{44}	ratio of m/z 44 to total organics
f_{43}	ratio of m/z 43 to total organics
O:C	ratio of oxygen to carbon

Publications resulting from this thesis

Peer-reviewed Publications

van Stratum, B. J. H., Vilá-Guerau de Arellano, J., Ouwersloot, H. G., van den Dries, K., van Laar, T. W., Martinez, M., Lelieveld, J., **Diesch, J.-M.**, Drewnick, F., Fischer, H., Hosaynali-Beygi, Z., Harder, H., Regelin, E., Sinha, V., Adame, J. A., Sörgel, M., Sander, R., Bozem, H., Song, W., Williams, J., and Yassaa, N.: Study of the diurnal variability of atmospheric chemistry with respect to boundary layer dynamics during DOMINO, Atmos. Chem. Phys., 12, 5329-5341, 2012.

Diesch, J.-M., Drewnick, F., Zorn, S. R., von der Weiden-Reinmüller, S.-L., Martinez, M., and Borrmann, S.: Variability of aerosol, gaseous pollutants and meteorological characteristics associated with changes in air mass origin at the SW Atlantic coast of Iberia, Atmos. Chem. Phys., 12, 3761-3782, 2012.

Sinha, V., Williams, J., **Diesch, J.-M.**, Drewnick, F., Martinez, M., Harder, H., Regelin, E., Kubistin, D., Bozem, H., Hosaynali-Beygi, Z., Fischer, H., Andrés-Hernández, M. D., Kartal, D., Adame, J. A., and Lelieveld, J.: OH reactivity measurements in a coastal location in Southwestern Spain during DOMINO, Atmos. Chem. Phys. Discuss., 12, 4979-5014, 2012.

Crowley, J. N., Thieser, J., Tang, M. J., Schuster, G., Bozem, H., Beygi, Z. H., Fischer, H., **Diesch, J.-M.**, Drewnick, F., Borrmann, S., Song, W., Yassaa, N., Williams, J., Pöhler, D., Platt, U., and Lelieveld, J.: Variable lifetimes and loss mechanisms for NO_3 and N_2O_5 during the DOMINO campaign: contrasts between marine, urban and continental air, Atmos. Chem. Phys., 11, 10853-10870, 2011.

Sörgel, M., Regelin, E., Bozem, H., **Diesch, J.-M.**, Drewnick, F., Fischer, H., Harder, H., Held, A., Hosaynali Beygi, Z., Martinez, M., and Zetzsch, C.: Quantification of the unknown HONO daytime source and its relation to NO_2, Atmos. Chem. Phys., 11, 10433-10477, 2011.

Diesch, J.-M., Drewnick, F., Sinha, V., Adame, J. A., Sorribas, M., Williams, J., Martinez, M., and Borrmann, S.: New particle formation and growth events observed under clean and polluted conditions and with superimposed pollution on the coast of SW Spain, submitted to Atmos. Environ., 2012.

Diesch, J.-M., Drewnick, F., Klimach, T., and Borrmann, S.: Investigation of gaseous and particulate emissions from various marine vessel types measured on the banks of the Elbe in Northern Germany, submitted to Atmos. Chem. Phys., in review, 2012.

Diesch, J.-M., Drewnick, F., Klimach, T., and Borrmann, S.: Particle and trace gas properties from ship exhaust plumes: Emission characteristics and impact on air quality, Proceeding of the TAC-Conference, 2012.

von der Weiden-Reinmüller, S.-L., Drewnick, F., Crippa, M., Prévôt, A. S. H., Meleux, F., Böttger, T., Gallavardin, S., Klimach, T., Zorn, S. R., **Diesch, J.-M.**, Baltensberger, U., Beekmann, M., and Borrmann, S.: Mobile aerosol and trace gas measurements to investigate characteristics and transformation processes of megacity emissions in the Paris metropolitan area – an overview, to be submitted to Atmos. Chem. Phys., in review, 2012.

Diesch, J.-M., Drewnick, F., and Borrmann, S.: Ship emission impact on local air quality and atmospheric chemistry, to be submitted to Environ. Sci. Technol., in review, 2012.

Conference contributions

Diesch, J.-M., Drewnick, F., Klimach, T., and Borrmann, S.: Particle and trace gas properties from ship exhaust plumes: Emission characteristics and impact on air quality, Conference on Transport, Atmosphere and Climate (TAC), Prien am Chiemsee, Germany, oral presentation, 2012.

Diesch, J.-M., Drewnick, F., Sinha, V., Williams, J., and Borrmann, S.: Characterization of key aerosol, trace gas and meteorological properties & particle formation and growth processes dependant on air mass origins in Southern Spain, American Geophysical Union (AGU), San Francisco, oral presentation, 2011.

Drewnick, F., **Diesch, J.-M.**, and Borrmann, S.: Characteristics of aerosol particles and trace gases in ship exhaust plumes, American Geophysical Union (AGU), San Francisco, poster presentation, 2011.

Diesch, J.-M., Drewnick, F., Sinha, V., Williams, J., and Borrmann, S.: Influence of key aerosol, trace gas and meteorological parameters on new particle formation in Southern Spain, European Aerosol Conference (EAC), Manchester, oral presentation, 2011.

Sörgel, M., Bozem, H., **Diesch, J.-M.**, Drewnick, F., Fischer, H., Harder, H., Held, A., Hosynali-Beygi, Z., Martinez, M., Regelin, E., and Zetzsch, C: Quantification of the unknown HONO daytime source and its relation to NO_2 and aerosol properties, International Conference on Chemistry and the Environment (ICCE), Zürich, oral presentation, 2011.

Diesch, J.-M., Zorn, S. R., von der Weiden, S.-L., Drewnick, F., and Borrmann, S.: Comparison of regional pollution and background air characteristics in coastal Southern Spain, European Geoscience Union (EGU), Vienna, poster presentation, 2011.

Adame, J. A., **Diesch, J.-M.**, Herández-Ceballos, M., Drewnick, F., and Martinez, M.: Surface meteorology overview for the DOMINO campaign. European Geoscience Union (EGU), Vienna, oral presentation, 2011.

Diesch, J.-M., Zorn, S. R., von der Weiden, S.-L., Drewnick, F., and Borrmann, S.: Aerosol/trace gas characteristics and particle formation depending on air mass origin: Results from the DOMINO campaign in Southern Spain, International Aerosol Conference (IAC), Helsinki, oral presentation, 2010.

Drewnick, F., von der Weiden, S.-L., Freutel, F., Klimach, T., Dzepina, K., Roth, A., Gallavardin, S., Schneider, S., Zorn, S. R., **Diesch, J.-M.**, Fachinger, J., Reitz, P., Schmale, J., Beekmann, M., and Borrmann, S.: Investigation of megacity emissions using combined mobile and stationary measurements during the MEGAPOLI field campaigns in Paris, International Aerosol Conference (IAC), Helsinki, oral presentation, 2010.

von der Weiden, S.-L., Drewnick, F., Zorn, S. R., **Diesch, J.-M.**, Dzepina, K., Beekmann, M., and Borrmann, S.: Urban pollution measurements in the Paris region using a mobile laboratory within the MEGAPOLI project, International Aerosol Conference (IAC), Helsinki, oral presentation, 2010.

Regelin, E., Martinez, M., Harder, H., Adame, J. A., Fischer, H., Bozem, H., Hosynali-Beygi, Z., Williams, J., Custer, T., Song, W., Lawrence, M., Sander, R., **Diesch, J.-M.**, Drewnick, F., Sörgel, M., Andrés-Hernández, L, and Lelieveld, J.: OH and HO_2 in the boundary layer as observed during DOMINO, European Geoscience Union (EGU), Vienna, oral presentation, 2010.

Acknowledgements

Curriculum Vitae

Appendix B

The Appendix B provides a brief overview of my contribution to the co-authored publications included in this thesis. Additionally, all co-authored publications are presented.

Publications A - D:

- van Stratum, B. J. H., Vilá-Guerau de Arellano, J., Ouwersloot, H. G., van den Dries, K., van Laar, T. W., Martinez, M., Lelieveld, J., **Diesch, J.-M.**, Drewnick, F., Fischer, H., Hosaynali-Beygi, Z., Harder, H., Regelin, E., Sinha, V., Adame, J. A., Sörgel, M., Sander, R., Bozem, H., Song, W., Williams, J., and Yassaa, N.: Study of the diurnal variability of atmospheric chemistry with respect to boundary layer dynamics during DOMINO, Atmos. Chem. Phys., 12, 5329-5341, 2012.

- Sinha, V., Williams, J., **Diesch, J.-M.**, Drewnick, F., Martinez, M., Harder, H., Regelin, E., Kubistin, D., Bozem, H., Hosaynali-Beygi, Z., Fischer, H., Andrés-Hernández, M. D., Kartal, D., Adame, J. A., and Lelieveld, J.: OH reactivity measurements in a coastal location in Southwestern Spain during DOMINO, Atmos. Chem. Phys. Discuss., 12, 4979-5014, 2012.

- Crowley, J. N., Thieser, J., Tang, M. J., Schuster, G., Bozem, H., Beygi, Z. H., Fischer, H., **Diesch, J.-M.**, Drewnick, F., Borrmann, S., Song, W., Yassaa, N., Williams, J., Pöhler, D., Platt, U., and Lelieveld, J.: Variable lifetimes and loss mechanisms for NO_3 and N_2O_5 during the DOMINO campaign: contrasts between marine, urban and continental air, Atmos. Chem. Phys., 11, 10853-10870, 2011.

- Sörgel, M., Regelin, E., Bozem, H., **Diesch, J.-M.**, Drewnick, F., Fischer, H., Harder, H., Held, A., Hosaynali Beygi, Z., Martinez, M., and Zetzsch, C.: Quantification of the unknown HONO daytime source and its relation to NO_2, Atmos. Chem. Phys., 11, 10433-10477, 2011.

These publications provide insights into atmospheric gas phase processes observed during the DOMINO campaign in the southwest of Spain. The main objectives within the publications are the study of the atmospheric oxidation chemistry, the comparison of the radical and nighttime chemistry and the characterization of the self-cleaning efficiency of the atmosphere in different air mass types. The mobile laboratory MoLa provides additional information for the investigation of physical and chemical aerosol parameters, meteorological and typical gas phase data. Using a combination of particulate and individual trace gas data (e.g. OH reactivity, HONO but also typical ones measured by MoLa), further aspects could be highlighted within each of the publications. For this reason, by providing a consistent, corrected dataset of the measured MoLa parameters which allows to efficiently investigate individual parameters, I was named as a co-author.

Additionally, some of the authors used the same separation in the individual source regions marine/urban/continental and the corresponding HYSPLIT trajectories as I used in the DOMINO publications.

Publication E:

- von der Weiden-Reinmüller, S.-L., Drewnick, F., Crippa, M., Prévôt, A. S. H., Meleux, F., Böttger, T., Gallavardin, S., Klimach, T., Zorn, S. R., **Diesch, J.-M.**, Baltensberger, U., Beekmann, M., and Borrmann, S.: Mobile aerosol and trace gas measurements to investigate characteristics and transformation processes of megacity emissions in the Paris metropolitan area – an overview, to be submitted to Atmos. Chem. Phys., in review, 2012.

This publication deals with mobile and stationary measurements performed in the Paris metropolitan area, France within the framework of the European Union FP7 MEGAPOLI project. The main focus was to investigate the megacity emission plume, their structure and transformation processes during plume dilution. During the summer 2009 and winter 2010 campaign, in each case for one week I operated the instruments. During all kinds of measurement strategies, including cross section measurements for the investigation of the plume structure, quasi-Lagrangian radial measurements and stationary measurements, high qualitative data were obtained. Also during the intercomparison measurement where the mobile laboratory MOSQUITA and the French aircraft ATR took part, data comparison show a good agreement which is presented in this publication as well.

A Study of the diurnal variability of atmospheric chemistry with respect to boundary layer dynamics during DOMINO

B. J. H. van Stratum[1], J. Vilà-Guerau de Arellano[1], H. G. Ouwersloot[1,2], K. van den Dries[1], T. W. van Laar[1], M. Martinez[2], J. Lelieveld[2], J.-M. Diesch[3], F. Drewnick[3], H. Fischer[2], Z. Hosaynali Beygi[2], H. Harder[2], E. Regelin[2], V. Sinha[4], J. A. Adame[5], M. Sörgel[6,*], R. Sander[2], H. Bozem[2], W. Song[2], J. Williams[2], and N. Yassaa[2,7]

[1]Wageningen University, Meteorology and Air Quality, Wageningen, The Netherlands
[2]Max Planck Institute for Chemistry, Department of Atmospheric Chemistry, Mainz, Germany
[3]Max Planck Institute for Chemistry, Particle Chemistry Department, Mainz, Germany
[4]Indian Institute of Science Education and Research Mohali, Sector 81, S. A. S. Nagar, Manauli PO, Punjab, 140306, India
[5]National Institute for Aerospace Technology, Atmospheric Sounding Station – El Arenosillo, Mazagón, Spain
[6]University of Bayreuth, Atmospheric Chemistry Research Laboratory, Bayreuth, Germany
[7]University of Sciences and Technology Houari Boumediene, Faculty of Chemistry, Algiers, Algeria
*now at: University of Bayreuth, Junior Professorship in Atmospheric Chemistry, Bayreuth, Germany

Published in Atmos. Chem. Phys., Volume 12, 5329-5341, 2012

Abstract

We study the interactions between atmospheric boundary layer (ABL) dynamics and atmospheric chemistry using a mixed-layer model (MXLCH) coupled to chemical reaction schemes. Guided by both atmospheric and chemical measurements obtained during the DOMINO campaign (2008), numerical experiments are performed to study the role of ABL dynamics and the accuracy of chemical schemes with different complexity: MOZART-4 and a reduced mechanism of this chemical system. Both schemes produce satisfactory results, indicating that the reduced scheme is capable of reproducing the O_3-NO_X-VOC-HO_X diurnal cycle during conditions characterised by a low NO_X regime and small O_3 tendencies (less than 1 ppb per hour). By focussing on the budget equations of chemical species in the mixed-layer model, we show that for species like O_3, NO and NO_2, the influence of entrainment and boundary layer growth is of the same order as chemical production/loss. This indicates that an accurate representation of ABL processes is crucial in understanding the daily cycle of chemical species. By comparing the time scales of chemical reactive species with the mixing time scale of turbulence, we propose a classification based on the Damköhler number to further determine the importance of dynamics on chemistry during field campaigns. Our findings advocate an integrated approach, simultaneously solving the ABL dynamics and chemical reactions, in order to obtain a better understanding of chemical path ways and processes and the interpretation of the results obtained during measurement campaigns.

1 Introduction

Present day research on atmospheric chemistry covers a vast range of scales and approaches. Focusing on isoprene, there are for instance highly fundamental studies, either based on a theoretical approach (Peeters et al., 2009) or on small scale laboratory experiments in reaction chambers (Paulot et al., 2009), and studies with a more applied approach. Examples of the latter are

controlled experiments in box models (Sander et al., 2011) and simulations at a global scale using global transport models (Stavrakou et al., 2010). However, in order to obtain a better understanding of the chemical system in real-life conditions, field experiments like e.g. TROFEE (Yokelson et al., 2007), DOMINO (Sörgel et al., 2011; Crowley et al., 2011; Diesch et al., 2012) and HUMPPA-COPEC (Williams et al., 2011) are conducted, the majority of which are strongly modulated by the diel variability of the atmospheric boundary layer (ABL). This adds further complexity to the interpretation of the data, which is often undervalued. Here, in analysing the diurnal variability of the reactants during DOMINO, we propose an integrated approach, simultaneously solving the ABL development and chemical transformation within a conceptual meteorological model in order to obtain a better understanding and representation of the daily cycle of chemical species.

The temporal evolution of atmospheric chemistry is controlled by both chemical processes and the development of the ABL (Ganzeveld et al., 2008; Vilà-Guerau de Arellano et al., 2011). Especially for convective cases characterised by a strong diel cycle, the influence of boundary layer growth and entrainment plays a crucial role in the diurnal cycle of atmospheric chemical species. As the influence of boundary layer dynamics acts on similar time-scales (~30 min) as certain chemical transformations, dynamics and chemistry have to be addressed as an integrated whole.

In this paper we systematically study the effect of boundary layer dynamics on atmospheric chemistry by quantifying their respective influence by means of a mixed-layer model coupled to a chemical reaction scheme. Under diurnal conditions, mixed-layer theory is a satisfactory compromise between a box model (no characterization of ABL dynamics) and more advanced 3-D (large-eddy simulation, mesoscale or global circulation) models. The simplicity of the mixed-layer model enables us to obtain insight on the underlying processes and is very suitable/complementary for the interpretation of measurement campaigns. More specifically, we use one day during the DOMINO (Diel Oxidant Mechanisms in relation to Nitrogen Oxides) measurement campaign, conducted in November 2008 near Mazagón, south western Spain. The campaign focussed on the diel cycle of chemistry in relation to meteorology, combining the measurement of chemical species with meteorological surface and upper air observations. With (amongst others) ozone, nitrogen oxides and vertical profiles of temperature and moisture, the dataset provides a unique opportunity to comprehensively study and validate the interplay between the dynamics and atmospheric chemistry in the ABL.

Using the measurement data, we reproduce the boundary layer development of a single day during DOMINO with the mixed-layer model. Two different reaction schemes are integrated in the mixed-layer model: the Model for Ozone and Related chemical Tracers, version 4 (MOZART-4, hereafter: MOZART) (Emmons et al., 2010) and an extended version of the reaction schemes used by Vilà-Guerau de Arellano et al. (2009, 2011) and Ouwersloot et al. (2011). The latter consists of a reduced mechanism of the chemical system. In absence of a complete set of measurements, this minimizes the assumptions made in the initial and boundary conditions, like e.g. the initial mixing ratios or surface emissions or deposition.

Our main objectives are: (1) to quantify the influence of boundary layer dynamics on atmospheric chemistry, (2) to show the benefits in using conceptual models as a method to obtain a better understanding and complementary information of measured data and (3) to discuss the current state of the art of modelling, comparing the complex MOZART chemical scheme with a simplified reaction scheme.

Our research approach and structure of the article is as follows: we start in Sect. 2 with a short description of the mixed-layer model and chemical reaction schemes. In Sect. 3 the large scale atmospheric synoptic and boundary layer dynamics of the studied day are addressed, followed by the design of the numerical experiments. In Sect. 4 we discuss the modelled results, comparing MOZART and the reduced scheme with measurements. Next, we examine the budget equations of chemical species, separating the influence of boundary layer dynamics (entrainment and boundary layer growth) from the contributions of other processes like surface emission/deposition or chemical transformations. This allows us to study the relative importance of boundary layer dynamics compared to chemical reactions. This is further supported by studying the characteristic time scales of chemistry and turbulence as an appropriate indicator of the relevance of chemistry versus dynamics for fast and slow reacting chemical species. In Sect. 5 we conclude the paper by summarizing the main conclusions.

2 Mixed-layer model

2.1 Representation boundary layer dynamics

The MiXed Layer CHemistry (MXLCH) model stems from the pioneering research of Lilly (1968); Betts (1973); Tennekes and Driedonks (1981) on the dynamics of clear and cloudy boundary layers. In short, the model solves the time development of idealized vertical profiles of dynamic variables (potential temperature (θ), specific humidity (q)) and chemical species (S) like nitrogen dioxide (NO_2) or ozone (O_3). As shown schematically in Fig. 1, the mixed-layer quantities are expected to be perfectly mixed by turbulence. Consequently, we can define the mixed-layer variables to be constant with height:

$$\langle \phi \rangle = \frac{1}{h}\int_s^h \phi(z)\,\mathrm{d}z, \tag{1}$$

with $\phi = \{\theta, q, S\}$ and "s" and "h" denote the surface and mixed-layer height. The equations governing (*Ø)* are derived by vertically integrating the one dimensional Reynolds averaged Navier-Stokes equations, resulting in:

$$\frac{\partial \langle \phi \rangle}{\partial t} = \frac{\overline{w'\phi'}_s - \overline{w'\phi'}_h}{h} + S_\phi. \tag{2}$$

Here $\overline{w'\phi'}$ denotes a turbulent flux and $S_Ø$ contains additional source and sink terms, for chemical species the production and/or loss rates in chemical reactions. An additional term for advection has been omitted, but can easily be included in a similar manner like $S_Ø$. The mixed-layer top discontinuity ΔØ, marking the interface between the unstable mixed-layer and stable free troposphere, evolves in time as the combined result of mixed-layer growth and changes in the bulk quantity:

$$\frac{\partial \Delta\phi}{\partial t} = \frac{\partial \phi_{FT}}{\partial t} - \frac{\partial \langle \phi \rangle}{\partial t} = \gamma_\phi \left(\frac{\partial h}{\partial t} - w_s \right) - \frac{\partial \langle \phi \rangle}{\partial t}, \tag{3}$$

where $Ø_{FT}$ and $\gamma_Ø$ represent respectively the condition directly above the inversion and the free 5 tropospheric lapse rate (Fig. 1). The mixed-layer grows due to entrainment, opposed by large scale vertical motions:

$$\frac{\partial h}{\partial t} = w_e + w_s, \tag{4}$$

where w_e and w_s represent the entrainment and subsidence velocity, the latter is defined as $w_s = (\nabla \times V_h)h$ with $\nabla \times V_h$ the horizontal velocity divergence. The entrainment 10 velocity is calculated as:

$$w_e = \frac{-\overline{w'\theta'}_{v;h}}{\Delta\theta_v}. \quad (5)$$

Note that virtual temperatures are used to include the influence of moisture on buoyancy (Stull, 1988). In order to close this set of equations, the entrainment flux of (virtual) heat is parametrized as a negative fixed fraction (β) of the surface heat flux:

$$\overline{w'\theta'}_{v;h} = -\beta\overline{w'\theta'}_{v;s}, \quad (6)$$

and written into Eq. (5). This relates the entrainment of not only heat, but also moisture and chemical species to the surface flux of heat and the thermodynamic structure as w_e is used to calculate the entrainment fluxes:

$$\overline{w'\phi'}_h = -w_e\Delta\phi. \quad (7)$$

Buoyancy (mainly controlled by heat) is therefore a key variable, actively influencing the budgets of chemical reactive species. Explained in words, the tendencies of heat, moisture and chemical species depend on the mixing of any input at the surface (latent and sensible heat fluxes and, for chemical species, the emission or deposition fluxes) and the entrained air from the free troposphere over the mixed-layer depth. Depending on the sign of $\Delta\emptyset$ and therefore the difference between the mixed-layer and free troposphere, the influence of entrainment on the budget of a chemical species can be negative or positive. For instance, for the examples shown in Fig. 1., entrainment will decrease (NO_2) as air with a lower mixing ratio is entrained into the mixed-layer. For O_3, the opposite occurs and entrainment will increase (O_3).

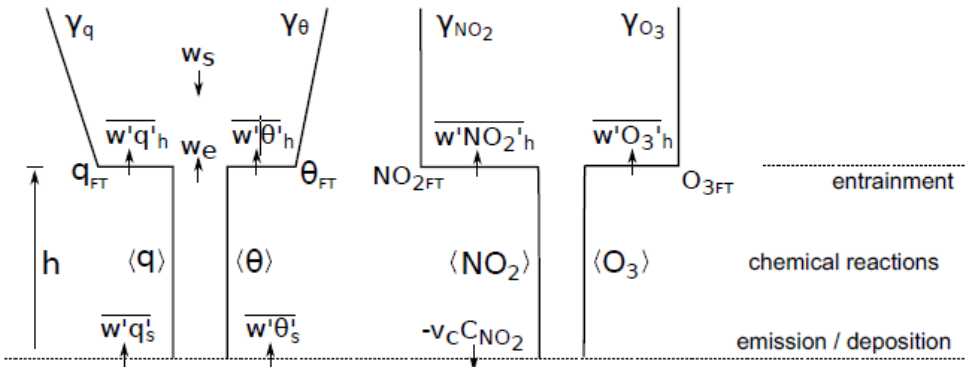

Figure 1: Conceptual representation of the vertical profiles of specific humidity (q), potential temperature (θ) and, as an example, nitrogen dioxide (NO_2) and ozone (O_3). Within the mixedlayer all variables are constant with height (Eq. 1), topped by an inversion defined as $\Delta\emptyset = \emptyset_{FT} - (\emptyset)$ (Eq. 3). On the right side for chemistry relevant processes are shown with emissions and deposition near the surface, chemical reactions within the mixed-layer and entrainment of free-tropospheric air at the mixed-layer top ($\overline{w'\phi'}$, Eq.2).

2.2 Representation of chemistry

As a representation for the chemical reactions, two chemical reaction schemes are implemented in MXLCH: MOZART (Emmons et al., 2010) and an extended version of the reaction schemes used by Vilà-Guerau de Arellano et al. (2009, 2011); Ouwersloot et al. (2011), where the latter consists of

a reduced mechanism of the chemical system. Despite being less complete in both the number of chemical species and reaction equations, the reduced scheme has a number of advantages over MOZART:

1. As the scheme contains less species and equations, the computational costs are minimized while the scheme still retains the essential components of the O_3-NO_X-VOC-HO_X cycle (Vilà-Guerau de Arellano et al., 2011). Although computational time is no limiting factor when using a conceptual model like MXLCH, use of the reduced scheme can act as a validation before implementing it in for instance large-eddy simulation (e.g. Ouwersloot et al., 2011) where the number of reactions does put a serious constraint on the computational possibilities.

2. Using a limited number of species and reactions, the chemical system remains tractable, resulting in a better understanding of the main underlying chemical pathways.

3. By including less species, the degrees of freedom are reduced, resulting in less uncertainty in the initialisation and boundary conditions (emission/deposition variability and initial properties of the mixed-layer and free troposphere) of the model.

The chemical reactions employed in the reduced scheme are presented in Table 1. The reaction rate coefficients are from the International Union of Pure and Applied Chemistry (IUPAC), Subcommittee for Gas Kinetic Data Evaluation (http://www.iupac-kinetic.ch.cam.ac.uk/) All chemical reactions are solved at each time step of dt = 1 s for both the mixed-layer and free troposphere.

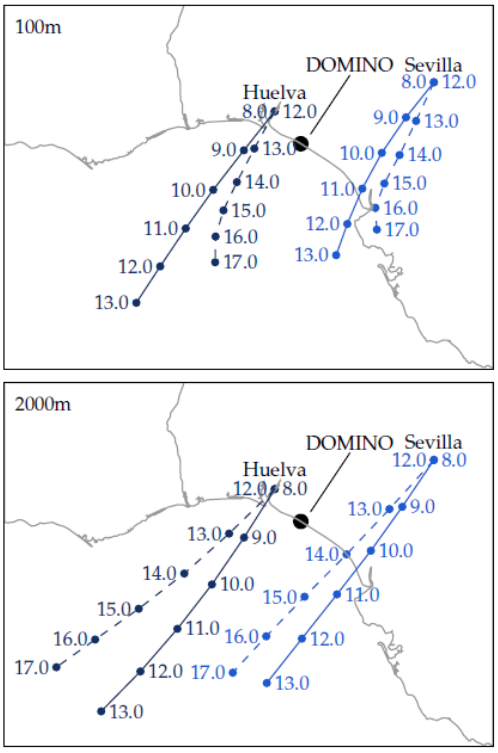

Figure 2: Forward trajectories at 100 m and 2000 m calculated by the NOAA HYSPLIT model using NCEP-GDAS meteorology, starting at Sevilla and Huelva at 08:00 UTC (solid lines) and 12:00 UTC (dashed lines) on 23 November 2008. The black dot indicates the DOMINO measurement location at El Arenosillo.

Table 1: Chemical reaction scheme used in the reduced scheme with T the absolute temperature in Kelvin and χ the solar zenith angle. First-order reaction rates are in s^{-1}, second-order reaction rates in cm^3 $molecule^{-1}s-1$. In R19 n=0 (no OH-recycling), P depicts a product which is not further evaluated in the chemical reaction scheme. ISO refers to isoprene, where all its oxidation products (MVK; methyl vinyl ketone and MACR; methacrolein) are lumped into a single species MVK.

Number	Reaction	Reaction Rate
R1	$O_3 + h\nu \rightarrow O^1D + O_2$	$3.00\times10^{-5}\times e^{\frac{-0.575}{\cos(\chi)}}$
R2	$O^1D + H_2O \rightarrow 2OH$	$1.63\times10^{-10}\times e^{\frac{60}{T}}$
R3	$O^1D + N_2 \rightarrow O_3 + \mathcal{P}$	$2.15\times10^{-11}\times e^{\frac{110}{T}}$
R4	$O^1D + O_2 \rightarrow O_3$	$3.30\times10^{-11}\times e^{\frac{55}{T}}$
R5	$NO_2 + h\nu \rightarrow NO + O_3 + \mathcal{P}$	$1.67\times10^{-2}\times e^{\frac{-0.575}{\cos(\chi)}}$
R6	$CH_2O + h\nu \rightarrow HO_2 + \mathcal{P}$	$1.47\times10^{-4}\times e^{\frac{-0.575}{\cos(\chi)}}$
R7	$OH + CO \rightarrow HO_2 + \mathcal{P}$	2.40×10^{-13}
R8	$OH + CH_4 \rightarrow CH_3O_2 + \mathcal{P}$	$2.45\times10^{-12}\times e^{\frac{-1775}{T}}$
R9	$OH + ISO \rightarrow RO_2$	1.00×10^{-10}
R10	$OH + MVK \rightarrow HO_2 + CH_2O + \mathcal{P}$	2.40×10^{-11}
R11	$OH + HO_2 \rightarrow H_2O + O_2$	$4.80\times10^{-11}\times e^{\frac{250}{T}}$
R12	$OH + H_2O_2 \rightarrow H_2O + HO_2$	$2.90\times10^{-12}\times e^{\frac{-160}{T}}$
R13	$OH + O_3 \rightarrow HO_2 + O_2$	$1.30\times10^{-12}\times e^{\frac{-956}{T}}$
R14	$HO_2 + NO \rightarrow OH + NO_2$	$3.50\times10^{-12}\times e^{\frac{250}{T}}$
R15	$CH_3O_2 + NO \rightarrow HO_2 + NO_2 + CH_2O + \mathcal{P}$	$2.80\times10^{-12}\times e^{\frac{300}{T}}$
R16	$RO_2 + NO \rightarrow HO_2 + NO_2 + MVK + CH_2O$	1.00×10^{-11}
R17	$OH + CH_2O \rightarrow HO_2 + \mathcal{P}$	$5.50\times10^{-12}\times e^{\frac{125}{T}}$
R18	$2HO_2 \rightarrow H_2O_2 + O_2$	*
R19	$CH_3O_2 + HO_2 \rightarrow \mathcal{P}$	$4.10\times10^{-13}\times e^{\frac{750}{T}}$
R20	$RO_2 + HO_2 \rightarrow n\mathrm{OH} + \mathcal{P}$	1.50×10^{-11}
R21	$OH + NO_2 \rightarrow HNO_3$	$3.50\times10^{-12}\times e^{\frac{340}{T}}$
R22	$NO + O_3 \rightarrow NO_2 + O_2$	$3.00\times10^{-12}\times e^{\frac{-1500}{T}}$
R23	$NO_2 + O_3 \rightarrow NO_3 + O_2$	$1.40\times10^{-13}\times e^{\frac{-2470}{T}}$

$^*k = (k1+k2)/k3;\ k1 = 2.21\times10^{-13}\times e^{\frac{600}{T}};\ k2 = 1.91\times10^{-33}\times e^{\frac{980}{T}}\times c_{air};\ k3 = 1+1.4\times10^{-21}\times e^{\frac{2200}{T}}\times c_{H_2O}$

3 Case description

Our numerical experiments are based on measurement data obtained during the DOMINO campaign, conducted at the *Atmospheric Sounding Station – El Arenosillo* (37.1°N, 6.7°W, +40 m a.m.s.l.), a platform of the Atmospheric Research and Instrumentation Branch of the Spanish National Institute for Aerospace Technology (INTA), dedicated to atmospheric measurements in the Southwest of Spain. From this dataset, we selected the 23 November 2008 as it was an ideal day; characterized by a relative small influence of large synoptic scales and with lower build up of ozone (less than 10 ppb in 10 h). Furthermore, this day was in an intense observation period with high frequency balloon soundings (hourly, measuring the location, temperature, humidity and pressure) and comprehensive coverage of the chemical measurements. With high pressure over Spain (Azores High), it was a cloudless day with a moderate (1–4 ms^{-1}) NNE flow in which an initially shallow stable boundary layer developed into a convective boundary layer with a depth of approximately 1400 m at 15:00 UTC. Figure 2 shows eight forward trajectories computed with the NOAA HYSPLIT model (Draxler and Rolph, 2011) using NCEP-GDAS as meteorological input files with 1° × 1° spatial resolution. The trajectories were calculated in the ABL (near surface, 100 m) and free troposphere (2000 m), starting at the city of Sevilla and the industrial area near Huelva (petrochemical industry) at 08:00 UTC (ending at 13:00 UTC) and 12:00 UTC (ending at 17:00 UTC). In spite of the low resolution, the trajectories indicate that relative clean air was advected from these areas during 23 November. This is further corroborated by the relative low NO_X and O_3

observations in Fig. 4. This ensures that the evolution in the observational chemical data is mainly controlled by local meteorological events: emission or deposition, chemical reactions or boundary layer dynamics, rather than transport.

The initial and boundary conditions used in MLXCH are presented in Tables 2 and 4. The initial temperature and moisture profiles are based on the atmospheric soundings and meteorological data measured at 50 m a.g.l. from a tall tower (100 m) available at El Arenosillo. As no measurements of the surface heat and moisture fluxes are available, we impose typical values given the location and time of the year. In addition to the experiments with MXLCH, a second experiment is conducted with a box model to provide a first quantification of the influence of ABL dynamics. With both the sensible and latent heat flux set to zero, MXLCH behaves as a box model with a fixed height, temperature and moisture content and no entrainment. The different experiments are summarized in Table 3. The initial mixed-layer and free tropospheric mixing ratios and surface forcings (emission/deposition) of chemical species are shown in Table 4. The initial mixing ratios are based on the DOMINO measurements. All other species (except for molecular oxygen and nitrogen) are initialized at zero.

Table 2: Initial and boundary conditions used in MXLCH. MXLCH is initiated at 07:00 UTC, t is the elapsed time since the start of the simulation and t_d is the time in seconds between 07:00–17:00 UTC.

Property	Value
Initial mixed-layer height h [m]	500
Horizontal velocity divergence $\nabla \times \mathbf{V}_h$ [s^{-1}]	5×10^{-6}
Geostrophic wind U_g, V_g [$m\,s^{-1}$]	(0,0)
Surface sensible heat flux $\overline{w'\theta'}_s$ [$K\,m\,s^{-1}$]	$0.22 \sin(\pi t/t_d)$
Entrainment/surface heat-flux ratio $\beta = -\overline{w'\theta'}_h/\overline{w'\theta'}_s$ [–]	0.2
Initial mixed-layer potential temperature $\langle\theta\rangle$ [K]	287
Initial free-troposphere potential temperature θ_{FT} [K]	288.5
Potential temperature lapse rate free troposphere γ_θ [$K\,m^{-1}$]	0.006
Surface latent heat flux $\overline{w'q'}_s$ [$kg\,kg^{-1}\,m\,s^{-1}$]	$0.03 \sin(\pi t/t_d)$
Initial mixed-layer specific humidity $\langle q\rangle$ [$g\,kg^{-1}$]	5.3
Initial free-troposphere specific humidity q_{FT} [$g\,kg^{-1}$]	4.5
Specific humidity lapse rate free troposphere γ_θ [$g\,kg^{-1}\,m^{-1}$]	−0.0012

Table 3: Overview experiments

Name	Dynamics	Chemistry
BOX750	NONE	Reduced
MOZART	MXLCH	MOZART
REDUCED	MXLCH	Reduced

4 Results

4.1 Temporal evolution dynamics and chemistry

The temporal evolution of the mixed-layer height (h) and slab averaged potential temperature (θ) and specific humidity (q) is shown in Fig. 3a–c. When around 09:00 UTC the surface sensible heat flux has broken the ground inversion by heating the ABL, the mixed-layer encounters a rapid growth of approximately 200 m h^{-1} between 09:00 UTC and 12:00 UTC. As the mixed-layer grows, air with properties of the free troposphere is entrained into the mixed-layer, causing an increase in potential temperature (entrainment of relative warm air) and decrease in specific humidity (entrainment of dry air). Comparison with the measurements show that the mixed-layer model correctly represents the dynamical evolution of the ABL. Subsidence (Eq. 4, Table 2) plays a relatively small role and decreases the mixed-layer growth with 200 m throughout the day. Especially the accurate representation of the mixed-layer height is crucial for the budgets of chemical species, not only because of its influence on entrainment, but also as h is the mixing-depth of any input or loss at the surface or mixed-layer top (Eq. 2). This encourages frequent probing of the atmosphere (like e.g. during DOMINO with balloon soundings at a 1 h interval) as the mixed-layer height is calculated as the maximum temperature gradient of the upper air soundings, and frequent measurements are needed to capture the rapid development in the early morning. In addition to the thermodynamic variables, we show in Fig. 3d the photolysis rate of NO_2, a quantity driven by ultraviolet radiation. To calculate the photolysis rate of NO_2, we use the empirical expression of Wiegand and Bofinger (2000). Both MOZART and the reduced scheme correctly reproduce the measured photolysis rate of NO_2 and in addition (not shown), produce similar results as the TUV model (Madronich et al., 2011) for the photolysis rates of O_3 and CH_2O.

Figure 4 shows the diurnal variation of O_3, NO, NO_2 and HNO_3. Although the ten dencies are similar, the results obtained with experiment BOX750 tend to overestimate the mixing ratio evolution. This is the combined effect of not taking mixed-layer growth and entrainment, the exchange between the ABL and free troposphere, into account. MXLCH with both MOZART and the reduced scheme is capable of reproducing the measured mixing ratios. The mixing ratio of O_3 is slightly underestimated with MOZART and NO_2 slightly overestimated using the reduced chemistry scheme. In spite of being a reduced scheme, the scheme presented in Table 1 is able to reproduce the observational trend of O_3, NO and NO_2 and same characteristic ratios like $NO_2/NO \approx 2–3$. This indicates that in regimes where ozone increases smoothly, the scheme performs satisfactorily. Also, given the differences between the observations, the box model and MXLCH with both reaction schemes, it needs to be stressed that ABL dynamics plays a key role in reproducing and understanding the measured mixing ratios.

The satisfactory results of the reduced scheme are further corroborated by the intercomparison of isoprene, OH, HO_2 and H_2O_2 in Fig. 5. For isoprene, MOZART and the reduced scheme both have different tendencies compared with the few observations, but the mixing ratios are of a similar order. For OH, HO_2 and H_2O_2, both MOZART and the reduced scheme are close to the measured data where, on average, MOZART underestimates the mixing ratios due to the introduction of additional reactions that destroy OH. However, the measured OH mixing-ratios are upper-limit values, possibly overestimating the mixing ratio by up to a factor two (Sörgel et al., 2011). It should also be mentioned that although we are not accounting for key chemical pathways like the formation of OH from HONO (Sörgel et al., 2011), our findings provide a comprehensible evolution of reactants in the ABL. In this respect, although we are missing details near the surface

(an example is given in Fig. 3 of Vilà-Guerau de Arellano et al. (2011)), we take advantage of the rapid mixing efficiency of the ABL, driven by convective turbulence.

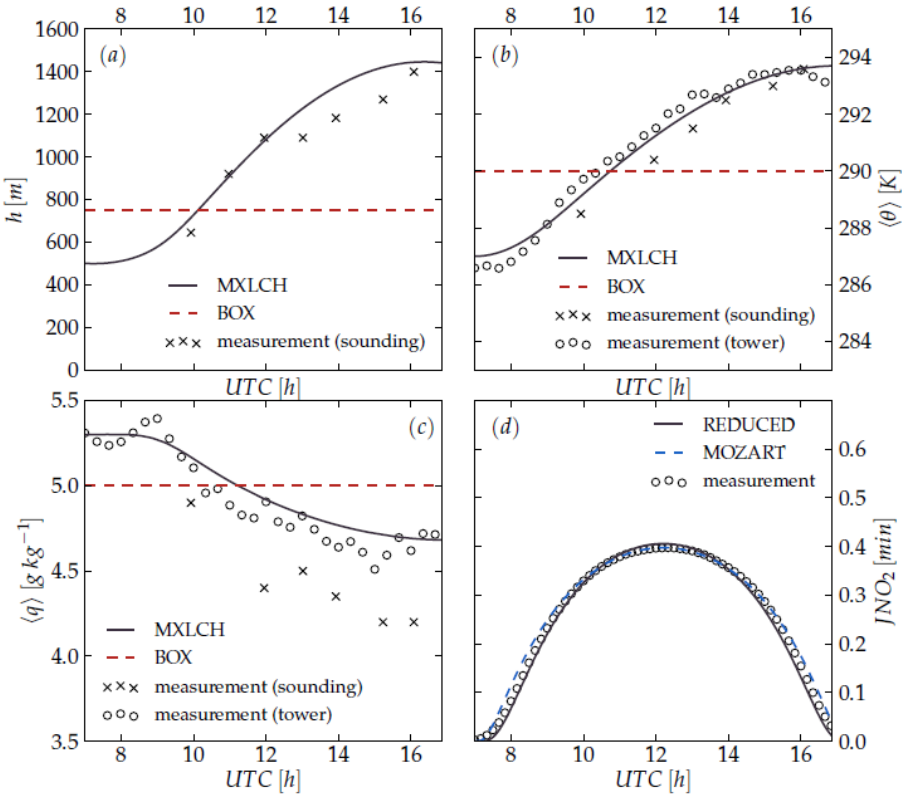

Figure 3: Time evolution of the **(a)** mixed-layer height, **(b)** slab averaged potential temperature, **(c)** slab averaged specific humidity and **(d)** photolysis rate of NO_2, compared to the measurements. In addition to the results of MXLCH, the fixed conditions of the box model are indicated.

4.2 Budgeting of chemical reactants

MXLCH enables us to further determine the individual contributions of emission/deposition, chemical transformation and entrainment to the evolution of the (reactive) species, i.e. the different terms of Eq. (2). We selected four species to examine the variation in time of the contribution of both dynamics and chemistry. The dynamic part is here defined as the mixing of both surface emissions/deposition and the entrained air over the mixed-layer depth h whereas the chemical contribution is the net production or loss rate from the equations in Table 1:

$$\frac{\partial \langle S \rangle}{\partial t} = \underbrace{\overbrace{\frac{\overline{w'S'_s}}{h}}^{Ds} - \overbrace{\frac{\overline{w'S'_h}}{h}}^{De}}_{\text{dynamics}} + \underbrace{\overbrace{S_{prod}}^{Cp} - \overbrace{S_{loss}}^{Cl}}_{\text{chemistry}}. \tag{8}$$

Figure 6 shows the budgets of O_3, NO, NO_2 and OH. As Fig. 6a shows, the net O_3 tendency is positive throughout almost the entire day (see Fig. 4a) with a maximum increase in O_3 around 09:30 UTC. The peak is closely related to the maximum in entrainment (De) of ozone originating in the free troposphere, at this time caused by (1) the rapid growing mixed-layer (Fig. 3) and (2) the relative large difference in mixing ratio between the mixed-layer and free troposphere ($\Delta O_3 \approx 7$ ppb). When during the day the O_3 mixing ratio increases (decreasing ΔO_3 towards zero) and the

mixedlayer growth decreases, the contribution of entrainment relative to the chemical term decreases to zero around 14:00 UTC. From 08:00 UTC onwards the net chemical tendency is positive and equals the contribution by entrainment around 11:00 UTC. After ~13:00 UTC the total ozone tendency is mainly driven by chemical reactions. This makes that the total O_3 tendency is mainly controlled by dynamics during the morning growth of the ABL and by chemistry in the afternoon.

The tendency of NO, shown in Fig. 6b, is positive up to 09:30 UTC and negative afterwards, in agreement with the peak observed in Fig. 4b. Since the initial mixing ratios and thus initial ΔNO is zero, the relative contribution of entrainment to the total tendency is small. Only when the mixed-layer mixing ratio has increased towards its maximum around 10:00 UTC, growth of the mixed-layer causes entrainment of air with a relative low mixing ratio ($\Delta NO \approx -0.14$ ppb), resulting in a small (negative) contribution to the total tendency. The total tendency is therefore the result of a balance between the surface emission and the net chemical loss. Despite being forced with a fixed surface emission (Table 4), Ds decreases throughout the day as the mixed-layer grows, because this term is inversely proportional to h (see Eq. 8). This demonstrates that, without having a strong influence of entrainment, ABL dynamics still influences the tendencies of chemical species, as shown by the first RHS term of Eq. (8).

Figure 6c shows the budget of NO_2. With a lower mixing ratio in the free troposphere, entrainment results in a decrease of NO_2 which, like for ozone, is the strongest around 09:30 UTC. At the same time, deposition causes an extra loss of NO_2. With the deposition calculated as $-v_C C_{NO_2}$ with v_C constant (Table 4), the contribution of deposition decreases as both the NO_2 mixing ratio decreases and the mixed-layer grows. Combined, the dynamical contribution causes a strong negative tendency during the day. Chemical transformations counter the dynamical contribution. However only during the morning (when the contribution of entrainment is still small) and late afternoon (when the mixed-layer reaches its maximum height) the net chemical production is sufficient to create a net positive tendency of NO_2.

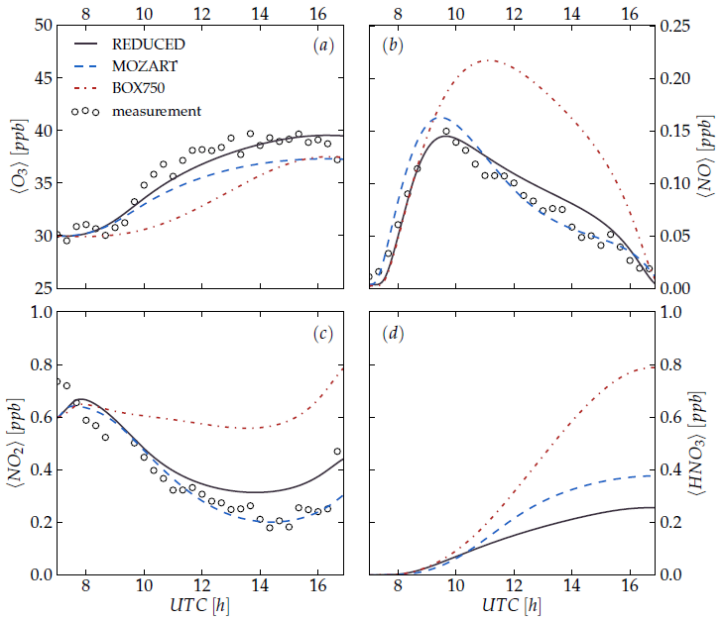

Figure 4: Measured and modelled mixed-layer mixing ratios of O_3, NO, NO_2 and HNO_3 as measured and modelled with MXLCH (using both MOZART and the reduced chemical scheme) and the box model (using the reduced chemistry scheme).

For faster reacting species like OH in Fig. 6d, the tendency is mostly controlled by chemical production and loss. This indicates that, for species with a short lifetime or high reactivity, the chemical part of Eq. (8) dominates and the influence of ABL dynamics decreases. This subject will be studied in more detail in the next section.

Table 4: Initial mixing ratio in both MOZART and the reduced scheme in the mixed-layer ($\langle S \rangle$) and free troposphere (S_{FT}), and surface emission or deposition. All other species except for molecular oxygen and nitrogen are initialized at zero. The chemistry scheme is initialised at 07:00 UTC, t is the elapsed time since the start of the simulation and t_d is the time in seconds between 07:00–17:00 UTC.

	O_3	NO	NO_2	CH_4	ISO	CO	H_2O_2
$\langle S \rangle$ [ppb]	31	0	0.6	1724	0	105	0.1
S_{FT} [ppb]	39	0	0	1724	0	105	0.1
$\overline{w'S'}$ [$\mu g\, m^{-2}\, s^{-1}$]	0	0.04	*	0	**	0	0

* Deposition flux of NO_2 is calculated as $-v_C C_{NO_2}$ with $v_C = 0.015\, m\, s^{-1}$

** $\overline{w'ISO'} = 0.09 \cdot \sin(\pi t / t_d)$

4.3 Time scales of turbulence and chemistry

To further substantiate the relative influence of mixed-layer dynamics compared to chemistry, and to provide a more robust quantification of the relative importance, we examine further the diurnal variability in terms of the characteristic time scales on which the different species and turbulence are acting. The Damköhler number (Damköhler, 1940), for mixing at large scales defined as the ratio of the typical turbulence time scale to the time scale of chemistry (Vilà-Guerau de Arellano, 2003), is the key dimensionless number to distinguish the influence of turbulence from chemistry:

$$Da_S = \frac{\tau_t}{\tau_{c;S}};\ \tau_t = \frac{h}{w_*};\ \tau_{c;S} = \frac{c_S}{C_l}, \tag{9}$$

with τ_t the time scale of turbulence, $\tau_{c;S}$ the time scale of chemical species S, c_S the concentration of species S and C_l the chemical loss rate of species S. w_* is the convective velocity scale, defined as (Stull, 1988):

$$w_* = \sqrt[3]{\frac{g\, h}{\langle \theta_v \rangle} \overline{w'\theta'}_{v;s}}, \tag{10}$$

where g is the gravitational acceleration. The time scale τ_t thus increases as the mixed layer grows, while a stronger virtual heat flux $(\overline{w'\theta'}_{v;s})$ enhances turbulent mixing and therefore decreases the time scale. Based on the Damköhler number we can define the following regimes:

- $Da_S \lesssim 0.1$ – Slow chemistry where the mixing ratio is controlled by emission/deposition and ABL dynamics

- $0.1 \lesssim Da_S \lesssim 10$ – Moderate chemistry where the mixing ratio is governed by ABL dynamics and chemical reactions

- $Da_S \gtrsim 10$ – Fast chemistry where the mixing ratio is determined by chemical reactions.

Under the regime of a Damköhler number $Da_S \gtrsim 10$, the influence of ABL dynamics is negligible for this chemical species and Eq. (8) reduces to only the chemical contributions. In contrast, a small

Damköhler number of $Da_S \lesssim 0.1$ indicates an atmospheric reactive flow where the contribution of chemical reactions is relatively small compared to ABL dynamics or large scale forcings. For ($0.1 \lesssim Da_S \lesssim 10$) chemistry and dynamics interact and both the dynamical and chemical term of Eq. (8) needs to be taken into account. Using MXLCH, we are able to calculate the time scales of turbulence and the individual chemical species and as such provide an indicator for the relative importance of dynamics and chemistry.

Figure 7 shows the time scale τ for both the convective ABL ("turbulence") and a number of fast and slow reaction species. For the analysed day during DOMINO the time scale of the ABL increases from ~400 s at 09:00 UTC to ~1000 s at 16:00 UTC. CO, here the slowest reacting species, acts on a time scale in the order of 10 days, resulting in a $Da_S \ll 0.1$, indicating that CO for example is mainly controlled by atmospheric turbulence and transport. In contrast, OH, acts on a time scale of seconds or less, resulting in $Da_S \gg 10$. This confirms the findings of Fig. 6d, where the OH budget was mainly determined by the chemical transformations. Closely connected with the chemical lifetime of OH is the OH-reactivity; the inverse of the lifetime (e.g. Di Carlo et al., 2004; Lelieveld et al., 2008; Sinha et al., 2008). During DOMINO, the reactivity of OH was directly measured with at 23 November values in the order of 40 s^{-1} (Sinha et al., 2012). With average reactivities of 1.4 s^{-1} (reduced scheme) and 2 s^{-1} (MOZART), MXLCH underestimates the reactivity. As the modelled OH mixing ratio fits well to the measurements (Fig. 5), this indicates that both chemical schemes are missing chemical pathways related to the production and destruction of OH. This is still an open issue, possibly caused by an incomplete initialization of anthropogenic volatile organic compounds (VOC). Intermediate species like O_3, NO and NO_2 act on a time scale of minutes to hours, within ± one order of magnitude of the typical time scale of the ABL, again corroborating the need to take dynamics and chemical transformations simultaneously into account.

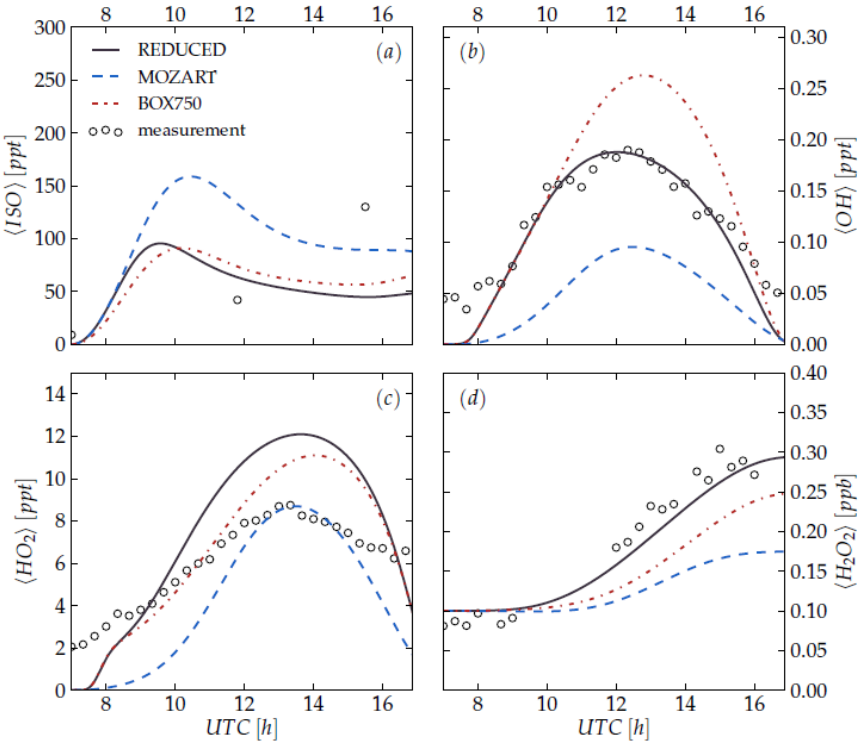

Figure 5: Measured and modelled mixed-layer mixing ratios of Isoprene, OH, HO_2 and H_2O_2 as measured and modelled with MXLCH (using both MOZART and the reduced chemical scheme) and the box model (using the reduced chemistry scheme).

5 Conclusions

In this study we used a mixed-layer model coupled to chemical reaction schemes to systematically study the influence of atmospheric boundary layer (ABL) dynamics on the time evolution of chemistry. We selected one day during the DOMINO measurement campaign and designed numerical experiments to determine the performance of two chemical schemes with different complexity (MOZART-4 and a reduced mechanism of this chemical system) under realistic dynamical conditions. Additional experiments with a box model, which neglects the influence ABL dynamics, display an overestimation in the mixing ratios of chemical species. The mixed-layer model with both MOZART and the reduced reaction scheme performs satisfactory, reproducing the measured mixing ratios of key chemical species like O_3 and NO_X. This indicates that, in conditions characterized by a low NO_X regime and small O_3 tendencies, the reduced scheme is capable of reproducing the O_3-NO_X-VOC-HO_X diurnal cycle. Under these conditions, the reduced scheme is a useful, more comprehensible and computationally less expensive alternative for complex schemes like MOZART, for e.g. use in large-eddy simulation.

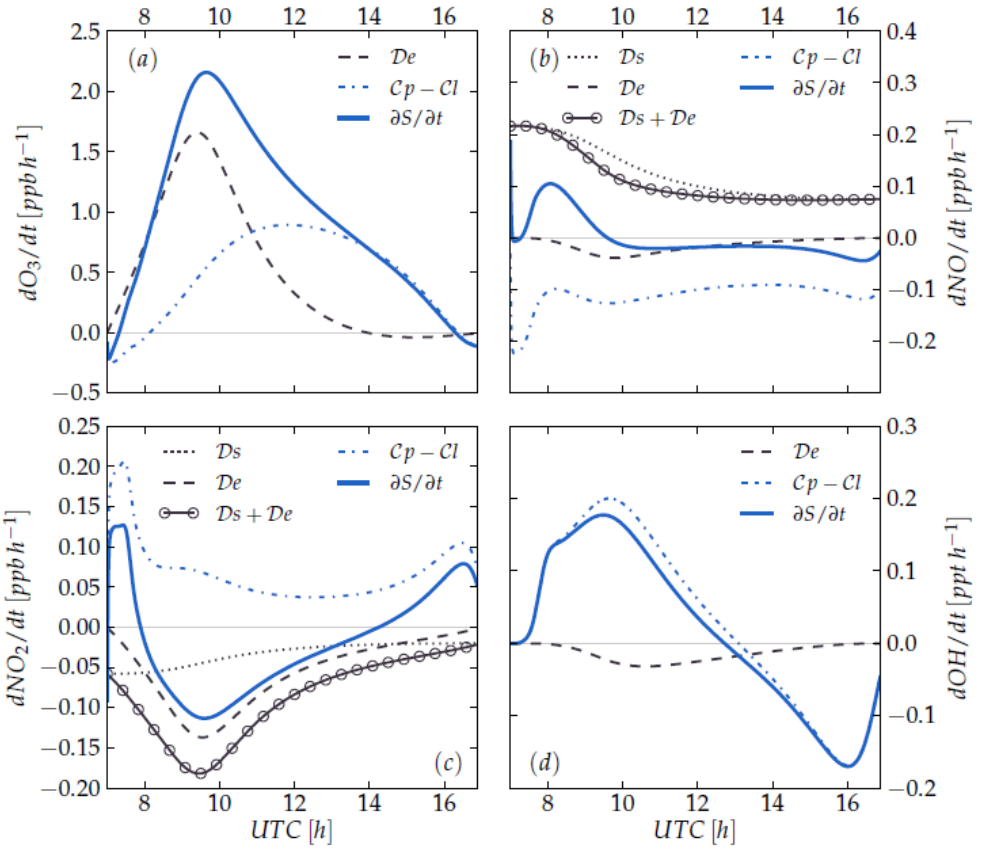

Figure 6: Individual budget terms of Eq. (8) for O_3, NO, NO_2 and OH. The labels of the individual terms refer to the notation defined in Eq. (8).

By studying the individual contribution of emission/deposition, chemical transformation, mixed-layer growth and entrainment to the evolution of the reactive species, it is found that for species like O_3, NO, NO_2, the contribution of boundary layer processes is of the same order as the contribution of chemical transformations. Both O_3 and NO_2 are strongly controlled by entrainment of relatively ozone rich and nitrogen dioxide poor air originated in the free troposphere. The change in mixed-layer height, the depth over which any input or loss at the surface or mixed-layer top is distributed, was shown to be important for the budget of NO.

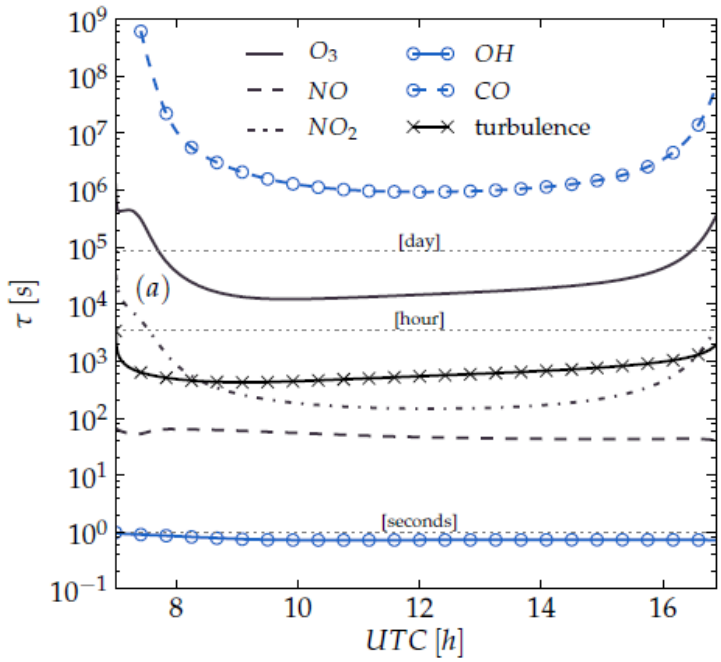

Figure 7. Calculated life times of key chemical species and the ABL (top) and the OH-reactivity (bottom), the inverse of the OH lifetime, as measured and modelled.

By comparing the lifetime of chemical active species with the boundary layer mixing time through the dimensionless Damköhler number, we demonstrated an effective method to obtain a first estimate of the relevance of dynamics and chemistry. When classified into three regimes, the Damköhler number provides a measure of whether chemistry is controlled by chemical transformations or ABL-dynamics. When calculated for a number of fast (OH), intermediate (O_3, NO, NO_2) and slow (CO) reacting species, this method confirmed the impact of ABL-dynamics on the time evolution of chemical active species.

Due to its simplicity and transparency, the mixed-layer model (MXLCH) used in this study can act as a useful tool towards a better understanding of (1) the main chemical pathways and processes that govern the temporal evolution of chemistry and (2) a better understanding of the results obtained during measurement campaigns. Also, gaining a better understanding of the core physical and chemical processes involve might be beneficial for the development of new measurement campaigns or strategies, or to understand new chemical pathways. MXLCH is available from the authors upon request.

References

Betts, A. K.: Non-precipitating convection and its parameterization, Q. J. Roy. Meteorol. Soc., 99, 178–196, 1973.

Crowley, J. N., Thieser, J., Tang, M. J., Schuster, G., Bozem, H., Beygi, Z. H., Fischer, H., Diesch, J.-M., Drewnick, F., Borrmann, S., Song, W., Yassaa, N., Williams, J., Pöhler, D., Platt, U., and Lelieveld, J.: Variable lifetimes and loss mechanisms for NO_3 and N_2O_5 during the DOMINO campaign: contrasts between marine, urban

and continental air, Atmos. Chem. Phys., 11, 10853–10870, doi:10.5194/acp-11-10853-2011, 2011.

Damköhler, G.: Influence of turbulence on the velocity flames in gas mixtures, Z. Elektrochem., 46, 601–626, 1940.

Di Carlo, P., Brune, W. H., Martinez, M., Harder, H., Lesher, R., Ren, X., Thornberry, T., Carroll, M. A., Young, V., Shepson, P. B., Riemer, D., Apel, E., and Campbell, C.: Missing OH Reactivity in a Forest: Evidence for Unknown Reactive Biogenic VOCs, Science, 304, 722–725, 2004.

Diesch, J.-M., Drewnick, F., Zorn, S. R., von der Weiden-Reinmüller, S.-L., Martinez, M., and Borrmann, S.: Variability of aerosol, gaseous pollutants and meteorological characteristics associated with continental, urban and marine air masses at the SW Atlantic coast of Iberia, Atmos. Chem. Phys. Discuss., 11, 31585–31642, doi:10.5194/acpd-11-31585-2011, 2011.

Draxler, R. R. and Rolph, G. D.: HYSPLIT (HYbrid Single-Particle Lagrangian Integrated Trajectory) Model access via NOAA ARL READY Website (http://ready.arl.noaa.gov/HYSPLIT. php), NOAA Air Resources Laboratory, Silver Spring, MD., 2011.

Emmons, L. K., Walters, S., Hess, P. G., Lamarque, J.-F., Pfister, G. G., Fillmore, D., Granier, C., Guenther, A., Kinnison, D., Laepple, T., Orlando, J., Tie, X., Tyndall, G., Wiedinmyer, C., Baughcum, S. L., and Kloster, S.: Description and evaluation of the Model for Ozone and Related chemical Tracers, version 4 (MOZART-4), Geosci. Model Dev., 3, 43–67, doi:10.5194/gmd-3-43-2010, 2010.

Ganzeveld, L., Eerdekens, G., Feig, G., Fischer, H., Harder, H., Königstedt, R., Kubistin, D., Martinez, M., Meixner, F. X., Scheeren, H. A., Sinha, V., Taraborrelli, D., Williams, J., Vilà- Guerau de Arellano, J., and Lelieveld, J.: Surface and boundary layer exchanges of volatile organic compounds, nitrogen oxides and ozone during the GABRIEL campaign, Atmos. Chem. Phys., 8, 6223–6243, doi:10.5194/acp-8-6223-2008, 2008.

Lelieveld, J., Butler, T., Crowley, 5 J., Dillon, T., Fischer, H., Ganzeveld, L., Harder, H., Lawrence, M., Martinez, M., Taraborrelli, D., and Williams, J.: Atmospheric oxidation capacity sustained by a tropical forest, Nature, 452, 737–740, 2008.

Lilly, D. K.: Models of cloud-topped mixed-layer under a strong inversion, Q. J. Roy. Meteorol. Soc., 94, 292–309, 1968.

Madronich, S., Flocke, S., Zeng, J., Petropavlovskikh, I., and Lee-Taylor, J.: Tropospheric Ultraviolet-Visible Model (TUV), http://cprm.acd.ucar.edu/Models/TUV/, 2011.

Ouwersloot, H. G., Vilà-Guerau de Arellano, J., van Heerwaarden, C. C., Ganzeveld, L. N., Krol, M. C., and Lelieveld, J.: On the segregation of chemical species in a clear boundary layer over heterogeneous land surfaces, Atmos. Chem. Phys., 11, 10681–10704, doi:10.5194/acp-11-10681-2011, 2011.

Paulot, F., Crounse, J. D., Kjaergaard, H. G., Kroll, J. H., Seinfeld, J. H., and Wennberg, P. O.: Isoprene photooxidation: new insights into the production of acids and organic nitrates, Atmos. Chem. Phys., 9, 1479–1501, doi:10.5194/acp-9-1479-2009, 2009.

Peeters, J., Nguyen, T. L., and Vereecken, L.: HO_X radical regeneration in the oxidation of isoprene, Phys. Chem. Chem. Phys., 11, 5935–5939, 2009.

Sander, R., Baumgaertner, A., Gromov, S., Harder, H., Jöckel, P., Kerkweg, A., Kubistin, D., Regelin, E., Riede, H., Sandu, A., Taraborrelli, D., Tost, H., and Xie, Z.-Q.: The atmospheric chemistry box model CAABA/MECCA-3.0, Geosci. Model Dev., 4, 373–380, doi:10.5194/gmd-4-373-2011, 2011.

Sinha, V., Williams, J., Crowley, J. N., and Lelieveld, J.: The Comparative Reactivity Method – a new tool to measure total OH Reactivity in ambient air, Atmos. Chem. Phys., 8, 2213–2227, doi:10.5194/acp-8-2213-2008, 2008.

Sinha, V., Williams, J., Diesch, J. M., Drewnick, F., Martinez, M., Harder, H., Regelin, E., Kubistin, D., Bozem, H., Hosaynali-Beygi, Z., Fischer, H., Andrés-Hernández, M. D., Kartal, D., Adame, J. A., and Lelieveld, J.: OH reactivity measurements in a coastal location in Southwestern Spain during DOMINO, Atmos. Chem. Phys. Discuss., 12, 4979–5014, doi:10.5194/acpd-12-4979-2012, 2012.

Sörgel, M., Regelin, E., Bozem, H., Diesch, J.-M., Drewnick, F., Fischer, H., Harder, H., Held, A., Hosaynali-Beygi, Z., Martinez, M., and Zetzsch, C.: Quantification of the unknown HONO daytime source and its relation to NO_2, Atmos. Chem. Phys., 11, 10433–10447, doi:10.5194/acp-11-10433-2011, 2011.

Stavrakou, T., Peeters, J., and Müller, J.-F.: Improved global modelling of HOx recycling in isoprene oxidation: evaluation against the GABRIEL and INTEX-A aircraft campaign measurements, Atmos. Chem. Phys., 10, 9863–9878, doi:10.5194/acp-10-9863-2010, 2010.

Stull, R. B.: An introduction to boundary layer meteorology, Kluwer Academic Publishers, 1988.

Tennekes, H. and Driedonks, A. G. M.: Basic entrainment equations for the atmospheric boundary layer, Bound-Lay. Meteorol., 20, 515–531, 1981.

Vilà-Guerau de Arellano, J.: Bridging the gap between atmospheric physics and chemistry in studies of small-scale turbulence, B. Am. Meteorol. Soc., 84, 51–56, 2003.

Vilà-Guerau de Arellano, J., van den Dries, K., and Pino, D.: On inferring isoprene emission surface flux from atmospheric boundary layer concentration measurements, Atmos. Chem. Phys., 9, 3629–3640, doi:10.5194/acp-9-3629-2009, 2009.

Vilà-Guerau de Arellano, J., Patton, E. G., Karl, T., van den Dries, K., Barth, M. C., and Orlando, J. J.: The role of boundary layer dynamics on the diurnal evolution of isoprene and the hydroxyl radical over tropical forests, J. Geophys. Res.-Atmos., 116, D07304, doi:10.1029/2010JD014857 2011.

Wiegand, A. N. and Bofinger, N. D.: Review of empirical methods for the calculation of the diurnal NO_2 photolysis rate coefficient, Atmos. Environ., 34, 99–108, 2000. 6529

Williams, J., Crowley, J., Fischer, H., Harder, H., Martinez, M., Petäjä, T., Rinne, J., Bäck, J., Boy, M., Dal Maso, M., Hakala, J., Kajos, M., Keronen, P., Rantala, P., Aalto, J., Aaltonen, H., Paatero, J., Vesala, T., Hakola, H., Levula, J., Pohja, T., Herrmann, F., Auld, J., Mesarchaki, E., Song, W., Yassaa, N., Nölscher, A., Johnson, A. M., Custer, T., Sinha, V., Thieser, J., Pouvesle, N., Taraborrelli, D., Tang, M. J., Bozem, H., Hosaynali-Beygi, Z., Axinte, R., Oswald, R., Novelli, A., Kubistin, D., Hens, K., Javed, U., Trawny, K., Breitenberger, C., Hidalgo, P. J., Ebben, C. J., Geiger, F. M., Corrigan, A. L., Russell, L. M., Ouwersloot, H. G., Vilà-Guerau de Arellano, J., Ganzeveld, L., Vogel, A., Beck, M., Bayerle, A., Kampf, C. J., Bertelmann, M., Köllner, F., Hoffmann, T., Valverde, J., González, D., Riekkola, M.-L., Kulmala, M., and Lelieveld, J.: The summertime Boreal forest field measurement intensive

(HUMPPA-COPEC-2010): an overview of meteorological and chemical influences, Atmos. Chem. Phys., 11, 10599–10618, doi:10.5194/acp-11-10599-2011, 2011.

Yokelson, R. J., Karl, T., Artaxo, P., Blake, D. R., Christian, T. J., Griffith, D. W. T., Guenther, A., and Hao, W. M.: The Tropical Forest and Fire Emissions Experiment: overview and airborne fire emission factor measurements, Atmos. Chem. Phys., 7, 5175–5196, doi:10.5194/acp-7-5175-2007, 2007.

B OH reactivity measurements in a coastal location in Southwestern Spain during DOMINO

V. Sinha[1,2], J. Williams[1], J.M. Diesch[3], F. Drewnick[3], M. Martinez[1], H. Harder[1], E. Regelin[1], D. Kubistin[1], H. Bozem[1,6], Z. Hosaynali-Beygi[1], H. Fisher[1], , M.D. Andrés-Hernández[4], D. Kartal[4], J. A. Adame[5], J. Lelieveld[1]

[1]Air Chemistry Division, Max-Planck-Institute for Chemistry, Mainz, Germany

[2]Indian Institute of Science Education and Research Mohali, Sector 81, S. A. S. Nagar, Manauli PO, Punjab, India 140306

[3]Particle Chemistry Department, Max-Planck-Institute for Chemistry, Mainz, Germany

[4]Institute of Environmental Physics, University of Bremen, Germany

[5]Atmospheric Research and Instrumentation Branch, National Institute for Aerospace Technology (INTA), Mazagón-Huelva, Spain

[6]Institute for Atmospheric Physics, University of Mainz, Germany

Published in Atmos. Chem. Phys. Discuss., Volume 12, 4979-5014, 2012

Abstract

In this study air masses are characterized in terms of their total OH reactivity which is a robust measure of the "reactive air pollutant loading". The measurements were performed during the DOMINO campaign (Diel Oxidant Mechanisms In relation to Nitrogen Oxides) held from 21.11.2008 to 08.12.2008 at the Atmospheric Sounding Station - El Arenosillo (37.1 N – 6.7 W, 40 m asl). The site was frequently impacted by marine air masses (arriving at the site from the southerly sector) and air masses from the cities of Huelva (located N.W of the site), Seville and Madrid (located N.N.E. of the site). OH reactivity values showed strong wind sector dependence. North eastern "continental" air masses were characterized by the highest OH reactivities (average: 31.4 ± 4.5 s^{-1}; range of average diel values: 21.3 - 40.5 s^{-1}), followed by north western "industrial" air masses (average: 13.8 ± 4.4 s^{-1}; range of average diel values: 7 – 23.4 s^{-1}) and marine air masses (average: 6.3 ± 6.6 s^{-1}; range of average diel values: below detection limit –21.7 s^{-1}), respectively. The average OH reactivity for the entire campaign period was ~18 s^{-1} and no pronounced variation was discernible in the diel profiles with the exception of relatively high values from 09:00 to 11:00 U.T.C. on occasions when air masses arrived from the north western and southern wind sectors. The measured OH reactivity was used to constrain both diel instantaneous ozone production potential rates and regimes. Gross ozone production rates at the site were generally limited by the availability of NO_x with peak values of around 20 ppbV O_3 /hr. Using the OH reactivity based approach, derived ozone production rates indicate that if NO_x would no longer be the limiting factor in air masses arriving from the continental north eastern sector, peak ozone production rates could double. We suggest that the new combined approach of in-situ fast measurements of OH reactivity, nitrogen oxides and peroxy radicals for constraining instantaneous ozone production rates, could significantly improve analyses of upwind point sources and their impact on regional ozone levels.

1 Introduction

The hydroxyl radical (OH·) plays a central role in the chemistry of the troposphere by controlling primary oxidation processes of volatile organic compounds (VOCs), daytime photochemical ozone production and formation of secondary organic aerosol. The hydroxyl radical reactivity (also termed

total OH reactivity) of an air mass is defined in terms of the total loss rate of OH radicals due to the presence of OH reactants in the air mass and is expressed as:

$$\text{Total OH reactivity } (s^{-1}) = \sum k_{(Xi + OH)} [X_i] \quad (1)$$

where $k_{(Xi + OH)}$ is the pseudo first order rate coefficient for the reaction of species X_i with OH, and X_i stands for individual OH reactants present in an air mass such as carbon monoxide (CO), sulphur dioxide(SO_2), nitrogen oxides (NO, NO_2), and VOCs. Direct OH reactivity measurements are an invaluable tool as they provide a robust measure of the reactive pollutant "loading" of an air mass, considering that most air pollutants react primarily with the OH radical (Lelieveld et al., 2004). In addition, by combining direct OH reactivity measurements with simultaneous measurements of known OH sinks (e.g. CO, NO_x and VOCs), it is possible to assess uncertainties in emissions and modeling of VOC budgets (e.g. Di Carlo et al., 2004). Despite such obvious importance, only few studies have reported direct OH reactivity measurements till date (e.g. Di Carlo et al., 2004; Hofzumahaus et al., 2010; Ingham, 2009; Kovacs et al., 2003; Ren et al., 2003; Sadanaga et al., 2004a; Sinha et al., 2010; Yoshino et al., 2006). One reason for this is that there are no commercial OH reactivity measurement instruments, and research instruments that are capable of making such measurements are based on sophisticated and expensive detectors such as laser induced fluorescence and proton transfer reaction mass spectrometers (Kovacs and Brune, 2001;Sadanaga et al., 2004b;Sinha et al., 2008). Amongst the available direct OH reactivity measurement dataset in literature, the sites that have been studied encompass urban, suburban and forested sites in the United States (e.g. Di Carlo et al., 2004; Martinez et al., 2003; Ren et al., 2006), Japan (e.g. Sadanaga et al., 2004a; Yoshino et al., 2006), China (e.g. Hofzumahaus et al., 2010), United Kingdom (e.g. Ingham, 2009), Germany, Suriname and Finland (e.g. Sinha et al., 2008; Sinha et al., 2010) and Malaysia (Ingham, 2009). Only one study has reported direct OH reactivity measurements from a coastal site, at the Weybourne Atmospheric Observatory on the North Norfolk coast, in the UK (Lee et al., 2009). Coastal sites provide the unique opportunity to contrast the chemistry of very different air masses such as marine influenced conditions, continental air or even urban and industrial air masses at a single location depending on the surrounding sources and the prevalent meteorology.

During the DOMINO campaign (Diel Oxidant Mechanisms In relation to Nitrogen Oxides) held from 21.11.2008 to 08.12.2008 at the Atmospheric Sounding Station -El Arenosillo, located on the Atlantic coast of southern Spain, direct OH reactivity measurements were made using the comparative reactivity method described by Sinha et al. (2008). These are the first OH reactivity measurements reported from Spain and enhance the direct OH reactivity measurement datasets in literature to include south western Europe.

While several previous field studies (Di Carlo et al., 2004; Hofzumahaus et al., 2010; Ingham, 2009; Kovacs et al., 2003; Ren et al., 2003; Sadanaga et al., 2004a; Sinha et al., 2010; Yoshino et al., 2006) have focussed on testing the completeness of the suite of measured OH reactants by comparing the directly measured OH reactivity with the summed up calculated OH reactivity due the measured reactants by applying Equation 1, in this study, we did not undertake this since the suite of VOCs measured during the campaign was not comprehensive enough to justify such an exercise.
Here, we focus on how the influence of air mass origin and history impacts the OH reactivity and ozone photochemistry at the coastal site El Arenosillo, which is downwind of several large cities in Spain such as Huelva, Seville and Madrid for substantial periods in the year. Employing in-situ measurements of OH Reactivity, organic peroxy radicals (RO_2^*), hydroxy and hydroperoxy radicals (OH, HO_2) and NO_x (NO, NO_2) we examine the diurnal instantaneous ozone formation regimes

and rates of production potential in different air masses arriving at the site by a variety of approaches with implications for the future air quality of the region.

2 Experimental

2.1 Site description and wind sector classification

Figure 1a shows the location of El Arenosillo, (37.1 N – 6.7 W, 40 m asl) in southwestern Spain. Stone pine trees (*Pinus pinea* ~ 5-10 m in height) were present in the immediate vicinity while the Atlantic Ocean was only 300 m south of the measurement site. The urban and industrial areas of Huelva city and the harbour (also shown in Figure 1a) were located about 35 km north west of the measurement site. Huelva houses one of Europe's larger oil refineries and air masses from this sector contain emissions from related industrial / shipping activity. Madrid (also shown in Figure 1a) was located about 600 km north-north east (~30 degrees) of the measurement site while the city of Seville was closer and only about 70 km east-north east of the measurement site (~60 degrees). The wind rose of the measured OH reactivity is shown in Figure 1 b (right panel). Note that the OH reactivity was highly dependent on the wind sector from which air masses arrived at the site. The highest OH reactivity was observed in air masses arriving from the north eastern sector, followed by the north western sector and the southern sector. In order to examine the impact of these "chemically" different air masses in a meaningful way, measurements of OH reactivity, nitrogen dioxide, nitric oxide, sulphur dioxide, ozone, formaldehyde, hydroxyl radical, hydroperoxy radical and the sum of all peroxy radicals (RO_2^*) were binned using three prevalent wind sectors and the rationale for the wind sector classification is presented shortly. It is worth noting that while short lived species such as OH radicals are not transported far from their point of production, their in-situ formation and destruction rates in an air mass does depend on the chemical composition and hence "history" of the air masses.

Based on dominant types of emission influencing the air masses, three different prevalent wind sectors were identified for this purpose, namely 1) the continental sector which was influenced mainly by aged air masses of continental origin (local wind direction: 0-60 degrees 2) the Huelva sector (local wind direction: 270-340 degrees) which was heavily influenced by industrial and shipping emissions 3) the ocean sector (local wind direction: 150-270 degrees) which was characterized by relatively clean marine air except for occasional ship traffic. During the campaign period, the site received air masses from each of these different source sectors at least 25 % of the time. Thus, the comparison of the measurements in air masses from these different wind sectors is statistically reasonable.

The classification of air masses in terms of local wind direction was also checked for consistency with back trajectories by combining information about the air mass back trajectories calculated using the NOAA HYSPLIT model with GDAS meteorology (Draxler and Rolph, 2011). For the Huelva sector and ocean sector the local wind direction was consistent with the calculated air mass back trajectories, for the continental sector, this was not always the case, the wind direction sometimes deviating by some 20 degrees from the direction of the corresponding 24-hour back trajectory. This fact was taken into consideration while choosing the 0-60 degree sector wind direction for the continental air mass influence, which could otherwise have been a narrower sector if only wind direction or only back trajectories had been used.

This is illustrated further in Figure 1a which shows selected back trajectories for each sector. Black and its lighter shades are for the continental sector, red and its lighter shades are for the Huelva

sector; dark blue and its lighter shades are for the ocean sector, and the different shades merely indicate trajectories calculated at multiple heights (20 m, 100m and 500m above ground level; darker the shade, higher the altitude). It should be noted from Figure 1a that the back trajectories show similar characteristics for air masses arriving at different heights at the site which indicates the homogeneity of the first few hundred meters. The back trajectories also showed that the air masses arriving at the site stayed within the convective boundary layer during transport.

The trajectory shown for the continental sector in Fig 1a (black) corresponds to the highest measured OH reactivity values for the entire campaign period of 63-83 s^{-1}(see Fig 1 b), observed between 12:00 U.T.C and 14:00 U.T.C on 22.11.2008. Interestingly this was also associated with the highest wind speeds of the campaign (> 5m/s), which would have favoured long distance transport. As indicated by the trajectory which arrived at the measurement site at 12:00 U.T.C. on 22.11.2008, the air masses had passed over Madrid less than 13 hours previously. There is a mountain range about 1 km high just south of Madrid. Thus, instead of direct advection to El Arenosillo, emissions from Madrid and surrounding areas may undergo upward and horizontal transport accompanied by photochemical processing during the daytime boundary layer growth, and mix in with emissions from Seville and other upwind areas before arriving at El Arenosillo. The red coloured trajectories (Fig 1 a) depict the air masses that arrived from the Huelva sector at 21:00 U.T.C on 30.11.2008 and was associated with the highest OH reactivity values measured in air masses from this sector of ~25-33 s^{-1}, from 21:00 – 23:00 U.T.C. on 30.11.2008, again at high wind speeds (> 4m/s). Finally the blue coloured trajectories show the air masses that arrived at the site at 02:00 U.T.C. on 07.12.2008. Air masses from this sector generally brought very clean air and were characterized by low OH reactivity except for the odd NO_x and SO_2 peak. Consequently in air sampled from this sector, OH reactivity values were often below the instrumental detection limit of 3.5 s^{-1}. For the blue trajectory shown in Fig 1a , measured OH reactivity values were always less than the detection limit.

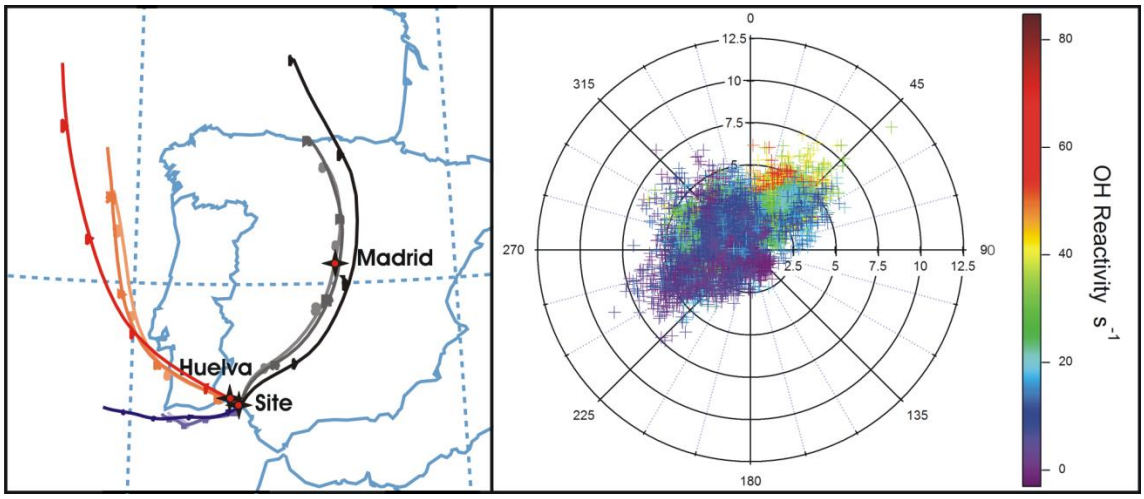

Figures 1 (a) and 1 (b): Location of the measurement site Base de Arenosillo, 37° 05' 58" N, 6° 44' 17" W) as well as Madrid and Huelva (shown with starts) in Spain with select back trajectories at multiple heights from each wind sector (left panel) and wind rose plot showing OH Reactivity measurements (coloured markers and scale), wind speed (radii) and wind direction (angle) for the measurements made during the campaign (right panel).

2.2 OH reactivity measurements

OH reactivity was measured using the comparative reactivity method. The method has been described in detail in previous publications (Sinha et al., 2008; Sinha et al., 2010) hence only a brief description and details pertinent to the operational parameters during the DOMINO campaign are described here.

The comparative reactivity method for OH reactivity measurement employs an in situ competitive kinetics experiment in which a proton transfer reaction mass spectrometer (PTR-MS) is coupled to a turbulent flow glass reactor. Pyrrole (C_4H_5N) is introduced into the reactor and its concentration C1 is monitored with a PTR-MS, in the air exiting the reactor. Then, synthetically generated OH radicals ([OH] < [Pyrrole]) are introduced into the reactor at a constant rate to react with pyrrole. This causes C1 to decrease to concentration C2. When ambient air is introduced into the reactor, the various species present in it compete with pyrrole for the available OH, so that the concentration of pyrrole increases to C3. Comparing the amount of pyrrole exiting the reactor in the zero air (C2) and ambient air (C3), allows the introduced air sample's OH reactivity to be determined, provided the system is suitably calibrated for pyrrole (Sinha et al., 2009). The following equation, a derivation of which is available elsewhere (Sinha et al., 2008), yields the measured OH reactivity signal in terms of C1, C2, C3 and the rate coefficient of pyrrole with the hydroxyl radical (k_p = 1.2 x 10^{-10} molecules cm^{-3} s^{-1}(Atkinson et al., 1984):

$$R_{air} = \frac{(C3 - C2)}{(C1 - C3)} \cdot k_p C1 \qquad (2)$$

The values obtained using Equation 2 are corrected for deviations from pseudo first order conditions using the pyrrole to OH ratio (i.e. C1/(C1-C2)), and for the dilution of ambient air within the reactor. For the DOMINO campaign the pyrrole /OH ratio was ~ 1.7 leading to a correction factor that lowers the values obtained from Equation 2 by ~ 30 %. Frequent tests (at least every other day) with air samples of known OH reactivity (a propane gas standard), were performed and excellent accountability for OH reactivity of the test samples was obtained. These measurement settings are similar to that employed previously for measurements within a boreal forest in Finland (Sinha et al., 2010). Only three differences are worth mentioning. The inlet residence time during the DOMINO campaign was < 4 s, compared to the inlet residence time of < 8 s during the previous study in Finland. The reactor residence time was ~ 20 s, resulting in a total sampling time of 24 s. The second difference was that the main sampling inlets were heated to a temperature of 40 degree Celsius for the entire campaign period during DOMINO. Thirdly, fast measurements of OH reactivity were performed by switching rapidly between baseline (corresponding to C2 of measured pyrrole signal) and the ambient air (corresponding to C3 of measured pyrrole signal) every 4 minutes.

Ambient air was sampled into the glass reactor at 180 ml min^{-1} in a total flow of 300 ml min^{-1} leading to a dilution factor of 1.7. A Teflon VOC pump was used to draw a fraction of the fast flow from the ~15 m long main inlet Teflon tubing (12.7 mm outer diameter) which was at a height of 12 m above ground, and fitted with a Teflon filter to prevent particles form clogging the lines.

The detection limit for the OH reactivity measurements during this study was 3.5 s^{-1}. The overall uncertainty of the measured OH reactivity was ~20 %, obtained by applying the root square propagation of uncertainties due to 1) rate coefficient of pyrrole + OH (14%), 2) overall flow fluctuation (10%), 3) uncertainty in value of the pyrrole standard (5%), 4) precision error of PTR-MS (4%), and 5) error in matching the humidity of the ambient air exactly (5%). NO mixing ratios

exceeding 10 ppbV in ambient air are known to cause underestimation of the measured OH reactivity in the comparative reactivity method (Sinha et al., 2008). However, the NO levels in the ambient air during DOMINO were too low to cause any interference. Values of NO during the campaign ranged from below 0.01 ppbV to a maximum of 8.2 ppbV in a single event on 05.12.2008 at 12:15 U.T.C. The average value of NO in ambient air for the entire campaign was only 0.21 ± 0.6 ppbV, hence no corrections were required for the OH reactivity data on account of the NO interference during DOMINO.

2.3 Simultaneous ancillary measurements

All other measurements used in this study were collocated and performed from the same mast with less than 1 m separating the inlets of individual instruments. The only exception were ozone and sulphur dioxide which were measured from a neighboring inlet (< 3 m away) installed on the mast of a mobile van at a height of 10 m above ground (Diesch et al., 2012). As details regarding the measurements of nitrogen oxides, formaldehyde, hydroxyl and hydroperoxy radicals during the DOMINO campaign have already been described elsewhere (Crowley et al., 2011; Sörgel et al., 2011) only a short description is given below..

2.3.1 NO_x (NO, NO_2) Measurements

NO and NO_2 measurements were made using a high resolution and high sensitivity chemiluminescence detector (ECO-Physics CLD 790 SR, originally manufactured by ECO-Physics, Durnten, Switzerland). NO is measured directly, however, NO_2 is measured indirectly after conversion to NO using a blue light converter which is a solid state photolytic converter (Droplet Measurement Technologies, Boulder, CO, USA). The total uncertainty including the precision and accuracy error was 6.04 ppt + 5% of the measured value for NO and 8.29 ppt + 8% of the measured value for NO2 for an integration period of 1s. A detailed description of the instrument and calibration techniques can be found Hosaynali Beygi et al. (2011).

2.3.2 OH and HO_2 measurements

OH and HO_2 measurements were made using laser induced fluorescence spectroscopy. Details of the instrument are available elsewhere (Martinez et al., 2010). The accuracy of the OH and HO_2 measurement was ± 18 % and the precision for OH was 0.034 pptv and 0.23 for HO_2, respectively.

After the DOMINO campaign, laboratory tests established an interference for the OH measurement. To estimate the magnitude of the interference follow up measurements were performed in the same season in 2009. They indicate an OH interference of about 60 % between 10 am and 3 pm (UTC) (E. Regelin, personal communication). In a recent paper by Fuchs et al. (2011), an HO_2 interference is discussed due to presence of RO_2-radicals, in particular if the RO_2 is originating from OH addition to alkenes or aromatics. The author reports for their instrument an interference of up to 95 % depending on the type of RO_2. In this study we cannot exclude this possible interference for the HO_2 measurement presented.

Hence for the purpose of this study, the presented OH and HO_2 measurements are considered as upper limits.

2.3.3 Formaldehyde (HCHO) measurements

A commercially available instrument (AERO Laser model AL 4021, Germany) was used for in-situ HCHO measurements. This instrument is based on the Hantzsch reagent method. The time resolution is 160 sec. Detection limit and precision were estimated from the 1σ -reproducibility of in-situ zero and calibration gas measurements as 22 pptv and ± 15 %, respectively. The total uncertainty is estimated to be 29 %.

2.3.4 Sum of peroxy radicals, $RO_2^* = HO_2 + \Sigma RO_2$ (R stands for organic chain)

RO_2^* were measured using a DUALER (**DUA**l channe**L** peroxy radical chemical amplifi**ER**) adapted for ground based measurements. The instrument uses the well known PeRCA (**Pe**roxy **R**adical **C**hemical **A**mplification) technique (Hastie et al., 1991; Cantrell et al., 1993). The technique converts ambient peroxy radicals into NO_2, which is detected by measuring the chemiluminiscence of its reaction with luminol. There are two identical lines working in alternate modes, i.e., an amplification mode resulting from the chemical conversion of RO_2^* into NO_2 in a chain reaction above the NO_2 background levels, and a background mode comprising NO_2 and all NO_2 sources other than radicals in the air sampled and up to the detector such as reaction of NO with O_3, the decomposition of PAN, etc. (Kartal et al., 2010). For the set up deployed within DOMINO the total uncertainty of 1 minute averages was 30% for RH at 60% (detection limit 1-3 pptv) and 60% for RH between 70- 90% ,(5-10 pptv detection limit).

2.3.5 Ozone (O_3), sulphur dioxide (SO_2) and meteorological measurements

O_3 and SO_2 were measured using commercial instruments (Airpointer, Recordum GmbH, Austria). Meteorological parameters like temperature, relative humidity (RH), atmospheric pressure, wind speed and wind direction were measured with a Vaisala WXT510 15125 (Vaisala, Helsinki, Finland) meteorological station equipped at 10 m above ground level on the mobile laboratory (MoLa) (Diesch et al., 2012). Limits of detection and precision were 1 ppb for both SO_2 and O_3.

3 Results and discussion

3.1 General trends in OH reactivity and dependency on air masses

Figure 2 (top panel) shows the time series of the 1 minute (gray dots; n = 11584 measurements) and 30 minute averages (black circles) of the OH reactivity data during the DOMINO campaign. The OH reactivity ranged from below detection limit (~3.5 s^{-1}) to 84 s^{-1}, the latter being observed between 12:00 U.T.C and 14:00 U.T.C on 22.11.2008 when air mass that had passed over Madrid and Seville region less than 13 hours earlier arrived at the site from the Continental sector (local wind direction: 0-60 Degrees; see also Fig 1 a and Section 2.1). Also shown in the top panel of Figure 2 are the 30 min averages of the formaldehyde (HCHO) mixing ratios (green circles) and in the bottom panel, a time series of the ambient temperature (solid black line) and nitrogen dioxide (NO_2) mixing ratios (red circles). Overall, there was considerable variability in the OH reactivity with an average of 18 ± 15 s^{-1} for the entire campaign. The ambient temperature ranged from 2 – 23°C with the first four days from 21.11.2008 - 24.11.2008 generally warmer than the other periods of the campaign. As shown in Figure 2, formaldehyde (HCHO) an oxidation product formed during the hydroxyl radical initiated oxidation of many VOCs (Atkinson, 2003), appeared to correlate with the profile of the measured OH reactivity for extended periods on certain days of the

campaign such as: 21.11.2008 - 23.11.2008; 30.11.2008 - 01.12.2008; 04.12.2008-06.12.2008 and 07.12.2008-08.12.2008. However, the correlation coefficient between the 30 minute OH reactivity and formaldehyde data for the entire campaign is only r = 0.5. High NO_2 values acted as a marker for pollution plumes arriving at the site. This happened quite frequently as can be seen in Figure 2, and although the average value for NO_2 was low (1.9 ± 1.9 ppbV for the entire campaign), occasionally peak values of ~ 13 ppbV were also observed during the campaign (see Fig 2). As mentioned in Section 2.1, the measurement site was surrounded by a forest of Stone pine trees. However, Song et al. (2012) who measured biogenic VOCs such as monoterpenes and isoprene during DOMINO, found their levels to be low (average value of terpenes for the entire campaign period: 10 pptV) with the highest value 140 pptV of isoprene. This is consistent with previous seasonal studies of this vegetation (Keenan et al. 2009: Staudt et al. 2000). Aromatic VOCs such as benzene, toluene and xylene, which were also measured by Song et al. (2011) were marginally higher with mean values in the range of 10-156 pptV for the entire campaign. Thus the contribution of the measured biogenic VOCs and the aromatic VOCs to the OH reactivity was negligible. Unfortunately, other anthropogenic VOCs such as the C2- C8 alkanes and alkenes which are known to be present in continental, urban and industrial emissions (e.g. Monks et al., 2009) were not measured during DOMINO so information about their levels is unavailable.

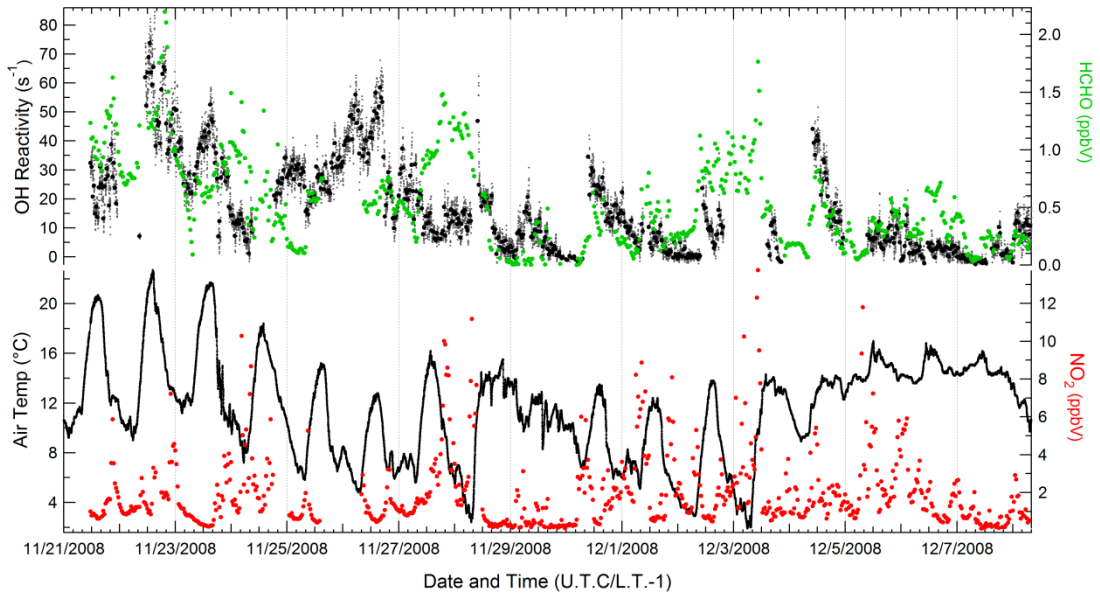

Figure 2: Time series of the 1 minute (gray dots; n = 11584 measurements) and 30 minute averages (black circles) of the OH reactivity data during the DOMINO campaign (top panel) and the 30 minute averages of the formaldehyde (HCHO) mixing ratios (green circles), the ambient temperature (solid black line) and nitrogen dioxide (NO_2) mixing ratios (red circles) (bottom panel).

Figure 3(a) shows a diel box and whisker plot of the measured total OH reactivity at El Arenosillo, derived from all measurements (n > 11500). The range of OH reactivity even for the same hour of the day shows considerable day to day variability (Below Detection .Limit. to 48 s^{-1}). We note that except at 10:00 and 11:00 U.T.C, every other time of the day has some values close to the detection limit of 3.5 s^{-1} in the 10^{th} percentile (lower whisker). These values correspond to periods when clean air masses from the ocean sector were sampled at the site (see also Fig 1 b). The average and median span a range of 9 - 25 s^{-1}, with the average always greater than or equal to the median, consistent with frequent pollution plumes being sampled at the site as indicated by the NO_2 time series shown in Figure 2. Both median and average OH Reactivity values are generally higher between 9:00 – 15:00 U.T.C but there does not seem to be a pronounced diel cycle. The strong

peak between 9:00 – 11:00 U.T.C was probably due to both ship emissions from the ocean (150-270 degrees) and traffic emissions from the Huelva wind sectors (270-340 degrees). The average diel profile for each wind sector, which is discussed next, and the high average NO_x and SO_2 values between 9:00-11:00 U.T.C in air masses from these sectors which are shown in Figure 4 and Figure 5 appears to support this hypothesis. Figure 3 (b) shows the average diel profile of OH reactivity for air masses from each wind sector, namely the continental (black markers), Huelva (red markers) and ocean (blue markers) sectors. Clearly, the highest average OH reactivity was always in air masses that arrived from the continental sector carrying aged and processed emissions followed by the Huelva sector and the ocean sector. The average and diel range of the OH reactivities for each of the sectors were: continental sector (average: 31.4 ± 4.5 s^{-1}; range: 21.3 - 40.5 s^{-1}), Huelva sector (average: 13.8 ± 4.4 s^{-1}; range: 7 – 23.4 s^{-1}), ocean sector (average: 6.3 ± 6.6 s^{-1}; range: below detection limit –21.7 s^{-1}). The highest average OH reactivity of 20 s^{-1} at 10:00 U.T.C. in the ocean sector air masses as discussed earlier is likely due to ship traffic and mixed in industrial emissions from the Huelva harbour area.

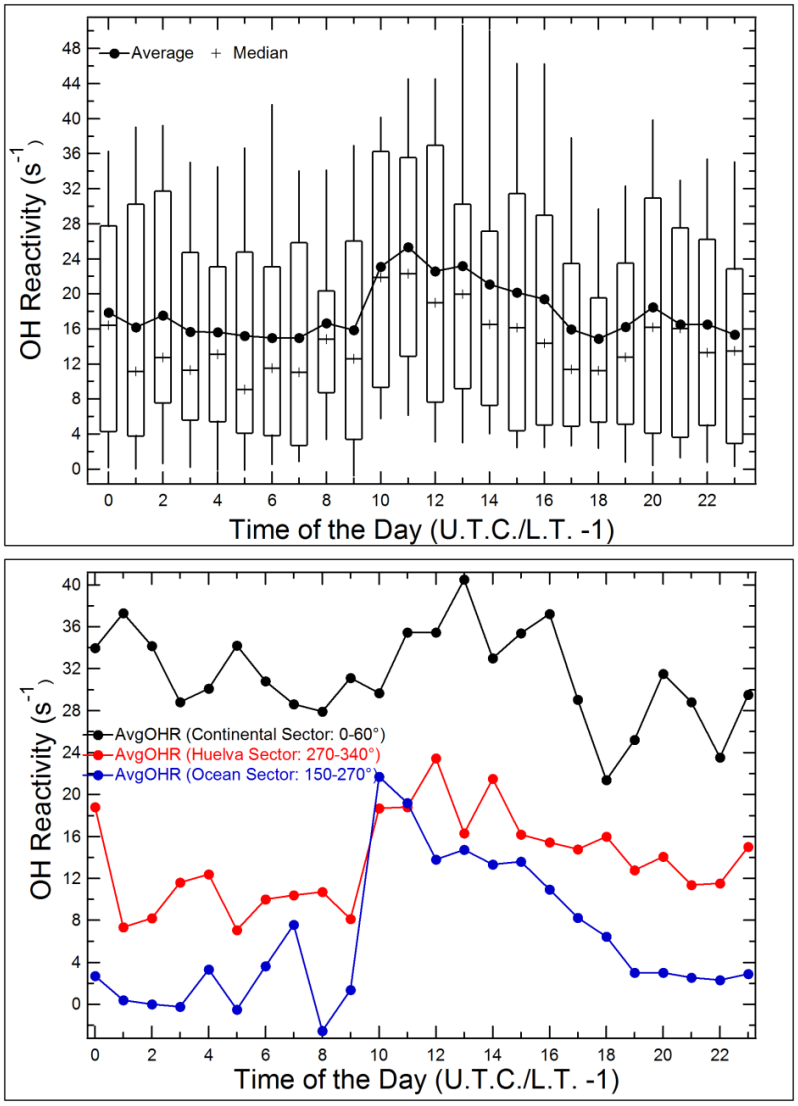

Figure 3 (a) and 3 (b): Diel box and whisker plot of the total OH reactivity at Base de Arenosillo, 37° 05' 58" N, 6° 44' 17" W) derived from all measurements (n > 11500) during the DOMINO campaign (top) and average diel profile of OH reactivity for air masses from the continental (black), huelva (red) and ocean (blue) wind sectors.

The average value of 6 s^{-1} for the ocean sector is comparable to the average value of 5 s^{-1} reported by Ingham et al. (2009) and Lee et al. (2009) from the Weybourne Atmospheric Observatory in UK, which is on the North Sea coast. They are also quite close to the average value of 4 s^{-1} reported by Mao et al. (2009) over the Pacific Ocean during the INTEX-B campaign between 0-2 km above sea level. Remarkably, the average value of 13.8 s^{-1} for the Huelva sector is quite similar to the median value of 11.3 s^{-1} reported by Kovacs et al. (2003) from a site 8 km downwind of Nashville TN in the United States. Both Huelva city and Nashville TN have large petrochemical industries. In addition, Huelva also houses Spain's largest pulp/paper mill. As the distance of these sources was less than 35 km from the measurement site during DOMINO, emissions from such anthropogenic sources are expected to have contributed significantly to the OH reactivity in air masses arriving from the Huelva sector.

The average OH reactivity of ~ 31 s^{-1} measured in continental sector air masses is remarkably high for the fact that there were no obvious nearby strong point emission sources in this sector. The fact that highest values were observed at the highest wind speeds (see Fig 1 b) and sustained levels of high average OH reactivity > 20 s^{-1} by day and night were observed whenever the air came from the continental sector, also indicates that the species responsible for the high OH reactivity did not have local sources. Aged air masses can contain significant amounts of reactive oxidation products formed due to photochemical processing of the primary anthropogenic emissions such as alkanes and alkenes (Butler et al., 2011). As shown in Figure 1a, the transport time of less than 13 hours for air masses that had passed over Madrid , implies that a significant fraction of the emissions from Madrid, and indeed more reactive secondary oxidation products from precursors such as alkanes and aromatic VOCs (Lee et al., 2009) would still be present in these air masses. Most of the NO_x would however have reacted away, and as shown later in Figure 5, this was indeed the case. Such high levels of OH reactivity have previously only been observed downwind of or within urban sites such as the Mexico Metropolitan Area (median: 33 s^{-1}; (Shirley et al., 2006), New York City (average: 19 s^{-1} (Ren et al., 2003) and Tokyo city (Average 30 s^{-1}; (Sadanaga et al., 2005). In Section 3.2, we examine the strong wind sector dependence in the diurnal profile of some of the other measured chemical species as well before discussing the implications of this on zone chemistry in Section 3.3.

3.2 Diurnal profile of radical species, formaldehyde and sulphur dioxide

Figure 4 shows the measured average diurnal profiles of the hydroxyl radical (OH), hydroperoxy radical (HO_2), sum of peroxy radicals (RO_2^*), formaldehyde (HCHO) and sulphur dioxide (SO_2) for all the three wind sectors. It can be seen that for all the species shown in Figure 4 with the exception of sulphur dioxide, the trend of measured values follows the same as that observed for the measured OH reactivity, namely, continental sector values > Huelva sector values > ocean sector values. In particular, note that HO_2, RO_2^* and HCHO are typically twice as high in air masses with strong continental influence compared to air masses from the Huelva and ocean sector, for most hours of the day. The RO_2^* data at 10:00 U.T.C is not shown due to insufficient number of RO_2^*measurements at this hour from this sector (n = 17) only due to calibration checks of this particular instrument, whereas all other RO_2^* data have n > 40. None of these species would contribute significantly in terms of absolute magnitude to the measured OH reactivity and most are not even transported due to their short lifetimes but rather produced in-situ. Yet they do suggest strongly and independantly from the OH reactivity measurements, that the continental air masses were very different from the other air masses in terms of chemical composition. Also in Figure 4, it should be noted that SO_2 is present at several ppb in air masses from the Huelva and ocean sector, but is almost zero in continental sector air masses. Crowley et al. (2011) have discussed the

influence of Spain's largest paper mill which is located in Huelva in terms of malodorous sulphur emissions at ppbV level. The SO_2 profile shown in Figure 4 suggests that the Huelva and ocean sector air masses are characterized by higher sulphur dioxide due to strong sources of sulphur (refineries, ship traffic, paper mill). The proximity of those strong sources to the measurement site, would favour more efficient transport of the primary emissions and lower photochemical processing in contrast to the continental sector air masses.

Such different "chemical" loadings and reactivity from different wind sectors at El Arenosillo, has important implications for the ozone chemistry at the site, and in the next few sections we examine the impact of the different air masses on the instantaneous diurnal ozone production regime and rates using different methods that have been proposed in previous works.

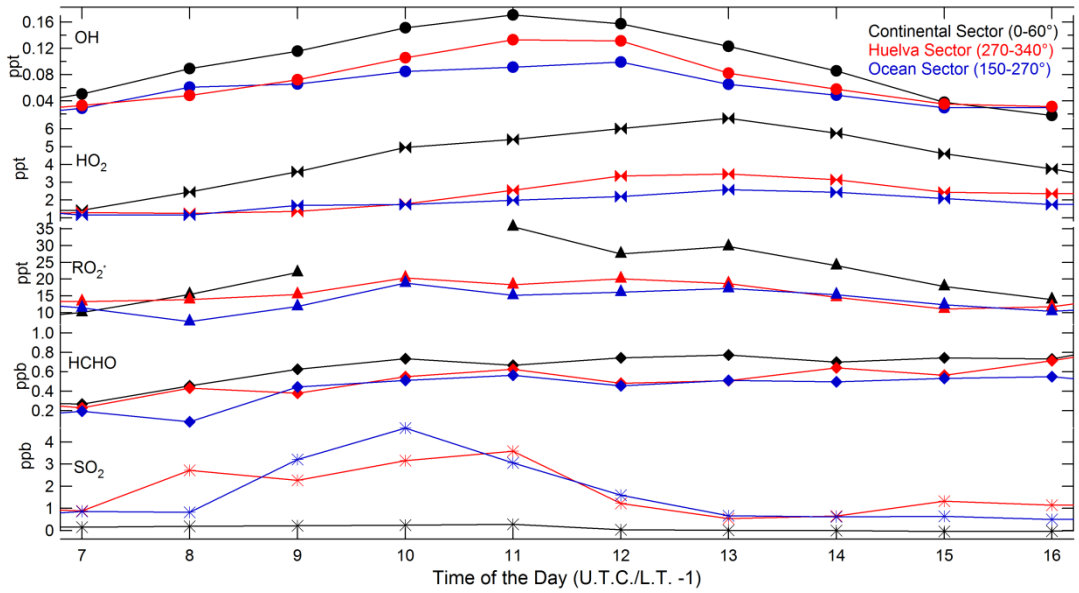

Figure 4: Average diurnal profiles of the hydroxyl radical (OH), hydroperoxy radical (HO_2), sum of peroxy radicals (RO_2*), formaldehyde (HCHO) and sulphur dioxide (SO_2) in air masses from the continental, huelva and ocean wind sectors.

3.3 Derivation of instantaneous ozone production regimes in air masses

In order to assess whether the ozone production regime was limited by NO_x or VOCs or both, two similar but differently formulated diagnostic methods were applied. The first method is based on the approach of Kirchner et al. (2001) while the second is a modified version of the traditional VOC/NO_x ratio method as given in Seinfeld and Pandis (2006). Both methods rely on accurate determination of the ratio of OH reactivity due to VOCs to OH reactivity due to NO_x and are elucidated in detail below.

Conventionally, OH reactivity due to VOCs would require measurements of all individual VOCs followed by summation of their individual OH reactivities, which is the product of the VOC concentration and its reaction rate coefficient with the OH radical. The tremendous advantage of the directly measured total OH reactivity of air masses is that the OH reactivity due to VOCs is easily obtained by subtracting the OH reactivity of NO_x from the directly measured total OH reactivity.

The NO_x OH reactivity for the air masses analyzed during DOMINO was calculated using NO and NO_2 concentrations (obtained by using respective temperatures and pressures for the measured mixing ratios) and their pseudo first order reaction rate constants with the OH radical (Atkinson et al., 2004) as given by Equation 1. Thus,

$$NO_x \text{ OH Reactivity} = k_{OH+NO2}[NO_2] + k_{OH+NO}[NO] \quad (3)$$

and

$$\text{VOC OH reactivity} = \text{Total OH Reactivity} - NO_x \text{ OH Reactivity} \quad (4)$$

The above approach assumes that OH reactants other than VOCs and NO_x, do not contribute significantly to the directly measured OH reactivity, which is a reasonable assumption since most other abundant inorganic species (e.g.O_3, H_2O_2) react only slowly with OH and SO_2 contribution to OH reactivity during DOMINO is negligible.

Method 1: This method is based on the approach of Kirchner et al. (2001) and is quite useful when both direct OH reactivity and NO_x measurements are available as was the case during DOMINO. Details about the extensive validation of this approach are available in the original work by Kirchner et al (2001). Briefly, this method makes use of an indicator ratio namely $\Theta = {}^{VOC}\Gamma_{OH} / {}^{NOx}\Gamma_{OH}$ which describes the ratio of the lifetime of the OH radical against the losses by reacting with VOCs and NO_x respectively. Since the reactivity is the inverse of the respective lifetime for the extremely short lived OH radical, Θ = NO_x OH Reactivity/ VOC OH Reactivity. Kirchner et al. (2001) tested the validity of this indicator extensively against other indicators such as the O_3/NO_z ratio and H_2O_2 / HNO_3 ratio and found it to be robust. In contrast to the other indicators, Θ is not based on long lived species and therefore permits finding the instantaneous ozone production regime of an air parcel. As per this indicator method, for $\Theta > 0.2$ ($\pm$ 0.1), the ozone production regime is VOC limited, whereas for indicator values below 0.01 the ozone production regime would be primarily NO_x limited. The intermediate range of $0.01 < \Theta < 0.2$, indicates that the ozone production depends strongly on both NO_x and VOC levels.

Method 2: This method employs the ratios of VOC to NO_x present in an air mass (Seinfeld and Pandis (2006) and is based on observed characteristics of the average VOC-OH reaction rate constant in a typical urban atmosphere. Accordingly, a VOC-to NO_x ratio > 5.5 is indicative of a NO_x limited ozone production regime, whereas a VOC-to NO_x ratio < 5.5 indicates a VOC limited ozone production regime. For the ratio to be valid, the VOC concentration must be expressed on a per carbon atom basis. Note that the term VOC as defined in both Method 1 and Method 2 does not exclude carbon monoxide and methane. As mentioned earlier, both carbon monoxide and methane and indeed most of the important C2-C8 VOCs were not measured during DOMINO. However, the ratio of VOC- OH reactivity to NO_x -OH reactivity should represent the rates of VOC and NO_x reactions better since reaction rate constants are also taken into account. So in our modified approach we replaced the ratio of VOC to NO_x mixing ratios by the VOC OH Reactivity to NO_x OH Reactivity. This enables us to examine how the modified approach compares with results obtained using Method 1 while retaining the threshold ratio of 5.5.

Figure 5 shows a summary of the results. The top two panels of Figure 5 show the instantaneous diurnal ozone production regime for each of the three air mass sectors, namely, continental (black markers), Huelva (red markers), and ocean (blue markers) using Method 1 and Method 2. The two

bottom panels show the measured NO_x (NO, NO_2) mixing ratios. Both Method 1 and Method 2 show good agreement within the uncertainty of the individual indicator ratio. This is also not surprising as the thresholds are not too different at least for the VOC limited ozone production regime (5 in Method 1 and 5.5 in Method 2). A noteworthy feature is that they seem to be consistent within the levels of NO_x present in the different air masses. For example the ozone production regime in the continental sector air masses is always a NO_x limited regime, and the NO_x mixing ratios measured in these air masses were also the lowest. A characteristic of NO_x limited regimes is that before the end of the day most of it reacts away and this also reflected in the diurnal trends of NO_x measured in air masses from the continental sector. From the data shown in Figure 5, it appears that there are occasions when ozone production in the Huelva and ocean sector air masses falls under a VOC limited regime. Looking at the high ppbV level NO_x during these hours for the Huelva and ocean sectors, this might not seem surprising. However it should also be noted that on several such occasions (e.g. from 10-14), the values of the indicator ratios in both methods for Huelva and ocean sector air masses are at the border of the NO_x and VOC limited regimes, making the case for a clear delineation of regimes weak for such cases. Towards the end of the day, as NO_x levels decrease and photooxidation products are formed, the ozone production regime tends to become NO_x limited.

In Section 3.3 we calculate rates of the instantaneous ozone production potential in air masses from the three sectors using two different methods that have been used in the literature.

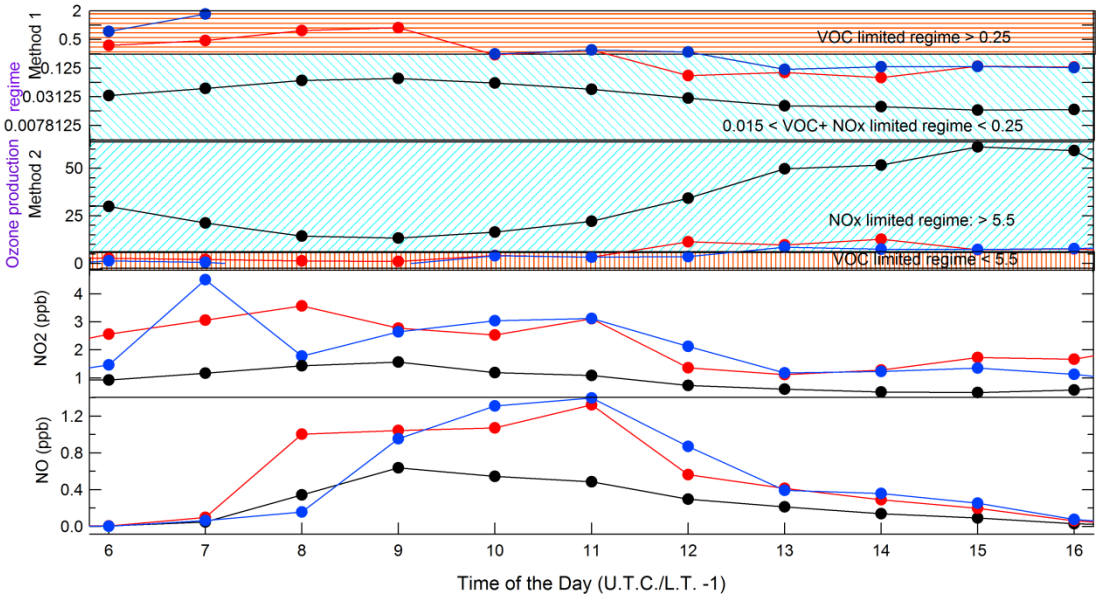

Figures 5: Instantaneous diurnal ozone production regime for each of the three air mass sectors, namely, continental (black markers), huelva (red markers), and ocean (blue markers) using Method 1 and Method 2 (top two panels) and average diurnal NOx (NO, NO_2) mixing ratios (bottom panels).

3.4 Derivation of rates of instantaneous ozone production potential

Before presenting the expressions used for calculating the rates of the instantaneous ozone production potential, it is helpful to recall the main steps in ozone production from hydrocarbons.

A generic hydrocarbon RH reacts with the OH radical in the presence of oxygen to form an alkyl peroxy radical (RO_2).

$RH + OH + O_2 \rightarrow RO_2 + H_2O$ (R1)

Next, the alkyl peroxy radical reacts with NO when present,

$RO_2 + NO \rightarrow RO + NO_2$ (R2)

to produce an alkoxy radical that reacts with O_2,

$RO + O_2 \rightarrow$ Carbonyl compound + HO_2 (R3)

The hydroperoxy radical formed can also react with NO as in Reaction (R2)

$HO_2 + NO \rightarrow OH + NO_2$ (R4)

The NO_2 molecules photodissociate to form oxygen atoms (O) that combine with molecular oxygen (O_2) and form ozone (O_3):

$2\ NO_2 + h\vartheta \rightarrow 2\ NO + 2\ O$ (R5)

$2O + 2\ O_2 \rightarrow 2\ O_3$ (R6)

Reactions (R1) to (R6) can be summarized as:

$RH + 4O_2 + h\vartheta \rightarrow H_2O + 2\ O_3 +$ Carbonyl compound (R7)

Based on typical reaction rate constants, generally Reactions (R2) to (R6), as shown above are faster than Reaction (R1), and thus the latter reaction of the hydrocarbon with the OH radical is the rate determining step in production of ozone, which actually occurs in two steps (shown below as R1 a and R1 b) of which the first Reaction (R1 a) is the slower and hence rate limiting:

$RH + OH \rightarrow R + H_2O$ (R1 a)

$R + O_2 \rightarrow RO_2$ (R1 b)

The number of O_3 molecules formed during the oxidation of a given hydrocarbon depends on the number of NO to NO_2 conversions that occur during its oxidation and assuming that all peroxy radicals react only with NO (a reasonable assumption under sufficient NO_x levels) and not amongst themselves, as a first approximation the ozone production potential due to a generic hydrocarbon can be expressed as:

O_3 production potential = k_{RH+OH} [RH] [OH] x n (5)

where n is the number of NO to NO_2 conversions that occur during the oxidation of RH.

As shown in the above example where two NO to NO_2 conversions took place, n=2 is a reasonable value and is frequently used in Eq. (5) for assessing the O_3 production potential of a given hydrocarbon (Hewitt, 1999) and policy for control of VOCs that act as ozone precursors.

Note that using n = 2, from Eq. (5) the total ozone production potential for an air mass can then be expressed as:

O_3 production potential = (VOC OH reactivity of air mass) x [OH] x 2 (6)

where the VOC OH reactivity of air mass = $\sum k_{RH+OH}$ [RH].

For DOMINO, the VOC OH Reactivity can be obtained from the directly measured OH reactivity as explained in Sect. 3.2. OH mixing ratios were also measured using laser induced fluorescence (Martinez et al., 2010).

The second method of estimating the O_3 production potential in an air mass is based on the approach used previously by Sommariva et al. (2011) that uses measured mixing ratios of RO_2, HO_2 and NO and is given by:

$$O_3 \text{ production potential} = k_{HO2+NO}\,[HO_2]\,[NO] + \sum k_{RO2i+NO}\,[RO_{2i}]\,[NO] \quad (7)$$

In order to apply Eq. (7) for analysis of the DOMINO data, $\sum RO_{2i}$ was obtained by subtracting the measured HO_2 from the measured total sum of peroxy radicals (RO_2^*) and the reaction rate constants were taken from Atkinson et al. (2004). The value used for k_{RO2+NO} was 1×10^{-11} cm^3 $molec^{-1}$ s^{-1}.

Note that both methods of estimating the total ozone production potential of air masses give complementary information. The VOC OH reactivity based ozone production approach gives an estimate of the total ozone production potential of a given air mass and not necessarily the in-situ gross local ozone production, unless the entire VOC oxidation process takes place at the same site (which is seldom the case). Also the expression is valid only for air masses where NO_x is not the limiting reactant. Nonetheless it is a very useful expression for a priori O_3 production control and VOC emission control and hence used widely in urban atmospheres where NO_x levels are usually high. The second approach which is based on in-situ measurements of RO_2, HO_2 and NO yields the gross local in-situ O_3 production but again as an upper limit since it also assumes that all the peroxy radicals react only with NO to form NO_2 and all the NO_2 formed thereby, photodissociates and forms O_3 with O_2. In reality NO_2 can also react with OH forming HNO_3, which reduces the O_3 formation rate in high NO_x environments by removing radicals from the system. As mentioned earlier, for the current analysis where the focus is on relative differences of the air masses sampled at the site and their impact on rates of the ozone formation potential, important inferences can be drawn by applying both methods to the measured data.

Figure 6 shows the diurnal profile of O_3 and the instantaneous rates of O_3 production potential (black: continental sector; red: Huelva sector; blue: ocean sector) derived from the in-situ measurements at El Arenosillo). The average O_3 mixing ratios between 07:00 and 16:00 U.T.C for each of the sectors differs by less than 2 ppb, with the peak values of ~ 40 ppbV occurring at 15:00 U.T.C in air masses from the continental sector. A linear fit (green dotted line in top panel of Fig 6) to the measured O_3 mixing ratios in air masses from the continental sector yields the slope for a net ozone production of 1.9 ppb/hr.

In stark contrast to similar values for the mixing ratios of ozone in air masses from the different sectors, the O_3 production potential derived using the measured VOC- OH reactivity and OH values (middle panel of Fig 6) shows the highest rates of O_3 production potential for the continental sector air masses with peak values of about 40 ppb/hr at 11:00 U.T.C., which are incredibly high considering the actual measured levels of O_3 at the site. The peak values in the Huelva and ocean sector air masses are less than 20 ppb/hr using the same method. Rates of ozone production potential for the different air masses derived using in-situ measurements of NO, HO_2 and RO_2 are shown in the bottom panel of Figure 6. These show a completely different trend with

higher rates of ozone production potential for the Huelva and ocean sectors compared to the continental sector which is the lowest. Remarkably, values of the ozone production potential using both methods are quite comparable for the Huelva and ocean sector air masses (0-20 ppb/hr). Note also that from 13:00 U.T.C onwards both methods shows a steady decrease in the instantaneous O_3 production rates in all air masses and converge to almost zero rates of O_3 production at 16:00 U.T.C. It is worth mentioning that the values for instantaneous rates of O_3 production observed are much lower than the 0- 160 ppb/hr range reported by Sommariva et al. (2011) during the TexAQS 2006 study. The main reason for this is that NO_x levels, in particular for NO were significantly lower during DOMINO (average range: ~0.1- 5 ppbV) compared to the TexAQS study (average range: ~0.7 – 15 ppbV).

The apparently irreconcilable trends in the rates of ozone production potential for different air masses using the two methods can be understood by noting from Section 3.2, that the ozone production regime at the site was mostly NO_x limited, with air masses from the continental sector always falling in the NO_x limited regime (Figure 5). As mentioned earlier during the description of the methods, the estimation method based on VOC-OH reactivity, would be expected to perform accurately (though still an upper limit) only when NO_x is not the limiting factor for O_3 production. In contrast the method based on measured HO_2, RO_2 and NO performs better in explaining the observed ozone production at the site because it represents the local in-situ O_3 production and includes the measured NO values in its formulation.

The combination of both methods however gives both the local and likely regional picture, for example in response to future NO_x increases. The high rates of O_3 production potential estimated by the VOC-OH reactivity based method, show that if strong sources of NO_x come up in the future in the continental wind sector close to the site, O_3 production rates at the site could increase by a factor of 2.

This also implies that places located in the continental wind sector that are currently upwind of El Arenosillo could potentially be subject to similar impacts in terms of high rates of O_3 production due to the addition of strong NO_x sources.

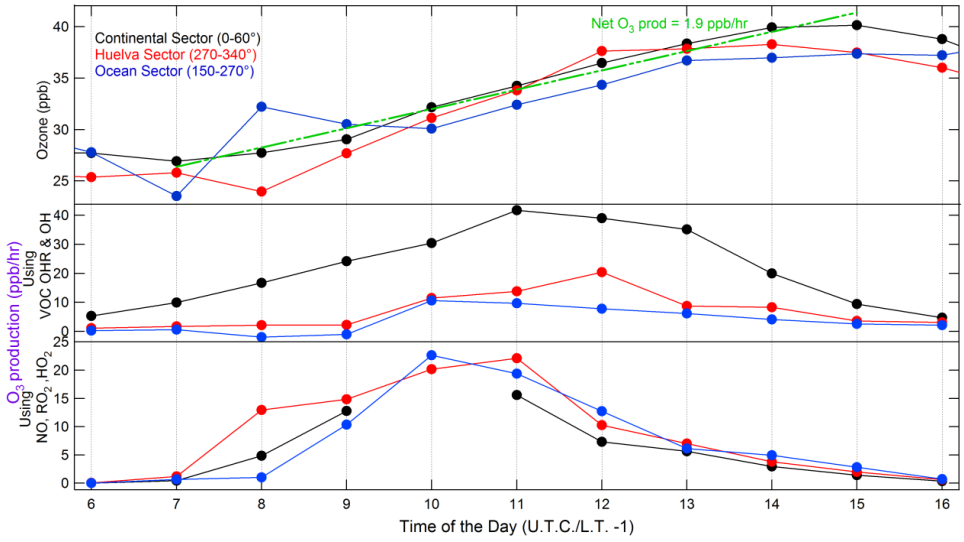

Figure 6: Diurnal profile of O_3 and the instantaneous rates of O_3 production potential (black: continental sector; red: huelva sector; blue: ocean sector) derived from the in-situ measurements made at Base de Arenosillo, 37° 05' 58" N, 6° 44' 17" W.

4 Conclusions

The first dataset of direct OH reactivity measurements in ambient air from Spain at the coastal site El Arenosillo highlights the importance of direct OH reactivity measurements for classifying air masses based on their pollutant loading and constraining the in-situ instantaneous ozone production regimes and rates in combination with measurements of five parameters namely nitrogen oxides (NO, NO_2), hydroxyl radical (OH) and the peroxy radicals (HO_2 and RO_2).

Although measurements of several important classes of VOCs (e.g. anthropogenic alkenes) were unavailable during DOMINO, direct OH reactivity measurements enabled classification of different air masses based on their reactive pollutant loading. Surprisingly, continental air masses from the north easterly direction with photochemically processed emissions from cities like Madrid and the Seville area were found to have significantly higher reactivity compared to the relatively "fresh" industrial emissions from Huelva which was north west of the measurement site at El Arenosillo. In stark contrast, clean marine air masses arriving at the site from the Atlantic ocean often had OH reactivity values which were below the instrument's detection limit (< 3.5 s^{-1}). Thus, extremely high variability was observed at this single site with values ranging from below detection limit to 85 s^{-1}, covering the average range of OH reactivity values that have been reported in the literature from more than three quarters of all sites where such measurements have been performed (e.g. Table 1 of Lou et al 2010.).

Using two methodologies prevalent in the literature we show that using measurements of three parameters namely NO, NO_2 and OH reactivity, one can determine the instantaneous ozone production regime in different air masses at a single site which may be very helpful for policy decisions regarding ozone reduction and emissions control at specific locations. Further by calculating instantaneous ozone production rates using two different methods, we demonstrate the complementary information provided by both.

In this particular study we found that the potential ozone production rates based on just the measured VOC OH reactivity and OH radicals at El Arenosillo are very high when air masses arrive from the continental sector. The other approach of calculating the in-situ ozone production rates which takes into account NO and peroxy radical levels yields lower values as the site is predominantly a NO_x limited regime.

The complementary information (one local and the other more regional) provided by employing both methods indicates that if upwind point sources of NO_x were to increase north east of El Arenosillo with VOC emission levels staying the same as observed in this study, then ozone production rates at the site could potentially increase by a factor of two to 40 ppbV/hr causing a dramatic increase in regional ozone levels. On the other hand addition of upwind point NO_x sources north west of El Arenosillo would not cause such high ozone production rates.

Such information made possible by direct OH reactivity measurements would be very useful for environmental impact assessment and policy decisions on urban planning efforts focussed on ozone reduction. With increasing urbanization and industrialization in the future, adding the OH reactivity measurements to pollution monitoring networks that already measure criteria air pollutants like ozone and NO_x would provide detailed in-situ ozone production regimes and rates.

Acknowledgements. We thank INTA (National Institute for Aerospace Technology) for providing facilities at the measurement site. NOAA Air Resources Laboratory (ARL) is gratefully acknowledged for the provision of the HYSPLIT transport and dispersion model (http://www.arl.noaa.gov/ready.html) used in this paper. All the participants of the DOMNIO campaign for logistical support, in particular Dr. Thomas Custer.

References

Atkinson, R.: Kinetics of the gas-phase reactions of OH radicals with alkanes and cycloalkanes, Atmos. Chem. Phys., 3, 2233–2307, doi:10.5194/acp-3-2233-2003, 2003.

Atkinson, R., Aschmann, S. M., Winer, A. M., and Carter, W. P. L.: Rate Constants for the Gas-Phase Reactions of OH Radicals and O_3 with Pyrrole at 295+/-1k and Atmospheric-Pressure, Atmos. Environ., 18, 2105–2107, 1984.

Atkinson, R., Baulch, D. L., Cox, R. A., Crowley, J. N., Hampson, R. F., Hynes, R. G., Jenkin, M. E., Rossi, M. J., and Troe, J.: Evaluated kinetic and photochemical data for atmospheric chemistry: Volume I – gas phase reactions of O_X, HO_X, NO_X and SO_X species, Atmos. Chem. Phys., 4, 1461–1738, doi:10.5194/acp-4-1461-2004, 2004.

Butler, T. M., Lawrence, M. G., Taraborrelli, D., and Lelieveld, J.: Multi-day ozone production potential of volatile organic compounds calculated with a tagging approach, Atmos. Environ., 45, 4082–4090, doi:10.1016/j.atmosenv.2011.03.040, 2011.

Cantrell, C. A., Shetter, R. E., Lind, J. A., McDaniel, A., Calvert, J., Parrish, D., Fehsenfeld, F., Buhr, M., and Trainer, M.: An Improved Chemical Amplifier Technique for Peroxy Radical Measurements, J. Geophys. Res., 98, 2897–28909, 1993.

Crowley, J. N., Thieser, J., Tang, M. J., Schuster, G., Bozem, H., Beygi, Z. H., Fischer, H., Diesch, J.-M., Drewnick, F., Borrmann, S., Song, W., Yassaa, N., Williams, J., Pöhler, D., Platt, U., and Lelieveld, J.: Variable lifetimes and loss mechanisms for NO_3 and N_2O_5 during the DOMINO campaign: contrasts between marine, urban and continental air, Atmos. Chem. Phys., 11, 10853–10870, doi:10.5194/acp-11-10853-2011, 2011.

Di Carlo, P., Brune, W. H., Martinez, M., Harder, H., Lesher, R., Ren, X. R., Thornberry, T., Carroll, M. A., Young, V., Shepson, P. B., Riemer, D., Apel, E., and Campbell, C.: Missing OH reactivity in a forest: Evidence for unknown reactive biogenic VOCs, Science, 304, 722–725, 2004.

Diesch, J., Drewnick, F., Sinha, V., Adame, J. A., Williams, J, Martinez, M., and Borrmann, S.: Influence of aerosol, trace gas and meteorological characteristics on new particle formation and growth events under clean and polluted conditions in coastal Southern Spain, submitted, 2011.

Draxler, R. R. and Rolph, G. D.: HYSPLIT (HYbrid Single-Particle Lagrangian Integrated Trajectory), Model access via NOAA ARL READY Website http://ready.arl.noaa.gov/HYSPLIT.php), NOAA Air Resources Laboratory, Silver Spring, MD, 2011.

Fuchs, H., Bohn, B., Hofzumahaus, A., Holland, F., Lu, K. D., Nehr, S., Rohrer, F., and Wahner, A.: Detection of HO2 by laser-induced fluorescence: calibration and interferences from RO_2 radicals, Atmos. Meas. Tech., 4, 1209–1225, doi:10.5194/amt-4-1209-2011, 2011.

Hastie, D. R., Weißenmayer, M., Burrows, J. P., and Harris, G.W.: Calibrated chemical amplifier for atmospheric RO_X measurements, Anal. Chem., 63, 2048–2057, 1991.

Hosaynali Beygi, Z., Fischer, H., Harder, H. D., Martinez, M., Sander, R., Williams, J., Brookes, D. M., Monks, P. S., and Lelieveld, J.: Oxidation photochemistry in the Southern Atlantic boundary layer: unexpected deviations of photochemical steady state, Atmos. Chem. Phys., 11, 8497–8513, doi:10.5194/acp-11-8497-2011, 2011.

Ingham, T., Goddard, A., Whalley, L. K., Furneaux, K. L., Edwards, P. M., Seal, C. P., Self, D. E., Johnson, G. P., Read, K. A., Lee, J. D., and Heard, D. E.: A flow-tube based laser-induced fluorescence instrument to measure OH reactivity in the troposphere, Atmos. Meas. Tech., 2, 465–477, doi:10.5194/amt-2-465-2009, 2009.

Kartal, D., Andrés-Hernández, M. D., Reichert, L., Schlager, H., and Burrows, J. P.: Technical Note: Characterisation of a DUALER instrument for the airborne measurement of peroxy radicals during AMMA 2006, Atmos. Chem. Phys., 10, 3047–3062, doi:10.5194/acp-10-3047- 2010, 2010.

Keenan, T., Niinemets, Ü., Sabate, S., Gracia, C., and Peñuelas, J.: Seasonality of monoterpene emission potentials in Quercus ilex and Pinus pinea: Implications for regional VOC emissions modeling, J. Geophys. Res., 114, D22202, doi:10.1029/2009JD011904, 2009.

Kirchner, F., Jeanneret, F., Clappier, A., Kruger, B., van den Bergh, H., and Calpini, B.: Total VOC reactivity in the planetary boundary layer 2, A new indicator for determining the sensitivity of the ozone production to VOC and NO_X, J. Geophys. Res.-Atmos., 106, 3095–3110, doi:10.1029/2000jd900603, 2001.

Kovacs, T. A. and Brune, W. H.: Total OH loss rate measurement, J. Atmos. Chem., 39, 105– 122, 2001.

Kovacs, T. A., Brune, W. H., Harder, H., Martinez, M., Simpas, J. B., Frost, G. J., Williams, E., Jobson, T., Stroud, C., Young, V., Fried, A., and Wert, B.: Direct measurements of urban OH reactivity during Nashville SOS in summer 1999, J. Environ. Monit., 5, 68–74, 2003.

Lee, J. D., Young, J. C., Read, K. A., Hamilton, J. F., Hopkins, J. R., Lewis, A. C., Bandy, B. J., Davey, J., Edwards, P., Ingham, T., Self, D. E., Smith, S. C., Pilling, M. J., and Heard, D. E.: Measurement and calculation of OH reactivity at a United Kingdom coastal site, J. Atmos. Chem., 64, 53–76, doi:10.1007/s10874-010-9171-0, 2009.

Lelieveld, J., Dentener, F. J., Peters, W., and Krol, M. C.: On the role of hydroxyl radicals in the self-cleansing capacity of the troposphere, Atmos. Chem. Phys., 4, 2337–2344, doi:10.5194/acp-4-2337-2004, 2004.

Lou, S., Holland, F., Rohrer, F., Lu, K., Bohn, B., Brauers, T., Chang, C. C., Fuchs, H., Häseler, R., Kita, K., Kondo, Y., Li, X., Shao, M., Zeng, L., Wahner, A., Zhang, Y., Wang, W., and Hofzumahaus, A.: Atmospheric OH reactivities in the Pearl River Delta – China in summer 2006: measurement and model results, Atmos. Chem. Phys., 10, 11243–11260, doi:10.5194/acp-10-11243-2010, 2010.

Mao, J., Ren, X., Brune, W. H., Olson, J. R., Crawford, J. H., Fried, A., Huey, L. G., Cohen, R. C., Heikes, B., Singh, H. B., Blake, D. R., Sachse, G. W., Diskin, G. S., Hall, S. R., and Shetter, R. E.: Airborne measurement of OH reactivity during INTEX-B, Atmos. Chem. Phys., 9, 163–173, doi:10.5194/acp-9-163-2009, 2009.

Martinez, M., Harder, H., Kovacs, T. A., Simpas, J. B., Bassis, J., Lesher, R., Brune, W. H., Frost, G. J., Williams, E. J., Stroud, C. A., Jobson, B. T., Roberts, J. M., Hall, S. R., Shetter, R. E., Wert, B., Fried, A., Alicke, B., Stutz, J., Young, V. L., White, A. B., and Zamora, R. J.: OH and HO_2 concentrations, sources, and loss rates during the Southern Oxidants Study in Nashville, Tennessee, summer 1999, J. Geophys. Res.-Atmos., 108, 4617, 17 pp., 2003.

Martinez, M., Harder, H., Kubistin, D., Rudolf, M., Bozem, H., Eerdekens, G., Fischer, H., Klüpfel, T., Gurk, C., Königstedt, R., Parchatka, U., Schiller, C. L., Stickler, A., Williams, J., and Lelieveld, J.: Hydroxyl radicals in the tropical troposphere over the Suriname rainforest: airborne measurements, Atmos. Chem. Phys., 10, 3759–3773, doi:10.5194/acp-10-3759- 2010, 2010.

Monks, P. S., Granier, C., Fuzzi, S., Stohl, A., Williams, M. L., Akimoto, H., Amann, M., Baklanov, A., Baltensperger, U., Bey, I., Blake, N., Blake, R. S., Carslaw, K., Cooper, O. R., Dentener, F., Fowler, D., Fragkou, E., Frost, G. J., Generoso, S., Ginoux, P., Grewe, V., Guenther, A., Hansson, H. C., Henne, S., Hjorth, J., Hofzumahaus, A., Huntrieser, H., Isaksen, I. S. A., Jenkin, M. E., Kaiser, J., Kanakidou, M., Klimont, Z., Kulmala, M., Laj, P., Lawrence, . G., Lee, J. D., Liousse, C., Maione, M., McFiggans, G., Metzger, A., Mieville, A., Moussiopoulos, N., Orlando, J. J., O'Dowd, C. D., Palmer, P. I., Parrish, D. D., Petzold, A., Platt, U., Poschl, U., Prevot, A. S. H., Reeves, C. E., Reimann, S., Rudich, Y., Sellegri, K., Steinbrecher, R., Simpson, D., ten Brink, H., Theloke, J., van der Werf, G. R., Vautard, R., Vestreng, V., Vlachokostas, C., and von Glasow, R.: Atmospheric composition change – global and regional air quality, Atmos. Environ., 43, 5268–5350, 2009.

Ren, X. R., Harder, H., Martinez, M., Lesher, R. L., Oliger, A., Shirley, T., Adams, J., Simpas, J. B., and Brune, W. H.: HO_X concentrations and OH reactivity observations in New York City during PMTACS-NY2001, Atmos. Environ., 37, 3627–3637, 2003.

Ren, X. R., Brune, W. H., Oliger, A., Metcalf, A. R., Simpas, J. B., Shirley, T., Schwab, J. J., Bai, C. H., Roychowdhury, U., Li, Y. Q., Cai, C. X., Demerjian, K. L., He, Y., Zhou, X. L., Gao, H. L., and Hou, J.: OH, HO_2, and OH reactivity during the PMTACS-NY Whiteface Mountain 2002 campaign: Observations and model comparison, J. Geophys. Res.-Atmos., 111, D10S03, 12 pp., 2006.

Sadanaga, Y., Yoshino, A., Kato, S., Yoshioka, A., Watanabe, K., Miyakawa, Y., Hayashi, I., Ichikawa, M., Matsumoto, J., Nishiyama, A., Akiyama, N., Kanaya, Y., and Kajii, Y.: The importance of NO_2 and volatile organic compounds in the urban air from the viewpoint of the OH reactivity, Geophys. Res. Lett., 31, L08102, 4 pp., 2004a.

Sadanaga, Y., Yoshino, A., Watanabe, K., Yoshioka, A., Wakazono, Y., Kanaya, Y., and Kajii, Y.: Development of a measurement system of OH reactivity in the atmosphere by using a laser-induced pump and probe technique, Rev. Sci. Instrum., 75, 2648–2655, 2004b.

Sadanaga, Y., Yoshino, A., Kato, S., and Kajii, Y.: Measurements of OH reactivity and photochemical ozone production in the urban atmosphere, Environ. Sci. Technol., 39, 8847–8852, 2005.

Seinfeld, J. H. and Pandis, S. N.: Chapter 6, Atmospheric Chemistry and Physics – From Air Pollution to Climate Change, 2nd Edn., John Wiley & Sons, Inc, New Jersey, 2006.

Shirley, T. R., Brune, W. H., Ren, X., Mao, J., Lesher, R., Cardenas, B., Volkamer, R., Molina, L. T., Molina, M. J., Lamb, B., Velasco, E., Jobson, T., and Alexander, M.: Atmospheric oxidation in the Mexico City Metropolitan Area (MCMA) during April 2003, Atmos. Chem. Phys., 6, 2753–2765, doi:10.5194/acp-6-2753-2006, 2006.

Sinha, V., Williams, J., Crowley, J. N., and Lelieveld, J.: The Comparative Reactivity Method – a new tool to measure total OH Reactivity in ambient air, Atmos. Chem. Phys., 8, 2213–2227, doi:10.5194/acp-8-2213-2008, 2008.

Sinha, V., Custer, T. G., Kluepfel, T., and Williams, J.: The effect of relative humidity on the detection of pyrrole by PTR-MS for OH reactivity measurements, Int. J. Mass Spectrom., 282, 108–111, 2009.

Sinha, V., Williams, J., Lelieveld, J., Ruuskanen, T. M., Kajos, M. K., Patokoski, J., Hellen, H., Hakola, H., Mogensen, D., Boy, M., Rinne, J., and Kulmala, M.: OH Reactivity Measurements within a Boreal Forest: Evidence for Unknown Reactive Emissions, Environ. Sci. Technol., 44, 6614–6620, 2010.

Sommariva, R., Brown, S. S., Roberts, J. M., Brookes, D. M., Parker, A. E., Monks, P. S., Bates, T. S., Bon, D., de Gouw, J. A., Frost, G. J., Gilman, J. B., Goldan, P. D., Herndon, S. C., Kuster, W. C., Lerner, B. M., Osthoff, H. D., Tucker, S. C., Warneke, C., Williams, E. J., and Zahniser, M. S.: Ozone production in remote oceanic and industrial areas derived from ship based measurements of peroxy radicals during TexAQS 2006, Atmos. Chem. Phys., 11, 2471–2485, doi:10.5194/acp-11-2471-2011, 2011.

Song, W., Williams, J., Yassaa, N., Reglin, E., Kubistin, D., Harder, H., Martinez, M., Carnero, J. A. A., Fernandez, P. H., Bozem, H., and Lelieveld, J. J.: Atmos. Chem., in review, 2012.

Sörgel, M., Regelin, E., Bozem, H., Diesch, J.-M., Drewnick, F., Fischer, H., Harder, H., Held, A., Hosaynali-Beygi, Z., Martinez, M., and Zetzsch, C.: Quantification of the unknown HONO daytime source and its relation to NO2, Atmos. Chem. Phys., 11, 10433–10447, doi:10.5194/acp-11-10433-2011, 2011.

Staudt, M., Bertin, N., Frenzel, B., and Seufert, G.: Seasonal variation in amount and composition of monoterpenes emitted by young Pinus pinea trees – Implications for emission modeling, J. Atmos. Chem., 35, 77–99, doi:10.1023/a:1006233010748, 2000.

Yoshino, A., Sadanaga, Y., Watanabe, K., Kato, S., Miyakawa, Y., Matsumoto, J., and Kajii, Y.: Measurement of total OH reactivity by laser-induced pump and probe technique – comprehensive observations in the urban atmosphere of Tokyo, Atmos. Environ., 40, 7869–7881, 2006.

C Variable lifetimes and loss mechanisms for NO_3 and N_2O_5 during the DOMINO campaign: contrasts between marine, urban and continental air

J. N. Crowley[1], J. Thieser[1], M. Tang[1], G. Schuster[1], H. Bozem[1], Z. Hosaynali Beygi[1], H. Fischer[1], J.-M. Diesch[2], F. Drewnick[2], S. Borrmann[2,3], W. Song[1], N. Yassaa[1,4], J. Williams[1], D. Pöhler[5], U. Platt[5], and J. Lelieveld[1]

[1]Max-Planck-Institut für Chemie, Division of Atmospheric Chemistry, Mainz, Germany
[2]Max-Planck-Institut für Chemie, Particle Chemistry Department, Mainz, Germany
[3]Institute for Atmospheric Physics, University of Mainz, Germany
[4]Faculty of Chemistry, University of Sciences and Technology Houari Boumediene (USTHB), Algiers, Algeria
[5]Institut of Environmetal Physics, University of Heidelberg, Germany

Published in Atmos. Chem. Phys., Volume 11, 10853-10870, 2011

Abstract

Nighttime mixing ratios of boundary layer N_2O_5 were determined using cavity-ring-down spectroscopy during the DOMINO campaign in Southern Spain (Diel Oxidant Mechanisms In relation to Nitrogen Oxides, 21.11.2008 - 08.12.2008). N_2O_5 mixing ratios ranged from below the detection limit (~ 5 ppt) to ~ 500 ppt. A steady-state analysis constrained by measured mixing ratios of N_2O_5, NO_2 and O_3 was used to derive NO_3 lifetimes and compare them to calculated rates of loss via gas-phase and heterogeneous reactions of both NO_3 and N_2O_5. Three distinct types of air masses were encountered, which were largely marine (Atlantic), continental or urban-industrial in origin. NO_3 lifetimes were longest in the Atlantic sector (up to ~ 30 min) but were very short (a few seconds) in polluted, air masses from the local city and petroleum-related industrial complex of Huelva. Air from the continental sector was an intermediate case. The high reactivity to NO_3 of the urban air mass was not accounted for by gas-phase and heterogeneous reactions, rates of which were constrained by measurements of NO, volatile organic species and aerosol surface area. In general, high NO_2 mixing ratios were associated with low NO_3 lifetimes, though heterogeneous processes (e.g. reaction of N_2O_5 on aerosol) were generally less important than direct gas-phase losses of NO_3. The presence of SO_2 at levels above ~ 2ppb in the urban air sector was always associated with very low N_2O_5 mixing ratios indicating either very short NO_3 lifetimes in the presence of combustion-related emissions or an important role for reduced sulphur species in urban, nighttime chemistry. High production rates coupled with low lifetimes of NO_3 imply an important contribution of nighttime chemistry to removal of both NO_x and VOC.

1 Introduction

The photochemically driven, OH-initiated oxidation processes during the day are supplemented by (or, for several classes of volatile organic compounds (VOCs) such as terpenes or CH_3SCH_3, surpassed by) night-time reactions with the NO_3 radical (Wayne et al., 1991). The interaction of NO_3 with VOCs leads to the formation of organic peroxy radicals, and via secondary reactions to HO_2 and OH (Platt et al., 1990; Sommariva et al., 2009). NO_3 can thus initiate and propagate nocturnal radical chemistry linking HO_2 and NO_x chemistry and significantly impacting on oxidation rates of several classes of atmospheric trace gases.

NO_3 is formed predominantly in the reaction of NO_2 with O_3 (R1) and is converted to N_2O_5 via further reaction with NO_2 (R2). The thermal decomposition of N_2O_5 links the concentrations of NO_3 and N_2O_5 via the equilibrium constant, K_2. Simultaneous measurements of NO_3 and N_2O_5 (Brown et al., 2003a; Crowley et al., 2010) confirm that (under most conditions) the timescales to acquire equilibrium are sufficiently short that the relative concentrations of NO_3 and N_2O_5 in the atmosphere are controlled only by the temperature and levels of NO_2.

$NO_2+O_3 \rightarrow NO_3+O_2$ (R1)

$NO_2+NO_3+M \rightarrow N_2O_5+M$ (R2)

$N_2O_5+M \rightarrow NO_2+NO_3+M$ (R3)

The impacts of NO_3 and N_2O_5 on nighttime chemistry depends on their relative rates of loss via gas-phase and heterogeneous reactions. Whereas NO_3 is lost mainly via gas-phase reactions with e.g. VOCs (see above), N_2O_5 is removed predominantly by heterogeneous hydrolysis on aqueous aerosol, which can substantially modify the amount of reactive nitrogen available for daytime photochemistry. In the polluted boundary layer, this process influences the fate of NOx emissions and their potential for photochemical ozone formation and also (via heterogeneous chemistry on sulphate particles) links O_3 production rates to emissions of SO_2 from e.g. power plants or shipping (Brown et al., 2006). It has recently been shown that heterogeneous reactions of N_2O_5 with chloride containing particles can also represent a significant source of photo-labile chlorine (in the form of $ClNO_2$ and Cl_2) (Roberts et al., 2009; Thornton et al., 2010).

The objectives of this study were to examine the roles and relative importance of gas phase and heterogeneous processing of NO_3 and N_2O_5 in chemically distinct air masses: urban (strong anthropogenic influence), continental (mainly biogenic emissions) and maritime. In order to achieve these objectives the NO_3 and N_2O_5 measurements were accompanied by instrumentation for trace gas and aerosol characterisation (see later).

1.1 NO_3 lifetimes

The production rate of NO_3 is given by $k_1[NO_2][O_3]$ (generally we write k_i as the rate coefficient for reaction (Ri)) so that its stationary state turnover lifetime, $\tau_{ss}(NO_3)$, can be calculated from observations of its concentration and those of O_3 and NO_2:

$$\tau_{ss}(NO_3) = \frac{[NO_3]}{k_1[NO_2][O_3]} \quad (1)$$

Whenever we use the term "NO_3 lifetimes" in the manuscript, we refer to $\tau_{ss}(NO_3)$.

NO_3 can be removed directly from the air by e.g. reaction with organic trace gases (Wayne et al., 1991) or indirectly via removal of N_2O_5 via e.g. heterogeneous loss to aqueous particles. As described previously (Geyer et al., 2001b; Aldener et al., 2006; Crowley et al., 2010) the contributions of direct and indirect losses of NO_3 to its lifetime can, in principal, be evaluated if K_2 (the equilibrium constant k_2 / k_{-2}) and $[NO_2]$ are known:

$$\tau_{ss}(\mathrm{NO_3}) \approx \frac{1}{f_{ss}(\mathrm{NO_3})} \quad (2)$$

where $f_{ss}(NO_3)$ is the overall loss frequency of NO_3 from stationary state and is equal to

$$\Sigma_i \left(k_i[X]_i\right) + 0.25\bar{c}\gamma(\mathrm{NO_3})A + f_{\mathrm{dd}}(\mathrm{NO_3}) + \left(0.25\bar{c}\gamma(\mathrm{N_2O_5})A + f_{\mathrm{dd}}(\mathrm{N_2O_5}) + f_{H2O}\right)K_2[\mathrm{NO_2}]$$

In this expression, k_i (cm^3 molecule^{-1} s^{-1}) is the rate coefficient for reaction of NO_3 with trace gas i at concentration $[X]_i$ (molecule cm^{-3}), A is the aerosol surface area density (cm^2 cm^{-3}), $\bar{c}$ (cm s^{-1}) is the mean molecular velocity of NO_3 or N_2O_5, $\gamma(NO_3)$ and $\gamma(N_2O_5)$ are the dimensionless uptake coefficients for irreversible reaction of NO_3 or N_2O_5 with aerosol, f_{dd} (s^{-1}) is the first-order rate constant for dry deposition of NO_3 or N_2O_5 and f_{H2O} (s^{-1}) represents the homogeneous, gas-phase loss of N_2O_5 via reaction with water vapour.

Recent measurements of long lifetimes of N_2O_5 even in the presence of high relative humidity (Brown et al., 2009; Crowley et al., 2010) imply that f_{H2O} is too small to be important under most conditions. The rate of uptake of a trace gas to airborne particles can be reduced by concentration gradients close to the particle surface, which requires modification of the simple expression for the heterogeneous loss rate, $k_{het} = 0.25\bar{c}\gamma A$, as used in Equation (2). The effective uptake coefficient ($\gamma_{\mathrm{effective}}$) is approximated by (Fuchs and Sutugin, 1970):

$$\frac{1}{\gamma_{\mathrm{effective}}} = \frac{1}{\gamma} + \frac{0.75 + 0.283Kn}{Kn(Kn+1)} \quad (3)$$

where $Kn = \frac{3D_g}{\bar{c} \cdot r_{sw}}$, r_{sw} is the radius of the particle at the maximum of the surface area weighted size distribution, and D_g is the gas phase diffusion coefficient of N_2O_5 or NO_3 at the appropriate pressure and temperature. For N_2O_5, D_g is 0.085 cm^2 s^{-1} at atmospheric pressure and 298 K (Wagner et al., 2008). During the nights of the campaign, the dominant contribution to aerosol surface area was by particles with diameters of less than ~200 nm. In this case, only uptake coefficients close to unity require significant correction. For example, an uptake coefficient of ~0.1 would be reduced by transport limitations to ~0.09, whereas a γ of 1 would reduce to ~0.5. A value of 0.5 is therefore the approximate maximum value of $\gamma(N_2O_5)$ or $\gamma(NO_3)$, which can be used to calculate NO_3 lifetimes using Equation (2). More realistic (lower) values of γ, derived from laboratory and field experiments are discussed later.

At low aerosol loading (or low values of γ) and negligible dry deposition the term (in Equation (2))

$\left(0.25\bar{c}\gamma(\mathrm{N_2O_5})A + f_{\mathrm{dd}}(\mathrm{N_2O_5}) + f_{H2O}\right)K_2[\mathrm{NO_2}]$ becomes diminishingly small and NO_3 lifetimes are largely independant of NO_2 concentrations. On the other hand, if gas-phase losses of NO_3 are slow, N_2O_5 chemistry can be important and NO_3 lifetimes will show a dependence on the inverse NO_2 concentration (Heintz et al., 1996; Martinez et al., 2000; Geyer et al., 2001b; Brown et al., 2003a; Brown et al., 2003b; Aldener et al., 2006; Brown et al., 2009).

Certain conditions must be fulfilled if Equation (2) is used to examine NO_3 lifetimes and draw conclusions regarding direct and indirect loss routes. Firstly, NO_3 production rates are governed by a slow reaction between NO_2 and O_3. Application of a stationary state analysis to NO_3 lifetimes is only suited to air-masses where the chemical lifetime of NO_3 (or N_2O_5) is sufficiently short that stationary state is achieved with the transport time from the emission region to the measurement site (Brown et al., 2003a).

Stationary state is formally achieved when the rate of change of NO_3 and N_2O_5 are zero, i.e. $d[NO_3]/dt = k_1[NO_2][O_3] + k_{-2}[N_2O_5] - k_2[NO_2][O_3] - k'(NO_3)[NO_3] = 0$ and $d[N_2O_5]/dt = k_2[NO_2][NO_3] - k_{-2}[N_2O_5] - k''[N_2O_5] = 0$, where $k'(NO_3)$ and $k''(N_2O_5)$ are summed first order loss rate constants for any reactions involving NO_3 and N_2O_5. The approximate time to achieve stationary state thus depends on the production and loss rates of both NO_3 and N_2O_5 and is longer at high NO_2 mixing ratio and low temperatures.

Time dependent values of $d[NO_3]/dt$ and $d[N_2O_5]/dt$ were determined for an unfavourable case (i.e. high NO_2 mixing ratio of 10 ppb) by numerical simulation in a manner similar to that described previously (Brown et al., 2003a). The low N_2O_5 and NO_3 concentrations observed (implying short lifetimes) meant that stationary state was achieved within 1-2 hours after dusk and within the time of transport from the major source of NO_x (e.g. Huelva).

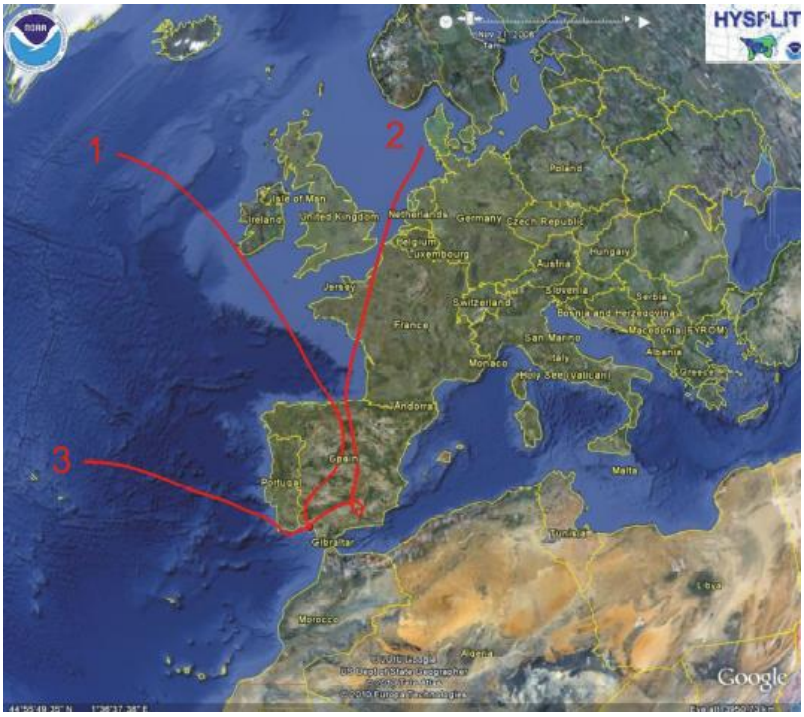

Figure 1: Location of the measurement site with three 72-h HYSPLIT back-trajectories of air masses reaching the site at 00:00 on the 24 November 2008 (1, Huelva sector), 27 November 2008 (2,continental sector) and 7 December 2008 (3, Atlantic sector).

Equation (2) has been used to derive the direct and indirect contributions to NO_3 loss rates (Brown et al., 2009; Crowley et al., 2010) via the dependence of the observed lifetime on NO_2 mixing ratios. This approach will however break down if the trace gases which react directly with NO_3 are correlated (e.g. have the same chemical source or spatial distribution of emissions) with NO_2. This is unlikely to apply to regions where NO_3 losses are dominated by e.g. reaction with biogenic volatile organic compounds (BVOC) in clean air masses, but might be the case where NO_3 reacts

with traces gases resulting from combustion processes in which NO_2 is also generated. In a similar vein, if aerosol surface area also co-varies with NO_2, use of Equation (2) to separate the contributions of homogeneous and heterogeneous loss rates of N_2O_5 to the NO_3 lifetime is not possible.

2 Site description

The DOMINO campaign (Diel Oxidant Mechanisms In relation to Nitrogen Oxides, (21.11.2008 - 08.12.2008) took place at the Atmospheric Sounding Station (Base de Arenosillo*, 37° 05' 58" N, 6° 44' 17" W) located on the Atlantic coast of the southern Spanish region of Moguer (Figure 1). Measurements were conducted in a forested area (mainly Stone pines, *Pinus pinea* ~ 5-10 m in height) with proximity to both extensive pollution sources and the Atlantic Ocean (the Atlantic coast was ~ 300 m distant and ~20 m lower) so that the chemical composition of air masses arriving at the site was highly dependent on wind direction. On-site wind directions between 290 and 340 degrees indicated that air masses had recently passed over the expansive industrial centre and port of Huelva (henceforth referred to as the "Huelva" sector) which was located about 30 km away, or with typical night-time wind-speeds of 8-18 km/hour about 2-3 hours upwind. Huelva houses one of Europe's larger oil refineries and pollution from this sector includes emissions from related industrial / shipping activity. Air from the Huelva sector arriving at the measurement site at night was frequently and strongly malodorous. Air arriving from the 150-270 degrees sector passed over the Atlantic (sector "Atlantic") and generally contained low levels of NO*x*. NO_2 plumes were occasionally observed in this sector, which were usually accompanied by enhanced levels of SO_2 indicating emissions from passing ships.

Wind directions between 0 and 45 degrees (sector "continental") were from mainland Spain and passed no large cities for several hours prior to arrival at the site. Air arriving from Sevilla (~ 60 degrees), following Huelva, the next largest potential source of pollutants, was rarely encountered during the night. Overall, during the nights of the campaign, the air arrived predominantly from the Huelva (~50 %) or continental sectors (~35 %), with air from the Atlantic sector (~15%) encountered less frequently. Air mass back-trajectories calculated using HYSPLIT with GDAS meteorology (Draxler and Rolph, 2011) confirmed the allocation of source region sector according to local wind directions. Figure 1 displays selected back-trajectories for air arriving at midnight from the Huelva sector (1), the continental sector (2) and the Atlantic sector (3).

3 Methods

3.1 NO_3 and N_2O_5

NO_3 and N_2O_5 mixing ratios were measured using a two-channel, off axis cavity-ring-down system (OA-CRD), which has recently been described in detail (Schuster et al., 2009; Crowley et al., 2010) and also by long-path, differential optical absorption spectroscopy (LP-DOAS). In the CRD instrument, one channel monitors NO_3 directly, the other is used to monitor the sum of NO_3 and N_2O_5 via thermal dissociation of N_2O_5. The instrument was located in the upper container of a two-container stack and sampled air through a few meters of ¼ or ½" PFA-tubing with the inlet

* El Arenosillo is a platform of the Atmospheric Research and Instrumentation Branch of the Spanish National Institute for Aerospace Technology (INTA) dedicated to atmospheric measurements in the Southwest of Spain.

sampling from a height of between 7 and 12 m above ground level (~1-5 m above the closest canopy).

The 1/2" inlet was operated with a large bypass flow to reduce the residence time. A 2 μm pore Teflon filter (replaced every hour) in a PFA filter holder was located at the end of the inlet outside the container. The losses of NO_3 and N_2O_5 to the filter (15 ± 3 % and <2 %, respectively) were characterised prior to and after the campaign. Loss rates in the Teflon coated (DuPont, FEP) glass cavities were also measured during the campaign. Operational pressures and flows resulted in residence times in the inlet lines and cavities of between 0.6 and 1 s. CRD noise-levels changed during the campaign and varied between ~ 3 and 7 pptv for N_2O_5 and between 2 and 5 pptv for NO_3 (both with 5 s integration per datapoint). The detection limit is partly defined by accuracy of the chemical zero (measured by adding NO as described in detail previously (Schuster et al., 2009)) and was between 2 and 3 pptv for NO_3 and 5-7 pptv for N_2O_5 (both assuming zero losses in the inlet tubing). However, NO_3 was not observed directly during the campaign even when N_2O_5 levels of several hundred pptv were present. As NO_2 levels were not sufficiently high and temperatures (controlling K_2) not sufficiently low to reduce NO_3 to below the detection limit, this indicates deviation of the NO_2-NO_3-N_2O_5 chemistry from equilibrium. With night-time temperatures occasionally as high as 15 °C, equilibrium should be established within in a few minutes, suggesting that any processes that rapidly drain NO_3 from equilibrium must be very local otherwise N_2O_5 would also have been completely removed.

A potential cause of dis-equilibrium between NO_2, O_3 and N_2O_5 is the loss of NO_3 in the PFA inlet. This had not been anticipated as it was not encountered on a previous campaign at a rural location (Crowley et al., 2010) in which a similar sampling strategy (long PFA line with 1 s residence time) had been periodically deployed in place of the normally used, FEP-coated high-volume flow glass sampling line. Use of new inlet lines did not result in observation of NO_3, even temporarily. On several occasions during the campaign a calibration source of NO_3 was added to the inlet to measure its transmission and also that of the NO_3 cavity. NO_3 was generated by the thermal decomposition (~ 90 °C) of N_2O_5, itself made by mixing NO_2 and O_3 in a blackened, FEP-coated glass reaction vessel as described previously (Schuster et al., 2009). Prior to heating, the mixture typically contained approximately 200-400 pptv N_2O_5, 150 ppbv O_3 and 5 ppbv NO_2. The results were rather surprising as the initial transmission of the inlet tubing to NO_3 was very low (on occasions less than 20 %) even if it was relatively fresh. The transmission increased with exposure to the O_3, NO_2, NO_3 mixture to a value (circa 70-80 %) commensurate with known loss rates of NO_3 in PFA tubing. This condition sometimes took as long as an hour to achieve. At the same time, loss rates of NO_3 in the cold cavity were recorded as high as 1 s^{-1}, a factor 5 larger than observed in the laboratory, whereas loss in the hot cavity (i.e. the N_2O_5 + NO_3 channel) proceeded at the usual rate (~0.2 s^{-1}). These observations indicate that the PFA tubing rapidly became reactive to NO_3 when exposed to the air and this reactivity could be reduced by extended passivation with high NO_3 / O_3 concentrations or by heating to 90 °C. Post-campaign tests of the inlets used also revealed high (initial) reactivity to NO_3.

Assuming that the loss of NO_3 occurred in our inlet, it took place on a timescale (1 s) which is considerably shorter than the thermal lifetime of N_2O_5 (minutes), so that the N_2O_5 mixing ratios would not have been significantly affected. In this case we can calculate NO_3 ambient mixing ratios from the measured N_2O_5 and NO_2 and the equilibrium constant, K_2 via Equation (4).

$$[NO_3] = \frac{[N_2O_5]}{K_2[NO_2]} \quad (4)$$

As the inlet tubing was protected with a Teflon filter we do not anticipate large losses of N_2O_5 due to coating of the wall with aerosol. The disadvantage with this indirect calculation of NO_3 is that it relies on high quality (accurate, low noise), and preferably high time resolution NO_2 measurements. Some uncertainty is also associated with K_2, though recent field measurements of NO_2, NO_3 and N_2O_5 suggest that this is not more than 20 % (Osthoff et al., 2007; Crowley et al., 2010). The uncertainty in NO_3 mixing ratios calculated this way is thus considerably larger than via direct measurements and are estimated as about 35 % if N_2O_5 < 7 ppt. At lower levels of N_2O_5 the uncertainty in N_2O_5 (~40 % at 5 ppt) dominates. Long-path differential optical absorption spectroscopy (LP-DOAS, see below) measurements of NO_3 taken at a similar height to the CRD inlet are however in good agreement with the CRD-NO_3 mixing ratios derived from N_2O_5 and NO_2.

The LP-DOAS instrument applies the set-up from (Merten et al., 2011) with a configuration described in (Pöhler et al., 2010). It uses a telescope of 1.5m focal length a 100 or 200µm fibre bundle a 75W XBO xenon arc lamp (Osram) and for spectral analysis an Acton 300i spectrometer with Roper Scientific CCD camera (Spec-10:2KBUV). The instrument was located at 9m above the ground about 800m north of the main sampling point. It was operated with three sets of retro-reflectors mounted on a tower at 20, 35 and 70 m above the ground at a distance of 4.8km to the east, resulting in a total optical path-length of 9.6 km. The data analysis of NO_3 was performed in the spectral range from 615.0 nm to 673.8 nm with a gap between 644.1 nm to 657.8 nm to avoid strong water absorption lines. The reference spectra used were: NO_3 (Yokelson et al., 1994), NO_2 (Vandaele et al., 1998), O_3 (Voigt et al., 2001), H_2O (Hitran 2006 from (Gordon et al., 2007)) and additionally a recorded spectrum at noon to correct for most H_2O absorption, a background spectrum and a 3rd order polynomial. The standard deviation σ of the measurements was estimated according to Stutz and Platt (Stutz and Platt, 1996) and resulted in an average uncertainty for the NO_3 mixing ratio of 1ppt. In this work we use data at from the lowest retro reflector only in order to compare with the CRD measurements.

3.2 NO_2 and NO

NO and NO_2 measurements were made with a modified commercial chemiluminescence detector (CLD 790 SR) originally manufactured by ECO Physics (Duernten, Switzerland). The quantitative detection of NO_2 is based on its photolytic conversion (Blue Light Converter, Droplet Measurement Technologies, Boulder, Co, USA) to NO, which was subsequently detected in the CLD (Kley and McFarland, 1980). The detection limits for the NO and NO_2 measurements were 6 pptv and 8 ppt, respectively for an integration period of 1s. The total uncertainties for the measurements of NO, NO_2 were determined both to be 10%, based on the reproducibility of in-field background measurements, calibrations, the uncertainties of the standards and the conversion efficiency of the photolytic converter. The drift in instrument zero was less than ~2 ppt over the duration of one night. The same device was described in more detail recently (Crowley et al., 2010).

3.3 O_3, SO_2 and H_2O

O_3 and SO_2 (Airpointer, Recordum GmbH) and H_2O (LICOR 840 gas analyser, LI-COR, Inc.) were measured using instrumentation onboard the MoLa mobile platform (Diesch et al., 2012).

Limits of detection and precision were 0.5 ppb and 1 ppb for both SO_2 and O_3, 0.4 ppb and 1 ppb for NO*x*. Whilst Airpointer measurements of NO and NO_2 mirrored the trends seen using the ECO Physics device described above, they were not sufficiently accurate (especially at low NO*x* levels) to perform NO_3 lifetime analyses.

3.4 Volatile organic compounds

A commercially available instrument (AERO Laser model AL 4021, Germany) was used for in-situ HCHO measurements. This instrument is based on the Hantzsch reagent method, following the design described in Kelly and Fortune (1994). The time resolution is 160 sec. Detection limit and precision were estimated from the 1σ -reproducibility of in-situ zero and calibration gas measurements as 22 pptv and ± 15 %, respectively. The total uncertainty is estimated to be 29 %. An on-line sampling Thermal Desorption-Gas Chromatograph-Mass Spectrometer (TD-GC-MS) measurement system was used for the in-situ observation of anthropogenic VOCs such as ethylbenzene, and all xylene isomers as well as biogenic species such as isoprene and monoterpenes (Song et al., 2011). C_1-C_4 alkenes and alkanes were not measured.

3.5 Aerosol measurements

Particle size information was obtained using MoLa instruments (see above). A Fast Mobility Particle Sizer (FMPS 3091, TSI, Inc.), an Aerodynamic Particle Sizer (APS 3321, TSI, Inc.) as well as an Optical Particle Counter (OPC 1.109, Grimm) covered a particle size range from 5.6 nm to 32 μm. The chemical composition of the non-refractory aerosol in the sub-micron range was measured by means of a High-Resolution Time-of-Flight Aerosol Mass Spectrometer (HR-ToF-AMS, Aerodyne Res., Inc.). The soot (black carbon) concentration in PM_1 was determined by a Multi Angle Absorption Photometer (MAAP, Thermo E.C.). The aerosol surface area (ASA) used for calculating rates of trace gas uptake was calculated only from the FMPS dataset as, for most nights (including those examined in detail later), this contributed ≥ 80 % of the total aerosol surface area and (in contrast to super-micron particles) was of known composition.

3.6 Meteorological parameters

Wind direction and speed, temperature and pressure and relative humidity and rain intensity at approximate inlet height were provided by MoLa instrumentation (WXT 510 weather station, Vaisala). Temperatures and wind directions were also available at heights of 25, 50 and 100 m from a local meteorological tower operated by INTA.

Several cloudless nights gave rise to a strong temperature inversion, with temperatures at a height of 100m up to 5-6 °C warmer than those measured at the inlet height (~10m). This inversion would have lead to a very stable nocturnal boundary layer with efficient accumulation of low altitude emissions from e.g. the Huelva industrial area.

4 Measurements and discussion

Measurements of N_2O_5 and NO_3 were made on all campaign nights with the exception of the 28th of November. N_2O_5 was observed on most nights, though it was never present above the detection limit throughout the night but rather appeared in bursts of a few hours duration, reflecting differences in production and loss rates with changes in air-mass origin and/or local emissions. The

observed mixing ratios of N_2O_5 are plotted for each night of the campaign in Figure 2. As described above, NO_3 could not be detected directly using CRD but its mixing ratio was calculated from those of N_2O_5 and NO_2 and the equilibrium constant, K_2. The NO_3 data are generally in good agreement with DOAS measurements considering the differences in location and heights of inlet (CRD) and optical path (LP-DOAS).

As shown in reactions R1-R2, the production rates of NO_3 and N_2O_5 are governed by the NO_2 and O_3 mixing ratios. During the DOMINO campaign, night-time mixing ratios of NO_2 were highly variable, fluctuating from local background levels of ~ 1 ppbv to more than 15 ppb. The highest levels of NO_2 were associated with air masses that had passed over the Huelva sector, often arriving in plumes with a duration of about 1-2 hours. Sub-ppbv levels of NO_2 were usually associated with the Atlantic sector. Apart from infrequent NO spikes presumably from traffic using local roads, night-time levels of NO were low. They were however, occasionally non-zero and on some nights 5-10 pptv of NO was present for a prolonged duration. Given that the lifetime of NO in the presence of > 15 ppbv O_3 is only a few minutes, the presence of NO implies a local source. Indeed, with an average night-time wind-speeds of just 2.8 m/s this implies a source located within about 500 m of the inlet. Possible sources of NO are emissions from the surrounding woodland soil. Apart from occasional plumes from Huelva, non-zero levels of NO were not associated with any single wind-direction which argues against a local, continuous point emission source (i.e. instrument exhaust-line.

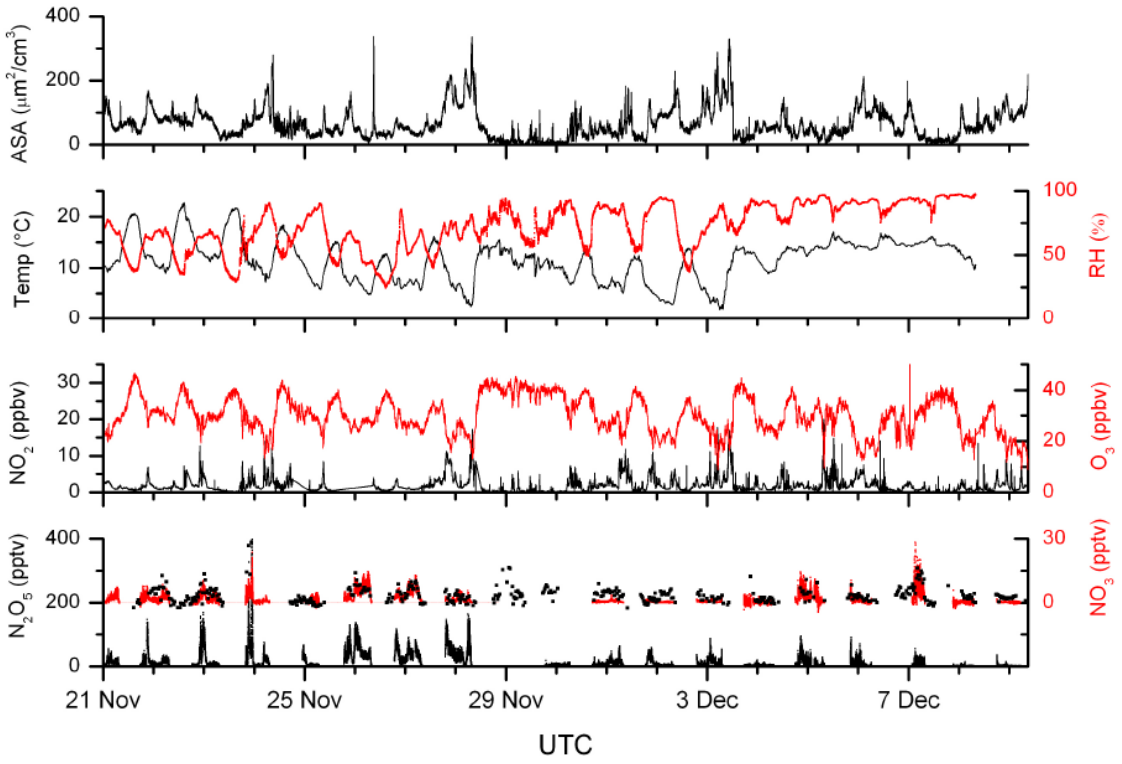

Figure 2: Campaign overview of measured N_2O_5, NO_2 and O_3 mixing ratios, aerosol surface area (ASA), temperature, relative humidity (RH) and calculated CRD-NO_3 mixing ratios (in red). The black NO_3 datapoints are LP-DOAS measurements. x-axis ticks are at midnight.

Night-time O_3 was strongly anti-correlated with NO_2 and thus also showed significant variability, with typical levels of 15-40 ppbv. Air masses passing over the Huelva and coastal region (and sometimes the open ocean) often contained SO_2, with maximum levels of ~ 40 ppbv in plumes

originating from the port or Huelva areas. The SO_2 plumes were always associated with high levels of NO_2 with a similar temporal profile, indicating a common process as source. This might have been the result of petrochemical industry activity as flaring at the petrochemical complex in Huelva was frequently visible at night. A further possible source of SO_2 was ship emissions, either at sea or entering the harbour at Huelva. Note that the strait of Gibraltar (~160 km distant) is one of the world's busiest shipping lanes. SO_2 was not observed above the limit of detection from the continental sector. We note that the presence of both SO_2 and NO_2 in a plume nearly always meant low levels or non-detection of N_2O_5, despite high NO_3 production rates. We discuss this particular aspect of NO_3 / N_2O_5 chemistry in more detail later when analysing individual days.

Particles measured at the site displayed number size distributions with mode diameters of between 40 and 80 nm with a generally dominant organic fraction but with a significant sulphate component with short term increases that correlated with SO_2 plumes. The ammonium to sulphate mole ratio was always less than unity during the campaign, indicating that the aerosol was acidic (ratio of 2 = neutral aerosol).

4.1 NO_3 lifetimes

Despite large NO_3 production rates N_2O_5 was only sporadically observed, indicating reactive air-masses and short NO_3 or N_2O_5 lifetimes. More than 50 % of the campaign data revealed NO_3 lifetimes of less than 1 minute, with lifetimes longer than 15 min representing only 0.5 % of the measurements. NO_3 lifetimes were found to be strongly dependent on wind direction, with the largest values measured in air masses originating from the Atlantic sector and the shortest lifetimes when air arrived from Huelva, with continental air an intermediate case. This is illustrated in Figure 3.

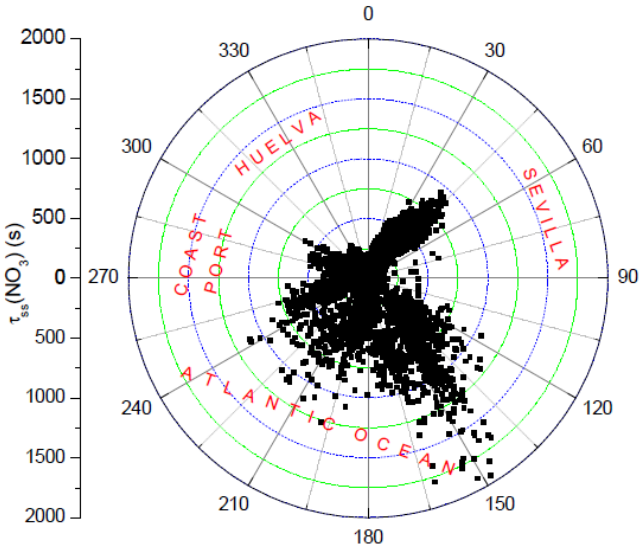

Figure 3: Wind-direction dependence of NO_3 lifetimes (nighttime only). ~50% of the airmasses encountered at night came from the Huelva sector, and were associated with very short NO_3 lifetimes.

During the campaign, NO_3 lifetimes were seen to be reduced at high NO_2 mixing ratios. Frequently, this is taken to be indicative of indirect losses of NO_3 (i.e. N_2O_5 driven, heterogeneous reactions). However, the NO_2 mixing ratio was also correlated with the available surface area, so that separation of the NO_3 losses into direct and indirect reactions (see E2) is problematic.

Below, we analyse three nights of the campaign in some detail, attempting to identify and quantify the various direct and indirect processes controlling NO_3 lifetimes. Each day represents a different air mass origin, covering each of the Atlantic, Huelva and continental sectors.

4.1.1 6-7th December: Clean air from the Atlantic sector

Local wind directions indicated that air masses encountered during the latter part of the night spanning the 6th – 7th December arrived from the Atlantic sector. Back trajectories (Figure 1) confirmed that the air had spent at least 3 days over the Atlantic Ocean prior to arriving at the site.

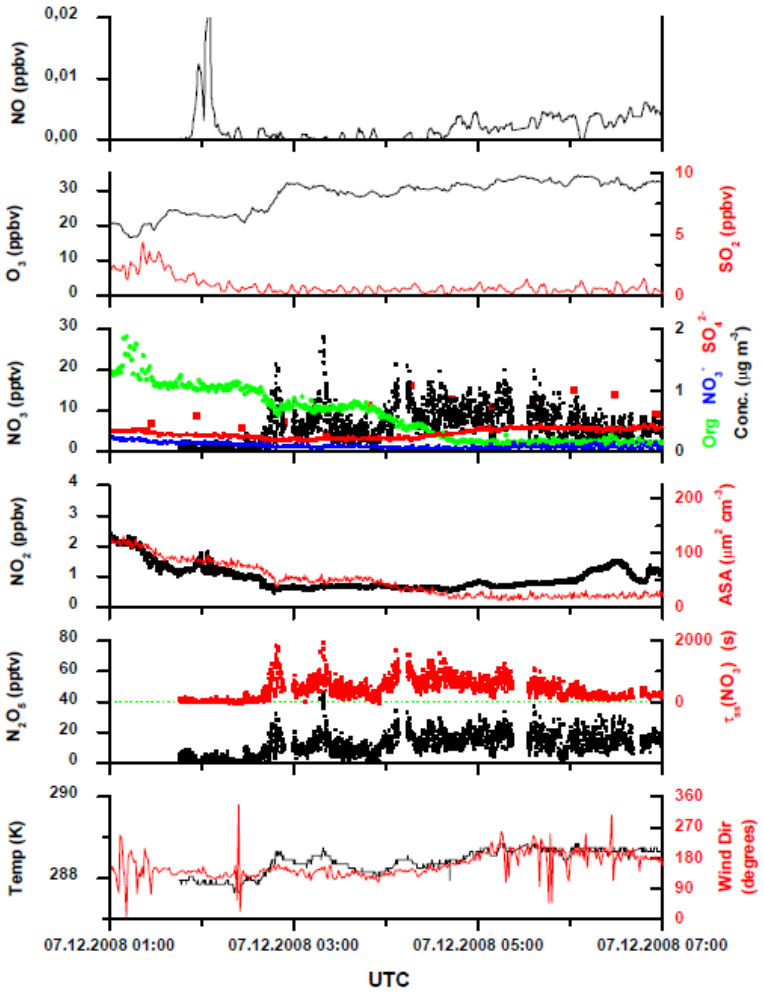

Figure 4: Overview of measurements on the night 6th–7th December (air from the Atlantic sector). ASA = Aerosol surface area. For NO_3, the black dataponts are derived from CRD measurements of N_2O_5, the red squares (at ~30 min intervals) are LP-DOAS measurements.

Selected trace gas and aerosol measurements, meteorological data and calculated NO_3 lifetimes are plotted in Figure 4. After 02:30, O_3 levels were between 25 and 35 ppb, with NO_2 close to 1 ppbv, resulting in comparatively low NO_3 production rates (~2×10^{-2} ppt s^{-1}). On this night, NO_3 and N_2O_5 measurements started only at 01:45 on the 7th due to instrument tests. N_2O_5 was observed at levels up to ~50 pptv with NO_3 lifetimes (calculated via E1) occasionally greater than 30 min. These represent the longest NO_3 lifetimes encountered during the campaign and are consistent with observations of extended NO_3 lifetimes in marine air at low NO_x mixing ratios (Heintz et al.,

1996; Carslaw et al., 1997a; Carslaw et al., 1997b; Allan et al., 2000). The CRD (calculated) and LP-DOAS derived NO_3 mixing ratios were in good agreement for most of the night. N_2O_5 was, however, not observed before ~02:30 and its calculated lifetime was less than ~100 s prior to this time. Similarly, NO_3 lifetimes decreased more or less constantly from 04:30 until dawn. In both cases the short NO_3 lifetime was accompanied by non-zero NO mixing ratios and enhanced NO_2 levels. Prior to 02:30 somewhat reduced O_3 mixing ratios were observed along with elevated levels of SO_2 (2-3 ppbv) and a ~ 20 pptv spike in the NO mixing ratio at 02:00, indicating some influence of local emissions. A rough estimate (ignoring dilution) of the age of the NO / NO_2 plume of ~ 350 s could be estimated from the enhancement in the NO_2 mixing ratio (~700 pptv), the NO and O_3 mixing ratios and rate constant for R1. The observation of a decrease in a biogenic trace gas (pinene) from 10-20 pptv before 02:30 to 2-3 pptv after 02:30 supports a change in air-mass origin at this time. An increase in NO after 04:30 indicated weak local emissions. The cleanest, maritime air was thus sampled between ~02:30 and 04:30 on this night.

Three rapid increases in the N_2O_5 mixing ratio (and τ NO_3) at 02:48, 03:20 and 04:06. are apparent in Figure 4. These features correlate with small increases (less than 1 °C) in the temperature and indicate an influx of air from higher (warmer) layers within the nocturnal inversion, which were less impacted by ground level emissions of e.g. NO or other reactive trace gases. This is a strong indication of large gradients in NO_3 (and N_2O_5) at the site, which were corroborated by DOAS measurements of NO_3 at three different levels (Thieser et al., manuscript in preparation for submission to the DOMINO special issue).

In order to understand the factors which limit the NO_3 lifetimes during this night we first estimate the contribution of each constrained loss process for NO_3 and N_2O_5 to see if the summed loss (in the case of N_2O_5 scaled by $K_{eq}[NO_2]$, see Equation (2) is consistent with observations. Figure 5 reveals that the lifetime of NO_3 was dependent on NO_2 mixing ratios, with the largest lifetimes associated with low NO_2 mixing ratios. Such observations are frequently taken as evidence for an important contribution of N_2O_5 losses to $f_{ss}(NO_3)$ (see E2) and we consider these first.

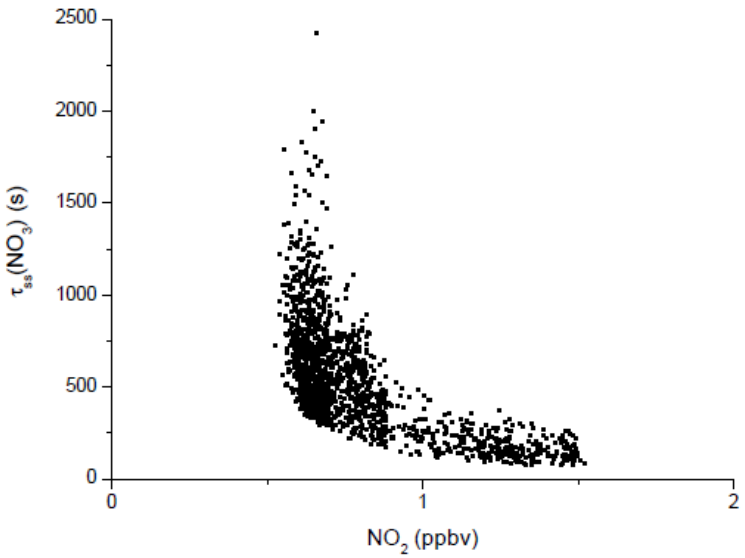

Figure 5: Dependence of NO_3 lifetime, $\tau_{ss}(NO_3)$, on NO_2 mixing ratios (night 6th–7th December). The NO_3 lifetime was calculated using K_2 and measurements of N_2O_5, NO_2 and O_3 (Eq. 1).

Loss of N_2O_5 to aerosols

The uptake coefficient for hydrolysis of N_2O_5 on aqueous, sulphate containing, tropospheric aerosol has been measured using laboratory surrogate aerosol (Mozurkewich and Calvert, 1988; Hu and Abbatt, 1997; Kane et al., 2001; Folkers et al., 2003; Badger et al., 2006; Griffiths and Cox, 2009) and a value of $\gamma \sim 0.04$ at high relative humidity has been recommended (IUPAC, 2010). This is consistent with the largest values of γ derived from calculations using field observations of NO_3 and N_2O_5 (Allan et al., 1999; Aldener et al., 2006; Ambrose et al., 2007; Bertram et al., 2009; Brown et al., 2009). Both laboratory and field work indicate that N_2O_5 uptake coefficients can be significantly lower in the presence of organic components or nitrate, although the presence of chloride can offset the nitrate effect (see e.g. (Mentel et al., 1999; Anttila et al., 2006; Bertram and Thornton, 2009; Griffiths et al., 2009; Riemer et al., 2009)). Riemer et al. (2009) showed that the uptake coefficient of N_2O_5 on a pure inorganic aerosol depended on the sulphate to nitrate ratio with maximum values of $\gamma(N_2O_5) = 0.02$ on pure sulphate, which reduced to ~0.01 when the sulphate and nitrate masses were equivalent. Bertram et al (2009) measured N_2O_5 reactivity on ambient aerosol and found for one air sample a maximum value of γ between 0.03 and 0.04 when the ratio of organic-to-sulphate particle mass was ~2.5. This decreased to 0.01 with an organic-to-sulphate ratio of 10. Bertram and Thornton (Bertram and Thornton, 2009) also describe the particle water molarity dependence of $\gamma(N_2O_5)$ on the uptake of N_2O_5 to NH_4HSO_4 aerosol. Maximum values of γ (N_2O_5) = 0.03 were found when the H_2O molarity was 20 or greater, but which decreased rapidly below this threshold. Given that the organic mass fraction of the particles was frequently above 50 % before 04:30, lower values of γ than 0.03 will apply irrespective of the nitrate content. Not only the organic mass fraction of the aerosol but also the oxidation state of the condensed organic species influences the rates of uptake of both N_2O_5 and NO_3, either indirectly via the water fraction of the aerosol (N_2O_5) or directly via the number of double bonds available for NO_3 to react with.

During the night 6th-7th December the total aerosol surface area was low, consistent with relatively clean maritime air masses, with maximum values of about 90 $\mu m^2\ cm^{-3}$ at the beginning of the NO_3 / N_2O_5 measurements and decreasing to ~ 30 $\mu m^2\ cm^{-3}$ at the end of the night. The organic-to-sulphate ratio was ~4 until 04:00 when it started decreasing to a value of ~0.3 to 0.4 clearly indicating a change in air mass to a more marine one at this time.

The sulphate to (sulphate + nitrate) ratio was between ~0.6 and 0.9. The RH was above 90 % all the time so that, late in the night, with high sulphate content and high RH, aqueous aerosol should support a large uptake coefficient, i.e. up to a maximum value of ~0.04. The total NO_3 loss rate, $f_{ss}(NO_3)$, calculated using an uptake coefficient of 0.04 for the entire night is displayed in Figure 6 where various contributors are compared. For most of the night, the low aerosol surface areas meant that N_2O_5 uptake to aerosol (RN2O5ASA) accounted for only a few percent to $f_{ss}(NO_3)$ with the exception of periods where the NO_3 lifetime was longest. For example, at 02:00 ~10 % of the calculated total loss was due to heterogeneous processing of N_2O_5. When we consider that, especially during the early stages of the measurement, the aerosol had a dominant organic component a lower value than 0.04 for γ would be more realistic, which would further decrease the contribution of N_2O_5 loss. From 04:00 onwards, the contribution of N_2O_5 uptake to $f_{ss}(NO_3)$ diminished as the NO_2 mixing ratio decreased (shifting the NO_3 / N_2O_5 equilibrium towards NO_3). At ~06:00 less than 5% of the measured loss frequency of NO_3 was due to N_2O_5 losses.

Reaction of N_2O_5 with water vapour

Laboratory experiments (Wahner et al., 1998) have provided evidence for a slow reaction between N_2O_5 and H_2O, which, under certain circumstances, (e.g. low aerosol loading) can contribute to the loss of N_2O_5.

$$N_2O_5 + nH_2O \rightarrow 2HNO_3 + (n-1)H_2O \qquad \text{(R4)}$$

The reaction was found to proceed with terms both linear and quadratic in $[H_2O]$ so that the loss rate coefficient (k_{H2O}) is described by $k_{H2O} = 2.5 \times 10^{-22} [H_2O] + 1.8 \times 10^{-39} [H_2O]^2$ s^{-1}. Measurements of long N_2O_5 lifetimes at high relatively humidity (Brown et al., 2009) strongly suggest that the true value may be a factor 10 lower. We therefore assess the impact of this reaction on NO_3 lifetimes using $0.1 \times k_{H2O}$. This is displayed as Rwater in the lower panel of Figure 6. At rates of $< 1 \times 10^{-4}$, reaction with H_2O has an insignificant impact on the overall loss rate of N_2O_5 (or NO_3) throughout the entire night.

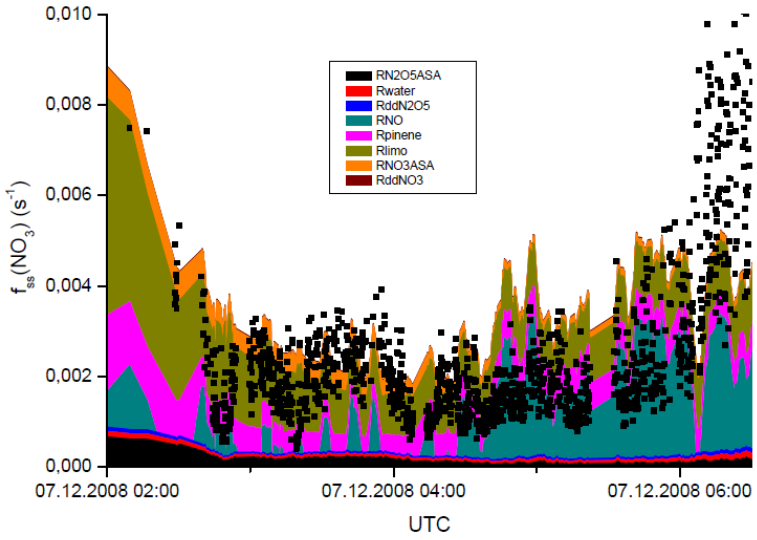

Figure 6: Apportioned NO_3 loss rates during the night 6th-7th December. The various contributions are: RN2O5ASA = uptake of N_2O_5 to aerosol, Rwater = homogeneous hydrolysis of N_2O_5 with water vapour, RddN2O5 = dry deposition of N_2O_5, RNO = reaction of NO_3 with NO, Rpinene = reaction of NO_3 with α-pinene, Rlimo = reaction of NO_3 with limonene, RNO3ASA = reaction of NO_3 on aerosol, RddNO3 = dry deposition of NO_3. The solid, black datapoints are measurements of the loss frequency of NO_3.

Dry deposition of N_2O_5

Assuming neutral stratification and zero surface resistance Geyer et al. (Geyer et al., 2001a) calculated an upper limit to the N_2O_5 loss frequency due to dry deposition within a 100m high nocturnal boundary layer as 0.3×10^{-4} s^{-1}. When multiplied by $K_2[NO_2]$, this results in a loss rate constant for NO_3 of $<1 \times 10^{-4}$ s^{-1}, contributing insignificantly to the NO_3 lifetime (RddN2O5 in lower panel of Figure 6). Assuming a factor two lower (or higher) boundary layer would not alter this conclusion.

Gas-phase reactions of NO_3

Known reaction partners for NO_3, which were constrained by measurements were NO, α-pinene, isoprene and HCHO. The reactions of NO_3 with both NO and α-pinene have large rate coefficients ($k_4 = 2.6 \times 10^{-11}$, $k_5 = 6.2 \times 10^{-12}$ cm^3 $molecule^{-1}$ s^{-1}) whereas HCHO reacts much more slowly ($k_7 = 5.6 \times 10^{-16}$ cm^3 $molecule^{-1}$ s^{-1}). Isoprene is an intermediate case with $k_6 = 7 \times 10^{-13}$ cm^3 $molecule^{-1}$ s^{-1} (Atkinson et al., 2004; Atkinson et al., 2006). At mixing ratios of less than 1 ppbv on this night HCHO did not contribute significantly to NO_3 removal and is not further considered. Likewise, isoprene mixing ratios on this night were less than those of α-pinene and limonene and as isoprene reacts a factor ~10 slower than α-pinene or limonene with NO_3, we do not need to consider R7).

$NO_3 + NO \rightarrow 2NO_2$ (R5)

$NO_3 + \alpha-pinene \rightarrow products$ (R6)

$NO_3 + isoprene \rightarrow products$ (R7)

$NO_3 + limonene \rightarrow products$ (R8)

$NO_3 + HCHO \rightarrow HNO_3 + HCO$ (R9)

The calculated, steady state, turnover loss rates of NO_3 for reaction with NO (RNO), α-pinene (Rpinene) and limonene (Rlimo) are illustrated in Figure 6. Loss of NO_3 due to reaction with α-pinene and limonene was slow reflecting the low concentrations and emission rates of biogenic trace gases during late autumn at this site (Song et al., 2011), but still significant in the early part of the night, where its contribution easily exceeds that of heterogeneous losses. The reaction with NO is unimportant until ~04:00 but thereafter becomes the dominant NO_3 sink for the rest of the night and even at mixing ratios of just 5 pptv can account for the entire observed NO_3 loss until ~6:00. After 06:00, the reaction of NO accounts for ~30 % of the observed NO_3 loss rate. Note that fine structure on the NO_3 loss rate due to R4 (RNO) is due to noise as the measurements were made close to the NO detection limit.

Loss of NO_3 to aerosols and via dry deposition

Laboratory experiments have characterised the efficiency of uptake of NO_3 to various environmental surfaces. Whereas the low solubility of NO_3 in water leads to low uptake coefficients ($\gamma_{NO3} \leq 10^{-3}$) for interaction with aqueous droplets (Rudich et al., 1996), large values ($\gamma_{NO3} \sim 0.1$) have been found for uptake to low volatility, unsaturated organic liquids (Moise et al., 2002; Gross and Bertram, 2009; Gross et al., 2009), such as those present in secondary organic aerosol. Uptake of NO_3 to urban aerosol (Tang et al., 2010) or organic aerosols (Gross et al., 2009) has been found to be orders of magnitude more efficient than N_2O_5 uptake to the same aerosol type. For the purpose of assessing the contribution of heterogeneous NO_3 loss to aerosol we have used a value of $\gamma = 0.1$, which most probably represents an upper limit to the true value. Despite the use of this large value, the loss of NO_3 to aerosol is not significant (RNO3ASA in the lower panel of Figure 6) but nonetheless exceeds N_2O_5 loss rates via uptake to aerosol when NO_2 is low (i.e. when the NO_3 / N_2O_5 equilibrium is not strongly partitioned towards N_2O_5) as seen between 02:00 and 04:00. As

for N_2O_5, dry deposition (RddNO3) is insignificant if a loss rate of 0.3×10^{-4} s^{-1} is adopted (Geyer et al., 2001a).

Summary

Some of the cleanest air-masses encountered at night in the campaign reached the measurement site on the night of 6th –7th December and NO_3 lifetimes were correspondingly long. A large fraction (and sometimes all) of the NO_3 reactivity was accounted for with measured parameters as summarised in Figure 6.

Although the results suggest that the aerosol loss of N_2O_5 contributed up to 20 % to NO_3 losses early in the night, recall that the γ used was most likely too high for aerosol with a dominant organic fraction and thus may be considered an upper limit. Missing reactivity (i.e. measured NO_3 lifetimes were shorter than calculated based on measured parameters) was apparent between circa 03:00 and 04:00 and also after 06:00. The deviation between measured and calculated NO_3 lifetimes is similar in direction and magnitude to that observed previously in marine air masses (Sommariva et al., 2007).

Considering that this air mass had spent several days over the ocean, CH_3SCH_3 (not measured) is a likely contributor to NO_3 reactivity. Strong evidence for CH_3SCH_3 in this air mass could be found in AMS measurements of significant methane-sulphonic acid concentrations on the morning of 07.12. Given a rate constant for reaction between NO_3 and CH_3SCH_3 of 1.1×10^{-12} cm^3 $molecule^{-1}$ s^{-1} (Atkinson et al., 2004) the missing reactivity observed at ~06:00 (about 0.005 s^{-1}) would be provided by ~200 pptv of CH_3SCH_3.

As already mentioned, the plot of NO_3 lifetime versus NO_2 (Figure 5) could be interpreted to indicate that indirect loss of NO_3 (i.e. via N_2O_5 removal) is an important contributor to NO_3 lifetimes. The discussion above indicates however, that the indirect losses are inefficient and a weak correlation between NO_2 and NO explains the dependence of NO_3 lifetimes on NO_2. At high NO_2 mixing ratios (e.g. 1-1.5 ppb) the calculated lifetimes are larger than measured. These data points were taken at the end of the night (after 06:00) and Figure 6 also indicates missing reactivity during this period. In the absence of a significant change in wind direction, the plume like NO_2 increases (about 0.5 ppb) during this part of the night may indicate local ship emissions and an increase in reactivity towards NO_3 due to other trace gases co-emitted.

As a significant fraction of the NO_3 reactivity is accounted for by measured NO (which must have a local source) the use of a steady-state analysis for the later part of this night is not entirely appropriate.

Low nighttime concentrations of NO have previously been reported to limit NO_3 lifetimes in a relatively clean coastal environment, which may be impacted by local NO emissions, e.g. from soil (Sommariva et al., 2007).

4.1.2 23rd – 24th November: Mixed air from the continental and Huelva sectors

Measurements of N_2O_5 on this evening started at 20:00 UTC, about 2.5 hours after sunset. The complete dataset, with meteorological information and other trace gas measurements is displayed in Figure **7**. Until midnight, the wind was mainly from the continental sector (close to 360 degrees)

whereas after midnight it came mainly from the Huelva / Port sectors. Following a warm, cloud-free day, the night of the 23rd-24th was characterised by low wind speeds and a strong temperature inversion (temperature at 50 m was ~7 °C higher than at inlet height), implying a highly stratified nocturnal boundary layer. Back trajectories (Figure 1) suggest that the air had travelled over the Atlantic before spending 1 day over central Spain- with the last 6-12 hours within the boundary layer.

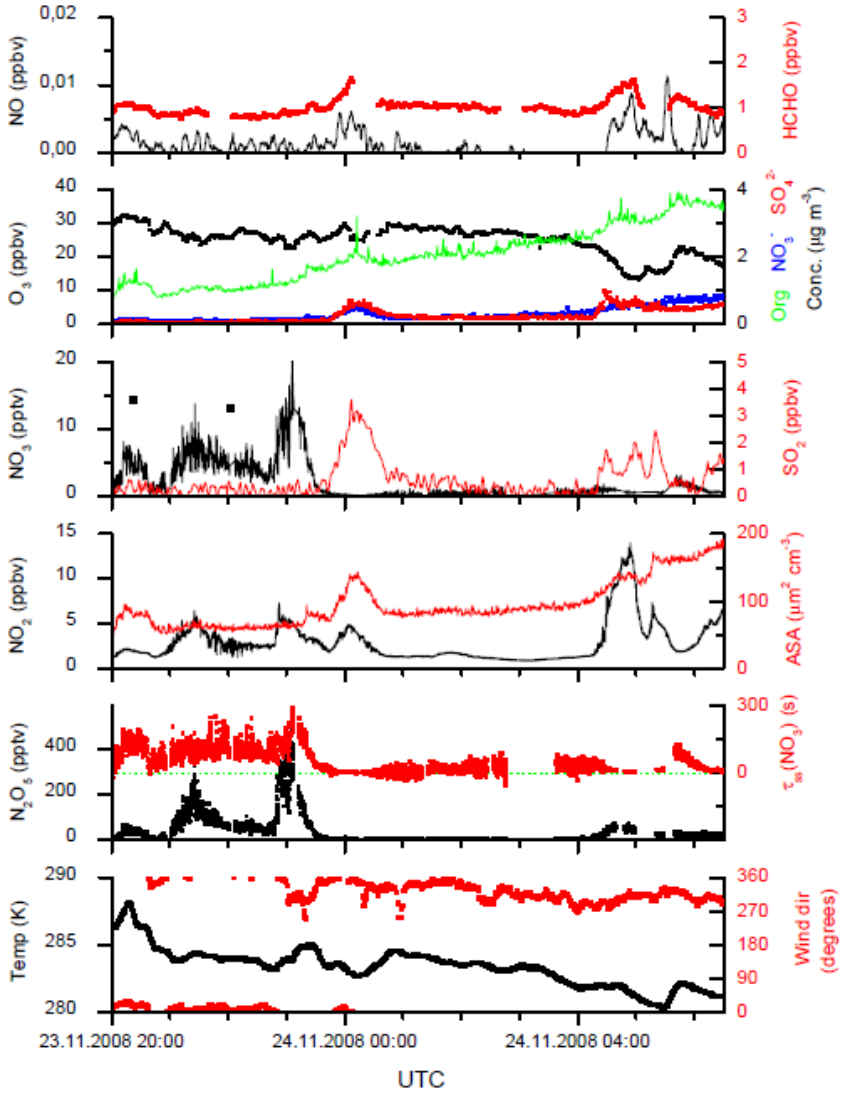

Figure 7: Overview of measurements on the night 23rd–24th in which wind direction swung from the continental to Huelva sector. Only limited LP-DOAS measurements (solid black symbols) were available from the lowest optical path on this night.

NO_2 levels showed large variability during the night with mixing ratios between 1 and 13 ppbv, whereas NO was always close to zero (< 2 pptv) until about 04:30 when a few pptv were observed. Some plume like NO_2 features were accompanied by plumes of similar duration in SO_2 (up to ~ 3 ppbv), HCHO (up to ~1.5 ppbv) and increases in the overall aerosol surface area, implying common, likely combustion related sources. This is especially apparent in the plumes at midnight and 05:00. For each of the NO_2 plumes at ~20:00, 21:30 and 23:00 there is a significant increase in the N_2O_5 mixing ratio, caused by an increase in the NO_3 production rate. In contrast, N_2O_5 remains close to the detection limit for the entire NO_2 plume at midnight and reaches only low

mixing ratios during the larger plumes at 05:00 and 06:30. Note that the NO_2 plume at ~23:00 (when SO_2 was close to zero) was accompanied by a positive gradient in the temperature, whereas the NO_2 / SO_2 plume at midnight was accompanied by a negative temperature gradient. Similarly the NO_2 / SO_2 plumes after 04:00 were accompanied by drops in temperature. The NO_2 / SO_2 plumes were also accompanied by an increase in the aerosol surface area, caused by an increase in mainly the sulphate and nitrate content, but also the organic fraction of the aerosol. This is especially apparent at midnight.

Prior to midnight, NO_2 mixing ratios between ~1 and 6 ppbv and ozone levels of > 25 ppbv resulted in large NO_3 production rates (up to ~0.12 pt s^{-1}) and the highest N_2O_5 concentrations in the entire campaign (~500 ppt) were measured. The high levels of NO_2 and moderately cold temperatures (283 K) meant that N_2O_5 was usually in greater than tenfold excess of the calculated NO_3 mixing ratio, and up to a factor of 50 greater at the peak of the NO_2 plumes. Prior to midnight, $\tau_{ss}(NO_3)$ was fairly constant at about 75-150 s but was essentially zero for the period between midnight and 01:00 during the SO_2 plume. Log-book entries report significant levels of malodorous gases at the site. The dependence of the NO_3 lifetime on NO_2 and SO_2 mixing ratios and aerosol surface area (ASA) is summarised in Figure 8. The shortest NO_3 lifetimes are clearly associated with large NO_2 concentrations (upper panel), likewise SO_2 mixing ratios above 1 ppbv are always associated with very short NO_3 lifetimes and there is also weak anti-correlation with aerosol surface area. The observed NO_2 and aerosol surface area dependencies would appear to indicate that heterogeneous loss of N_2O_5 is important. Similar to the treatment above for the Atlantic sector we therefore assess (via E2) gas-phase and heterogeneous loss mechanisms for NO_3 and N_2O_5 which were constrained by measurements and also identify potential (unmeasured) reactive trace gases.

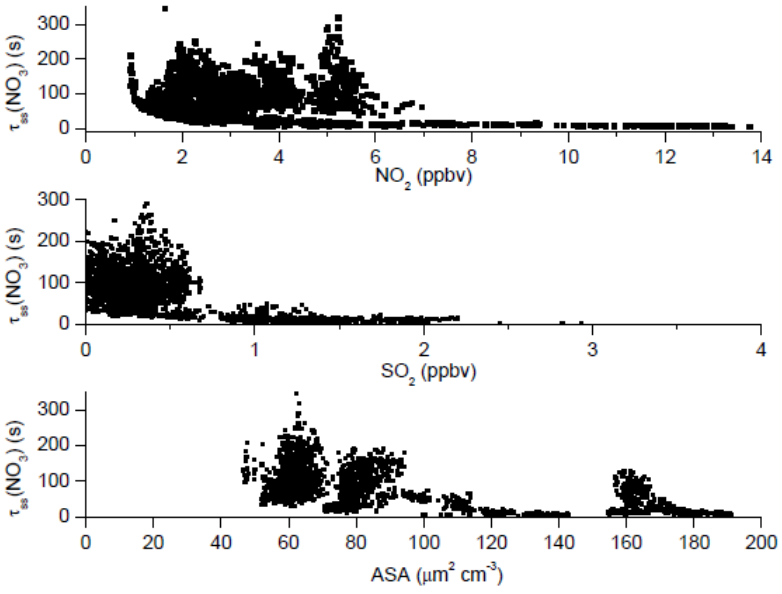

Figure 8: 23rd-24th November: Dependence of $\tau_{ss}(NO_3)$ on NO_2 and SO_2 mixing ratios and the aerosol surface area (ASA). $\tau_{ss}(NO_3)$ was calculated using measurements of N_2O_5, NO_2 and O_3 (E1).

Heterogeneous loss of NO_3 and N_2O_5

Compared to the 7th of December, the surface area available for interaction of aerosol with N_2O_5 or NO_3 was significantly larger on this night (factor of 2-3). The high levels of NO_2 observed result in large N_2O_5 / NO_3 ratios, so that the heterogeneous losses would be expected to be more important for N_2O_5 than for NO_3. For this night the aerosol contained a very high organic component (up to 75 % of the aerosol mass) with organic / sulphate ratios as high as 15 early in the night and never decreasing below about 3. The sulphate / (sulphate + nitrate) ratio was also quite low (0.3-0.7).

As discussed above, $\gamma(N_2O_5)$ on such particles would be expected to be less than 0.04. The uptake coefficient for NO_3 is poorly defined but potentially a factor of 10 larger (Tang et al., 2010). An absolute upper limit to the sum of direct and indirect NO_3 loss rates via heterogeneous uptake to aerosol was thus calculated using uptake coefficients of 0.04 for N_2O_5 and 0.5 for NO_3, the later representing diffusion limited uptake. This provides an estimate of the maximum contribution of heterogeneous reactions on aerosols to the NO_3 lifetime.

Figure 9 (lower panel) provides an overview of the relative importance of the constrained, direct and indirect loss processes for NO_3 on this night. Even though the uptake coefficients employed were upper limits, the calculated loss of N_2O_5 (RN2O5ASA) and NO_3 (RNO3ASA) to aerosols does not account entirely for the observed NO_3 loss frequency (black dots) before ~ 23:30 on the 23rd. Despite the much larger uptake coefficient used for NO_3, its contribution to the total heterogeneous loss was similar to that of N_2O_5 as the NO_3 – N_2O_5 partitioning was shifted towards N_2O_5 on this night with high NO_2 mixing ratios.

During the first SO_2 / NO_2 plume (centred at midnight) the NO_3 lifetime was drastically shortened and heterogeneous processes contribute an upper limit of ~10 % to the overall measured loss frequency of NO_3 (RN2O5ASA + RNO3ASA). Similarly, the summed effect of dry deposition of NO_3 and N_2O_5 (using the dry deposition rates listed above) can be disregarded as a major loss of either NO_3 or N_2O_5 (Rdd).

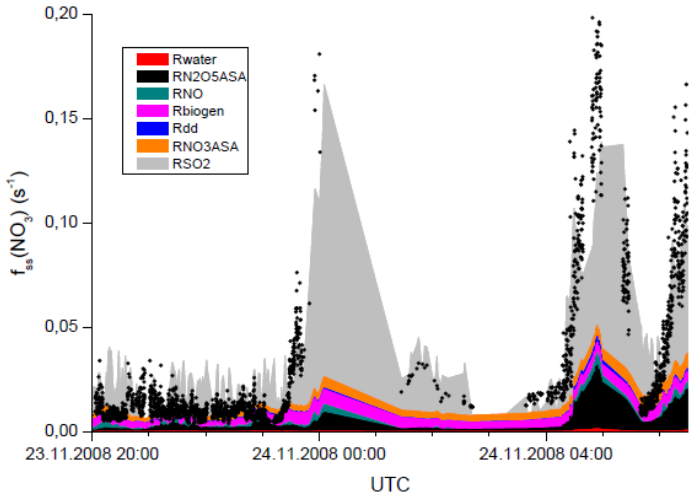

Figure 9: Apportioned NO_3 loss rates on the night 23rd-24th of November. The various contributions are: Rwater = homogeneous hydrolysis of N_2O_5 with water vapour, RN2O5ASA = uptake of N_2O_5 to aerosol, RNO = reaction of NO_3 with NO, Rbiogen = reaction of NO_3 with isoprene, limonene and α-pinene, Rdd = summed dry deposition of N_2O_5 and NO_3, RNO3ASA = reaction of NO_3 on aerosol, RSO2 is the missing reactivity which has been scaled to correlate with SO_2 mixing ratios. The black dots datapoints are the calculated loss frequency of NO_3.

Gas-Phase reactions of NO_3 and N_2O_5

Similar to the 7th of December, the homogeneous hydrolysis of N_2O_5 is not an important loss process in this air mass, contributing less than 1 % to the NO_3 reactivity (Rwater in the lower panel of Figure 9). Close to zero levels of NO during most of this night also rule out a significant impact (RNO). The sum of the direct NO_3 loss rates due to BVOC (the sum of α-pinene, limonene and isoprene, Rbiogen) contributes significantly to NO_3 loss before 23:00, but only a few percent during the SO_2 plumes. Further measured trace gases which can react with NO_3 are HCHO and aromatics. At a mixing ratio of close to 1 ppbv and a rate coefficient close to 5×10^{-16} cm^3 $molecule^{-1}$ s^{-1} (Atkinson et al., 2006) HCHO can contribute a negligible 1×10^{-5} s^{-1} to the overall NO_3 loss rate. Similarly, with respective room temperature rate coefficients of $<3 \times 10^{-17}$, 7×10^{-17}, $\sim 4 \times 10^{-16}$ and $<6 \times 10^{-16}$ cm^3 $molecule^{-1}$ s^{-1} (Atkinson and Arey, 2003), benzene (~80 pptv), toluene (~100 pptv), xylenes (sum of *p,m* and *o*-xylene was ~20 pptv) and ehylbenzene (8 pptv) all react too slowly with NO_3 to contribute significantly.

Under certain circumstances, RO_2 (formed e.g. from NO_3 initiated oxidation of CH_3SCH_3 or ozonolysis of BVOC) has been shown to contribute to NO_3 loss (Sommariva et al., 2009). On this night, RO_2 mixing ratios of up to 80 pptv were observed between ~midnight and 04:00 (Andrés-Heranández et al., to be submitted to the DOMINO special issue). In the absence of speciated RO_2 measurements we calculate the loss rate of NO_3 due to reaction with RO_2 assuming a rate coefficient of 2.3×10^{-12} cm^3 $molecule^{-1}$ s^{-1} taken from evaluated kinetic data (Atkinson et al., 2006). This results in NO_3 loss rates of $\sim 5 \times 10^{-3}$ s^{-1}, which again is only a small fraction of the total loss rate (~ 4 % at midnight).

Clearly, the sum of constrained indirect and direct losses of NO_3 do not explain the short lifetimes observed during the SO_2 plumes. As heterogeneous processing cannot be enhanced in rate beyond that calculated using measured aerosol surface areas and upper limits for $\gamma(NO_3)$ and $\gamma(N_2O_5)$ we turn to potential gas-phase reactions, that were not constrained by measurements at the site.

Unknown or undetermined reactions/loss processes

The aerosol surface area and trace gases which were measured provided only a fraction of the observed reactivity after midnight on the 23rd-24th. A clue to the missing reactivity may be provided by the very short NO_3 lifetimes (or absence of N_2O_5) when SO_2 was present at levels above ~1 ppbv (Figures 7 and 8).

Whilst SO_2 itself does not react with NO_3, it may be co-emitted or co-located with emissions of more reactive traces gases. Two scenarios are considered below in which reduced sulphur species or unsaturated VOCs are responsible for efficient NO_3 loss during periods of enhanced SO_2 on this night.

A log-book entry describes strongly malodorous air at the measurement site on this (and several other) nights. Malodorous, reduced sulphur compounds (RSC) are often associated with oil refining, pulp/paper mill and waste treatment activities (Nunes et al., 2005; Pal et al., 2009; Toda et al., 2010) and we note that not only a huge oil-refinery complex but also Spain's largest pulp/paper mill is located in Huelva.

RSC with high reactivity to NO_3 are CH_3SCH_3 (DMS), CH_3SSCH_3 (DMDS) and CH_3SH. NO_3 lifetimes are known to be strongly influenced by DMS emissions in marine air masses (Allan et al., 2000; Aldener et al., 2006; Sommariva et al., 2009) but a large contribution to NO_3 loss in urban air has also been reported (Shon and Kim, 2006). The oxidation of RSC by NO_3 results in the formation of SO_2, HCHO and RO_2 (Jensen et al., 1992) with (modelled) RO_2 levels often exceeding those observed during daylight (Sommariva et al., 2009). The rate coefficients for reaction of DMS, DMDS and CH_3SH with NO_3 are all close to 1×10^{-12} cm^3 molecule^{-1} s^{-1}, so that a total mixing ratio of these RSC of 4 ppbv would provide an equivalent reactivity of 0.1 s^{-1}. Whilst no measurements of RSC were available to support their potential role, we note that ppbv mixing ratios are not unrealistic as RSC emitted into a shallow, highly stratified boundary layer at night have no gas-phase loss mechanisms apart from reaction with NO_3. Human odour thresholds for H_2S, CH_3SH, CH_3SCH_3 and CH_3SSCH_3 are also in the ppbv regime (Kim et al., 2007; Pal et al., 2009). In order to capture the NO_3 lifetime dependence on SO_2, a reactive term, considering the presence of a trace gas at a constant fraction of the SO_2 mixing ratio and reacting with NO_3 with a rate constant of 1×10^{-12} cm^3 molecule^{-1} s^{-1} (i.e. like RSC) was added to E2. The result is the grey area (RSO2) of Figure 9**.** The RSC to SO_2 ratio was adjusted (to ~two) to approximately capture the large NO_3 loss rates at midnight, bringing the measured and modelled steady state lifetime in rough agreement.

The co-incidental increases in nighttime aerosol surface area and the sulphate component of the aerosol is difficult to account for in the RSC scenario unless a sufficient rate of oxidation of SO_2 (i.e. by reaction with OH) is available. Nighttime OH could conceivably be generated by reactions of RO_2 with NO_3 (Platt et al., 1990; Geyer et al., 2003). The increase in particle sulphate at the maximum of the 3 ppbv SO_2 plume was ~ 0.5 μg m^{-3}, which would require oxidation via reaction with OH of 100 pptv of SO_2 and efficient transfer of the H_2SO_4 product to the particle phase. Assuming a total reaction time of 4 hours (maximum transport time from Huelva), this would still require a constant nighttime OH concentration en route of ~ 2×10^6 molecule cm^{-3}.

Interactions between NO_x and reduced sulphur thus provide an interesting but highly speculative explanation for some of the observations on this and other campaign nights, including short NO_3 lifetimes, high RO_2 levels and formation of HCHO and SO_2, though we note that plume like increases in SO_2 were not always accompanied by increases in HCHO as illustrated for this night in Figure 7.

In a second scenario, we consider the coincident arrival of the SO_2, NO_2 and HCHO plumes to be due to their formation in a common combustion source, either related to shipping or oil-refinery activity. During this night the wind direction swept slowly from the continental sector to the Huelva sector with the plumes in NO_2 reflecting emissions from various point sources in the coastal-Huelva region. The short lifetimes of NO_3 after midnight reflect highly reactive air masses from Huelva, but not necessarily due to RSC. Hydrocarbon emissions related to the petrochemical industry, including unsaturated VOC such as 1,3-butadiene (Roberts et al., 2003) which are reactive towards NO_3 could then be responsible for the short NO_3 lifetimes. In this scenario, the source of the peroxy radicals observed on this night would be reaction of unsaturated hydrocarbons with either NO_3 or O_3. In this context note that NO_3 reacts at least a factor 10 more slowly with unsaturated, petrochemical-related hydrocarbons (e.g. the rate coefficient for NO_3 with 1,3-butadiene is 1.0×10^{-13} cm^3 molecule^{-1} s^{-1}) than with RSC so that mixing ratios of several tens of ppbv of the alkene would be necessary to explain the short NO_3 lifetimes. In summary, air from the Huelva sector and the port/coastal region close to Huelva was highly reactive towards NO_3

resulting in very short lifetimes which were controlled by gas-phase reactions and a diminished role for heterogeneous processes (either for NO_3 or N_2O_5). Whilst RSC and unsaturated VOC were proposed as potential reaction partners for NO_3 they were not constrained by measurements and for extended periods of the night (especially when SO_2 was observable) much of the reactivity is not accounted for.

4.1.3 26th – 27th November: Air from the continental sector

On the night of the 26th-27th of November, local wind directions indicated air masses originating from continental Spain which avoided large local cities and industrial centres such as Huelva or Sevilla. Back trajectories suggested that the air had spent the last two days over central Spain and northern France before reaching the site, gradually descending from ~3500m to ground level over this period with only the last 4-6 hours spent at altitudes of less than 500 m. Local wind speeds during the night were between 2.5 and 5 m s^{-1}.

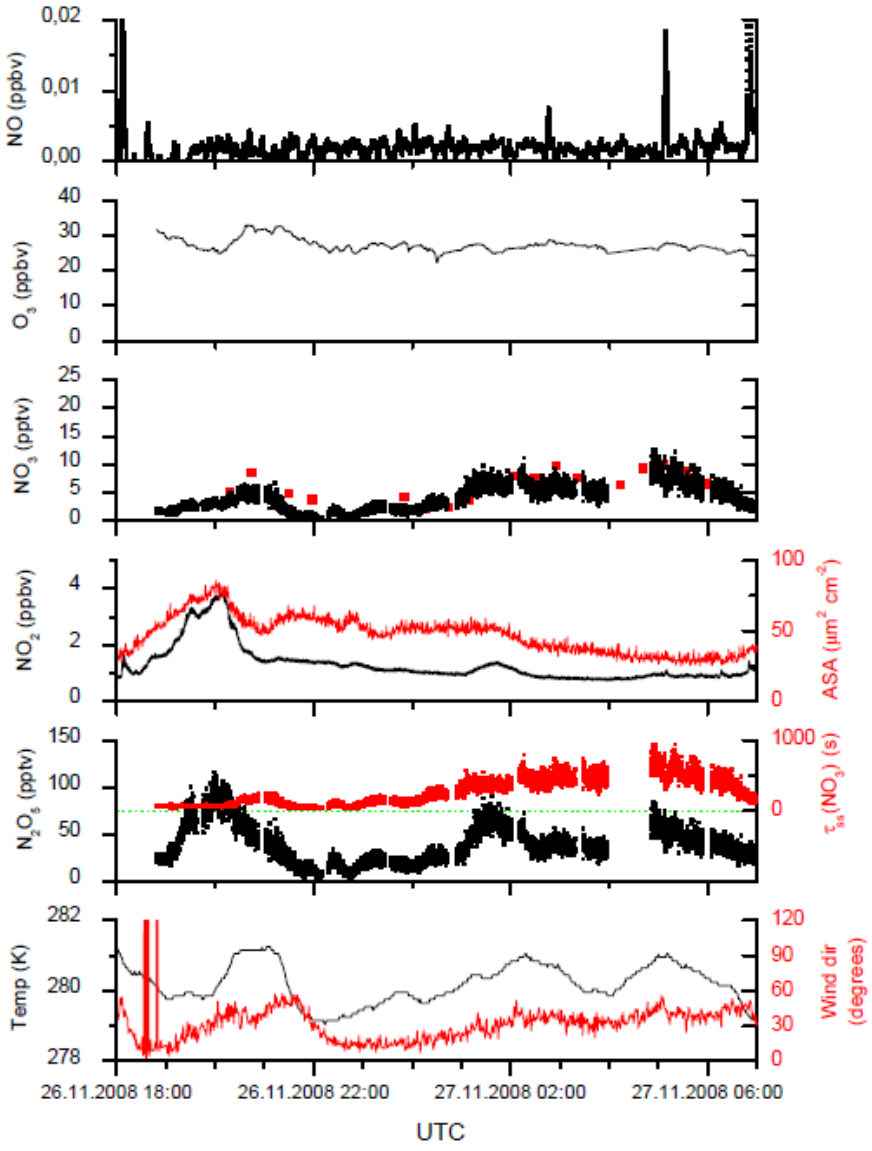

Figure 10: Overview of measurements on the night 26th-27th of November (air from the continental sector). For NO_3, the black dataponts are CRD measurements, the red squares (~30 min resolution) are DOAS measurements.

On this night, NO_2 levels were generally under 2 ppbv except for a plume-like increase to ~4 ppbv at ~20:00 on the evening of the 26th (Figure 10). As was frequently observed for the continental sector, NO_2 was correlated with black carbon but not with SO_2, indicating that emission by road traffic was the most likely source. NO was close to the detection limit (2 ppt) during the whole night, except for some spikes due to very local (likely vehicular) emissions. The constancy of the NO mixing ratio through the night strongly suggests that the true value is zero and the 2pptv is a residual from zero correction. O_3 levels were constant at ~25-30 ppbv. Levels of biogenic hydrocarbons (isoprene, pinene) were low (~10 ppt) as on other nights of the campaign. Mixing ratios of aromatics were similar to the 23rd (less than 100 pptv). Aerosol surface areas were between 25 and 80 $\mu m^2\ cm^{-3}$ and were correlated with NO_2. The aerosol was acidic (NH_4^+/ SO_4^{2-} = 0.6) with a dominant organic fraction (the organic to sulphate ratio was ~4 until 04:00 when it slowly decreased to 2).

N_2O_5 could be measured above the detection limit at almost all times during this night, with maximum mixing ratios of ~100 pptv and steady-state NO_3-lifetimes up to 900 s. Intermediate to those observed for the Huelva and Atlantic sectors. The CRD and DOAS-derived NO_3 mixing ratios were in good agreement, especially after midnight. The observations are summarised in Figure 10.

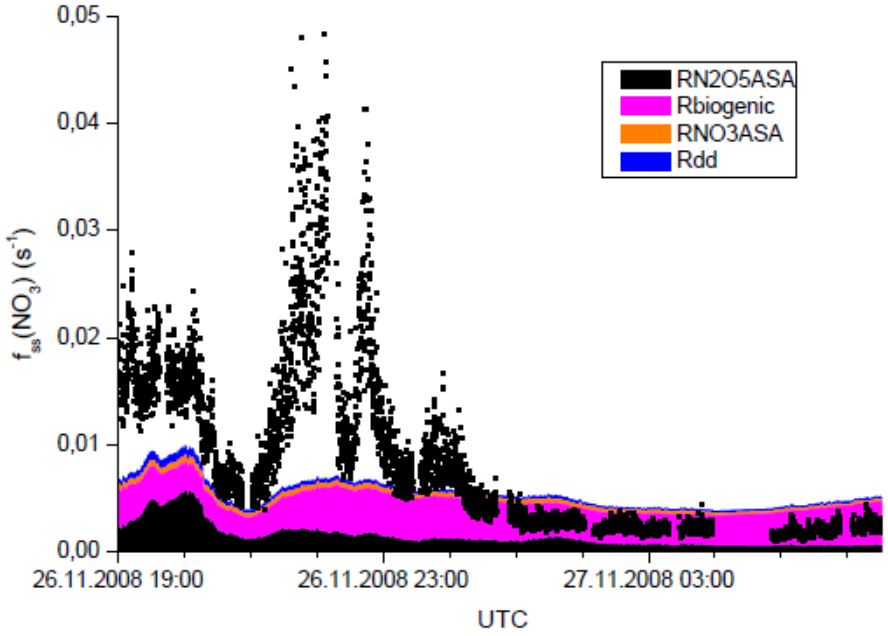

Figure 11: Apportioned NO_3 loss rates on the night 26th-27th of November. The various contributions are: RN2O5ASA = uptake of N_2O_5 to aerosol (using γ = 0.04), Rbiogen = reaction of NO_3 with isoprene, limonene and α-pinene, RNO3ASA = reaction of NO_3 on aerosol (using γ = 0.1), Rdd = summed dry deposition of N_2O_5 and NO_3. The black datapoints are measurements of loss frequency of NO_3.

As in the discussion of the previous case studies, direct and indirect losses of NO_3 were assessed based on measured aerosol surface areas and trace gases. For this purpose, NO mixing ratios were assumed to be zero. The calculations are summarised in Figure 11. Between midnight and 07:00, the presence of α-pinene and limonene at mixing ratios of 5-10 pptv results in loss rates of ~4 × 10^{-3} s^{-1}. The calculated NO_3 loss rate in this period thus exceeds that measured suggesting that reactivity is entirely accounted for by reasonably well constrained gas-phase reactions. This allows us to estimate upper bounds for the rates of all other loss mechanisms, including uptake to aerosol

on this night. The rate of direct loss of NO_3 to the organic component of the aerosol is of major uncertainty as the nature of the organic fraction (and thus availability of e.g. double bonds with which NO_3 can react) is unknown. A value of $\gamma\ NO_3 = 0.1$ contributes only insignificantly to the NO_3 lifetime whereas a value of 0.5 (diffusion limited uptake) would increase the discrepancy between observed and calculated lifetimes. A similar effect would be obtained by use of a large value (e.g. 0.1) for $\gamma(N_2O_5)$.

On this night, the organic to sulphate ratio was ~2-4 and the sulphate to (sulphate + nitrate) ratio was fairly constant at 0.6, implying a more likely value of γ (N_2O_5) of ~0.01 (Riemer et al., 2009), which is also consistent with our observations.

In the first half of the night (up to ~midnight) NO_3 lifetimes were much shorter and highly variable, with loss rates up to 0.05 s^{-1} (lifetimes of just 200s). We can rule out that this increase in the NO_3 loss frequency is due to a change in reactivity of the aerosol to either N_2O_5 or NO_3. Neither the aerosol composition (i.e., organic, nitrate and sulphate fractions and acidity) nor the relative humidity changed significantly during the night so a large change in γ (factor 10) is not anticipated. Also, the large variability in the loss frequency is not mirrored by changes in aerosol surface area, but is most likely associated with fluctuations in rates of vertical mixing within a highly stratified nocturnal boundary layer, with longer lived NO_3 present in higher layers. Inspection of the temperature and N_2O_5 trends during this night reveals significant correlation, with higher temperatures (i.e. air from higher altitudes) bringing more NO_3. Measurements of a strong vertical gradient in N_2O_5 on this night (Thieser et al, manuscript in preparation for submission to the DOMINO special issue) confirm this interpretation.

4.2 Nocturnal loss of NOx and VOCs

During DOMINO, the efficiency of nocturnal loss of NO_x to particulate phase or to long-lived reservoir species (e.g. HNO_3) which may undergo deposition, will depend both on the absolute and relative rates of processing of NO_3 (in gas-phase reactions) and N_2O_5 (in heterogeneous reactions). If direct loss processes of NO_3 are slow and N_2O_5 uptake to particles is inefficient, the NO_3-N_2O_5 equilibrium-pair represents only a temporary NO_x reservoir. N_2O_5 or NO_3 formed in the night will release NO_x at sunrise as NO_3 lifetimes are shortened by photolysis (to form both NO and NO_2) and reaction with NO (to form NO_2). N_2O_5 decomposes thermally to NO_2 and NO_3, so that NO_x is recovered and available for O_3 production. In the present campaign, nighttime lifetimes of NO_3 were generally so short that efficient irreversible loss of NO_x occurred. NO_3 lifetimes of just a few minutes imply that the rate of loss of boundary layer NO_x is approximately equal to the rate of NO_3 formation i.e.

$$L_{NOx} \approx n \cdot k_1 [NO2][O3] \quad (5)$$

where the factor *n* is 1 if NO_3 is lost only directly (e.g. by reaction with VOC) and is 2 if NO_3 is lost indirectly only via N_2O_5 formation and reaction as two NO_2 are required to make each N_2O_5 molecule. For the present campaign we have shown that, when produced at high rates, NO_3 is lost predominantly by direct routes, so that *n* should be close to 1. Figure 1**2** displays the integrated NO_x losses via reaction of NO_2 with O_3 for the three case studies outlined above. These calculations indicate that over the course of a 12 hour night, 0.8, 1.0 and 1.8 ppbv of NO_x were removed from the boundary layer on the 23-24th, 26-27th and 06-07th, respectively. This is equivalent to ~ 70 % of NO_2 as mean mixing ratios were 1.2, 2.7 and 1.3 ppbv on these nights. The

average loss rates were in the range 1.9-4.2 × 10^{-5} ppbv of NO_2 per second. Assuming that NO_3 is lost entirely by reaction with VOC (and not reaction with NO or by NO_3 or N_2O_5 uptake to aerosol), this is also the loss rate of VOC over the same period. For comparison, a 12 hour, daytime loss of NO_2 via reaction with OH of 2 × 10^{-5} s^{-1} would be obtained for average OH and NO_2 mixing ratios of 0.04 and 2000 ppt, respectively, though the greater daytime boundary layer depth would favour the OH mechanism.

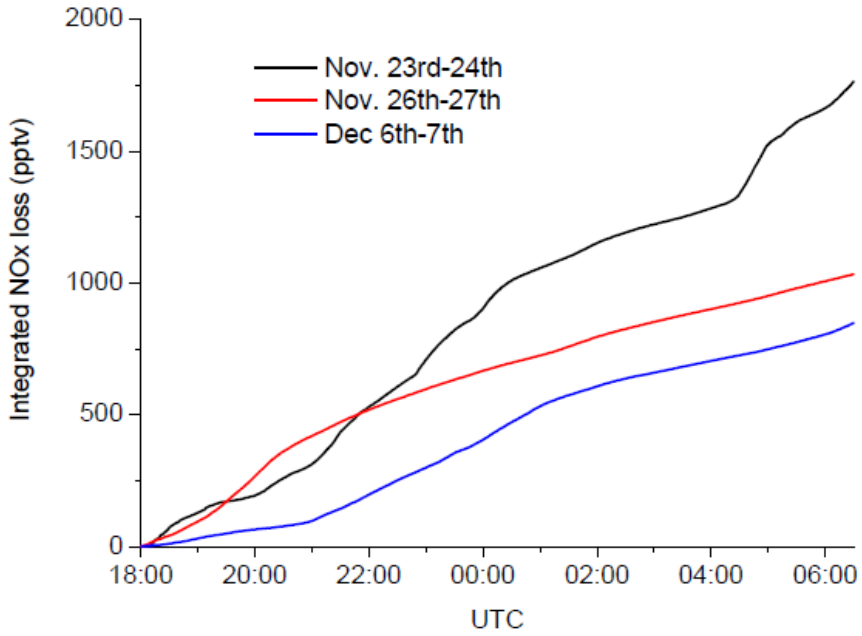

Figure 12: Integrated loss of NO*x* on three campaign nights with air from the Huelva sector (black line), the continental sector (red line) and the Atlantic sector (blue line). Mean NO_2 concentrations on these nights (18:00 til 06:30) were 2,7, 1,3 and 1,2 ppbv, for the 23-24th, 26-27th and 06-17th, respectively.

5 Summary and conclusions

Measurements of N_2O_5 and steady-state calculations of NO_3 lifetimes during the DOMINO campaign revealed stark differences according to the type of air mass encountered. The longest lifetimes (~ 30 min) of NO_3 were encountered in air masses arriving from the Atlantic sector. Air from the Huelva urban (petrochemical and industrial) sector had high production rates of NO_3, but frequently concentrations close to the detection limit and lifetimes of only a few seconds. The high reactivity could only be partially accounted for by measured trace gases and aerosol surface areas. Lifetimes of NO_3 were always very short when SO_2 was observed at the site, either due to reactions of NO_3 with RSC or due to common or co-located emissions (e.g. combustion) sources of other reactive trace gases. The relationship between the NO_3 lifetime, SO_2, NO_2 and ASA over the course of the entire campaign is illustrated in Figure 1**3**. Clearly, polluted air masses (NO_2 or SO_2 > 2 ppbv) do not support long NO_3 lifetimes.

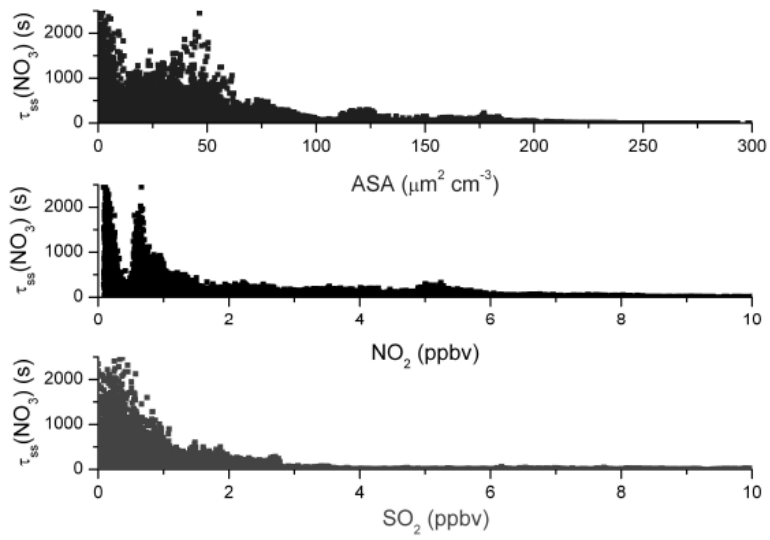

Figure 13: Relationship between NO_3 lifetimes, $\tau_{ss}(NO_3)$ and the mixing ratios of NO_2, SO_2 and aerosol surface area (ASA) during the entire campaign.

NO_3 in air from the continental sector had lifetimes which were similar to other forested areas (e.g. Crowley et al., 2010), but which were occasionally significantly shortened, presumably due to the impact of anthropogenic emissions. In general these results show that NO_3 (or N_2O_5) mixing ratios in air masses from urban and industrial centres were controlled by gas-phase reactions of NO_3 and cannot be accurately estimated from production terms (e.g. NO_2 and O_3 mixing ratios) and measured BVOC and aerosol. However, the combination of high NO_3 production rates and short lifetimes frequently observed during the campaign implies large nocturnal processing rates for the VOCs mainly responsible for NO_3 loss, and thus a high production rate of organic peroxy radicals and secondary oxidation products, such as carbonyl compounds and organic nitrates/ nitric acid.

Acknowledgements. We are indebted to the National Institute for Aerospace Technology (INTA) for hosting the campaign and to Monica Martinez (Max-Planck-Institut) for campaign organisation and management. We thank Pablo Hidalgo for information related to industrial activity in the Huelva area. We thank DuPont for providing us with the FEP dispersion.

References

Aldener, M., Brown, S. S., Stark, H., Williams, E. J., Lerner, B. M., Kuster, W. C., Goldan, P. D., Quinn, P. K., Bates, T. S., Fehsenfeld, F. C., and Ravishankara, A. R.: Reactivity and loss mechanisms of NO_3 and N_2O_5 in a polluted marine environment: Results from in situ measurements during New England Air Quality Study 2002, J. Geophys. Res.-Atmos., 111, D23S73, doi:10.1029/2006JD007252, 2006.

Allan, B.J., Carslaw, N., Coe, H., Burgess, R.A., and Plane, J.M.C.: Observations of the nitrate radical in the marine boundary layer, J. Atmos. Chem., 33, 129-154, 1999.

Allan, B.J., McFiggans, G., Plane, J.M.C., Coe, H., and McFadyen, G.G.: The nitrate radical in the remote marine boundary layer, J. Geophys. Res.-Atmos., 105, 24191-24204, 2000.

Allan, B.J., Plane, J.M.C., Coe, H., and Shillito, J.: Observations of NO_3 concentration profiles in the troposphere, J. Geophys. Res.-Atmos., 107, 4588, doi: 10.1029/2002jd002112, 2002.

Ambrose, J.L., Mao, H., Mayne, H.R., Stutz, J., Talbot, R., and Sive, B.C.: Nighttime nitrate radical chemistry at Appledore island, Maine during the 2004 international consortium for atmospheric research on transport and transformation, J. Geophys. Res.-Atmos., 112, D21302, doi:101.1029/2007JD008756, 2007.

Anttila, T., Kiendler-Scharr, A., Tillmann, R., and Mentel, T.F.: On the reactive uptake of gaseous compounds by organic-coated aqueous aerosols: Theoretical analysis and application to the heterogeneous hydrolysis of N_2O_5, J. Phys. Chem. A, 110, 10435-10443, 2006.

Atkinson, R., and Arey, J.: Atmospheric degradation of volatile organic compounds, Chem. Rev., 103, 4605-4638, 2003.

Atkinson, R., Baulch, D.L., Cox, R.A., Crowley, J.N., Hampson, R.F., Hynes, R.G., Jenkin, M.E., Rossi, M.J., and Troe, J.: Evaluated kinetic and photochemical data for atmospheric chemistry: Volume I - gas phase reactions of Ox, HOx, NOx and SOx species, Atmos. Chem. Phys., 4, 1461-1738, 2004.

Atkinson, R., Baulch, D.L., Cox, R.A., Crowley, J.N., Hampson, R.F., Hynes, R.G., Jenkin, M.E., Rossi, M.J., and Troe, J.: Evaluated kinetic and photochemical data for atmospheric chemistry: Volume II - reactions of organic species, Atmos. Chem. Phys., 3625-4055, 2006.

Badger, C.L., Griffiths, P.T., George, I., Abbatt, J.P.D., and Cox, R.A.: Reactive uptake of N_2O_5 by aerosol particles containing mixtures of humic acid and ammonium sulfate, J. Phys. Chem. A, 110, 6986-6994, 2006.

Bertram, T.H., and Thornton, J.A.: Toward a general parameterization of N_2O_5 reactivity on aqueous particles: the competing effects of particle liquid water, nitrate and chloride, Atmos. Chem. Phys., 9, 8351-8363, 2009.

Bertram, T.H., Thornton, J.A., Riedel, T.P., Middlebrook, A.M., Bahreini, R., Bates, T.S., Quinn, P.K., and Coffman, D.J.: Direct observations of N_2O_5 reactivity on ambient aerosol particles, Geophys. Res. Lett., 36, L19803, doi:10.1029/2009GL040248, 2009.

Brown, S.S., Dube, W.P., Fuchs, H., Ryerson, T.B., Wollny, A.G., Brock, C.A., Bahreini, R., Middlebrook, A.M., Neuman, J.A., Atlas, E., Roberts, J.M., Osthoff, H.D., Trainer, M., Fehsenfeld, F.C., and Ravishankara, A.R.: Reactive uptake coefficients for N_2O_5 determined from aircraft measurements during the Second Texas Air Quality Study: Comparison to current model parameterizations, J. Geophys. Res.-Atmos., 114, art. D00F10, 2009.

Brown, S.S., Dube, W.P., Osthoff, H.D., Wolfe, D.E., Angevine, W.M., and Ravishankara, A.R.: High resolution vertical distributions of NO_3 and N_2O_5 through the nocturnal boundary layer, Atmos. Chem. Phys., 7, 139-149, 2007.

Brown, S.S., Ryerson, T.B., Wollny, A.G., Brock, C.A., Peltier, R., Sullivan, A.P., Weber, R.J., Dube, W.P., Trainer, M., Meagher, J.F., Fehsenfeld, F.C., and Ravishankara, A.R.: Variability

in nocturnal nitrogen oxide processing and its role in regional air quality, Science, 311, 67-70, 2006.

Brown, S.S., Stark, H., and Ravishankara, A.R.: Applicability of the steady state approximation to the interpretation of atmospheric observations of NO_3 and N_2O_5, J. Geophys. Res.-Atmos., 108, Art. 4539, doi:10.1029/2003JD003407, 2003a.

Brown, S.S., Stark, H., Ryerson, T.B., Williams, E.J., Nicks, D.K., Trainer, M., Fehsenfeld, F.C., and Ravishankara, A.R.: Nitrogen oxides in the nocturnal boundary layer: Simultaneous in situ measurements of NO_3, N_2O_5, NO_2, NO, and O_3, J. Geophys. Res.-Atmos., 108, art. 4299, 2003b.

Carslaw, N., Carpenter, L.J., Plane, J.M.C., Allan, B.J., Burgess, R.A., Clemitshaw, K.C., Coe, H., and Penkett, S.A.: Simultaneous observations of nitrate and peroxy radicals in the marine boundary layer, J. Geophys. Res.-Atmos., 102, 18917-18933, 1997a.

Carslaw, N., Plane, J.M.C., Coe, H., and Cuevas, E.: Observations of the nitrate radical in the free troposphere at Izana de Tenerife, J. Geophys. Res.-Atmos., 102, 10613-10622, 1997b.

Crowley, J.N., Schuster, G., Pouvesle, N., Parchatka, U., Fischer, H., Bonn, B., Bingemer, H., and Lelieveld, J.: Nocturnal nitrogen oxides at a rural mountain site in south-western Germany, Atmos. Chem. Phys., 10, 2795-2812, 2010.

Diesch, J.-M., Drewnick, F., von der Weiden-Reinmüller, S.L., Martinez-Harder, M., and Borrmann, S.: Variability of Aerosol, Trace Gas and Meteorological Characteristics associated with Continental, Urban and Marin Air Masses in the Southwestern Mediterranean, Atmos. Chem. Phys. Discuss., to be submitted, 2011.

Draxler, R.R., and Rolph, G.D.: HYSPLIT (HYbrid Single-Particle Lagrangian Integrated Trajectory) Model access via NOAA ARL READY Website (http://ready.arl.noaa.gov/HYSPLIT.php). NOAA Air Resources Laboratory, Silver Spring, MD., 2011.

Folkers, M., Mentel, T.F., and Wahner, A.: Influence of an organic coating on the reactivity of aqueous aerosols probed by the heterogeneous hydrolysis of N_2O_5, Geophys. Res. Lett., 30, 1644, doi: 10.1029/2003GL017168, 2003.

Geyer, A., Ackermann, R., Dubois, R., Lohrmann, B., Muller, T., and Platt, U.: Long-term observation of nitrate radicals in the continental boundary layer near Berlin, Atmospheric Environment, 35, 3619-3631, 2001a.

Geyer, A., Alicke, B., Konrad, S., Schmitz, T., Stutz, J., and Platt, U.: Chemistry and oxidation capacity of the nitrate radical in the continental boundary layer near Berlin, J. Geophys. Res.-Atmos., 106, 8013-8025, 2001b.

Geyer, A., Bachmann, K., Hofzumahaus, A., Holland, F., Konrad, S., Klupfel, T., Patz, H.W., Perner, D., Mihelcic, D., Schafer, H.J., Volz-Thomas, A., and Platt, U.: Nighttime formation of peroxy and hydroxyl radicals during the BERLIOZ campaign: Observations and modeling studies, J. Geophys. Res.-Atmos., 108, 2003.

Geyer, A., and Stutz, J.: Vertical profiles of NO_3, N_2O_5, O_3, and NOx in the nocturnal boundary layer: 2. Model studies on the altitude dependence of composition and chemistry (vol 109, art no D16399, 2004), J. Geophys. Res.-Atmos., 109, 2004.

Gordon, I.E., Rothman, L.S., Gamache, R.R., Jacquemart, D., Boone, C., Bernath, P.F., Shephard, M.W., Delamere, J.S., and Clough, S.A.: Current updates of the water-vapor line list in HITRAN: A new "diet" for air-broadened half-widths, J. Quant. Spectrosc. Radiat. Transfer, 108, 389-402, 2007.

Griffiths, P.T., Badger, C.L., Cox, R.A., Folkers, M., Henk, H.H., and Mentel, T.F.: Reactive uptake of N_2O_5 by aerosols containing dicarboxylic acids. Effect of particle phase, composition, and nitrate content, J. Phys. Chem. A, 113, 5082-5090, 2009.

Griffiths, P.T., and Cox, R.A.: Temperature dependence of heterogeneous uptake of N_2O_5 by ammonium sulfate aerosol, Atmospheric Science Letters, 10, 159-163, 2009.

Gross, S., and Bertram, A.K.: Products and kinetics of the reactions of an alkane monolayer and a terminal alkene monolayer with NO_3 radicals, J. Geophys. Res.-Atmos., 114, D02307, doi:10.1029/2008JD010987, 2009.

Gross, S., Iannone, R., Xiao, S., and Bertram, A.K.: Reactive uptake studies of NO_3 and N_2O_5 on alkenoic acid, alkanoate, and polyalcohol substrates to probe nighttime aerosol chemistry, Phys. Chem. Chem. Phys., 11, 7792-7803, 2009.

Heintz, F., Platt, U., Flentje, H., and Dubois, R.: Long-term observation of nitrate radicals at the tor station, Kap Arkona (Rugen), J. Geophys. Res.-Atmos., 101, 22891-22910, 1996.

Hu, J.H., and Abbatt, J.P.D.: Reaction probabilities for N_2O_5 hydrolysis on sulfuric acid and ammonium sulfate aerosols at room temperature, jpc-A, 101, 871-878, 1997.

IUPAC. Subcommittee for gas kinetic data evaluation. (Ammann, M., Atkinson, R., Cox, R.A., Crowley, J.N., Hynes, R. G., Jenkin, M.E., Mellouki, W., Rossi, M. J., Troe, J. and Wallington, T. J.) Evaluated kinetic data: http://www.iupac-kinetic.ch.cam.ac.uk/,, 2010.

Jensen, N.R., Hjorth, J., Lohse, C., Skov, H., and Restelli, G.: Products and mechanisms of the gas-phase reactions of NO_3 with CH_3SCH_3, CD_3SCD_3, CH_3SH and CH_3SSCH_3, J. Atmos. Chem., 14, 95-108, 1992.

Kane, S.M., Caloz, F., and Leu, M.T.: Heterogeneous uptake of gaseous N_2O_5 by $(NH_4)_2SO_4$, NH_4HSO_4, and H_2SO_4 aerosols, J. Phys. Chem. A, 105, 6465-6470, 2001.

Kelly, T.J., and Fortune, C.R.: Continuous monitoring of gaseous formaldehyde using an improved fluorescence approach, Int. J. Environ. Anal. Chem, 54, 249-263, 1994.

Kim, K.H., Jeon, E.C., Choi, Y.J., and Koo, Y.S.: The emission characteristics and the related malodour intensities of gaseous reduced sulfur compounds (RSC) in a large industrial complex (vol 40, pg 4478, 2006), Atmospheric Environment, 41, 3728-3728, 2007.

Kley, D., and McFarland, M.: Chemiluminescence detector for NO and NO_2, Atmos. Technol., 12, 63-69, 1980.

Martinez, M., Perner, D., Hackenthal, E.M., Kulzer, S., and Schutz, L.: NO_3 at Helgoland during the NORDEX campaign in October 1996, JGR, 105, 22685-22695, 2000.

Mentel, T.F., Sohn, M., and Wahner, A.: Nitrate effect in the heterogeneous hydrolysis of dinitrogen pentoxide on aqueous aerosols, Phys. Chem. Chem. Phys., 1, 5451-5457, 1999.

Merten, A., Tschritter, J., and Platt, U.: Design of differential optical absorption spectroscopy long-path telescopes based on fiber optics, Appl. Opt., 50, 738-754, 2011.

Moise, T., Talukdar, R.K., Frost, G.J., Fox, R.W., and Rudich, Y.: Reactive uptake of NO_3 by liquid and frozen organics, J. Geophys. Res.-Atmos., 107, D2, doi: 10.1029/2001JD000334, 2002.

Mozurkewich, M., and Calvert, J.G.: Reaction probability of N_2O_5 on aqueous aerosols, J. Geophys. Res.-Atmos., 93, 15889-15896, 1988.

Nunes, L.S.S., Tavares, T.M., Dippel, J., and Jaeschke, W.: Measurements of atmospheric concentrations of reduced sulphur compounds in the All Saints Bay area in Bahia, Brazil, J. Atmos. Chem., 50, 79-100, 2005.

Osthoff, H.D., Pilling, M.J., Ravishankara, A.R., and Brown, S.S.: Temperature dependence of the NO_3 absorption cross-section above 298 K and determination of the equilibrium constant for $NO_3 + NO_2 <-> N_2O_5$ at atmospherically relevant conditions, Phys. Chem. Chem. Phys., 9, 5785-5793, 2007.

Pal, R., Kim, K.H., Jeon, E.C., Song, S.K., Shon, Z.H., Park, S.Y., Lee, K.H., Hwang, S.J., Oh, J.M., and Koo, Y.S.: Reduced sulfur compounds in ambient air surrounding an industrial region in Korea, Environmental Monitoring and Assessment, 148, 109-125, 2009.

Platt, U., Lebras, G., Poulet, G., Burrows, J.P., and Moortgat, G.: Peroxy-radicals from nighttime reactions of NO_3 with organic compounds, Nature, 348, 147-149, 1990.

Pöhler, D., Vogel, L., Friess, U., and Platt, U.: Observation of halogen species in the Amundsen Gulf, Arctic, by active long-path differential optical absorption spectroscopy, Proc. Natl. Acad. Sci. U. S. A., 107, 6582-6587, 2010.

Riemer, N., Vogel, H., Vogel, B., Anttila, T., Kiendler-Scharr, A., and Mentel, T.F.: Relative importance of organic coatings for the heterogeneous hydrolysis of N_2O_5 during summer in Europe, J. Geophys. Res.-Atmos., 114, art. Nr D17307, 2009.

Roberts, J.M., Jobson, B.T., Kuster, W., Goldan, P., Murphy, P., Williams, E., Frost, G., Riemer, D., Apel, E., Stroud, C., Wiedinmyer, C., and Fehsenfeld, F.: An examination of the chemistry of peroxycarboxylic nitric anhydrides and related volatile organic compounds during Texas Air Quality Study 2000 using ground-based measurements, J. Geophys. Res.-Atmos., 108, 2003.

Roberts, J.M., Osthoff, H.D., Brown, S.S., Ravishankara, A.R., Coffman, D., Quinn, P., and Bates, T.: Laboratory studies of products of N_2O_5 uptake on Cl- containing substrates, Geophys. Res. Lett., 36, 2009.

Rudich, Y., Talukdar, R.K., Ravishankara, A.R., and Fox, R.W.: Reactive uptake of NO_3 on pure water and ionic solutions, JGR, 101, 21023-21031, 1996.

Schuster, G., Labazan, I., and Crowley, J.N.: A cavity ring down / cavity enhanced absorption device for measurement of ambient NO_3 and N_2O_5, Atmos. Meas. Tech., 2, 1-13, 2009.

Shon, Z.H., and Kim, K.H.: Photochemical oxidation of reduced sulfur compounds in an urban location based on short time monitoring data, Chemosphere, 63, 1859-1869, 2006.

Sommariva, R., Osthoff, H.D., Brown, S.S., Bates, T.S., Baynard, T., Coffman, D., de Gouw, J.A., Goldan, P.D., Kuster, W.C., Lerner, B.M., Stark, H., Warneke, C., Williams, E.J., Fehsenfeld, F.C., Ravishankara, A.R., and Trainer, M.: Radicals in the marine boundary layer during NEAQS 2004: a model study of day-time and night-time sources and sinks, Atmos. Chem. Phys., 9, 3075-3093, 2009.

Sommariva, R., Pilling, M.J., Bloss, W.J., Heard, D.E., Lee, J.D., Fleming, Z.L., Monks, P.S., Plane, J.M.C., Saiz-Lopez, A., Ball, S.M., Bitter, M., Jones, R.L., Brough, N., Penkett, S.A., Hopkins, J.R., Lewis, A.C., and Read, K.A.: Night-time radical chemistry during the NAMBLEX campaign, Atmos. Chem. Phys., 7, 587-598, 2007.

Song, W., Williams, J., Yassaa, N., Regelin, E., Harder, H., Martinez, M., Carnero, J.A.A., Hidalgo, P.J., Bozem, H., and Lelieveld, J.: Characterization of biogenic enantiomeric monoterpenes and anthropogenic BTEX Compounds at a Mediterranean Stone pine Forest site in Southern Spain, to be submitted, 2011.

Stutz, J., and Platt, U.: Numerical analysis and estimation of the statistical error of differential optical absorption spectroscopy measurements with least-squares methods, Appl. Opt., 35, 6041-6053, 1996.

Tang, M.J., Thieser, J., Schuster, G., and Crowley, J.N.: Uptake of NO_3 and N_2O_5 to Saharan dust, ambient urban aerosol and soot: a relative rate study, Atmos. Chem. Phys., 10, 2965-2974, 2010.

Thornton, J.A., Kercher, J.P., Riedel, T.P., Wagner, N.L., Cozic, J., Holloway, J.S., Dube, W.P., Wolfe, G.M., Quinn, P.K., Middlebrook, A.M., Alexander, B., and Brown, S.S.: A large atomic chlorine source inferred from mid-continental reactive nitrogen chemistry, Nature, 464, 271-274, 2010.

Toda, K., Obata, T., Obolkin, V.A., Potemkin, V.L., Hirota, K., Takeuchi, M., Arita, S., Khodzher, T.V., and Grachev, M.A.: Atmospheric methanethiol emitted from a pulp and paper plant on the shore of Lake Baikal, Atmospheric Environment, 44, 2427-2433, 2010.

Vandaele, A.C., Hermans, C., Simon, P.C., Carleer, M., Colin, R., Fally, S., Merienne, M.F., Jenouvrier, A., and Coquart, B.: Measurements of the NO_2 absorption cross-section from 42 000 cm^{-1} to 10 000 cm^{-1} (238-1000 nm) at 220 K and 294 K, J. Quant. Spectrosc. Radiat. Transfer, 59, 171-184, 1998.

Voigt, S., Orphal, J., Bogumil, K., and Burrows, J.P.: The temperature dependence (203-293 K) of the absorption cross sections of O_3 in the 230-850 nm region measured by Fourier-transform spectroscopy, J. Photochem. Photobiol. A-Chem., 143, 1-9, 2001.

Wagner, C., Hanisch, F., de Coninck, H.C., Holmes, N.S., Schuster, G., and Crowley, J.N.: The interaction of N_2O_5 with mineral dust: Aerosol flow tube and Knudsen reactor studies, Atmos. Chem. Phys., 8, 91-109, 2008.

Wahner, A., Mentel, T.F., and Sohn, M.: Gas-phase reaction of N_2O_5 with water vapor: Importance of heterogeneous hydrolysis of N_2O_5 and surface desorption of HNO_3 in a large teflon chamber, Geophys. Res. Lett., 25, 2169-2172, 1998.

Wayne, R.P., Barnes, I., Biggs, P., Burrows, J.P., Canosa-Mas, C.E., Hjorth, J., Le Bras, G., Moortgat, G.K., Perner, D., Poulet, G., Restelli, G., and Sidebottom, H.: The nitrate radical: Physics, chemistry, and the atmosphere, AE, 25A, 1-206, 1991.

Yokelson, R.J., Burkholder, J.B., Fox, R.W., Talukdar, R.K., and Ravishankara, A.R.: Temperature-dependence of the NO_3 absorption spectrum, J. Phys. Chem., 98, 13144-13150, 1994.

D Quantification of the unknown HONO daytime source and its relation to NO_2

M. Sörgel[1,2], E. Regelin[3], H. Bozem[3,*], J.-M. Diesch[4], F. Drewnick[4], H. Fischer[3], H. Harder[3], A. Held[2], Z. Hosaynali-Beygi[3], M. Martinez[3], and C. Zetzsch[1,5]

[1]University of Bayreuth, Atmospheric Chemistry Research Laboratory, Bayreuth, Germany

[2]University of Bayreuth, Junior Professorship in Atmospheric Chemistry, Bayreuth, Germany

[3]Max Planck Institute for Chemistry, Atmospheric Chemistry Department, P.O. Box 3060, 55020 Mainz, Germany

[4]Max Planck Institute for Chemistry, Particle Chemistry Department, P.O. Box 3060, 55020 Mainz, Germany

[5]Fraunhofer Institute for Toxicology and Experimental Medicine, Hannover, Germany

[*]now at: University Mainz, Institute for Atmospheric Physics, Mainz, Germany

Published in Atmos. Chem. Phys., Volume 11, 10433-10447, 2011

Abstract

During the DOMINO (**D**iel **O**xidant **M**echanism **I**n relation to **N**itrogen **O**xides) campaign in southwest Spain we measured simultaneously all quantities necessary to calculate a photostationary state for HONO in the gas phase. These quantities comprise the concentrations of OH, NO, and HONO and the photolysis frequency of NO_2, $j(NO_2)$ as a proxy for j(HONO). This allowed us to calculate values of the unknown HONO daytime source. This unknown HONO source, normalized by NO_2 mixing ratios and expressed as a conversion frequency (% h^{-1}), showed a clear dependence on $j(NO_2)$ with values up to 43%h^{-1} at noon. We compared our unknown HONO source with values calculated from the measured field data for two recently proposed processes, the light-induced NO_2 conversion on soot surfaces and the reaction of electronically excited NO_2* with water vapour, with the result that these two reactions normally contributed less than 10 % (<1 % NO_2 + soot + *hν*; and <10 % NO_2* +H_2O) to our unknown HONO daytime source. OH production from HONO photolysis was found to be larger (by 20 %) than the "classical" OH formation from ozone photolysis ($O(^1D)$) integrated over the day.

1 Introduction

Nitrous acid (HONO) is an important OH radical precursor which serves as the "detergent" of the atmosphere due to its oxidizing power. Besides its importance for the atmospheric oxidation potential, HONO is part of acid and nutrient deposition to the biosphere. Moreover, growing concern exists about possible health effects due to the formation of nitrosamines (Hanst et al., 1977; Pitts et al., 1978) where HONO acts as the nitrosating agent, especially in indoor environments after wall reactions of HONO with nicotine (Sleiman et al., 2010). Despite three decades of research since the first unequivocal detection of HONO in the atmosphere (Perner and Platt, 1979), HONO formation processes in the atmosphere are still under discussion, especially during daytime where large discrepancies were found between mixing ratios calculated from known gas phase chemistry and measured daytime mixing ratios (Kleffmann et al., 2005). In the absence of light, the most favoured formation reaction is the heterogeneous disproportionation of nitrogen dioxide (NO_2):

$$2NO_2 + H_2O \rightarrow HONO + HNO_3 \quad \text{(R1)}$$

This reaction has been extensively studied on different materials like fluorinated polymers and different types of glass as reviewed by Lammel and Cape (1996), but also on building materials like concrete (Trick, 2004). It was found to be first order in NO_2 and water vapour (Sakamaki et al., 1983; Svennson et al., 1987; Pitts et al., 1984; Jenkin et al., 1988). A mechanism involving the formation of the NO_2 dimer (N_2O_4) in the gas phase was proposed (Finlayson-Pitts et al., 2003), but is not important in the real atmosphere (Kleffmann et al., 1998; Gustafsson et al., 2008). Recently, evidence for a mechanism involving reaction between adsorbed NO_2 and H (NO_2 (ads) + H(ads) → HONO (ads)) present on the surface following the dissociation of chemisorbed H_2O was found in a study on mineral dust particles with isotopically labelled water (Gustafsson et al., 2008), but the results are probably not transferable from laboratory to field conditions (Finlayson-Pitts, 2009). The disproportionation Reaction (R1) was found to be catalysed by anions at the surface of droplets (Yabushita et al., 2009; Kinugawa et al., 2011). In the absence of light, HONO formation from NO_2 on soot deactivates quite rapidly and thus was concluded to be less important for atmospheric HONO formation except for freshly emitted soot (Kleffmann et al., 1999; Arens et al., 2001; Aubin and Abbatt, 2007). The mechanism was summarized as the Reaction (R2) of reducing organic compounds $\{C\text{-}H\}_{red}$ with NO_2 (Gutzwiller et al., 2002a). A reaction similar to Reaction (R2) was postulated for the aqueous phase (Gutzwiller et al., 2002b; Ammann et al., 2005), but only proceeds at a relevant rate at high pH levels, since it is based on the well-known charge transfer reaction of phenolate with NO_2.

$$NO_2 + \{C-H\}_{red} \rightarrow HONO + \{C\}_{ox} \quad \text{(R2)}$$

$$NO + NO_2 + H_2O \rightarrow 2HONO \quad \text{(R3)}$$

$$HNO_3(ads) + NO(g) \rightarrow HONO + NO_2 \quad \text{(R4)}$$

The Reactions (R3) (via the intermediate N_2O_3) and (R4) proposed from field measurements (Calvert et al., 1994; Andres-Hernandez et al., 1996; Saliba et al., 2001) could neither explain laboratory results under low NO_X conditions (Svensson et al., 1987; Jenkin et al., 1988; Kleffmann et al., 1998, 2004) nor field experiments with low NO mixing ratios (Harrison and Kitto, 1994; Alicke et al., 2003; this study). During daytime the dominant sink for HONO is photolysis according to Reaction (R5), which forms OH.

$$HONO + h\nu \rightarrow NO + OH \quad \text{(R5)}$$

An additional sink is the reaction of HONO with OH (R6).

$$HONO + OH \rightarrow NO_2 + H_2O \quad \text{(R6)}$$

The back reaction (R7) regenerates HONO.

$$NO + OH + M \rightarrow HONO + M \quad \text{(R7)}$$

At high insolation, Reactions (R5–R7) are supposed to be in a photostationary state (PSS) (Cox, 1974; Kleffmann et al., 2005). Only few studies (Kleffmann et al., 2005; Acker et al., 2006) measured all quantities necessary to calculate the photostationary state (no net OH formation), some with j(HONO) calculated from UV measurements (Ren et al., 2003, 2006). In all these studies measured HONO values exceeded the HONO values calculated from PSS. The "dark"

heterogeneous formation (via Reactions (R1)/(R2)) was too slow (20–60 times) to explain this discrepancy (Kleffmann et al., 2003, 2005). This stimulated laboratory studies about a light-induced conversion of NO_2 to HONO or other photolytic sources of HONO as recently summarized by Kleffmann (2007). There are a variety of proposed sources dealing with light-induced NO_2 reduction including NO_2 reduction on irradiated mineral surfaces like TiO_2 (Gustafsson et al., 2006; Ndour et al., 2008). Many studies focussed on the reduction of NO_2 involving organic photosensitizers (George et al., 2005) like hydrocarbons on soot (Monge et al., 2010) or humic acids (Stemmler et al., 2006, 2007).

As already proposed from smog chamber experiments (Killus and Whitten, 1990), photolysis of deposited HNO_3/nitrate on surfaces was suggested as a daytime HONO source for rural forested environments by Zhou et al. (2002a, b, 2003) and Raivonnen et al. (2006). This mechanism is still controversial since the photolysis of HNO_3 was not found to be a photolytic source of HONO in chamber experiments (Rohrer et al., 2005), and quantum yields for HNO_3/nitrate photolysis are too low in the gas phase and in solution (Kleffmann, 2007). The photolysis of HNO_3 might be enhanced at surfaces (Finlayson-Pitts, 2009) or via organic photosensitizers as speculated by Kleffmann (2007). Recent studies showed the enhanced light absorption of surface adsorbed HNO_3 compared to the gas phase (Zhu et al., 2008, 2010), and thus higher photolysis rates of adsorbed HNO_3. These laboratory studies identified NO_2* as the main photolysis product. Zhou et al. (2011), who found that their HONO daytime source is correlated to the product of surface nitrate loading and the photolysis frequency of HNO_3, concluded that HONO formation by HNO_3 photolysis at the surface occurs via the mechanism proposed by Stemmler et al. (2006).

A direct HONO source is the photolysis of nitrophenols (Bejan et al., 2006) depending on pollution levels which govern the formation of nitrophenols.

The contribution of the reaction of electronically excited NO_2* with water vapour (R8) to the oxidation capacity of the troposphere was investigated in recent modelling studies (Wennberg and Dabdub, 2008; Sarwar et al., 2009; Ensberg et al., 2010). These studies focussed on ozone formation and concluded that there is an impact on oxidant formation for high NO_X emissions when using the rate constant of Li et al. (2008) for reactive quenching of NO_2*. Even with low NO_X emissions the influence is still noticeable, whereas using the rate constant of Crowley and Carl (1997) the impact is negligible. The portion of the reactive quenching of NO_2* by H_2O (and thus the rate constant of Reaction (R8), k_8) is still under discussion (Carr et al., 2009; Li et al., 2009; Fang et al., 2010; Blitz, 2010). In their laboratory study, Crowley and Carl (1997) did not observe any OH production via Reaction (R8) and thus derived an upper limit for the reactive quenching of NO_2* by H_2O of $k_8 = 1.2 \times 10^{-14}$ cm^3 molecules^{-1} s^{-1}. A recent study by Carr et al. (2009) confirmed these findings. In contrast to these studies which used unfocused laser beams, Li et al. (2008) observed OH production and report a one order of magnitude higher value for $k_8 = 1.7 \times 10^{-13}$ cm^3 molecules^{-1} s^{-1}.

$$NO_2^* + H_2O \rightarrow HONO + OH \qquad \text{(R8)}$$

In this study we quantify the gas phase photostationary state for HONO from measured values in Spain, calculate the values of the unknown HONO daytime source, and compare the latter with HONO formation from Reaction (R8) and the light-induced NO_2 conversion on soot (Monge et al., 2010).

2 Experimental

The **D**iel **O**xidant **M**echanism **I**n relation to **N**itrogen **O**xides (DOMINO) campaign took place at the "Atmospheric Sounding Station – El Arenosillo", a platform of the Atmospheric Research and Instrumentation Branch of the Spanish National Institute for Aerospace Technology (INTA) dedicated to atmospheric measurements in the southwest of Spain (37°05´48.03´´ N, 6°44´07.47´´ W). The measurement site was about 300 m inland from the coast of the Atlantic Ocean in a large area of uniform pine (*Pinus pinea* L.) forest with sandy soil. Only sparse buildings and streets were located around the site. The average canopy height was about 6 m. The leaf area index (LAI) for this forested area is about 1–1.5 (Gonçalves et al., 2010). About 15 km to the northwest is the industrial area of Huelva, with refineries and other heavy industry. The metropolitan area of Seville is about 70 km to the east-north-east. The campaign took place from mid November to mid December 2008.

Measurements of HONO were conducted at a height of 10 m above ground (~4 m above canopy) on a scaffold and at 1 m above ground, by commercial LOPAP instruments (**LO**ng **P**ath **A**bsorption **P**hotometer, QUMA Elektronik & Analytik, Wuppertal, Germany). The LOPAP is based on a wet chemical technique, with fast sampling of HONO as nitrite in a stripping coil and subsequent detection as an azo dye using long path absorption in 2.4 m long Teflon AF tubing. A detailed description of the instrument has been given by Heland et al. (2001) and Kleffmann et al. (2002). The instruments were placed outside directly on the scaffolds in ventilated aluminium boxes without temperature control. The temperature of the stripping coils was kept constant at 20 °C by thermostats to assure constant sampling conditions. The overall relative error of the LOPAP instruments was found to be 12 % in a recent side by side intercomparison in the field (Sörgel et al., 2011). Detection limits during DOMINO, calculated as 3σ of the noise during zero air measurements, were between 1 and 2.5 ppt.

The instrument used to measure NO_X was a high resolution and high sensitivity chemiluminescence detector (ECOPhysics CLD 790 SR, ECO-Physics, Dürnten, Switzerland) which carries out simultaneous in situ measurements of NO and NO_2. NO is measured directly, however, NO_2 is measured indirectly after conversion to NO using a blue light converter which is a solid state photolytic converter (Droplet Measurement Technologies, Boulder, Co, USA). A detailed description of the instrument, the calibration techniques and the error calculation has been given by Hosaynali-Beygi et al. (2011). Air was sampled through a polytetrafluoroethylene (PTFE) inlet line which was mounted on top of a scaffold at the measurement site at a height of 10m above the ground. From there an inlet line which consisted of 1/2´´ PTFE tubing was installed to the container. The last meter of the inlet line consisted of 1/4´´ PTFE tubing. The total uncertainty for the original 1 s data (at 2σ) based on the calculations of precision and accuracy is 6.04 ppt + 5 % of reading for NO and 8.29 ppt + 8 % of reading for NO_2 measurements. The residence time in the tubing was about 3 s. The shift in the tubing due to the reaction of NO with O_3 was thus less than 5 % for NO and less than 2 % for NO_2 during the campaign.

OH was measured by Laser Induced Fluorescence (LIF) with the "HORUS" (**H**ydr**O**xyl **R**adical measurement **U**nit based on fluorescence **S**pectroscopy) instrument (Martinez et al., 2010). The detection system was placed next to the LOPAP on top of the scaffold (10 m). The measurement uncertainty was ±18 %. Measured OH values present an upper limit due to interferences which can be up to a factor of two for some conditions (H. Harder, personal communication, 2011). The inlets for HONO, NO_X and HO_X measurements were collocated at 10 m above ground on the scaffold.

NO_2 photolysis frequencies $j(NO_2)$ were measured by filter radiometers (Meteorologie consult, Königstein, Germany) on top of the scaffold, with an uncertainty of ±5 %. The HONO photolysis frequency (j(HONO)) was calculated by multiplying $j(NO_2)$ with a factor of 0.175 (Trebs et al., 2009). By comparing different parameterizations (Kraus and Hofzumahaus, 1998; Trebs et al., 2009), the uncertainty for the calculation of j(HONO) was estimated to be 5 %. The overall (4π) photolysis frequency was calculated by increasing values of the downwelling radiation by 5 %, i.e. the portion of the upwelling radiation (albedo of UV radiation) at this site (Cancillo et al., 2005).

Photolysis frequencies for $O(^1D)$ formation ($j(O(^1D))$ were calculated using the TUV model (Version 4.1, e.g. Madronich et al., 1998) taking the ozone column from the NASA webpage (http://jwocky.gsfc.nasa.gov/teacher/ozone overhead.html).We firstly derived a factor for scaling modeled $j(NO_2)$ to measured $j(NO_2)$. This factor was then applied for scaling modelled $j(O^1D)$.

Meteorological parameters like temperature, relative humidity (RH), atmospheric pressure, wind speed and wind direction were measured with a Vaisala WXT510 (Vaisala, Helsinki, Finnland) meteorological station on top of the MoLa (**Mo**bile **La**boratory) inlet system, which was at 10m height 10m southeast of the scaffold. For details see Diesch et al. (2011). MoLa measured ozone by UV absorption with the "Airpointer" (Recordum, Mödling, Austria), water vapour mixing ratios by infrared absorption (LICOR 840, Li-COR, Lincol, USA) and black carbon with a Multi Angle Absorption Photometer (MAAP, Model 5012, Thermo Fischer Scientific, Whatman, USA).

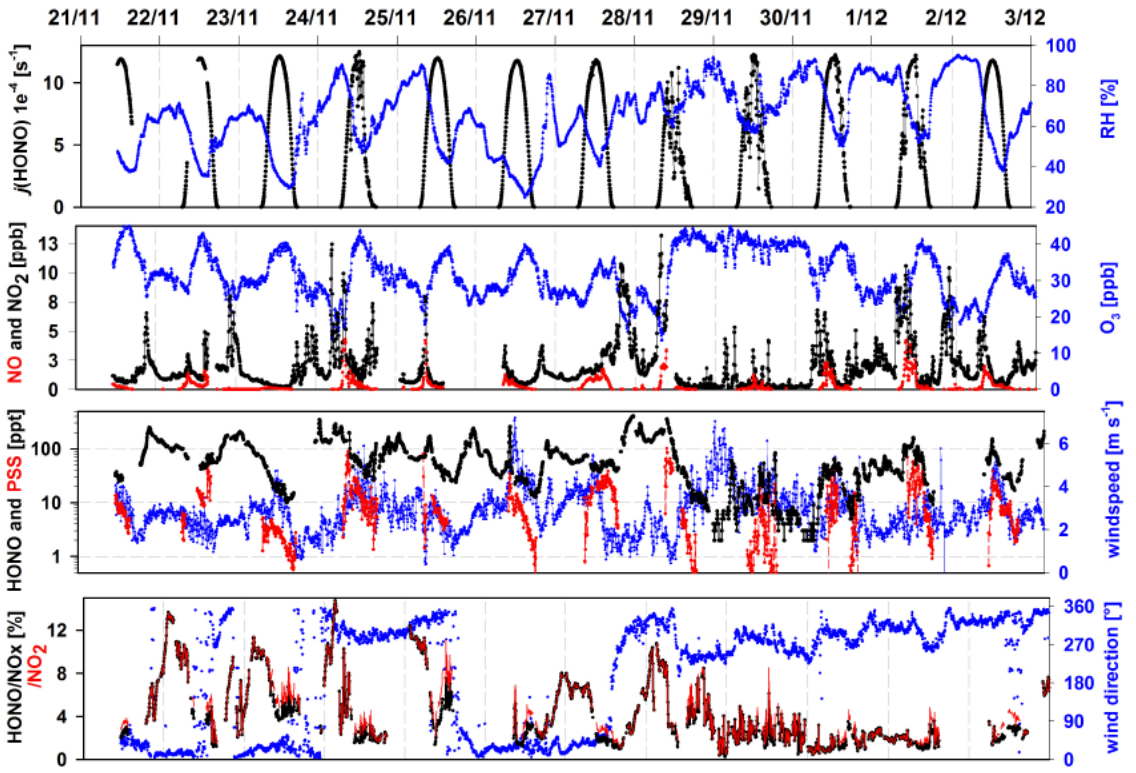

Figure 1: Overview of meteorological (RH, wind speed and wind direction) and chemical quantities (O_3, NO, NO_2, HONO, $HONO_{PSS}$ (calculated), $HONO/NO_X$ and $HONO/NO_2$ ratios and j(HONO)).

3 Results and discussion

3.1 Meteorological and chemical conditions

Figure 1 gives an overview of meteorological and chemical measurements during the experiment in November/ December 2008. In the beginning of the campaign there was a fair weather period with moderate (about 3 ms^{-1}) north-easterly winds (from inland Seville region). On 24 November, the wind direction changed to northwest (along the coast from Huelva). From the 28 to 30 November, clean marine air with some plumes arrived at the site from the west. This was also the only period with rainfall, and HONO values were often around the detection limit (2 ppt). Ozone mixing ratios were about 30 ppb and showed a diurnal variation except for the clean air period with higher values (40 ppb) and no diurnal variation. A more detailed analysis of the ozone behaviour and the different wind sectors has been given by Diesch et al. (2011).

3.2 Photostationary state (PSS)

3.2.1 Calculating the photostationary state/gas phase

Regarding only the well-established gas phase formation (R7) and gas phase sink processes (R5 and R6) one can calculate the photostationary state (PSS) mixing ratio of HONO (Cox, 1974; Kleffmann et al., 2005),

$$[HONO_{PSS}] = k_7[NO][OH] / k_6[OH] + j(HONO) \quad (1)$$

$[HONO_{PSS}]$ is the equilibrium concentration, [NO] and [OH] are the measured NO and OH concentrations, and j(HONO) is the photolysis frequency of HONO. Rate constants for the termolecular Reaction (R7) were calculated at atmospheric pressure from the fall-off curves (high and low pressure limit rate constants) according to the formulas given by the respective references (Atkinson et al., 2004; Sander et al., 2006). Values of k_7 differed by 24 % (constantly over the temperature and pressure range of our study): from IUPAC (Atkinson et al., 2004) $k_{7,(298K)} = 9.8 \times 10^{-12}$ cm^3 $molecules^{-1}$ s^{-1} and from JPL (Sander et al., 2006) $k_{7,(298K)} = 7.4 \times 10^{-12}$ cm^3 $molecules^{-1}$ s^{-1}. The calculated JPL value is consistent with the value ($k_{7,(\sim 298K)} = (7.4 \pm 1.3) \times 10^{-12}$ cm^3 $molecules^{-1}$ s^{-1}) measured directly at atmospheric pressure by Bohn and Zetzsch (1997). We therefore prefer this value and use it for our calculations of the PSS. For the bimolecular reaction of HONO and OH (R6), a rate constant of $k_{6298K} = 6.0 \times 10^{-12}$ cm^3 $molecules^{-1}$ s^{-1} was taken from Atkinson et al. (2004).

Uncertainties in the PSS mainly originate from OH measurements with an accuracy of ±18 %. This has some influence on HONO formation via Reaction (R7) but not much influence on the loss term, since HONO loss via Reaction (R7) was mostly less than 5% of the total loss (R5 and R6) during the whole campaign. As OH measurements may possibly suffer from interferences, the $[HONO_{PSS}]$ values are rather an upper limit. As a consequence, the unknown HONO source discussed in Sect. 3.3 is rather a lower limit. There is also some uncertainty in the j(HONO) values since the portions of the upwelling part of the radiation measured at the site were about 0.3–0.5 of the downwelling (direct + diffuse). These high albedo values were presumably caused by the white container roofs and the aluminium scaffold below the sensor. As the minimum HONO lifetime (inverse photolysis frequency) is about 15 min around noon, our measurements at the 10m scaffold do not reflect the local situation but an integration over a "footprint area" (Schmid, 2002; Vesala et

al., 2008). Therefore, we chose an albedo value for UV radiation of the surrounding pine forest of 0.05 (Cancillo et al., 2005) which is more representative.

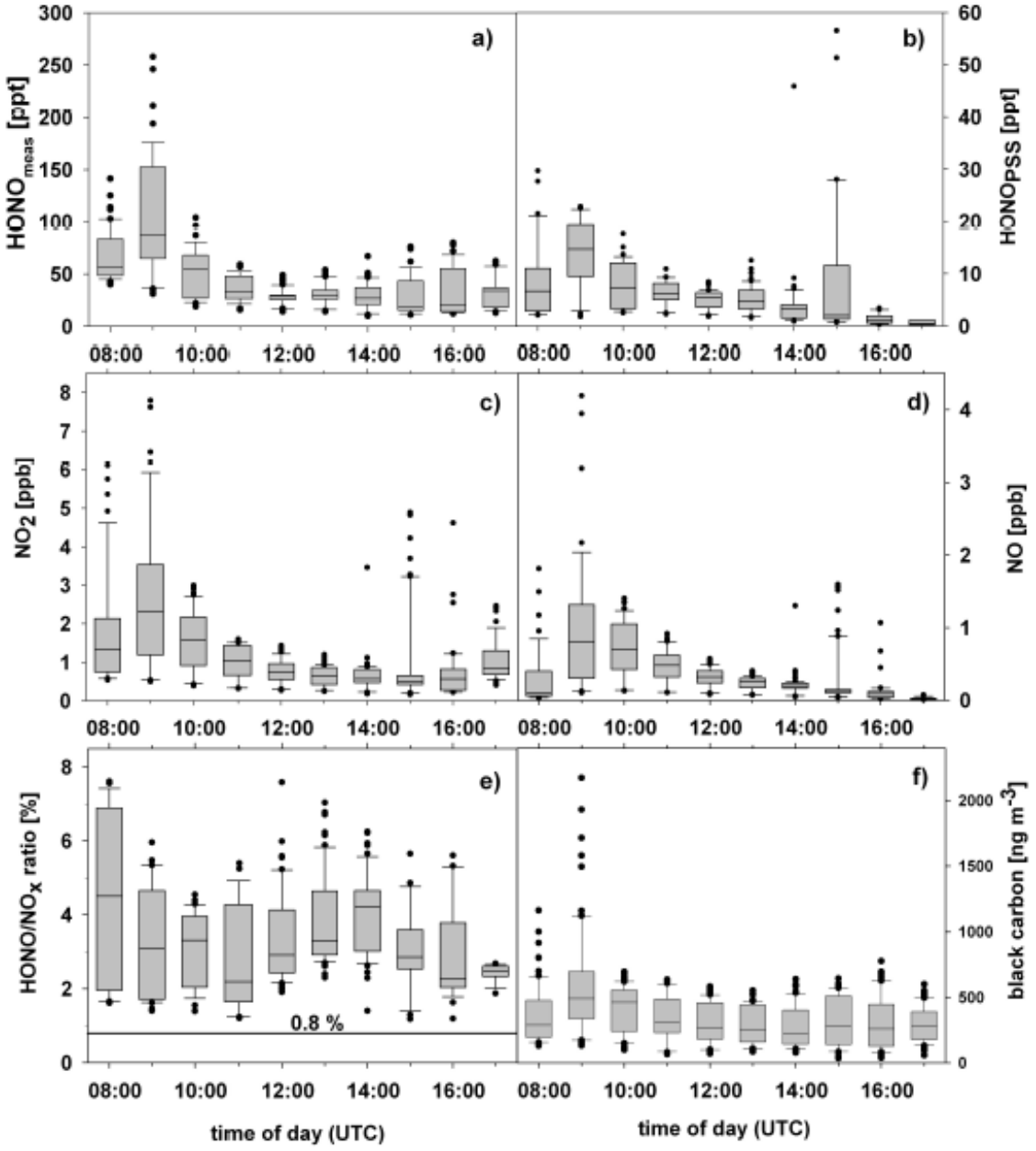

Figure 2: Daytime cycles of **(a)** measured HONO mixing ratios, $HONO_{meas}$ **(b)** calculated HONO mixing according to Eq. (1), $HONO_{PSS}$ **(c)** NO_2 and **(d)** NO mixing ratios as well as **(e)** $HONO/NO_X$ ratios with the value of 0.8 % for direct emissions (Kurtenbach et al., 2001) marked as black line and black carbon concentration **(f)**. The boxes and whiskers represent a one hour time interval (centred in the middle) of five minute data (22–72 data points) of 7 cloud free days (21 ,22, 23, 25, 26, 27 November and 2 December). The upper ends of the boxes represent the 75th percentile, the lower bounds the 25th percentile and the line within the boxes the median. The upper whisker marks the last point within the 90th percentile and the lower whisker that of the 10th percentile. Data points outside the 10th and 90th percentile are marked individually as dots.

Figure 2 summarizes the diurnal courses of HONO and NO_X for 7 cloud free days. On the 27th around noon, fair weather clouds were passing. These data points were rejected for further analysis to exclude effects from fluctuations in *j*(HONO). On 2 December, data was taken from a second LOPAP at 1 m height as there were no data available from the 10 m instrument. Both instruments have been demonstrated to agree within 12 % under dry field conditions in side-byside measurements (Sörgel et al., 2011). Assuming efficient vertical mixing during the day, HONO mixing ratios at 1 m and 10 m height can be expected to be similar (Sörgel et al., 2011).

The portion of HONO formed by known reactions in the gas phase ([$HONO_{PSS}$], Fig. 2b) is not negligible. The median contribution is 20 % (25 percentile is 13 %) of the measured HONO mixing ratios. On the other hand, the gas phase formation can explain only part of the measured HONO, as 75 % of the [$HONO_{PSS}$] values contribute less than 30 % to the measured values. $HONO_{meas}$, $HONO_{PSS}$, NO and NO_2 have a similar diurnal cycle with the most pronounced feature being the maximum values around 09:00 UTC. This could be explained by local emissions which were trapped in the stable boundary layer before the breakup of the inversion in the morning. In the afternoon (15:00–16:00), this peak occurs less pronouncedly in NO and NO_2 but very clearly in the PSS values, as OH values are about twice (~3×10^6 molecules cm^{-3}) those at 09:00. From Fig. 2b and d one can infer that [$HONO_{PSS}$] values are correlated to NO mixing ratios (r^2 =0.78). Correlations to other input parameters of the PSS are low ([OH] r^2 =0.006; *j*(HONO) r^2 = 0.01). Therefore, NO availability seems to be a driving force for HONO gas phase chemistry. Measured HONO mixing ratios (Fig. 2a) have a coefficient of determination r^2 = 0.49 with [NO_2], and r^2 = 0.36 with [NO]. The relation of the HONO formation rate (which is more appropriate than HONO mixing ratios) and NO_2 is discussed in detail in Sect. 3.3.

$HONO/NO_X$ ratios reach their daytime maximum in the early afternoon with median values around 4 % (Fig. 2e), implying efficient NO_X conversion. On the other hand, the maximum can also be attributed to sources independant from ambient NO_X values such as soil emissions (Su et al., 2011), and HNO_3 photolysis at surfaces (Zhou et al., 2011), which are not affected by the declining NO_X values in the early afternoon.

3.2.2 Including the parameterized heterogeneous HONO formation into PSS calculations

To sum up known HONO formation pathways, the heterogeneous formation ((R1)/(R2)) which was measured during nighttime may be included as an additional source in the PSS (e.g. Alicke et al., 2002, 2003) with the assumption that (R1/R2) continue at daytime in the same manner as at night.

This assumption may not be true because even at night HONO formation (release) is not proceeding at the same rate all night. Studies about HONO fluxes (Harrison and Kitto, 1994; Harrison et al., 1996; Stutz et al., 2002, 2004) explained that measured HONO formation is a net process (pseudo steady state) of release and deposition (see also discussion in Vogel et al., 2003). A recent study by Wong et al. (2011) provides detailed information about HONO formation and deposition in the **N**octurnal **B**oundary **L**ayer (NBL) by combining vertical gradient measurements with 1-D model calculations. According to their results the ground surface accounts for most (~70 %) of the HONO formation by NO_2 conversion but also for most of the loss (~70 %). This confirms previous results from ground based field measurements (Harrison and Kitto, 1994; Stutz et al., 2002; Veitel, 2002; Kleffmann et al., 2003; Zhang et al., 2009; Sörgel et al., 2011), aircraft profiles (Zhang et al., 2009) and modelling (Vogel et al., 2003) that the ground surface is a major source of HONO. Hence, turbulent exchange has a significant impact on near surface HONO

mixing ratios as already proposed by Febo et al. (1996). These authors found a good correlation of HONO with radon, which is exclusively emitted from the ground. Furthermore, profiles from recent aircraft measurements were closely related to atmospheric stability with higher HONO values close to the ground and steeper gradients during stable conditions (Zhang et al., 2009). Therefore, mixing ratios are also expected to be controlled by the mixed volume which determines the surface to volume ratio (S/V). The conventional way to account for changes in S/V is the scaling of HONO or HONO production (P_{HONO}) by NO_2 or NO_X (e.g. Alicke et al., 2002, 2003). It is assumed that NO_X is also emitted close to the ground, and therefore is also sensitive to S/V and NO_2 is the precursor of HONO. As local sources/sinks of the compounds used for scaling (e.g. NO_X) may disturb the $HONO/NO_X$ ratio, Su et al. (2008a) proposed a combined scaling using also black carbon (BC) and carbon monoxide (CO). To our knowledge, only two recent studies (Yu et al., 2009; Sörgel et al., 2011) tried to address S/V (ground and aerosol) directly by using inversion layer heights from SODAR measurements to estimate mixed volumes. However, at night a stable boundary layer is formed where only intermittent turbulence provides some mixing (Stull, 1988). Therefore, a mixed volume cannot easily be defined. Apart from that, NO_2 conversion frequencies measured in different environments around the world are all within a quite narrow range from 0.4 to 1.8%h^{-1} as summarized by Su et al. (2008a) and Sörgel et al. (2011). Conversion frequencies ($F_{HONO,night}$) of 0.9–2%h^{-1} for individual nights and a mean value of 1.5±0.6%h^{-1} were derived in this study using the approach of Alicke et al. (2002).

In our study, nighttime HONO formation occurs presumably by Reactions (R1) and (R2). Formation through Reactions (R3), (R4) and (R7), all involving NO, is not considered to be important since HONO typically increased from sunset (17:30 UTC) to midnight, when NO mixing ratios were mostly (93 %) below the detection limit (LOD) of 6 ppt. Only 87 of 1232 five-minute mean values were above the LOD with median mixing ratios of 8 ppt, respectively. Therefore, a linear regression of the $HONO/NO_X$ ratio and $HONO/NO_2$ ratio for all night time data yields a slope of 1.0 and an intercept of 0.02 % (r^2 =0.9986). Thus, both ratios can be regarded as equivalent during nighttime. There are no clear indications about the contribution of direct emissions. The closest emissions sources were the industrial area of Huelva (shortest distance ~15 km) and the city of Huelva (city centre about 20 km). Thus, transport times are in the range from one to two hours. Applying a conversion frequency for NO_2 to HONO of about 1%h^{-1}, which is within the range of published values (see above), yields a 1–2% increase in $HONO/NO_X$ during the transport. Thus, HONO mixing ratios reaching the site are already two to threefold those originally emitted ($HONO/NO_X$ ~0.8 %, Kurtenbach et al., 2001). Using the wind sector classification for the DOMINO site of Diesch et al. (2011) we found indeed lower $HONO/NO_X$ values at night for air masses passing Huelva than for other air masses from the continent. If this can be attributed to direct emissions is unclear. The transport occurs along the coast and therefore also mixing with HONO depleted marine air can cause lower $HONO/NO_X$. $HONO/NO_X$ values for Huelva are indeed within the range of those for the "clean" marine sector. Therefore, we assume that Reactions (R1)/(R2) is the dominant nightime HONO formation pathway at the DOMINO site.

Generally, a stable boundary layer is formed at nighttime in which turbulence is suppressed, whereas during daytime a mixed layer develops which is much more turbulent (e.g. Stull, 1988). This has two opposing effects on Reactions (R1) and (R2) (especially if the ground surface is the dominant source).

1. During daytime turbulence is enhanced which means that NO_2 is efficiently transported to the reactive surface.

2. The surface to volume ratio (S/V) is lower during daytime, as the mixed volume increases (mixed layer), thus less reactive surface area per volume is available.

If no deposition or advection occurs, $HONO/NO_X$ will rise continuously from sunset to sunrise, as photolysis is absent. We found decreasing $HONO/NO_X$ in the late night until sunrise which may point to the dominance of loss processes of HONO, e.g. deposition. Therefore, it is questionable if Reactions (R1) and (R2), i.e. heterogeneous formation, can simply be transferred to daytime conditions. As will be shown in Sect. 3.3 (Figs. 3 and 4), including this dark heterogeneous source as a daytime source in Eq. (3) to calculate the magnitude of the unknown daytime source $P_{unknown}$ yields mainly negative values in the early morning. This points to a missing sink like deposition (or a smaller source or both). Therefore, we did not consider this heterogeneous source for the PSS calculations.

3.3 Missing daytime source

As shown in Sect. 3.2 (Fig. 2) measured HONO values ($HONO_{meas}$) almost always exceed the $[HONO]_{PSS}$ values. Thus, an additional (unknown) HONO daytime source exists. Equation (2), which is similar to that of Su et al. (2008b), sums up the processes influencing HONO mixing ratios.

$$\begin{aligned} d\mathrm{HONO}/dt &= \text{sources} - \text{sinks} = \\ &= (P_{NO+OH} + P_{emis} + P_{het} + P_{unknown}) - (L_{phot} + L_{HONO+OH} + L_{dep}) + T_v + T_h \end{aligned} \quad (2)$$

The source/production (P_x) terms consist of the gas phase formation (P_{NO+OH}, R7), the dark heterogeneous formation (P_{het}, via R1/R2) and direct emissions (P_{emis}). $P_{unknown}$ is the unknown HONO daytime source. The sink/loss processes (L_y) are photolysis (L_{phot}, R5), reaction of HONO with OH ($L_{HONO+OH}$, R6), and dry deposition (L_{dep}). Note that the terms for vertical (T_v) and horizontal advection (T_h) can mimic source or sink terms depending on the HONO mixing ratios of the advected air relative to that of the measurement site (and height). If HONO has a ground source (or near surface aerosol source), T_v mimics a sink term, as vertical mixing dilutes HONO formed near the ground (see also discussion Sect. 3.2.2). The magnitude of T_v (without the contribution of the rising boundary layer in the morning) can be estimated by using a parameterization for dilution by background air provided by Dillon et al. (2002), i.e. $T_v = k_{(dilution)}$ ($[HONO]-[HONO]_{background}$). Assuming a $k_{(dilution)}$ of 0.23 h^{-1} (Dillon et al., 2002), a $[HONO]_{background}$ value of about 10 ppt (Zhang et al., 2009) and taking mean noontime [HONO] values of 35 ppt we can derive that T_v is about 4 ppt h^{-1}. This value is about the same magnitude as L_{dep} as already suggested by Su et al. (2008b).

L_{dep} can be parameterized by multiplying the measured HONO concentration with the dry deposition velocity and then scaling by the mixing height, in order to scale the loss at the ground to its contribution to total HONO loss in the mixed volume. Taking a deposition velocity of 2 cm s^{-1} (Harrison et al., 1996; Su et al., 2008b) and a mixing height of 1000 m, L_{dep} is in the order of a few ppt h^{-1} in our study which is indeed small (<3% of L_{phot} 09:00–15:30 UTC for 7 clear days N = 312) compared to L_{phot}. As is discussed in more detail later, the relative contribution of L_{dep} might be higher in the morning and evening hours, as L_{phot} is smaller and a stable boundary layer is formed (mixed height ≪1000 m, or stable conditions). Overall, T_v and L_{dep} are small loss terms (compared to L_{phot}). If their contributions are larger than assumed (especially in the morning and evening), $P_{unknown}$ is underestimated during these periods.

P_{emis} cannot easily be determined, because its contribution varies with the source strength, the HONO lifetime, the horizontal wind speed and wind direction. Again, this contribution is assumed to be highest in the morning and in the evening (longer lifetimes = longer transport range). As there were no collocated emission sources, directly emitted HONO only contributed to the horizontal advection term (T_h). Measured HONO/NO_X ratios were always higher than those reported for direct emissions (max. reported 0.8 %) (Pitts et al., 1984; Kirchstetter et al., 1996; Kurtenbach et al., 2001; Kleffmann et al., 2003). Thus, no pure direct emissions were measured. Therefore, the contribution of directly emitted HONO to the HONO budget is uncertain, but P_{emis} can be assumed to be of minor importance around noon, as NO_X values exhibit a minimum and show low variability. Furthermore, HONO lifetime is only about 15 min, so at typical wind speeds of about 3 ms^{-1}, emissions have to occur within 3 km to reach the site within their lifetime. Additionally, minimum values of HONO/NO_X, which indicate fresh emissions, are independant of wind direction.

Simplifying Eq. (2), we can derive the unknown HONO daytime source, $P_{unknown}$, from Eq. (3).

$$P_{unknown} = L_{HONO+OH} + L_{phot} + L_{dep} - P_{NO+OH} - P_{het} + \Delta HONO/\Delta t \quad (3)$$

P_{unknow} is not equal to OH production from HONO as for net OH formation a simple balancing of gas phase sources and sinks without further assumptions is applicable ($P_{OH} = L_{phot} - L_{HONO+OH} - P_{NO+OH}$). Mean diurnal contributions of the single terms and the values of $P_{unknown}$ are presented in Fig. 3. P_{NO+OH}, L_{phot}, $L_{HONO+OH}$ were calculated from measured values as already described for the PSS (Sect. 3.2.1). P_{het} was parameterized from the nighttime NO_2 conversion by $P_{het}(t) = F_{HONO,night}[NO_2]$ (Alicke et al., 2002) using $F_{HONO,night}$ =1.5%h^{-1} (Sect. 3.2.2). The differential dHONO/dt was substituted by the difference $\Delta HONO/\Delta t$, which is the mixing ratio difference from the centre of the interval (5 min) to the centre of the next interval (LOPAP has 5 min time resolution) and accounts for changes in mixing ratio levels. It became obvious that point to point changes in HONO ($\Delta HONO/\Delta t$) were mostly smaller than the relative error of the instrument (±12 %), and so we could not account for these changes. Values above this threshold were mainly caused by sharp HONO peaks which were accompanied with peaks in NO and BC. These plumes passed the site mainly in the morning hours (see Figs. 2, 3 and 4) with maximum HONO values comparable to the nighttime maxima (Fig. 1). This indicates that especially in the morning, the advective term T_h does play a role and the arrival of plumes at the site mimics a source term ($\Delta HONO/\Delta t > 0$), whereas their fading ($\Delta HONO/\Delta t < 0$) mimics a sink (Figs. 3 and 4). Also, the contribution of $\Delta HONO/\Delta t$ to the HONO budget depends on the integration time of the HONO signal. Comparing 5, 15, 30 and 60 min values, the highest contribution is associated with the 5 min values and the lowest with the 30 min values (60 min values are possibly already influenced by the diurnal cycle). Besides less influence from advection, the lower contribution of $\Delta HONO/\Delta t$ to the source and sink terms during the PRIDE-PRD-2004 experiment (Su et al., 2008b) compared to our study could at least partly be caused by the lower time resolution for HONO measurements in that study.

The contributions of the terms of Eq. (3) to the HONO budget (Fig. 3) are as follows. The reaction between HONO and OH ($L_{HONO+OH}$) has a very small contribution to HONO loss (mostly less than 5% of L_{phot}). Dry deposition (L_{dep}) is also very small (mostly less than 3% of L_{phot}). Around noon the main known HONO source is P_{NO+OH}. Due to low NO_2 levels around noon (see Fig. 2) P_{het} is also very low during that period. The noon period is clearly dominated by loss via L_{phot} (the overall dominant loss process) and formation by the unknown HONO source ($P_{unknown}$). P_{het} is higher in the morning and evening, respectively, provided that the parameterization (Sect. 2.3.2) is

valid. $P_{unknown}$ is negative (Figs. 3 and 4) in the early morning and evening indicating a missing sink, since more HONO is formed by the "known sources" than is destroyed via photolysis. A likely sink is non-negligible deposition of HONO, whose relative contribution might be higher in the morning and evening hours (mixed height ≪1000 m).

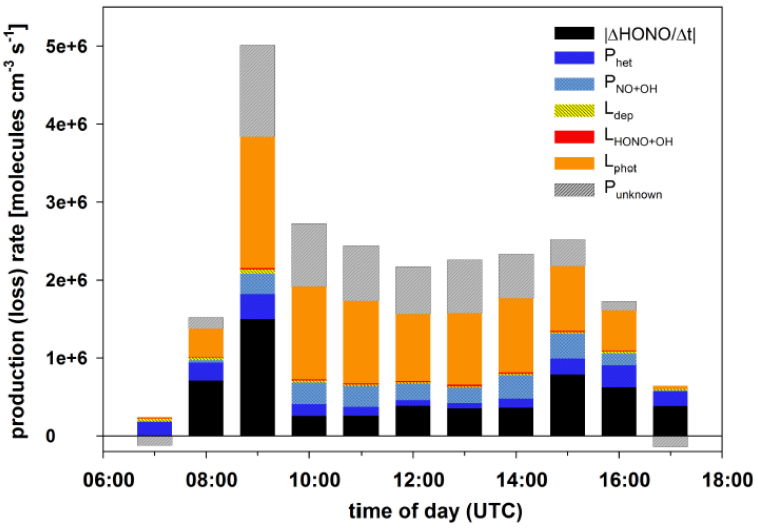

Figure 3: Contributions of production (bluish colours) and loss terms (hourly means 21 November to 5 December) as well as the unknown daytime HONO source $P_{unknown}$ from Eq. (3).

Figure 4a shows all calculated values of the unknown HONO source ($P_{unknown}$) in ppt h^{-1} (=7.37 × 10^3 molecules cm^{-3} s^{-1} at 1000 hPa and 273.15 K) versus $j(NO_2)$, as former studies (e.g. Vogel et al., 2003; Su et al., 2008b) proposed a correlation of this source to $j(NO_2)$. Values for $P_{unknown}$ range from about −700 to 1800 ppt h^{-1} (at noontime 10:00 – 14:00 UTC: 105±39 ppt h^{-1} for 7 clear days N =195) which is within the range of other rural and urban studies (Kleffmann, 2007). The filled red dots in Fig. 4 are points where ΔHONO/Δt values were larger than the respective relative errors of the HONO measurements, and thus included in Eq. (3). Applying a linear fit to the data in Fig. 4 a yields a coefficient of determination (r^2) of 0.16, and thus a rather weak linear correlation of $P_{unknown}$ versus $j(NO_2)$.

As light-induced conversion of NO_2 is thought to be the most probable source of HONO daytime formation, we normalized the unknown source by the NO_2 mixing ratios to improve comparability to other environmental conditions (remote, urban, laboratory). This normalized $P_{unknown}$ presented in Fig. 4b has the same units (% h^{-1}) as the nighttime conversion frequency ($F_{HONO,night}$) and can be referred to as a daytime conversion frequency assuming NO_2 is the direct precursor as indicated by recent studies of light-induced NO_2 conversion (e.g. Stemmler et al., 2006). Figure 4b indicates that NO_2 levels indeed play an important role, as peak values of the daytime source, when scaled by NO_2 mixing ratios, fall below an upper limit of conversion of $P_{unknown,norm,max}$ =(7490· $j(NO_2)$−1.2)%h^{-1} . The coefficient of determination of the linear fit to all values (Fig. 4b blue dashed line) increased from 0.16 without to 0.38 with NO_2 scaling. The correlation further improved to r^2 =0.47 if only data from clear days were taken and advection events were excluded (Fig. 5 insert). Nevertheless, this means that less than 50 % of the variance is explained by the linear model of the normalized unknown HONO source increasing linearly with $j(NO_2)$. A possible reason are HONO sources which are independant of the NO_X values such as HNO_3 photolysis (Zhou et al., 2011) or soil emissions (Su et al., 2011). These sources would cause an overestimation of the conversion frequencies at low ambient NO_X levels. Nevertheless, normalizing by NO_2 values seems to efficiently remove peak values in HONO formation during advection events.

As can be seen from a comparison with the diurnal cycle of the normalized $P_{unknown}$ in Fig. 5, the contribution of P_{het} to daytime HONO is very low during most of the day. While the maximum dark heterogeneous conversion rates are around 2%h^{-1}, the normalized unknown source (presumably daytime NO_2 conversion frequency) reaches median values of about 14%h^{-1} around noontime, with maximum values up to 43%h^{-1}. Around noon $P_{unknown}$ is thus about 7 to 20 times faster than the parameterized nighttime conversion, which is in agreement with Kleffmann et al. (2003), but a factor of three lower than found by Kleffmann et al. (2005).

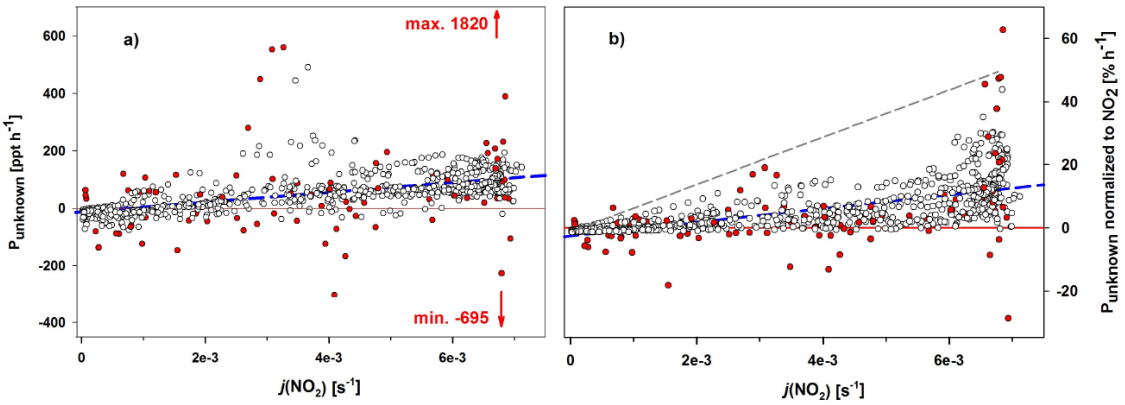

Figure 4: (a) Unknown HONO daytime source ($P_{unknown}$) in ppt h^{-1} for all days versus $j(NO_2)$. **(b)** $P_{unknown}$ normalized by NO_2 mixing ratios yielding a conversion frequency (% h^{-1}). Panel **(a)** contains only data points (N =753) which could be normalized to NO_2. Points where $\Delta HONO/\Delta t$ was larger than the relative error of the LOPAP (±12 %) are marked as filled red points. Blue dashed lines are linear fits to the data with **(a)** r^2 =0.16 and **(b)** r^2 =0.38. The grey dashed line in Fig. 4a presents an upper limit based on the mean of the five lowest points at $(jNO_2)_{min}$ and five highest points at $(jNO_2)_{max}$.

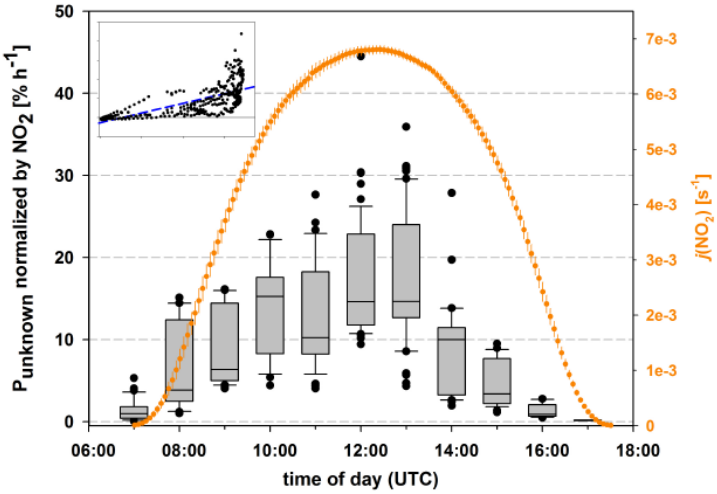

Figure 5: Diurnal cycle (only daytime) of the unknown HONO source ($P_{unknown}$), normalized by NO_2 mixing ratios from 7 cloud-free days (same as Fig. 2). To reflect more stationary conditions, only values where $\Delta HONO/\Delta t$ was lower than the relative error of the LOPAP were included in this graph. The upper ends of the bars reflect the 75th percentiles, the lower bounds the 25th percentiles and the line in between the medians. The upper whiskers represents the 90th percentiles and the lower the 10th percentiles. The minimum number of data points per hour is 17 (07:00), the maximum is 59 (13:00), except for the values close to sunset (17:00) with only 8 data points. Orange dots and bars represent the mean and standard deviation of $j(NO_2)$ for these days, respectively. The insert shows the same data, but as correlation plot of normalized $P_{unknown}$ versus $j(NO_2)$. The r^2 of the regression line is 0.47.

3.4 Potential contributions to the unknown HONO daytime source

In this section we investigate the contributions of two possible reaction pathways recently investigated in laboratory studies following a light-induced conversion of NO_2.

3.4.1 NO_2 conversion on irradiated soot

We calculated HONO production rates from the reaction of NO_2 on irradiated soot surfaces by extrapolating the reactive uptake coefficients (γ-values) derived in a laboratory study (Monge et al., 2010) to conditions we measured in the field. These γ -values were normalized to the Brunauer-Emmett- Teller surface (BET-surface) of the soot samples yielding a mass independant uptake (γ - BET). This γ -BET for NO_2 was found to increase with increasing irradiance and with decreasing NO_2 mixing ratios (Monge et al. 2010). Therefore, we used an extrapolation to lower NO_2 values (≪16 ppb) provided by B. D'Anna et al. (personal communication, 2010) leading to higher reactive NO_2 uptake in our study (median daytime NO_2 = 0.9 ppb). For simplicity, we took a value of 100 $m^2\ g^{-1}$ as the BET surface for soot, which is between the values (120–140 $m^2\ g^{-1}$ from a propane flame) used by Monge et al. (2010) and a value of 97 $m^2\ g^{-1}$ published for freshly emitted (81 $m^2\ g^{-1}$ for oxidized) soot (Daly and Horn, 2009). It can be regarded as an upper limit for soot from natural and anthropogenic combustion (Rockne et al., 2000; Fernandes et al., 2003). Black carbon (BC) measurements were taken as proxy soot values. As a further simplification, we used a constant upper limit integrated (300–420 nm) photon flux of 1.91×10^{16} photons $cm^{-2}\ s^{-1}$ instead of varying it with the solar zenith angle. Therefore, the diurnal variation of the calculated values (Fig. 6) has to be viewed with caution. High values in the morning hours due to NO_2 and BC peaks are actually lower due to lower irradiance values in the morning, and thus lower reactivity. Following Monge et al. (2010), we assumed a HONO production of 60 % of the reactive NO_2 uptake. Although we used upper limits for all calculations, the resulting values for the HONO production by this source (Fig. 6) are below 0.6 % of $P_{unknown}$ in 75 % of all cases (25 percentile = 0.2 % and median = 0.3 %). Thus, for conditions encountered during our campaign (daytime BC_{median} ~300 ng m^{-3} and $NO_{2,median}$ ~0.9 ppb) this reaction has no noticeable influence on HONO daytime values.

3.4.2 Electronically excited NO_2 reacting with water vapour

In order to study the potential contribution of the controversially discussed reaction of electronically excited NO_2 with water vapour (R8), we calculated its contribution to HONO and OH formation using the expression for OH production (= HONO production) from Crowley and Carl (1997).

$$R_{OH} = j_{ex}(NO_2)[NO_2]/(1 + k_{air}[M]/k_8[H_2O]) \quad (4)$$

$j_{ex}(NO_2)$ is the frequency of electronic excitation of NO_2 beyond the dissociation threshold (>420 nm), and k_{air} (~3×10^{-11}, Crowley and Carl, 1997) the rate constant for non-reactive quenching with air. k_8 is the rate constant for the reactive quenching with H_2O, $k_{8,Crowley} = 1.2 \times 10^{-14}$ cm^3 $molecules^{-1}\ s^{-1}$ according to Crowley and Carl (1997) and $k_{8,Li} = 1.7 \times 10^{-13}$ cm^3 $molecules^{-1}\ s^{-1}$ according to Li et al. (2008). We estimated $j_{ex}(NO_2)$ from measured $j(NO_2)$ by multiplying with a factor of 3.5 (Crowley and Carl, 1997) which is consistent with solar zenith angles <70° (~60° around noontime).

Referring to $k_{8,Li}$ as an upper limit, HONO and OH production rates calculated via Eq. (4) are in the order of a few ppt h^{-1}. This contribution to $P_{unknown}$ is less than 8% for 75% of our data, with a

median contribution of 4 %. Using $k_{8,Crowley}$, the values are one order of magnitude lower and thus negligible. These findings are in line with calculations from Crowley and Carl (1997) and with recent modeling studies (Wennberg and Dabdub, 2008; Sarwar et al., 2009; Ensberg et al., 2010) where this reaction was found to have a noticeable impact only at very high pollution levels, when using $k_{8,Li}$. As we do not expect the value for k_8 to be higher than reported by Li et al. (2008), we do not follow the approach of Wentzell et al. (2010) to explain the unknown HONO source by Reaction (R8) with varying k_8 alone. A very recent paper by Amedro et al. (2011) confirms that the reaction of Li et al. (2008) followed a multi photon absorption process, and provides an upper limit for reactive quenching which is even lower than that of Crowley and Carl (1997).

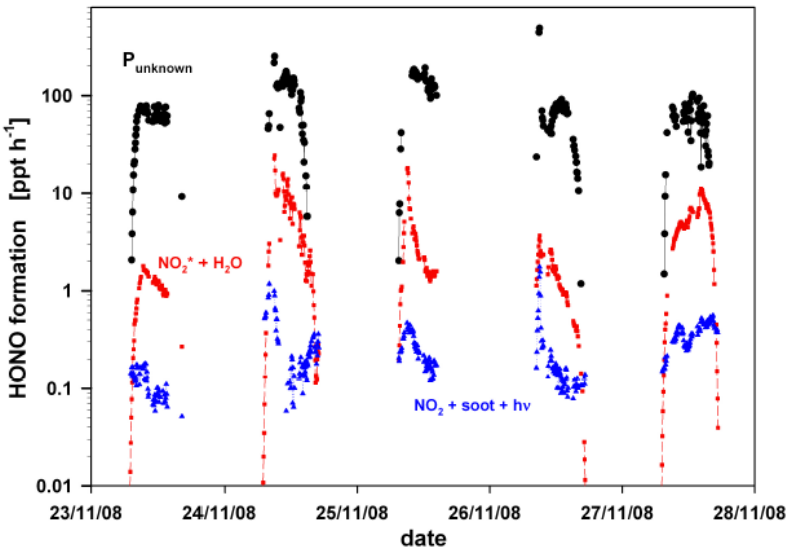

Figure 6: Comparison of different HONO daytime source strengths (blue: NO_2 + soot + *hv* (Monge et al., 2010); red: NO_2* + H_2O, Li et al., 2008) with the unknown HONO daytime source (black).

3.4.3 Important ground sources

The proposed formation of nitrous acid on the ground follows two major pathways. The light induced NO_2 conversion via organic photosensitizers (George et al., 2005; Stemmler et al., 2006) and the microbiological formation of nitrite in the soil and the volatilization to the atmosphere as HONO (Kubota and Asami, 1985; Su et al., 2011). As recent measurements of the photolysis of adsorbed HNO_3 (Zhu et al., 2010) found NO_2* as the main photolysis product, Zhou et al. (2011) assume that HONO formation by HNO_3 photolysis also follows the mechanism of NO_2 conversion provided by George et al. (2005) and Stemmler et al. (2006). Adsorbed HNO_3 therefore acts as a reservoir or a source of NO_X in rural environments (Zhou et al., 2002b, 2003, 2011). One might speculate if the reaction of NO_2* formed by HNO_3 photolysis at the surface with adsorbed water is also enhanced with regard to the gas phase Reaction (R8), and thus can act as source of HONO from HNO_3 photolysis. The relative contribution of HNO_3 photolysis to direct NO_2 conversion increases with surface nitrate loading and decreasing NO_X values. This might be reflected in our measurements as some of the highest conversion frequencies (Fig. 4b) were measured on a "clean day" (NO_X < 0.5 ppb). For a rough estimate of the contribution of direct NO_2 conversion (on aerosol and ground surfaces) we took the estimates of Stemmler et al. (2007) which are about 1 ppt h^{-1} for humic acid aerosol and about 700 ppt h^{-1} for conversion at the soil surface in a 100 m mixed height at 20 ppb NO_2. We scaled these values to 1 ppb NO_2 (observed NO_2 values). As already concluded by Stemmler et al. (2007) the contribution of the aerosol is

negligible (~0.05 ppt h^{-1}). The ground source would contribute about 35 ppt h^{-1}, i.e. one third of the missing source, applying a linear scaling with NO_2.

Regarding the soil emissions, there are no soil acidity and nitrate loading data available for the DOMINO campaign. Therefore, it is at best speculative to derive a HONO source based on the numbers given by Su et al. (2011) as the resulting HONO fluxes vary by orders of magnitude. But as HONO soil flux values in the lowest range (low nitrogen loading and rather high pH) can already produce source strength in the right order of magnitude for $P_{unknown}$, this HONO source might be a substantial contribution during DOMINO.

All calculations about source strength at the ground are very sensitive to vertical mixing. Thus, as already addressed by Zhou et al. (2011), vertical transport determines the discrepancy between the effective source strength relative to that calculated at the measurement height. We conclude that only modelling which takes vertical transport into account can yield reliable estimates of the ground source contribution to the missing HONO source.

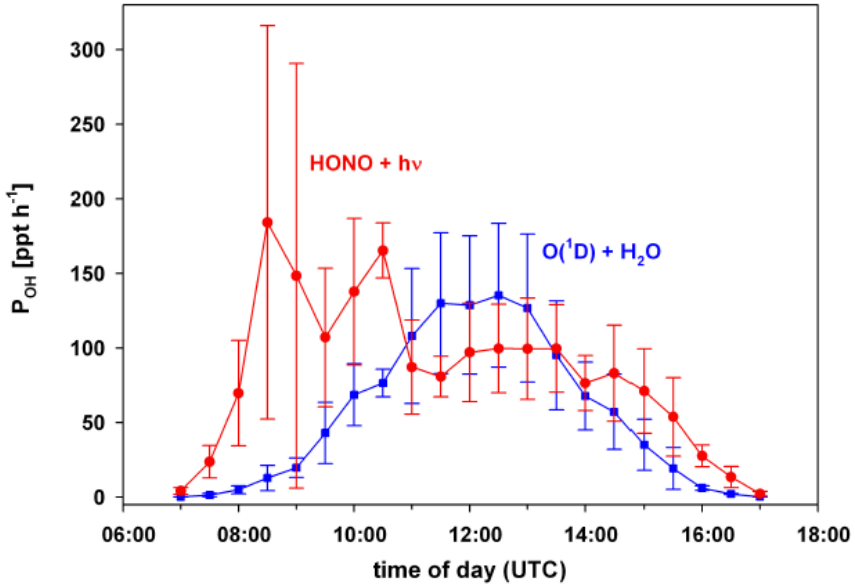

Figure 7: Comparison for the seven clear days of the campaign of calculated primary OH production by HONO and ozone photolysis (means and standard deviations).

3.5 Comparison of OH radical production from ozone and HONO photolysis

OH production rates from ozone photolysis were calculated from ozone, H_2O measurements and modelled $j(O(^1D))$ values which were scaled by the ratio of measured and modeled $j(NO_2)$. OH production from $O(^1D)$ was calculated according to Crowley and Carl (1997) using the rate constants for $O(^1D)$ quenching by O_2, N_2 and O_3 and the reaction with H_2O taken from the IUPAC recommendations (Atkinson et al., 2004 and updated values from the IUPAC homepage, http://www.iupac-kinetic.ch.cam.ac.uk/). These values are in good agreement (~3 % higher) with the same calculations using the recommendations from Sander et al. (2006). The net OH production by HONO was calculated by balancing source and sink terms of OH by HONO in the gas phase (for k values see Sect. 3.2):

$$P_{OH} = j(HONO)[HONO] - k_7[NO][OH] - k_6[HONO][OH] \quad (5)$$

Although HONO mixing ratios (mean: 30 ppt) are three orders of magnitude lower than O_3 mixing ratios (mean: 35 ppb) around noon and OH production rates by $O(^1D)$ exceed those of HONO photolysis by about 50 % around noon (11:00 – 13:00), the integrated daily OH production is about 20 % lower than that of HONO. Figure 7 shows the higher contribution of HONO photolysis to the OH formation in the morning and evening hours due to longer wavelengths (up to ~400 nm) associated with HONO photolysis. A special feature of our measurement site are the very high HONO values between 08:00 and 11:00, which can be attributed to advection (see Sects. 3.2 and 3.3). This leads to high P_{OH} values from HONO photolysis during that period.

4 Conclusions

The unknown HONO daytime source derived from our measurements was normalized by NO_2 mixing ratios to improve comparability of HONO source strengths in different environmental and laboratory conditions. For the nighttime formation of HONO, we can exclude that NO plays an important role as NO was mostly below the detection limit of about 6 ppt. Inclusion of the parameterized nighttime HONO formation from NO_2 ($1.5\%h^{-1}$ in this study) as an additional source into the calculations of the unknown HONO daytime source ($P_{unknown}$) yields mainly negative values in the early morning. This indicates the relevance of loss terms not taken into account (e.g. deposition) or overestimation of the dark heterogeneous formation in the morning and evening. Restricting the analysis only to cloud free days and the time around noon, when faster HONO photolysis leads to lifetimes around 15 min and other loss processes for HONO are small compared to loss by photolysis, establishment of a PSS can be assumed. The mean source strength of $P_{unknown}$ under these conditions was about 100 ppt h^{-1} and thus in the lower range of values reported in the literature. Nevertheless $P_{unknown}$ was the dominant HONO source during day. The normalized unknown HONO source (or NO_2 conversion frequency, if we assume that NO_2 is the precursor) varied from slightly negative values in the morning and evening to an upper limit correlated with $j(NO_2)$. High median daytime NO_2 conversion frequencies of $\sim 14\%h^{-1}$ were found around noon, in addition to the $1.5\%h^{-1}$ HONO formation rate observed during night.

Our results indicate light-induced HONO formation, possibly via conversion of NO_2 as indicated by lab experiments. This source is about an order of magnitude stronger than HONO formation during nighttime. We compared the HONO net source to values calculated for light-induced NO_2 uptake on soot (Monge et al., 2010) and the reaction of electronically excited NO_2* with water vapour. The contribution of these reactions to HONO daytime values was mostly less than 10% and cannot explain the HONO source strength derived in our study. Other processes like light-induced conversion of NO_2 on irradiated organic materials like humic acids (Stemmler et al., 2006), or soil emissions (Su et al., 2011) might be more important. Additional measurements including detailed speciation of organic aerosols and determination of humic acids on ground and canopy surfaces are needed to quantify their contribution. Furthermore, a detailed assessment of the contribution of the ground sources requires profound knowledge of boundary layer processes. The unknown HONO daytime source is essential contribution to primary OH production, as photolysis of HONO exceeded the OH formation by ozone photolysis by 20 %.

Acknowledgements. The authors gratefully acknowledge financial support by the German Science foundation (DFG projects ZE 792/4-1 and HE5214/4-1) and by the Max Planck Society. We are grateful to Ralph Dlugi and Thomas Foken for intensive and fruitful discussions. We thank Ivonne Trebs and Franz-Xaver Meixner from the Max Planck Institute for Chemistry for providing instruments and equipment, and the Spanish National Institute of Aerospace Technology (INTA) for hosting the campaign.

References

Acker, K., Möller, D., Wieprecht, W., Meixner, F. X., Bohn, B., Gilge, S., Plass-Dülmer, C., and Berresheim, H.: Strong daytime production of OH from HNO_2 at a rural mountain site, Geophys. Res. Lett., 33, L02809, doi:10.1029/2005GL024643, 2006.

Alicke, B., Platt, U., and Stutz, J.: Impact of nitrous acid photolysis on the total hydroxyl radical budget during the Limitation of Oxidant Production Pianura/Padana Produzione di Ozono study in Milan, J. Geophys. Res., 107, 8196, doi:10.1029/2000JD000075, 2002.

Alicke, B., Geyer, A., Hofzumahaus, A., Holland, F., Konrad, S., Pätz, H.W., Schäfer, J., Stutz, J., Volz-Thomas, A., and Platt, U.: OH formation by HONO photolysis during the BERLIOZ experiment, J. Geophys. Res., 108, 8247, doi:10.1029/2001JD000579, 2003.

Amedro, D., Parker, A. E., Schoemaecker, C., and Fittschen, C.: Direct observation of OH radicals after 565 nm multi-photon excitation of NO_2 in the presence of H_2O, Chem. Phys. Lett., 513, 12–16, 2011

Ammann, M., Rössler, E., Strekowski, R., and George, C.: Nitrogen dioxide multiphase chemistry: Uptake kinetics on aqueous solutions containing phenolic compounds, Phys. Chem. Chem. Phys., 7, 2513–2518, 2005.

Andres-Hernandez, M. D., Notholt, J., Hjorth, J., and Schrems, O.: A DOAS study on the origin of nitrous acid at urban and nonurban sites, Atmos. Environ., 30, 175–180, 1996.

Arens, F., Gutzwiller, L., Baltensperger, U., Gäggler, H. W., and Ammann, M.: Heterogeneous reaction of NO_2 on diesel soot particles, Environ. Sci. Technol., 35, 2191–2199, 2001.

Atkinson, R., Baulch, D. L., Cox, R. A., Crowley, J. N., Hampson, R. F., Hynes, R. G., Jenkin, M. E., Rossi, M. J., and Troe, J.: Evaluated kinetic and photochemical data for atmospheric chemistry: Volume I – gas phase reactions of O_x, HO_x, NO_x and So_x species, Atmos. Chem. Phys., 4, 1461–1738, doi:10.5194/acp-4- 1461-2004, 2004.

Aubin, D. G. and Abbatt, J. P. D.: Interaction of NO_2 with hydrocarbon soot: focus on HONO yield, surface modification, and mechanism, J. Phys. Chem. A, 111, 6263–6273, 2007.

Bejan, I., Abd el Aal, Y., Barnes, I., Benter, T., Bohn, B., Wiesen, P., and Kleffmann, J.: The photolysis of ortho-nitrophenols: a new gas phase source of HONO, Phys. Chem. Chem. Phys., 8, 2028–2035, doi:10.1039/b516590c, 2006.

Blitz, M. A.: Comment on "The conical intersection dominates the generation of tropospheric hydroxyl radicals from NO_2 and H_2O", J. Phys. Chem. A, 114, 8016, 2010.

Bohn, B. and Zetzsch, C.: Rate constants of HO_2 + NO covering atmospheric conditions. 1. HO_2 formed by OH + H_2O_2, J. Phys. Chem. A, 101, 1488–1493, 1997.

Calvert, J. G., Yarwood, G., and Dunker, A. M.: An evaluation of the mechanism of nitrous acid formation in the urban atmosphere, Res. Chem. Intermediat., 20, 463–502, 1994.

Cancillo, M. L., Serrano, A., Antón, M., García, J. A., Vilaplana, J. M., and de la Morena, B.: An improved outdoor calibration procedure for broadband ultraviolet radiometers, Photochem. Photobiol., 81, 860–865, 2005.

Carr, S., Heard, D. E., and Blitz, M. A.: Comment on "Atmospheric Hydroxyl Radical Production from Electronically Excited NO_2 and H_2O", Science, 324, p. 336b, doi:10.1126/science.1166669, 2009.

Cox, R. A.: The photolysis of nitrous acid in the presence of carbon monoxide and sulphur dioxide, J. Photochem., 3, 291–304, 1974.

Crowley, J. N. and Carl, S. A.: OH formation in the photoexcitation of NO_2 beyond the dissociation threshold in the presence of water vapor, J. Phys. Chem. A, 101, 4178–4184, 1997.

Daly, H. M. and Horn, A. B.: Heterogeneous chemistry of toluene, kerosene and diesel soots, Phys. Chem. Chem. Phys., 11, 1069– 1076, 2009.

Diesch, J.-M., Drewnick, F., Zorn, S. R., von der Weiden-Reinmüller, S.-L., Martinez, M., and Borrmann, S.: Variability of aerosol, gaseous pollutants and meteorological characteristics associated with continental, urban and marine air masses at the SW Atlantic coast of Iberia, in preparation, 2011.

Dillon, M. B., Lamanna, M. S., Schade, G. W., Goldstein, A., and Cohen, R. C.: Chemical evolution of the Sacramento urban plume: Transport and oxidation, J. Geophys. Res., 107, 4045, doi:10.1029/2001JD000969, 2002.

Ensberg, J. J., Carreras-Sospedra, M., and Dabdub, D.: Impacts of electronically photo-excited NO_2 on air pollution in the South Coast Air Basin of California, Atmos. Chem. Phys., 10, 1171– 1181, doi:10.5194/acp-10-1171-2010, 2010.

Fang, Q., Han, J., Jiang, J., Chen, X., and Fang, W.: The conical intersection dominates the generation of tropospheric hydroxyl radicals from NO_2 and H_2O, J. Phys. Chem. A, 114, 4601–4608, 2010.

Febo, A., Perrino, C., and Allegrini, I.: Measurement of nitrous acid in Milan, Italy, by DOAS and diffusion denuders, Atmos. Environ., 30 3599–3609, 1996.

Fernandes, M. B., Skjemstad, J. O., Johnson, B. B., Wells, J. D., and Brooks, P.: Characterization of carbonaceous combustion residues. I. Morphological, elemental and spectroscopic features, Chemosphere, 51, 785–795, 2003.

Finlayson-Pitts, B. J.: Reactions at surfaces in the atmosphere: integration of experiments and theory as necessary (but not necessarily sufficient) for predicting the physical chemistry of aerosols, Phys. Chem. Chem. Phys., 11, 7760–7779, 2009.

Finlayson-Pitts, B. J., Wingen, L. M., Sumner, A. L., Syomin, D., and Ramazan, K. A.: The heterogeneous hydrolysis of NO_2 in laboratory systems and in outdoor and indoor atmospheres: An integrated mechanism, Phys. Chem. Chem. Phys., 5, 223–242, 2003.

George, C., Strekowski, R. S., Kleffmann, J., Stemmler, K., and Ammann, M.: Photoenhanced uptake of gaseous NO_2 on solid organic compounds: a photochemical source of HONO?, Faraday Discuss., 130, 195–210, 2005.

Gonçlves, M., Dabdub, D., Chang, W. L., Saiz, F., Jorba, O., and Baldasano, J. M.: The impact of different nitrous acid sources in the air quality levels of the Iberian Peninsula, Atmos. Chem. Phys. Discuss., 10, 28183–28230, doi:10.5194/acpd-10-28183-2010, 2010.

Gustafsson, R. J., Orlov, A., Griffiths, P. T., Cox, R. A., and Lambert, R. M.: Reduction of NO_2 to nitrous acid on illuminated titanium dioxide aerosol surfaces: implications for photocatalysis and atmospheric chemistry, Chem. Commun., 37, 3936–3938, 2006.

Gustafsson, R. J., Kyriakou, G., and Lambert, R. M.: The molecular mechanism of tropospheric nitrous acid production on mineral dust surfaces, Chem. Phys. Chem., 9, 1390–1393, 2008.

Gutzwiller, L., Arens, F., Baltensberger, U., Gäggler, H. W., and Ammann, M.: Significance of semivolatile diesel exhaust organics for secondary HONO formation, Environ. Sci. Technol., 36, 677–682, 2002a.

Gutzwiller, L., George, C., Rössler, E., and Ammann, M.: Reaction kinetics of NO_2 with resorcinol and 2,7-naphthalenediol in the aqueous phase at different pH, J. Phys. Chem. A, 106, 12045–12050, 2002b.

Hanst, P. L., Spence, J. W., and Miller, M.: Atmospheric chemistry of n-nitroso dimethylamine, Environ. Sci. Technol., 11, 403–405, 1977.

Harrison, R. M. and Kitto, A.-M. N.: Evidence for a surface source of atmospheric nitrous acid, Atmos. Environ., 28, 1089–1094, 1994.

Harrison, R. M., Peak, J. D., and Collin, G. M.: Tropospheric cycle of nitrous acid, J. Geophys. Res., 101, 14429–14439, 1996.

Heland, J., Kleffmann, J., Kurtenbach, R., and Wiesen, P.: A new instrument to measure gaseous nitrous acid (HONO) in the atmosphere, Environ. Sci. Technol., 35, 3207–3212, 2001.

Hosaynali Beygi, Z., Fischer, H., Harder, H. D., Martinez, M., Sander, R., Williams, J., Brookes, D. M., Monks, P. S., and Lelieveld, J.: Oxidation photochemistry in the Southern Atlantic boundary layer: unexpected deviations of photochemical steady state, Atmos. Chem. Phys., 11, 8497–8513, doi:10.5194/acp-11- 8497-2011, 2011.

IUPAC Subcommittee on Gas Kinetic Data Evaluation: http://www.iupac-kinetic.ch.cam.ac.uk/, access 10 January 2011.

Jenkin, M. E., Cox, R. A., andWilliams, D. J.: Laboratory studies of the kinetics of formation of nitrous acid from the thermal reaction of nitrogen dioxide and water vapour, Atmos. Environ., 22 487– 498, 1988.

Killus, J. P. and Whitten, G. Z.: Background reactivity in smog chambers, Int. J. Chem. Kinet., 22, 547–575, 1990.

Kinugawa, T., Enami, S., Yabushita, A., Kawasaki, M., Hoffmann, M. R., and Colussi, A. J.: Conversion of gaseous nitrogen dioxide to nitrate and nitrite on aqueous surfactants, Phys. Chem. Chem. Phys., 13, 5144–5149, doi:10.1039/C0CP01497D, 2011.

Kirchstetter, T. W., Harley, R. A., and Littlejohn, D.: Measurement of nitrous acid in motor vehicle exhaust, Environ. Sci. Technol., 30, 2843–2849, 1996.

Kleffmann, J.: Daytime sources of nitrous acid (HONO) in the atmospheric boundary layer, Chem. Phys. Chem., 8, 1137–1144, 2007.

Kleffmann, J., Becker, K. H., and Wiesen, P.: Heterogeneous NO_2 conversion processes on acid surfaces: possible atmospheric implications, Atmos. Environ., 32, 2721–2729, 1998.

Kleffmann, J., Becker, K. H., Lackhoff, M., and Wiesen, P.: Heterogeneous conversion of NO_2 on carbonaceous surfaces, Phys. Chem. Chem. Phys., 1, 5443–5450, 1999.

Kleffmann, J., Heland, J., Kurtenbach, R., Lörzer, J., and Wiesen, P.: A new instrument (LOPAP) for the detection of nitrous acid (HONO), Environ. Sci. Pollut. R., 4, 48–54, 2002.

Kleffmann, J., Kurtenbach, R., Lörzer, J., Wiesen, P., Kalthoff, N., Vogel, B., and Vogel, H.: Measured and simulated vertical profiles of nitrous acid – Part I: Field measurements, Atmos. Environ., 37, 2949–2955, 2003.

Kleffmann, J., Benter, T., and Wiesen, P.: Heterogeneous reaction of nitric acid with nitric oxide on glass surfaces under simulated atmospheric conditions, J. Phys. Chem. A, 108, 5793–5799, 2004.

Kleffmann, J., Gavriloaiei, T., Hofzumahaus, A., Holland, F., Koppmann, R., Rupp, L., Schlosser, E., Siese, M., and Wahner, A.: Daytime formation of nitrous acid: A major source of OH radicals in a forest, Geophys. Res. Lett., 32, L05818, doi:10.1029/2005GL022524, 2005.

Kraus, A. and Hofzumahaus, A.: Field measurements of atmospheric photolysis frequencies for O_3, NO_2, HCHO, CH_3CHO, H_2O_2, and HONO by UV spectroradiometry, J. Atmos. Chem., 31, 161–180, 1998.

Kubota, M. and Asami, T.: Source of nitrous acid volatilized from upland soils, Soil Sci. Plant Nutr., 31, 35–42, 1985.

Kurtenbach, R., Becker, K. H., Gomes, J. A. G., Kleffmann, J., Lörzer, J. C., Spittler, M., Wiesen, P., Ackermann, R., Geyer, A., and Platt, U.: Investigations of emissions and heterogeneous formation of HONO in a road traffic tunnel, Atmos. Environ., 35, 3385–3394, 2001.

Lammel, G. and Cape, J. N.: Nitrous acid and nitrite in the atmosphere, Chem. Soc. Rev., 25, 361–369, 1996.

Li, S., Matthews, J., and Sinha, A.: Atmospheric hydroxyl radical production from electronically excited NO_2 and H_2O, Science, 319, 1657–1660, doi:10.1126/science.1151443, 2008.

Li, S., Matthews, J., and Sinha, A.: Response to comment on "Atmospheric hydroxyl radical production from electronically excited NO_2 and H_2O", Science, 324, p. 336c, 2009.

Madronich, S. and Flocke, S., The role of solar radiation in atmospheric chemistry, in: The Handbook of Environmental Chemistry/Reactions and Processes/Environmental Photochemistry Part I: BD 2/Part L, edited by: Boule, P., Springer-Verlag, Heidelberg, 373 (pp. 1-26), 1998.

Martinez, M., Harder, H., Kubistin, D., Rudolf, M., Bozem, H., Eerdekens, G., Fischer, H., Klüpfel, T., Gurk, C., Königstedt, R., Parchatka, U., Schiller, C. L., Stickler, A., Williams, J., and Lelieveld, J.: Hydroxyl radicals in the tropical troposphere over the Suriname rainforest: airborne measurements, Atmos. Chem. Phys., 10, 3759–3773, doi:10.5194/acp-10-3759-2010, 2010.

Monge, M. E., D'Anna, B., Mazri, L., Giroir-Fendler, A., Ammann, M., Donaldson, D. J., and George, C.: Light changes the atmospheric reactivity of soot, P. Natl. Acad. Sci. USA, 107, 6605– 6609, 2010.

NASA.: Ozone over your house, http://jwocky.gsfc.nasa.gov/ teacher/ozone overhead.html, last access: January 2011.

Perner, D. and Platt, U.: Detection of nitrous acid in the atmosphere by differential optical absorption, Geophys. Res. Lett., 6, 917–920, 1979.

Pitts Jr., J. N., Grosjean, D., Cauwenberghe, K. V., Schmid, J. P., and Fitz, D. R.: Photooxidation of aliphatic amines under simulated atmospheric conditions: formation of nitrosamines, nitramines, amides, and photochemical oxidant, Environ. Sci. Technol., 12 946–953, 1978.

Pitts Jr., J. N., Biermann, H. W., Winer, A. M., and Tuazon, E. C.: Spectroscopic identification and measurement of gaseous nitrous acid in dilute auto exhaust, Atmos. Environ., 18, 847–854, 1984.

Raivonen, M., Bonn, B., Sanz, M. J., Vesala, T., Kulmala, M., and Hari, P.: UV-induced NOy emissions from Scots pine: Could they originate from photolysis of deposited HNO_3?, Atmos. Environ., 40, 6201–6213, 2006.

Ren, X., Harder, H., Martinez, M., Lesher, R. L., Oliger, A., Simpas, J. B., Brune, W. H., Schwab, J. J., Demerjian, K. L., He, Y., Zhou, X., and Gao, H.: OH and HO_2 chemistry in the urban atmosphere of New York City, Atmos. Environ., 37, 3639–3651, 2003.

Ren, X., Brune, W. H., Mao, J., Mitchell, M. J., Lesher, R. L., Simpas, J. B., Metcalf, A. R., Schwab, J. J., Cai, C., Li, Y., Demerjian, K. L., Felton, H. D., Boynton, G., Adams, A., Perry, J., He, Y., Zhou, X., and Hou, J.: Behavior of OH and HO_2 in the winter atmosphere in New York City, Atmos. Environ., 40, 252–263, 2006.

Rockne, K. J., Taghon, G. L., and Kosson, D. S.: Pore structure of soot deposits from several combustion sources, Chemosphere, 41, 1125–1135, 2000.

Rohrer, F., Bohn, B., Brauers, T., Brüning, D., Johnen, F.-J., Wahner, A., and Kleffmann, J.: Characterisation of the photolytic HONO-source in the atmosphere simulation chamber SAPHIR, Atmos. Chem. Phys., 5, 2189–2201, doi:10.5194/acp-5-2189-2005, 2005.

Sakamaki, F., Hatakeyama, S., and Akimoto, H.: Formation of nitrous acid and nitric oxide in the heterogeneous dark reaction of nitrogen dioxide and water vapour, Int. J. Chem. Kinet., 15, 1013–1029, 1983.

Saliba, N. A., Yang, H., and Finlayson-Pitts, B. J.: Reaction of gaseous nitric oxide with nitric acid on silica surfaces in the presence of water at room temperature, J. Phys. Chem. A, 105, 10339–10346, 2001.

Sander, S. P., Friedl, R. R., Golden, D. M., Kurylo, M. J., Moortgat, G. K., Keller-Rudek, H., Wine, P. H., Ravishankara, A. R., Kolb, C. E., Molina, M. J., Finlayson-Pitts, B. J., Huie, R. E., and Orkin, V. L.: Chemical kinetics and photochemical data for use in atmospheric studies evaluation number 15, Jet Propulsion Laboratory, Pasadena, 523, 2006.

Sarwar, G., Pinder, R. W., Appel, K. W., Mathur, R., and Carlton, A. G.: Examination of the impact of photoexcited NO_2 chemistry on regional air quality, Atmos. Environ., 43, 6383–6387, 2009.

Schmid, H. P.: Footprint modeling for vegetation atmosphere exchange studies: a review and perspective, Agr. Forest. Meteorol., 113, 159–183, 2002.

Sleiman, M., Gundel, L. A., Pankow, J. F., Jacob, P., Singer, B. C., and Destaillats, H.: Formation of carcinogens indoors by surfacemediated reactions of nicotine with nitrous acid, leading to potential thirdhand smoke hazards, P. Natl. Acad. Sci. USA, 107, 6576–6581, 2010.

Sörgel, M., Trebs, I., Serafimovich, A., Moravek, A., Held, A., and Zetzsch, C.: Simultaneous HONO measurements in and above a forest canopy: influence of turbulent exchange on mixing ratio differences, Atmos. Chem. Phys., 11, 841–855, doi:10.5194/acp- 11-841-2011, 2011.

Stemmler, K., Ammann, M., Donders, C., Kleffmann, J., and George, C.: Photosensitized reduction of nitrogen dioxide on humic acid as a source of nitrous acid, Nature, 440, 195–198, 2006.

Stemmler, K., Ndour, M., Elshorbany, Y., Kleffmann, J., D'Anna, B., George, C., Bohn, B., and Ammann, M.: Light induced conversion of nitrogen dioxide into nitrous acid on submicron humic acid aerosol, Atmos. Chem. Phys., 7, 4237–4248, doi:10.5194/acp-7-4237-2007, 2007.

Stull, R. B.: An introduction to boundary layer meteorology, Atmospheric and Oceanographic Sciences Library, Kluwer Academic Publishers, Dordrecht, 670 pp., 1988.

Stutz, J., Alicke, B., and Neftel, A.: Nitrous acid formation in the urban atmosphere: Gradient measurements of NO_2 and HONO over grass in Milan, Italy, J. Geophys. Res., 107, 8192, doi:10.1029/2001JD000390, 2002.

Stutz, J., Alicke, B., Ackermann, R., Geyer, A.,Wang, S., White, A. B.,Williams, E. J., Spicer, C.W., and Fast, J. D.: Relative humidity dependence of HONO chemistry in urban areas, J. Geophys. Res., 109, D03307, doi:10.1029/2003JD004135, 2004.

Su, H., Cheng, Y. F., Cheng, P., Zhang, Y. H., Dong, S., Zeng, L. M., Wang, X., Slanina, J., Shao, M., and Wiedensohler, A.: Observation of nighttime nitrous acid (HONO) formation at a nonurban site during PRIDE-PRD2004 in China, Atmos. Environ., 42, 6219–6232, 2008a.

Su, H., Cheng, Y. F., Shao, M., Gao, D. F., Yu, Z. Y., Zeng, L. M., Slanina, J., Zhang, Y. H., and Wiedensohler, A.: Nitrous acid (HONO) and its daytime sources at a rural site during the 2004 PRIDE-PRD experiment in China, J. Geophys. Res., 113, D14312, doi:10.1029/2007JD009060, 2008b.

Su, H., Cheng,Y., Oswald, R., Behrendt, T., Trebs, I., Meixner, F.- X., Andreae, M. O., Cheng, P., Zhang, Y., and Pöschl, U.: Soil Nitrite as a Source of Atmospheric HONO and OH Radicals, Science, 333, 1616–1618, doi:10.1126/science.1207687, 2011.

Svennsson, R., Ljungstrom, E., and Lindqvist, O.: Kinetics of the reaction between nitrogen dioxide and water vapour, Atmos. Environ., 21 1529–1539, 1987.

Trebs, I., Bohn, B., Ammann, C., Rummel, U., Blumthaler, M., Königstedt, R., Meixner, F. X., Fan, S., and Andreae, M. O.: Relationship between the NO_2 photolysis frequency and the solar global irradiance, Atmos. Meas. Tech., 2, 725–739, doi:10.5194/amt-2-725-2009, 2009.

Trick, S.: Formation of nitrous acid on urban surfaces – a physicalchemical perspective, Ph.D. thesis, University Heidelberg, Germany, 290 pp., 2004.

Veitel, H.: Vertical profiles of NO_2 and HONO in the boundary layer, Ph.D. thesis, University, Heidelberg, Germany, 270 pp., 2002.

Vesala, T., Kljun, N., Rannik, Ü., Rinne, J., Sogachev, A., Markkanen, T., Sabelfeld, K., Foken, T., and Leclerc, M. Y.: Flux and concentration footprint modelling: State of the art, Environ. Pollut., 152, 653–666, 2008.

Vogel, B., Vogel, H., Kleffmann, J., and Kurtenbach, R.: Measured and simulated vertical profiles of nitrous acid – Part II. Model simulations and indications for a photolytic source, Atmos. Environ., 37, 2957–2966, 2003.

Wennberg, P. O. and Dabdub, D.: Rethinking ozone production, Science, 319, 1624–1625, 2008.

Wentzell, J. J. B., Schiller, C. L., and Harris, G. W.: Measurements of HONO during BAQS-Met, Atmos. Chem. Phys., 10, 12285–12293, doi:10.5194/acp-10-12285-2010, 2010.

Wong, K. W., Oh, H.-J., Lefer, B. L., Rappenglück, B., and Stutz, J.: Vertical profiles of nitrous acid in the nocturnal urban atmosphere of Houston, TX, Atmos. Chem. Phys., 11, 3595-3609, doi:10.5194/acp-11-3595-2011, 2011.

Yabushita, A., Enami, S., Sakamoto, Y., Kawasaki, M., Hoffmann, M. R., and Colussi, A. J.: Anion-catalyzed dissolution of NO_2 on aqueous microdroplets, J. Phys. Chem. A, 113, 4844–4848, 2009.

Yu, Y., Galle, B., Panday, A., Hodson, E., Prinn, R., and Wang, S.: Observations of high rates of NO_2-HONO conversion in the nocturnal atmospheric boundary layer in Kathmandu, Nepal, Atmos. Chem. Phys., 9, 6401–6415, doi:10.5194/acp-9-6401-2009, 2009.

Zhang, N., Zhou, X., Shepson, P. B., Gao, H., Alaghmand, M., and Stirm, B.: Aircraft measurement of HONO vertical profiles over a forested region, Geophys. Res. Lett., 36, L15820, doi:10.1029/2009GL038999, 2009.

Zhou, X., Civerolo, K., Dai, H., Huang, G., Schwab, J., and Demerjian, K.: Summertime nitrous acid chemistry in the atmospheric boundary layer at a rural site in New York State, J. Geophys. Res., 107, 4590, doi:10.1029/2001JD001539, 2002a.

Zhou, X., He, Y., Huang, G., Thornberry, T. D., Carroll, M. A., and Bertman, S. B.: Photochemical production of nitrous acid on glass sample manifold surface, Geophys. Res. Lett., 29, 1681, doi:10.1029/2002GL015080, 2002b.

Zhou, X., Gao, H., He, Y., Huang, G., Bertman, S. B., Civerolo, K., and Schwab, J.: Nitric acid photolysis on surfaces in low-NO_X environments: Significant atmospheric implications, Geophys. Res. Lett., 30, 2217, doi:10.1029/2003GL018620, 2003.

Zhou, X., Zhang, N., TerAvest, M., Tang , D., Hou, J., Bertman, S., Alaghmand, M., Shepson, P. B., Carroll, M. A., Griffith, S., Dusanter, S., and Stevens, P. S.: Nitric acid photolysis on forest canopy surface as a source for tropospheric nitrous acid, Nat. Geosci., 4, 440–443, doi:10.1038/ngeo1164, 2011.

Zhu, C., Xiang, B., Zhu, L., and Cole, R.: Determination of absorption cross sections of surface-adsorbed HNO_3 in the 290–330 nm region by Brewster angle cavity ring-down spectroscopy, Chem. Phys. Lett., 458, 73–377, 2008.

Zhu, C., Xiang, B., Chu, L. T., and Zhu, L.: Photolysis of nitric acid in the gas phase, on aluminum surfaces, and on ice films, J. Phys. Chem. A, 114, 2561–2568, 2010.

E On the applicability of mobile aerosol and trace gas measurements for the investigation of characteristics and transformation of megacity emissions: The Paris metropolitan area

S.-L. von der Weiden-Reinmüller[1], F. Drewnick[1], M. Crippa[2], A. S. H. Prévôt[2], F. Meleux[3], T. Böttger[1], T. Klimach[1], S. R. Zorn[1,*], J.-M. Diesch[1], U. Baltensperger[2], M. Beekmann[4] and S. Borrmann[1,5]

[1]Particle Chemistry Department, Max Planck Institute for Chemistry, Mainz, Germany
[2]Laboratory of Atmospheric Chemistry, Paul Scherrer Institute, Villigen, Switzerland
[3]Institut National de l´Environment Industriel et des Risques, Verneuil en Halatte, France
[4]Laboratoire inter-universitaire des Systèmes Atmosphériques, Créteil Cedex, France
[5] Institute of Physics of the Atmosphere, Johannes Gutenberg University Mainz, Germany
[*]now at: AeroMegt GmbH, Hilden, Germany

To be submitted to Atmos. Chem. Phys., in review, 2012

Abstract

For the investigation of megacity emissions mobile aerosol and trace gas measurements have been carried out in the Paris metropolitan area. The measurements took place between 1 July and 31 July 2009 and 15 January and 15 February 2010 in the framework of the European Union FP7 MEGAPOLI project. The focus of this manuscript is to give an overview of these mobile measurements and to discuss the applicability of such measurements for the investigation of megacity emissions. The used mobile laboratories MoLa and MOSQUITA as well as their instrumental details are presented. The applied measurement strategies include cross section measurements for the investigation of plume structure and quasi-Lagrangian measurements radially away from the city to study plume aging processes. Results of intercomparison measurements between the two mobile laboratories represent the adopted data quality assurance procedures. A special challenge is the preparation of data from mobile ground-based platforms for analysis like removal of local pollution contamination from the data sets. Furthermore advanced analysis tools like positive matrix factorization (PMF) and peak integration by key analysis (PIKA) applied to high-resolution time-of-flight aerosol mass spectrometer data are used for in-depth data analysis. We give several measurement examples, including a combination of MoLa and MOSQUITA data on a cross section through the Paris emission plume, to demonstrate how such mobile measurements can be used to investigate the emission plume of a megacity. A critical discussion of the potential and limitations of the presented mobile measurements completes this work.

1 Introduction

A growing fraction of the world´s population is living in cities or large urban agglomerations of increasing size. In 2008 more than 50 % of the human beings lived in an urban environment seeking for higher living standards. Considering the actual world´s population of more than 7 billion people (United Nations, 2011) this leads to a huge concentration of activities onto a relatively small area. The number of so-called megacities, defined as metropolitan areas with more than 10 million inhabitants (Molina and Molina, 2004), grew from 3 in 1975 to 20 in 2008. It is predicted, that in 2025 about 30 cities worldwide will classify as megacities (United Nations, 2009). Along with major challenges as urban planning, industrial development and transportation these intense pollution hot-spots cause a number of scientific questions concerning their influence on

local and regional air quality, with its impact on human health, flora and fauna as well as atmospheric chemistry and climate (e.g. Kunkel et al., 2012).

In Europe the metropolitan areas of London, Paris, the Rhine-Ruhr and the Po valley regions, Moscow and Istanbul are qualified as megacities. Within the framework of the European Union FP7 MEGAPOLI project (**M**egacities: **E**missions, urban, regional and **G**lobal **A**tmospheric **POL**lution and climate effects, and **I**ntegrated tools for assessment and mitigation, MEGAPOLI Project, 2012) two major field campaigns have been carried out in the greater Paris region in summer 2009 and winter 2010. The focus of these measurement campaigns is to characterize the Paris emission plume, to assess its impact on the local and regional air quality and to investigate aerosol transformation processes within this plume as it travels away from its source. Additionally, the influence of meteorology on the emission plume was studied due to different environmental conditions in summer and winter.

Typically, aerosol and trace gas measurements take place at stationary sites which leads to a strong spatial limitation of the data. Especially for the investigation of emissions from spatially extended aerosol sources like cities and their formation and transformation during transport, stationary measurements are only suitable to a limited extent. For this purpose, in the past few years several mobile laboratories equipped with high-time resolution instrumentation have been developed which allow measurements with large spatial flexibility (Bukowiecki et al., 2002; Kolb et al., 2004; Pirjola et al., 2004; Pirjola et al., 2009; Drewnick et al., 2012).

Here we focus on mobile ground-based measurements of aerosol and trace gas characteristics that have been carried out during both campaigns by two research groups with two different mobile aerosol laboratories. These mobile measurements were embedded in a network of stationary ground-based, additional mobile ground-based remote sensing and aircraft measurements, satellite observations and local, regional and global modelling (Beekmann et al., 2012). To integrate the presented measurements in a greater context of urban pollution investigations we refer to the comprehensive number of publications focused on this topic (e.g. Nunnermarcker et al., 1998; McMurry, 2000; Raga et al., 2001; Gros et al., 2007; Pey et al., 2008; Elanskii et al., 2010; Crippa et al., 2012a; Freutel et al., 2012).

Both mobile laboratories are equipped with state-of-the-art instrumentation to measure aerosol particle and trace gas properties. Important parameters that characterize the aerosol are particle number and mass concentration and chemical composition. Especially, for the measurement of the sub-micron particle chemical composition new sophisticated on-line measurement devices as the aerosol mass spectrometer have been developed (Jayne et al., 2000; Drewnick et al., 2005; DeCarlo et al., 2006; Lanz et al., 2010). In combination with complex analysis tools as positive matrix factorization (PMF) (Paatero and Tapper, 1994; Paatero, 1997; Lanz et al., 2007; Ulbrich et al., 2009) and peak integration by key analysis (PIKA) (ToF-AMS Analysis Software Homepage, 2012) a large amount of information can be obtained about aerosol properties (Zhang et al., 2005; Canagaratna et al., 2007; Sun et al., 2010; Zhang et al., 2011). The additional measurement of major trace gases like carbon dioxide, ozone and nitrogen oxides together with meteorological parameters helps to improve the insight into atmospheric processes, especially in urban environments (e.g. Fenger, 1999; Akimoto, 2003; Crutzen, 2004; Gurjar and Lelieveld, 2005).

Here we present an overview of several measurement applications of two mobile laboratories in the framework of urban aerosol studies. In Sect. 2 we focus on a detailed description of the MEGAPOLI field campaigns. We give an introduction to the two mobile laboratories including specification and intercomparison of the on-board instruments. The different measurement

strategies applied during different environmental conditions are described. A general overview of the advanced data preparation for analysis completes this section. In Sect. 3 four examples of mobile measurements are presented. These measurements give insight into the differences between long-range transported and locally produced pollution. A combination of both mobile laboratories data allows a detailed view of the spatial structure of the emission plume. Radial measurement trips show the decrease in pollution burden with increasing distance to the source. In a final example of stationary measurements at various locations around Paris the influence of the Paris emission plume on local air quality is illustrated. Sect. 4 provides a critical discussion of possibilities, challenges and limitations of mobile measurements. Finally, the information content of the MEGAPOLI mobile data sets with respect to further analysis is examined.

2 Methods

2.1 MEGAPOLI field campaigns

MEGAPOLI project: The European Union FP7 MEGAPOLI project is a collaborative project that involves several European research groups and also scientists from non-European countries. The main goals are first to assess impacts of megacities and large air-pollution hot-spots on local, regional, and global air quality and climate, second to quantify feedbacks between megacity emissions, air quality, local and regional climate, and global climate change and third to develop and implement improved, integrated tools to assess the impacts of air pollution from megacities on regional and global air quality and climate and to evaluate the effectiveness of mitigation strategies (MEGAPOLI Project, 2012). The project combines modeling and measurement efforts to achieve the mentioned objectives.

MEGAPOLI field campaigns: In the context of this project two major field campaigns took place in the greater Paris region in France. As mentioned above the Paris urban area which classifies as megacity with currently about 10.5 million inhabitants (population living in areas classified as urban according to the criteria used by France) (United Nations, 2009). The greater Paris metropolitan area, defined as the territory with high residential density and additional surrounding areas that are also influenced by the city, for example by frequent transport or road linkages (United Nations, 2009) has actually a population of more than 12 million inhabitants (Aire urbaine, 2012). The summer measurement period has been carried out between 1 July and 31 July 2009, the winter field campaign between 15 January and 15 February 2010. The main objective of these field measurements is to characterize and quantify sources of primary and secondary aerosol in and around a large agglomeration and to investigate its evolution and impacts on local and regional air quality as well as atmospheric chemistry in the megacity emission plume. In addition to three ground-based stationary measurement sites – two suburb and one downtown site (for details see MEGAPOLI project (2012), Freutel et al. (2012) and Crippa et al. (2012a)) –, aircraft-based measurements and specialized mobile measurements (DOAS instrument operated on top of a regular passenger vehicle, a LIDAR instrument installed on a pick-up (Royer et al., 2011)), two mobile laboratories for state-of-the-art aerosol and trace gas measurements have been deployed. These mobile laboratories measured while driving through atmospheric background and emission plume influenced air masses, carried out several stationary measurements at various places in and around Paris and have also been used for intercomparison studies with the other measurement sites for data quality assurance. In the following section the two mobile laboratories are introduced in more detail.

2.2 Mobile laboratories and on-board instrumentation

2.2.1 Mobile laboratory "MoLa"

Mobile Laboratory: The Max-Planck-Institute for Chemistry developed a compact **Mo**bile aerosol research **La**boratory ("MoLa") for stationary and mobile measurements of aerosol and trace gas characteristics. MoLa utilizes a Ford Transit delivery vehicle as platform that has been modified to meet the requirements of a fully equipped mobile research laboratory. The main inlet system for mobile measurements is located above the driver´s cabin in a height of approximately two meters and it is equipped with a nozzle optimized for an average driving velocity of about 50 km h^{-1}. Stationary measurements have been performed using an extendable mast (up to 10 m) on the roof of the vehicle for aerosol sampling. A detailed description of MoLa including technical details can be found in Drewnick et al. (2012).

Measurement instruments: During both field campaigns MoLa has been equipped with the High-Resolution Time-of-Flight Aerosol Mass Spectrometer (HR-ToF-AMS) to measure size resolved mass concentrations of non-refractory species (together with black carbon this includes most species found in the sub-micron aerosol) approximately in the PM_1 (< 1 μm) size range (DeCarlo et al., 2006). Additionally, black carbon and particle-bound polycyclic aromatic hydrocarbon mass concentrations have been measured to achieve detailed chemical information about total PM_1 particle composition. The aerosol particle concentration has been investigated by total number concentration as well as particle size distribution measurements, applying three different techniques (electrical mobility, aerodynamic sizing, light scattering). The detected trace gases include O_3, SO_2, NO, NO_2, CO, CO_2 and H_2O. Meteorological parameters have been recorded as well as GPS vehicle position. Additionally, environmental conditions (e.g. traffic situation) using a webcam and nuclear radiation applying a Geiger counter have been detected. In Table 1 a list of measurement devices (introducing their abbreviations used in this publication) applied during the MEGAPOLI campaigns is presented, including instrument details and measured parameters. In the following section the working principles of these instruments are explained in more detail. During other field campaigns slightly different sets of instruments have been used in MoLa (e.g. Diesch et al., 2012a; Diesch et al., 2012b).

A specific feature of the MoLa aerosol inlet system is its optimization and characterization for minimal sampling and transport losses using the Particle Loss Calculator (von der Weiden et al., 2009). The residence time of the aerosol during its way through the inlet system to the individual instruments has been measured and calculated for sampling time correction (see Sect. 2.3 and Drewnick et al., 2012).

2.2.2 Mobile laboratory "MOSQUITA"

Mobile Laboratory: The Paul Scherrer Institute in Villigen, Switzerland, developed in 2000 a first version of an aerosol and trace gas mobile laboratory (**M**easurements **O**f **S**patial **QU**antitative **I**missions of **T**race gases and **A**erosols: "MOSQUITA"), that was remodeled in 2009 (Weimer et al., 2009; Mohr et al., 2011). The mobile laboratory utilizes an IVECO Turbo Daily Transporter as platform and has been modified to a fully equipped research laboratory. The main aerosol inlet is located in a height of 3.2 m in the front part of the vehicle. A nozzle with a diameter of 1 cm allows isokinetic sampling at a driving velocity of 50 km h^{-1}. A heavy-duty blower eliminates the influence of driving speed on the aerosol transportation by providing a constant flow velocity of 0.5 m s^{-1} in

Table 1: Summary of measurement devices – including information about measured parameters, size range, time resolution and detection limit – installed in the mobile laboratory MoLa (Max-Planck-Institute for Chemistry) during the summer and winter MEGAPOLI field campaigns. AMS detection limit (using the method described in Drewnick et al., 2009) is calculated for summer (S) and winter field campaign (W) separately, because the AMS detection limit can change over time.

Measurement device	Measured parameter	Size range	Time resolution	Detection limit
AMS[6]	Size-resolved aerosol chemical composition	50 nm – ~1 μm	1 min	organics: 0.03 (S) / 0.01 (W) μg m^{-3} nitrate: 0.05 (S) / < 0.01 (W) μg m^{-3} sulfate: < 0.01 (S) / 0.01 (W) μg m^{-3} ammonium: 0.06 (S) / 0.03 (W) μg m^{-3}
MAAP[7]	Black carbon mass concentration	10 nm – 1 μm	1 min	0.1 μg m^{-3}
PAS[8]	PAH mass concentration	10 nm – 1 μm	12 s	1 ng m^{-3}
CPC[9]	Particle number concentration	2.5 nm – 3 μm	1 s	N/A
FMPS[10]	Particle size distribution based on electrical mobility	5.6 nm – 560 nm (32 channels)	1 s	N/A
APS[11]	Particle size distribution based on aerodynamic sizing	0.5 μm – 20 μm (52 channels)	1 s	N/A

[6] HR-ToF-AMS, Aerosol Mass Spectrometer (AMS), Aerodyne Research, Inc., USA, (http://aerodyne.com, last accessed 11.01.2012)
[7] Multi-Angle Absorption Photometer (MAAP), Carusso / Model 5012 MAAP, Thermo Electron Corp., USA, (http://thermoscientific.com, last accessed 11.01.2012)
[8] PolyAromatic Hydrocarbon Sensor (PAS), EcoChem Model PAS2000, Ansyco, Germany, (http://ansyco.de, last accessed 11.01.2012)
[9] Condensation Particle Counter (CPC), Model 3786, TSI, Inc., USA, (http://tsi.com, last accessed 11.01.2012)
[10] Fast Mobility Particle Sizer Spectrometer (FMPS), Model 3091, TSI, Inc., USA
[11] Aerodynamic Particle Sizer Spectrometer (APS), Model 3321, TSI, Inc., USA

OPC[12]	Particle size distribution based on light scattering	0.25 μm – 32 μm (31 channels)	6 s	N/A
Airpointer[13]	O_3, SO_2, CO, NO, NO_2 mixing ratio	N/A	1 min	O_3: < 1.0 ppbV SO_2: < 1.0 ppbV CO: < 0.2 ppmV NO_x: < 1.0 ppbV
LI-840[14]	CO_2, H_2O mixing ratio	N/A	1 s	CO_2: < 1 ppmV (RMS noise) H_2O: < 10 ppmV (RMS noise)
Meteorological Station[15]	Wind speed, wind direction, temperature, precipitation, pressure, relative humidity	N/A	1 s	Accuracy: WindSp: 0.3 m s^{-1} WindDir: 3° Temp: 0.3 C° RH: 3% Precipitation: 5% Pressure: 0.5 hPa
Geiger Counter[16]	α, β, □□ radiation	N/A	10 s	N/A
GPS[17]	Vehicle location and speed	N/A	1 s	N/A
Webcam[18]	Driver´s view through windshield	N/A	1 s	N/A

[12] Optical Particle Counter (OPC), Model 1.109, Grimm Aerosoltechnik, Germany, (http://grimm-aerosol.com, last accessed 11.01.2012)
[13] Airpointer, Recordum Messtechnik GmbH, Austria, (http://recordum.com, last accessed 11.01.2012)
[14] LI-COR, Model LI-840, Corp., USA, (http://licor.com, last accessed 11.01.2012)
[15] Model WXT520, Vaisala, Finland, (http://vaisala.com, last accessed 11.01.2012)
[16] Model Gamma-Scout online, GAMMA-SCOUT GmbH, Germany, (http://gamma-scout.de, last accessed 11.01.2012)
[17] Garmin, GPSmap 278, Garmin Ltd., USA, (http://garmin.com, last accessed 11.01.2012)
[18] Model EDIMAX IC7000, Edimax Technology Co., Ltd., Taiwan, (http://edimax.com, last accessed 11.01.2012)

the sampling system. A detailed description of this mobile laboratory is given by Bukowiecki et al. (2002) and on the Paul Scherrer Institute´s website (Mobile Laboratory MOSQUITA, 2012).

Measurement instrumentation: MOSQUITA investigated PM_1 particle chemical composition by applying a HR-ToF-AMS and additional black carbon mass concentration measurements. Aerosol particle concentrations have been measured in total as well as size resolved applying different techniques in summer (electrical mobility) and winter (light scattering). Additionally, the aerosol active surface area has been investigated. The recorded trace gases are O_3, NO, NO_2, CO, CO_2 and H_2O. Meteorological parameters as well as GPS information and webcam videos complete the MOSQUITA data set. In Table 2 a list of measurement devices applied during the MEGAPOLI campaigns is presented. The instrumentation of MOSQUITA can also be altered depending on the scientific targets. Examples for different instrumental set-ups are given in Weimer et al. (2009) and Mohr et al. (2011).

In the following Section comparisons for those instruments that measure similar parameters in both mobile laboratories are presented. This is an essential step if both data sets are combined during further analysis (see Sect. 3.2).

2.2.3 Intercomparison of similar measurement devices

To assure comparable data quality for both mobile laboratories it is necessary to compare those instruments with each other that measure the same or a related quantity. Intercomparison measurements have been carried out several times during both field campaigns. Not only MoLa and MOSQUITA have been compared, but also both mobile laboratories with the other stationary ground-based measurement sites and the research aircraft. These intercomparison measurements resulted in comparable agreements of the respective instruments like those described in this publication. A detailed description of the results of these intercomparison exercises can be found in Freutel et al. (2012) and Crippa et al. (2012a).

For the two mobile laboratories the instruments measuring the following parameters have been compared in this study (for instrument abbreviations see Table 1 and 2):

1. Particle number size distribution (FMPS, UHSAS, APS, OPC)
2. Particle number concentration (CPC3786, CPC3010s)
3. Non-refractory chemical aerosol composition (two HR-ToF-AMS)
4. Black Carbon mass concentration (two MAAP)
5. CO_2 mixing ratio (LI-840, LI-7000)
6. O_3 mixing ratio (Airpointer, Ozone-monitor)
7. NO_x mixing ratio (Airpointer, Luminox monitor)

CO mixing ratio has not been compared, because due to issues with the MoLa instrument all measurements have been below detection limit during both campaigns and thus were not used for further analysis. An intercomparison of H_2O mixing ratio and meteorological parameters has not been performed in this context, because these quantities have a minor importance for the further combined analysis of the mobile data sets. However, the intercomparison of the MoLa weather

Table 2: Summary of measurement devices – including information about measured parameters, size range, time resolution and detection limit – installed in the mobile laboratory MOSQUITA (Paul Scherrer Institute) during the summer and winter MEGAPOLI field campaigns. AMS detection limits are calculated and averaged for the two mobile measurements presented in this work.

Measurement device	Measured parameter	Size range	Time resolution	Detection limit
AMS[19]	Size-resolved aerosol chemical composition	50 nm – ~1 μm	5 s (S) / 10 s (W)	organics: 0.3 μg m^{-3} nitrate: 0.07 μg m^{-3} sulfate: 0.06 μg m^{-3} ammonium: 0.25 μg m^{-3}
MAAP[20]	Black carbon mass concentration	10 nm – 1 μm	1 s	0.1 μg m^{-3}
CPC[21]	Particle number concentration	10 nm – 3 μm	1 s	N/A
FMPS[22] (only summer)	Particle size distribution based on electrical mobility	5.6 nm – 560 nm (32 channels)	1 s	N/A
UHSAS[23] (only winter)	Particle size distribution based on light scattering	60 nm – 1 μm (100 channels)	1 – 150 s	N/A
DC[24]	Aerosol active surface area	1 nm – 1 μm	1 s	10 μm^2 cm^{-3}
Ozone-monitor[25]	O_3 mixing ratio	N/A	2 s	1 ppbV
CO analyzer[26]	CO mixing ratio	N/A	1 s	2 ppbV
LI-7000[27]	CO_2 and H_2O mixing ratio	N/A	1 s	CO_2: 0.035 ppmV (RMS noise) H_2O: 2 ppmV (RMS noise)

[19] HR-ToF-AMS, Aerosol Mass Spectrometer, Aerodyne Research, Inc., USA
[20] Multi-Angle Absorption Photometer, Carusso / Model 5012 MAAP, Thermo Electron Corp., USA
[21] Condensation Particle Counter, Model 3010s, TSI, Inc., USA
[22] Fast Mobility Particle Sizer Spectrometer, Model 3091, TSI, Inc., USA
[23] Ultra High Sensitivity Aerosol Spectrometer (UHSAS), PMT Partikel-Messtechnik GmbH, Germany, (http://pmt.eu, http://dropletmeasurements.com last accessed 11.01.2012)
[24] Diffusion Charging Sensor (DC), Model LQ1-DC, Matter engineering AG (now: Matter aerosol AG), Switzerland, (http://matter-aerosol.ch, http://labs.ti.bfh.ch/uploads/media/NP_Messtechnik_EN.pdf last accessed 11.01.2012)
[25] Ozone-monitor (UV absorption), constructed by Paul Scherrer Institute, Switzerland
[26] Model AL 5002 VUV Fast Fluorescence CO Analyser, Aerosolaser GmbH, Germany, (http://aero-laser.com, last accessed 11.01.2012)
[27] LI-COR, Model LI-7000, Corp., USA

NO_x analyzer[28]	NO_x mixing ratio	N/A	1 s	< 100 pptV
Ambient temperature sensor[29]	Temperature	N/A	< 1 min	Accuracy: 0.15 °C
Pressure sensor[30]	Pressure	N/A	< 1 min	Common standard
HUMICAP sensor[31]	Relative humidity	N/A	< 1 min	Accuracy: 2 % (0 – 80 % RH) 3 % (80 – 100 % RH)
Wind sensor[32]	Wind direction	N/A	1 s	Common standard
Pyranometer[33]	Global radiation	N/A	< 1 min	< 1% (40°/60° zenith angle) < 3% (80° zenith angle)
GPS[34]	Vehicle location and speed	N/A	2 s	N/A
Webcam[35]	Driver´s view through windshield	N/A	1 s	N/A

parameters showed excellent agreement with the meteorological parameters measured at the North-East suburb measurement site (Freutel et al., 2012).

Intercomparison time periods: The intercomparison time periods in the summer campaign are 11 July 2009 from 12:05:00 till 17:39:00 (at Pontoise airport) and 23 July 2009 from 11:22:00 till 19:00:00 (at the South-West suburb measurement site). The winter intercomparison took place on 9 February 2010 from 11:42:00 till 19:30:00 also at the South-West suburb measurement site. All given times are in local time. For details about the mentioned measurement sites we refer to the MEGAPOLI project´s website (MEGAPOLI Project, 2012) and Beekmann et al. (2012).

Particle number size distribution: During the summer field campaign both mobile laboratories applied identical FMPS devices. The measured particle number size distributions are in the same order of magnitude and the averaged size distributions during the two intercomparison periods show the same modes (nucleation mode around 20 nm particle diameter and accumulation mode around 100 nm). The temporal trends of the size distribution are reproduced by both instruments. Smaller differences of the absolute concentration in some size channels mainly during the first intercomparison can be explained by an instrumental calibration error of the MOSQUITA instrument. During the second intercomparison this difference is no longer visible. In summer the FMPS size distribution measurements are consistent within the range of uncertainty of the devices.

[28] Model LMA-3 Luminox Monitor, SCINTREX Ltd., Canada, (http://scintrexltd.com, last accessed 11.01.2012)
[29] Model YSI 44203 Thermilinear thermistor network, Inteltronics Instrumentation, South Africa (http://inteltronics.co.za, last accessed 11.01.2012)
[30] Pressure sensor, constructed by Paul Scherrer Institute, Switzerland
[31] Model HMP 31UT HUMICAP sensor, Vaisala, Finland
[32] Wind sensor, constructed by Paul Scherrer Institute, Switzerland
[33] Solarimeter, Model CM10, Kipp&Zonen, Netherlands, (http://kippzonen.com, last accessed 11.01.2012)
[34] Garmin IIplus, Garmin Ltd., USA
[35] BISCHKE Model CCD-FX-5612, EverFocus Electronics GmbH, Germany, (http://everfocus.com, last accessed 11.01.2012)

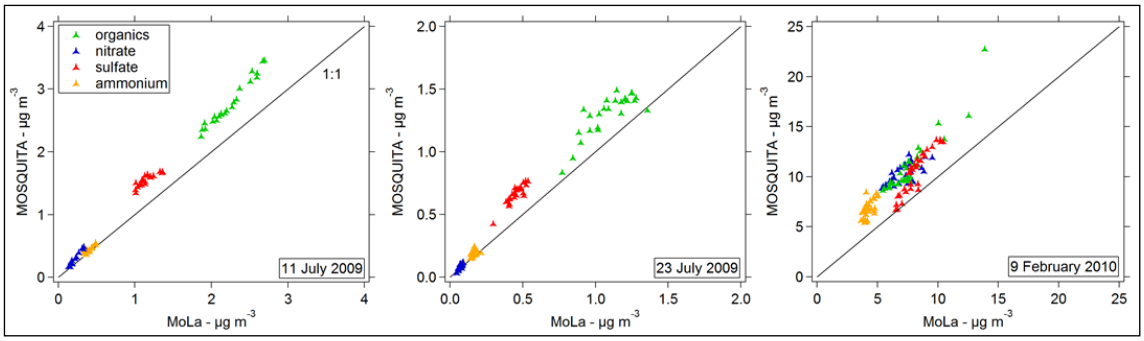

Figure 1: Correlation of sub-micron particulate organics (green), nitrate (blue), sulfate (red) and ammonium (orange) simultaneously measured by the mobile laboratories MoLa (x-axis) and MOSQUITA (y-axis) during the three intercomparison periods of the summer and winter campaign. The data are averaged to a common 15 min time base. The fit parameters (slope and Pearson´s R^2) of linear fits through zero of the presented data are listed in Table 3.

During the winter campaign a different instrument for the particle size distribution measurement has been applied in MOSQUITA. The UHSAS and FMPS device overlap only in the size range between 55 and 560 nm. In this size range temporal variations are presented by both instruments and the derived absolute number concentrations are in the same order of magnitude. The UHSAS shows some instrumental artifacts which are probably caused by internal conversion calculations, however they are of minor relevance for this intercomparison. The UHSAS can also be compared to OPC and APS in MoLa, because these instruments overlap in the size range from 0.25 µm (OPC) and 0.5 µm (APS) up to 1 µm. The density and shape of the measured particles is not exactly known, so the different equivalent diameters (FMPS: electrical mobility diameter, UHSAS: optical diameter, OPC: optical diameter, APS: aerodynamic diameter) have not been converted into a common diameter for this intercomparison. The concentrations measured by the UHSAS are in average between the concentration values measured by OPC and APS. Additionally, the three size distribution devices in MoLa have been compared during both field campaigns. Here the average particle concentrations are in the same order of magnitude regarding the different equivalent particle diameters. In summary, with respect to the different measurement principles the agreement of all size distribution devices is sufficient for further combined analysis.

Particle number concentration: For the particle number concentration measurements we expect significant differences because the lower size cut-off of the CPCs is different. While the MoLa-CPC has a lower cut-off of 2.5 nm the MOSQUITA-CPC measures particles larger 10 nm. As expected, the MoLa instruments detects always equal or more particles than the other instrument. Accounting for the different size ranges the agreement of total number and temporal variations is satisfying and approximate comparability of the two measurements is given if no extreme concentrations of nucleation mode particles are present.

Non-refractory chemical particle composition: For the intercomparison of non-refractory particle chemical composition the time series of particulate organics, nitrate, sulfate, ammonium and chloride have been compared. While for both HR-ToF-AMS data sets the same data processing routines have been applied (m/z calibration, baseline correction, instrument background measurements, additional calibration parameters) different values for the collection efficiency are used during the summer campaign. For the MoLa data set a standard collection efficiency of 0.5 (Matthew et al., 2008) is applied during both campaigns, for the MOSQUITA data set the same value was used in winter, however a value of 1.0 was applied for the summer data set . This unusual collection efficiency is justified on the one hand by instrumental features and is based on long-term experience with the MOSQUITA instrument. On the other hand including all intercomparison measurements (not only AMS intercomparisons, but also AMS comparison with additional PM_1 measurements) carried out during both campaigns it seems to be appropriate to apply different

collection efficiencies for the MOSQUITA summer and winter AMS data. A second difference between the data sets is the mode of operation of the two HR-ToF-AMSs. The MoLa instrument switched between 10 s in the mass spectrum mode and 10 s in the particle time-of-flight mode, both in V-mode (medium resolution but high sensitivity) only. The MOSQUITA instrument applied shorter mode switching times, and also measured in V-mode only. During the summer campaign the AMS switched between 3 s in mass spectrum mode and 2 s in particle time-of-flight mode. In winter it switched between 5 s in mass spectrum mode and 5 s in particle time-of-flight mode. Due to the shorter measurement time a higher temporal resolution of the AMS data has been achieved compared to the MoLa instrument.

In Fig. 1 the AMS data measured by MOSQUITA versus those measured by MoLa during the three intercomparison times are presented. Chloride data are not shown, because ambient values have been below the detection limit most of the time. The data are averaged to a common 15 min data base. In Table 3 the correlation parameters (slope and Pearson´s R^2) of linear fits forced through zero of the respective AMS data are listed, as well as average ratios of mass concentrations of MoLa to MOSQUITA data and mean concentration values of both instruments. The given uncertainties represent the standard deviations of the respective parameters, which include ambient variations as well as instrumental noise. In Fig. 1 as well as from Table 3 can be seen, that the MOSQUITA AMS measured always higher species mass concentrations than the MoLa instrument. During the summer campaign the average ratio of the MoLa to the MOSQUITA AMS concentrations is about 0.80; during the winter campaign this ratio seems to be lower with about 0.70. The Pearson´s R^2 values are between 0.84 and 0.97 for the first intercomparison period, which implies that temporal variations are observed by both instruments similarly. The low Pearson´s R^2 values for nitrate and ammonium during the second intercomparison (summer) can be explained by low ambient concentrations of these components near or below the detection limit of the MOSQUITA AMS. In winter ambient concentrations have been well above the detection limits of both instruments, however, especially for ammonium the Pearson´s R^2 value (0.39) is still low. Calibration errors of one or both instruments can be the reason for the observed differences in absolute mass concentrations (indicated by the slope and the MoLa to MOSQUITA AMS averaged mass concentrations ratio) and discrepancies in the temporal behavior of the AMS time series (indicated by Pearson´s R^2) could be explained by local emissions, which have been detected only by one of the AMSs. Nevertheless, general temporal trends are represented similarly by both instruments during all three intercomparion periods.

The overall uncertainty of AMS data is, including all uncertainties of operation mode, instrumental differences, different inlet setups, calibrations and analysis variations, about 30 % (Canagaratna et al., 2007), so the observed differences are within the range of uncertainty. Similar ranges of uncertainty were experienced during other intercomparison exercises as well (Bahreini et al., 2009). Intercomparisons of the MoLa and the MOSQUITA aerosol mass spectrometers with AMS instruments at the stationary measurement sites show discrepancies of the same order of magnitude (Freutel et al., 2012; Crippa et al., 2012a).

Black carbon mass concentration: Although black carbon mass concentrations are measured with two identical instruments during the summer campaign the MOSQUITA device measured on average about 40 % more than the MoLa device. In winter the difference is slightly lower with about 30 %. Temporal variations are similarly represented by both instruments. However, this significant difference can only be explained by calibration errors, deterioration of instrumental components and / or differences in the inlet systems. The MoLa MAAP sampled the aerosol through a PM_1 cyclone (only particles up to 1 μm have been measured) while the MOSQUITA device was not

operated in combination with a specific size selective aerosol inlet. Comparison results of the MoLa instrument with other black carbon measurements can be found in Freutel et al. (2012). In this publication the difference of identical MAAP instruments is satisfyingly small with about 10 %.

CO_2 mixing ratio: CO_2 mixing ratios can only be compared during the summer campaign, because of data recording problems of the MOSQUITA CO_2 device during the winter intercomparison. During the second intercomparison in summer there also seems to be a calibration problem of this device. However, during the first time period temporal variations are satisfyingly represented by both instruments and the difference of the absolute concentrations is less than 1 %.

Table 3: Average ratios of MoLa data to MOSQUITA data, average concentration values in µg m^{-3} of both HR-ToF-AMS instruments and two correlation parameters[36] (slope and Pearson´s R^2) for the three intercomparison time intervals for the measured parameters sub-micron particulate organics, nitrate, sulfate and ammonium. The given uncertainties represent the standard deviations.

	organics	nitrate	sulfate	ammonium
11.07.2009				
MoLa / MOSQUITA	0.81 +/- 0.05	0.79 +/- 0.21	0.74 +/- 0.05	0.92 +/- 0.14
Average MoLa	2.24 +/- 0.29	0.20 +/- 0.07	1.15 +/- 0.11	0.39 +/- 0.06
Average MOSQUITA	2.77 +/- 0.40	0.27 +/- 0.13	1.55 +/- 0.12	0.43 +/- 0.07
Slope	1.24 +/- 0.01	1.36 +/- 0.02	1.34 +/- 0.01	1.10 +/- 0.01
Pearson´s R^2	0.97	0.97	0.76	0.84
23.07.2009				
MoLa / MOSQUITA	0.83 +/- 0.08	0.91 +/- 0.34	0.69 +/- 0.05	0.89 +/- 0.22
Average MoLa	1.09 +/- 0.23	0.07 +/- 0.02	0.45 +/- 0.05	0.16 +/- 0.03
Average MOSQUITA	1.30 +/- 0.18	0.08 +/- 0.03	0.66 +/- 0.07	0.19 +/- 0.04
Slope	1.19 +/- 0.02	1.20 +/- 0.04	1.46 +/- 0.02	1.14 +/- 0.03
Pearson´s R^2	0.68	0.61	0.82	0.38
09.02.2010				
MoLa / MOSQUITA	0.70 +/- 0.07	0.69 +/- 0.08	0.80 +/- 0.09	0.63 +/- 0.06

[36] Linear fit through zero for MOSQUITA AMS data versus MoLa AMS data (15 min averages of organics, nitrate, sulfate and ammonium, respectively).

Average MoLa	7.64 +/- 2.68	6.79 +/- 1.08	8.14 +/- 1.13	4.21 +/- 0.42
Average MOSQUITA	10.97 +/- 3.38	10.14 +/- 1.03	10.46 +/- 2.12	6.78 +/- 0.87
Slope	1.43 +/- 0.02	1.43 +/- 0.03	1.29 +/- 0.02	1.60 +/- 0.03
Pearson´s R^2	0.88	0.53	0.84	0.39

O_3 mixing ratio: O_3 mixing ratios also show comparable temporal variations. On average the MoLa instrument measures about 5 % more than the MOSQUITA device during the first summer intercomparison and 25 % more during the second one. In winter the difference is about 30 %. The MoLa instrument is less sensitive than the one in MOSQUITA and the difference could be explained by different instrument designs and calibration errors. Additional intercomparisons of both instruments to O_3 devices at the fixed measurement sites show very good agreement for the MoLa instrument (summer and winter) and good comparability for the MOSQUITA device (only validated for summer, because in winter no additional intercomparison data are available).

NO_x mixing ratio: The comparison of the two NO_x instruments presented here has only limited significance, because the MoLa device had problems with this parameter during both campaigns and the MOSQUITA instrument during the summer campaign. The MOSQUITA NO_x monitor showed significant offsets of the measured absolute NO_x concentrations due to calibration issues. Internal operation mode settings of the MoLa NO_x module caused extended increased temporal averaging intervals of this parameter during times with low NO_x variations like the intercomparison periods. So only the mean values of both instruments for the three intercomparison periods can be compared. Here the MOSQUITA device measured in summer by a factor of approximately 7 higher NO_x concentrations and in winter 30 % less than the MoLa device. This large difference especially during the summer campaign is most likely caused by incorrect calibration of the MOSQUITA instrument and is only minimal biased by the averaging settings of the MoLa device. During mobile measurements with higher temporal variations of the NO_x mixing ratio the influence of the averaging algorithm is negligible and the data can be used for analysis. Additionally, the detection limit of the MoLa device is higher than that of the MOSQUITA device. Especially during the first intercomparison period in summer ambient NO_x concentrations have been in the same order of magnitude as the MoLa NO_x detection limit. Intercomparisons of these two instruments with instruments at the fixed measurements sites show good results for the MoLa device in summer and winter and also a large offset of the MOSQUITA instrument during summer (no additional intercomparison data are available for the MOSQUITA device in winter).

In summary, the agreement of most parameters, except black carbon and NO_x, is within the range of uncertainty of the instruments and the data are sufficiently accurate for combined analysis. Aerosol sampling artifacts occurring in the two inlet systems and small scale (few meters) aerosol concentration differences should not have influenced the intercomparison in a significant way.

2.3 Data preparation for analysis

Mobile data are adversely influenced by additional factors that are often negligible during stationary measurements. Especially local contamination caused by, for example, vehicles driving in front of the mobile laboratory or emission sources near the street is problematic for the processing of the measurement data. Pollution from these sources can dominate the measured data, since typically

the emitted local concentrations are large compared to ambient values. Those contaminations have to be removed from the data set when ambient air is supposed to be measured, e.g. when background and plume emissions are investigated. Otherwise misinterpretation of the data set is possible. Details about contamination removal procedures are given in Sect. 2.3.1.

Another issue especially important for mobile measurements is the residence time of the aerosol in the inlet system. High temporal resolution (seconds) of the data is desired for analysis of mobile measurements and time shifts caused by transport of the aerosol should be corrected. For both mobile laboratories the residence times for each instrument has been calculated and verified by measurements. All mobile measurement data are corrected for the sample residence time in the inlet system. Due to the optimization and characterization of both inlet systems particle losses during transport to the instruments are known and in a negligible order of magnitude. For more details see Bukowiecki et al. (2002), Mohr et al. (2011) and Drewnick et al. (2012). Further processing of the data like removal of calibration periods and outliers, application of calibration and correction factors, averaging on a common time base and general tests for reasonability is self-evident.

To obtain as much information as possible especially from HR-ToF-AMS data several advanced analysis methods are available. Two of them, PMF and PIKA, have been used for the processing of this data set and are introduced in Sect. 2.3.2 and 2.3.3.

2.3.1 Removal of local contamination

Local pollution – e.g. emissions from a vehicle in front of the mobile laboratory or from strong sources next to the road that are passed – is problematic if the phenomena investigated are not strongly distinct compared to the local emissions. The influence of local contamination can only be neglected when the probed concentrations are either extremely high or when the composition or other features of the intended sample differs strongly from those of the local emissions. In our case, as in most cases, the Paris emission plume characteristics can only be successfully extracted if in a first step all measurement data significantly influenced by local pollution are eliminated from the data set. Several methods have been tested to obtain uncontaminated mobile data sets (Drewnick et al., 2012). The finally applied "video tape analysis procedure" is explained below.

Video tape analysis procedure: During the analysis of the MEGAPOLI data set it has become apparent that the most consistent method to identify local contamination is to analyze the video tapes of mobile measurements recorded by the webcam in the driver´s cabin. Therefore several criteria for contaminated time periods have been defined:

- Times whiles driving through a village / town due to higher traffic, heating, cooking and other human activities.

- Times when a vehicle is less than about 150 m in front of the mobile laboratory or when there is significant traffic on the road including the opposite lane.

- Times while the driving velocity of the mobile laboratory is low increasing the possibility of contamination by the own exhaust.

- Times while next to the street a source of local contamination is visible, for example a burning fire or a working tractor.

- Times while driving through a tunnel, because exhaust emissions might be accumulated.

All 1-second intervals fulfilling at least one of these criteria are marked as contaminated and corresponding data points are removed before further analysis. For data with lower time resolution minutes with more than 20 contaminated 1-second intervals are also removed. This criterion is somewhat arbitrary, but seems to be a good balance between removing partly contaminated data and keeping as much data as possible. This method treats all instrument time series equally and it is best possible objective due to the direct pollution source identification.

Only for a first interpretation of the individual measurement trips the contaminated data sets can be used to avoid the time consuming pollution removal procedure for data sets that are not used for later analysis. For all further analysis of the Paris emission plume only the uncontaminated data have been used to obtain best results and conclusions.

2.3.2 Positive Matrix Factorization

Positive Matrix Factorization: Positive Matrix Factorization (PMF) is used to identify and apportion sources of aerosol particles in the atmosphere based on the principle of mass conservation. Such methods, that use measured ambient concentrations as inputs and estimate source contributions, are generally known as receptor models. They are used to reduce large data sets by estimation of number and composition of potential aerosol sources ("factors" that explain the data variability). Part of this study is to identify different sources of organic aerosol contributing to the emission plume from the Paris agglomeration. The importance of organic aerosol is demonstrated by its high fraction of the total submicron aerosol mass. It can consist of multiple organic components and the scientific interest in formation and transformation processes in the atmosphere is high (Jimenez et al., 2009; Lanz et al., 2010). Therefore PMF became one of the standard analysis techniques for HR-ToF-AMS data in the past few years (Zhang et al., 2011). With this method it is possible to extract factors representing not only organic aerosol of different sources but also organic aerosol of different oxidation state which is correlated to the age of the aerosol. However, the mathematic algorithm of PMF has several uncertainties by itself (e.g. start value "seed" of the calculation and rotational freedom of the solution given by the parameter "fpeak") and the freedom of the user inputs and interpretation adds additional uncertainty. Comparison of PMF results with external time series of other instruments and with mass spectra from known sources are tools for embedding those results in a greater context to identify the chemical nature of a certain PMF factor. For more details about the underlying mathematical algorithm and the applied software we refer to Paatero et al. (1994), Paatero et al. (1997), Lanz et al. (2007) and Ulbrich et al. (2009).

PMF of MEGAPOLI mobile data sets: PMF has been applied to both mobile unit mass resolution AMS data sets. For the MoLa data set four factors (hydrocarbon-like organic aerosol (HOA), low-volatile organic aerosol (LV-OOA) and two types of organic aerosol with higher volatility) have been extracted for the summer data set and five factors (HOA, LV-OOA, two types of organic aerosol with higher volatility and one factor associated with biomass burning) for the winter data set. PMF for the MOSQUITA mobile data sets resulted in mainly two factors for the summer (HOA and LV-OOA) and an additional third factor for the winter campaign which is also associated with biomass burning. HOA and LV-OOA are especially interesting for the identification of the Paris emission plume. HOA is mainly connected with fresh emissions e.g. from traffic like in the emission plume air masses, while LV-OOA represents highly oxidized long-range transported air masses which characterize the ambient background atmosphere. In Sect. 3.3 an example of the MoLa PMF results is presented. For further description of the mentioned factors (HOA, LV-OOA, etc.) we refer to Zhang et al. (2011). Details about the extracted factors and their identification using correlations with external time series and mass spectra, quantified uncertainties

and interpretation of the scientific content of the PMF results would exceed the frame of this overview paper. There will be further publications based on these mobile data sets including a detailed PMF discussion (Crippa et al., 2012b; von der Weiden-Reinmüller et al., 2012).

2.3.3 Peak integration by key analysis

PIKA (Peak Integration by Key Analysis, ToF-AMS Analysis Software Homepage, 2012) is another advanced analysis software tool for the speciation and quantification of HR-ToF-AMS data. PIKA is based on SQUIRREL (**S**e**QU**ential **I**gor data **R**et**R**i**E**va**L,** ToF-AMS Analysis Software Homepage, 2012), the standard software for basic analysis of AMS data, e.g. for application of calibration parameters and to obtain chemically resolved mass concentration time series or particle size distributions. In newer versions PIKA includes Apes (**A**nalytcial **P**rocedure for **E**lemental **S**eparation, ToF-AMS Analysis Software Homepage, 2012), a software tool for the separation of high resolution AMS ions to their elemental components. PIKA is a powerful tool for the extraction of detailed chemical information about single peaks (e.g. elemental or molecular information and on its isotopes for individual peaks) in the measured complex high resolution mass spectra. In this study PIKA has mainly been applied for the retrieval of the O/C ratio of the organic aerosol which is a marker for the oxidation state and therewith the age of the aerosol. In Sect. 3.2 an example of low O/C ratio as marker for fresh emissions in the Paris plume is presented. More details about PIKA, SQUIRREL and Apes can be found on the developers' website (ToF-AMS Analysis Software Homepage, 2012).

The applied PMF software tool as well as PIKA, SQUIRREL and Apes are based on the scientific graphing, data analysis, image processing and programming software tool IGOR Pro 6 (Wavemetrics, 2012)

2.4 Measurement strategies

The major advantage of mobile laboratories is the opportunity to measure while driving and to change within very short time the location for stationary measurements. The electrical power supply for the instruments and necessary installations, like for example air conditioning, is either produced by the engine of the vehicle that serves as platform or can be provided from external sources. MoLa has been operated in combination with an external power generator on a separate vehicle during both campaigns to carry out stationary measurements at various places in the greater Paris region. MOSQUITA has been applied for mobile measurements only. More details can be found in Drewnick et al. (2012) and Bukowieki et al. (2002).

Depending on environmental conditions like predicted plume strength, intensity and direction different measurement strategies have been applied. In the following sections the three main measurement scenarios are explained in detail. For the decision which type of measurement is most useful for a specific day regional plume prediction maps for pollutant markers like primary organic matter have been provided by Prev'Air (Honoré et al., 2008).

Prev'Air plume prediction maps: The Prev'Air forecast system (Prev'Air, 2012) started in 2003 and is based on global, European and national forecast simulations. The aim is to provide daily air quality forecast and re-analysis maps of pollutant markers like O_3, NO_2, PM_{10} and $PM_{2.5}$ for Europe and France. Air quality maps are provided as 2-day (e.g. simulating on Monday the air quality situation occurring on Wednesday), 1-day and actual day forecast and as retrospective re-analysis. These re-analysis maps – a combination of posteriori simulations and observations – are the most objective presentation of the pollution situation (Earthobservations, 2012). They have been also used for our

mobile measurements analysis (e.g. to check which part of the measurement route has been located in the Paris emission plume). Especially for the MEGAPOLI project detailed modeling forecasts of the Paris emission plume have been available focused on the greater Paris region.

Measurement planning: For the measurement planning 1-day forecast maps have been applied for a rough route planning on the evening before the measurement day. A combination of high resolution printed fold-up maps and actual day forecast maps has been used in the morning of the measurement day to decide on the actual driving route. Ideal routes for the investigation of a megacity emission plume avoid woods, streets with heavy traffic, larger villages and towns and regions with strong local pollution like near industrial plants. In general, mobile measurements have been carried out on minor roads with less traffic to avoid local pollution sources as much as possible. Stationary measurement sites have been chosen regarding similar considerations. Additional attention has been paid to provide a free undisturbed flow of the air masses to the sampling location. So places behind woods or in valleys have been avoided as well as places downwind of local pollution sources like villages or major streets. The appropriate weather and plume conditions for the three measurement scenarios are described in the following sections.

In summary MoLa performed a total of 31 mobile (including 6 radial trips) and 25 stationary measurements during both campaigns. MOSQUITA measured 17 times on the road, including one mobile measurement late in the evening. Stationary measurements have been performed with MOSQUITA only for intercomparison purposes.

2.4.1 Cross section measurements

To distinguish between ambient background and emission plume influenced aerosol and trace gas loadings of the ground level atmosphere cross section measurements are most beneficial. A cross section measurement usually starts in a region not influenced by the emission plume, then crosses the plume at a constant distance to the city and ends again in background air masses. Several cross section measurements at different distances from the city provide additional information about dilution and aging processes in the plume during transport. Applying this type of measurement it is also possible to investigate the structure of the plume and dilution processes at the plume border. If the predicted emission plume was distinct and reasonably stable in direction over a sufficient number of hours to finish a significant fraction of the measurement cross sections measurements have been carried out. Problems with this type of measurement occur when the plume is changing its direction during the day. To cover plume as well as background air masses usually takes several. So a shifting plume can appear deformed in the measured data with a broader, narrower or more heterogeneous shape than it was in reality.

In Fig. 2 an example of the emission plume forecast maps is shown for 31 January 2010 during the winter field campaign. The concentrations of the presented primary organic matter in the aerosol are represented by the color code. Purple and pink areas indicate low concentrations while blue to green and red areas indicate high values. The yellow arrows demonstrate cross section measurements at several distances from Paris. In Sect. 3.2 a measurement example of several cross sections performed during the summer campaign by MoLa and MOSQUITA is presented.

2.4.2 Radial measurements

To get insight into the spatial extent of the plume, i.e. up to which distance from the city it can be observed, radial measurements are most beneficial. The quasi-Lagrangian character (following an

individual air parcel along its trajectory) of such measurements also allows investigating atmospheric conversion processes, like oxidation of organic aerosol or ozone build-up from precursor gases, during transport and dilution with increasing distance to Paris. In Fig. 2 the black arrow demonstrates radial measurements starting at the outer suburbs of Paris and reaching as far as about 200 km away from the city. For this type of measurement a distinct emission plume with constant wind conditions is necessary. A wind shift of a few degrees over several hours is tolerable and the radial measurement route still should be located inside the plume. The megacity Paris is an area source of pollution and therewith the emission plume can be expected to have a width of more than ten kilometers. Appropriate weather conditions have been identified only on few days during both campaigns. An additional issue with this type of measurement appears when major roads or larger towns are located in the predicted plume direction. Fresh pollution from these local sources will mix with the Paris emission plume and change its physical and chemical properties like oxidation state of the organic aerosol or number concentration of small particles.

MoLa has carried out three radial trips during the summer campaign, two trips up to 160 km and one trip up to 180 km away from the city border. In winter one radial trip up to 100 km distance from Paris, two shorter radial trips up to 90 km on the same day and one combination of cross sections in several distances and a radial trip up to 60 km have been performed. MOSQUITA performed most of the mobile measurements as a combination of cross sections and radial trips to cover a wide area. With this strategy it is easier to measure the emission plume even if the plume direction is slightly uncertain or changing. The disadvantage of this method is that the distance to Paris that can be covered within several hours is not as large as on a straight radial trip. In Sect. 3.3 a measurement example of a radial trip performed during the summer campaign by MoLa is presented.

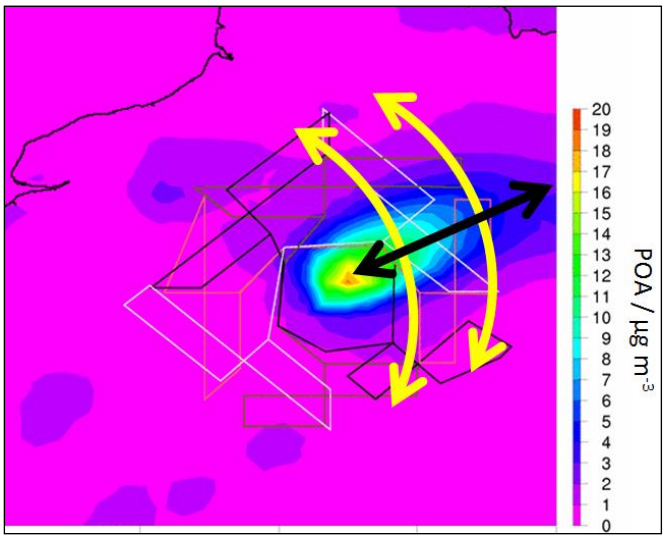

Figure 2: PrevAir Paris emission plume actual day forecast for 31 January 2010 18:00:00 UTC during the winter field campaign. The color code indicates the concentration of primary organic matter, a marker for fresh air pollution which is emitted by various sources in and around Paris. The yellow arrows demonstrate cross section measurements at several distances to Paris. The black arrow indicates radial measurements starting at the outer areas of Paris up to about 200 km away from the city.

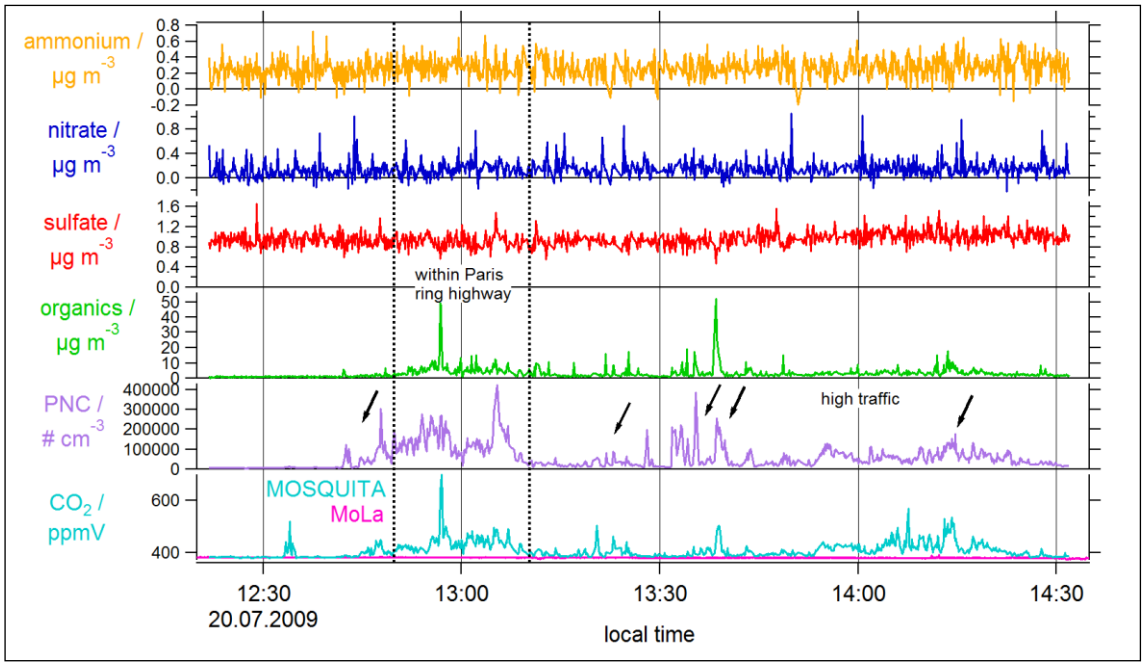

Figure 3: Different temporal behavior of measurement parameters primarily associated with long-range transported pollution (ammonium – yellow, nitrate – dark blue and sulfate – red) and parameters reflecting locally and regionally produced pollution (organics – green, particle number concentration (PNC) – purple and CO_2 – light blue (MOSQUITA), pink (MoLa)). The two vertical dashed lines frame the measurement range within the inner region of Paris; the arrows indicate measurement times with heavy traffic on the street. The time series have been measured by MOSQUITA during the summer campaign (20 July 2009).

2.4.3 Stationary measurements

Supported by electrical power supply from the external power generator as mentioned above, MoLa carried out several stationary measurements around Paris. This type of measurement was often chosen when plume predictions were not sufficiently robust for mobile measurements. Measurement sites downwind of Paris allow measuring the emission plume for several hours in a certain distance and locations upwind of Paris have been used for ambient background measurements. Stationary measurements give insight into temporal variations of plume as well as background air masses, depending on weather influence (e.g. rain fall wash out of particles), solar radiation, boundary layer effects and pollution source variation (e.g. rush hour in the morning and evening).

Several stationary measurements have been carried out in background air masses far away from the city without any impact by emissions from Paris. These measurements contain valuable information about real background concentrations for comparison with the fixed measurement sites that have been influenced by local emissions most of the time (Beekmann et al., 2012; Freutel et al., 2012). A few measurements show both, the Paris emission plume and the atmospheric background values when the wind direction was shifting. For these data sets the investigation of plume structure and homogeneity is possible. An example of such a measurement is presented in Sect. 3.4. Other stationary measurements have been performed as intercomparison measurements at the fixed stationary measurements sites of the MEGAPOLI field campaigns. For measurements located in the direction of the predicted plume and in line with stationary measurement sites (connected flow between all measurement locations (Freutel et al., 2012) investigation of conversion and dilution processes during transport is also possible.

MOSQUITA had no flexible external power supply for stationary measurements, so with this mobile laboratory only cross sections, radial measurements and stationary intercomparisons at the fixed measurement sites have been performed.

3 Examples of measurements

In this Section four examples of mobile measurements (including one stationary measurement performed by MoLa) during the summer and winter MEGAPOLI field campaigns are presented. These examples provide insight into the variety of mobile measurements for the investigation of megacity emissions and the potential information that can be derived from those data.

3.1. Long-range transport of pollution versus local and regional pollution

Long-range transported pollution: Long-range transported pollution has significantly different characteristics than freshly produced local or regional pollution. Due to transformation processes during transport the aerosol can for example be expected to be more oxidized represented by a higher O/C ratio of the aerosol particles (Aiken et al., 2007; Aiken et al., 2008). Aerosol species like particulate sulfate and nitrate evolve during transport from precursor gases (generation of secondary aerosol) and a variety of formerly volatile substances can condense onto existing particles. These transformation processes need several hours of time depending on environmental conditions like solar radiation and the corresponding aerosol products are therefore not or to a lesser extent present in freshly produced (minutes up to few hours) air pollution. Dilution processes cause large-scale dispersion of secondary particulate and long living gas phase components and result (after days of transportation without input of additional pollution) in well-mixed air masses with homogeneous distributions. Time series of mass concentrations of related components are therefore dominated by slow variations depending mainly on changes in the long-range transported air masses (e.g. air masses influenced from different regions).

Local and regional pollution: In contrast to this, local (from a local point source) and regional (from a spatial extended source and / or a mixture of multiple local sources) pollution shows frequent concentration changes in marker time series. If a measurement takes place near a pollution source high concentrations of the emitted substances can be observed. The substances are quickly diluted or transformed in the surrounding air masses and with increasing distance from the source the concentrations decrease to background values. The occurrence of components correlated with fresh pollution is highly inhomogeneous in the atmosphere and strongly depends on the distance to the pollution source and its emission strength.

Measurement example: On 20 July 2009 the mobile laboratory MOSQUITA performed a radial trip up to 50 km from the border of the Paris metropolitan area in the North-East direction of Paris, including passes through the town center of Paris (a large and inhomogeneous source of fresh pollution) on the outward and return journey from the starting point (fixed suburb measurement site in the South-West of Paris). At the same time MoLa performed a stationary measurement in about 35 km distance in the same direction of Paris. The Paris emission plume was also advected in the North-East direction, so both mobile laboratories should have measured Paris influenced air masses.

In Fig. 3 six time series of aerosol and gas phase parameters measured by MOSQUITA during the outward trip (the AMS instrument stopped recording during the return trip due to computer problems) can be seen. Additionally, CO_2 mixing ratios measured stationary by MoLa are shown. Three time series represent species that are associated with long-range transported pollution

(ammonium, nitrate, sulfate) and the other three are dominated by local and regional pollution (organics, particle number concentration, CO_2). For a better illustration of the different temporal and spatial behavior of freshly produced and long-range transported pollution markers no local pollution removal procedure as described in Sect. 2.3.1 has been applied to the presented data.

The time series of particulate organic matter shows signatures of both pollution types. It is likely a mixture of long-range transported highly oxidized (aged) organic aerosol, semi-volatile medium-aged organic aerosol, freshly produced hydrocarbon-like organic aerosol (mainly connected with traffic emissions (Zhang et al., 2005)) and freshly produced organic aerosol caused by various emission sources (e.g. cooking, biomass burning). In Fig. 3 the fresh and local fraction of the organic aerosol can be clearly identified by the various concentration peaks. The long-range transported part of the organic aerosol is represented by an underlying slowly varying concentration level of about 1 to 2 $\mu g\ m^{-3}$.

The time series of the particle number concentration is also dominated by frequent concentration changes due to the various sources measured during the drive. The long-range transported fraction (accumulated and grown particles with several hundred nanometers particle diameter) of the particle number concentration is small compared to the large number of freshly emitted small particles with a few nanometers particle diameter.

In Fig. 3 due to the axis scaling mainly the CO_2 peak concentrations from fresh pollution is shown. After several hours of transportation the fresh CO_2 contributions are totally diluted in the surrounding air masses, but momentary CO_2 concentrations measured near the source can reach about twice the global background concentrations which can be seen in the presented time series measured by MOSQUITA. CO_2 mixing ratios measured by MoLa show nearly constant values, because no nearby local emission sources influenced the measurement location. A similar temporal behavior (not shown in this graph) can be seen for particle number and organic aerosol mass concentrations during the stationary measurement.

In contrast to this the time series of ammonium, nitrate and sulfate measured with both mobile laboratories (in Fig. 3 presented for MOSQUITA) show only small and slow variations in time despite rapid fluctuations around the actual background value, mainly caused by the instrument itself (especially for ammonium, where the measured values are close to the detection limit of this substance). This is a typical behavior for substances that change only on large temporal and spatial scales under the influence of different air masses. Of course, in reality there are not only the two extremes of very local fresh pollution plumes and completely homogeneously distributed long-rang transported air masses. There are also air masses where secondary aerosol is inhomogeneously mixed because at the beginning the fresh precursor substances have been distributed inhomogeneously. This can also be a reason for some of the more rapid changes in the time series of ammonium, nitrate and sulfate.

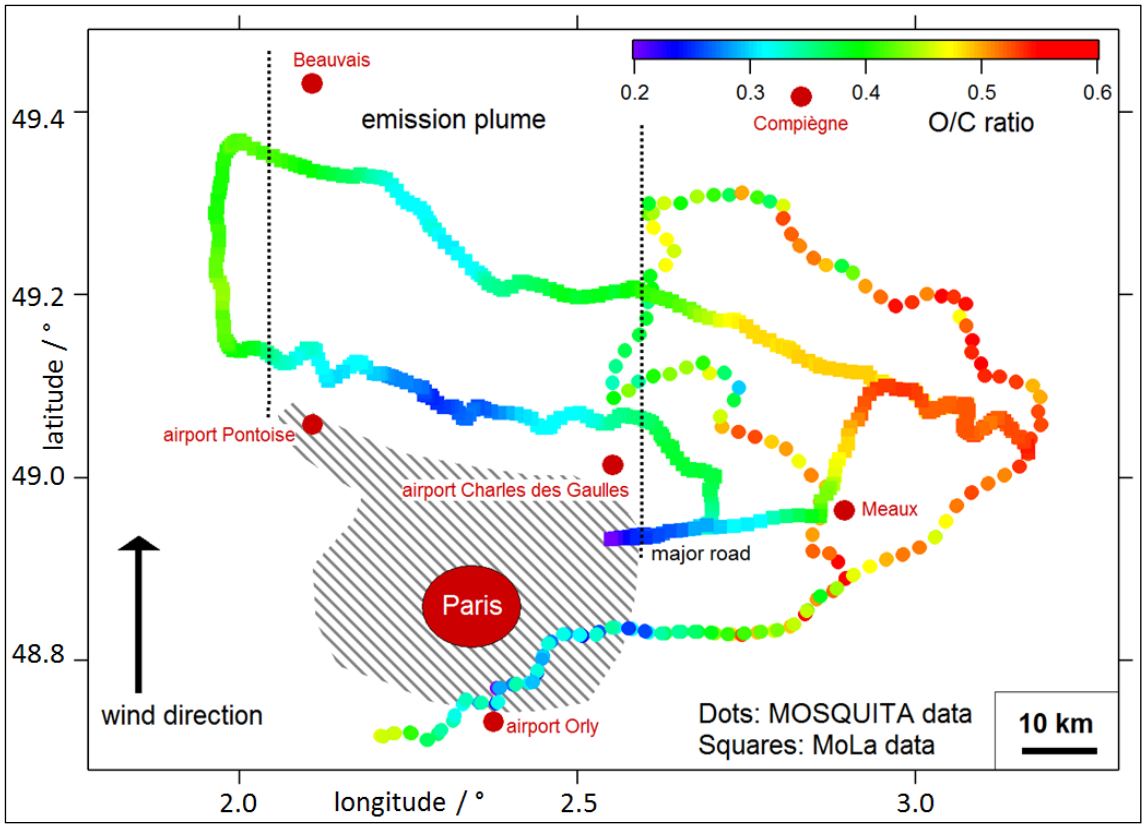

Figure 4: Combined results of MoLa (line of squares) and MOSQUITA (dotted line) mobile appliations during several cross section measurements through the Paris emission plume during the summer campaign (29 July 2009). The regional wind direction was constantly from South on this day (black arrow). The track is color-coded by the O/C ratio. Blue colors indicate low values (fresh organic aerosol) and red colors high values (aged organic aerosol). The urban area of Paris is marked by the big red dot, the Paris metropolitan area is indicated by the gray shaded area. For a better orientation 6 places are also marked in the map (red dots).

3.2 Cross section through the Paris emission plume: Combination of MoLa and MOSQUITA data

Megacity emission plume – cross section: An emission plume generated by a large inhomogeneous area source like Paris can be expected to have a complex structure at least near the city where dilution processes had not much time to mix the air masses homogeneously. To investigate the structure of the emission plume it is useful to cross it at a constant distance to the emission source to avoid the simultaneous influence of additional transportation and dilution effects. These effects can additionally be measured by performance of several cross sections in different distances to the source.

Measurement example: On 29 July 2009 the Paris emission plume was constantly transported to the North direction. Both mobile laboratories carried out several cross section measurements in the North and North-East region around Paris. MoLa performed two cross sections at 20 km and 40 km distance to the Paris metropolitan area and MOSQUITA two cross sections in 30 km and 50 km distance. In Fig. 4 the measurement tracks of both mobile laboratories color-coded with the O/C ratio are presented on a map of the region. Both data sets have 1 min time resolution, but for a clear distinction between MoLa and MOSQUITA data different types of lines (MoLa – solid line, MOSQUITA – dotted line) for visualization have been used. Low O/C ratios indicate less oxidized fresh organic aerosol (blue colors), high O/C ratios indicate strongly oxidized aged organic aerosol

(red colors). The low O/C ratio values (< 0.2) in the South and East of Paris are caused by high traffic on major roads and thus local contamination. The interesting result of this measurement is the low values measured in the North of Paris – carried out on minor roads with less traffic – that are clearly connected with the Paris emission plume. At the same distance to the city but in the North-East direction much higher O/C ratios (> 0.6) were observed indicating background air masses not influence by the city.

The same map but with the measured tracks of markers for (long-range transported) background air masses like particulate ammonium shows different spatial distribution of these substances. There is no enhancement in concentrations in emission plume influenced regions. Higher values are also detected in the most Eastern part of the cross sections, where the highest O/C ratios have been seen. This is a further indication that in this region primarily an aged air mass containing long-range transported pollution has been measured on this day.

This detailed picture of plume and background air masses in a wide range around Paris is especially possible due to the combination of both mobile laboratories data. With only one mobile laboratory it would be difficult to cover such a wide spatial range and also impossible to measure at different locations at the same time. Especially the simultaneous measurement at different places is useful to avoid temporal influences (e.g. wind shift) on the investigation of the spatial plume structure.

Interestingly, the emission plume as visible in the O/C ratios in Fig. 4 looks rather homogeneous with a definite structure (like a Gaussian form: highest values in the center of the plume, with constantly decreasing values to both sides) even in the nearest cross section performed by MoLa only 20 km away from the border of Paris. In this distance one could expect a more inhomogeneous structure due to the short transportation time of about 1 hour (averaged wind speed about 20 km h^{-1} on this day) from this large diversified emission source. However, a detailed analysis of the emission plume structure under various influences like weather conditions would exceed the scope of this publication. For more details about the plume structure analysis we refer to the continuative publication by von der Weiden-Reinmüller et al. (2012).

3.3 Radial measurement: Exploring the spatial extent of the emission plume

Megacity emission plume – radial measurement: A radial measurement inside the emission plume with a mobile laboratory has the advantage that the vehicle driving velocity can be in the same order of magnitude as the transportation speed of the plume. So on the one hand the spatial extent of the emission plume can be investigated and on the other hand transformation processes in the same air parcel travelling "together" with the mobile laboratory (Lagrangian measurement).

Measurement example: On 1 July 2009 weather conditions and the predicted plume have been sufficiently stable and well defined for a radial measurement within the emission plume. The North-Eastern wind advected the Paris emission plume to the South-West, where MoLa performed a radial trip up to 160 km from the Paris center. On this day only MoLa has been measuring, so no results of MOSQUITA are shown here. In Fig. 5 black carbon, HOA and sulfate mass concentrations in μg m^{-3} versus the distance to the center of Paris in km are presented. In the upper part of the graph results from the outward trip carried out during the morning can be seen, in the lower part results from the return trip during the afternoon are shown. Although the contamination removal has been applied to the data, still few locally influenced high concentration values can be seen.

Nevertheless, a clear decrease of black carbon and HOA concentrations in the emission plume can be observed with increasing distance to Paris. On the outward trip the emission plume that is observable with our measurements extends approximately up to 40 km distance from the outer areas of Paris (equals to 60 km distance to Paris center). During the day the emission plume seems to develop and intensify. On the return trip the range of the detected plume increased to a distance of about 80 to 100 km from Paris center. The decrease in concentration with increasing distance from the city is mainly caused by dilution of the emission plume in surrounding background air masses. We expect no significant black carbon sinks like dry deposition (there has not been any rain causing wet deposition on this day) of particles in this time frame of several hours. Also HOA does not lose its typical characteristics (for details see Zhang et al. (2005)) and is transformed into secondary organic aerosol within this time frame. In regions near the city black carbon concentrations are up to 10 times higher (7 to 10 µg m^{-3}) than in background air masses (0.5 to 1 µg m^{-3}). HOA concentrations vary from 1.5 µg m^{-3} near the city to around 0.5 µg m^{-3} in background air masses. To put this into perspective local emissions of black carbon and HOA can exceed typical background values by a factor of 100 e.g. in tunnels with heavy traffic (which has also been measured during the MEGAPOLI campaigns by the mobile laboratories on trips through the city center of Paris).

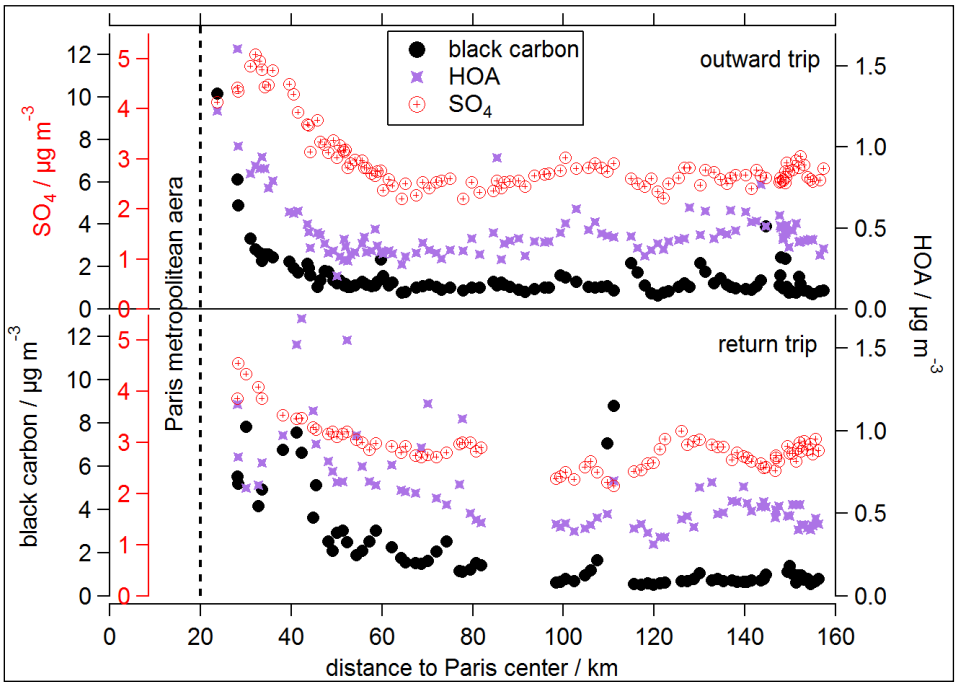

Figure 5: Black carbon (black dots), HOA (purple stars) and sulfate (red dots and crosses) mass concentrations in µg m^{-3} versus distance to Paris center in km measured during a radial trip on 1 July 2009 by the mobile laboratory MoLa. In the upper part of this graph results of the outward trip carried out during the morning are presented, in the lower part results from the return trip during the afternoon.

During the return trip in a distance of about 110 km to Paris also very high concentrations (especially black carbon) have been measured, although local contamination has been removed by video analysis. In this region two larger villages with a commercial area are located resulting in a higher traffic volume and therefore cause a local pollution hot spot. Here the limits of the applied local pollution removal procedure become obvious, because only "visible" (in the video tapes) contamination sources in front of the car can be identified. Measurements on a near bypass road (where no local pollution source is recorded by the webcam) can still be affected by locally

distributed emissions. A detailed discussion of the limitations of mobile measurements due to local pollution contamination is presented in Sect. 4. Nevertheless, the spatial extent of the Paris emissions plume can be clearly seen and also quantified in the presented data.

The described decreasing concentrations with increasing distance from Paris were not only observed in black carbon and HOA mass concentrations, but also in related fresh pollution markers like PAH and CO_2 (not shown in Fig. 5). An enhancement of the measured concentrations was detected on the outward trip up to 40 km distance from Paris center and on the return trip up to 60 km, respectively. The quantified enhancement of emission plume concentrations reaches a factor of 100 for PAH and about 20 for excess CO_2 (when a typical background value of 370 ppmV has been subtracted). Of course, these enhancement factors depend on the emission source strength and typical ambient background values, which is different for each substance.

For these two substances the emissions from Paris seem to experience either a removal process in addition to dilution in the surrounding air masses (further analysis of processes occurring during transport of the emission plume is discussed in von der Weiden-Reinmüller et al. (2012)) or the measurement principles of the applied devices overestimate the decrease of the substances. E.g. the PAH monitor installed in MoLa can only detect PAH molecules bound to the surface of the particles. When the aerosol particles are coated with previously volatile material during the transport, this device will no longer detect the PAH molecules although they are still part of the emission plume aerosol particles (Kulkarni et al., 2011).

Surprisingly, during this radial trip also long-range transported secondary pollution markers like sulfate (see Fig. 5) and nitrate show a decrease in concentration (a factor of 2 to 3 for sulfate and a factor of 4 to 10 for nitrate) with increasing distance to Paris. It is possible that long-range transported pollution has been mixed in the measured air masses. As mentioned above also long-range transported pollution is not necessarily completely homogeneously distributed in ambient air masses. Also at the downtown and suburb South-West measurement sites an increase in sulfate was observed during the morning of 1 July 2009, followed by decreasing concentrations in the afternoon and enhanced values again in the evening. In contrast to this, fresh pollutant markers showed a different temporal behavior on this day. Additionally, during other radial trips like the one performed with MoLa on 25 July 2009 increased concentrations of sulfate are not measured near Paris but in a distance of about 100 km. These are both indicators that we measured the Paris emission plume with some mixed-in long-range transported pollution.

Another explanation for the observed decrease in concentration of most of the measured parameters with increase in distance to Paris could be that the few radial trips carried out had been performed mainly during the same time of day (starting in the morning in Paris and returning in the evening). The atmospheric boundary layer develops during the day and shrinks again in the evening. High measured concentrations could therefore also be correlated to a low boundary layer height, accidentally associated with measurements near the city. However, the measured data of the radial trip on 25 July 2009 show a contrary trend for some of the measured parameters: No enhancement of ammonium and sulfate could be observed during the morning and evening hours (near the city), but around noon (in a distance of more than 100 km away from Paris) the concentrations are approximately two times higher. So we assume that the boundary layer effect is small compared to the emission plume strength.

3.4 Stationary measurements: Plume crossing during wind shift

Megacity emission plume – stationary measurements: Stationary measurements with a mobile laboratory have the advantage over mobile measurements that the measurement location can be chosen in a way that no local pollution source influences the measurement. A disadvantage is the lost spatial flexibility compared to a mobile measurement, but during an appropriate wind shift it is also possible to measure e.g. a cross section of an emission plume.

Measurement example: On 27 July 2009 the wind direction was predicted to shift from South to West during the day. This was no sufficiently stable meteorological condition for a mobile measurement, but it was ideal for a stationary measurement located North-East of Paris in a distance of about 20 km to the Paris metropolitan area carried out by MoLa. The measurement site was enclosed by open fields with no near upwind local pollution sources (e.g. villages, roads) and so an undisturbed flow of the air masses to the sampling location was guaranteed. Due to the wind shift both a measurement of background and emission plume air masses was possible. This wind shift is represented by three wind rose plots in the upper part of Fig. 6. The wind rose plots are centered at the measurement location and the red dots symbolize the direction of Paris in relation to the measurement site. In the morning and late afternoon the measurement site was not affected by Paris influenced air masses, however during the hours around noon the wind was shifting advecting air masses directly from Paris and the emission plume was successfully detected (time between the grey dashed lines in Fig. 6).

In Fig. 6 time series of O_3 and CO_2 mixing ratios as well as black carbon, PAH, particulate organics and sulfate mass concentrations are presented for this measurement. There is a clear enhancement in CO_2, black carbon, organics and PAH concentrations around noon caused by Paris emissions. The concentrations increase about seven times compared to background values measured on this day for black carbon, about ten times for PAH and about four times for CO_2 (again subtracting a Northern summer hemisphere background value of 370 ppmV). O_3 shows a reduced mixing ratio due to high NO_x concentrations (not shown in this graph) associated with fresh emissions in the Paris area.

In contrast to this sulfate concentrations show no significant enhancement during this time. SO_2 (not in this graph) shows a minor increase during this time period, but has obviously not yet been transformed into sulfate until the arrival of the air masses at the measurement site. On the other hand a clear enhancement in sulfate can be seen in the afternoon around 14:30 local time on this day. This seems to be long-range transported pollution (e.g. from industrial plants emitting SO_2 more far away from Paris), because no simultaneous enhancement can be seen in black carbon or PAH concentrations. CO_2 and O_3 show slightly higher (lower) concentrations in the afternoon but with different temporal behavior so this has likely a different reason.

In Fig. 7 averaged particle number size distributions measured by the MoLa FMPS device (a) and chemically resolved size distributions (particulate organics and sulfate, m/z 57 as marker for HOA) detected by the AMS (b) on the same day are presented. The particle size in nm is the particle electrical mobility diameter measured by the FMPS device; for the AMS data it was calculated from the particle vacuum-aerodynamic diameter measured by the instrument (DeCarlo et al., 2004). For this diameter conversion an average particle density of 1.65 g cm^{-3} and a spherical shape of the particles has been assumed. "Background 1" corresponds to the time period before Paris influenced air masses have been detected and "background 2" to the time interval thereafter.

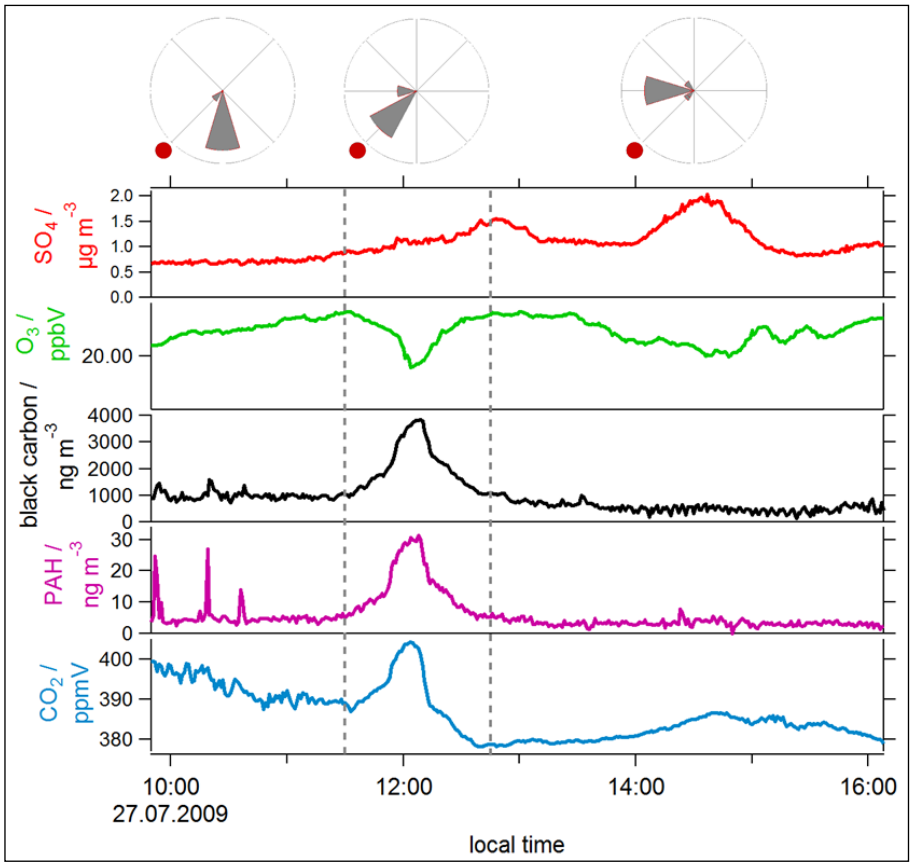

Figure 6: O_3 (yellow) and CO_2 (blue) mixing ratios as well as black carbon (black), PAH (purple), particulate organics (green) and sulfate (red) mass concentrations measured during a stationary measurement on 27 July 2009 by the mobile laboratory MoLa. The measurement location (center of windrose plots) was in the North-East of Paris (red dot in windrose plots) with about 20 km to the city border. The wind was shifting from South to West during the measurement as indicated by the three wind rose plots above the time series graph. The grey vertical dashed lines frame the time period when the Paris emission plume has been measured.

During all three time periods the aerosol particle number distribution measured by the FMPS shows a bimodal structure with a nucleation mode containing particles smaller than 20 nm and an accumulation mode between 30 nm and 200 nm. Although the three particle number distributions are similar, the absolute particle number concentrations show large differences. Paris emissions clearly enhance the particle number concentrations in both modes compared to background values (factor of two compared to background 1, factor of three compared to background 2). This can on the one hand be explained by secondary produced particles resulting from precursor gases and / or freshly produced particles directly emitted in Paris (nucleation mode) and on the other hand by accumulated and grown particles (e.g. due to condensation of low volatile (oxidized) vapors onto existing particles) that originate from sources in Paris (accumulation mode). Additionally, the differences in absolute values for the two background time periods show that also in background air masses variations of the pollution burden can be expected depending on regional origin.
The chemically resolved particle mass size distributions measured by the AMS (Fig. 7b) show for particulate organics, sulfate and m/z 57 mainly one mode in the accumulation size range. For organics this mode peaks approximately between 130 and 170 nm and for sulfate between 210 and 270 nm. In the air masses influenced by Paris emissions the maximum diameters of this mode differ strongest with 135 nm for organics and 270 nm for sulfate. This indicates that the measured particles are especially in plume air masses partly externally mixed. This statement is supported by the size distributions of m/z 57 which is used as marker for traffic-related HOA (Canagaratna et al.,

2007). Here the maximum of the mode is at approximately 70 nm, which is in clear contrast to the mode diameter of long-range transported sulfate. Especially particles with a diameter below 100 nm seem to contain mainly fresh organic material, while particles above 100 nm additionally contain sulfate, nitrate and ammonium.

For the HOA marker also the differences between plume and background air masses can be seen well. In background (and more aged) air masses the particles containing traffic-related m/z 57 are shifted to much larger particle sizes compared to particles that have been freshly emitted in the Paris region. Around 70 nm the concentration of m/z 57 is more than two times higher in plume than in background air masses. This can be explained – as mentioned above – by condensation of low volatile substances onto existing particles and accumulation of particles, both processes that need several hours to days to increase the particle diameter significantly.

In summary, these measurement results provide strong evidence for an emission plume that is transported away from the megacity and has a clear influence on local air quality of the surrounding regions. It also shows that the emissions are visible in many measurement parameters as expected due to the various emission sources in the Paris metropolitan area.

Although during the MEGAPOLI field campaigns mostly stationary measurements have been carried out when the meteorological conditions have not been sufficiently stable for mobile measurements they often provide very valuable results. Because they are almost not influenced by local contamination due to the choice of measurement location with no sources in the immediate upwind vicinity they are often a valuable addition to the fixed measurement sites within the metropolitan area.

4 Potential and limitations of mobile measurements for megacity emission plume characterization

Benefits of mobile measurements: Mobile measurements with fully equipped research laboratories are unique in their flexibility. The opportunities range from mapping experiments of whole regions to chasing experiments of single vehicles. Stationary measurements are possible at nearly every location. In the context of detailed investigation of megacity plume emission characteristics three applications have shown to be of high benefit. Cross section measurements through the emission plume allow investigation of the plume structure, caused mainly by emission source distribution, orographic and meteorological conditions and dilution processes. When performed in different distances to the megacity also information about transformation (aging) processes of the plume during transport away from the source can be obtained. Radial trips are beneficial due to their quasi-Lagrangian character. Transformation processes of plume emissions can be studied while the air masses travel away from the city. The spatial extent of an emission plume can only be reliably measured by driving as far as the emission plume ranges. Stationary measurement sites can be chosen according to minimum influence by local pollution sources and can be quickly changed if necessary. Measurements far away or upwind of the megacity allow unaffected atmospheric background measurements. Measurement locations downwind of the megacity allow on the other hand investigation of temporal variations of megacity emissions. Stationary measurements in combination with appropriate wind shifting allow studying the plume structure like during a mobile cross section measurement but with negligible influence of local pollution.

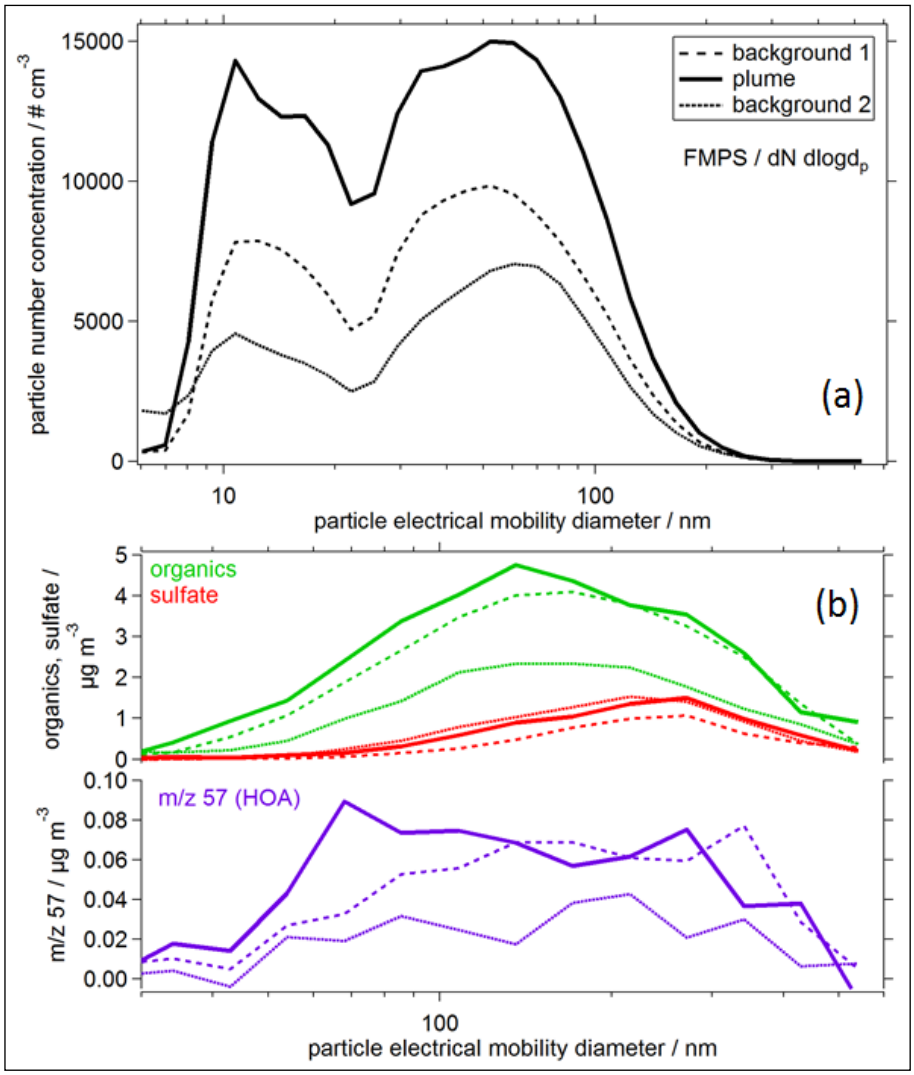

Figure 7: Averaged particle number size distributions (dN / dlogd$_p$) recorded by the FMPS (a) and chemically resolved mass size distributions (particulate organics – green, sulfate – red, m/z 57 as marker for HOA – purple) detected by the AMS (b) during the stationary measurement on 27 July 2009 by the mobile laboratory MoLa. The particle size in nm describes the particle electrical mobility diameter measured by the FMPS device and calculated from the particle vacuum-aerodynamic diameter measured by the AMS. Corresponding to the time periods defined in Fig. 6 "background 1" (dashed lines) corresponds to the time period before plume emissions (solid lines) have been measured and "background 2" (dotted lines) to the time period thereafter.

Such measurements are only possible with mobile laboratories, which can continuously change their measurement location. So it is not necessary to wait for appropriate measurement conditions, the measurement method and location can be adjusted to the current ambient conditions. Due to online measurement techniques the actual observed concentrations can directly be observed on a display. This makes it possible to quickly correct the measurement route according to ambient condition changes. For example, if it becomes apparent in the measurement data that the plume is broader than expected the cross section route can be extended.

Limitations of mobile measurements due to local pollution contamination: Besides the high potential of mobile measurements in the framework of megacity emission investigations there are also limitations of the obtained data sets. As mentioned above one major problem affecting mobile measurements is local pollution contamination of the data. Often high concentrations of fresh emissions dominate the measured values of substances like black carbon, PAH, particulate organic matter, particle number

concentration, CO_2 and NO_x. When the research is focused on phenomena that are not strongly distinct compared to local pollution it is necessary to remove this local influence from the data. Several removal procedures have been discussed in this publication. Some procedures are very time consuming and subjective, e.g. manual removal of contamination peaks in the data set. Automatic removal algorithms are not applicable to each data set, e.g. low time resolution data sets or data sets containing a large density of local contamination so that no individual pollution peaks can be identified. The time consuming but more objective video tape analysis method has shown to be most useful for mobile laboratories applied under the explained conditions, even if not every pollution source can be identified in the video tapes. The removal of local contamination makes the preparation of mobile data more time consuming, but in most cases it is possible to extract a nearly uncontaminated data set for further analysis.

Limitation due to temporal and spatial range of mobile measurements: Another limitation of the described mobile measurements is that they can only provide snap shots of the present situation at a certain location. E.g. if the emission plume is changed in its structure and / or direction during the measurement, the measured data will show a distorted picture of the plume. Boundary layer effects can also affect the measurements, e.g. when radial trips always start and end at the same time of the day. On the other hand, fixed measurement sites are affected by the same effects and so the mentioned limitations are not only relevant for mobile measurements. Nevertheless obtained data from mobile measurements have to be handled with care not to accidentally interpret features in the data set caused by temporal effects wrongly as spatial effects. The snap shot taken by a mobile laboratory still covers a much wider spatial range than those of a stationary measurement. Measurements always deliver a spatial and also temporal limited view of the real ambient situation. Here it is useful to combine as many measurements as possible, e.g. stationary measurements at several sites with mobile measurements, especially when regional phenomena like the emission plume of megacities are investigated.

Limitations due to the quality of the emission plume forecast maps: Limitation of the success of a mobile measurement in the context of megacity emission plume investigation is also given by the quality of forecast maps used for measurement planning. The local and regional forecast models have limitations e.g. due to inaccuracy of the input data and approximate parameterizations of small scale processes. For example, local or regional wind deviations from the forecast can have a significant influence on the measurement results. If the direction of the emission plume is shifted only by a few degrees the measurement track can be next to the plume and not inside it. However, the risk of missing the emission plume due to uncertainties in the forecasts can be reduced by selecting appropriate measurement routes. For this purpose MOSQUITA often performed combinations of cross sections and radial trips to cover a wider area around Paris.

Limitations due to the instrumental setup: The applied measurement devices themself bring additional limitations and uncertainties, which of course also applies for stationary measurement sites. There is limited space in a mobile laboratory (as in a fixed measurement container) and a certain set of instruments depending on the phenomena investigated has to be chosen. The transport of the aerosol through the inlet system to the individual devices causes bias of the measurement results, even if the occurring particle losses are below 10 % as for the two described mobile laboratories. On the other hand, the permanent inlet systems of MoLa and MOSQUITA are possibly better optimized and characterized than the inlet systems of fixed measurement containers build up only for a certain field campaign. However, all measurements experience at least some limitations. When handling additional mobile measurement issues with the appropriate care, mobile measurements are of high scientific value outweighing the discussed limitations.

5 Summary

We present a detailed overview of mobile aerosol and trace gas measurements carried out in the framework of the European Union MEGAPOLI project in the greater Paris area. During two major field campaigns, one in summer 2009 and one during winter 2010, several mobile and also stationary measurement have been carried out including application of the mobile laboratories MoLa and MOSQUITA. These mobile measurements are embedded in a framework of stationary measurements at several fixed measurement sites across the agglomeration, special mobile measurements (e.g. remote sensing measurements) and also measurements by a research aircraft. To provide an insight into the variety of measured parameters all applied measurement devices within both mobile laboratories are described. Intercomparison exercises of similar devices have been performed to guaranty high quality of the data set. Depending on the predicted weather and plume conditions three different measurement strategies have been carried out. Radial measurements allow special insight into the spatial extent of the emission plume as well as on transformation processes during its transport away from the city. Cross sections are most useful for differentiation between background and plume emission loadings of the atmosphere and to determine the plume direction and width. Stationary measurements are best suited for unstable weather conditions or as real background measurements outside the influence range of the Paris region and also not influenced by local pollution.

Before further analysis of the data set, the data have to be carefully treated to remove local contamination. Several advanced analysis methods are presented to give an overview of the possible information content of mobile data.

To present the types of applications during the MEGAPOLI field campaign we show four measurement examples. The first example demonstrates the difference between long-range transported and local or regional pollution. Second, we present a combination of MoLa and MOSQUITA data sets for extended information about the spatial structure of the Paris emission plume. The spatial extent of the emission plume can be seen in example three, a radial measurement trip carried out during the summer campaign. The last example illustrates the influence of Paris emissions on local air quality. During a stationary measurement the wind shifted, causing the plume to pass over the measurement location, allowing the direct comparison of background and polluted air masses.

A critical discussion of the potential and limitations of mobile measurements in the framework of megacity emission investigations completes this work. Special focus lies on the removal of local contamination, an issue usually not appearing during stationary measurements, provided that the measurement location has been chosen well. To largely avoid the problem of local pollution contamination during mobile measurements in the lower-most troposphere e.g. a zeppelin could be applied as mobile laboratory. Then real cross-country measurements in a height of a few meters unaffected by most local pollution sources would be possible.

The high scientific potential of mobile measurements is given due to spatial flexibility of the measurement location. Changes in environmental conditions can instantaneously be accounted for by adaption of the measurement route due to online access to the measured data. Some phenomena like e.g. emission plume structure and spatial extent can only be reasonably measured by applying mobile measurements. Limitations are given on the one hand by the still limited spatial range covered by a single mobile laboratory in a certain time and on the other hand by uncertainties in the emission plume forecast. To improve the spatial coverage of measurement locations the combination of several mobile laboratories and also fixed measurement sites is useful.

Based on the data sets obtained within the framework of this study, further publications are in preparation. They focus on the one hand on the spatial distribution of organic aerosol sources (Crippa et al., 2012b). On the other hand transformation processes in the plume are analyzed, the structure of the emission plume is investigated and a statistical characterization of the Paris emission plume is presented with a focus on differences due to summer and winter environmental conditions (von der Weiden-Reinmüller et al., 2012).

Acknowledgements. The MoLa team (Max-Planck-Institute for Chemistry) thanks Katja Dzepina, Johannes Fachinger, Friederike Freutel, Stéphane Gallavardin, Paul Reitz, Anja Roth, Julia Schmale and Johannes Schneider for support during organization, preparation and realization of the measurement campaigns. The Golf Départemental de la Poudrerie is thanked for hosting the suburb North-East stationary measurement and MoLa parking site. The contribution of Max-Planck-Institute for Chemistry´s scientists and the campaign participation was fully covered by internal funds of Max-Planck-Institute for Chemistry.

The MOSQUITA team (Paul Scherrer Institute) thanks Claudia Mohr, René Richter and the Paul Scherrer Institute´s team working at the suburb South-West measurement site during the campaigns. The contribution of Paul Scherrer Institute´s, Laboratoire Inter-universitaire des Systèmes Atmosphériques´s and Institut National de l'Environnement Industriel et des Risques´s scientists and the campaign participation was supported by the European Union´s Framework Program FP/2007-2011 within the project MEGAPOLI, grant agreement n°212520.

Aurélie Colomb is thanked for providing additional gas phase instruments intercomparison data.

References

Aiken, A. C., DeCarlo, P. F., and Jimenez, J. L.: Elemental Analysis of Organic Species with Electron Ionization High-Resolution Mass Spectrometry, Anal. Chem., 79, 8350-8358, 2007.

Aiken, A. C., DeCarlo, P. F., Kroll, J. H., Huffman, J. A., Docherty, K. S., Ulbrich, I. M., Mohr, C., Kimmel, J. R., Sueper, D., Sun, Y., Zhang, Q., Trimborn, A., Northway, M., Ziemann, P. J., Canagaratna, M. R., Onasch, T. B., Alfarra, M. R., Prévôt, A. S. H., Dommen, J., Duplissy, J., Metzger, A., Baltensperger, U., and Jimenez, J. L.: O/C and OM/OC Ratios of Primary, Secondary, and Ambient Organic Aerosols with High-Resolution Time-of-Flight Aerosol Mass Spectrometry, Environ. Sci. Technol., 42, 4478-4485, 2008.

Aire urbaine: http://recensement.insee.fr (last accessed 05.02.2012)

Akimoto, H.: Global Air Quality and Pollution, Science, 302, 1716-1719, 2003.

Ansyco: http://ansyco.de (last accessed 11.01.2012)

Aerolaser: http://aero-laser.com (last accessed 17.01.2012)

Bahreini, R., Ervens, B., Middlebrook, A. M., Warneke, C., de Gouw, J. A., DeCarlo, P. F., Jimenez, J. L., Brock, C. A., Neuman, J. A., Ryerson, T. B., Stark, H., Atlas, E., Brioude, J., Fried, A., Holloway, J. S., Peischl, J., Richter, D., Walega, J., Weibring, P., Wollny, A. G., and Fehsenfeld, F. C.: Organic aerosol formation in urban and industrial plumes near Houston and Dallas, Texas, J. Geophys. Res., 114, D00F16, 2009.

Beekmann et al.: Science-Paper (2012)

Brunekreef, B., and Holgate, S. T.: Air pollution and health, The Lancet, 360, 1233-1242, 2002.

Bukowiecki, N., Dommen, J., Prévôt, A. S. H., Richter, R., Weingartner, E., and Baltensperger, U.: A mobile pollutant measurement laboratory – measuring gas phase and aerosol ambient concentrations with high spatial and temporal resolution, Atmos. Environ., 36, 5569-5579, 2002.

Canagaratna, M. R., Janye, J. T., Jimenez, J. L., Allan, J. D., Alfarra, M. R., Zhang, Q., Onasch, T. B., Drewnick, F., Coe, H., Middelbrook, A., Delia, A., Williams, L. R., Trimborn, A. M., Northway, M. J., DeCarlo, P. F., Kolb, C. E., Davidovits, R., and Worsnop, D. R.: Chemical and microphysical characterization of ambient aerosols with the Aerodyne aerosol mass spectrometer, Mass Spectrom. Rev., 26, 185-222, 2007.

Crippa, M., DeCarlo, P. F., Slowik, J. G., Mohr, C., Heringa, M. F., Chirico, R., Poulain, L., Freutel, F., Sciare, J., Cozic, J., Di Marco, C. F., Elsasser, M., Nicolas, J., Marchand, N., Abidi, E., Wiedensohler, A., Drewnick, F., Schneider, J., Borrmann, S., Nemitz, E., Zimmermann, R., Jaffrezo, J.-L., Prévôt, A. S. H., and Baltensperger, U.: Wintertime aerosol chemical composition and source apportionment of the organic fraction in the metropolitan area of Paris, Atmos. Chem. Phys., To be Submitted, 2012a.

Crippa, M. et al.: Paper about PSI mobile measurements, In Preparation, 2012b.

Crutzen, P. J.: New Directions: The growing urban heat and pollution "island" effect – impact on chemistry and climate, Atmos. Environ., 38, 3539-3540, 2004.

Davidson, C. I., Phalen, R. F., and Solomon, P. A.: Airborne Particulate Matter and Human Health: A Review, Aerosol Sci. Tech., 39, 737-749, 2005.

DeCarlo, P. F., Slowik, J. G., Worsnop, D. R., Davidovits, P., and Jimenez, J. L.: Particle Morphology and Density Characterization by Combined Mobility and Aerodynamic Diameter Measurements. Part 1: Theory, Aerosol Sci. Tech., 38, 1185-1205, 2004.

DeCarlo, P. F., Kimmel, J. R., Trimborn, A., Northway, M. J., Jayne, J. T., Aiken, A. C., Gonin, M., Fuhrer, K., Horvath, T., Docherty, K. S., Worsnop, D. R., and Jimenez, J. L.: Field-Deployable, High-Resolution, Time-of-Flight Aerosol Mass Spectrometer, Anal. Chem., 78, 8281-8289, 2006.

Diesch, J.-M., Drewnick, F., Zorn, S. R., von der Weiden-Reinmüller, S.-L., Martinez, M., and Borrmann, S.: Variability of aerosol, gaseous pollutants and meteorological characteristics associated with changes in air mass origin at the SW Atlantic coast of Iberia, Atmos. Chem. Phys., 12, 3761-3782, 2012a.

Diesch, J.-M., Drewnick, F., Klimach, T., and Borrmann, S.: Investigation of gaseous and particulate emissions from various marine vessel types measured on the banks of the Elbe in Northern Germany, In Preparation, 2012b.

Drewnick, F., Hings, S. S., DeCarlo, P., Jayne, J. T., Gonin, M., Fuhrer, K., Weimer, S., Jimenez, J. L., Demerjian, K. L., Borrmann, S., and Worsnop, D. R.: A New Time-of-Flight Aerosol Mass Spectrometer (TOF-AMS) – Instrument Description and First Field Deployment, Aerosol Sci. Tech., 39, 637-658, 2005.

Drewnick, F., Hings, S. S., Alfarra, M. R., Prévôt, A. S. H., and Borrmann, S.: Aerosol quantification with the Aerodyne Aerosol Mass Spectrometer: detection limits and ionizer background effects, Atmos. Meas. Techn., 2, 33-46, 2009.

Drewnick, F., Böttger, T., von der Weiden-Reinmüller, S.-L., Zorn, S. R., Klimach, T., Schneider, J., and Borrmann, S.: Design of a mobile aerosol research laboratory and data processing

tools for effective stationary and mobile field measurements, Atmos. Meas. Techn., 5, 2273-2313, 2012. Akzeptiert, finale Citation noch ergänzen!!

Droplet Measurements: http://dropletmeasurements.com (last accessed 13.01.2012)

Earth System Research Laboratory: http://.esrl.noaa.gov/gmd/ccgg/trends/ (last accessed 07.03.2012)

Earthobservations: http://earthobservations.com (last accessed 06.03.2012)

Edimax Technology: http://edimax.com (last accessed 12.01.2012)

Elanskii, N. F., Belikov, I. B., Golitsyn, G. S., Grisenko, A. M., Lavrova, O. V., Pankratova, N. V., Safronov, A. N., Skorokhod, A. I., and Shumskii, R. A.: Observations of the atmosphere composition in the Moscow megapolis from a mobile laboratory, Dokl. Earth Sci., 432, 649-655, 2010.

Ever-Focus Electronics: http://everfocus.com (last accessed 17.01.2012)

Fenger, J.: Urban air quality, Atmos. Environ., 33, 4877-4900, 1999.

Freutel, F., Schneider, J., Drewnick, F., von der Weiden-Reinmüller, S.-L., Crippa, M., Prévôt, A. S. H., Baltensperger, U., Poulain, L., Wiedensohler, A., Sciare, J., Sarda-Estève, R., Burkhart, J. F., Eckhardt, S., Stohl, A., Gros, V., Colomb, A., Michoud, V., Doussin, J. F., Borbon, A., Haeffelin, M., Morille, Y., Beekmann, M., and Borrmann, S.: Aerosol particle measurements at three stationary sites in the megacity of Paris during summer 2009: Meteorology and air mass origin dominate aerosol particle composition and size distribution, Atmos. Chem. Phys., To be Submitted, 2012.

GAMMA-SCOUT: http://gamma-scout.de (last accessed 12.01.2012)

Garmin: http://garmin.com (last accessed 12.01.2012)

Grimm: http://dustmonitor.eu (last accessed 12.01.2012)

Gros, V., Sciare, J., and Yu, T.: Air-quality measurements in megacities: Focus on gaseous organic and particulate pollutants and comparison between two contrasted cities, Paris and Beijing, C. R. Geosci., 339, 764-774, 2007.

Gurjar, B. R., and Lelieveld, J.: New Directions: Megacities and global change, Atmos. Environ., 39, 391-393, 2005.

Honoré, C., Rouïl, L., Vautard, R., Beekmann, M., Bessagent, B., Dufour, A., Elichegaray, C., Flaud, J.-M., Malherbe, L., Meleux, F., Menut, L., Martin, D., Peuch, A., Peuch, V.-H., and Poisson, N.: Predictability of European air quality: Assessment of 3 years of operational forecasts and analyses by the PREV'AIR system, J. Geophys. Res., 113, D04301, 2008.

Inteltronics Instrumentation: http://inteltronics.co.za (last accessed 17.01.2012)

Jayne, J. T., Leard, D. C., Zhang, X., Davidovits, P., Smith, K. A., Kolb, C. E., and Worsnop, D. R.: Development of an Aerosol Mass Spectrometer for Size and Composition Analysis of Submicron Particles, Aerosol Sci. Tech., 33, 49-70, 2000.

Jimenez, J. L., Canagaratna, M. R., Donahue, N. M., Prévôt, A. S. H., Zhang, Q., Kroll, J. H., DeCarlo, P. F., Allan, J. D., Coe, H, Ng, N. L., Aiken, A. C., Docherty, K. S., Ulbrich I. M., Grieshop, A. P., Robinson, A. L., Duplissy, J., Smith, J. D., Wilson, K. R., Lanz, V. A., Hueglin, C., Sun, Y. L., Tian, J., Laaksonen, A., Raatikainen, T., Rautianinen, J., Vaattovaara, P., Ehn, M., Kulmala, M., Tomlinson, J. M., Collins, D. R., Cubison, M.

J., Dunlea, E. J., Huffman, J. A., Onasch, T. B., Alfarra, M. R., Williams, P. I., Bower, K., Kondo, Y., Schneider, J., Drewnick, F., Borrmann, S., Weimer, S., Demerjian, K., Salcedo, D., Cottrell, L., Griffin, R., Takami, A., Miyoshi, T., Hatakeyama, S., Shimono, A., Sun, J. Y., Zhang, Y. M., Dzepina, K., Kimmel, J. R., Sueper, D., Jayne, J. T., Herndon, S. C., Trimborn, A. M., Williams, L. R., Wood, E. C., Middlebrook, A. M., Kolb, C. E., Baltensperger, U., and Worsnop, D. R.: Evolution of Organic Aerosol in the Atmosphere, Science, 326, 1525-1529, 2009.

Kipp&Zonen: http://kippzonen.com (last accessed 17.01.2012)

Kolb, C. E., Herndon, S. C., McManus, J. B., Shorter, J. H., Zahniser, M. S., Nelson, D. D., Jayne, J. T., Canagaratna, M. R., and Worsnop, D. R.: Mobile Laboratory with Rapid Response Instruments for Real-Time Measurements of Urban and Regional Trace Gas and Particulate Distributions and Emission Source Characteristics, Environ. Sci. Tech., 38, 5694-5703, 2004.

Kulkarni, P., Baron, P. A., and Willeke, K.: Aerosol Measurement: Principles, Techniques and Applications, 3. Edition, John Wiley and Sons, New Jersey, 2011.

Kunkel, D., Lawrence, M. G., Tost, H., Kerkweg, A., Jöckl, P., and Borrmann, S.: Urban emission hot spots as sources for remote aerosol deposition, Geophys. Res. Lett., 39, L01808, 2012.

Lanz, V. A., Alfarra, M. R., Baltensperger, U., Buchmann, B., Hueglin, C., and Prévôt, A. S. H.: Source apportionment of submicron organic aerosols at an urban site by factor analytical modelling of aerosol mass spectra, Atmos. Chem. Phys., 7, 1503-1522, 2007.

Lanz, V. A., Prévôt, A. S. H., Alfarra, M. R., Weimer, S., Mohr, C., DeCarlo, P. F., Gianini, M. F. D., Hueglin, C., Schneider, J., Favez, O., D´Anna, B., George, C., and Baltensperger, U.: Characterization of aerosol chemical composition with aerosol mass spectrometry in Central Europe: an overview, Atmos. Chem. Phys., 10, 10453-10471, 2010.

LI-COR: http://licor.com (last accessed 12.01.2012)

Matter Aerosol: http://matter-aerosol.ch (last accessed 17.01.2012)

Matter Engineering: http://labs.ti.bfh.ch/uploads/media/NP_Messtechnik_EN.pdf (last accessed 23.03.2012)

Matthew, B. M., Middlebrook, A. M., and Onasch, T. B.: Collection Efficiencies in an Aerodyne Aerosol Mass Spectrometer as a Function of Particle Phase for Laboratory Generated Aerosols, Aerosol Sci. Tech., 42, 884-898, 2008.

McMurry, P.: A review of atmospheric aerosol measurements, Atmos. Environ., 34, 1959-1999, 2000.

MEGAPOLI Project: http://megapoli.info (last accessed 10.01.2012)

Mobile Laboratory MOSQUITA: http://psi.ch/lac/mobile-laboratory (last accessed 11.01.2012)

Mohr, C., Richter, R., DeCarlo, P. F., Prévôt, A. S. H., and Baltensperger, U.: Spatial variation of chemical composition and sources of submicron aerosol in Zurich during wintertime using mobile aerosol mass spectrometer data, Atmos. Chem. Phys., 11, 7465-7482, 2011.

Molina, M. J., and Molina, L. T.: Megacities and Atmospheric Pollution, J. Air Waste Ma., 54, 644-680, 2004.

Nunnermacker, L. J., Imre, D., Daum, P. H., Kleinman, L., Lee, Y.-N., Lee, J. H., Springston, S. R., Newman, L., Weinstein-Llyod, J., Luke, W. T., Banta, R., Alvarez, R., Senff, C., Sillman, S., Holdren, M., Keigley, G. W., and Zhou, X.: Characterization of the Nashville urban plume on July 3 and July 18, 1995, J Geophys. Res., 103 (D21), 28129-28148, 1998.

Paatero, P., and Tapper, U.: Positive matrix factorization: a non-negative factor model with optimal utilization of error estimated of data values, Environmetrics, 5, 111-126, 1994.

Paatero, P.: Least squares formulation of robust non-negative factor analysis, Chemometr. Intell. Lab., 37, 23-35, 1997.

Pey, J., Rodriguez, S., Querol, X., Alastuey, A., Moreno, T., Putaud, J. P., and van Dingenen, R.: Variations of urban aerosols in the western Mediterranean, Atmos. Environ., 42, 9052-9062, 2008.

Pirjola, L., Parviainen, H., Hussein, T., Valli, A., Hämeri, K., Aaalto, P., Virtanen, A., Keskinen, J., Pakkanen, T. A., Mäkelä, T., and Hillamo, R. E.: „Sniffer“ – a novel tool for chasing vehicles and measuring traffic pollutants, Atmos. Environ., 38, 3625-3635, 2004.

Pirjola, L., Kupiainen, K. J., Perhoniemi, P., Tervahattu, H., and Vesala, H.: Non-exhaust emission measurement system of the mobile laboratory SNIFFER, Atmos. Environ., 43, 4703-4713, 2009.

PMT Partikel-Messtechnik: http://pmt.eu (last accessed 13.01.2012)

Pöschl, U.: Atmospheric aerosols: composition, transformation, climate and health effects, Angewandte Chemie, International Edition, 44, 7520-7540, 2005.

Prev'Air: http://prevair.org (last accessed 18.01.2012)

Recordum Messtechnik: http://recordum.com (last accessed 12.01.2012)

Royer, P., Chazette, P., Sartelet, K., Zhang, Q. J., Beekmann, M., and Raut, J.-C.: Comparison of lidar-derived PM10 with regional modeling and ground-based observations in the frame of MEGAPOLI experiment, Atmos. Chem. Phys., 11, 10705-10726, 2011.

SCINTREX Ltd.: http://scintrexltd.com (last accessed 17.01.2012)

Seinfeld, J. H., and Pandis, S. N.: Atmospheric Chemistry and Physics: From Air Pollution to Climate Change, John Wiley and Sons, 2. Edition, New Jersey, 2006.

Solomon, S., Quin, D., Manning, M., Chen, Z., Marquis, M., KAveryt, K. B., Tignor, M., and Miller, H. L. (eds.): Climate Change 2007: The Physical Science Basis. Cambridge University Press, Cambridge UK, 2007.

Sun, J., Zhang, Q., Canagaratna, M. R., Zhang, Y., Ng, N. L., Sun, Y., Jayne, J. T., Zhang, X., Zhang, X., and Worsnop, D. R.: Highly time- and size-resolved characterization of submicron aerosol particles in Beijing using an Aerodyne Aerosol Mass Spectrometer, Atmos. Environ., 44, 131-140, 2010.

Thermo Scientific: http://thermoscientific.com (last accessed 11.01.2012)

ToF-AMS Analysis Software Homepage: http://cires.colorado.edu/jimenez-group/wiki/index.php/ToF-AMS_Analysis_Software (last accessed 19.01.2012)

TSI: http://tsi.com (last accessed 12.01.2012)

Ulbrich, I. M., Canagaratna, M. R., Zhang, Q., Worsnop, D. R., and Jimenez, J. L.: Interpretation of organic components from Positive Matrix Factorization of aerosol mass spectrometric data, Atmos. Chem. Phys., 9, 2891-2918, 2009.

United Nations: World Urbanization Prospects: The 2009 Revision. http://esa.un.org/unpd/wup/index.htm (last accessed 10.01.2012), New York, 2009.

United Nations: World Populations Prospects: The 2010 Revision. http://esa.un.org/unpd/wpp/index.htm (last accessed 10.01.2012), New York, 2011.

Vaisala: http://vaisala.com (last accessed 12.01.2012)

von der Weiden, S.-L., Drewnick, F., and Borrmann, S.: Particle Loss Calculator – a new software tool for the assessment of the performance of aerosol inlet systems, Atmos. Meas. Techn., 2, 479-494, 2009.

von der Weiden-Reinmüller, S.-L., Drewnick, F., Zhang, Q., Freutel, F., Beekmann, M., and Borrmann, S.: Megacity emission plume characteristics in summer and winter investigated by mobile aerosol and trace gas measurements: The Paris metropolitan area, In Preparation, 2012.

Wavemetrics: http://wavemetrics.com (last accessed 19.01.2012)

Weimer, S., Mohr, C., Richter, R., Keller, J., Mohr, M., Prévôt, A. S. H., and Baltensperger, U.: Mobile measurements of aerosol number and volume size distributions in an Alpine valley: Influence of traffic versus wood burning, Atmos. Environ., 43, 624-630, 2009.

Zhang, Q., Worsnop, D. R., Canagaratna, M. R., and Jimenez, J. L.: Hydrocarbon-like and oxygenated organic aerosols in Pittsburgh: insights into sources and processes of organic aerosols, Atmos. Chem. Phys., 5, 3289-3311, 2005.

Zhang, Q., Jimenez, J. L., Canagaratna, M. R., Ulbrich, I. M., Ng, N. L., Worsnop, D. R., and Sun, Y.: Understanding atmospheric organic aerosols via factor analysis of aerosol mass spectrometry: a review, Anal. Bioanal. Chem., 401 (10), 3045-3067, 2011.